

**STUDY OF MAGNETIC AND TRANSPORT ANOMALIES IN
RARE - EARTH BASED INTERMETALLICS AND OXIDES**

Thesis submitted to

THE KLE ACADEMY OF HIGHER EDUCATION AND RESEARCH,

BELAGAVI

(KLE DEEMED UNIVERSITY)

[Declared as Deemed-to-be-University u/s 3 of the UGC Act, 1956 vide

Govt. of India Notification No.F.9-19/2000-U.3 (A)]

(Accredited 'A+' Grade by NAAC) (3rd Cycle)

[Placed in Category 'A' by MHRD (GoI)]

*For the award of the degree of
Doctor of Philosophy in the Faculty of
Interdisciplinary Sciences*

by

Iyer Karthik Krishnan

(Registration No: KLEU/Ph.D./2021-22/ DO1221013)



Under the Guidance of

Guide: **Dr. Suneel Dodamani** Co-guide: **Dr. Shidaling Matteppanavar**

July/2024

UNDERTAKING

I, **Karthik Krishnan Iyer** hereby declare that the information and the data mentioned in my thesis entitled **Study of Magnetic and Transport Anomalies in Rare - Earth based Intermetallics and Oxides** belongs to me and is original.

I am aware of definition of plagiarism as detailed below:

- An act or instance of using or closely imitating the language and thoughts of another author without authorization and the representation of that author's work as one's own, as by not crediting the original author.
- A piece of writing or other work reflecting such unauthorized use or imitation.
- The deliberate or reckless representation of another's words, thoughts or ideas as one's own without attribution in connection with submission of academic work, whether graded or otherwise.

I hereby declare that the thesis prepared by me is original-one and does not involve plagiarism anywhere. In case at a later stage it is found that I have indulged in plagiarism, then I am solely responsible for the same and the Institution is at liberty to take any disciplinary action against me including cancellation of dissertation or any other penalties imposed by the University.

Signature of the Research Scholar

Date:

Place: Belagavi

PLAGARISM REPORT



Ref. No. KAHER/AA/24-25/D-223

18th July 2024

Sir,

The soft copy of Ph.D. research thesis of **Mr. Iyer Karthik Krishnan, Faculty of Interdisciplinary Science** of KAHER, Belagavi has been submitted for anti-plagiarism check at the office of the undersigned through “Turn-it-in” package. The scan has been carried out and the scanned output reveals a match percentage of **5%** which is within the acceptable limit of 10%.

To obtain the comprehensive report of the plagiarism test, research scholar can send a mail to diracademic@kledeemeduniversity.edu.in along with the Registration Number, Name of the Scholar, Name of Guide/Co-guide and title of the thesis.



Jyoti M. Nagamoti
Dr.(Mrs.) Jyoti M. Nagamoti
Director, Academic Affairs

To,

Mr. Iyer Karthik Krishnan
Full-Time Ph.D. Scholar, 2021-22 Batch A
Faculty of Interdisciplinary Science, KAHER
Belagavi.

Cc to :

- 1) The Director, Dr. Prabhakar Kore Basic Science Research Centre, KAHER, Belagavi.
- 2) Dr. Suneel Dodamani, Scientist Grade-I, BSRC, KAHER, Belagavi – Guide
- 3) Dr. Shidaling Matteppanavar, Associate Prof., KLE's Basavaprabhu Kore College of Science, Arts and Commerce, Chikodi- Co-guide

KLE ACADEMY OF HIGHER EDUCATION AND RESEARCH

(Deemed-to-be-University established u/s 3 & 12B of the UGC Act, 1956)
Accredited **A*** Grade by NAAC (3rd Cycle) Placed in Category **A** by MoE (Govt)

📍 JNMC Campus, Nehru Nagar, Belagavi - 590 010, Karnataka, India 📞 0831-2444444 🌐 kledeemeduniversity.edu.in

**KLE ACADEMY OF HIGHER EDUCATION AND RESEARCH,
(KLE DEEMED UNIVERSITY)**

[Declared as Deemed-to-be-University u/s 3 of the UGC Act, 1956 vide Govt. of India Notification No.F.9 19/2000-U.3 (A)]

(Accredited 'A+' Grade by NAAC) (3rd Cycle)

[Placed in Category 'A' by MHRD (GoI)]

BELAGAVI



COPYRIGHT DECLARATION

*We hereby declare that **KLE ACADEMY OF HIGHER EDUCATION AND RESEARCH, BELAGAVI, KARNATAKA, shall have the rights to preserve, use and disseminate this thesis in print or electronic format for academic/research purpose.***

Signature
Iyer Karthik Krishnan

Signature
Dr. Suneel Dodamani,
Research Scientist,
KAHER's BSRC, Belagavi – 10.

Place: Belagavi

Date:

**© KLE ACADEMY OF HIGHER EDUCATION AND RESEARCH,
BELAGAVI**

**KLE ACADEMY OF HIGHER EDUCATION AND RESEARCH,
(KLE DEEMED UNIVERSITY)**

[Declared as Deemed-to-be-University u/s 3 of the UGC Act, 1956 vide Govt. of India Notification No.F.9-19/2000-U.3 (A)]

(Accredited 'A+' Grade by NAAC) (3rd Cycle)

[Placed in Category 'A' by MHRD (GoI)]

BELAGAVI



DECLARATION

I hereby declare that the thesis entitled "Study of Magnetic and Transport Anomalies in Rare - Earth based Intermetallics and Oxides" is a bonafide and original research carried out by me under the guidance of Dr. Suneel Dodamani, Research Scientist, KAHER's BSRC, Belagavi – 10. The thesis or any part thereof has not formed the basis for the award of any degree/ fellowship or similar title to any candidate of any University.

Place: Belagavi

Signature

Date:

Iyer Karthik Krishnan
KAHER's BSRC
Belagavi-10

**KLE ACADEMY OF HIGHER EDUCATION AND RESEARCH,
(KLE DEEMED UNIVERSITY)**

[Declared as Deemed-to-be-University u/s 3 of the UGC Act, 1956 vide Govt. of India Notification No.F.9-19/2000-U.3 (A)]

(Accredited 'A+' Grade by NAAC) (3rd Cycle)

[Placed in Category 'A' by MHRD (GoI)]

BELAGAVI



CERTIFICATE

This is to certify that the thesis entitled “Study of Magnetic and Transport Anomalies in Rare - Earth based Intermetallics and Oxides” is a bonafide and genuine research carried out by Karthik Krishnan Iyer under the guidance of Dr. Suneel Dodamani, Research Scientist, KAHER's BSRC, Belagavi – 10.

Place: Belagavi
Date:

Signature
Name & Address of Dean

**KLE ACADEMY OF HIGHER EDUCATION AND RESEARCH,
(KLE DEEMED UNIVERSITY)**

[Declared as Deemed-to-be-University u/s 3 of the UGC Act, 1956 vide Govt. of India Notification No.F.9-19/2000-U.3 (A)]

(Accredited ‘A+’ Grade by NAAC) (3rd Cycle)

[Placed in Category ‘A’ by MHRD (GoI)]

BELAGAVI



CERTIFICATE

This is to certify that the thesis entitled “Study of Magnetic and Transport Anomalies in Rare - Earth based Intermetallics and Oxides” is a bonafide record of original research carried out by Karthik Krishnan Iyer for the award of degree of DOCTOR OF PHILOSOPHY IN FACULTY OF INTERDISCIPLINARY SCIENCES under my supervision and guidance

Place: Belagavi

Date:

Signature

Dr. Suneel Dodamani,
Research Scientist,
KAHER’s BSRC,
Belagavi – 10.

Acknowledgement

First of all, I would like to thank Prof. Dr. Ramesh Paranjape (Director and Head, BSRC- KAHER) for giving me an opportunity to carry on my research work in this premier institution.

I would like to express my gratitude and thanks to my thesis supervisors Dr. Suneel Dodamani and Dr. Shidaling Mattepanavar for giving me an opportunity to carry out my research work under their guidance.

With a deep sense of gratitude, I would like to specially thank Prof. Dr. E.V. Sampathkumaran and Prof. Dr. Kalobaran Maiti who have been instrumental in this entire process, while providing me with the much-needed guidance, encouragement and help from the beginning till the completion of my PhD., whilst ensuring to bring my thesis work to completion in a stipulated time period. Their vast physics knowledge and ideas have been a source of inspiration and an education for me. Words are not enough to describe the kind of help and support I have got from them. I would also like to thank Dr. Bahadur Singh for his constant encouragement and support.

I would like to thank my colleagues, Dr. Sudhindra Rayaprol, Ms. Smita Gohil and Dr. Ram Kumar for their valuable suggestions, timely help as and when needed and their support from time to time

which helped me tremendously in completing my research work and completing my thesis well in time.

I would like to thank my lab members, Dr. Saswata Halder, Dr. Sawani Dutta, Ms. Ayusa Biswal and Mr. Shrinivas Chinnababu for their help and support.

I am thankful to Ms. Sayali Manjerekar of BSRC- KAHER who has helped me in completion of my antimicrobial efficacy studies well in time. Being new to this field, her help and guidance has been valuable in bringing the study to a proper conclusion.

I am also grateful to Mrs. B.A. Chalke, Mr. Rudheer Bapat, Mr. Jayesh Parmar and Mr. Vilas Mhatre for their help in carrying out the SEM-TEM and XRD measurements. I would also like to thank Mr. Jadhav who has been helpful in providing various help and support during the course of measurements. I am also thankful to Mr. Ganesh Jangam who has helped me in carrying out magnetization measurements on my samples.

I would also like to thank the office staff of KAHER, Belagavi, for helping me through various office procedures during the entire tenure of my PhD.

Finally, I would like to thank my family members who have always been a source of strength and inspiration. My sisters who always had a strong faith in my capabilities and their constant

persuasion which forced me to pursue my higher studies. Their perseverance is what has actually helped me in completion of my PhD, even at this stage of my life. It is the faith they had on me and their valuable advice from time to time which has always guided me through all the difficult situations in my life and my career.

A special thanks to all my Friends of Batch 2021-22 A, who have always been nice and helpful to me, especially Mr. Anilkumar who has been ever helpful at any point of time for providing any kind of help that was needed. In our batch I never felt that I'm actually age apart from them and they ensured that I always felt the same warmth of being together throughout the journey of my Ph.D.

And finally, the blessings of my parents and my almighty, who have always guided me in my life through highs and lows to do what is correct that needs to be done at that moment of time, ensuring that I reach the place and position, I ought to be at the end of my various journey's.

Iyer Karthik Krishnan

Date :

Place: Belagavi

TABLE OF CONTENTS

Sl. No.	Particulars	Page No.
1	List of Abbreviations	XV
	List of Tables	XVII
	List of Figures	XVII
	Synopsis	XXVI
	Chapter 1	
	Introduction	
1.1	Preliminary remarks	1
1.2	Elementary aspects of magnetism in solids	2
	1.2.1 Paramagnetism, diamagnetism, and magnetic ordering	2
	1.2.2 Spin-glasses	8
1.3	Crystal-field effects	10
1.4	Geometrically Frustrated magnetism	12
1.5	Types of exchange interactions	14
1.6	Transport properties	21
	1.6.1 Electrical resistance	21
	1.6.2 Magnetoresistance	24
1.7	Thermal Properties	26
	1.7.1 Heat Capacity	26
	1.7.2 Magnetocaloric effect (MCE)	28
1.8	Basics of rare-earth based systems	30
1.9	Kondo effect	32
1.10	Antimicrobial and Therapeutic applications.	37
1.11	Thrust of the thesis	38
1.12	Bibliographical references	41
	Chapter 2	
	Experimental Details	
2.1	Preliminary remarks	59

2.2		Sample preparation	59
	2.2.1	Intermetallic samples	59
	2.2.2	Oxide samples	60
	2.2.3	Nanoform specimens	60
2.3		Sample characterization	61
	2.3.1	X-ray diffraction and Rietveld analysis of powder sample	61
	2.3.2	Energy dispersive x-ray analysis	62
	2.3.3	DC electrical resistivity	62
	2.3.4	Heat Capacity	63
	2.3.5	SQUID magnetometer	65
	2.3.6	Vibrating sample magnetometer	67
	2.3.7	High pressure cells	69
	2.3.8	Antimicrobial susceptibility studies	71
2.4		Bibliographical references	76
		Chapter 3	
		Magnetic and transport anomalies in R₂RhSi₃ (R= Nd and Er) compounds	
3.1		Introduction	78
3.2		Crystal Structure	80
3.3		Sample preparation and characterization.	82
3.4		Results and discussion for Nd ₂ RhSi ₃	84
	3.4.1	Dc magnetization behavior	84
	3.4.2	Heat capacity and isothermal entropy behavior	89
	3.4.3	Ac magnetic susceptibility and isothermal remnant	92
	3.4.4	Electrical resistivity and magnetoresistance	95
3.5		Results and discussion for Er ₂ RhSi ₃	99
	3.5.1	Dc Magnetization behavior	99
	3.5.2	Ac Susceptibility and Isothermal remanent magnetization	102
	3.5.3	Heat capacity and Isothermal entropy	105
	3.5.4	Isothermal magnetization behavior	107
	3.4.5	Resistivity and magnetoresistance behavior	110

3.6		Discussions	114
3.7		Conclusions	116
3.8		Bibliographical references	118
		Chapter 4	
		Magnetic and transport anomalies in Er₄PtAl, Ho₄PtAl and Dy₄RhAl compounds	
4.1		Introduction	128
4.2		Crystal Structure	130
4.3		Sample preparation, characterization & experimental details.	131
4.4		Results and discussion for Ho ₄ PtAl	133
	4.4.1	Dc magnetization behavior	133
	4.4.2	Ac susceptibility and Isothermal remanent magnetization	136
	4.4.3	Heat capacity and isothermal entropy change behavior	139
	4.4.4	Electrical resistivity and magnetoresistance behavior	141
4.5		Results and discussion for Er ₄ PtAl	145
	4.5.1	dc Magnetization behavior	145
	4.5.2	ac susceptibility and Isothermal remanent magnetization	148
	4.5.3	Heat capacity and isothermal entropy change behavior	150
	4.5.4	Resistivity and magnetoresistance behavior	153
4.6		Results and discussion for Dy ₄ RhAl	156
	4.6.1	Dc Magnetization behavior	157
	4.6.2	Heat capacity and isothermal entropy change behavior	160
	4.6.3	Ac susceptibility and isothermal remnant magnetization	163
	4.6.4	Electrical resistivity and magnetoresistance behavior	165
4.7		Discussions and Conclusions	168
4.8		Bibliographical references	170
		Chapter 5	
		Pressure effects on the magnetic properties of spin-chain compounds Tb₂BaNiO₅ and Tb₂BaCoO₅	
5.1		Introduction and motivation	176
5.2		Crystal structure	179

5.3		Sample preparation, characterization & experimental details.	180
5.4		Magnetic susceptibility under external pressure	183
	5.4.1	Tb ₂ BaNiO ₅	183
	5.4.2	Tb ₂ BaCoO ₅	187
	5.4.3	Magnetic susceptibility under chemical pressure by partial doping of Sr at the Ba Site in Tb ₂ BaNiO ₅ : Tb ₂ Ba _{1-x} Sr _x NiO ₅ (x= 0, 0.025, 0.05, 0.075 and 0.1)	189
5.5		Isothermal magnetization behavior under pressure	194
	5.5.1	Tb ₂ BaNiO ₅	194
	5.5.2	Tb ₂ BaNiO ₅	195
	5.5.3	Isothermal magnetization under chemical pressure by partial doping of Sr at the Ba Site in Tb ₂ BaNiO ₅ : Tb ₂ Ba _{1-x} Sr _x NiO ₅ (x= 0, 0.025, 0.05, 0.075 and 0.1)	197
5.6		Temperature dependent x-ray diffraction behavior	199
5.7		Discussion and Conclusions	201
5.8		Bibliographical references	202
		Chapter 6	
		Magnetic behavior of nanoform of intermetallic compounds and antimicrobial properties.	
6.1		Introduction	208
6.2		Sample preparation, characterization & experimental details.	212
6.3		Magnetic and thermal properties of Dy ₄ RhAl	215
6.4		Study of the antimicrobial efficacy	224
6.5		Conclusions	241
6.6		Bibliographical references	241
		Appendix	
A.1		Nd ₂ RhSi ₃	251
A.2		Er ₂ RhSi ₃	255
A.3		Ho ₄ PtAl	258
A.4		Er ₄ PtAl	261
		Conclusion	265
		List of Publications	266
		Annexures (Published articles & Presentation certificates)	278

List of abbreviations used

Symbols Used	
R	Rare-earths
KL	Kondo lattice
M	Magnetization
T	Temperature
H	Magnetic-field
P	High pressure
TM	Transition Metal
C	Heat-capacity
T_C	Ferromagnetic ordering temperature known as the Curie temperature
T_N	Antiferromagnetic ordering temperature known as the Néel temperature
$\chi = M/H$	Magnetic susceptibility
N	Avogadro number
k	Boltzmann constant
θ_p	Curie-Weiss parameter (also called 'paramagnetic Curie temperature')
μ_{eff}	Effective magnetic moment, in Bohr-magneton units in the paramagnetic state
J	Total angular momentum
g_J	Lande's g factor
k_B	Boltzmann constant
M_{IRM}	Isothermal remanent magnetization
χ'	Real part of Ac susceptibility
χ''	Imaginary part of Ac susceptibility
T_g	Transition temperature for glassy state
τ	Relaxation time
T_w	Temperature at which the sample is held for a particular duration
t_w	Waiting time at a particular temperature
F_m	Degree of magnetic frustration
N_{at}	Total number of atoms in a volume V
n_r	Conduction electron to atom ratio
Γ	Exchange integral between the 4f electron and the conduction electron
E_F	Fermi energy
k_F	Fermi wave vector
$\langle S_z \rangle$	Expectation value of the spin moment
a	Interionic distances

P	Resistivity
ρ_0	Contributions from lattice defects
ρ_{phonon}	Due to lattice vibrations
Z_A	Atomic weight
α	Interaction parameter
θ_D	Debye temperature
ρ_{mag}	Magnetic contributions to ρ due to the scattering of the conduction electrons from thermally disordered localized spins
RKKY	Ruderman Kittel Kasuya Yosida
ϑ_0	Atomic volume
m^*	Effective mass
G	de Gennes factor
ρ_s	Spin-disorder resistivity in the paramagnetic regime
ζ	Average scattering time
l	Electron mean free path
r_c	Cyclotron orbit radius
ω_c	Cyclotron angular frequency
R	Gas constant
S	Entropy
γ	Electronic heat capacity
C_{lattice}	Lattice heat capacity
C_{4f}	Magnetic heat capacity
S_{4f}	Magnetic entropy
ΔS_m	Isothermal entropy change
ΔT_{ad}	Adiabatic temperature change
KL	Kondo lattices
CKS	Concentrated Kondo systems
DOS	Density of states
HF	Heavy Fermions
ZFC	Zero field cooled
FC	Field cooled
FCW	Field cooled warming
FCC	Field cooled cooling
HF	Heavy fermions
KL	Kondo lattice
FL	Fermi liquid
ϵ_0	Binding energy

List of tables

Sl. No.	Particulars	Page No.
1.1	Some properties of free rare earth ions, like 4f electronic configuration, ground state term symbol spin, orbital and total angular momentum, Lande g factor (g_J), effective magnetic moment and de Gennes factor.	33
3.1	Rietveld refined fitting parameters for $R_2\text{RhSi}_3$	84
4.1	Rietveld refined fitting parameters for $R_4\text{TmAl}$	131
5.1	Rietveld refined fitting parameters for $\text{Tb}_2\text{Ba}_{1-x}\text{Sr}_x\text{NiO}_5$ and $\text{Tb}_2\text{BaCoO}_5$.	182
A.1	Comparison of the magnetic features of the bulk and ball milled Nd_2RhSi_3 .	251
A.2	Comparison of the features of the bulk and ball milled Er_2RhSi_3 .	255
A.3	Comparison of changes in magnetic features observed in ball milled Ho_4PtAl	258
A.4	Comparison of changes in magnetic features observed in ball milled Er_4PtAl .	261

List of figures

Sl. No.	Particulars	Page No.
1.1	Schematics of isothermal magnetization behavior of a paramagnet.	3
1.2	The Brillouin function simulated for various J values, which is attributed to the total angular momentum.	4
1.3	Schematic representation of a ferromagnet, hysteresis loop for a hard ferromagnet.	6
1.4	Illustrative example of antiferromagnet with a typical behavior of temperature dependence of magnetic susceptibility.	7
1.5	Illustrative example of ferrimagnetic behavior.	8
1.6	Illustrative example of conventional spin-glass.	9
1.7	(i) Degenerate d-orbitals of a transition metal ion, (ii) Splitting of the d-orbitals into higher energy e_g and low energy t_{2g} orbitals in the octahedral environment, and (iii) Further splitting due to Jahn-Teller distortion for Cu^{2+} ion.	11
1.8	Geometric frustration in (a) Square lattice (b) triangular lattice with nearest neighbor antiferromagnetic interaction. (c) hyper-kagome lattice.	13
1.9	Illustrative example of super exchange interaction.	16
1.10	Schematic of RKKY interaction.	18
1.11	Schematic of double exchange interaction.	20
1.12	Typical temperature dependent ρ behavior in a ferromagnet (upper panel), and an antiferromagnet with super-zone boundary anomalies (lower panel).	23
1.13	Representation of Isothermal entropy change and adiabatic change in temperature.	28
1.14	Illustrative example of isothermal entropy obtained for single crystalline dysprosium metal.	29
1.15	Comparison of radial charge distribution of $4f$, $5s$, $5p$, $5d$ and $6s$ electrons in Gd atom.	31

1.16	Rare earth magnetic ordering temperatures (T_0) and magnetic spin disorder contribution (ρ_{mag}) to electrical resistivity (normalized to the values of Gd) based on the de Gennes model.	32
1.17	Schematic representation of the temperature dependence of electrical resistivity (ρ) of single-ion Kondo and Kondo lattice systems.	36
2.1	Schematic diagram of a SQUID detection circuit.	66
2.2	Schematic diagram for VSM.	68
2.3	Schematic diagram of a MCell 10.	70
2.4	Schematic diagram of a disk diffusion and/or well diffusion technique.	72
2.5	Schematic diagram of steps involved in broth dilution and MIC/MBC technique.	74
3.1	Crystallographic features of R_2RhSi_3 .	81
3.2	Rietveld refined powder x-ray diffraction pattern of R_2RhSi_3 using CuK_α radiation.	83
3.3	a) Magnetic susceptibility and inverse of magnetic susceptibility of Nd_2RhSi_3 in 5 kOe and b) data obtained in a field of 100 Oe in both zero-field-cooled and field-cooled conditions.	86
3.4	(a) Magnetic hysteresis loops in a field range of -20 kOe to 20 kOe at various temperatures from 1.8 K to 35 K of Nd_2RhSi_3 . (b) Magnetic hysteresis loops in a field range of -20 kOe to 20 kOe at various temperatures from 40 K to 300 K of Nd_2RhSi_3 .	87
3.5	Heat-capacity of Nd_2RhSi_3 .	90
3.6	Isothermal entropy changes, derived using heat capacity data.	91
3.7	Real part and imaginary part of Ac magnetic susceptibility of Nd_2RhSi_3 .	93
3.8	Isothermal remnant magnetization of Nd_2RhSi_3 .	94
3.9	Electrical resistivity of Nd_2RhSi_3 , below 100 K.	96
3.10	Magnetoresistance as a function of magnetic field for Nd_2RhSi_3 .	98
3.11	Magnetic susceptibility and inverse of magnetic susceptibility of Er_2RhSi_3 in 5 kOe and the data obtained in a field of 100 Oe in both zero-field-cooled and field-cooled conditions.	100

3.12	Magnetic susceptibility obtained in a field of 10, 20, 50 and 100 Oe in the zero-field cooled and field cooled conditions for Er ₂ RhSi ₃ .	101
3.13	Real part and imaginary part of ac susceptibility of Er ₂ RhSi ₃ .	103
3.14	Isothermal remnant magnetization of Er ₂ RhSi ₃ .	104
3.15	Heat-capacity as a function of temperature for Er ₂ RhSi ₃ and isothermal entropy change as a function of temperature derived from the heat capacity data.	106
3.16	Isothermal magnetization of Er ₂ RhSi ₃ .	108
3.17	Electrical resistivity as a function of temperature for Er ₂ RhSi ₃ .	111
3.18	Magnetoresistance behavior for Er ₂ RhSi ₃ .	112
4.1	Crystal structure of R ₄ TAl.	130
4.2	Rietveld refined powder x-ray diffraction patterns for R ₄ TAl obtained using Cu K _α radiation.	132
4.3	Temperature dependent dc magnetic susceptibility and inverse susceptibility for Ho ₄ PtAl measured in 5 kOe and magnetic susceptibility measured in zero field cooled and field cooled conditions in a field of 100 Oe.	134
4.4	Isothermal magnetization for Ho ₄ PtAl and low-field hysteresis loops.	135
4.5	Real and imaginary part of ac susceptibility for Ho ₄ PtAl and time dependence of isothermal remnant magnetization.	137
4.6	Heat-capacity as a function of temperature for Ho ₄ PtAl and isothermal entropy change as a function of temperature, derived from the heat capacity data.	140
4.7	Electrical resistivity as a function of temperature for Ho ₄ PtAl, measured in zero field and the presence of external magnetic fields.	142
4.8	Magnetoresistance as a function of magnetic fields for Ho ₄ PtAl.	144
4.9	Temperature dependent dc magnetic susceptibility and inverse susceptibility for Er ₄ PtAl measured in 5 kOe and magnetic susceptibility measured for zero field cooled and field cooled conditions in a field of 100 Oe.	146
4.10	Isothermal magnetization for Er ₄ PtAl and low-field hysteresis loops.	147

4.11	Real part and imaginary part of ac susceptibility for Er ₄ PtAl and time dependence of isothermal remnant magnetization.	149
4.12	Heat-capacity as a function of temperature and isothermal entropy change derived from the heat capacity data.	151
4.13	Electrical resistivity as a function of temperature, measured in zero field and in the presence of external magnetic fields for Er ₄ PtAl.	154
4.14	Magnetoresistance as a function of magnetic field for Er ₄ PtAl.	155
4.15	Temperature dependent dc magnetic susceptibility and inverse susceptibility measured in 5kOe and temperature dependent dc magnetic susceptibility measured in 100 Oe (for zero-field-cooled and field-cooled conditions) for Dy ₄ RhAl.	158
4.16	Isothermal magnetization for Dy ₄ RhAl.	159
4.17	Heat-capacity as a function of temperature for Dy ₄ RhAl.	161
4.18	Isothermal entropy change as a function of temperature for Dy ₄ RhAl.	162
4.19	Real part and imaginary part of ac susceptibility for Dy ₄ RhAl and time dependence of isothermal remnant magnetization.	164
4.20	Electrical resistivity for Dy ₄ RhAl.	166
4.21	Magnetoresistance as a function of field for Dy ₄ RhAl.	167
5.1	Crystal structure of Tb ₂ BaNi/(Co)O ₅ .	179
5.2	Rietveld refined powder x-ray diffraction patterns of Tb ₂ BaNiO ₅ and Sr doped Tb ₂ BaNiO ₅ using Cu K _α radiation.	181
5.3	Rietveld refined powder x-ray diffraction pattern for Tb ₂ BaCoO ₅ using Cu K _α radiation.	182
5.4	Magnetic susceptibility measured as a function of temperature for ambient and applied external pressures in a field of 5 kOe For Tb ₂ BaNiO ₅ .	185
5.5	Magnetic susceptibility measured as a function of temperature for ambient and applied external pressures in a field of 100 Oe for Tb ₂ BaNiO ₅ .	186
5.6	Magnetic susceptibility measured as a function of temperature for ambient and applied external pressures in a field of 100 Oe for Tb ₂ BaCoO ₅ .	188

5.7	Magnetic susceptibility measured as a function of temperature for ambient and applied external pressures in a field of 5 kOe for Tb_2BaCoO_5 .	189
5.8	Magnetic susceptibility measured as a function of temperature for Sr doped samples in a field of 100 Oe.	191
5.9	Magnetic susceptibility measured as a function of temperature for Sr based samples in a field of 5 kOe.	192
5.10	Isothermal magnetization at 5 K for Tb_2BaNiO_5 under external applied pressure and profile of the curve in the range 0-160 kOe measured under ambient pressure.	195
5.11	Isothermal magnetization at 4 K for Tb_2BaCoO_5 under external applied pressure and profile of the curve in the range 0-70 kOe measured under ambient pressure at 2 K.	196
5.12	Isothermal magnetization at 5 K for the Sr doped specimens for Tb_2BaNiO_5 and profile of the curve in the range 0-120 kOe for $x=0.1$ composition, at 5 K.	198
5.13	Synchrotron based powder x-ray diffraction (S-PXRD) patterns of selected temperatures for (a) Tb_2BaNiO_5 , (b) $Tb_2Ba_{0.9}Sr_{0.1}NiO_5$ and (c) Tb_2BaCoO_5 .	200
6.1	Comparison of powder X-ray diffraction patterns for R_2RhSi_3 bulk and nanoform specimens using $Cu K_\alpha$ radiation.	213
6.2	Comparison of powder X-ray diffraction patterns for R_4TAl bulk and nanoform specimens using $Cu K_\alpha$ radiation.	214
6.3	(a) SEM image showing the particle size of ground specimen of Dy_4RhAl (b) TEM image showing diffraction rings obtained on one of the particles; diffraction rings indexed with the (hkl), which matched with the XRD pattern confirming the phase of ground specimen.	215
6.4	a) Magnetic susceptibility as a function of temperature obtained in a field of 100 Oe in both zero-field-cooled and field-cooled conditions for nanoform specimen of Dy_4RhAl . b) Magnetic susceptibility and inverse of magnetic susceptibility in a field of 5 kOe. c) Isothermal magnetization d) Heat-capacity as a function of temperature. e)	217

	Heat-capacity divided by temperature. (f) Isothermal entropy change derived from heat capacity data.	
6.5	Magnetic hysteresis loops in a field range of -15 kOe to 15 kOe for nanoform specimen of Dy ₄ RhAl.	219
6.6	Isothermal remnant magnetization as a function of time for nanoform specimen of Dy ₄ RhAl.	220
6.7	Inverse magnetic susceptibility as a function of temperature in the presence of dc magnetic fields and data for 100 Oe, plotted as log ($\chi-1$) verses log(T/T ₀ -1) for nanoform specimen of Dy ₄ RhAl.	222
6.8	Agar Plate with Ho ₄ PtAl (A), Er ₄ PtAl (B), Ho ₂ RhSi ₃ (C), Nd ₂ RhSi ₃ (D), Er ₂ RhSi ₃ (E) sample disks.	225
6.9	Agar Plate with Ho ₄ PtAl (A), Er ₄ PtAl (B), Ho ₂ RhSi ₃ (C), Nd ₂ RhSi ₃ (C), Er ₂ RhSi ₃ (D) disks, lawned with E. coli and incubated for 2 days	226
6.10	Agar Plate lawned with sixth dilution of mixture of E. coli, BHI broth and powders of Dy ₄ RhAl (A), Er ₄ PtAl (D), Ho ₄ PtAl (G), Er ₂ RhSi ₃ (M), Ho ₂ RhSi ₃ (P), Nd ₂ RhSi ₃ (J) and incubated for 2 days.	227
6.11	Agar Plate lawned with sixth dilution of mixture of Pseudomonas, BHI broth and powders of Dy ₄ RhAl (B), Er ₄ PtAl (E), Ho ₄ PtAl (H), Er ₂ RhSi ₃ (N), Ho ₂ RhSi ₃ (Q), Nd ₂ RhSi ₃ (K) and incubated for 2 days.	228
6.12	Agar Plate lawned with sixth dilution of mixture of S. Aureus, BHI broth and powders of Dy ₄ RhAl (C), Er ₄ PtAl (F), Ho ₄ PtAl (I), Er ₂ RhSi ₃ (O), Ho ₂ RhSi ₃ (R), Nd ₂ RhSi ₃ (L), and incubated for 2 days.	229
6.13	Left image shows agar plate with wells filled with Dy ₄ RhAl (A), Ho ₄ PtAl (B), Er ₄ PtAl (C) and Ho ₂ RhSi ₃ (D) on day 0 and right image shows the growth after 28 hours of Incubation at 37°C for P. Acne.	231
6.14	S. Aureus with Er ₄ PtAl nano powder and K region acts as control.	232
6.15	E. coli with Er ₄ PtAl nano powder and K region acts as control.	233
6.16	Pseudomonas with Er ₄ PtAl nano powder and K region acts as control.	233

6.17	E. Faecalis with Er ₄ PtAl nano powder and K region acts as control.	233
6.18	S. Aureus with Ho ₄ PtAl nano powder and K region acts as control.	234
6.19	E. coli with Ho ₄ PtAl nano powder and K region acts as control.	234
6.20	Pseudomonas with Ho ₄ PtAl nano powder and K region acts as control.	234
6.21	E. Faecalis with Ho ₄ PtAl nano powder and K region acts as control.	235
6.22	S. Aureus with Dy ₄ RhAl nano powder and K region acts as control.	235
6.23	E. coli with Dy ₄ RhAl nano powder and K region acts as control.	235
6.24	Pseudomonas with Dy ₄ RhAl nano powder and K region acts as control.	236
6.25	E. Faecalis with Dy ₄ RhAl nano powder and K region acts as control.	236
6.26	S. Aureus with Er ₂ RhSi ₃ nano powder and K region acts as control.	236
6.27	E. coli with Er ₂ RhSi ₃ nano powder and K region acts as control.	237
6.28	Pseudomonas with Er ₂ RhSi ₃ nano powder and K region acts as control.	237
6.29	E. Faecalis with Er ₂ RhSi ₃ nano powder and K region acts as control.	237
6.30	S. Aureus with Ho ₂ RhSi ₃ nano powder and K region acts as control.	238
6.31	E. coli with Ho ₂ RhSi ₃ nano powder and K region acts as control.	238
6.32	Pseudomonas with Ho ₂ RhSi ₃ nano powder and K region acts as control.	238
6.33	E. Faecalis with Ho ₂ RhSi ₃ nano powder and K region acts as control.	239
6.34	S. Aureus with Nd ₂ RhSi ₃ nano powder and K region acts as control.	239
6.35	E. coli with Nd ₂ RhSi ₃ nano powder and K region acts as control.	239
6.36	Pseudomonas with Nd ₂ RhSi ₃ nano powder and K region acts as control.	240
6.37	E. Faecalis with Nd ₂ RhSi ₃ nano powder and K region acts as control.	240
A.1	a) Magnetic susceptibility as a function of temperature obtained in a field of 100 Oe in both zero-field-cooled and field-cooled conditions for nanoform specimen of Nd ₂ RhSi ₃ . b) Magnetic susceptibility and inverse of magnetic susceptibility in a field of 5 kOe. Curie-Weiss fitting above 100 K is also shown. c) Isothermal magnetization measured at 2 K. d) Heat-capacity as a function of temperature (<60	254

	K) measured in the presence of external magnetic fields as well. e) Heat-capacity divided by temperature f) Isothermal entropy change as a function of temperature (2-100 K) for different final fields starting from zero-field.	
A.2	a) Magnetic susceptibility as a function of temperature obtained in a field of 100 Oe in both zero-field-cooled and field-cooled conditions for nanoform specimen of Er_2RhSi_3 b) Magnetic susceptibility and inverse of magnetic susceptibility in a field of 5 kOe. Curie-Weiss fitting above 100 K is also shown, see red line through the data points. c) Isothermal magnetization measured at 2 K. d) Heat-capacity as a function of temperature (<15 K) measured in the presence of external magnetic fields as well. e) Isothermal entropy change as a function of temperature (2-40 K) for different final fields starting from zero-field.	257
A.3	a) Magnetic susceptibility as a function of temperature obtained in a field of 100 Oe in both zero-field-cooled and field-cooled conditions for nanoform specimen of Ho_4PtAl . b) Magnetic susceptibility and inverse of magnetic susceptibility in a field of 5 kOe. Curie-Weiss fitting above 100 K is also shown. c) Isothermal magnetization measured at 2 K. d) Heat-capacity as a function of temperature (<50 K) measured in the presence of external magnetic fields as well. e) Isothermal entropy change as a function of temperature (2-60 K) for different final fields starting from zero-field.	260
A.4	a) Magnetic susceptibility as a function of temperature obtained in a field of 100 Oe in both zero-field-cooled and field-cooled conditions for nanoform specimen of Er_4PtAl . b) Magnetic susceptibility and inverse of magnetic susceptibility in a field of 5 kOe. c) Isothermal magnetization measured at 2 K d) Heat-capacity as a function of temperature (<40 K) measured in the presence of external magnetic fields as well. e) Heat-capacity divided by temperature. (f) Isothermal entropy change as a function of temperature (2-50 K) for different final fields starting from zero-field.	264

Synopsis

Abstract

There has been a considerable interest in understanding the physical properties of the compounds containing rare-earths, not only from the angle of basic science but also considering growing application potential. Current trends in condensed matter area suggest that investigation of new materials in particular are important in this respect, as such studies often paved the way for new concepts and resultant applications. Keeping this in mind, some ternary compounds – less investigated in the literature – have been taken up for magnetic investigations, and also for exploring antibacterial studies. Such compounds for our studies are: Nd_2RhSi_3 , Er_2RhSi_3 , Ho_4PtAl , Er_4PtAl , and Dy_4RhAl among metals and spin-chain insulators $\text{Tb}_2\text{BaNiO}_5$ and $\text{Tb}_2\text{BaCoO}_5$, in both bulk and nanoforms. There are structural features facilitating ‘geometrically frustrated magnetism’ – a current trend in magnetism - in the above-mentioned metallic compounds. While many novel features (revealing structure-property relation) in the magnetic behavior of these compounds are reported in this thesis, main highlights are:

(i) Establishment of an exceptional magnetism of Nd_2RhSi_3 .

(ii) Establishment of antiferromagnetism at 5 K in Er_2RhSi_3 ,

however, with concurrent cluster spin-glass features, attributable to partially disordered antiferromagnetism; $1/3$ magnetization plateau – less known among metals – and corresponding magnetoresistance plateau are intriguing findings.

(iii) Ho_4PtAl and Er_4PtAl exhibit a re-entrant cluster spin-glass behavior, with the onset of an antiferromagnetic ordering; isothermal entropy change is very large at the onset of magnetic order, making these compounds useful for magnetic refrigeration applications. Dy_4RhAl exhibits spin-glass features which coexists with

antiferromagnetic order (18 K); this magnetic behavior is interestingly different from that of Dy₄PtAl, which is ferromagnetic.

(iv) Pressure studies on the magnetic ordering temperatures of well-known ‘exotic’ multiferroic systems. Tb₂BaNiO₅ and Tb₂BaCoO₅ bring out how magnetism of localized 4*f* electrons behave in a complex fashion to the application of external and chemical pressures, influencing other coupled phenomena.

(v) A reduction in particle to nanoform in Dy₄RhAl, leads to the evolution of a Griffiths-phase like behavior (a novel concept in magnetism), suppressing antiferromagnetic order – a rare demonstration in magnetic metals. In other cases, the changes in magnetic properties in nanoform are subtle.

This reinforces the fact that one needs to be cautious while employing nanoparticles for medicinal applications based on the properties of the bulk forms, though none of these compounds are efficacious in inhibition of bacterial and fungal growths. The studies serve as a classic study for exploration of such rare-earth intermetallic materials for medicinal applications.

Background

The rare-earth (*R*) compounds have been subjected to intense research for the past few decades in condensed matter physics due to a variety of unusual phenomena exhibited by such materials. In these materials, the magnetic properties are determined by the incomplete 4*f* shell which undergoes progressive filling when one moves from La to Lu. The incomplete 4*f* orbital in the *R*-based compounds was historically considered localized, shielded by filled 5*s*² and 5*p*⁶ shells. This initial belief got changed during last few decades for lighter rare earths (Ce, Sm and Eu) where manifestations of some degree of delocalization have been found in many physical properties. The basic aim of the studies for this thesis is to explore novelties in magnetism associated with heavy

rare-earth compounds in which $4f$ electrons are strictly localized, and also to explore such materials for antibacterial applications.

The materials under study contain transition metal (TM) ions also. In the case of transition metals, the d electrons, responsible for magnetism, are known to be essentially itinerant, often losing its moment due to bonding with other atoms. The compounds with moment-carrying rare-earths elements and transition metal elements ($3d, 4d, 5d$) elements have especially attracted considerable interest in materials physics as well as applications area, since the interaction between $4f$ of rare-earth and d of the transition metal has been often reported to promote magnetic and transport properties. A survey of the current research areas in condensed matter reveals the following trends:

- (i) While disorder in the lattice can create a competition between antiferromagnetic and ferromagnetic interactions leading to magnetic frustration, certain crystallographic arrangement (e.g., triangular) of magnetic ions can also induce magnetic frustration without disorder and this phenomenon is called ‘geometrically frustrated magnetism’.
- (ii) Investigation of new rare-earth materials, particularly those with strictly localized $4f$ electrons, brings out hitherto unknown concepts. Therefore, there is a need to probe such rare-earth materials which have not been paid much attention in the literature. Understanding various magnetic interactions and in turn the properties exhibited by these compounds can offer inputs for various industrial, technological and biomedical applications. These observations are central to this thesis work, and the three families of materials are chosen accordingly.

Objectives

Many of the members in the family of compounds, having a general formula R_2TMX_3 ($X =$ silicon/ germanium), derived from AlB_2 - type hexagonal structure have

been of great current interest due to novel anomalies exhibited by Pd-based series in the field of magnetism and superconductivity. This structure is of honey-comb type, in which TM -Si (Ge) layers are sandwiched by R layers. R ions form triangular lattice, interestingly with multiple areas, thereby favoring geometrically frustrated magnetism. Despite wide interest in Pd-based compounds, less work had been done on other isostructural families, in particular Rh-based family. There is a need to probe other families of compounds in depth and two such compounds were taken up for this thesis work.

Another family of interest in this respect is with 4:1:1 stoichiometry, like R_4PtAl , R_4RhAl etc., which are characterized by fascinating structural features, that is, these compounds are made up of magnetic layers, with triangular as well as kagomé-lattice arrangement of atoms, therefore, there is a potential for geometrically frustrated magnetism, as evidenced for some members of these families in the recent literature. Besides, 3 sites for R offer an opportunity to probe magnetism in the event of competing R - R magnetic interactions. Therefore, it is worthwhile to probe hitherto unexplored compounds in these families. Interestingly, complications in the magnetic and transport properties were seen not only in the magnetically ordered state, but also in the paramagnetic state in this family in the recent literature. Therefore, there is a need to extend such investigations for other members of this family.

The above two families are metallic in character, in which magnetism is mediated by Ruderman-Kittel-Kasuya-Yosida (RKKY) indirect exchange interaction. Insulating rare-earth materials, in which RKKY interaction is absent, were also studied for the aim of this thesis. The spin-chain family, R_2BaNiO_5 ($R = Gd, Dy, Er, Sm, Nd, Ho$ and Tb) crystallizing in a centrosymmetric orthorhombic structure ($Immm$ space-group) has been recently reported to exhibit novel multiferroic behavior. Among these,

Tb₂BaNiO₅ and also isomorphous Tb₂BaCoO₅ have been reported to be unique in the field of multiferroics in multiple ways. It is of interest to explore how external and chemical pressure tune the respective magnetic ordering temperatures to enable factors influencing exotic multiferroicity.

Metals and bimetallic compounds have also been extensively studied in the past literature and have been found to exhibit excellent physiochemical and biological properties. These properties have been used in drug delivery, therapeutic and other biomedical applications including bio-imaging and magnetic resonance imaging. Recently, there has been renewed interest in Au, Ag and Ga based binary compounds (bimetals), because these metals have been known to exhibit excellent antibacterial properties. Therefore, it is important to collect such data on the magnetism of rare-earth based intermetallic compounds, particularly in nanoform, for any such future applications.

Thus, our study focusses on those materials (both intermetallic and oxides), which have not been paid much attention in the existing literature, with the intention of sowing seed to discover new rare-earth metallic materials for medical applications. The magnetic and transport properties of these compounds were studied for the aim of this thesis in bulk polycrystalline form and also to understand the effects of particle size reduction on their magnetic properties, at least for some cases. The main measurement techniques are ac and dc magnetization, electrical and magnetoresistance and heat-capacity, depending on the material under study. We explored the antibacterial properties of these compounds to ascertain if their properties can be made useful for biomedical applications.

In a nutshell, the objectives can be stated as follows:

- To study the magnetic and transport properties of R_2RhSi_3 ($R = Nd$ and Er) in bulk and nano forms
- To study the magnetic and transport properties of R_4PtAl ($R = Ho$ and Er) and Dy_4RhAl in bulk and nano forms
- To assess the pressure effects [chemical and external] on the magnetic properties of Tb_2BaNiO_5 and Tb_2BaCoO_5 .
- To study the antimicrobial and antifungal efficacy of the nanocrystalline intermetallic compounds.

Methodology

- Intermetallic samples R_2RhSi_3 and R_4TMAI were prepared by arc melting technique.
- Oxide compounds R_2BaNiO_5 and R_2BaCoO_5 and other chemical doping viz. Sr for Ba etc. were prepared by a standard solid-state reaction route.
- Nanoform specimens of the intermetallic compounds were prepared by high-energy ball milling technique.
- For all the samples, phase purity and stoichiometry were determined by x-ray diffraction and SEM-EDAX measurements.
- Magnetic properties of these compounds were studied using SQUID or VSM magnetometers.
- Magneto-transport and heat capacity measurements were done using a commercial physical property measurement system.
- High pressure magnetic studies on the oxide compounds were carried out under hydrostatic pressure conditions using high pressure cells.

- Anti-microbial activity was carried out in gram positive bacteria *S. Aureus*, *E. Faecalis*, *P. Acnes* and the gram-negative bacteria *E. coli* and *Pseudomonas aeruginosa*. The anti-fungal studies were carried out on *Candida albicans*. To carry out the efficacy studies, we employed the disk diffusion technique, well diffusion technique and serial dilution bio-reaction technique.

Results and Conclusions

Chapter 3 of the thesis presents the results of *exhaustive* investigations by dc and ac magnetization, heat-capacity and transport measurements for the two compounds, R_2RhSi_3 ($R= Nd$ and Er), crystallizing in a AlB_2 -derived hexagonal structure. The results reveal that these compounds exhibit interesting properties – unique in their own way – due to a competition between ferromagnetic and antiferromagnetic interactions, which can be tuned by temperature and magnetic-field. While there are many interesting features in the properties, the key findings are only summarized below for each of these compounds.

The compound Nd_2RhSi_3 is established to exhibit long range ordering of a ferromagnetic type (at $T_C = 16.5$ K). The observed value of T_C is essentially the same as that of isostructural Nd_2PdSi_3 , unlike the antiferromagnetic behavior at different temperatures for a given R within the two families, thereby suggesting the dominant role of Nd $4f$ -Si $3p$ hybridization. This hybridization in addition causes a significant enhancement of T_C , disobeying de Gennes scaling. Such demonstrations of $4f$ hybridization effects on magnetism are rather scarce previously for Nd compounds. The ferromagnetism shows cluster spin-glass dynamics and complexities at temperatures lower than ~ 10 K with magnetic properties pointing to the development

of an antiferromagnetic component as in the Pd analogue. However, there are subtle differences between Nd_2PdSi_3 and Nd_2RhSi_3 well below T_C (e.g., in the nature of virgin isothermal magnetization behavior in the magnetic hysteresis loop, suggesting dominance of ferromagnetic component in the latter). The point to be stressed is that there is a remarkable difference between these two Nd compounds in the magnetic behavior above T_C ; that is, there are evidences for the gradual onset of ferromagnetic clusters with spin-glass dynamics (as revealed by the bifurcation of ZFC-FC dc χ curves, frequency -dependent ac χ peaks and slow decay of isothermal remanent magnetization) as the temperature is lowered towards T_C for the Rh case, as though Nd 4*f*-Rh 4*d* interaction is a triggering factor for its origin. Given that this family is characterized by a triangular arrangement of rare-earth ions and that there is a crystallography-favored bond disorder, the local variations in Nd 4*f* covalency should be the key for above-mentioned frustrated magnetism (that is, reflected in the form of cluster spin-glass dynamics). It is intriguing that some other heavy rare-earth members of this family do not show spin-glass anomalies in polycrystalline form. The temperature dependence of electrical resistivity and the features (including sign reversals) in the magnetoresistance are in conformity with the conclusions made above for the Rh compound. The results overall reveal this Nd compound is an exotic magnetic material.

With respect to Er_2RhSi_3 , Er is known to contain 4*f* electrons of localized character only, unlike Nd 4*f*, and hence offers an opportunity to explore anomalous magnetism of 4*f* in the localized limit. The results provide evidence for a proposal of onset of long-range antiferromagnetic order at 5 K, however, interestingly, with cluster spin-glass features at the same temperature (just as the Nd case, which is however ferromagnetic). A notable finding is that this compound exhibits a characteristic feature

of partially disordered antiferromagnetism (PDA), viz., $1/3$ magnetization plateau. This is fascinating as such a PDA magnetism has been proposed for some insulators with geometrically frustrated magnetism. But this is not so common among metals, that is, in a material with RKKY interaction, that too without any interference from other $4f$ -related hybridization phenomena. Additionally, none of the isostructural ternary rare-earth compounds has been known to show such PDA characteristics in the past, in particular, other rare-earth compounds of this Rh family (R= Gd, Dy and Ho) as well as the Er counterpart in the Pd-based family, Er_2PdSi_3 . Clearly, this compound is also a unique magnetic material. It is also demonstrated that this compound should also serve as a prototype for transport behavior across $1/3$ magnetization plateau.

Chapter 4: In the 4:1:1 family, the three compounds discussed in this chapter are: Ho_4PtAl , Er_4PtAl and Dy_4RhAl . While Ho_4PtAl and Er_4PtAl exhibit a re-entrant cluster spin-glass behavior, with the onset of an antiferromagnetic type of magnetic order. Antiferromagnetism has been known for other rare-earth members in the family, except Dy_4PtAl , which is known to exhibit a ferromagnetic ordering. From the degree of suppression of ac susceptibility peaks by the application of the magnetic fields, it is concluded that the spin glass dynamics in Dy_4RhAl is relatively weaker. Within this family of compounds, both Ho_4PtAl and Er_4PtAl exhibit the largest value of isothermal entropy change at the onset of magnetic order with a large tail above T_N . Since the values exceed that of an S -state ion, this finding suggests that the topology of the $4f$ orbital can enhance the magnetocaloric effect. The intriguing conclusion inferred from the comparison of the magnetocaloric effect (MCE) between the Pt-based family and the Rh-based family, is the following: It seems that the Pt $5d$ spin-orbit coupling also plays a role in the enhancement of the MCE values. Such a correlation should provide

clues for the advancement of theories in the field of *MCE*. This will in turn be helpful in engineering of materials for magnetic refrigeration at room temperature. The reversible isothermal entropy curves establish that the Er compound meets the criterion for magnetocaloric applications in the low temperature range.

In the case of Dy_4RhAl , the results establish that the compound undergoes antiferromagnetic order which is different from the ferromagnetic ordering seen in the case of Dy_4PtAl (as stated above). This result provides an indirect support to the fact that the ferromagnetism seen in the case of Dy_4PtAl is interesting and unusual. It is quite possible that the Pt $5d$ orbital, extended more spatially when compared to Rh $4d$ orbital, plays an important role by strong interaction with crystal-field-split anisotropic orbitals of Dy giving rise to the anomalous magnetism seen in the case of Dy_4PtAl . In addition, the $5d$ electrons are relatively less correlated with stronger spin-orbit coupling than the $4d$ electrons. These results suggest an important role of transition metal bands, which interact with the Dy $4f$ electrons, determining the magnetism of these systems.

In addition, there are various other interesting features, e.g. antiferromagnetic energy gap formation, large magnetoresistive behavior, not only in the magnetically ordered state but also in the paramagnetic state, well above T_N extending to $T > 3T_N$, and spin-orientation effects as a function of T and H in the magnetically ordered state, leading to complex sign reversals with the variation of such external parameters. Thus, the work brings out the complex nature of magnetism in these compounds, in the magnetically ordered state, arising from the different sites of rare-earth ions. Thus, this work offers a family of materials to theorists to explore how the interaction among three sites of rare-earth plays a role in deciding the magnetic behavior of the system.

Chapter 5: This chapter presents the results of high-pressure magnetization studies on the exotic multiferroic compounds, $\text{Tb}_2\text{BaNiO}_5$ and $\text{Tb}_2\text{BaCoO}_5$. The maximum external hydrostatic pressure applied being 10 kbar. In addition, the effects of chemical pressures induced by doping of Sr at the Ba site in $\text{Tb}_2\text{BaNiO}_5$ have also been probed for comparison. It is known that under ambient pressure conditions, both Tb and Ni/Co moments order at the same temperature (interestingly with the involvement of Tb $4f$ in inducing ferroelectricity, a situation which is not encountered in the case of rare-earth based manganites). Our study shows that the externally applied pressure does not have any effect on the magnetic properties of $\text{Tb}_2\text{BaCoO}_5$, indicating a robust nature of magnetism, in contrast to the opposite effect on the two magnetic transitions ($T_{N1} = 63$ K and $T_{N2} = 25$ K) in the case of $\text{Tb}_2\text{BaNiO}_5$. T_{N1} is found to get enhanced to higher temperatures, and T_{N2} , at which multiferroicity sets in, is interestingly depressed to lower temperatures. Such an effect of applied external pressures, on the two magnetic features, at two different temperatures, in the same compound, is quite interesting, particularly noting that both Tb and Ni have been known to order magnetically at the same temperature establishing coupling between these two moments. Since there is no change in magnetic symmetry across T_{N2} , one would expect that both the transitions behave in the same way with the application of external pressure. This observation is different from that noted for the Mn sublattice in the well-known type-II multiferroic materials, TbMnO_3 and RMn_2O_5 , including the magnetic transition temperature at which ferroelectric transition sets-in in these examples. Therefore, it can be concluded that the local distortions due to ferroelectricity in this compound influence the pressure dependence of corresponding magnetic transition temperature.

In addition, the study of the magnetic properties under the influence of chemical pressures induced by doping of Sr at the Ba site shows a difference in

variations of both the magnetic transition temperatures under the influence of chemical pressures. If these results are compared with the reported changes in the magnetic features seen by other isoelectronic substitution at Tb and Ba sites, it is concluded that the subtle distortions cause a profound effect on magnetic characteristics of this compound.

Thus, this chapter brings out a case of rare-earth in insulating environment (that is without *RKKY* interaction), in which localized $4f$ electrons (as far as magnetization is concerned) behave in a complex fashion to the application of external and chemical pressures.

Chapter 6 presents the results of nanocrystalline Dy_4RhAl where the dominant antiferromagnetic ordering seen in the case of bulk specimen disappears when the particle size is reduced to nanoform, with the evolution of a Griffiths-phase like behavior (a novel magnetic state proposed by P.W. Anderson) in the range 10–30 K. Demonstration of such a particle-size induced transformation to Griffith's phase-like features in an intermetallic compound due to localized $4f$ electrons is generally quite rare. In the case of other intermetallic compounds studied here, there is no result leading to a conceptual change in magnetism, though subtle changes are noted for each compound. Thus, these results overall suggest that a reduction in particle size may in some cases lead to a conceptual change in magnetic behavior, whereas in some other cases, the changes could be minor, reinforcing the fact that one needs to be cautious while employing nanoparticles for medicinal applications based on the properties of the bulk forms. The efficacy studies on the bulk and nanocrystalline intermetallic samples revealed that none of these compounds are efficacious in inhibition of microbial growth

Keywords

Rare-earths, Transition metals, $4f$ correlations, ferromagnetism, antiferromagnetism, spin-glass, Griffiths phase, magnetoresistance, magnetic coupling, nanocrystals antimicrobial and antifungal efficacy.

Chapter 1

Introduction

1.1 Preliminary remarks

The rare-earths (R) and their compounds play crucial roles in our day-to-day life in multiple ways, in terms of high-tech consumer products, permanent magnets etc. The applications of these materials have been expanding in a variety of directions and therefore there has been a constant demand for new rare-earth materials. Naturally, there is an absolute need to understand the fundamental physical properties of new materials, to provide inputs for exploring applications, to mention a few more, magnetic refrigeration, multiferroic and medicinal applications. In that direction of research over a period about six decades, the basic science researchers discovered a variety of exotic phenomena, e.g., valence fluctuations, Kondo lattice (KL) anomalies, heavy-fermion superconductivity, high-temperature superconductivity, and other phenomena (not specific to rare-earth systems alone) like multiferroicity, giant magnetoresistance, metal-insulator transitions, magnetization (M) reversal etc. While it is outside the scope of this thesis to elaborate all these phenomena, some of these will figure in this thesis. Several experimental tools have been employed in the literature as a function of temperature (T), magnetic-field (H), high pressure (P), and chemical substitution/doping in all these investigations to gain in-depth knowledge of the physics and chemistry of the materials. Considerable efforts have also gone in to understand the structure-property relationships and there are theoretical advancements as well.

Compounds containing R and TM (also carrying magnetic moments) have attracted special interest in the field of magnetism [1]. The $3d/4d/5d$ orbitals of TM responsible for

magnetism exhibit in general more itinerancy, often losing magnetic moment due to bonding with other atoms, compared to $4f$ orbitals of rare-earths. When the magnetic-moment is retained on TM , its coupling with $R 4f$ present interesting anomalies. The degree of delocalization of magnetic moments determines the type of exchange interactions that could arise in the compound [2].

This thesis focusses on some of these rare-earth transition metal (TM) compounds. In this chapter, the following concepts relevant to the understanding of the results presented in this thesis are briefly outlined: Elementary aspects of magnetism in solids including commonly known well-ordered magnetic structures and disordered magnetism (spin-glass and geometrically frustrated magnetism), different types of exchange interactions, and rare-earth magnetism, apart from a brief introduction to the basics of electrical transport and heat-capacity (C).

1.2 Elementary aspects of magnetism in solids

1.2.1 Paramagnetism, diamagnetism, and magnetic ordering

The nature of magnetism of a material depends upon the magnetic moment each ion possesses due to the presence of unpaired electrons, orbital motion of electrons and how these moments get internally arranged below a particular characteristic temperature, called ‘magnetic ordering temperature’ (Curie temperature T_C or Néel temperature T_N), by intersite magnetic interaction [3,4]. Paramagnetism and diamagnetism basically are intrasite effects, whereas the magnetic ordering is a cooperative effect when the magnetic centers interact with the neighboring magnetic centers, resulting in various magnetic structures, depending on material and other physical variables. In addition, the electrostatic

forces from the ions in the lattices result in the ‘so-called’ ‘crystal field’, which has an influence on determining the electronic ground state and hence the magnetic moment and magnetic structure. Some of these fundamentals are briefed below.

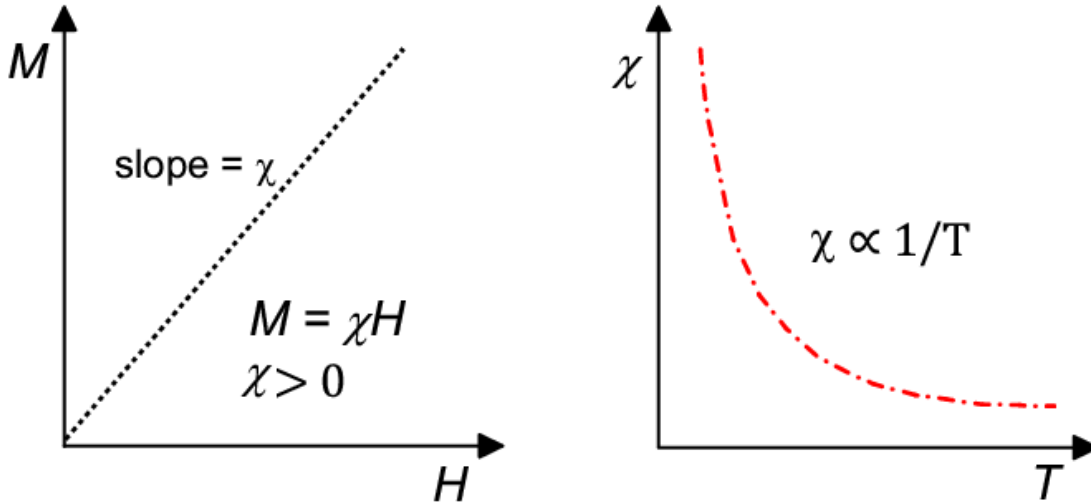


Figure 1.1: Schematics of isothermal magnetization behavior of a paramagnet. The right figure (magnetic susceptibility as a function of temperature), is strictly for localized moments.

In a paramagnetic material (that is, those containing at least one unpaired electron), when an external magnetic field is applied, these spins tend to align in the direction of the applied magnetic field. But thermal effect opposes this tendency for alignment. Naturally, as the temperature is increased, this influence of thermal effect increases. The parameter, ‘magnetic susceptibility’ ($\chi = M/H$) shown in figure 1.1 demonstrates this for an electron localized in an orbital, for the fields that can be applied in the laboratories in a T -range which is generally low (<200 kOe). The curve obeys Curie-Weiss law, $\chi = N\mu_{eff}^2 / 3k(T-\theta_p)$, where N is the Avogadro number, k is the Boltzmann constant, and θ_p is the Curie-Weiss parameter (also called ‘paramagnetic Curie temperature’) and μ_{eff} is the effective magnetic moment in Bohr-magneton units in the paramagnetic state, defined as

$$\mu_{\text{eff}} = g_J [J(J + 1)]^{1/2} \dots \quad (1.1)$$

where J is the total angular momentum and g_J is the Lande g factor. In the event that there is no interaction between the magnetic moments at different sites, θ_p is zero (see also, below), and when there is an interaction, the value is finite. The left figure (figure 1.1) shows M as a function of H , and the right one depicts behavior as a function of T (when $\theta_p = 0$). The sign of χ is positive in paramagnets. The spin alignment is not retained when the external magnetic field is removed, and the moment undergoes thermal fluctuation leading to ‘zero’ spontaneous magnetization. In metals, the unpaired electrons which are band-like exhibit ‘Pauli paramagnetism’, i.e., T -independent susceptibility, and this contribution often is superimposed over that from localized moment.

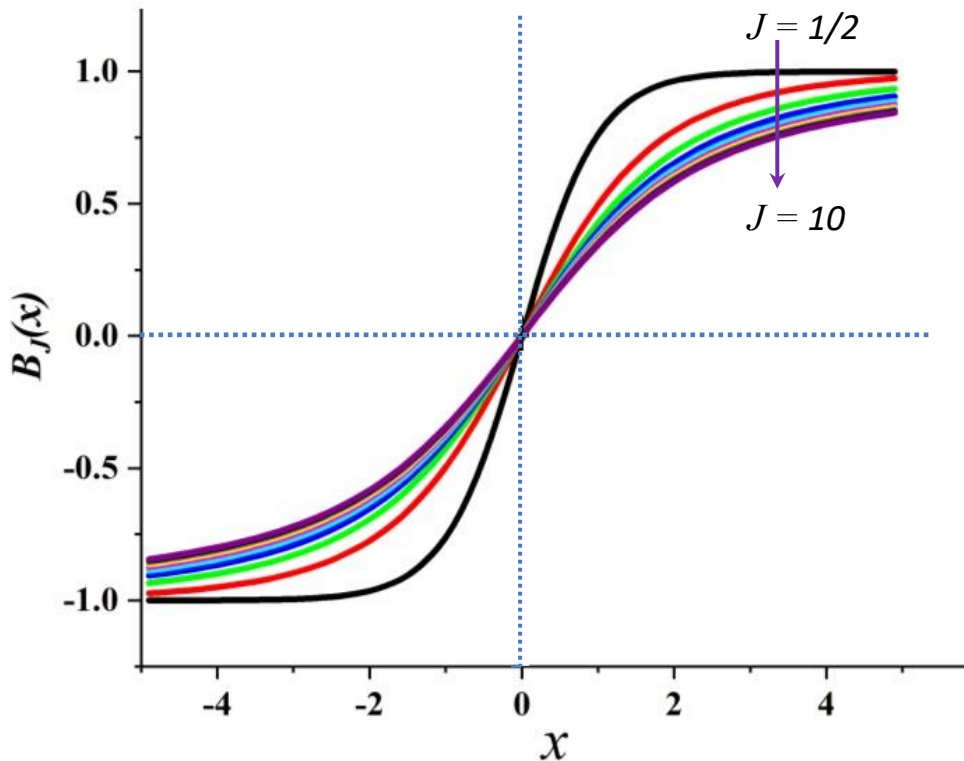


Figure 1.2: The Brillouin function is simulated for various J , the total angular momentum values.

Before closing this section on ‘paramagnetism’, a brief mention on Brillouin function is made here. Magnetization strength (M) of a paramagnetic material depends upon the ratio of the strength of individual magnetic dipole in the paramagnet to the thermal energy. This is dependence which is calculated using the quantum theory is given by the Brillouin function. The Brillouin function $B_J(x)$, applicable to non-interacting spin system is defined as

$$B_J(x) = \frac{2J+1}{2J} \coth\left(\frac{2J+1}{2J}x\right) - \frac{1}{2J} \coth\left(\frac{x}{2J}\right) \dots\dots\dots (1.2)$$

here, $x = \frac{g_J J \mu_B H}{k_B T}$, k_B is the Boltzmann constant. At low magnetic fields, the magnetization is linearly proportional to the applied magnetic field and magnetization reaches its maximum saturation value when the magnetic energy is much greater than the thermal energy (figure 1.2). One can estimate the magnetization of a system in the paramagnetic state. An approximation to this magnetization at high temperatures and low magnetic field was made by Perrie Curie, considering $x \ll 1$, and the paramagnetic susceptibility was determined as

$$\chi = \frac{M}{H} \sim \frac{NJ(J+1)g_J^2 \mu_B^2}{3k_B T} = \frac{C}{T} \dots\dots\dots (1.3)$$

Equation 1.3 is known as the Curie Law, which shows that in a non-interacting system the susceptibility is inversely proportional to the temperature. When there is finite interaction then χ is given by $\left(\frac{C}{T-\theta_P}\right)$.

Diamagnetism arises from the orbital motion of electrons (including those which are paired up in an atom). According to the classical electromagnetic theory, when a

charged particle like an electron moves in the external magnetic field, it experiences a force which is perpendicular to its velocity and magnetic field. This force causes the charged particle to move in a circular or elliptical path generating a magnetic field which opposes the external magnetic field. Hence, the sign of χ is negative (that is diamagnetism), exhibiting usually a linear variation with H and a T -independent behavior. But the magnitude is usually smaller compared to paramagnetic contribution. However, superconducting materials exhibit a strong diamagnetism, as the diamagnetism arises due to large super current which is known as the Meissner effect; here the magnetic field is completely expelled from the sample in the superconducting state.

Returning to cooperative ordering, in which unpaired electrons at different sites interact with each other through an exchange interaction, a few simple situations are discussed in the rest of this section.

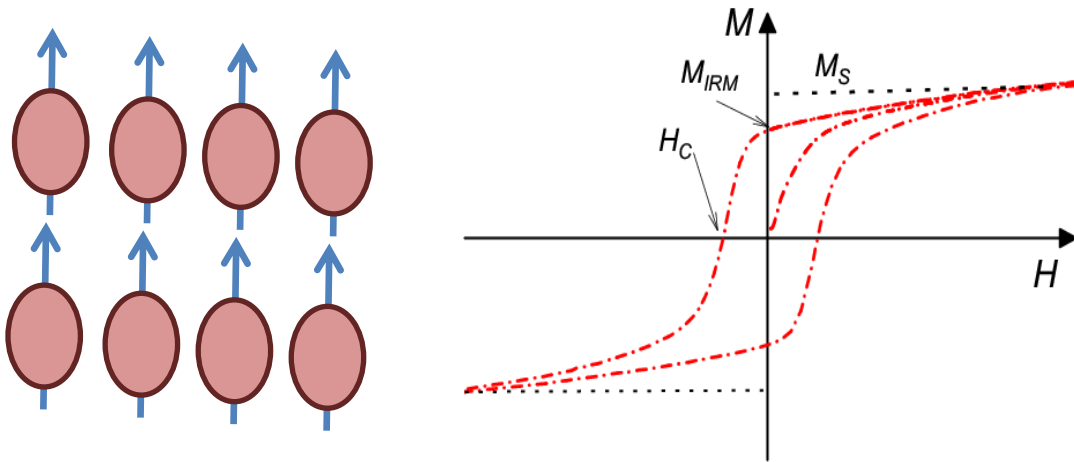


Figure 1.3: Schematic representation of a ferromagnet, circles represent the magnetic centers of the atoms or ions and the arrows represent the direction of spins. In the right, hysteresis loop for a hard ferromagnet is shown.

For instance, in ‘ferromagnetism’, there is a long-range collinear alignment of all the moments in the absence of an external magnetic field (figure 1.3, left), resulting in a net non-zero magnetization below the characteristic temperature, T_C , called Curie temperature. A typical $M(H)$ curve is shown in Fig. 1.3 (right) for a ‘hard’ ferromagnet for which a hysteretic loop can be seen; a finite remnant magnetization (M_{IRM}) is observed when the external field is removed, and thus such ferromagnets are characterized by a finite ‘coercive’ field (H_c). The saturation magnetization M_s is the maximum magnetic moment per unit volume. ‘Soft’ ferromagnets are characterized by zero remnant magnetization. In antiferromagnetism, the spins at different sites pair up and align in the opposite direction (figure 1.4, left) below a characteristic temperature, T_N , called the Néel temperature. This results in a net zero moment in a perfect antiferromagnet.

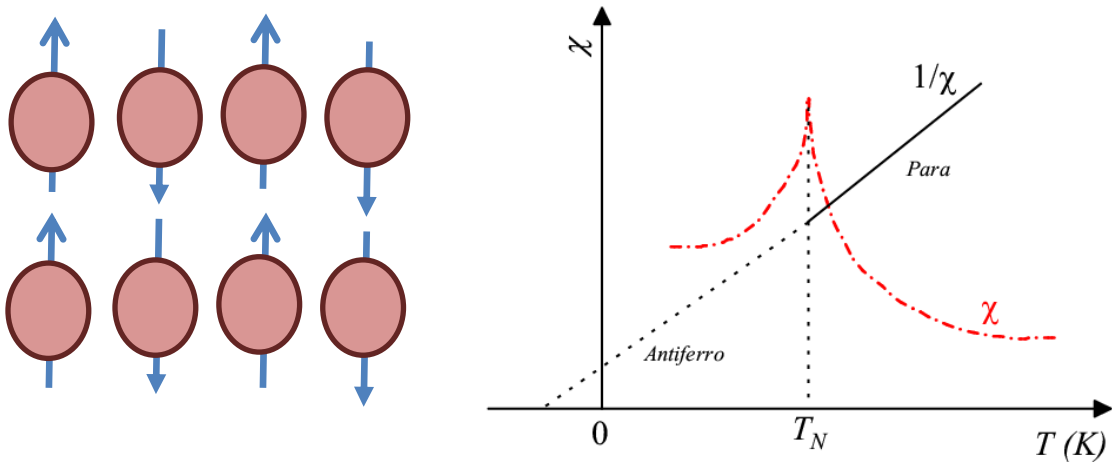


Figure 1.4: Illustrative example of antiferromagnetic behavior(left). Arrows show the direction of spin. Right figure shows a typical behavior of temperature dependence of magnetic susceptibility.

A typical $\chi(T)$ behavior for an antiferromagnet is shown in the right panel of figure 1.4. It is also possible that there is a canting of the magnetic moments with respect to that at the neighboring site (that is, with a ferromagnetic component), which can lead to a finite

value of magnetic moment. There are more complex situations, like sinusoidal modulation, that are often met with in real materials. In principle, the sign of θ_p defines the nature of magnetic interaction; positive (negative) sign implies ferromagnetic (antiferromagnetic) interaction in the paramagnetic state, though ultimate magnetic structure in the magnetically ordered state as the temperature is lowered can be different or can be more complex due to other details like crystallographic features, crystal-field effects etc.

Ferrimagnetism usually occurs in materials when the magnetic ions (either same or different ion) occupying two different crystallographic sites bear different magnetic moments, but couple antiparallel to each other. As a result, there is a partial cancellation of magnetic moment (figure 1.5). Hence, there is a net non-zero magnetic moment in the material, leading to ferromagnetic-like behavior.

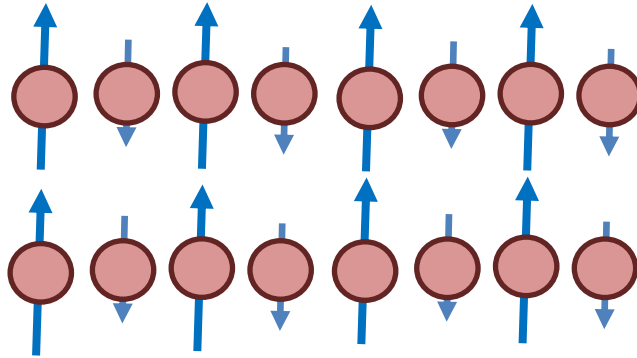


Figure 1.5: Illustrative example of ferrimagnetic behavior

1.2.2 Spin-glasses

Spin-glass freezing is a type of cooperative phenomenon different from the magnetic structures briefed above. Unlike in other cases, below the magnetic ordering temperature, the magnetic moments are frozen randomly in space [6,7]. The response of the spins to a measurement technique depends on probing time scale. Note that, in the paramagnetic

state, the spins are random in time domain also. The spin-glass freezing (figure 1.6) was originally observed in systems containing magnetic impurities dispersed in non-magnetic matrix, like CuMn [8]; subsequently, this was noted even in concentrated magnetic systems with well-defined crystal structure and the randomness of exchange interaction induced by various factors like defects and geometry. There are various signatures of spin-glass freezing:

- i) Bifurcation between zero-field-cooled (ZFC) and field-cooled (FC) curve in dc susceptibility below spin glass freezing temperature (T_g).

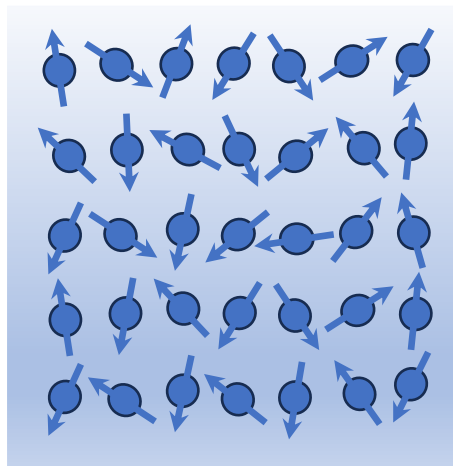


Figure 1.6: Illustrative example of a conventional spin-glass.

- ii) A frequency (ν) dependent behavior in ac χ , both in real (χ') and imaginary (χ'') parts. For a canonical spin glass like CuMn [8], the ac susceptibility shows frequency dependence with values shifting (weakly upwards typically about 0.5K) in response to increasing ac frequency from 1 Hz to 1 kHz. The peak temperature in χ'' vs T is often fitted with some power law (like Vogel-Fulcher law [9], Arrhenius law, etc.) which enables to understand slow spin relaxation [10].

iii) Isothermal remnant magnetization (M_{IRM}) below T_g shows a slow decay (often logarithmically/exponentially) with time (t) [11]. From this data, one learns about relaxation strength of spins to infer more details about spin glass freezing (such as, cluster glass or canonical spin glass), because the relaxation time, τ , for a cluster spin glass is significantly higher than that for canonical spin glasses like CuMn.

iv) Memory effect (aging and rejuvenation) [12] should be observed below T_g . In this case, if the sample is cooled and held at a particular temperature (T_w) for some time duration (t_w), it will show a local dip around the T_w in temperature dependent magnetization data while warming. The depth of the local dip depends on the duration of the wait; it increases with increasing t_w . If one waits at additional T below the spin-glass transition, additional local dips appear at each T_w .

1.3 Crystal-field effects

The $4f$ multiplets ($2J+1$ levels) of an isolated lanthanide ion are degenerate, but when lanthanide ions are incorporated into a crystal lattice, the crystal field created by surrounding ligands can perturb the degeneracy of the $4f$ orbitals and these orbitals can undergo partial splitting. This splitting is termed as the crystal field effects and is denoted by Δ_{CF} (figure 1.7). This crystal field in some cases decides the spin value of the magnetic ions which determines the magnetic state of a system. The nature of coordination, orbital arrangement and hybridization around the lanthanide ion decide the ultimate value of the magnetic moment. However, the degree to which the $4f$ orbitals are split by crystal-fields is smaller than what is observed for the d orbitals in transition metals because of the shielding effect and relatively large extension of the d orbitals. The partially filled orbitals

following crystal-field effects can be further split by a phenomenon called ‘Jahn-Teller effect’ [13] which is explained as follows. When there is an electronic degeneracy of the partially filled orbital (e.g., d^9 configuration of transition metal ions), this electronic system is unstable and undergoes a geometrical distortion for adopting a structure with a lower symmetry as well as lower energy. This lifts the degeneracy of the orbital concerned. For instance, for Cu^{2+} in an octahedral geometry, the d^9 electronic configuration results in 3 electrons in the 2-fold degenerate e_g orbitals. Thus, the polyhedra undergoes distortion along the four-fold axis (usually along z-axis) for lifting the degeneracy of the e_g orbitals while lowering of the overall energy.

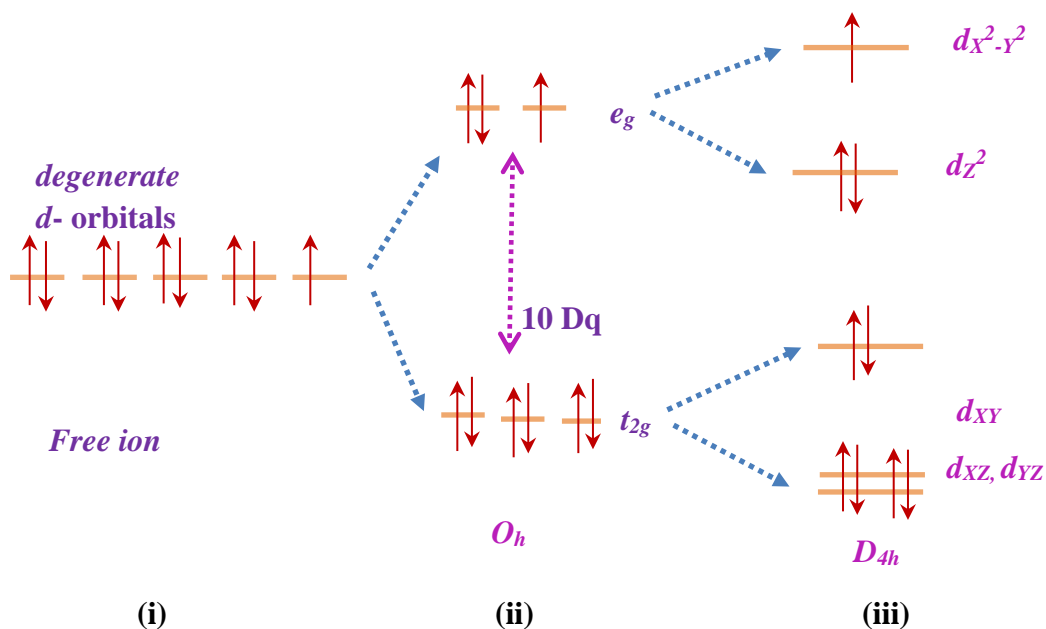


Figure 1.7: (i) Degenerate d-orbitals of a transition metal ion, (ii) Splitting of the d-orbitals into higher energy e_g and low energy t_{2g} orbitals in the octahedral environment, and (iii) Further splitting due to Jahn-Teller distortion for Cu^{2+} ion.

In octahedral symmetry the d -orbitals split into two sets with an energy difference, $10Dq$ that is ten times the "differential of quanta" (the crystal-field splitting parameter),

while the d_{xy} , d_{xz} and d_{yz} orbitals having t_{2g} symmetry will be lower in energy than the d_z^2 and $d_{x^2-y^2}$ (e_g symmetry), because the former group is farther from the ligands than the latter and therefore experiences lesser repulsive force. The lattice may distort to further lowering of energy as shown in the extreme right of the figure. Such a distortion can occur through the elongation of the metal-ligand bonds along z -axis as shown in the figure. In some cases it may take place through the contraction of the metal ligand bonds as well.

1.4 Geometrically Frustrated magnetism

It is known that disorder can result in randomization of exchange interaction, possibly giving rise to magnetic frustration leading to spin-glass anomalies, avoiding a long-range magnetic structure, as discussed in section 1.2.2. However, due to the geometrical arrangement of the magnetic ions and the presence of competing neighbor interactions, there can be situations in which there is a conflict in minimizing the exchange interaction energies associated with different spin pairs [14,15]. Such a conflict can also result in magnetic frustration leading to different interesting types of magnetism and such magnetic systems are termed as “*geometrically frustrated magnetic systems*” [16].

Here, we will brief some lattice geometries in which frustration is possible. For lattices such as square lattices (figure 1.8-a), simple cubic lattices, etc., where the ground state is such that each spin is antiparallel to its neighbors, every bond interaction is fully satisfied. However, in the event that both the first nearest neighbor interaction and second nearest neighbor interactions are antiferromagnetic, there is a magnetic frustration. In the case of lattices containing magnetic ions at the vortices of triangles, frustration can occur

(figure 1.8b). The reason is, in such cases, one cannot construct a ground state where all bond interactions are fully satisfied for antiferromagnetic nearest neighbor interaction.

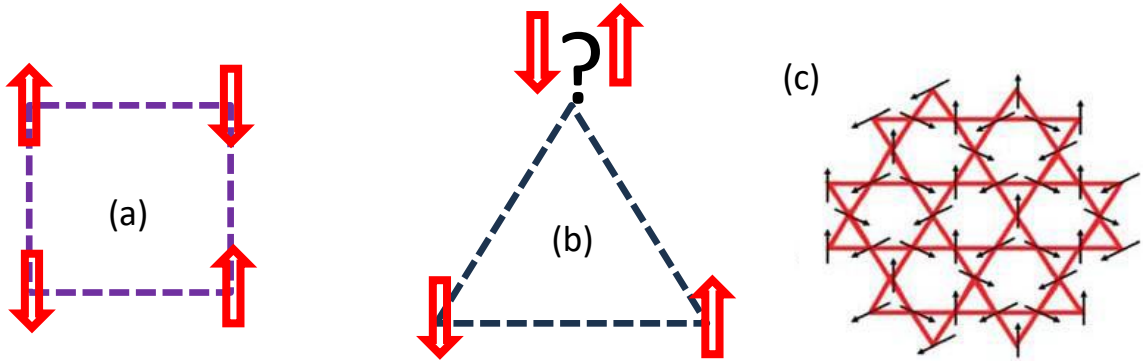


Figure 1.8: (a) Square lattice (b) triangular lattice with nearest neighbor antiferromagnetic interaction. (c) hyper-kagome lattice

Some of the best examples for geometrically frustrated triangular lattice arrangement are: ABO_2 system ($A = \text{Li, Na, Cu, Pd, etc.}$ $B = \text{V, Cr, Co, Mn, etc.}$) [17-19], R_2T_2X ($R = \text{rare earth, T = transition metal, X = Pb, Mg, etc.}$) [18], $A_3BB^*O_6$ ($A = \text{Ca, Sr, B = Co, Cu, Ni, B}^* = \text{Co, Mn, Rh, Ir}$) [20-22], etc. Another example of a frustrated lattice is the kagome lattice (as shown in figure 1.8-c), such as, $ZnCu_3(OH)_6Cl_2$ [23]. 3-dimensional (3D) kagome lattice is called ‘hyper-kagome’ lattice; one compound to our knowledge belonging to this category is $Na_4Ir_3O_8$. [24]. The spinel structure is another class of frustrated lattice structure in 3D [25]. It is possible that the 2D honeycomb lattice may also show frustration, and the magnetism in such systems is dominated by what is known as ‘Kitaev interaction [26]; the prototype example for such a frustrated magnetism is proposed to be Na_2IrO_3 in the literature [27]; this is a vast subject of research in the current literature and it is outside the scope of this thesis to discuss this aspect further. The degree of magnetic frustration (F_m) is measured as [28],

$$F_m = \frac{\theta_p}{|T_N|} \dots\dots\dots (1.4)$$

In some systems, the magnetic frustration is so large that the system can in principle not undergo any magnetic ordering, even when there is a finite intersite magnetic interaction, indicated by a large value of θ_p . Such systems are termed as ‘quantum spin-liquids’. Though many examples have been proposed in the literature, a consensus is yet to be reached for a convincing example for ‘spin liquids.’

In short, geometrically frustrated magnetic systems have been shown to exhibit a variety of magnetic anomalies, most common consequences under discussion in the literature being spin-glass, spin-ice, spin-liquid etc. It is also possible that there is a partial magnetic order and this phenomenon known as ‘partially disordered antiferromagnetism (PDA), has been known among insulators like CsCoCl_3 , $\text{Ca}_3\text{Co}_2\text{O}_6$, $\text{Ca}_3\text{CoRhO}_6$ [29-36]

1.5 Types of exchange interactions

Exchange interactions can be categorized into direct exchange interaction and indirect exchange interaction. Depending upon how these interactions influence magnetic ordering of the magnetic moments, one can observe ferromagnetic, antiferromagnetic, spin glass like, ferrimagnetic properties or a combination of various magnetic properties. These kinds of interactions have been explained, for instance, originally using the Heisenberg model [37], where there is an underlying assumption that the magnetic ions would interact only with their next nearest neighbors and also that these interactions are isotropic in nature. While direct exchange [38,39] and super exchange interaction [40] commonly control magnetic ordering in insulators, indirect exchange interactions, common in metals, can occur between the localized moments via the conduction electrons. The double exchange interaction is also a type of indirect exchange interaction which is seen in oxides containing

the transition metals. This interaction is generally mediated via the partially filled d -shell which is located near the magnetic ion of another element in a crystal structure.

Direct exchange interaction

Direct exchange interaction is seen in materials where there is an overlap of the orbitals of interacting ions. Based on the types of interactions, direct interactions can be categorized into different types as magnetic exchange interaction, van der Waals interaction, chemical exchange interaction, Coulombic exchange interaction, hydrophobic interaction etc. [41] Even though there are many kinds of direct interactions, we would restrict our focus on the magnetic exchange interactions.

In magnetic direct exchange, neighbouring magnetic moments (usually nearest neighbours) interact directly with each other with no intermediary involved in the interaction. There is a direct overlap of the electron wavefunctions and such interactions can give rise to both ferromagnetism and antiferromagnetism in compounds. Direct magnetic exchange interaction is generally seen in materials consisting of transition metals with partially filled d orbitals.

Indirect Exchange interaction

In the indirect exchange interaction, the interaction happens via a mediator which can be a nonmagnetic ion or a ligand in a complex compound. The two magnetic ions which are close to each other can interact via the overlap of the individual wavefunctions with the nonmagnetic mediator. Super-exchange interaction [42-44] and double exchange interaction [44] belong to this class. Ruderman Kittel Kasuya Yosida (RKKY) interaction

discussed below [40] can be also considered as ‘indirect exchange interaction. We try to elaborate each of these interactions in brief.

Superexchange interaction: The superexchange mechanism (figure 1.9) was first proposed by H A Kramers [45] and P W Anderson [46, 47]. In the case of transition metal compounds, generally the metal ions are connected via anions, say for example, oxygen in case of transition metal oxides.

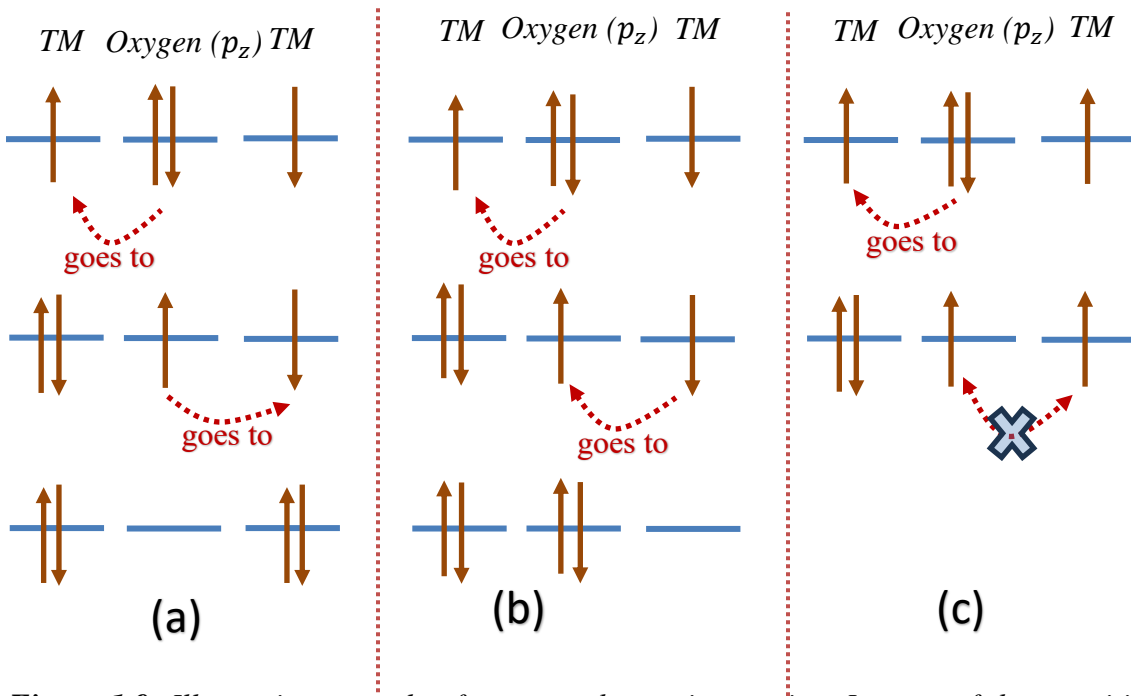


Figure 1.9: Illustrative example of super-exchange interaction. In most of the transition metal complexes, the TM d orbitals are coupled via oxygen $2p$ orbitals; (a) and (b) shows the possible electron hopping in 180° superexchange mechanism for antiferromagnetic arrangements of the transition metal spins and (c) ferromagnetic arrangement of the transition metal spins.

In such cases, the overlap between the wavefunctions of the two nearest transition metals is extremely small. As a result, it is not possible for the transition metals to interact via the direct exchange mechanism. In such cases, the interaction is mediated via hopping of electrons between the transition metal ion and oxygen $2p$ orbitals, since there is a

significant overlap between the d -orbitals of TM and the oxygen $2p$ orbitals. The exchange interaction mediated via the intermediate oxygen atom is called superexchange.

One of the examples of such an interaction has been demonstrated in the case of MnO and MnF_2 , where both these compounds are known to be antiferromagnetic insulators. In these compounds, the oxygen p orbital is located in between two d orbitals from the transition metals ions, (schematic illustration shown in figure 1.9). In such a scenario, if the spins are aligned antiparallely in the d -orbitals, there are two possible ways of two successive hoppings, while, if the spins are aligned parallelly, Pauli's exclusion principle forbids the second hopping, as this principle favours an antiferromagnetic exchange coupling only. In this example, the transition metals and oxygen are located in one line. In case of a 90° geometry, superexchange mechanism would favour a ferromagnetic coupling. Thus, it can be seen that depending on the relative orientation of the electron spins on the two magnetic ions, superexchange interaction can either lead to a ferromagnetic or antiferromagnetic nature of magnetism.

RKKY Interaction: This interaction [40] is seen in metallic compounds, most commonly discussed ones being the rare earth containing metals. In the case of rare earths, the incomplete localized $4f$ -orbital results in a lattice of localised magnetic moments. The $4f$ electrons can hybridize with the conduction band states, forming a complex electronic structure. At the beginning of the rare-earth series the R spin \vec{S}_i localized at the site i interacts with a conduction spin $\vec{S}(\vec{r})$ at position \vec{r} , which leads to a polarization of the spin $\vec{S}(\vec{r})$. This polarization in turn interacts with the spin of the R ion \vec{S}_j at site j , thus leading to an indirect exchange interaction known as the *RKKY* interaction (figure 1.10) between the spins \vec{S}_i and \vec{S}_j . The interaction results in a spatial polarization of conduction band

$$P(r) = -\frac{9\pi n_r^2 N_{at}}{2E_F V} \Gamma \langle S_Z \rangle F(2k_F r) \dots\dots \quad (1.5)$$

Here $P(r)$ is the electronic polarization (not to be confused with the notation for pressure), N_{at} is the total number of atoms in a volume V , n_r is the conduction electron to atom ratio, Γ is the exchange integral between the $4f$ electron and the conduction electrons, E_F is the Fermi energy, k_F is the Fermi wave vector and $\langle S_Z \rangle$ is the expectation value of the spin moment. The function

$$F(2k_F r) = \frac{(2k_F r) \cos(2k_F r) - \sin(2k_F r)}{(2k_F r)^4} \dots\dots \quad (1.6)$$

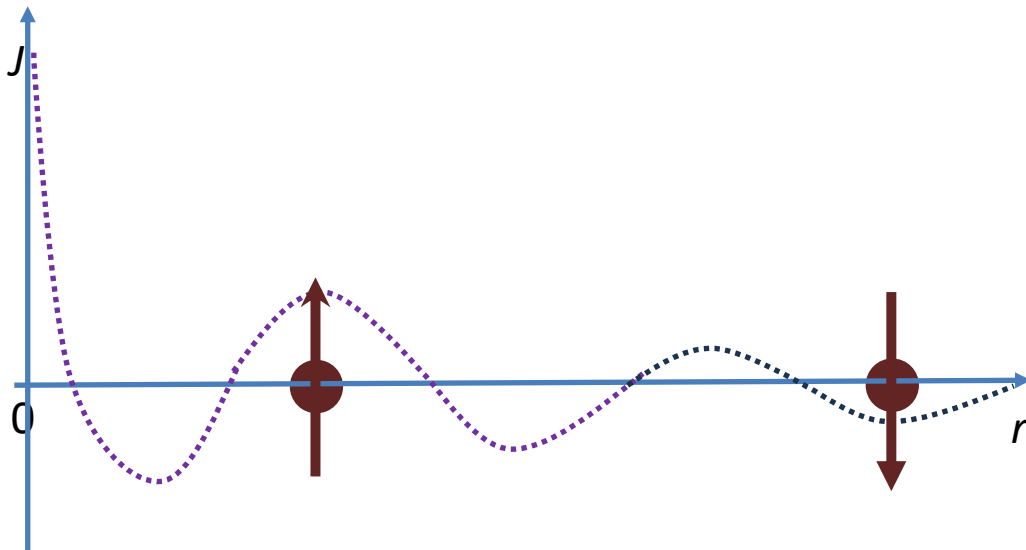


Figure 1.10: Schematic of RKKY interaction. illustrating an oscillatory nature of exchange coefficient with increasing distance, dotted lines represent the direction of polarized conduction electrons.

is oscillatory in space (figure 1.10), and can therefore give rise to positive (ferromagnetic) and negative (antiferromagnetic) interactions between R ions, depending on their interionic distances. The local conduction electron polarization at an R site is a sum $P = \sum_i P(R_i)$ over all magnetic moment sites at distance R_i .

Double exchange interaction: The double exchange interaction [44] is a type of indirect exchange interactions seen in certain types of transition metal oxides with partially filled d orbitals having different oxidation states. In this exchange, an electron gets exchanged between two magnetic centres giving rise to ferromagnetism or antiferromagnetism. An example for such an interaction is a manganese oxide (figure 1.11) in which the Mn e_g orbitals interact via the oxygen $2p$ orbitals. The exchange involves the outermost orbitals for each atom, which are $3d^4$ for Mn^{3+} , $3d^3$ for Mn^{4+} , and $2p^6$ for the O^{2-} . If the oxygen gives its spin 'up' electron to Mn^{4+} , the vacancy can be filled by an electron from Mn^{3+} . In this process an electron has moved between the neighbouring ions while retaining its spin confirming the Hund's rule. This hopping of the electron reduces the overall energy and gives rise to ferromagnetic alignment of neighbouring ions, leading to electrical conductivity.

The double exchange interaction is somewhat similar to that of super exchange interaction, with the following difference between the two interactions. In the case of a superexchange interaction, the alignment of the spins of the two magnetic centers, giving rise to ferromagnetic or antiferromagnetic interactions, can only happen between when the two interacting atoms have the same valency. However, in the case of double exchange, the interaction occurs only when one of the interacting atoms has an extra electron as compared to the other atom involved in the interaction process.

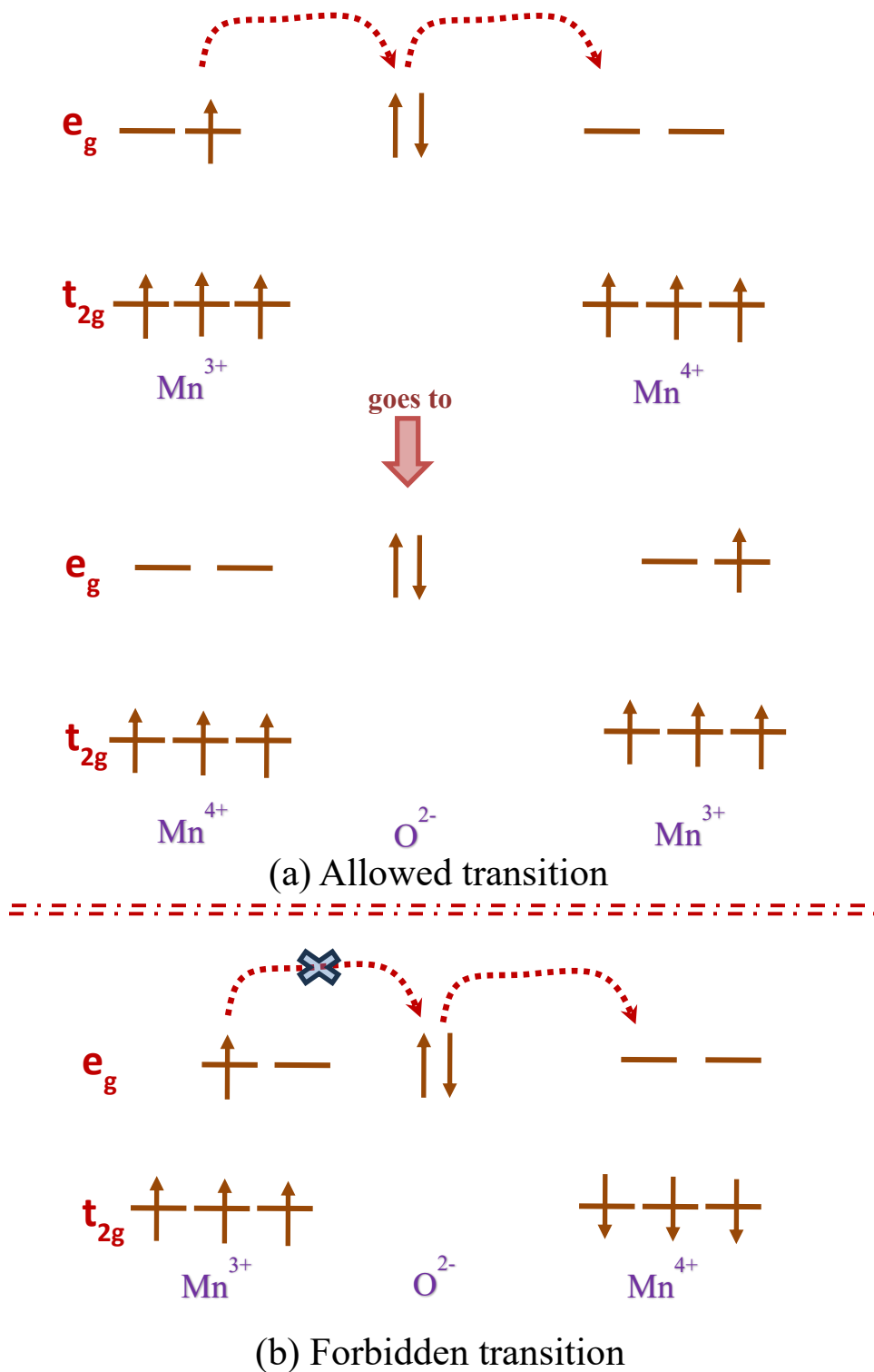


Figure 1.11: Schematic representation of double exchange interaction in an octahedral crystal field. In (a) up electron of O moves to e_g of Mn^{4+} , then up electron in e_g of Mn^{3+} moves to O. (b) movement of the up electron of O is forbidden for retaining the spin confirming Hund's rule.

1.6 Transport properties

1.6.1 Electrical resistance

As far as this property is concerned, since this thesis focuses on intermetallic systems, this part of the discussion is restricted to the behavior of electrical resistivity (ρ) in metallic environment only. The ρ in metals is a sum of the contributions from lattice defects (which is T -independent) and from that due to lattice vibrations (Mattheisen's rule, see e.g., ref. [48]) which is T -dependent, and may be written as

$$\rho = \rho_0 + \rho_{\text{lattice}}(T) \quad \dots\dots\dots 1.7$$

where the first term denotes all the static scattering mechanisms and the second one due to phonons. In the simplest electron-phonon scattering mechanism, where conduction electrons are scattered within the same s -conduction band, the general result for the resistivity contribution due to electron-phonon interactions is given by the Bloch equation [49].

$$\rho_{\text{lattice}}(T) = \frac{\alpha}{Z_A \theta_D} \left(\frac{T}{\theta_D}\right)^5 \int_0^{\theta_D/T} \frac{x^5 dx}{(e^x - 1)(1 - e^{-x})} \quad \dots\dots\dots 1.8$$

Here Z_A is the atomic weight, α is an interaction parameter which is almost constant and θ_D is the Debye temperature. The above expression is obtained under the assumptions that the compound being studied has a spherical Fermi surface completely contained within the first brouillon zone and the Debye phonon spectrum is described by θ_D . In the high temperature limit, the integral reduces to $0.25(\theta_D/T)^4$. Thus, $\rho_{\text{lattice}}(T) \propto T$ at high temperatures, and $\rho_{\text{lattice}}(T) \propto T^5$ at lower temperatures. At very low temperatures ($T \rightarrow 0$), where $\rho_{\text{lattice}} \approx 0$, one may have to consider the effects of electron-electron scattering also, which ideally can lead to T^2 dependence [50] and this is one way to identify electron-

electron interactions. However, this functional form can be modified by the contributions from complicated magnetic ordering.

Now turning to the magnetic-moment containing rare-earth metals, there are additional *magnetic* contributions to ρ due to the scattering of the conduction electrons from thermally disordered localized spins. In the paramagnetic state, this contribution (ρ_{sd}) is therefore also known as the spin-disorder resistivity, say, in the paramagnetic state. With the assumptions of the *RKKY* theory, the electron scattering problem can be solved using the Born approximation [51,52], and one obtains

$$\rho_{sd}(T \gg T_C) = \frac{3\pi m^*}{8\hbar e^2} \Gamma^2 \frac{G}{\vartheta_0 E_F} \dots\dots\dots 1.9$$

where ϑ_0 is the atomic volume, m^* is the effective mass, G is the de Gennes factor (see section 1.8) and Γ is the exchange integral between the $4f$ electron and the conduction electron. Thus, the spin-disorder resistivity (ρ_{sd}) in the paramagnetic regime is temperature independent, and provides a large constant addition to the total ρ of magnetic materials (see fig 1.13). [This spin-disorder contribution scales by the de Gennes factor G in a given R series, to be discussed later].

On magnetic ordering, the spin-disorder contribution to ρ is reduced, and ρ when plotted as a function of T should exhibit a sharp drop/slope change at T_c or T_N (see fig 1.12). In the ordered state ($T \ll T_c$), the spin-disorder resistivity contribution to ρ arises due to the scattering from spin waves or magnons, and the magnetic contribution (ρ_{mag}) is expected to give rise to a temperature dependence which is proportional to T^2 for ferromagnets [53]. [ρ_{sd} can be considered as a terminology of ρ_{mag} in the paramagnetic state].

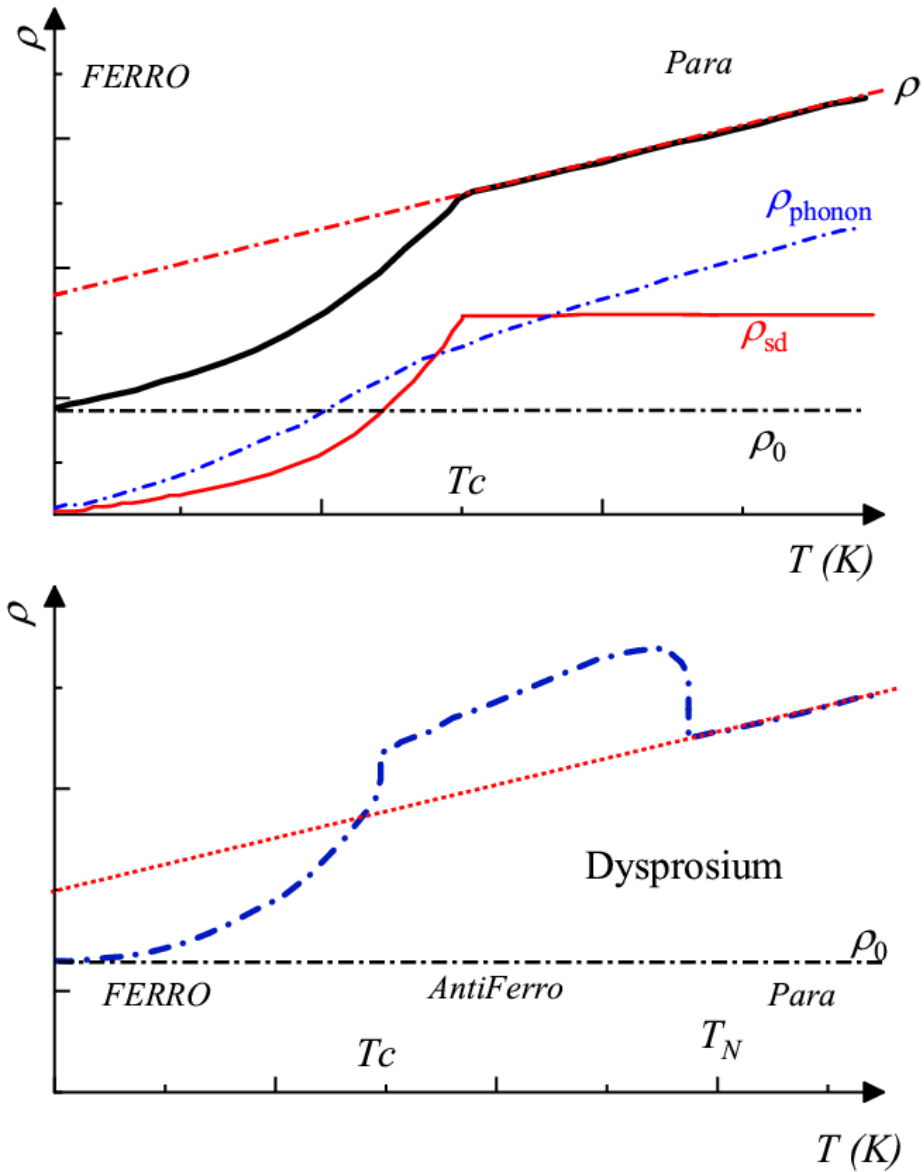


Figure 1.12: Typical temperature dependent ρ behavior in a ferromagnet (upper panel), and the magnetic spin-disorder (ρ_{sd}), static disorder (ρ_0) and lattice ($\rho_{lattice}$) contributions are shown. Lower panel shows c -axis ρ in Dy metal, which is an antiferromagnet with super-zone boundary anomalies below $T_N=178$ K, and a ferromagnetic transition at a lower temperature $T_c=86$ K.

It may be noted that interpretation of experimental ρ is often difficult due to the difficulties in separating out the contributions from several scattering processes. As compared to ferromagnets, in antiferromagnetic R systems such as Dy, Ho etc. [54] the

tendency towards antiparallel spin arrangement below T_N results in a very different and distinctive ρ anomaly (see fig 1.13) in the form of a "hump-backed" curve with a ρ maximum below T_N . This happens due to the additional spin-symmetry of the antiferromagnetic magnetic lattice below T_N . This antiferromagnetism introduces new periodicities in the lattice thereby producing an additional "magnetic" gaps, also known as a *magnetic super zone gaps*. If these super zone gaps lie near E_F , a sharp increase in the resistivity occurs [54], as seen for Dy metal (see fig 1.13) which shows a jump in the c -axis $\rho(T)$ below ($T_N=$) 178 K and another sharp drop upon ferromagnetic ordering below ($T_c=$) 86 K.

1.6.2 Magnetoresistance

The effect of an external magnetic field on the conduction electrons in a metal induces cyclotron-like motion of the electrons due to the action of a Lorentz force. The electrons move along curves given by the intersection of surfaces of constant energy (Fermi surfaces) with planes perpendicular to H [40,55], and this results in a positive MR [defined as $\{\rho(H)-\rho(0)\}/\rho(0)$] also referred to as *classical* (cyclotron-motion induced) MR . A relevant parameter [55] to characterize the resistivity in a field is the dimensionless quantity $\omega_c \zeta$, with,

$$\omega_c \zeta = \frac{l}{r_c} = \frac{H}{\rho_{H=0} n e} \quad \dots\dots\dots (1.10)$$

where l is the electron mean free path, and ζ is the average scattering time, r_c is the cyclotron orbit radius and ω_c is the cyclotron angular frequency. $\omega_c \zeta$ can be varied by changing H , and the following different regimes may be accessed: (i) for $\omega_c \zeta \gg 1$, the electrons complete many orbits before getting scattered, and the field dependence of MR is

determined by the topology of the Fermi surface; it is in this limit (i.e., for "clean" samples at low T , and in high fields) that the MR is significant (a few %); (ii) for $\omega_c \zeta < 1$, the orbits are never completed, and scattering processes dominate the MR . Generally, the magnitude of MR in non-magnetic metals is $\approx 1\%$. The importance of the parameter $\omega_c \zeta$ is further emphasized by the Kohler's rule [55,56] which states that if the scattering processes at the Fermi Surface can be approximated by a single relaxation time, the MR (see eqn. 1.10) should be a function of only $\omega_c \zeta$ (or $H/\rho_{H=0}$). Thus, MR as a function of $H/\rho_{H=0}$ is expected to be a single curve. Although some authors expect the Kohler's rule to be obeyed for a given sample at all temperatures [57,58], however there are contrasting views in the literature [55].

In the case of metals containing magnetic moments, in the paramagnetic region, the application of H suppresses the paramagnetic spin fluctuations (paramagnons), thereby leading to a very small negative MR varying quadratically with H , superimposed over that from classical contribution. However, the MR behavior in magnetically ordered systems is often more complex. For ferromagnets in the ordered state, one expects a small ($\sim 1\%$) negative MR due to suppression of residual spin fluctuations. However, if other phenomena are present, one can see a large value. A classic example is the giant magnetoresistance (GMR) in manganites, in which there is a metal-insulator transition with the ferromagnetism controlled by double-exchange mechanism [59]. Such materials bear immense application potential. For a simple two-sublattice antiferromagnet, a field in the direction of a particular sublattice suppresses these fluctuations in that lattice, but enhances the same in the antiparallel lattice; this combination gives a positive MR which is proportional to H^2 [60]. With the application of magnetic field, however, a spin-flop

metamagnetic transition might also occur, and then the MR should ideally be similar to the ferromagnetic case, leading to negative MR at this transition.

For the antiferromagnets, an additional complication may arise due to the existence of super-zone boundaries (*vide infra*) and resultant Fermi surface gaps [54]. The applied field, due to Zeeman splitting of the bands, may modify these Fermi surface gaps, thereby giving rise to a large negative MR . Thus, the MR in the AF ordered state can have several contributions of possibly different signs due to complications in magnetic ordering.

Usually, for simple *non-magnetic* metals and alloys, longitudinal and transverse magnetoresistances are *positive*. At low magnetic fields, $\Delta\rho \propto H^2$, and at large fields and at low temperature, $\Delta\rho$ tends to saturate. In the *magnetically ordered states*, there are several contributions to the magnetoresistance. Major factors could be changes in the relaxation time due to different parameters (spin fluctuation) or/ and changes in carrier density (due to change in band structure). Amplitude of spin fluctuations gets suppressed when the external magnetic field is applied, thereby reducing ρ of the material. As a result, when the field is small, $\Delta\rho/\rho$ is *negative* and is proportional to respectively H and H^2 for weakly and nearly *ferromagnetic* metals [61]; in the vicinity of the Curie point, $\Delta\rho/\rho$ is proportional to $H^{2/3}$.

1.7 Thermal Properties

1.7.1 Heat Capacity

The heat capacity of an ideal crystalline solid at finite temperatures can be approximated using the Debye model or the Einstein model [39, 63, 64]. Both of these models take into account the vibrational modes of atoms in the solid lattice. The heat capacity increases with

temperature and approaches the Dulong-Petit law [39,64] in the limit of high temperatures, which states that the molar heat capacity of a crystal is $3R$, where R is the gas constant. Heat capacity measurement is important for characterizing the fundamental excitations involved in a phase transition. Phase transitions involving spin, charge, phonons, orbital degrees of freedom, Schottky-like anomalies in doped compounds, electronic levels in correlated systems, etc. can be inferred using the heat capacity measurements. Entropy (S) changes due to a phase transition, can be directly obtained by integrating heat-capacity over temperature, i.e., $C(T)/T$ as a function of temperature. Heat capacity of a simple magnetic-moment containing metal in the paramagnetic state is due to the following contributions: Electronic heat capacity (γ) which arises from the density of states at E_F and lattice heat capacity ($C_{lattice}$) which comes from the thermal vibration of atoms in the metal lattice.

In the magnetically ordered state, there is an additional contribution to the heat capacity from the magnetic moments. This contribution is known as the magnetic heat capacity (C_{4f}). The magnetic part (S_{4f}) of the entropy, derived from C_{4f} , is given by $R \ln(2J+1)$, here R is the gas constant (not to be confused with the notation for rare-earths). Heat-capacity data, being related to J , is a measure of the magnetic moment in the magnetically ordered state. Thus, at temperatures much less than Debye temperature, the magnetic heat capacity can become significant, compared to electronic and lattice parts.

In the case of a ferromagnetic material, at very low temperatures, the temperature dependence of heat capacity is often characterized by $T^{3/2}$ dependence where phonon excitations are limited to low-energy states. In the case of antiferromagnets, the temperature dependence of heat capacity shows a T^3 dependence at low temperatures, and

the behavior is determined primarily by the quantized spin-wave excitations of magnons. There are often deviations from the functional forms due to complexities of magnetism

1.7.2 Magnetocaloric effect (MCE)

Magnetocaloric effect arises from the entropy changes in response to the application of external magnetic field. An external magnetic field usually tends to align the magnetic spins and thus decreases the entropy of the spin system.

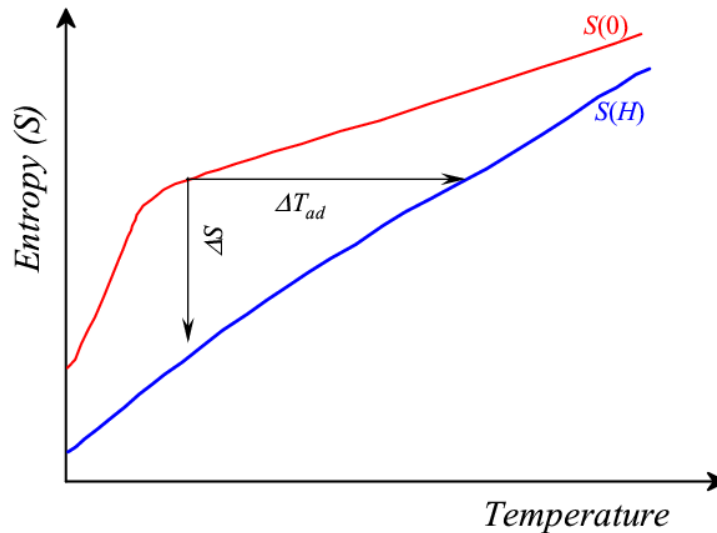


Figure 1.13: A schematic scenario of isothermal entropy change and adiabatic change in temperature when a magnetic field is applied.

MCE has important practical applications in the field of refrigeration due to energy-efficiency and environmental friendliness compared to traditional refrigeration methods that rely on the vapor compression cycle and refrigerant gases. MCE [65] is derived from the isothermal entropy change (ΔS) or the adiabatic temperature (ΔT_{ad}) change by the application or removal of magnetic field. See, figure 1.13 to understand how the entropy

changes when a field is applied. ΔS and ΔT_{ad} are related to M , H , and C and absolute temperature by one of the fundamental Maxwell's relations [66]

$$\left(\frac{\partial S(T,H)}{\partial H}\right)_T = \left(\frac{\partial M(T,H)}{\partial T}\right)_H \quad \dots\dots 1.11$$

$$\Delta S(T_{av}H) = \int_0^H \left(\frac{\partial M(T,H)}{\partial T}\right) dH$$

$$T_{av} = (T_{i+1} + T_i)/2 \quad \dots\dots\dots 1.12$$

Figure 1.13 shows a scenario of changes in entropy when a field is applied. $S(0)$ and $S(H)$ is the total entropy of the material for zero field and applied external magnetic field. It has been shown that in the case of antiferromagnets, the increasing field increases magnetic entropy, while in the case of ferromagnets the increasing field decreases the

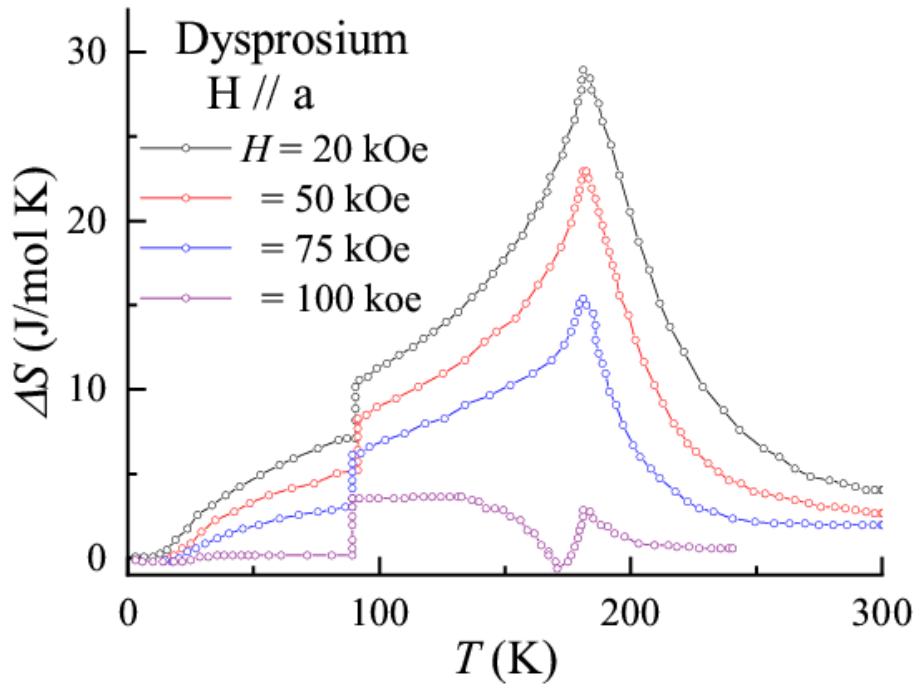


Figure 1.14: Illustrative example of isothermal entropy obtained for single crystalline dysprosium metal [69].

magnetic entropy [67]. Figure 1.14 shows the magnetocaloric effect for a single crystalline Dy metal which is known to order antiferromagnetically around 180 K, followed by a transition from antiferromagnet to ferromagnet at 90 K [68]. Accordingly, the magnetocaloric effect shows a sharp change because of ferromagnetic to antiferromagnetic transition around 90 K followed by a minimum and a negative entropy at 180 K [69].

1.8 Basics of rare-earth based systems

In the case of rare earth elements, the magnetic properties are determined by the incomplete $4f$ shell, which undergoes progressive filling when one traverses from La to Lu, with an electronic configuration given by $[\text{Xe}]4f^n(5d^16s^2)$. Thus, n varies from 0 to 14 from La to Lu. The $5d^16s^2$ electrons participating in chemical bonding impart trivalency for these elements. The incomplete $4f$ orbital in the R -based compounds was historically considered localized well within the ionic core (radius $\approx 0.3\text{\AA}$, being an order of magnitude less than the interatomic spacing) and shielded by filled $5s^2$ and $5p^6$ shells which can be seen in the plot of relative radial extension of various orbitals in the case of Gd (figure 1.15). This initial belief got changed during last few decades for lighter rare earths where manifestations of some degree of delocalization have been found in many physical properties. Various parameters characterizing the free R ions are given in table 1.1. Since the overall crystal-field splitting for rare-earths is around 100 K, the effective moment determined from higher temperatures in the paramagnetic state from the $\chi(T)$ data using Curie-Weiss law in the event $4f$ orbital is strictly localized, is expected to be in agreement with the values listed in the table 1.1. In some alloys, one can get an excess effective moment because of the polarization of the conduction band induced by the $4f$ magnetic

moment. Indirect exchange interactions between these moments usually results in long range magnetic order in metallic systems.

Within RKKY formalism, de Gennes [37] with a molecular field model arrived at an expression for θ_P and ρ_{mag} for rare-earth systems, according to which, θ_P and ρ_{mag} are $\propto (g_J - 1)^2 J(J + 1)$, which is known as the de Gennes factor.

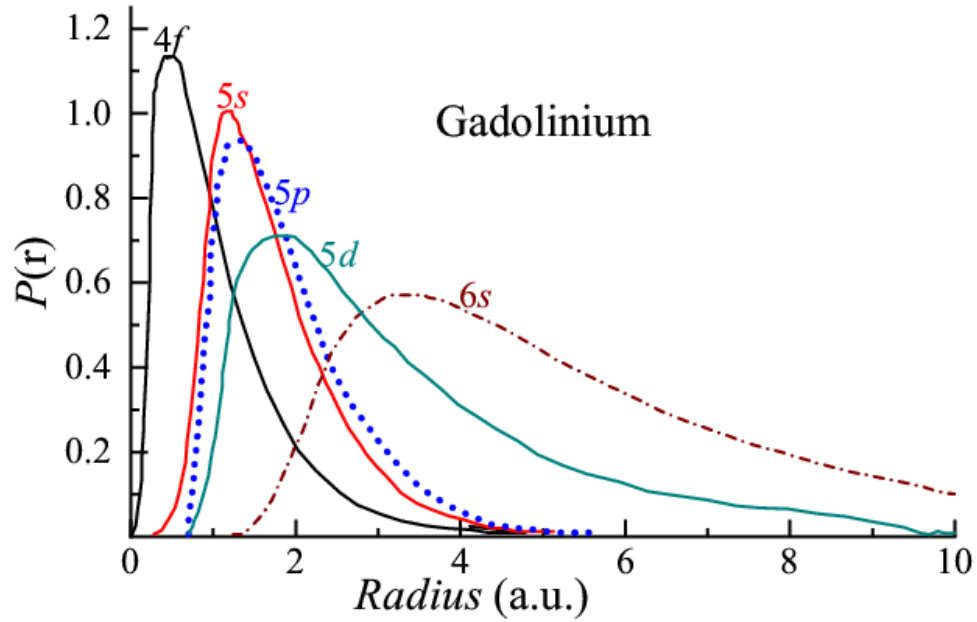


Figure 1.15: Comparison of radial charge distribution of 4f, 5s, 5p, 5d and 6s electrons in Gd atom.

Thus, the magnetic ordering temperature T_0 within a given R series is expected to scale with G , as shown in figure. 1.16. There are often deviations from this general rule due to competing phenomena in the R systems due to some degree of 4f delocalization, particularly at the beginning of a rare-earth series. Further modifications, from de Gennes scaling can occur also by the crystal field splitting of 4f levels [38]. In the case of Gd^{3+} and Eu^{2+} ions, the total orbital angular momentum is zero and hence crystal -field effects can be ignored.

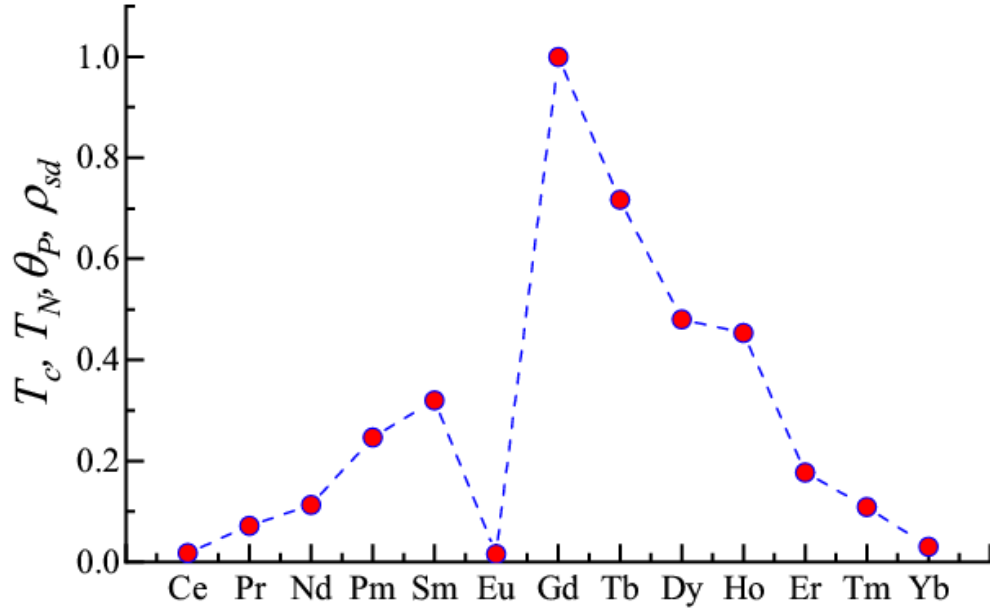


Figure 1.16: Rare earth magnetic ordering temperatures (T_0) and magnetic spin disorder contribution (ρ_{sd}) to electrical resistivity (normalized to the values of Gd) based on the de Gennes model.

1.9 Kondo effect

Experiments performed on dilute magnetic alloys revealed richness in low temperature anomalies, one of them being the Kondo effect [70]. By definition, the Kondo effect results from an antiferromagnetic exchange interaction between the local moment and the conduction electrons and is a *single-ion* effect.

Above a characteristic temperature, called Kondo temperature (T_K), only spin-flip scattering is observed among the impurity spin and the conduction electrons; below T_K , the impurity spins get compensated by the spins of the conduction electrons and a singlet state is formed. The compensation of local moment by the conduction electrons can be thought of as a formation of electron cloud around the impurity spin [71]. An extra peak in the

density of states (DOS) at E_F develops and it is called *Abrikosov-Suhl resonance* (ASR)

[72, 73] or *Kondo resonance* leading to enhancement of γ .

Table 1.1: Some properties of free rare earth ions, like 4f electronic configuration, ground state term symbol spin, orbital and total angular momentum, Lande g factor (g_J), effective magnetic moment and de Gennes factor.

Rare earth Ion	4f configuration	Ground state term	S	L	J	g_J	$g_J\sqrt{J(J+1)}$	g_JJ	de Gennes factor G
La ³⁺ , Ce ⁴⁺ , Y ³⁺	4f ⁰	¹ S ₀	0	0	0	-	0	0	0
Ce ³⁺	4f ¹	² F _{5/2}	1/2	3	5/2	6/7	2.54	2.14	0.011
Pr ³⁺	4f ²	³ H ₄	1	5	4	4/5	3.58	3.20	0.051
Nd ³⁺	4f ³	⁴ I _{9/2}	3/2	6	9/2	8/11	3.62	3.28	0.116
Pm ³⁺	4f ⁴	⁵ I ₄	2	6	4	3/5	2.68	2.40	0.217
Sm ³⁺	4f ⁵	⁶ H _{5/2}	5/2	5	5/2	2/7	0.84	0.72	0.283
Eu ³⁺ Sm ²⁺	4f ⁶	⁷ F ₀	3	3	0	0	0	0	0
Gd ³⁺ Eu ²⁺	4f ⁷	⁸ S _{7/2}	7/2	0	7/2	2	7.94	7	1
Tb ³⁺	4f ⁸	⁷ F ₆	3	3	6	3/2	9.72	9	0.667
Dy ³⁺	4f ⁹	⁶ H _{15/2}	5/2	5	15/2	4/3	10.63	10	0.450
Ho ³⁺	4f ¹⁰	⁵ I ₈	2	6	8	5/4	10.60	10	0.386
Er ³⁺	4f ¹¹	⁴ I _{15/2}	3/2	6	15/2	6/5	9.59	9	0.162
Tm ³⁺	4f ¹²	³ H ₆	1	5	6	7/6	7.57	7	0.074
Yb ³⁺ Tm ²⁺	4f ¹³	² F _{7/2}	1/2	3	7/2	8/7	4.54	4	0.020
Lu ³⁺ Yb ²⁺	4f ¹⁴	¹ S ₀	0	0	0	-	0	0	0

The bench mark of this local interaction is a low temperature upturn in ρ leading to a minimum in the plot of $\rho(T)$. A logarithmic rise in $\rho(T)$ with decreasing temperature was first observed for systems like magnetic Fe impurities in non-magnetic Au/Cu [74]. Kondo [70] used a third order perturbation calculation to reproduce the observed low temperature upturn in $\rho(T)$ behavior.

T_K (generally ranges from few mK to several hundred Kelvin) is identified as the only characteristic energy scale in the single-ion Kondo problem. Though the Kondo effect was first observed mainly in non-magnetic metals containing traces of magnetic transition ions, a behavior associated with the Kondo effect can also occur in rare-earth *compounds* or *concentrated 4f* (also *5f*) impurities [78]. This is because of relatively smaller spatial extension of the *4f* orbital ($\sim 0.5 \text{ \AA}$). Such systems are termed as *Kondo lattices (KL)* or *concentrated Kondo systems (CKS)*. The value of T_K is different for different *CEF* states [75,76]. If the hybridization between the local moment and the conduction electron is reasonably strong, not only the spin but also the electron from the *4f* level can go to the conduction band and come back, giving rise to a phenomenon known as ‘valence fluctuation’ or ‘intermediate valence’. Depending on the strength of hybridization energy $\Delta = \pi V_{kf}^2 N(E_F)$ (V_{kf} is the matrix element that admixes the Ce-*4f* and conduction electron states) with respect to the binding energy (ε_0) of the *4f* level, one can distinguish the different regimes:

- $\Delta \ll \varepsilon_0 \Rightarrow$ stable *4f* shell
- $\Delta < \varepsilon_0 \Rightarrow$ Kondo regime
- $\Delta \geq \varepsilon_0 \Rightarrow$ intermediate valence

The strength of the hybridization Δ depends on the proximity of the $4f$ level to Fermi level. Ce and Yb are very prone to the Kondo effect and intermediate valence because the mixing is energetically favorable for these compounds. It is found that Pr and Sm [77, 78] show Kondo effect occasionally, under favorable conditions. But for other heavy rare earths, hybridization is almost negligible due to deeply localized nature of the $4f$ orbital.

Due to the hybridization, enhanced linear coefficient of heat capacity compared to normal metals results in the Kondo systems at low temperatures is observed. For Kondo systems, MR is negative and the magnitude of $\rho(T)$ decreases monotonically with increasing magnetic fields and decreasing temperature. The negative $\Delta\rho/\rho$ arises from the suppression of the Kondo spin fluctuations by the application of magnetic field.

Since in Kondo lattices, there is an enhanced DOS at E_F due to Abrikosov-Suhl, or Kondo resonance electronic effective mass (m^*) becomes very large. Therefore, KL systems are also referred to as *heavy fermions (HF)* [79, 80]. Though thermodynamic properties of HF are similar to that of single ion impurities, the electrical transport behavior at low temperatures is quite different. The $\rho(T)$ behavior of (non-magnetic) KL s is schematically shown in figure 1.17. A drop is observed below a characteristic temperature, called T_{coh} , due to coherent scattering among the Kondo impurities, in the Kondo lattices.

Sometimes T_{coh} and T_K are related by a simple scaling factor [81, 82] but not always true. Rough estimation of Kondo temperature may be obtained from the value of θ_p ($T_K \sim \theta_p/n$ where $n = 2$ to 6 , [83]). In short, the non-magnetic KL are expected to obey the Landau Fermi liquid (FL) behaviour [84], not only in heat capacity, but also in magnetic

susceptibility leading to enhance Pauli contribution (χ_0) that is $\gamma \propto \chi_0 \propto A$, where A is the coefficient of T^2 term in resistivity.

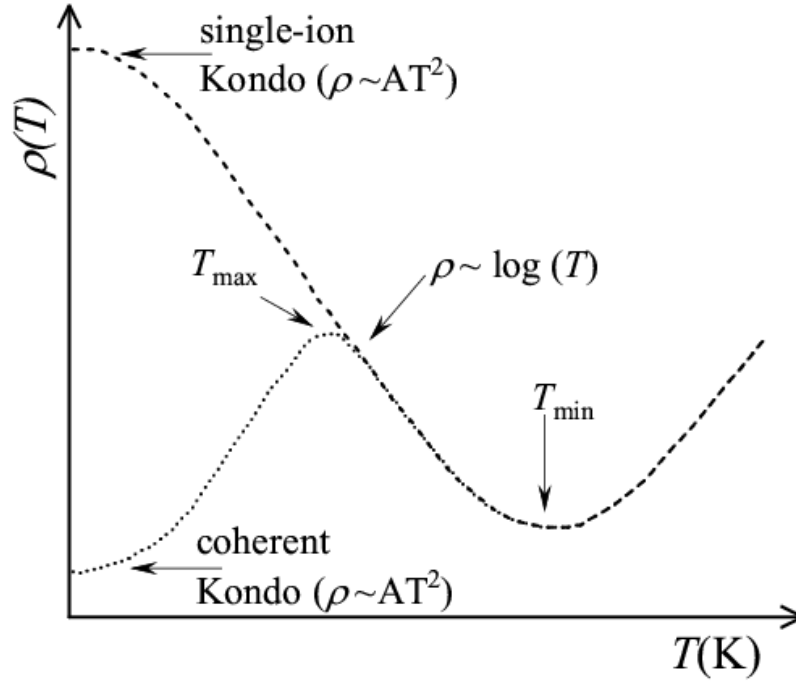


Figure 1.17: Schematic representation of the temperature dependence of electrical resistivity of single-ion Kondo and Kondo lattice systems.

Finally, it may be mentioned that, due to large concentrations of magnetic centres in the Kondo lattices, the Kondo interaction and the RKKY interaction can compete, leading to features in the properties attributable to both the Kondo effect and magnetic ordering. This can be tuned by varying chemical and external pressures. The physics of Kondo lattices on the verge of losing magnetic ordering, that is quantum critical point, is known to lead to complications in properties called ‘non-fermi liquid behaviour’. Since this modern topic is not being studied for this thesis, this aspect will not be elaborated further here.

1.10 Antimicrobial and Therapeutic applications.

In the field of biomedicine, antibiotics have been crucial in the treatment of bacterial infections [85]. During the “golden era” in antimicrobial research, almost all groups of important antibiotics (cephalosporins, tetracyclines, aminoglycosides and macrolides) were discovered and the main problems of chemotherapy were solved around 1960s. Over a period of time some antibiotics appear to be rendered useless due to the emergence of “superbugs” which show resistance to even various combinations of the widely used antibiotics, thus making available treatments ineffective [86, 87]. The impact of drug resistance is considerable with treatment failures associated with multidrug-resistant bacteria and it has become a global concern to public health. Hence it has been imperative to study and discover new antibiotics. Natural products are still one of the major sources of new drug molecules today, which are derived from prokaryotic bacteria, eukaryotic microorganisms, plants and various animal organisms. These microbial and plant products occupy the major part of the antimicrobial compounds in the field of biomedicine. Meanwhile, metal complexes to be used as antibiotics have only a niche presence in biomedical field, even though some compounds like cisplatin, have been shown to have profound impact for treatment of cancer and still being used extensively in cancer treatments. In addition, platinum-based chemotherapeutics are used widely in majority of cancer treatments [88]. The gold-containing auranofin is an approved drug used for the treatment of rheumatoid arthritis and is currently under investigation for its anticancer as well as antimicrobial properties [89-94]. Metal complexes have been largely been ignored for antibiotic development even when these compounds have access to unique modes of action and exist in a wider range of three-dimensional geometries than purely organic

compounds. Such properties make these compounds interesting for the development of new drugs. Study in this field has now extended other elements as well in the past few decades, with complexes of titanium, iron, ruthenium, gallium, palladium, silver, gold, bismuth, and copper being widely used for development of biomedicine for treatment from anticancer to antimalaria over to neurodegenerative diseases and has been subjected to variety of clinical trials [95-109].

Recently bimetallic nanoparticles have also attracted some attention because of their unique optical, electronic, magnetic, and catalytic properties, which, are significantly distinguishable from their monometallic counterparts in many cases. In many of these nanoparticles a synergistic antibacterial effect is being targeted. Ag–Cu, Ag–Au, Fe–Ag, and Cu–Ni complexes have been studied to understand their antibacterial efficiency [101-109]. There is no literature which focuses on the antimicrobial properties of ternary and quaternary compounds, particularly the ones carrying magnetism and it is worthwhile to focus the studies on such compounds to see if they have potential applications in the field of biomedicine.

1.11 Thrust of the thesis

Even though a lot of research has been published on compounds containing the rare-earth and transition metals, many novel behaviors emerge even today on new materials. While Ce, Eu and Yb compounds have been attracting attention for the past five decades due to some degree of $4f$ delocalization, those rare-earths containing strictly localized $4f$ electrons attracted less attention from the angle of new concepts. However, recent advances suggest the magnetism of such compounds have not been completely understood. Therefore, there is a need to probe those rare-earth materials not paid much attention in the past literature.

Understanding various magnetic interactions and in turn the properties exhibited by these compounds can offer inputs for various industrial, technological and biomedical applications. Thus, our study focusses on those materials (both intermetallic and oxides), which have not been paid much attention in the existing literature, with the intention of sowing seed to discover new materials for medical applications. The magnetic and transport properties of these compounds were studied for the aim of this thesis in bulk polycrystalline form and also to understand the effects of particle size reduction on their magnetic properties, at least for some cases. The main measurement techniques are ac and dc magnetization, electrical and magnetoresistance and heat-capacity, depending on the material under study. We also tried to study the antibacterial properties of these compounds to ascertain if their properties can be useful for biomedical applications.

Chapter 2 focuses on the details of the various measurement techniques which have been employed for the study of various properties exhibited by these compounds.

Chapter 3 focuses on the magnetic and transport properties of the intermetallic family having a general formula $R_2(TM)X_3$ (R = rare-earth, TM = transition-metal, X = silicon/germanium), derived from AlB_2 - type hexagonal structure [109, 110]. These compounds have been of great interest, considering the fact that properties exhibited by many of them bear relevance to current trends in the field of magnetism and superconductivity [111]. This structure is of honey-comb type, in which T-Si (Ge) layers are sandwiched by R layers. R ions form triangular lattice, thereby favoring geometrically frustrated magnetism. Considerable work has been carried out in the literature in the past few decades on this family of compounds, and yet many new properties keep emerging [112-115]. In this

Chapter, the results of the measurements on the bulk polycrystalline forms of some heavy rare-earth members of the family having general formula R_2RhSi_3 (namely for $R = Nd, Er$) are reported, one (Nd) in which $4f$ level is expected to be closer and, in another case, (Er) far away from the Fermi level having relatively less contributions in the conduction band. The results bring out hitherto unknown magnetic anomalies for these compounds.

Chapter 4 focuses on the study of the magnetic and transport properties of a few compounds (Ho_4PtAl , Er_4PtAl and Dy_4RhAl) belonging to the families R_4PtAl [117] and R_4RhAl [116], which are characterized by interesting structural features in particular, the presence of three sites for R leading to exotic magnetic and transport anomalies in all the compounds reported within these families. The present results add value to a systematic understanding of magnetic and transport anomalies, due to competing magnetic interactions in these families. Such studies on rare-earth materials with multiple sites for R are rare in literature.

Chapter 5 focuses on the spin-chain compound of the type, R_2BaNiO_5 , [117-135] which have been known to be exotic with respect to magnetism for the past few decades. But these compounds being centrosymmetric, are of special interest due to multiferroic anomalies reported in recent years. Our focus is to study the effects of external hydrostatic pressure and chemical pressure caused by the isoelectronic doping at Ba site by Sr on the magnetic properties of one of the exotic multiferroic compound Tb_2BaNiO_5 , and to study the effects of external hydrostatic pressure on the Co analogue, Tb_2BaCoO_5 .

Chapter 6 focuses on the study particle size reduction on the magnetic and thermal properties of the compounds in the $R_2\text{RhSi}_3$ and $R_4(TM)\text{Al}$ families, in addition to studying the antibacterial and antifungal properties of these compounds in bulk and nano forms. This work is of importance, since most of the study of efficacy is concentrated either on the d block transition metal elements or to some extent on the bimetallic compounds [136-140]. This work serves as a seed for further work, for potential medical applications, of nanoform rare-earth intermetallics.

1.12 Bibliographical references

1. Buschow K. Intermetallic compounds of rare earths and non-magnetic metals. Reports on Progress in Physics. 1979 Aug 1; 42(8):1373.
2. Coronado, E., Tsukerblat, B.S., Georges, R. (1996). Exchange Interactions I: Mechanisms. In: Coronado, E., Delhaès, P., Gatteschi, D., Miller, J.S. (eds) Molecular Magnetism: From Molecular Assemblies to the Devices. NATO ASI Series, vol 321. 1996 Jan 1; 65–84.
3. Hurd CM. Varieties of magnetic order in solids. Contemporary Physics. 1982 Sep 1; 23(5):469-93.
4. Landau, L. D., & Lifshitz, E. M. Statistical Physics: Volume 2, Theory of the Condensed State. . (1980). Butterworth-Heinemann
5. Yamaguchi Y, Nakano T, Nozue Y, Kimura T. Magnetoelectric Effect in an X Y-like Spin Glass System $\text{Ni}_x\text{Mn}_{1-x}\text{TiO}_3$. Physical Review Letters. 2012 Jan 30; 108(5):057203.
6. Binder K, Young AP. Spin glasses: Experimental facts, theoretical concepts, and open questions. Reviews of Modern physics. 1986 Oct 1; 58(4):801.

7. Mydosh JA. Spin glasses: an experimental introduction. CRC Press; 1993 May 13.
8. Mulder CA, AJ vanDuyneveldt, and JA Mydosh. Phys. Rev. B. 1981; 23(1384):31.
9. Shtrikman S, Wohlfarth EP. The theory of the Vogel-Fulcher law of spin glasses. Physics Letters A. 1981 Oct 19; 85(8-9):467-70.
10. Souletie J, Tholence JL. Critical slowing down in spin glasses and other glasses: Fulcher versus power law. Physical Review B. 1985 Jul 1; 32(1):516.
11. Suzuki IS, Suzuki M. Stretched-exponential relaxation in the three-dimensional short-range Ising spin-glass $\text{Cu}_{0.5}\text{Co}_{0.5}\text{Cl}_2\text{-FeCl}_3$ graphite bi-intercalation compound. Physical Review B. 2008 Dec 3; 78(21):214404.
12. Shvartsman VV, Bedanta S, Borisov P, Kleemann W, Tkach A, Vilarinho PM. (Sr, Mn) TiO_3 : A Magnetoelectric Multiglass. Physical review letters. 2008 Oct 16; 101(16):165704.
13. Jahn HA, Teller E. Stability of polyatomic molecules in degenerate electronic states—I—Orbital degeneracy. Proceedings of the Royal Society of London. Series A-Mathematical and Physical Sciences. 1937 Jul 15; 161(905):220-35.
14. Vannimenus J, Toulouse G. Theory of the frustration effect. II. Ising spins on a square lattice. Journal of Physics C: Solid State Physics. 1977 Sep 28; 10(18):L537.
15. Blundell S. Magnetism in condensed matter. OUP Oxford; 2001 Oct 5.
16. Ramirez AP. Strongly geometrically frustrated magnets. Annual Review of Materials Science. 1994 Aug; 24(1):453-80.
17. Takatsu H, Yoshizawa H, Yonezawa S, Maeno Y. Critical behavior of the metallic triangular-lattice Heisenberg antiferromagnet PdCrO_2 . Physical Review B. 2009 Mar 24; 79(10):104424.

18. Mazin II. Electronic structure and magnetism in the frustrated antiferromagnet LiCrO_2 : First-principles calculations. *Physical Review B*. 2007 Mar 6; 75(9):094407.
19. Onoda M. Geometrically frustrated triangular lattice system Na_xVO_2 : superparamagnetism in $x=1$ and trimerization in $x \approx 0.7$. *Journal of Physics: Condensed Matter*. 2008 Mar 18; 20(14):145205.
20. Whangbo MH, Dai D, Koo HJ, Jovic S. Investigations of the oxidation states and spin distributions in $\text{Ca}_3\text{Co}_2\text{O}_6$ and $\text{Ca}_3\text{CoRhO}_6$ by spin-polarized electronic band structure calculations. *Solid state communications*. 2003 Feb 1; 125(7-8):413-7.
21. Aasland S, Fjellvåg H, Hauback B. Magnetic properties of the one-dimensional $\text{Ca}_3\text{Co}_2\text{O}_6$. *Solid state communications*. 1997 Jan 1; 101(3):187-92.
22. Rayaprol S, Sengupta K, Sampathkumaran EV. Magnetic frustration in the stoichiometric spin-chain compound $\text{Ca}_3\text{CoIrO}_6$. *Physical Review B*. 2003 May 19; 67(18):180404.
23. Pati SK, Rao CN. Kagome network compounds and their novel magnetic properties. *Chemical communications*. 2008(39):4683-93.
24. Helton JS, Matan K, Shores MP, Nytko EA, Bartlett BM, Yoshida Y, Takano Y, Suslov A, Qiu Y, Chung JH, Nocera DG. Spin dynamics of the spin-1/2 kagome lattice antiferromagnet $\text{ZnCu}_3(\text{OH})_6\text{Cl}_2$. *Physical review letters*. 2007 Mar 9; 98(10):107204.
25. Okamoto Y, Nohara M, Aruga-Katori H, Takagi H. Spin-liquid state in the $S=1/2$ hyperkagome antiferromagnet $\text{Na}_4\text{Ir}_3\text{O}_8$. *Physical review letters*. 2007 Sep 27; 99(13):137207.

26. Kitaev A. Anyons in an exactly solved model and beyond. *Annals of Physics*. 2006 Jan 1; 321(1):2-111.
27. Tristan N, Hemberger J, Krimmel A, Von Nidda HK, Tsurkan V, Loidl A. Geometric frustration in the cubic spinels MAl_2O_4 (M= Co, Fe, and Mn). *Physical Review B*. 2005 Nov 1; 72(17):174404.
28. Ramirez AP, Hayashi A, Cava RJ, Siddharthan R, Shastry BS. Zero-point entropy in 'spin ice'. *Nature*. 1999 May 27; 399(6734):333-5.
29. Mekata M. Antiferro-ferrimagnetic transition in triangular Ising lattice. *Journal of the Physical Society of Japan*. 1977 Jan; 42(1):76-82.
30. Yelon WB, Cox DE, Eibschütz M. Magnetic ordering in CsCoBr_3 . *Physical Review B*. 1975 Dec 1; 12(11):5007.
31. Niitaka S, Kageyama H, Kato M, Yoshimura K, Kosuge K. Synthesis, crystal structure, and magnetic properties of new one-dimensional oxides $\text{Ca}_3\text{CoRhO}_6$ and $\text{Ca}_3\text{FeRhO}_6$. *Journal of Solid State Chemistry*. 1999 Aug 1;146(1):137-43. Niitaka S, Kageyama H, Yoshimura K, Kosuge K, Kawano S, Aso N, Mitsuda A, Mitamura H, Goto T. High-field magnetization and neutron diffraction studies of one-dimensional compound $\text{Ca}_3\text{CoRhO}_6$. *Journal of the physical society of japan*. 2001 May; 70(5):1222-5.
32. Sampathkumaran EV, Niazi A. Superparamagnetic-like ac susceptibility behavior in the partially disordered antiferromagnetic compound $\text{Ca}_3\text{CoRhO}_6$. *Physical Review B*. 2002 Apr 22; 65(18):180401.

33. Kageyama H, Yoshimura K, Kosuge K, Mitamura H, Goto T. Field-induced magnetic transitions in the one-dimensional compound $\text{Ca}_3\text{Co}_2\text{O}_6$. *Journal of the Physical Society of Japan*. 1997 Jun 1; 66(6):1607-10.
34. Maignan A, Michel C, Masset AC, Martin C, Raveau B. Single crystal study of the one-dimensional CaCoO compound: five stable configurations for the Ising triangular lattice. *The European Physical Journal B-Condensed Matter and Complex Systems*. 2000 Jun; 15(4):657-63.
35. Rayaprol S, Sengupta K, Sampathkumaran EV. Magnetic behaviour of quasi-one-dimensional oxides, $\text{Ca}_3\text{Co}_{1+x}\text{Mn}_{1-x}\text{O}_6$. *Solid state communications*. 2003 Oct 1; 128(2-3):79-84.
36. Levy F, Sheikin I, Berthier C, Horvatić M, Takigawa M, Kageyama H, Waki T, Ueda Y. Field dependence of the quantum ground state in the Shastry-Sutherland system $\text{SrCu}_2(\text{BO}_3)_2$. *Europhysics Letters*. 2008 Feb 29; 81(6):67004.
37. De Gennes PG. Interactions indirectes entre couches 4f dans les métaux de terres rares. *Journal de Physique et le Radium*. 1962 Aug 1; 23(8-9):510-21.
38. Seitz F, Turnbull D. *Solid state physics*. Academic Press; 1960.
39. Kittel C, McEuen P. *Introduction to solid state physics*. John Wiley & Sons; 2018.
40. Ruderman MA, Kittel C. Indirect exchange coupling of nuclear magnetic moments by conduction electrons. *Physical Review*. 1954 Oct 1; 96(1):99
Kasuya T. A theory of metallic ferro-and antiferromagnetism on Zener's model. *Progress of theoretical physics*. 1956 Jul 1; 16(1):45-57.
Yoshida K. Thermally assisted MRAM. *Phys. Rev. B*. 1957; 106(5):893.
41. Jacobs IS, Bean CP, Rado GT, Suhl H. *Magnetism III*. New York: Academic. 1963.

42. Anderson PW. Antiferromagnetism. Theory of superexchange interaction. *Physical Review*. 1950 Jul 15; 79(2):350.
43. Kramers HA. L'interaction entre les atomes magnétogènes dans un cristal paramagnétique. *Physica*. 1934 Jan 1; 1(1-6):182-92.
44. Zener C. Interaction between the d-shells in the transition metals. II. Ferromagnetic compounds of manganese with perovskite structure. *Physical Review*. 1951 May 1; 82(3):403.
45. Gardner JS. Geometrically frustrated magnetism. *Journal of Physics: Condensed Matter*. 2011 Apr 27; 23(16):160301.
46. Freeman AJ, Nesbet RK, Watson RE. Two-Electron Heisenberg Exchange Interaction between Neighboring Atoms. *Physical Review*. 1962 Mar 15; 125(6):1978.
47. Anderson PW. New approach to the theory of superexchange interactions. *Physical Review*. 1959 Jul 1; 115(1):2.
48. Ashcroft NW. ND Mermin *Solid State Physics* Saunders College. Philadelphia, PA, USA. 1976; 491.
49. Kadanoff LP, Götze W, Hamblen D, Hecht R, Lewis EA, Palciauskas VV, Rayl M, Swift J, Aspnes D, Kane J. Static phenomena near critical points: theory and experiment. *Reviews of Modern Physics*. 1967 Apr 1; 39(2):395
- Ma SK. *Modern theory of critical phenomena*. Routledge; 2018 May 4.
50. Kasuya T. Effects of s-d Interaction on Transport Phenomena. *Progress of theoretical physics*. 1959 Aug 1; 22(2):227-46.

51. Kasuya T. Electrical resistance of ferromagnetic metals. *Progress of Theoretical Physics*. 1956 Jul 1; 16(1):58-63.
52. De Gennes PG, Friedel J. Anomalies de résistivité dans certains métaux magnétiques. *Journal of Physics and Chemistry of Solids*. 1958 Jan 1; 4(1-2):71-7.
53. Mannari I. Electrical resistance of ferromagnetic metals. *Progress of Theoretical Physics*. 1959 Sep 1; 22(3):335-43.
Kasuya T. Effects of s-d Interaction on Transport Phenomena. *Progress of theoretical physics*. 1959 Aug 1; 22(2):227-46.
54. Elliott R, editor. *Magnetic properties of rare earth metals*. Springer Science & Business Media; 2013 Jun 29.
55. Pippard AB. *Magnetoresistance in metals*. Cambridge university press; 1989 Jan 26.
56. Verbanck G, Temst K, Mae K, Schad R, Van Bael MJ, Moshchalkov VV, Bruynseraede Y. Large positive magnetoresistance in Cr/Ag/Cr trilayers. *Applied physics letters*. 1997 Mar 17; 70(11):1477-9.
57. Ziman JM. *Electrons and phonons: the theory of transport phenomena in solids*. Oxford university press; 2001.
58. Verbanck G, Temst K, Mae K, Schad R, Van Bael MJ, Moshchalkov VV, Bruynseraede Y. Large positive magnetoresistance in Cr/Ag/Cr trilayers. *Applied physics letters*. 1997 Mar 17; 70(11):1477-9.
59. Dagotto E, Hotta T, Moreo A. Colossal magnetoresistant materials: the key role of phase separation. *Physics reports*. 2001 Apr 1; 344(1-3):1-53.

60. Dagotto E, Hotta T, Moreo A. Colossal magnetoresistant materials: the key role of phase separation. *Physics reports*. 2001 Apr 1; 344(1-3):1-53.
61. Ueda K. Effect of magnetic field on spin fluctuations in weakly ferromagnetic metals. *Solid State Communications*. 1976 Aug 1; 19(10):965-8.
62. Yamada H, Takada S. On the electrical resistivity of antiferromagnetic metals at low temperatures. *Progress of Theoretical Physics*. 1974 Oct 1; 52(4):1077-93.
63. Magnus A. Die spezifische Wärme des Platins und des Diamanten bei hohen Temperaturen. *Annalen der Physik*. 1915; 353(23):983-1004.
64. Gopal E. Specific heats at low temperatures. Springer Science & Business Media; 2012 Dec 6.
65. V.K. Pecharsky, K.A. Gschneidner. Magnetocaloric Effect. Elsevier eBooks. 2005 Jan 1;236–44
66. Maxwell, James C. Cambridge Philosophical Society Transactions: 27–83. 1855-56.
67. Gschneidner Jr KA, Pecharsky VK. Magnetocaloric materials. *Annual review of materials science*. 2000 Aug; 30(1):387-429.
68. Gschneidner KA, Bunzli JC, Pecharsky VK, editors. Handbook on the physics and chemistry of rare earths. Elsevier; 2005 Mar 9.
69. Chernyshov AS, Tsokol AO, Tishin AM, Gschneidner Jr KA, Pecharsky VK. Magnetic and magnetocaloric properties and the magnetic phase diagram of single-crystal dysprosium. *Physical Review B*. 2005 May 23; 71(18):184410.
70. Kondo J. Resistance minimum in dilute magnetic alloys. *Progress of theoretical physics*. 1964 Jul 1; 32(1):37-49.

71. Schlottmann P. Some exact results for dilute mixed-valent and heavy-fermion systems. *Physics Reports*. 1989 Sep 1; 181(1-2):1-19.
72. Abrikosov AA. Electron scattering on magnetic impurities in metals and anomalous resistivity effects. *Physics Physique Fizika*. 1965 Sep 1; 2(1):5.
73. Suhl H. Paramagnetic impurities in metals at finite temperatures. *Physics Physique Fizika*. 1965 Sep 1; 2(1):39.
74. De Haas WJ, De Boer J, Van den Berg GJ. The electrical resistance of gold, copper and lead at low temperatures. *Physica*. 1934 May 1; 1(7-12):1115-24.
75. Coqblin B, Schrieffer JR. Exchange interaction in alloys with cerium impurities. *Physical Review*. 1969 Sep 10; 185(2):847.
76. Cornut B, Coqblin B. Influence of the crystalline field on the Kondo effect of alloys and compounds with cerium impurities. *Physical Review B*. 1972 Jun 1; 5(11):4541.
77. Kalkowski G, Sampathkumaran EV, Laubschat C, Domke M, Kaindl G. Screening channels in 4f photoemission from light rare earth compounds. *Solid state communications*. 1985 Sep 1; 55(11):977-9.

Kucherenko Y, Finken M, Molodtsov SL, Heber M, Boysen J, Laubschat C, Behr G. Giant hybridization effects in 4 f photoemission spectra of Pr and Nd transition-metal compounds. *Physical Review B*. 2002 Apr 12; 65(16):165119.
78. Gschneidner KA, Bunzli JC, Pecharsky VK. *Handbook on the physics and chemistry of rare earths: optical spectroscopy*. Elsevier; 2011 Sep 22.
79. Stewart SG. Heavy-fermion systems. *Reviews of Modern Physics*. 1984 Oct 1; 56(4):755.

80. Hewson AC. The Kondo problem to heavy fermions. Cambridge university press; 1997 Apr 28.
81. Leopoldo Maximo Falicov, Hanke W, M. Brian Maple. Valence Fluctuations in Solids. North Holland; 1981.
82. Coleman P. 1 N expansion for the Kondo lattice. Physical Review B. 1983 Nov 1; 28(9):5255.
83. Brewer DF. Progress in low temperature physics. Elsevier; 1986 Sep 1.
84. Nozieres P. A “Fermi-liquid” description of the Kondo problem at low temperatures. In Basic Notions Of Condensed Matter Physics 2018 Mar 9 (pp. 441-452). CRC Press.
85. Nauc ler P, Huttner A, Van Werkhoven CH, Singer M, Tattevin P, Einav S, T ngd n T. Impact of time to antibiotic therapy on clinical outcome in patients with bacterial infections in the emergency department: implications for antimicrobial stewardship. Clinical Microbiology and Infection. 2021 Feb 1; 27(2):175-81.
86. Truman A. Antibiotics: Past, present and future Matthew I Hutchings, Andrew W Truman 2 and Barrie Wilkinson 2. Curr. Opin. Microbiol. 2019; 51:72-80.
87. Mehta G, Sengupta S, Pabbaraja S. Natural products from human microbiome: an emergent frontier in organic synthesis and drug discovery. Organic & Biomolecular Chemistry. 2024.
88. Johnstone TC, Suntharalingam K, Lippard SJ. The next generation of platinum drugs: targeted Pt (II) agents, nanoparticle delivery, and Pt (IV) prodrugs. Chemical reviews. 2016 Mar 9; 116(5):3436-86.

89. Champion GD, Graham GG, Ziegler JB. Chrysotherapy, treatment with gold-based drugs. *Ballieres Clin. Rheumatol.* 1990; 4: 491-534.
90. Kean WF, Kean IR. Clinical pharmacology of gold. *Inflammopharmacology.* 2008 Jun; 16(3):112-25.
91. Barnard PJ, Berners-Price SJ. Targeting the mitochondrial cell death pathway with gold compounds. *Coordination Chemistry Reviews.* 2007 Jul 1; 251(13-14):1889-902.
92. Mirzadeh N, Reddy TS, Bhargava SK. Advances in diphosphine ligand-containing gold complexes as anticancer agents. *Coordination Chemistry Reviews.* 2019 Jun 1; 388:343-59.
93. Harbut MB, Vilchèze C, Luo X, Hensler ME, Guo H, Yang B, Chatterjee AK, Nizet V, Jacobs Jr WR, Schultz PG, Wang F. Auranofin exerts broad-spectrum bactericidal activities by targeting thiol-redox homeostasis. *Proceedings of the National Academy of Sciences.* 2015 Apr 7; 112(14):4453-8.
94. Wu B, Yang X, Yan M. Synthesis and structure–activity relationship study of antimicrobial auranofin against ESKAPE pathogens. *Journal of medicinal chemistry.* 2019 Aug 6; 62(17):7751-68.
95. ClinicalTrials.gov a Database of Privately and Publicly Funded Clinical Studies Conducted around the World. Available online: www.clinicaltrials.gov (accessed on 5 December 2019).
96. Biot C, Nosten F, Fraisse L, Ter-Minassian D, Khalife J, Dive D. The antimalarial ferroquine: from bench to clinic. *Parasite: journal de la Société Française de Parasitologie.* 2011 Aug; 18(3):207.

97. Monro S, Colon KL, Yin H, Roque III J, Konda P, Gujar S, Thummel RP, Lilge L, Cameron CG, McFarland SA. Transition metal complexes and photodynamic therapy from a tumor-centered approach: challenges, opportunities, and highlights from the development of TLD1433. *Chemical reviews*. 2018 Oct 8; 119(2):797-828.
98. Zeng L, Gupta P, Chen Y, Wang E, Ji L, Chao H, Chen ZS. The development of anticancer ruthenium (II) complexes: from single molecule compounds to nanomaterials. *Chemical Society Reviews*. 2017; 46(19):5771-804.
99. Kenny RG, Marmion CJ. Toward multi-targeted platinum and ruthenium drugs—a new paradigm in cancer drug treatment regimens? *Chemical reviews*. 2019 Jan 14; 119(2):1058-137.
100. Korfel A, Scheulen ME, Schmoll HJ, Gründel O, Harstrick A, Knoche M, Fels LM, Skorzec M, Bach F, Baumgart J, Sass G. Phase I clinical and pharmacokinetic study of titanocene dichloride in adults with advanced solid tumors. *Clinical cancer research: an official journal of the American Association for Cancer Research*. 1998 Nov 1; 4(11):2701-8.
101. Marková Z, Šišková KM, Filip J, Cuda J, Kolar M, Safarova K, Medrik I, Zboril R. Air stable magnetic bimetallic Fe–Ag nanoparticles for advanced antimicrobial treatment and phosphorus removal. *Environmental science & technology*. 2013 May 21; 47(10):5285-93.
102. Perdikaki A, Galeou A, Pilatos G, Karatasios I, Kanellopoulos NK, Prombona A, Karanikolos GN. Ag and Cu monometallic and Ag/Cu bimetallic nanoparticle–

- graphene composites with enhanced antibacterial performance. *ACS Applied Materials & Interfaces*. 2016 Oct 19; 8(41):27498-510.
103. Perdikaki A, Galeou A, Pilatos G, Prombona A, Karanikolos GN. Ion-based metal/graphene antibacterial agents comprising mono-ionic and bi-ionic silver and copper species. *Langmuir*. 2018 Aug 26; 34(37):11156-66.
104. Perdikaki AV, Tsitoura P, Vermisoglou EC, Kanellopoulos NK, Karanikolos GN. Poly (ethylene oxide)-b-poly (propylene oxide) amphiphilic block copolymer-mediated growth of silver nanoparticles and their antibacterial behavior. *Langmuir*. 2013 Sep 10; 29(36):11479-88.
105. Pilatos G, Perdikaki AV, Sapalidis A, Pappas GS, Giannakopoulou T, Tsoutsou D, Xenogiannopoulou E, Boukos N, Dimoulas A, Trapalis C, Kanellopoulos NK. Graphene by one-step chemical vapor deposition from ferrocene vapors: Properties and electrochemical evaluation. *Journal of Applied Physics*. 2016 Feb 14; 119(6).
106. Pilatos G, Vermisoglou EC, Perdikaki A, Devlin E, Pappas GS, Romanos GE, Boukos N, Giannakopoulou T, Trapalis C, Kanellopoulos NK, Karanikolos GN. One-step, in situ growth of unmodified graphene–magnetic nanostructured composites. *Carbon*. 2014 Jan 1; 66: 467-75.
107. Abd-Elsalam KA. Bimetallic Nanoparticles as Antimicrobials. (2016) *J Nanotech Mater Sci* 3 (1): 1-2. *J Nanotech Mater Sci.*; 3(1).
108. Arora N, Thangavelu K, Karanikolos GN. Bimetallic nanoparticles for antimicrobial applications. *Frontiers in Chemistry*. 2020 May 28;8:412.
109. Frei A. Metal complexes, an untapped source of antibiotic potential. *Antibiotics*. 2020 Feb 18; 9(2):90.

110. Gladyshevskii RE, Cenozal K, Parthé E. Er₂RhSi₃ and R₂CoGa₃ (R = Y, Tb, Dy, Ho, Er, Tm, Yb) with Lu₂CoGa₃ type structure: new members of the A1B2 structure family. *Journal of alloys and compounds*. 1992 Dec 7; 189(2):221-8.
111. Sampathkumaran EV, Bitterlich H, Iyer KK, Löser W, Behr G. Magnetic behavior of single-crystal Ho₂ PdSi₃. *Physical Review B*. 2002 Aug 9; 66(5):052409.
112. Mallik R, Sampathkumaran EV, Strecker M, Wortmann G. Observation of a minimum in the temperature-dependent electrical resistance above the magnetic-ordering temperature in Gd₂PdSi₃. *Europhysics Letters*. 1998 Feb 1; 41(3):315.
113. Kurumaji T, Nakajima T, Hirschberger M, Kikkawa A, Yamasaki Y, Sagayama H, Nakao H, Taguchi Y, Arima TH, Tokura Y. Skyrmion lattice with a giant topological Hall effect in a frustrated triangular-lattice magnet. *Science*. 2019 Aug 30; 365(6456):914-8.
114. Sampathkumaran EV, Das I, Rawat R, Majumdar S. Magnetocaloric effect in Gd₂ PdSi₃. *Applied Physics Letters*. 2000 Jul 17; 77(3):418-20.
115. Kumar R, Iyer KK, Paulose PL, Sampathkumaran EV. Magnetic and transport anomalies in R₂RhSi₃ (R= Gd, Tb, and Dy) resembling those of the exotic magnetic material Gd₂PdSi₃. *Physical Review B*. 2020 Apr 29; 101(14):144440.
116. Kumar R, Sharma J, Iyer KK, Sampathkumaran EV. Reentrant spin-glass and transport behavior of Gd₄PtAl, a compound with three sites for Gd. *Journal of Magnetism and Magnetic Materials*. 2019 Nov 15; 490:165515.
117. Daniel MC, Astruc D. Gold nanoparticles: assembly, supramolecular chemistry, quantum-size-related properties, and applications toward biology, catalysis, and nanotechnology. *Chemical reviews*. 2004 Jan 14; 104(1):293-346.

118. Müller-Buschbaum H. The Crystal Chemistry of High-Temperature Oxide Superconductors and Materials with Related Structures. *Angewandte Chemie International Edition in English*. 1989 Nov; 28(11):1472-93.
119. Schiffler ST, Müller-Buschbaum H. BaNiYb₂O₅—eine Verbindung, die nicht im BaNiLn₂O₅-Typ kristallisiert Mit einem Beitrag über BaCuSm₂O₅. *Zeitschrift für anorganische und allgemeine Chemie*. 1986 Sep; 540(9-10):243-50.
120. Schiffler S, Müller-Buschbaum H. New compounds of the BaNiNd₂O₅-type: BaNiLn₂O₅ (Ln= Sm, Gd, Ho, Er, Tm). *Monatshefte für Chemie/Chemical Monthly*. 1987 Jun; 118:741-7.
121. Müller-Buschbaum H, Lang C. Notiz über synthese und kristallstruktur von BaPtEu₂O₅ und BaNiEu₂O₅. *Journal of the Less Common Metals*. 1988 Sep 1; 142:L1-3.
122. Mevs H, Müller-Buschbaum H. Ein wechsel des strukturtyps in den oxiden BaCoGd₂O₅, BaCoDy₂O₅ und BaCoY₂O₅. *Zeitschrift für anorganische und allgemeine Chemie*. 1989; 573(1):128-32.
123. Mevs H, Müller-Buschbaum H. Zwei neue Verbindungen vom BaNiLn₂O₅-TYP: BaCoNd₂O₅ und BaCoSm₂O₅. *Journal of the Less Common Metals*. 1989 Jun 1; 152(1):139-44.
124. Mevs H, Müller-Buschbaum HK. Neue Oxometallate vom BaCuSm₂O₆-Typ: BaCoHo₂O₅, BaCoYb₂O₅ und vom BaNiLn₂O₅-Typ: BaCoEr₂O₅. *Zeitschrift für anorganische und allgemeine Chemie*. 1989 Jul; 574(1):172-6.
125. Garcia-Matres E, Martinez JL, Rodriguez-Carvajal J, Alonso JA, Salinas-Sánchez A, Saez-Puche R. Structural characterization and polymorphism of R₂BaNiO₅ (R=

- Nd, Gd, Dy, Y, Ho, Er, Tm, Yb) studied by neutron diffraction. *Journal of Solid-State Chemistry*. 1993 Apr 1; 103(2):322-33.
126. Michel C, Raveau B. Les Oxydes A_2BaCuO_5 (A= Y, Sm, Eu, Gd, Dy, Ho, Er, Yb). *Journal of Solid-State Chemistry*. 1982 Jun 1; 43(1):73-80.
127. Salinas-Sanchez A, Garcia-Munoz JL, Rodriguez-Carvajal J, Saez-Puche R, Martinez JL. Structural characterization of R_2BaCuO_5 (R= Y, Lu, Yb, Tm, Er, Ho, Dy, Gd, Eu and Sm) oxides by X-ray and neutron diffraction. *Journal of Solid-State Chemistry*. 1992 Oct 1; 100(2):201-11.
128. Golosovsky IV, Böni P, Fischer P. Magnetic structure of the “brown phase” Nd_2BaCuO_5 . *Physics Letters A*. 1993 Nov 8; 182(1):161-4.
129. Abrashev MV, Zlateva GA, Iliev MN, Gyulmezov M. Optical phonons in Nd_2BaMO_5 (M= Zn, Cu). *Physical Review B*. 1994 May 1; 49(17):11783.
130. Taibi M, Aride J, Darriet J, Moquine A, Boukhari A. Structure cristalline de l'oxyde Nd_2BaZnO_5 . *Journal of Solid-State Chemistry*. 1990 Jun 1; 86(2):233-7.
131. Mori K, Ogawa H, Kan A, Ohsato H, Ishihara S. Crystal structural characterization of Nd_2BaZnO_5 -type microwave dielectric ceramics with rare-earth substitutions for Nd. *Materials chemistry and physics*. 2003 Apr 10; 79(2-3):273-5.
132. Salinas-Sanchez A, Garcia-Munoz JL, Rodriguez-Carvajal J, Saez-Puche R, Martinez JL. Structural characterization of R_2BaCuO_5 (R= Y, Lu, Yb, Tm, Er, Ho, Dy, Gd, Eu and Sm) oxides by X-ray and neutron diffraction. *Journal of Solid-State Chemistry*. 1992 Oct 1; 100(2):201-11.

133. Hadjünskü YA, Levitin RZ, Mill BV, Paukov IV, Popova MN, Snegirev VV. Spectral and magnetic studies of nickelates $\text{Lu}_2\text{BaNiO}_5$ and $\text{Yb}_2\text{BaNiO}_5$. Solid state communications. 1993 Mar 1; 85(9):743-8.
134. Kumar R, Rajput S, Maitra T, Hoser A, Rayaprol S, Upadhyay SK, Iyer KK, Maiti K, Sampathkumaran EV. Origin of destruction of multiferroicity in $\text{Tb}_2\text{BaNiO}_5$ by Sr doping and its implications. Journal of Alloys and Compounds. 2021 May 5; 862:158514.
135. Upadhyay SK, Sampathkumaran EV. Multiferroicity in a spin-chain compound, $\text{Tb}_2\text{BaCoO}_5$, with exceptionally large magnetodielectric coupling in polycrystalline form. Applied Physics Letters. 2018 Jun 25; 112(26).
136. Sekar RP Journal of Biomedical and Pharmaceutical Sciences 3: 28 (2018).
137. Weindling P. Epidemics and genocide in Eastern Europe, 1890-1945. OUP Oxford; 2000 Feb 3.
138. Apostolou P, Toloudi M, Chatziioannou M, Ioannou E, Knocke DR, Nester J, Komiotis D, Papasotiriou I. AnvirezTM in combination with cisplatin in breast, colon, lung, prostate, melanoma and pancreatic cancer cell lines. BMC Pharmacology and Toxicology. 2013 Dec; 14:1-6.
139. Akbar Vaseghi, Babak Bakhshinejd, Majide Sadeghizade et.al. (2014) Science and Researcher Branch, Islamic Azad University, Ardabil, Iran
140. Idris DS, Roy A. Synthesis of bimetallic nanoparticles and applications—an updated review. Crystals. 2023 Apr 7; 13(4):637.

Chapter 2

Experimental Details

2.1 Preliminary remarks

In this chapter, various experimental methods employed for the investigations are briefly outlined. In the case of intermetallic samples, we studied the magnetic, transport and thermal properties in the polycrystalline bulk form as well as in ball-milled nanoform as a function of T and H , while we studied the effects of pressures (external and chemical) on the magnetic properties of some oxides. Materials those were prepared and investigated are

Chapter 3: Nd_2RhSi_3 and Er_2RhSi_3

Chapter 4: Er_4PtAl , Ho_4PtAl and Dy_4RhAl

Chapter 5: $\text{Tb}_2\text{Ba}_{1-x}\text{Sr}_x\text{NiO}_5$ ($x = 0, 0.025, 0.05, 0.075$ and 0.1) and $\text{Tb}_2\text{BaCoO}_5$

Chapter 6: In addition to the study of the magnetic and transport properties, we have also carried out the study of antimicrobial efficacy on some of the intermetallic samples in both bulk and nanocrystalline form.

2.2 Sample preparation

2.2.1 Intermetallic samples

Intermetallic samples were prepared by arc-melting technique. In this technique stoichiometric amounts of respective high-purity (>99.95%) elements, were weighed and melted together several times on a water-cooled Cu hearth, in an inert atmosphere of high purity argon gas (0.3 – 0.5 bar). A commercial mini arc-melter (MAM-1, Edmund Bühler) was employed for this purpose. The arc furnace consists of two electrodes, one of them is a water-cooled copper hearth and the other electrode consists of a water-cooled tungsten

carbide tip. The electric arc is struck by touching the electrode tip with the copper hearth. First the arc was used to melt a Titanium ball, which adsorbs any oxygen impurity present in the chamber before actual melting of sample. The arc was then brought in contact with the sample and the current was increased till the sample melts congruently. This process is followed by flipping the sample several times till the sample is homogeneously melted. The mass of the molten ingots were checked after first and fifth melt, to ensure that the losses (if any) in the weights during melting remained below the acceptable limits (<2%). While most of the as-melted compounds were found to be in single phase composition, some of the molten ingots required annealing in evacuated sealed quartz tubes at temperatures mentioned in the literature to remove any stray phases present in the final study specimens, further details have been mentioned in respective chapters.

2.2.2 Oxide samples

Oxide samples were prepared by a conventional solid-state reaction technique. In this method, the high purity (>99.999%) oxides constituting the sample were weighed in respective stoichiometric ratios and ground together, to attain homogeneity. The ground powders were then calcined at 800 C for 24 hours in argon atmosphere. The calcined samples were further reground, pelletized and sintered several times in argon atmosphere at temperatures as specified in chapter 5.

2.2.3 Nanofom specimens

In order to get nanocrystalline samples, 5gms of the single-phase polycrystalline samples were ground to fine powder form using a commercial high energy ball mill (Pulversitte 7,

Fritsch GMBH). The hand-ground polycrystalline powders were mixed with toluene (to avoid oxidation of the metallic samples) and ground in zirconia bowls of 50 ml capacity, containing 65 zirconia balls of 5 mm diameter each. The grinding speed used was 500 RPM for a period of 30 minutes with a pause for 10 minutes after every 10 minutes. The final ground specimen after 150 minutes of grinding was used for studies.

Since the sintering and annealing temperatures and the heat treatment profiles in the case of oxides are different, we have specified those details in the respective chapters.

2.3 Sample characterization

2.3.1 X-ray diffraction and Rietveld analysis of powder sample

The samples were characterized by powder x-ray diffraction (XRD) using a commercial powder x-ray diffractometer, procured from PANalytical co. The instrument operates in the Gonio mode of θ - θ geometry and for all samples, Cu K α ($\lambda_1 = 1.5406 \text{ \AA}$ and $\lambda_2 = 1.5444 \text{ \AA}$) x-ray source was used in measurements. In our measurements, the sample stage is kept fixed while both source and detector was rotated. The data was collected from a low angle (mostly 10°) to 80° with a step size of 0.02° . Power of the x-ray source was 1.2 kV-A (40 kV and 30 mA). Rietveld refinement of the powder XRD pattern was done using the FullProf Suite software [1] to determine the phase formation and purity of the sample. It is confirmed that all the compounds form in single phase in desired structure within the detection limit of the x-ray diffractometer, unless otherwise stated in respective chapters.

2.3.2 Energy dispersive x-ray analysis

In order to ascertain that there is no detectable secondary phase and the stoichiometric ratio is uniform for the samples within the detection limit ($< 2\%$), we carried out the scanning electron microscopy (SEM) and energy dispersive x-ray analysis (EDAX) on the samples, using commercial SEM (Ultra Field Emission SEM of Zeiss). Backscattered electron images have been obtained to check the homogeneity and phase of the samples. However, this technique cannot measure the accurate compositions of low atomic number elements (like oxygen), which is the limitation of this technique. Hence, in the case of oxide samples, off-stoichiometry of oxygen (if present) cannot be verified through this equipment accurately.

2.3.3 DC electrical resistivity

The electrical resistivity measurements were done using the standard four probe technique, from 1.8 K to 300 K using the resistivity option of the commercial PPMS (Physical Property Measurement system, QDUSA), which adds a configurable resistance bridge board, called the user bridge board to the model 6000 PPMS controller. The four-probe method is a standard technique used for measurement of resistivity, in which four colinear contacts are placed on the measurement sample. A fixed current is passed between the outer two leads, while the voltage difference is measured using the middle leads. This technique eliminates the error due to the contact resistance between the sample and the contacts. The samples for the four probe measurements were mounted on standard PPMS sample pucks. Using the resistivity option, one can measure up to three samples in one set of measurement. The bridge board automatically adjusts the excitation current of its active channels, but one can specify the maximum allowable current ($\pm 0.01 - 5000 \mu\text{A}$), power

(0.0001 – 1000 μ W), and voltage (1- 95 mV) for each channel. The maximum measurable resistance is computed from the maximum potential drop that can be measured and from the minimum useful excitation current, which is determined by the user bridge's DAC (digital – to – analog converter) resolution.

2.3.4 Heat Capacity

Heat capacity measurements (at constant pressure) have been performed using the PPMS, by the relaxation technique [2,3,4]. The heat capacity puck utilizes the standard 12-pin format for electrical connections, and it provides a small micro-calorimeter platform for mounting the sample. Samples were mounted to this platform by a standard cryogenic grease or adhesive such as Apiezon N- grease. The sample platform is suspended by eight thin wires which serve as the electrical leads for an embedded heater and thermometer. The wires also provide a well-defined thermal connection between the sample platform and the puck. An additional thermometer embedded in the puck provides a highly accurate determination of the puck temperature, and a thermal shield aids in maintaining stable sample temperature and uniformity. To ensure that the heat is not lost via exchange gas, the heat capacity option includes the PPMS high-vacuum system, which maintains (using turbo pump or cryopump) the sample chamber pressure near 0.01 mbar and is automatically controlled by the software.

In the PPMS heat capacity option, the sample mass was limited to 1 – 20 mg. Given the thermal characteristics of the calorimeter, this range of mass produces varying relaxation time constants that may be a fraction of a second at 1.9 K or many minutes at 300 K. The addenda heat capacity limits the size of the smallest sample. After each

measurement cycle which is a heating period followed by a cooling period the heat capacity was fit in the entire temperature response [3] of the sample platform to a model that accounts for both the thermal relaxation (τ_1) of the sample platform to the bath temperature and the relaxation (τ_2) between the sample platform and the sample itself. The simple model assumes that the sample and the sample platform are in good thermal contact with each other. In this model, the temperature of the platform as a function of time t obeys the equation

$$C_{total} \frac{dT}{dt} = -K_w (T - T_b) + P(t), \quad \dots (2.1)$$

where, $C_{total} = (C_{sample} + C_{addenda})$ is the total heat capacity of the sample and sample platform, K_w is the thermal conductance of the supporting wire, T_b is the temperature of the thermal bath, and $P(t)$ is the power applied by the heater. The solution of this equation is given by exponential functions with a characteristic time constant $\tau = C_{total} / K_w$. The heat capacity software uses two-tau model to measure the heat capacity of the sample when poor thermal attachment of the sample to the platform produces a temperature difference between the two. The two-tau model simulates the effect of heat flowing between the sample platform and puck.

Using the non-linear, least square fitting algorithm, the system compares the solution to the simple model to the actual measurement. The values of the parameter that give the smallest fit deviation determine the heat capacity. The sensitivity of the fit deviation to small variations in the fitting parameters is used to estimate the standard errors for the heat capacity.

2.3.5 SQUID magnetometer

SQUID magnetometer uses a superconducting quantum interference device (SQUID) which is used to measure extremely weak signals ($\sim 10^{-7}$ emu). SQUID consists of two superconductors separated by thin insulating layers to form two parallel Josephson junctions. The electrical current density through a weak electric contact between the superconductors, depends on the phase difference $\Delta\phi$ of the two superconducting wavefunctions. The time derivation of $\Delta\phi$ is correlated with the voltage across the weak contacts. In addition, $\Delta\phi$ is influenced by the magnetic flux ϕ through its ring. Such a structure can be used to convert magnetic flux into an electric voltage. This principle forms the heart of the squid magnetometer.

The system has two major hardware components: (1) the MPMS dewar and probe assembly, and (2) the associated control system in the MPMS control console. Automatic control and data collection are provided by a computer and two independent subsystem controllers. Gas control and ancillary functions in the system are also automated. It is equipped with a 70 kOe superconducting magnet. The system provides rapid precision measurements over a temperature range of 1.8 K to 400 K. SQUID consisting of two Josephson junctions employed in parallel so that electron tunneling through the junctions demonstrate quantum interference, dependent upon the strength of the magnetic field within a loop. The linear motion of the sample induces an electric current in the coils; this current is sensed by the SQUID sensor via an isolation transformer. The external flux (ϕ_{ext}) couples into the single turn (for example) pickup coil with inductance L_p . This induces a current (I) in the circuit, which couples a flux through the input coil of the inductances.

The mutual inductance of the input coil and the SQUID shows as M_i (moment induced in the detection coil).

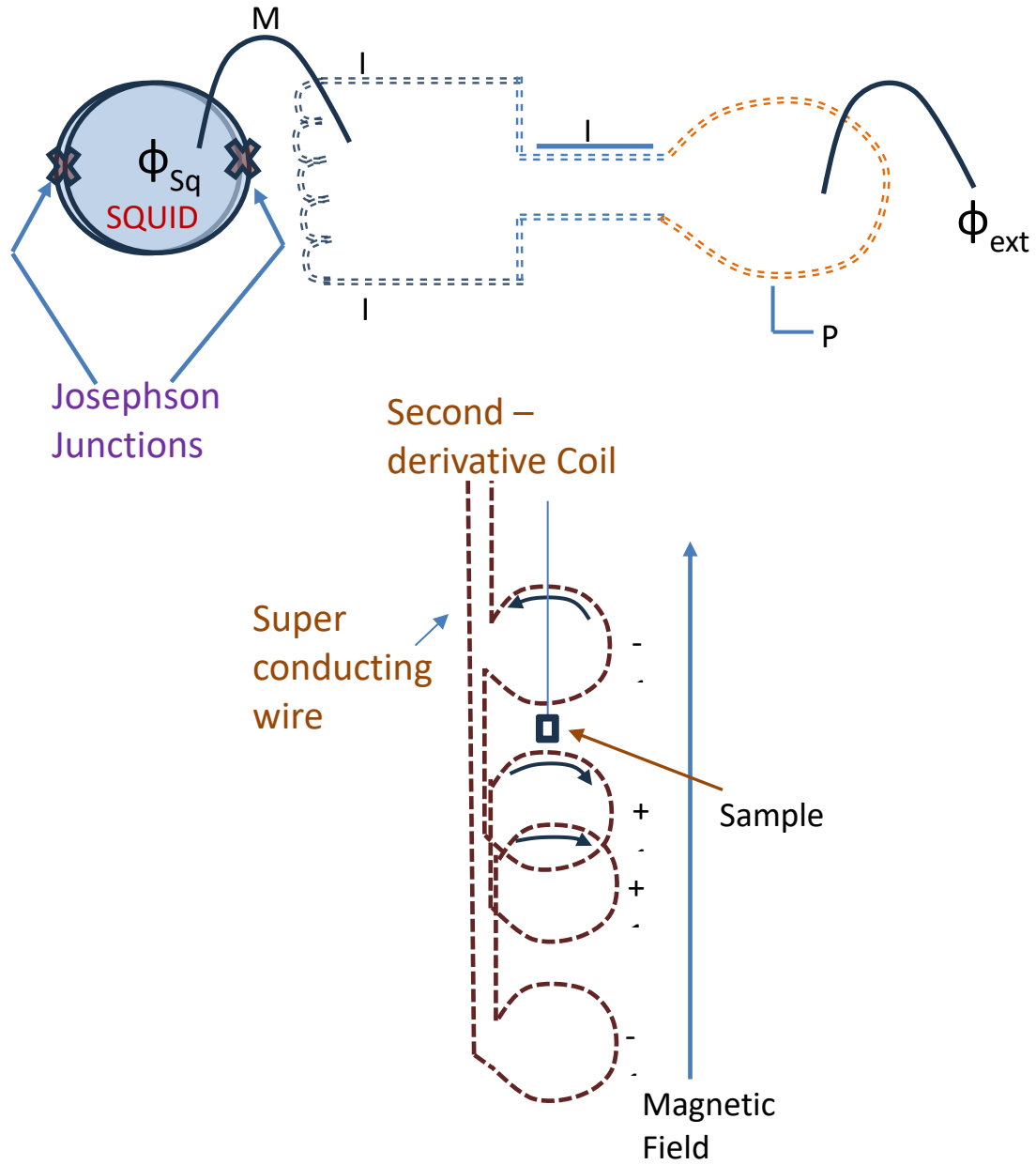


Figure 2.1: SQUID detection circuit.

The expression for the external flux coupled into the circuit to the flux in the SQUID is given by

$$\Phi_{\text{ext}} = (L_p + L_i) \left(\frac{\Phi_{sq}}{M_i} \right) \quad \dots (2.2)$$

Since the SQUID functions on the basis of a highly linear current to voltage conversion, the variations of the current in the detection coil produce corresponding variations in the SQUID output voltage which is proportional to the magnetic moment in the sample. This is the only system where the magnetic moment of the sample is directly measured.

2.3.6 Vibrating sample magnetometer

A Vibrating sample magnetometer (VSM) operates on Faraday's law of induction, which states that a changing magnetic field will produce an induced voltage (e.m.f). In the VSM the sample is placed in a constant external magnetic field, which magnetizes the sample by aligning the magnetic domains or spins of the sample along the applied field. This magnetization of the sample will produce a magnetic field around the sample which is also known as the stray magnetic field. When this magnetized sample is vibrated using a vibration controller, it causes the stray magnetic field to vary as a function of time. Such an alternating magnetic field can be sensed by the pick-up coils, due to the Faraday's laws of induction. This forms the basic working principle for a VSM. The induced current in the coils is proportional to the degree of magnetization of the sample under investigation. The sample under investigation is mounted in a sample holder at the end of a carbon fiber rod and inserted into an Oxford Instruments continuous flow helium cryostat and made to oscillate vertically, typically over 1- 1.5 mm range with frequencies 40 – 80 Hz.

If the sample is magnetized, the oscillation will induce an AC signal in a set of suitably placed pick-up or sense coils [5,6]. The lock-in amplifier is tuned to vibration frequency using a reference signal from the vibrator controller and detects the in-phase

voltage from the sense coils. The instrument (see figure 2.2) is equipped with a 120 kOe superconducting magnet.

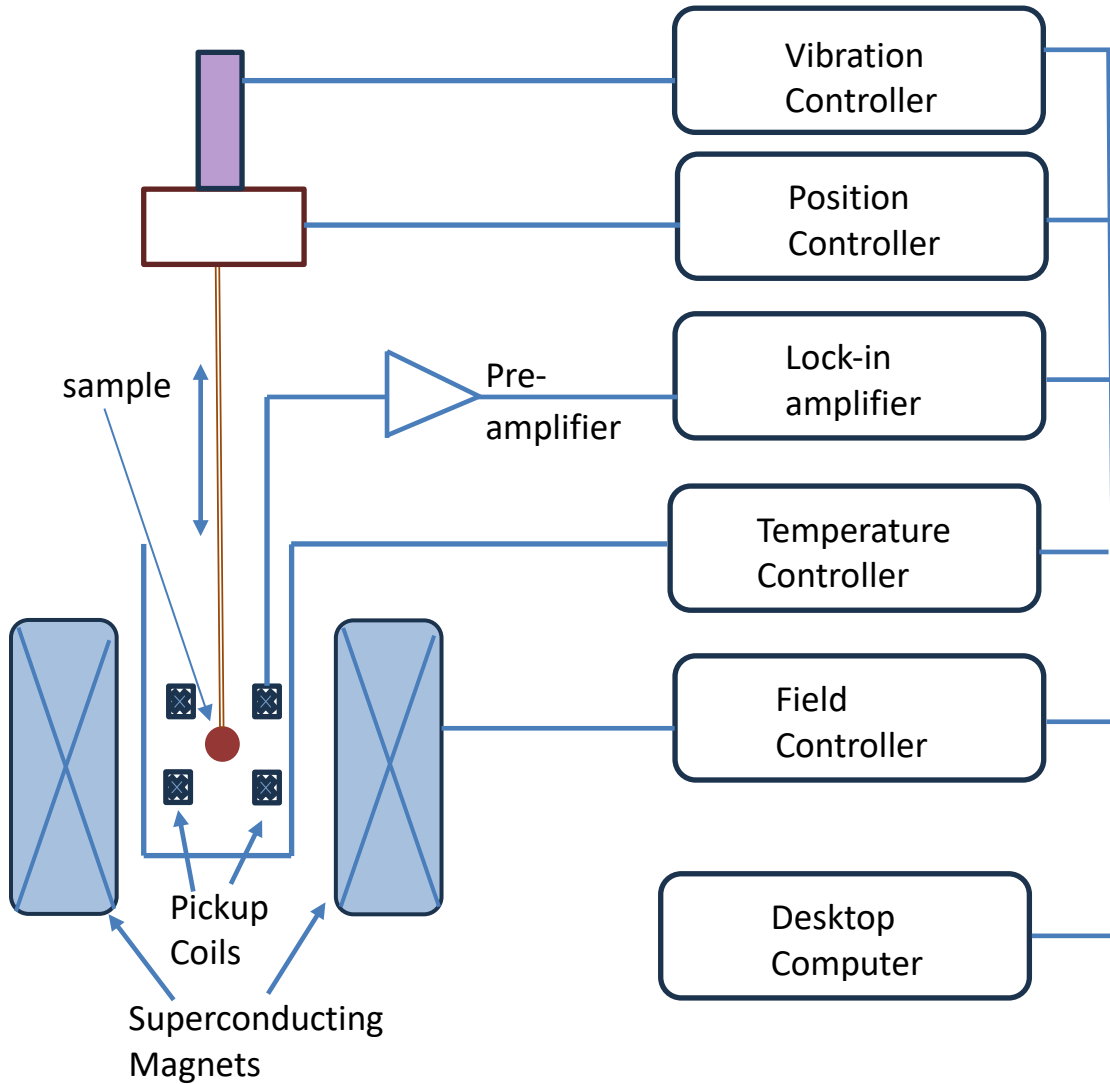


Figure 2.2: Schematic diagram for VSM

The induction current is amplified by a transimpedance analyzer and a lock in amplifier. The various components are hooked up to a computer interface. Using controlling and monitoring software the system can provide the degree of magnetization of the test samples.

2.3.7 High pressure cells

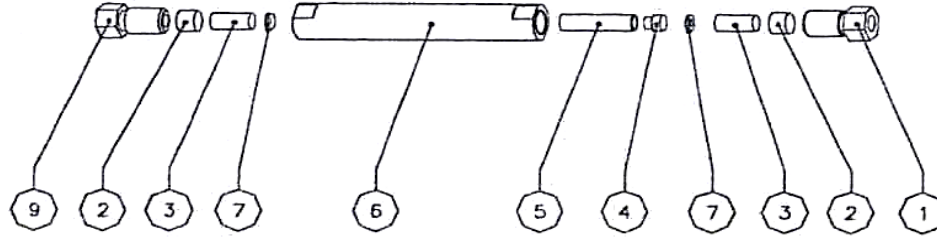
The cell used for carrying out magnetization (MCell 10) measurements under external hydrostatic pressures was a commercial cell procured from Easylab technologies U.K. The maximum attainable pressure for magnetization studies is 10 kbar (1 GPa) at 300 K.

The Mcell 10 [7] has been designed for carrying out magnetization measurements under high pressure up to 10kbar and down to a low temperature of 2 K using the squid magnetometer (MPMS) of Quantum design USA. The cell is designed in such a way that it can be directly attached to the lower end of the normal sample holder used in the SQUID magnetometer. It consists of a cylinder made up of copper beryllium, as shown in the figure 2.3. The sample was loaded in a teflon bucket filled with daphne oil as a pressure transmitting medium. The teflon bucket was then loaded at the center of the cell and fitted on both sides with antiextrusion disc which was pressed by ceramic pistons and ceramic disc. This disc when pressed transmitted the pressure on the daphne oil because of compression of teflon bucket. Finally, the daphne oil transmits the pressure onto the sample. There is a mild reduction in pressure when the sample is cooled, but below 200 K daphne oil solidifies sealing the applied pressure on the sample. The cell is pressurized using a hydraulic pressurizing system.

To determine the pressure in the cell at low temperature, a small piece of tin was added to teflon bucket along with the sample. Depending upon the shift in the superconducting transition of the tin, the pressure in the cell at low temperature can be determined using the polynomial function [8]:

$$P = a*[T_c(0) - T_c(P)]^2 + b [T_c(0) - T_c(P)], \quad \dots (2.3)$$

where P is pressure in kbar, a and b are constants with value $a = 5.041489$ and $b = 17.81287$.
 T_c is the superconducting transition temperature of Sn.



1) Upper locking nut, 2) Piston cap, 3) Piston, 4) Plug, 5) Cap, 6) Pressure cell body, 7) Anti extrusion ring, 8) Lower locking nut.

Figure 2.3: Schematic diagram of a MCell 10.

Generally, it was observed that there is a drop of around 1.5 kbar of pressure when one cools the system from 300 K to 4 K. To compensate for this drop, a marginally higher pressure is applied to the system at room temperature when the cell was being pressurized. The cell was then attached to the sample holder of MPMS and the magnetization measurements were performed similar to that of the normal measurements. In order to obtain a correct sample center in the cell when the cell was loaded in the MPMS, the system center was accurately calculated using a nickel standard at room temperature and accordingly calibrated to the cell to ensure that the measurements being carried out is for the sample. To account for the background contribution to the data from the cell, the empty cell background was measured earlier and subtracted from the measured data continuously using the MPMS software. The entire magnetization measurement was performed for a few sets of pressures which is determined on the basis of the magnetization data of the sample being measured.

2.3.8 Antimicrobial susceptibility studies

Antimicrobial susceptibility testing has been regularly used for drug discovery, epidemiology and prediction of the therapeutic outcome. In order to determine the antimicrobial efficacy, we carried out our studies on *E. coli*, *Pseudomonas*'s, *S. Aureus*, *E. Faecalis* and *Candida Albicans* using the Agar disk diffusion technique [9,10, 11], Agar well Diffusion technique and the Broth dilution technique for determining the MIC [minimum inhibitory concentration, which is the lowest concentration of antimicrobial agent that completely inhibits growth of the organism in the well plates] and MBC [minimum bactericidal concentration (MBC) or minimum fungicidal concentration (MFC), also known as the minimum lethal concentration (MLC)]; MBC is defined as the lowest concentration of antimicrobial agent needed to kill 99.9% of the final inoculum after incubation for 24 h under a standardized set of conditions described in document M26-A [12]. Each of this standard technique have been described in detail in the further sections below.

Since the intermetallic samples were in powder form, we had to determine the solubility of our samples, for which we carried out solubility studies on our samples using the standard solutions. The solubility of the compounds was tested in polar solvents like DMF, DMSO, Water, Acetone, Methanol, isopropanol, Acetonitrile as well as non-polar solvents like Benzene, Toluene, Acetic Acid, Chloroform, Diethyl ether etc. It was found that the intermetallic compounds are highly insoluble in any of the available solutions and any of the antimicrobial susceptibility testing has to be done using the direct dispersive technique.

Agar Disk Diffusion technique

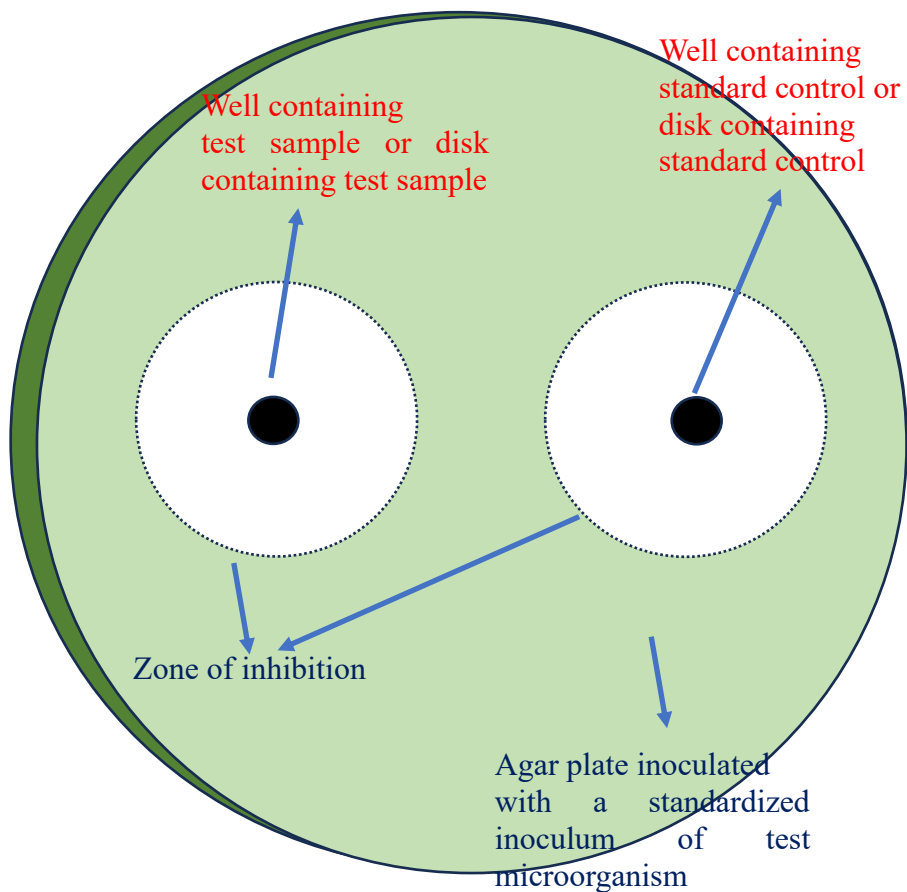


Figure 2.4: Schematic representation of a disk diffusion and/or well diffusion technique.

Agar disk-diffusion testing method was developed in 1940 [9]. This technique is one of the official methods used in many clinical microbiology laboratories for routine antimicrobial susceptibility testing. In this technique, the agar plates are inoculated with a standardized inoculum of the test microorganism. On this inoculated disk filter paper disk (about 6 mm in diameter), containing the test compound at a desired concentration, are placed on the agar surface. The Petri dishes are incubated under suitable conditions based on the type of microbe being tested. In normal cases the antimicrobial agent will diffuse

into the agar medium and inhibit the germination and growth of the test microorganism. After a particular incubation period say 24 hours, the diameters of inhibition growth zones are measured.

Agar well diffusion method

Agar well diffusion method is widely used to evaluate the antimicrobial activity of plants or microbial extracts [13,14]. In this method, Similar to the procedure used in disk-diffusion method, the agar plate surface is inoculated by spreading a volume of the microbial inoculum over the entire agar surface. A hole with a diameter of 6 to 8 mm is aseptically punched with a sterile cork borer or a tip, and a volume (20–100 mL) of the antimicrobial agent or extract solution at desired concentration is introduced into the well. These, agar plates are then incubated under suitable conditions depending upon the test microorganism. The antimicrobial agent diffuses in the agar medium and inhibits the growth of the microbial strain tested. Since the intermetallic samples are insoluble and has to be used in the dispersive mode, we modified the well diffusion technique by using a fixed weight of the test powder in the well instead of a volume of the antimicrobial agent. In addition, we tried to disperse this powder in the agar media when it was slightly hot and in a semi-solid state, and tried to make a localized well so that our powder was dispersed well inside the agar media in form of well.

Broth micro- or macro-dilution is one of the most basic anti-microbial susceptibility testing methods. This technique involves, preparation of two-fold dilutions of the antimicrobial agent (e.g. 1, 2, 4, 8, 16 and 32 mg/mL) in a liquid growth medium (Broth)

Broth Dilution method

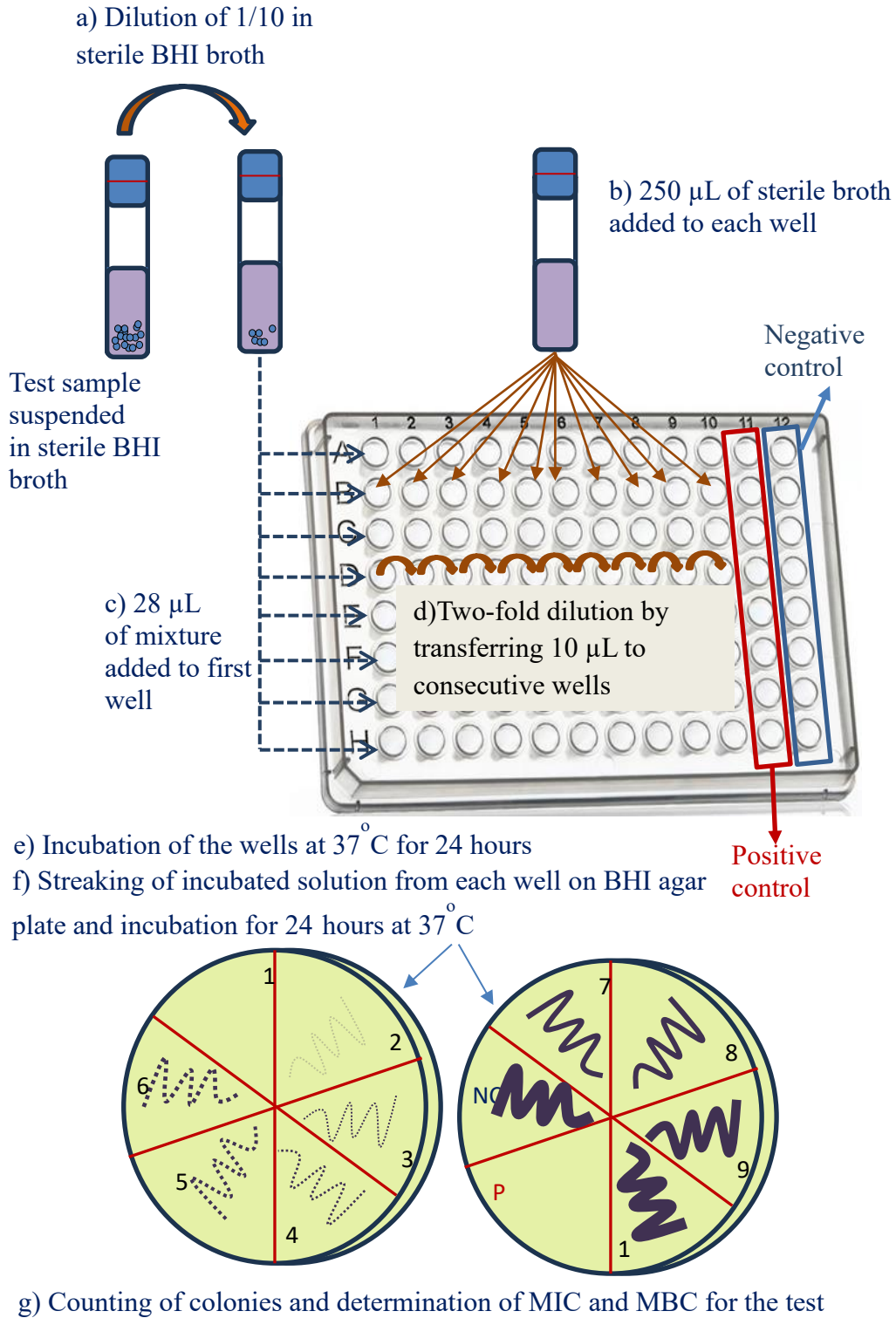


Figure 2.5: Schematic diagram of steps involved in broth dilution and MIC/MBC technique.

dispensed in tubes containing a minimum volume of 2 mL (macrodilution) or with smaller volumes using 96-well microtitration plate (microdilution).

Each of this tube are then inoculated with a microbial inoculum which is prepared in the same medium after dilution of standardized microbial suspension adjusted to 0.5 McFarland scale. Once a fixed amount of microbial inoculum is added to each tubes or wells, the tubes or wells is inoculated (mostly without agitation) under suitable conditions depending upon the test microorganism. The inoculated liquid is streaked onto a n freshly prepared agar plate along with positive and negative controls. These plates are further inoculated for another 24 hours to count the growth of microbial colonies and determine the MIC and MBC of the test materials. The experimental methodology to perform accurately the microdilution is schematized in figure. MIC is the lowest concentration of antimicrobial agent that completely inhibits growth of the organism in tubes or micro-dilution wells as detected by the unaided eye [15].

Unlike micro-dilution method, the main disadvantages of the macrodilution method are the tedious, manual undertaking, risk of errors in the preparation of antimicrobial solutions for each test, and the comparatively large amount of reagents and space required. Thus, the reproducibility and the economy of reagents and space that occurs due to the miniaturization of the test are the major advantages of the microdilution method. Nevertheless, the final result is significantly influenced by approach, which must be carefully controlled if reproducible results (intralaboratory and interlaboratory) are to be attained.

2.4 Bibliographical references

1. J. Rodríguez-Carvajal, *Physica B* **192**, 55 (1993).
2. P. F. Sullivan, G. Seidel, *Phys Rev* **173**, 679 (1968).
3. R. Bachmann et al., *Rev. Sci. Instr.* **43**, 205 (1972). (2012)
4. Kausik Sengupta, Ph. D Thesis, TIFR, March 2006.
5. S.Foner, *Rev.Sci.Instr.***30**, 548 (1959)
6. J.Mallison, *Appl. Phys.* **37**, 2514 (1966).
7. Pressure Cell Manual, Easy lab technologies U.K.
8. T.F. Smith, C.W. Chu and M.B. Maple, *Cryogenics* **53**, **9** (1969)
9. N.G. Heatley, A method for the assay of penicillin, *Biochem. J.* **38** (1944)
10. CLSI, Performance Standards for Antimicrobial Disk Susceptibility Tests, Approved Standard, 7th ed., CLSI document M02-A11. Clinical and Laboratory Standards Institute, 950 West Valley Road, Suite 2500, Wayne, Pennsylvania 19087, USA, 2012.
11. CLSI, Method for Antifungal Disk Diffusion Susceptibility Testing of Yeasts, Approved Guideline. CLSI document M44-A. CLSI, 940 West Valley Road, Suite 1400, Wayne, Pennsylvania 19087-1898, USA, 2004.
12. CLSI, Methods for Determining Bactericidal Activity of Antimicrobial Agents. Approved Guideline, CLSI document M26-A. Clinical and Laboratory Standards Institute, 950 West Valley Roadn Suite 2500, Wayne, Pennsylvania 19087, USA, 1998.
13. S. Magaldi, S. Mata-Essayag, C. Hartung de Capriles, et al., *Int. J. Infect. Dis.* **8**, 39–45 (2004).
14. C. Valgas, S.M. De Souza, E.F.A. Smânia, et al., *Braz. J. Microbiol.* **38**, 369–380 (2007).

15. CLSI, Methods for Dilution Antimicrobial Susceptibility Tests for Bacteria that Grow Aerobically, Approved Standard, 9th ed., CLSI document M07-A9. Clinical and Laboratory Standards Institute, 950 West Valley Road, Suite 2500, Wayne, Pennsylvania 19087, USA.

16. Manuals of PPMS and MPMS, QDUSA

Chapter 3

Magnetic and transport anomalies in R_2RhSi_3 ($R = Nd$ and Er) compounds

3.1 Introduction

Due to some degree of radial extension of $4f$ orbital, compounds containing Ce have been known to exhibit exotic magnetic and transport properties, which is an important direction of research in solid state physics as briefed in chapter 1. It is an accepted fact now that this extension of $4f$ orbitals reduces gradually with the increasing atomic number in the rare-earth series. As a result, there is a gradual reduction in the $4f$ hybridization with the conduction electronic states as one moves from Ce to Sm. However, the influences of partial $4f$ radial extension on the magnetic properties of other light rare-earth members have not been well demonstrated. There is growing evidence for exotic magnetic properties of the heavy rare-earth members also, though these may not be due to the $4f$ delocalization. In this context, for the past three decades, exhaustive studies have been performed on the R_2TMX_3 compounds, especially for the R_2PdSi_3 family, crystallizing in a AlB_2 -derived hexagonal crystal structure [1-23], using several experimental techniques, revealing exotic properties exhibited by these compounds, including heavy rare-earths. For example; Ce_2PdSi_3 has been reported to be an antiferromagnetic Kondo lattice with T_N at 3K [6]. Nd_2PdSi_3 has been shown to exhibit exceptional magnetic behavior, due to the onset of ferromagnetism (at about 16 K which is rather high, disobeying Gennes scaling), while the other rare-earth members of R_2PdSi_3 order antiferromagnetically. Such an exotic magnetism, uncommon for Nd compounds, has been found [17] to be due to subtlety in the

hybridization of Nd 4*f* states with the valence electrons in the PdSi-layer [18]. Eu₂PdSi₃ has been reported to exhibit a magnetism which is of a quasi-one-dimensional type above 10 K [2]. It has been shown that the Si hexagon network plays a dominant role in mediating magnetism among *R* ions, (called *R1* in its immediate vicinity) than the *R* ions surrounded by PdSi network (called *R2*). It is now exciting that the compound Gd₂PdSi₃ was shown to exhibit anomalous Hall properties across the two metamagnetic transitions [6] in the magnetically ordered state, which is now called the ‘Topological Hall effect’ in current literature, as well as unusual paramagnetic transport [3] behavior. The compounds Tb₂PdSi₃ and Dy₂PdSi₃ have been reported to exhibit antiferromagnetism with T_N of 23 K and 8 K respectively, with additional magnetic features at low temperature [4]. These compounds have been reported to exhibit a large magnetoresistive behavior. Ho₂PdSi₃ has been reported to show no anisotropic features in the magnetically ordered state with T_N at 8 K, [10] in contrast to the situation encountered for other members in the family. In this compound the spin-glass freezing has been attributed to the role of the *f*-ligand hybridization, rather than just Pd-Si disorder. Thus, it can be seen that each and every rare-earth member in the family, irrespective of the degree of 4*f* radial extension, have been known to exhibit exotic magnetic and transport properties. Most notably, Gd₂PdSi₃ is attracting considerable attention in the current literature, leading to new theoretical approaches in recent years [20, 21]. This recent upsurge in exploring the interesting properties exhibited by the heavy rare-earth members has prompted the investigation of isostructural Rh based compounds. Ce₂RhSi₃ [25] was studied in depth earlier, while there was very little work done on the other rare-earth members barring some preliminary reports in literature [1, 6, 21, 22]. A recent study of *R* = Gd, Tb and Dy members of R₂RhSi₃

family [26], reported the properties of these compounds to be comparable to the properties of Gd_2PdSi_3 .

We have therefore undertaken a study of some of the remaining members of the Rh series viz, Nd_2RhSi_3 and Er_2RhSi_3 . In the case of Nd_2RhSi_3 , the radial extension of Rh $4d$ -orbitals is slightly larger than Pd $4d$ -orbitals, which enables us to understand role of Nd $4f$ -hybridization on the properties of Nd in comparison with the Pd-analogue. While the study of the magnetic properties of heavy rare-earth member like Er, will provide an insight as to how the magnetic properties of this member evolve, when the $4f$ states are further away from the Fermi level, thus making less contribution to the conduction band. It may be noted that an initial dc magnetization study of Rh series indicated ferromagnetic ordering around 16.5 K for Nd case and antiferromagnetic ordering around 5.2 K for Er case. A neutron diffraction study of the Nd compound by Szytula et.al. [27] at 4.2 K suggested ferromagnetic ordering, whereas a similar study on Er compound [24] suggested antiferromagnetism. Subsequently there was no further detailed work to understand the properties of this compound. The present investigations reveal that these compounds exhibit more exotic magnetic and transport properties, than envisaged earlier.

3.2 Crystal Structure

The R_2RhSi_3 family of compounds crystallize in a AlB_2 - derived hexagonal structure. However, the space group of these compounds is still unresolved, that is whether the space group is $P\bar{6}2c$ or $P6_3/mmc$, because the atomic positions are very close for both the space groups [1, 24, 28]. The deviation from the centrosymmetry for the former acentric group is negligible [28].

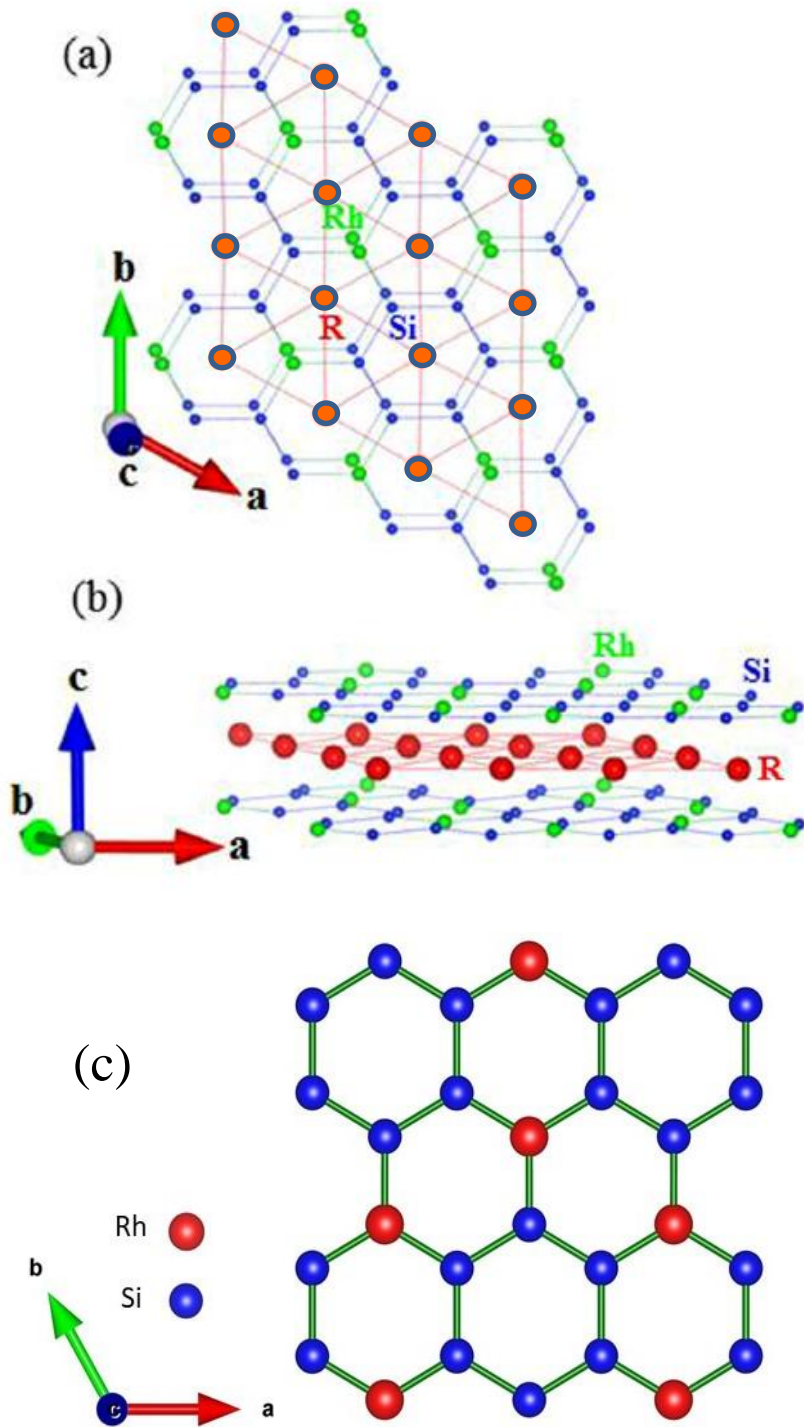


Figure 3.1: Crystallographic features of R_2RhSi_3 , shown in different ways. (a) Slightly angled top view of the lattice showing hexagonal network of R – lattice. (b) show the layered structure (c) Rh-Si conduction layer

In figure 3.1 (a), a view of the unit cell along c -direction is shown. To get a better idea of the crystallographic features, the structure is projected differently in figures 3.1 (a) and 3.1 (b). As shown in the figure 3.1 (b), R_2RhSi_3 is made up of Rh-Si and R layers stacked along c -direction alternatively. Due to the short Si-Si distances ($\sim 2.32 \text{ \AA}$), Si atoms form hexagons connecting via the Rh atoms, forming a honeycomb network (figure 3.1(c)). The Si-Si and the Rh-Rh distances ($\sim 3.86 \text{ \AA}$) along the c -axis are very long and therefore the Rh and Si atoms may be considered as forming a two-dimensional sublattice [1]. Each rare-earth layer is intercalated between two Rh-Si layers with the R forming triangular network (figure 3.1 (a), (b)). The R ion can be viewed as occupying two crystallographically inequivalent positions. 25% of the ions (called $R2$) are in the 2(b) site, while 75 % of the ions (called $R1$) are at the 6(h) sites.

The honeycomb network of the Rh-Si ions in the a - b plane results in a tube-like structure along the c -axis. As shown for case of Er [1], the common faces are alternatively larger and smaller, thus resulting in an asymmetry of the nearest neighbor interatomic distances for $R1$ and $R2$ sites.

3.3 Sample preparation and characterization.

For both the samples, magnetic, transport and thermal properties were studied in the bulk form as well as in the nano form. In this chapter we report our studies carried out on the bulk polycrystalline specimens, while the properties of nanoform specimens would be discussed in chapter 6.

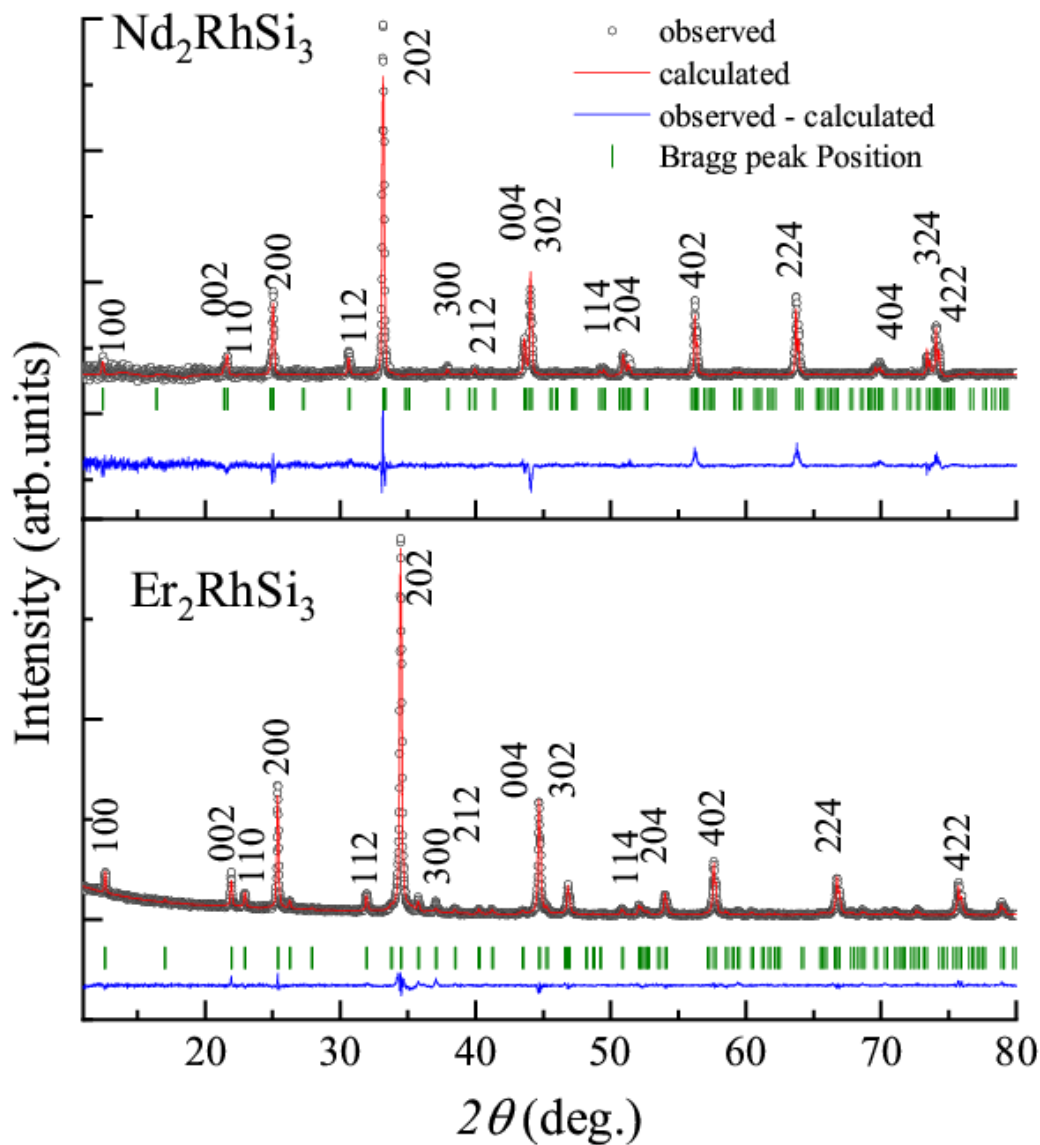


Figure 3.2: Rietveld refined powder x-ray diffraction patterns for R_2RhSi_3 ($R = Nd, Er$) using $Cu K_\alpha$ radiation.

The bulk specimens were prepared using the arc melting technique. The ingots were sealed in a quartz tube and annealed at 1073 K for one week. After annealing, the samples were characterized by powder x-ray diffraction. The diffraction data was analyzed using Rietveld refinement and the refined diffraction patterns for both the compounds are shown in Fig. 3.2. All the fitted parameters are tabulated in table 1.

Table 3.1: Rietveld refined fitting parameters for R_2RhSi_3 ($R = Nd, Er$)

Composition	$a = b$ (Å)	c (Å)	R_p	R_{wp}	R_{exp}	χ^2
Nd ₂ RhSi ₃	8.214 (2)	8.296(7)	42	27	28	1
Er ₂ RhSi ₃	8.1043(1)	7.7518(3)	6	8	13	2.04

This Rietveld refinement of the x-ray diffraction pattern for Nd₂RhSi₃ showed the compound to be in single phase, with the best fit being obtained in the hexagonal space group P6₃/mmc; the refinement pattern is shown in figure 3.2 (a) and the derived lattice constants and fitting results are given in table 3.1. The fits for the XRD patterns clearly reveal that there is a doubling of unit-cell parameters along a - and c - axis with respect to the AlB₂ structure. Scanning electron microscopic images revealed homogeneity of the ingots and energy dispersive x-ray analysis confirmed that the composition corresponds to 2:1:3 (R: Rh: Si).

3.4 Results and discussion for Nd₂RhSi₃.

3.4.1 Dc magnetization behavior

Temperature dependent χ behavior (1.8 -300 K), in a field of 5 kOe and 100 Oe are shown in figure 3.3. For a field of 5 kOe, (see figure 3.3 (a)) inverse $\chi(T)$ shows a gradual deviation from high temperature linearity below 50 K, and $\chi(T)$ exhibits a sharp upturn below ($T_C =$) 16.5 K, due to the onset of long-range magnetic ordering. This feature due to magnetic ordering is much more evident from the derivative plot of susceptibility, shown in the inset, for low temperature range. The deviation seen at a temperature of 50 K, far above the magnetic ordering temperature in the inverse χ plot could possibly due to crystal-field effects. The gradual formation of magnetic clusters (discussed below) can also

contribute to this. The value of μ_{eff} obtained from the Curie-Weiss fit of the linear region is $\sim 3.7 \mu_{\text{B}}/\text{Nd}$, which is very close to that for free trivalent Nd ion ($3.6 \mu_{\text{B}}$). The value of θ_{p} is interestingly very close to zero ($\sim 0.7 \text{ K}$). This means that either magnetic exchange interaction strength is very weak or the ferromagnetic and antiferromagnetic components are of equal strength. In light of relatively large value of magnetic ordering temperature compared to that of θ_{p} , the possibility of a weak magnetic exchange interaction strength is ruled out. In order to further understand the magnetically ordered state of the system, in a field of 100 Oe (for ZFC and FC conditions) was measured by cooling the sample from 50 K, the results of which are shown in figure 3.3 (b). Similar to the features seen in 5 kOe, there is an upturn seen below 16.5 K in both ZFC and FC curves. As the temperature is lowered below 16.5 K, a bifurcation is seen in the ZFC-FC curves around 14.5 K, which is a characteristic feature of spin-glasses [29]. While the ZFC curve peaks at 14.5 K, the FC curve keeps increasing, before attaining flatness a feature which is known for conventional spin glasses [29]. An upturn in FC curve has its origin in magnetic clusters with spin-glass dynamics [see, for instance, Refs. 30-35]. A careful look of the ZFC curve reveals that there is a change of slope in χ at about 10 K, as though there is an additional magnetic feature. Besides, the ZFC-FC curves actually do not merge up to about 40 K, as though there are strange magnetic correlations persisting far above T_{C} , and such behavior of ZFC-FC curves was not seen in Nd_2PdSi_3 [17].

The isothermal magnetization behavior was tracked at various temperatures in the magnetically ordered state to get additional information about the nature of zero field and

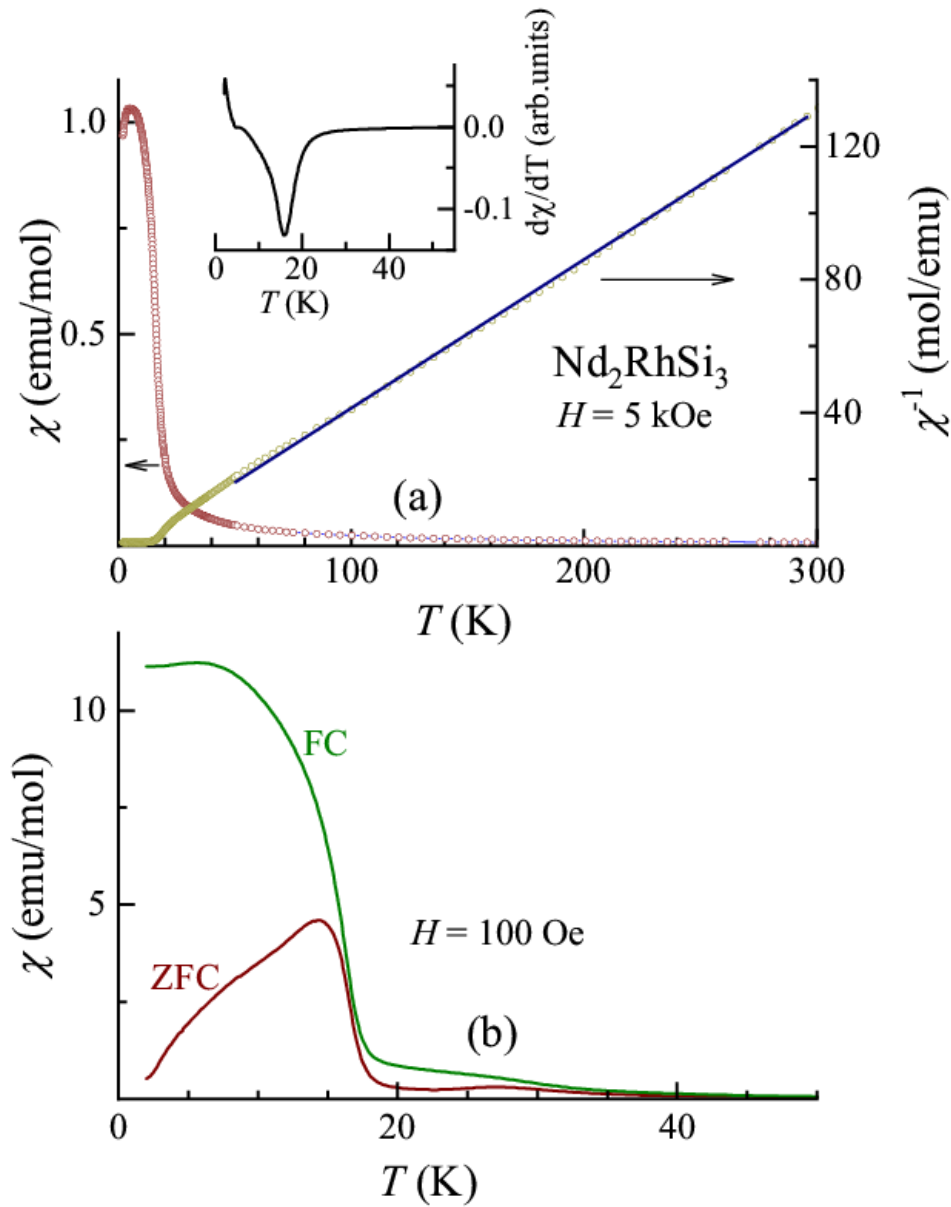


Figure 3.3: a) Magnetic susceptibility and inverse of magnetic susceptibility. A line above 50 K in the inverse χ plot shows Curie-Weiss fitting above 50 K. Inset shows the derivative of the magnetic susceptibility below 60 K. b) Magnetic susceptibility as a function of temperature obtained in a field of 100 Oe for both the zero-field-cooled and field-cooled conditions.

in-field magnetic states. The isothermal magnetization was measured up to a magnetic field of 70 kOe and the data was also collected in the form of hysteresis loops. The results are shown in figure 3.4 (a) and 3.4 (b) in the range of +40 to -40 kOe. In high fields (data not

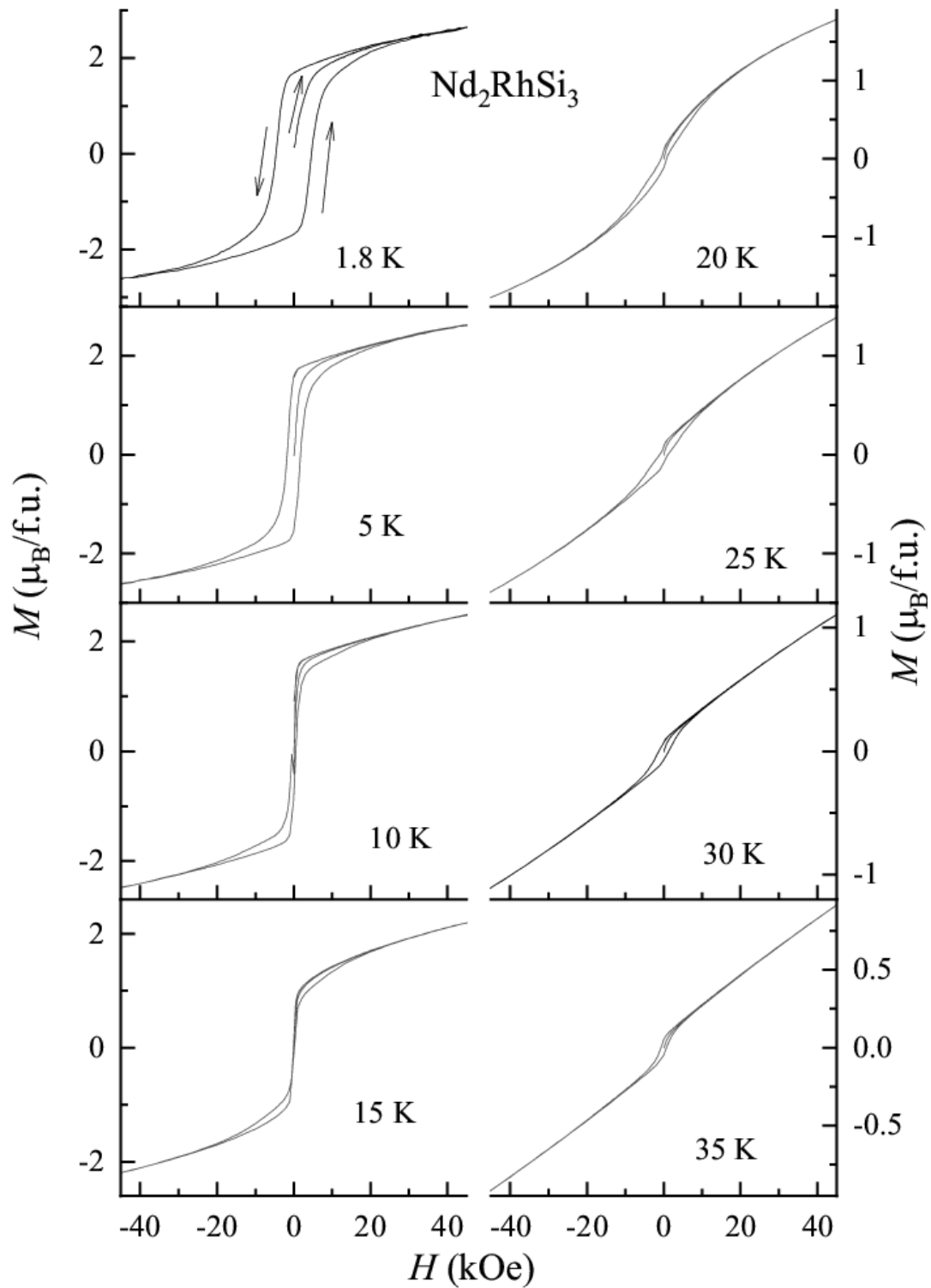


Figure 3.4: a) Magnetic hysteresis loops in a field range of -40 kOe to 40 kOe at various temperatures from 1.8 K to 35 K. Arrows shown in the 1.8 K data are for tracking the path of data with increasing magnetic field

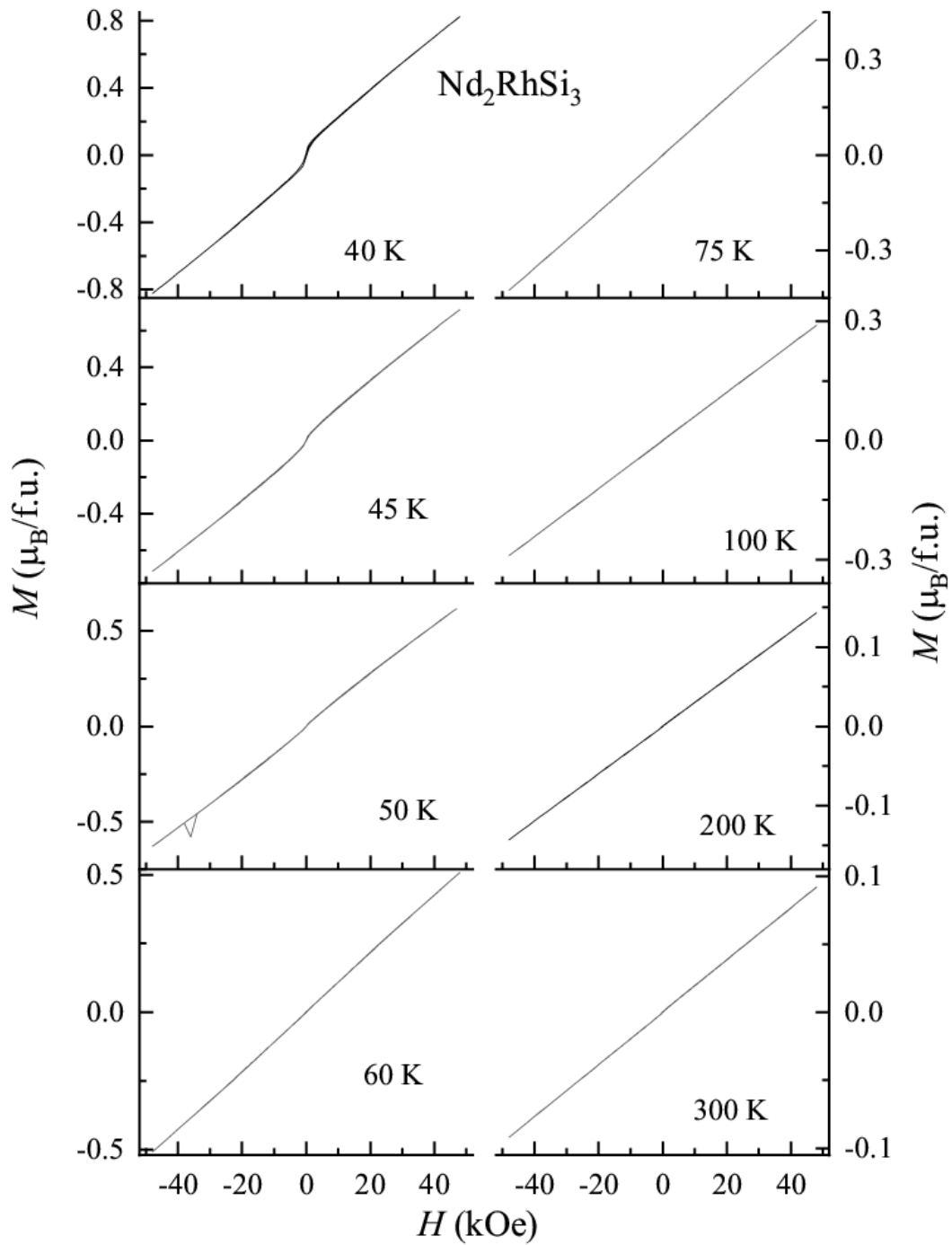


Figure 3.4: b) Magnetic hysteresis loops in a field range of -50 kOe to 50 kOe at various temperatures from 40 K to 300 K.

shown here), the only point of emphasis is that the magnetization curves do not saturate upto the highest measured field of 70 kOe, even for the lowest measured temperature of 1.8 K; the highest value of the magnetic moment attained is $\sim 1.5\mu_B$ per formula unit, say at 70 kOe, which is far below the expected value for trivalent Nd ion. This finding implies that there is an antiferromagnetic component in zero field and/or magnetic-field induced occupation of higher lying crystal field levels. While these observations are similar to that seen for Nd_2PdSi_3 [17], there is a difference in the behavior of the hysteresis loop as compared with the Pd case, in the sense that the virgin curve in the present case lies well inside the loop in the low temperature range, indicating that the ferromagnetic correlations dominate over antiferromagnetic correlations. It may be noted that the $M(H)$ curves are weakly hysteretic even above T_C , say at 35 K, establishing that the ferromagnetic clusters form before long range magnetic ordering sets in. This hysteretic feature gradually disappears with increasing temperature; correspondingly there is a simultaneous decrease of remnant magnetization values. The $M(H)$ plots are found to be linear beyond 50 K.

3.4.2 Heat capacity and isothermal entropy behavior

We measured the heat capacity of the compound in zero field and applied magnetic fields, to throw light on whether a long-range type of magnetism with a well-defined magnetic structure exists in this compound. Heat-capacity behavior as a function of temperature, below 50 K is shown in figure 3.5. In the zero-field curve (figure 3.5(a)), following a gradual decrease with T , there is an upturn at 18 K, with a peak at 15 K. The midpoint of the rising part which is the magnetic ordering temperature is around 16.5 K. Such a prominent λ -like anomaly around 16.5 K supports the existence of a well-defined magnetic

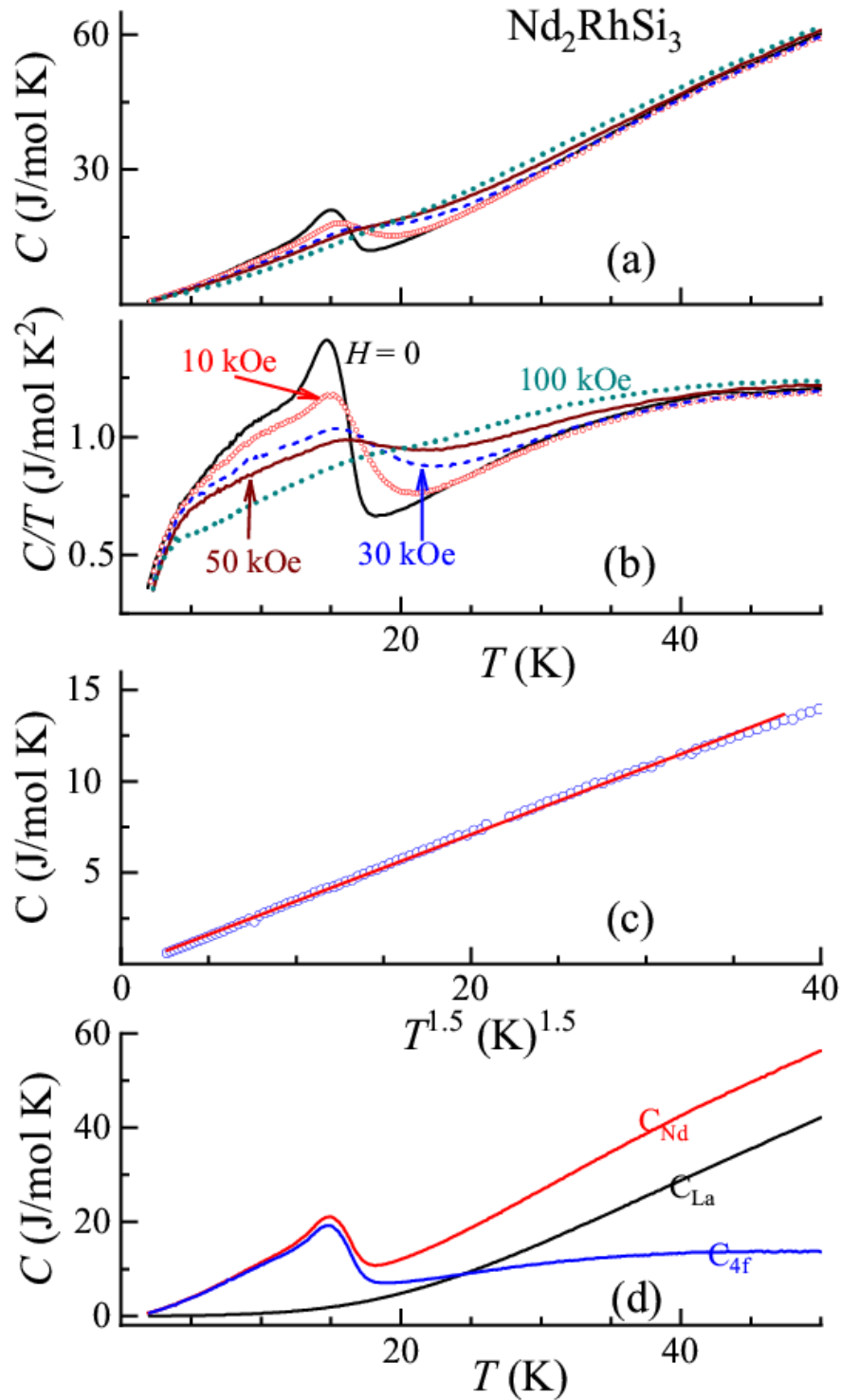


Figure 3.5: (a) Heat-capacity as a function of temperature (<50 K) for Nd_2RhSi_3 , measured in the presence of external magnetic fields as well. (b) Heat-capacity divided by temperature. (c) $T^{1.5}$ form at low temperatures is shown with the continuous line representing the fit to this form. (d) Zero-field heat-capacity as a function of temperature for Nd_2RhSi_3 and La_2RhSi_3 and the 4f contribution to heat-capacity for the former.

structure. In addition, there is an additional weak antiferromagnetic component seen around 10 K (in zero-field) which is much clearer from the plot of C/T versus T shown in figure 3.5 (b). It may also be noted that $C(T)$ in zero field exhibits a power-law behavior ($T^{1.5}$) well below 10 K (figure 3.5 (c)), which is different from T^3 behavior, expected for three-dimensional antiferromagnets, indicating complexities of antiferromagnetism and/or spin-glasses [36]. Above T_c , there is no evidence for long-range magnetic ordering. A careful look into the zero-field C/T data shows a tendency for a broad peak around 40 K.

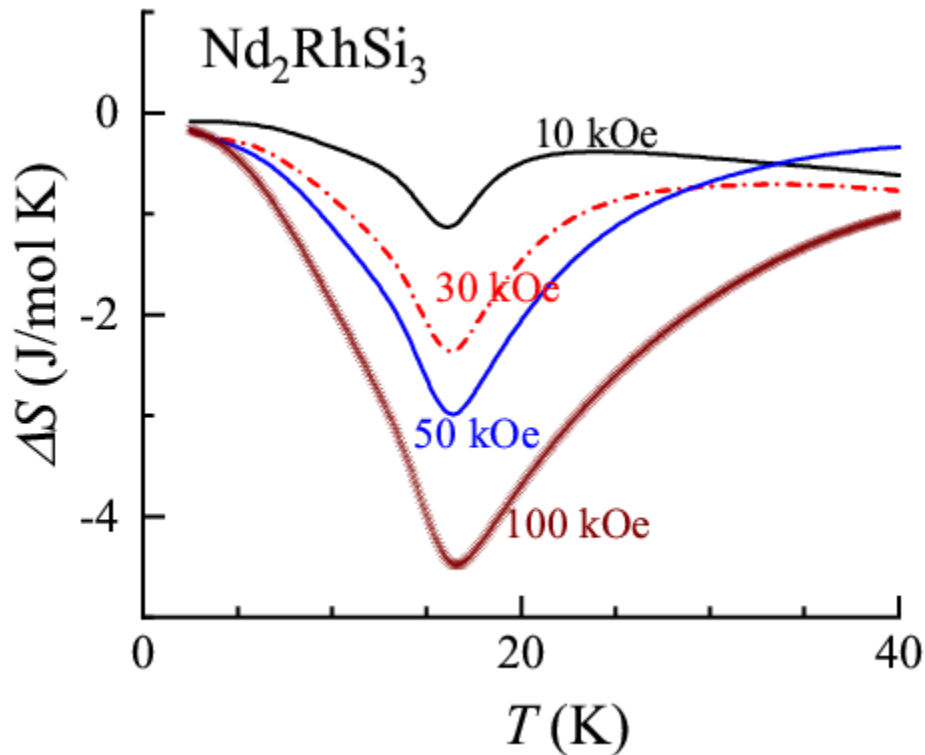


Figure 3.6: Isothermal entropy changes for a change of the magnetic field from zero to a finite value, derived using heat capacity data.

This feature can arise from the formation of short-range magnetic clusters as well as from the crystal-field effects indicated by magnetization data. This feature is clearly visible (figure 3.5 (d)) in the magnetic contribution obtained after subtracting the lattice part, using the heat capacity data of La_2RhSi_3 [26] as per the procedure suggested in Ref.

36. We have derived the isothermal entropy change, ΔS [defined as $S(H) - S(0)$], using the area under the curves of the C/T versus T plots and the curves thus obtained are plotted in figure. 3.6. ΔS shows a well-defined peak at the onset of long-range magnetic order at 16.5 K. The notable point is that the sign of ΔS is negative at all fields, supporting [38] that the ferromagnetism sets in at 16.5K. The tails of the entropy curve extend over a wide temperature range well above 16.5 K at higher fields. This is also supportive of our proposal for the gradual formation of ferromagnetic clusters before the compound enters a long range magnetically ordered state.

3.4.3: Ac magnetic susceptibility and isothermal remnant magnetization

Since dc magnetic susceptibility data for Nd_2RhSi_3 show one of the signatures of a spin glass freezing at low temperatures (ZFC-FC curves divergence), we consider it important to measure ac susceptibility as a function of temperature, for different frequencies, as well as isothermal remanent magnetization in the magnetically ordered state to look for other signature of spin- glass. In zero-field, the ac χ shows a cusp like feature at 16.5 K, that is at T_C , in the real part (see figure 3.7, top). The peak temperature shifts upward marginally with increasing ν . In addition, the peak intensity decreases slightly with increasing ν . While in the imaginary part, a peak appears with a peak temperature of 15.5 K, which is marginally lower than that at 16.5 K for χ' (as in other spin glasses). These peaks are completely destroyed when measurements were carried out in a magnetic field applied externally 5 kOe (not shown) and all these findings are typical of spin-glasses [29]. A surprising finding is that, there are relatively weaker, ν -dependent broad peaks, even above

16.5 K, say, at near 20 and 25 K, suggesting that the clusters, that are formed before long range magnetic order sets in, behave like spin-glasses.

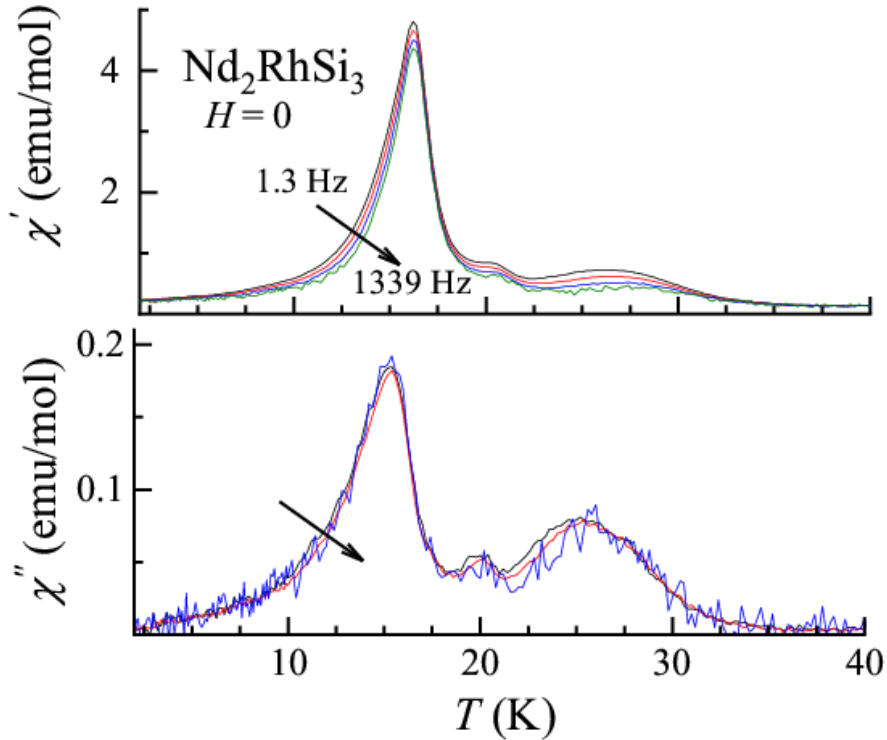


Figure 3.7: Real part (top) and imaginary part (bottom) of ac magnetic susceptibility measured with 1.3, 13, 133, and 1339 Hz frequencies in the absence of external magnetic field.

Possible impurity effects are ruled out as XRD pattern and SEM images reveal single phase nature of specimens. Viewing together the heat-capacity and the ac and dc susceptibility data, it is concluded that ferromagnetism arises from clusters and the inter-cluster dynamics is of spin-glass type.

M_{IRM} was measured as a function of time at selected temperatures and plotted in figure 3.8. The temperatures at which M_{IRM} is measured includes the regions not only below T_C , but also for temperatures above. The data has been obtained in the following manner: First the sample was zero-field cooled to the measurement temperature, a field of 5 kOe

was applied and the specimen was left in this field for a period of 5 minutes; after 5 minutes, the field was switched off and immediately after switching off the field, M_{IRM} was measured as a function of t for about 150 minutes.

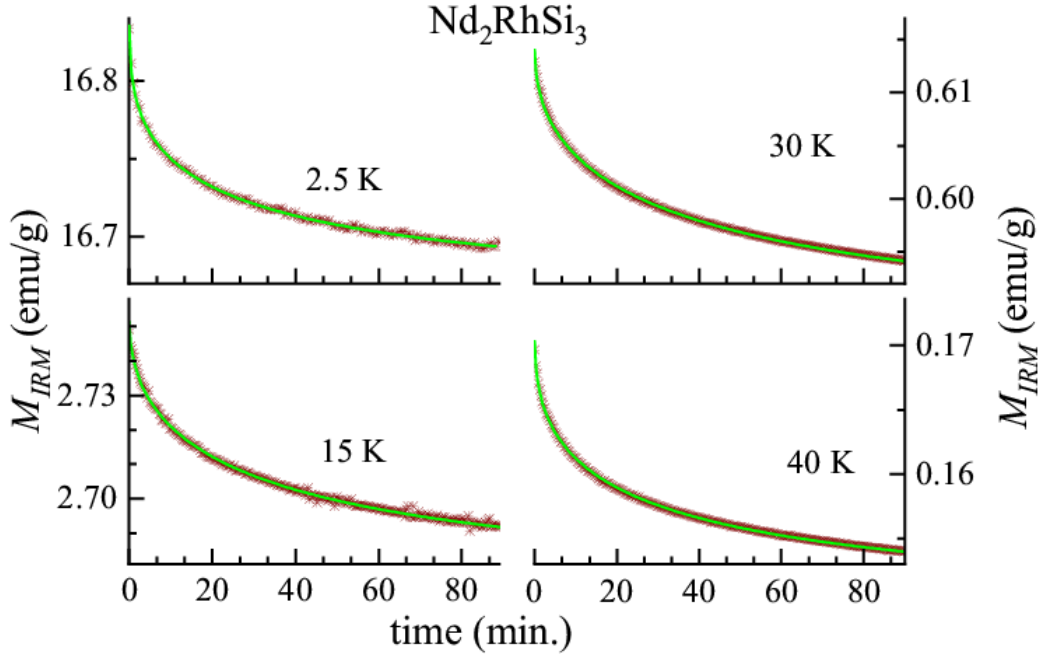


Figure 3.8: Isothermal remnant magnetization as a function of time, obtained at 2.5, 15, 30 and 40 K. Continuous lines through the data points are obtained by a fit to a stretched exponential form as described in the text.

The value of M_{IRM} is significantly large at 2.5 K (well below T_C) as soon as the field is switched off, and the value undergoes a slow decay with increasing t , which is expected for spin-glasses. The magnitude of M_{IRM} at $t = 0$ keeps decreasing as the measurement temperature is increased, indicating that the spin-glass component becomes gradually weaker. It is quite interesting to see that, a weak decay can be observed even at 40 K, which is consistent with the conclusions from ac χ data above. These curves could be fitted to a stretched exponential form [39], $M_{IRM}(t) = M_{IRM}(0) + A \exp(-t/\tau)^{1-n}$, where the constant A , the time constant τ and the exponent n are related to the relaxation rate of the cluster

spin-glass phase at respective temperatures. From the fit, it can be seen that the magnitude of τ falls in the range 1000 to 2500 s, which is typical of cluster spin-glasses [30-35].

3.4.4 Electrical resistivity and magnetoresistance

Electrical resistivity data measured for this compound is shown in figure 3.9. The resistivity data in the range 60-300 K are featureless, with a positive slope, establishing metallicity. Hence the data has been shown only below 55 K.

In the figure 3.9 (a), one can see a sudden drop in ρ (in the zero-field curve) at 16.5 K due to the loss of spin-disorder contribution, strongly supporting the conclusion above that a well-defined magnetic structure sets in at this temperature. This drop persists even at higher applied magnetic fields, say in 10 kOe and 30 kOe; a slope change can be seen even in 50 kOe data. A weak upward shift of the ordering temperature with H , which is a characteristic feature of ferromagnetic ordering can be inferred from the plots. This is also obvious from the derivate curve shown in figure 3.9 (b), from the temperature where a sudden change of slope (above 15 K) occurs. In the case of spin-glass freezing alone, these features would have got smeared around 16.5 K. No other worthwhile drop/peak is observed above 16.5 K, which is consistent with the proposal that the features seen in ac χ features at slightly higher temperatures are due to glassy magnetism. At lower temperatures (<6 K), there is a quadratic T -dependence of ρ (figure 3.9 (c)), as though transport occurs through the ferromagnetic part [40], though another weak (antiferromagnetic) component also sets in below 10 K (see figure 3.9 (a)). This reveals the existence of complex magnetism and transport behavior at low temperatures.

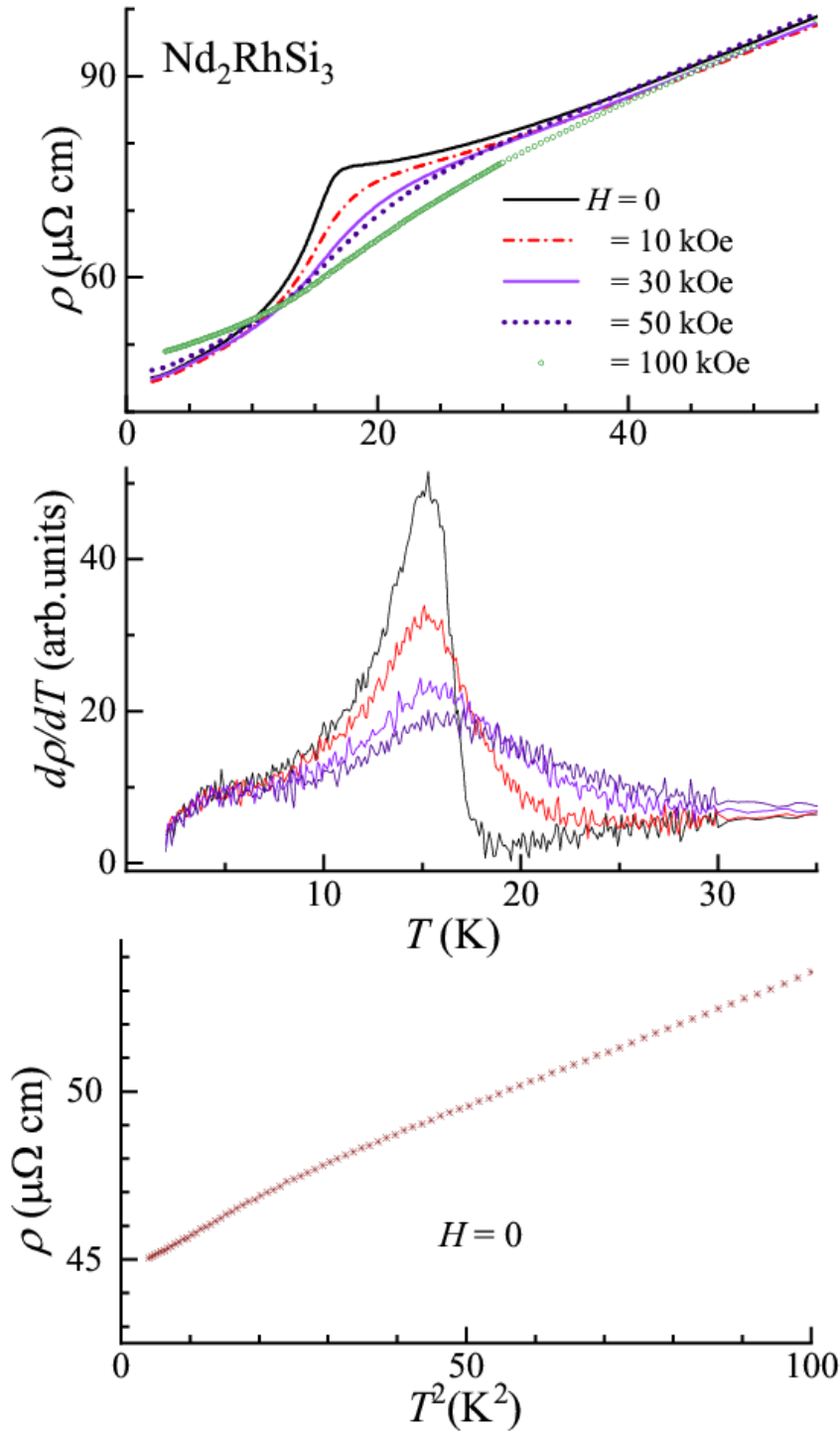


Figure 3.9: a) Electrical resistivity of Nd_2RhSi_3 as a function of temperature in zero field and various applied magnetic fields. b) Derivative curves are shown to infer magnetic ordering temperature from the temperature where an increase in the slope occurs c) Plot of (zero-field) resistivity as a function of square of temperature, below 100 K.

It can be inferred from the resistivity curves shown in figure 3.9, that the magnitude of MR keeps increasing as the temperature is decreased below 50 K, which is similar to the magnetic precursor effects [41] seen for many other rare-earth systems.

Figure 3.10 shows the MR behavior as a function of H at selected temperatures to get a reliable information on sign reversals. In the low temperature regime from 2 to 10 K, the sign of MR is initially negative for low magnetic fields, in the forward cycle. This is consistent with ferromagnetism or spin-glass freezing. As the field is increased, we see a sign crossover with almost a quadratic field-dependence, which is attributable to the dominant classical contribution from conduction electrons. It is difficult to guess whether there is any contribution from the weak antiferromagnetic component (below 10 K) to the positive sign of MR . A weak hysteretic behavior is observed in the reverse direction as the field is approached towards zero, which is consistent with behavior seen in $M(H)$. Just above T_C , e.g., at 20 and 30 K, the ferromagnetic cluster component overrides the classical contribution. The classical contribution usually weakens with increasing T . Once the cluster glass region is almost crossed the classical contribution should start dominating again leading to positive sign of MR . This is what is observed at 50 and 100 K. Near 40 K, compensation of the positive and negative contributions occurs as a result of which negligibly small values of MR ($\ll 1\%$) are seen. Thus, it is evident, that this compound exhibits an interesting interplay between the positive and negative contributions to MR , which is somewhat similar to that observed for Nd_2PdSi_3 [17].

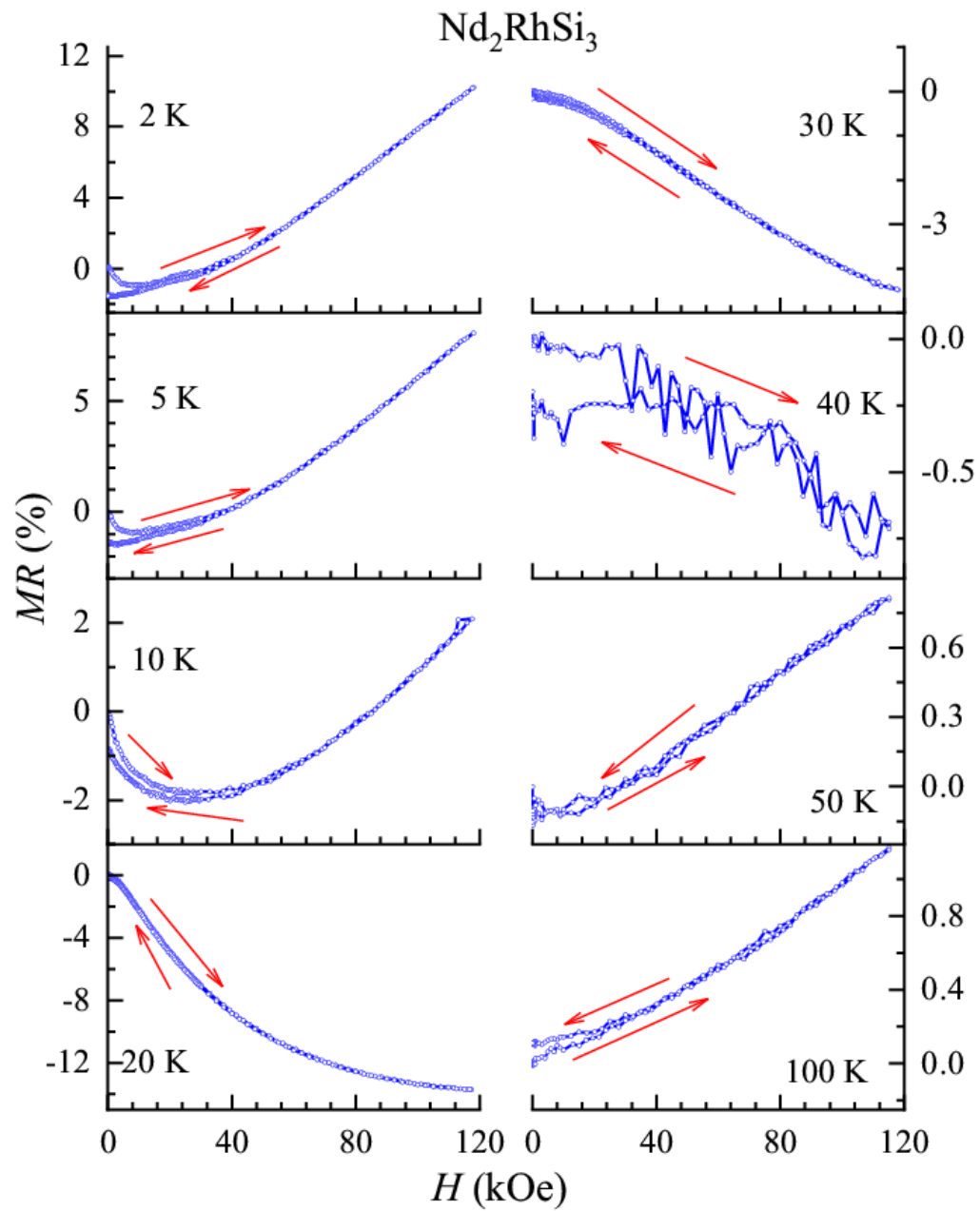


Figure 3.10: Magnetoresistance as a function of H at 2, 5, 10, 20, 30, 40, 50 and 100 K. Arrows serve as guides to show how the magnetic field is varied.

3.5 Results and discussion for Er_2RhSi_3 .

3.5.1 Dc Magnetization behavior

Susceptibility behaviors as a function of temperature for an applied magnetic field of 5 kOe and 100 Oe are plotted in figure 3.11. Inverse susceptibility shows a linear behavior over a wide T -range well above 10 K. The Curie-Weiss fit of the inverse susceptibility in the paramagnetic temperature range from 70 K to 300 K, yields a value of around $\sim 9.69 \mu_B$ for μ_{eff} which is close to the theoretical value of $9.7 \mu_B$, expected for trivalent Er ions. The value of θ_p is found to be around 1.4 K and the positive sign indicates ferromagnetic correlations between Er ions.

This is different from that for other rare-earth members in the same family except for Nd as discussed earlier. With a further lowering of temperature, the susceptibility shows a broad upturn around 5 K, indicating the onset of magnetic ordering at this temperature, which is much beyond the value expected from the high temperature Curie-Weiss behavior.

For understanding the nature of magnetism in the magnetically ordered state, a low-field magnetization curves, in a field of 100 Oe (for ZFC, FCC and FCW conditions) were measured by cooling the sample from 50 K, the results of which are shown in figure 3.11 (b). In the ZFC curve, we see a sharp jump in the susceptibility around 5.2 K, as though the virgin state exhibits a first-order-like transition. In the FCC and FCW conditions the curves are broadened and are shifted strangely to a lower temperature marginally (say by about 0.4 K, the reason for which is unclear) and the FCC and FCW curves show a hysteretic behavior. In addition to these features, the ZFC curve shows a broad shoulder around 3.2 K, while the FCW curve deviates from the ZFC curve at this temperature, with an increasing trend down to 2 K. The bifurcation seen in the ZFC-FC curves, with the FC

curve continuing to rise down to 2 K as in the case of Nd_2RhSi_3 , is typical of cluster spin-glasses [30, 32-35]. This broad feature seen in the 100 Oe field at 3.2 K is not seen in the 5 kOe data, suggesting its sensitivity to external fields.

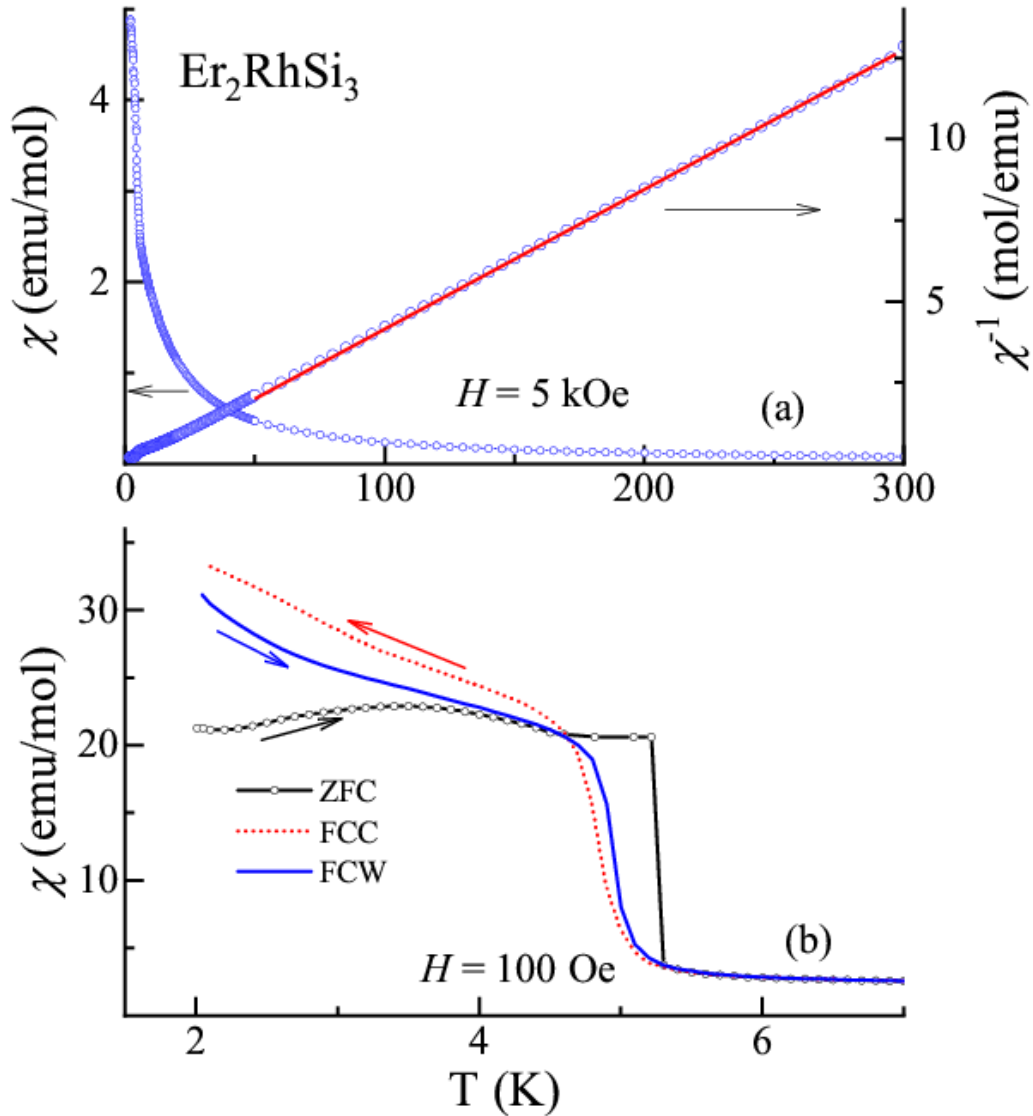


Figure 3.11: a) Magnetic susceptibility (χ) obtained in a field of 5 kOe and inverse of magnetic susceptibility with a line showing Curie-Weiss fitting above 60 K b) Magnetic susceptibility (χ) as a function of temperature obtained in a field of 100 Oe in zero-field-cooled and field-cooled-cooling and field-cooled-warming conditions. Arrows show the direction in which the data were collected while varying the temperature.

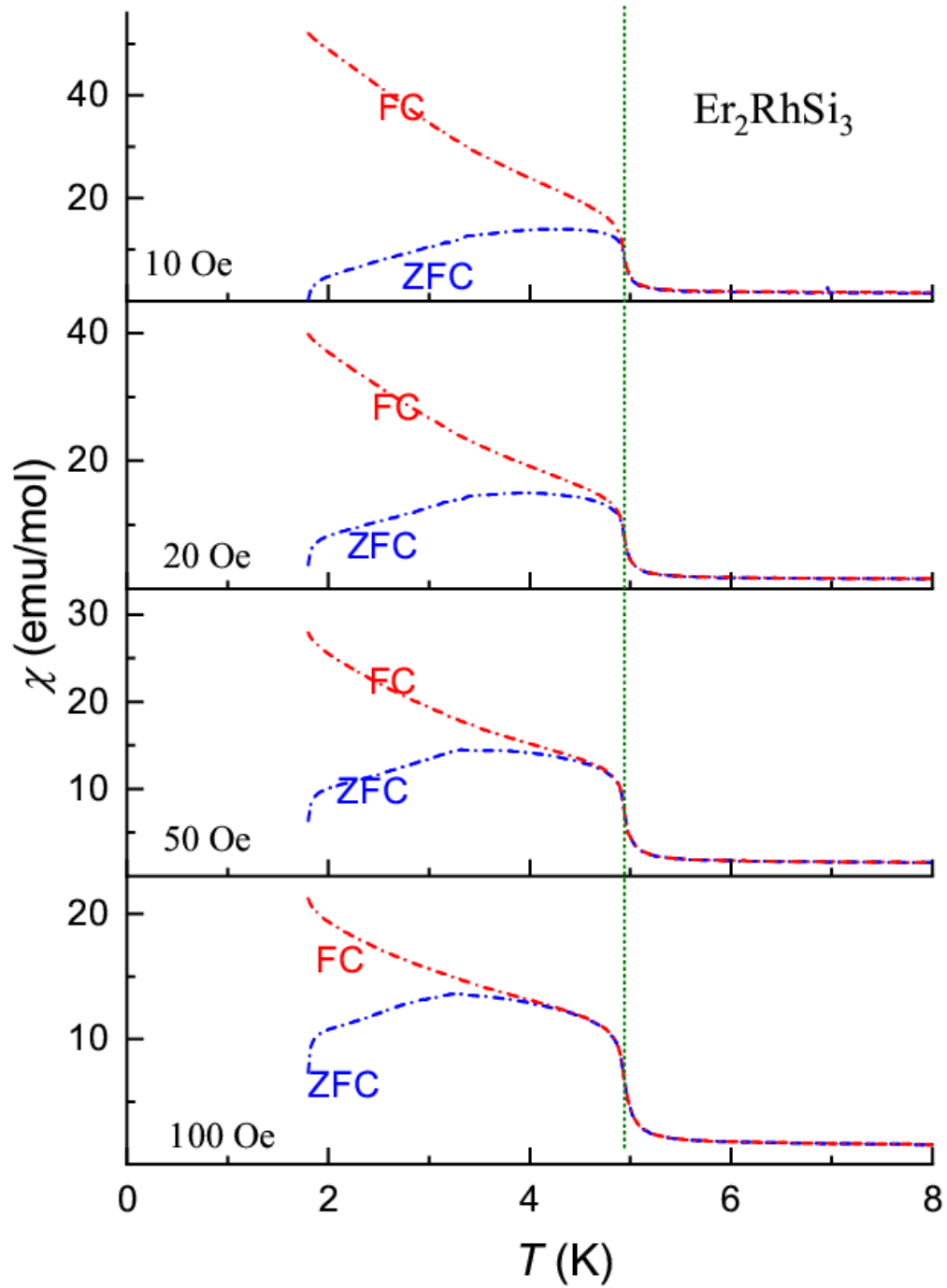


Figure 3.12: Magnetic susceptibility obtained in a field of 10, 20, 50 and 100 Oe for the zero-field cooled and field cooled conditions. Green vertical line serves as a guide to show how the ZFC-FC bifurcation temperature shifts to low temperature with increasing magnetic field.

Novelty of the magnetic features is revealed when the $\chi(T)$ curves were obtained for several low fields (10, 20, 50 and 100 Oe) in both ZFC and FC conditions, in the vicinity of the T -region between 2-20 K (figure 3.12). Since, there are no features to be emphasized beyond 8 K, the curves are been plotted below 8 K only for clarity of the low temperature features. An important point to be emphasized in the low field ZFC-FC curves is that the temperature at which the deviation in the curves begins, reduces with increasing H (*see the dotted vertical green line serving as a guide to the eyes*); for instance, this deviation in curves for a 100 Oe measuring field, is seen at about 3.2 K, while, for a field of 10 Oe, this bifurcation is seen exactly at the onset of magnetic order of 5.2 K itself, as though possible spin-glass freezing occurs at 5.2 K in the absence of any external field. Thus, in the ZFC-FC $\chi(T)$ curves, a high sensitivity of this characteristic temperature is seen to small applications of dc H .

3.5.2 Ac Susceptibility and Isothermal remanent magnetization behavior

In order to ascertain the possible glassiness at low temperature, we measured ac χ in the low temperature region, with frequencies 1.3, 13, 133 and 1333 Hz., and the plot is shown in figure 3.13. Since, at higher temperatures, there are no features to be emphasized, the plot is restricted to the vicinity of the magnetic ordering temperatures.

Both χ' (shown in 3.13 (a)), and χ'' (shown in 3.13 (b)), exhibit prominent peaks with a sharp upturn occurring around 5 K. The peak temperature in χ' shows a weak ν -dependence that is about 0.2 K for a variation of ν from 1.3 to 133 Hz. Similar to what is seen in the case of Nd, a curious point of emphasis is that the peak values also undergo a

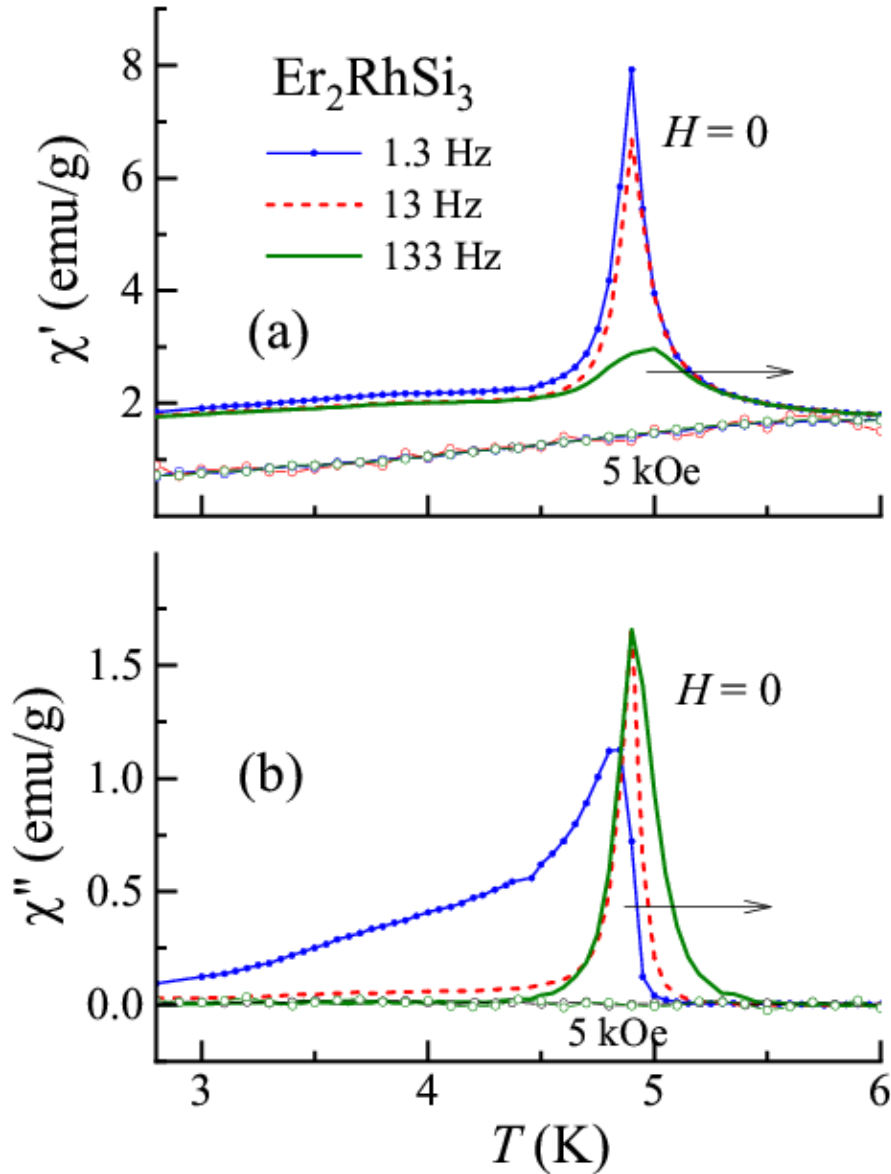


Figure 3.13: a) Real part of ac susceptibility below 6 K, obtained with different frequencies in zero and applied magnetic field of 5 kOe. b) Imaginary part of ac susceptibility below 6 K, obtained with different frequencies in zero field. For both real and imaginary parts, the curves for 5 kOe are flat, featureless and overlap for all frequencies.

dramatic decrease as ν increases, with a significant suppression for the higher frequency of 1333 Hz unlike other spin glasses. With the application of a dc magnetic field of 5 kOe, these peaks are suppressed. Nevertheless, these results establish that this compound undergoes spin-glass freezing at low temperatures. The most important point of emphasis,

as inferred from the peak temperature in χ' , is that the spin freezing occurs exactly at the onset of magnetic ordering.

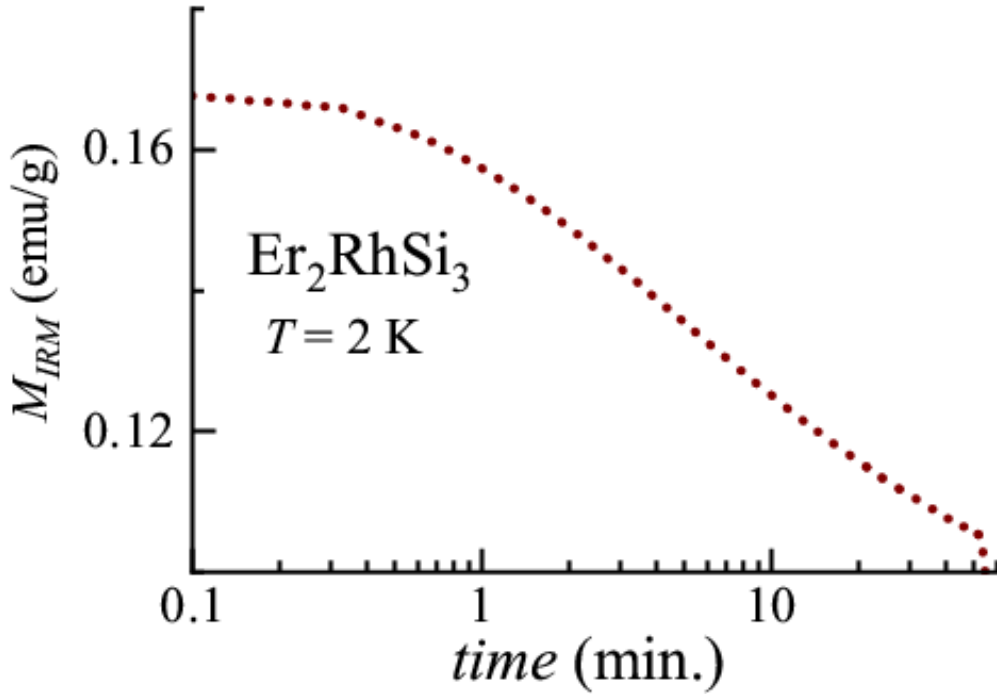


Figure 3.14: Isothermal remnant magnetization at 2 K.

M_{IRM} as a function of time at 2 K (figure 3.14) exhibits a slow decay, varying essentially logarithmically with time (except for the initial few seconds of the data). While all the results establish conclusively, that Er_2RhSi_3 undergoes spin glass freezing at low temperatures, viewing together all the features seen in magnetization (ac and dc) and heat capacity, it is evident that spin-glass freezing and a well-defined magnetic structure set in essentially at the same temperature, that is at 5 K. The results thus establish that partially disordered antiferromagnetism (PDA) occurs at the onset of magnetic ordering temperature at ($T_{\text{N}=\text{}}$) 5.2 K.

3.5.3 Heat capacity and isothermal entropy

The heat capacity behavior of this compound is shown in figure 3.15. For sake of clarity of the low temperature features, $C(T)$ and C/T versus T have been plotted in the T -region of interest only ($\ll 10$ K) (figure 3.15 (a) and (b)), since there is no worthwhile feature to be emphasized in the data measured up to 150 K. Heat capacity data in zero field exhibits a strong λ -anomaly with a sharp upturn at 5 K. This feature is characteristic of the existence of long-range magnetic ordering arising from a well-defined magnetic structure. This is in agreement with the neutron diffraction data that points to the presence of a well-defined magnetic structure at low temperatures [63]. The existence of only spin-glass freezing alone at low temperatures would have smeared the distinct peak in heat capacity seen at low temperatures. The field dependent curves show that the sharp peak gets gradually smeared and broadened, with the peak shifting towards lower temperature for increasing magnetic fields. For example, the peak for 30 and 50 kOe shifts to 4.5 and 3.8 K respectively. This feature establishes that the strong λ -anomaly arises from antiferromagnetism. The $4f$ contribution, C_{4f} , to heat capacity $C(T)$ obtained as for Nd_2RhSi_3 shows a broad peak well above T_N (figure 3.15c), due to combined effects of short-range magnetic order and crystal-field effects.

Isothermal entropy change behavior, is shown in figure 3.15 (d). The magnetic entropy, S_{4f} , is also shown in inset of figure 3.15d, which is obtained by integrating the C_{4f}/T versus T data. It can be seen that S_{4f} has a value less than that expected (46.1 J/mol K) for fully degenerate $4f$ of trivalent Er ion at T_N , suggesting the presence of crystal-field effects.

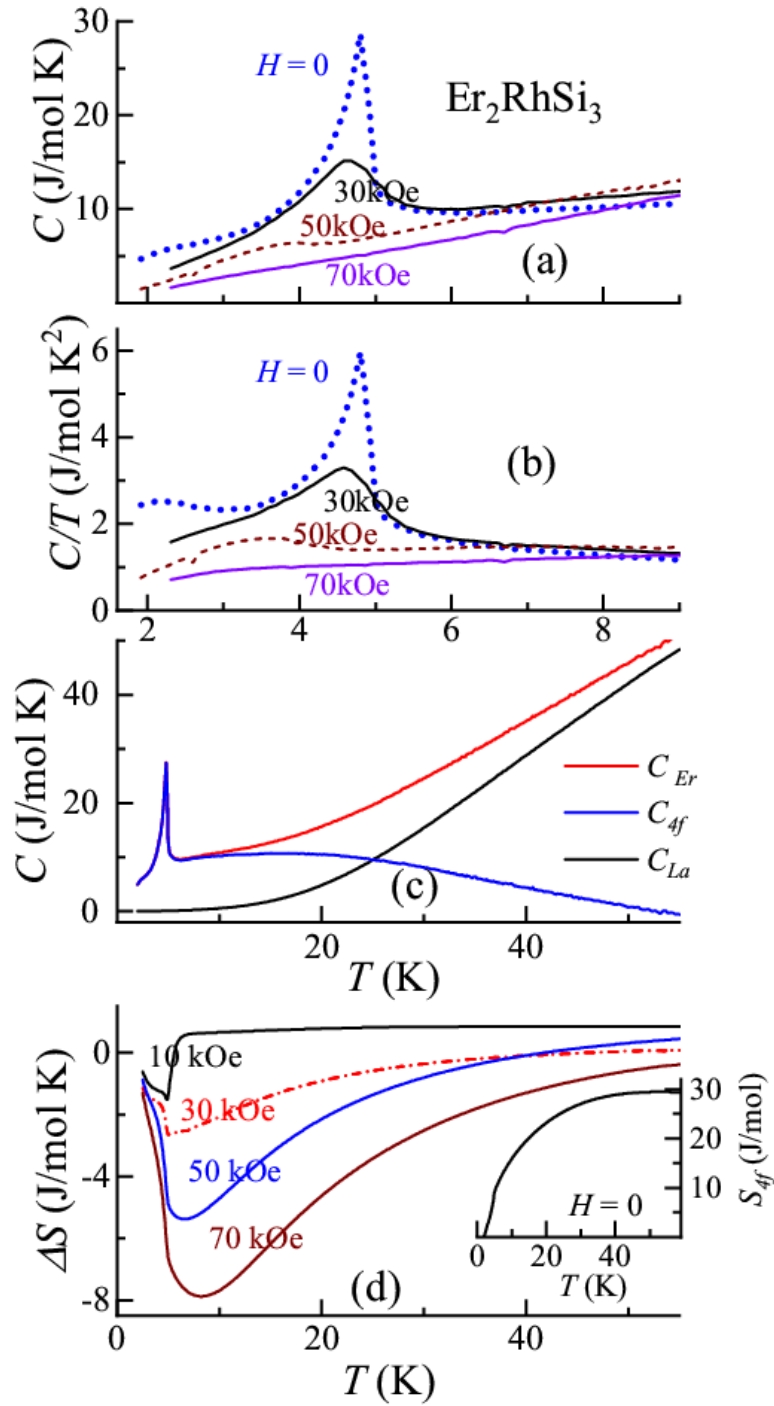


Figure 3.15: (a) Heat-capacity as a function of temperature (<10 K) for Er_2RhSi_3 , measured in the presence of external magnetic fields as well. (b) Heat-capacity divided by temperature. (c) Zero-field heat-capacity as a function of temperature for Er_2RhSi_3 and La_2RhSi_3 and the 4f contribution to heat-capacity for the former. (d) Isothermal entropy change as a function of temperature (2-55 K) for different final fields starting from zero-field with 4f contribution to zero-field entropy in the inset.

It can be seen that the curves of the isothermal entropy change, falls in the negative quadrant with a negative peak, revealing a dominant ferromagnetic component in such fields [38]. These features demonstrate the existence of field-induced changes in the magnetic structure, seen in the magnetically ordered state. The values of the isothermal entropy at the peaks are reasonably large, spreading over a reasonably wide temperature range, above T_N . It is surprising to see that ΔS changes sign sharply at the loss of magnetic order, i.e. above 5 K for 10 kOe, and the positive sign seen in the isothermal entropy, above T_N implies possible field-induced magnetic fluctuations, in such low fields. The sign turns negative in the paramagnetic state for $H > 10$ kOe as expected. However, the large magnitude over a wide T -range may be due to the formation of antiferromagnetic clusters, which gives rise to an effective ferromagnetic alignment with the application of magnetic field. Overall, the results show, that this compound is an example for interesting magnetic precursor effects [3, 21, 41, 58-59] over a wide T -range in the paramagnetic state.

3.5.4 Isothermal magnetization behavior

The isothermal magnetization behavior was measured at 1.8, 4 and 6 K and the results are plotted in figure 3.16a-c. The magnetization data showed an extremely weak hysteretic behavior; hence the curves have been plotted for the increasing magnetic fields only. At 1.8 K, we see a sharp rise in the magnetization for the initial application of a small magnetic field, and a plateau (very sluggish variation) is seen till 20 kOe. These features get smeared with increasing temperature, as shown for the magnetization measured at 4 K. When the field is ramped up further, an upturn in magnetization near about 20 kOe after the plateau occurs.

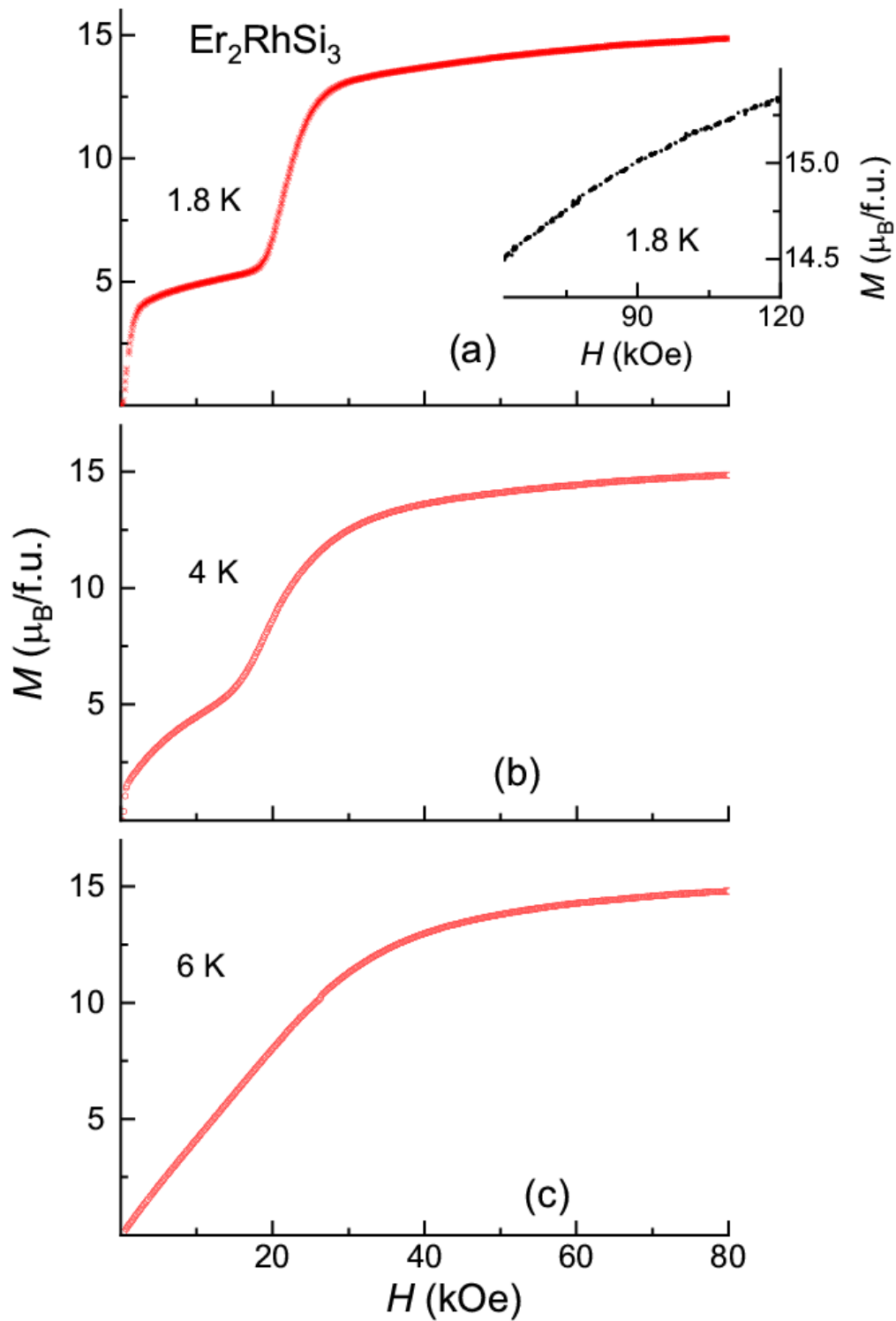


Figure 3.16: Isothermal magnetization of Er_2RhSi_3 plotted below 80 kOe measured at 1.8, 4 and 6 K (shown only for increasing magnetic fields). Inset shows the behavior in the range 60 – 120 kOe measured at 1.8 K.

The variation in magnetization is weak beyond about 30 kOe. We see a continuous increase in magnetization behavior, which tends to flatten, varying weakly beyond 60 kOe till the measured field of 120 kOe, without any further step (figure 3.17 (a), inset), as though the magnetization shows a tendency to saturate. If we try to linearly extrapolate the high-field curve to zero, a magnetization value of about $6.5 \mu_B/\text{Er}$, is obtained. This value is far below the saturation value expected for fully degenerate trivalent Er ions ($9 \mu_B$ per Er). This reduced value can be attributed to the presence of crystal-field effects in the system. The most intriguing observation is that, if we similarly extrapolate the magnetic moment in the plateau region between 20 kOe to 30 kOe, the value is $\sim 2.15 \mu_B/\text{Er}$. This is essentially one-third of the extrapolated value obtained above from the high-field data. Such a feature of 1/3 magnetization plateau can arise only when Er ion at one of the three vortices of the triangular lattice is magnetically disordered, as evidenced by the glassy features exhibited by the compound below the magnetically ordered state, while the other two are coupled antiparallely in zero field in the virgin state.

The plateau region seen in the magnetization data can be explained using a simple-minded picture. As introduced in chapter 1, when the magnetic interaction between the R ions in a triangular lattice is antiferromagnetic, one of the three sites become frustrated or magnetically disordered. The magnetic moment of this ‘disordered’ Er ion gets oriented along the field, thereby leaving the other two Er ions aligned antiparallel to each other. This leads to a net spontaneous moment. It is quite surprising to see such an intermediate state to be stable against the perturbation by a magnetic field of 20 kOe. It appears that the antiparallel interaction between the two Er ions is so strong that a field of 20 kOe is enough to flip the Er moment direction. When the field crosses a magnetic field of 30 kOe, all the

three sites tend to align ferromagnetically, resulting in thrice of magnetic moment of the plateau region. Thus, there is distinct support for ‘Partially Disordered Antiferromagnetism’ attributable to geometrical frustration of the magnetic moments from the isothermal magnetization data. From the $M(H)$ curve for 6 K (shown in figure 3.16 (c)), it is obvious, that the plateau region vanishes, thereby establishing that the plateau is a characteristic feature of the magnetically ordered ground state in this compound.

3.5.5 Resistivity and magnetoresistance behavior

In view of the partially disordered antiferromagnetic state attributable to geometrical frustration of the magnetic moments, the magnetization of this compound is exotic, particularly noting that the PDA features are generally not exhibited by RKKY governed magnetic materials, that is metallic magnets. Therefore, it is worthwhile to study the magnetoresistive behavior of such systems to understand the behavior in the 1/3 plateau regime, since such features cannot be studied in the case of corresponding insulators.

Resistivity curves as a function of temperature (1.8 – 200 K) for zero and applied magnetic fields, are plotted in figure 3.17. As seen in figure 3.20 (a), $\rho(T)$ (both in the presence of zero field and applied magnetic fields), show metallic behavior at temperatures higher than the magnetic ordering temperature due to positive temperature coefficient. Resistivity behavior below 20 K, is plotted in the figures 3.20 (b), 3.20 (c), 3.20 (d) and 3.20 (e). In zero-field, the resistivity as a function of temperature, shown in figure 3.20 (b), shows a distinct drop, due to the onset of magnetic ordering at 5.2 K. This feature strongly supports the conclusion, that a well- defined magnetic structure sets in at T_N as inferred

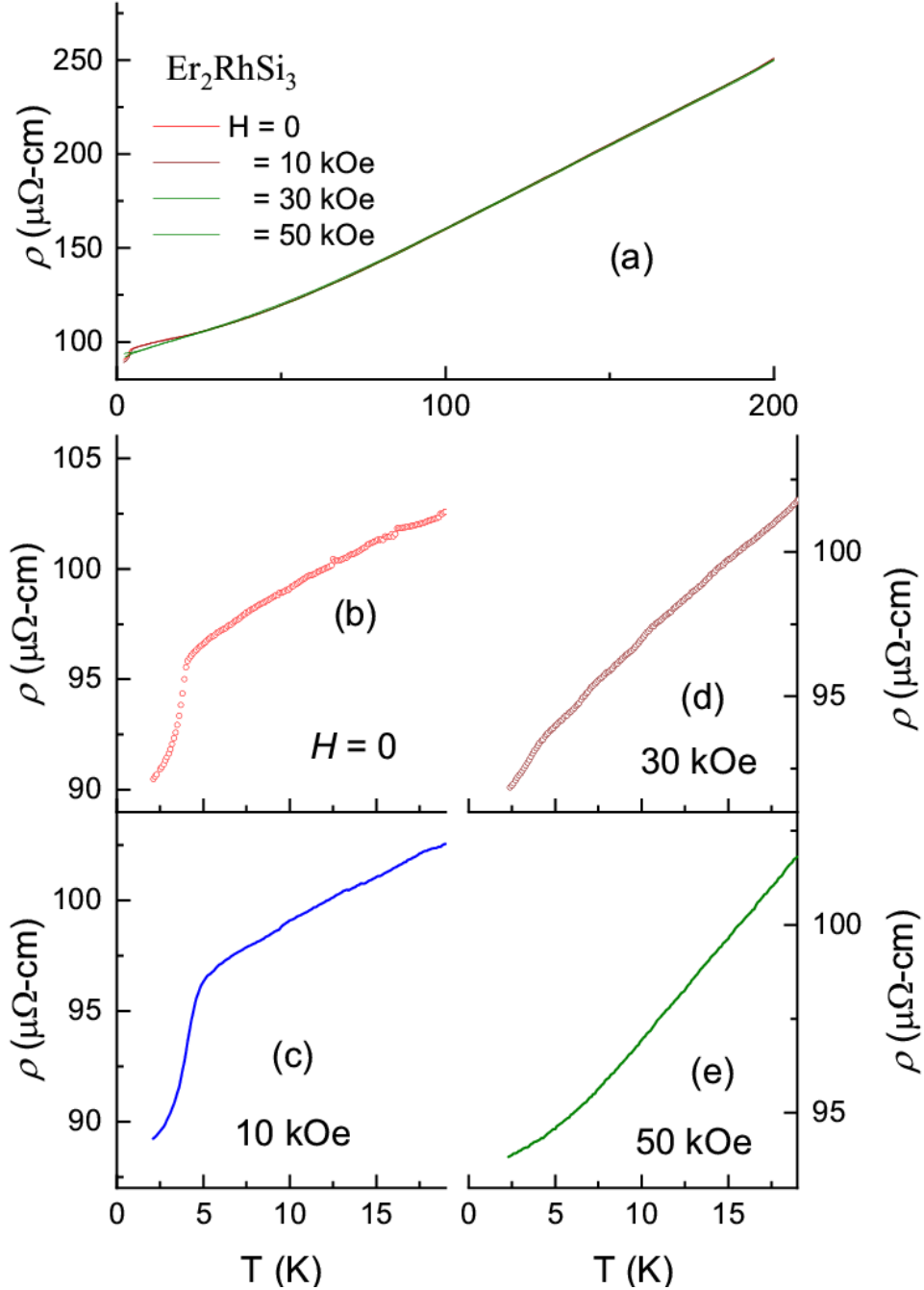


Figure 3.17: (a) Electrical resistivity as a function of temperature for Er_2RhSi_3 , measured in the presence of external magnetic fields as well. (b), (c), (d), (e) the plots below 20 K for $H = 0$, 10 kOe, 30 kOe and 50 kOe respectively are shown.

from the $C(T)$ and χ data. This drop persists even for a field of 10 kOe, but the feature gets suppressed with a distinct change in slope seen in a field of 30 kOe. Beyond 50 kOe, this feature is completely smeared.

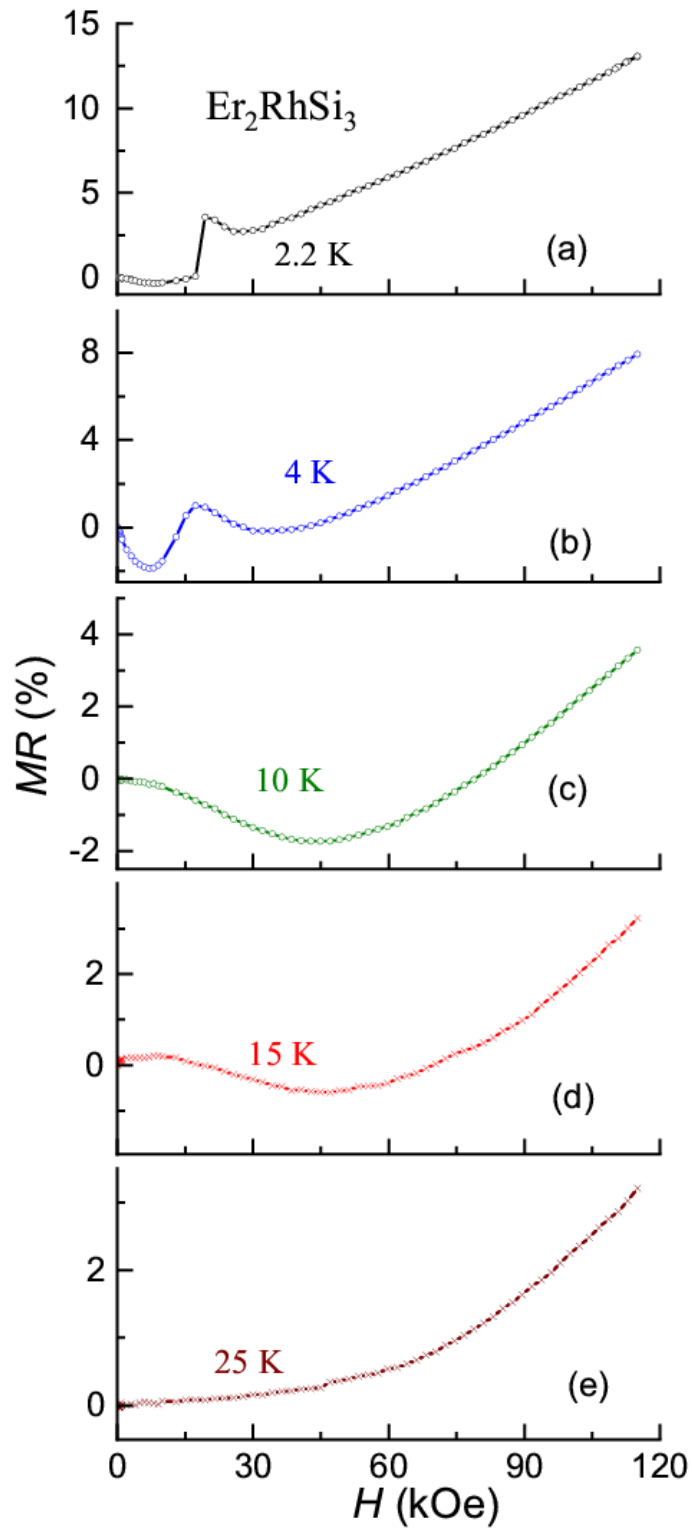


Figure 3.18: Magnetoresistance behavior as a function of magnetic field for Er_2RhSi_3 , measured at 2.2 K, 4K, 10 K, 15 K and 25 K.

Figures 3.18a-e show the behavior of isothermal magnetoresistance, at various temperatures across T_N . The MR curves are essentially nonhysteretic in nature. For a temperature of 2.2 K, the magnitude of MR is negligibly small below 20 kOe, but a negative sign emerges after a small change in applied magnetic field (attributable to grain boundaries or spin-glass component); otherwise, MR is almost flat in the 1/3 magnetization plateau region, interestingly avoiding even conventional magnetic and non-magnetic contributions for scattering process. Once this plateau region is crossed, there is a distinct upturn in MR behavior to positive quadrant. This is followed by a weak drop around 30 kOe due to ferromagnetic alignment contribution. When the magnetic field is increased further to the region where magnetization tends to saturate, MR keeps increasing remaining in the positive quadrant. Such a linear MR variation in the essentially ferromagnetically aligned state is puzzling (as one would expect a negative MR with a non-linear dependence on H for ferromagnets). It is possible that the positive classical contribution due to conduction electrons dominates ferromagnetic contribution at higher fields. At 4 K, the features are similar, except that the initial drop in MR is more prominent. Just above T_N , say at 10 K, there is a competition between well-known paramagnetic contribution (negative sign with H^2 -dependence) and positive classical contribution, which leads to a minimum at the intermediate field range. As the temperature is further increased say, for 10, 15 and 25 K (Fig. 3.21 (b) – (d)), it is expected that the paramagnetic contribution should get gradually weakened, and hence the minimum gradually vanishes.

3.6 Discussions

Let us now compare the systematics in the long-range magnetic ordering temperatures of rare-earths in Pd and Rh ternary series, to pin point an intriguing observation.

Antiferromagnetism sets in for Rh (Pd) family as follows: For Ce [6, 8, 42-44], 3 K (6 K); for Gd [3, 5, 26], 13.5 K (21 K); for Tb [4, 7, 12, 26], 13.5 K (23.6 K); for Dy [4, 26], 6.5 K (8 K); for Ho [10] 5.2 K (8 K) and for Er [13] 5 K (7 K). Obviously, the long-range magnetic ordering temperatures of the R ions (other than Nd) are by and large higher for the Pd series, with respect to those for the Rh series. This implies that the exchange interactions in these systems are dominated by the $R 4f$ with Pd/Rh $4d$. Now making a similar comparison for the Nd compounds, when Pd is replaced by Rh, this value essentially remains the same (~ 16 K). It is important to note that in both these compounds ferromagnetic ordering takes place, despite the fact that, for all other members including Ce, the onset of magnetic ordering is of an antiferromagnetic-type. As pointed out earlier, the $4f$ hybridization in the case of Ce systems is stronger than in Nd systems. If Nd $4f$ hybridization with Pd/Rh $4d$ states is responsible for anomalous magnetism, the magnetic behavior of Nd in both the series should have been similar to that of respective Ce compound. This is in contrast to the observation. Thus, from the above comparison of the magnetic behavior of Ce cases with the Nd compounds, it is concluded that Nd $4f$ hybridization with $3p$ orbitals of Si is the dominant factor to make the magnetism of Nd compounds different from other members within the respective ternary family. Similar inference can be made for Nd_2PtSi_3 ($T_C = 17.5$ K) also [45, 46]. However, we find there are subtle differences in the magnetic properties of Nd_2RhSi_3 with respect to Nd_2PdSi_3 . (i) In the Rh case there are ferromagnetic-like $M(H)$ loop at very low temperatures which is in contrast to dominating antiferromagnetic-like loop in the case of Pd and (ii) clear evidence for cluster-glass anomalies in the χ data above T_C in the former case only. So, we speculate that the hybridization with d band of transition metals play a subtle role to decide

magnetism. From the results presented above, we propose that the size of ferromagnetic clusters evolves gradually with decreasing temperature below 50 K eventually leading to sufficiently large sizes of these magnetic clusters, resulting in long range magnetic ordering. Such a finding was not reported for other members of this family [6, 64, 65]. Like some of them (e.g. Gd, Tb, Ho) do not even show spin glass anomalies. Clearly cluster formation must be due to special behavior of $4f$ orbital in the present cases, which needs to be understood theoretically. As an indirect support for cluster formation due to Nd $4f$ hybridization, real space high resolution transmission electron spectroscopic studies [48] on Ce and Nd analogues in a related family R_2CuSi_3 revealed relatively large sizes of clusters for the latter compared to the former.

Several magnetic phases forming such clusters competing as discussed above with a gradual lowering of temperature towards magnetic ordering temperature is attributed to geometrical frustration in a triangular network of magnetic ions, as emphasized for $Tb_3Ru_4Al_{12}$ [55], and theoretically [21, 56, 58], though such a magnetic state appearing before long-range magnetic order has been called differently by different approaches namely, “correlated paramagnetic state”, “classical spin liquid state” and, more broadly “magnetic precursor effects”.

We now relate the properties to an intriguing crystallographic feature. As stated at the introduction, the lattice is quite strained with multiple bond distances for a given pair of atoms of R . Therefore, the crystal structure (figure 3.1b) is made up of non-equilateral triangles of Er/Nd. This implies that there is a bond disorder. This kind of geometry-induced bond disorder naturally results in randomness in exchange interactions. This is a source of ‘partially disordered magnetic’ and long range ordered components in a

stoichiometric compound. Such a bond-disorder induced magnetic frustration was also theorized about a decade ago [60, 61].

3.7 Conclusions

In this chapter, the results of *exhaustive* investigations by dc and ac magnetization, heat-capacity and transport measurements for the two compounds, R_2RhSi_3 ($R= Nd$ and Er), crystallizing in a AlB_2 -derived hexagonal structure, are reported for the first time. The results reveal that these compounds exhibit interesting properties – unique in their own way – due to a competition between ferromagnetic and antiferromagnetic interactions, which can be tuned by temperature and magnetic-field. While there are many interesting features in the properties as elaborated in previous sections, the essence of key findings are only summarized below for each of these compounds.

The compound Nd_2RhSi_3 is established to exhibit long range ordering of a ferromagnetic type (at 16.5 K). The observed value of T_C is essentially the same as that of isostructural Nd_2PdSi_3 , unlike the antiferromagnetic behavior at different temperatures for a given R within the two families, thereby suggesting the dominant role of Nd $4f$ -Si $3p$ hybridization. This hybridization in addition causes a significant enhancement of T_C , disobeying de Genne scaling. Such demonstrations of $4f$ hybridization effects on magnetism are not known previously for Nd compounds. The magnetism is complex at temperatures lower than ~ 10 K with magnetic properties pointing to the development of an antiferromagnetic component as in the Pd analogue. However, there are subtle differences between Nd_2PdSi_3 and Nd_2RhSi_3 well below T_C (e.g., in the nature of virgin isothermal magnetization behavior in the magnetic hysteresis loop, suggesting dominance of

ferromagnetic component in the latter). The point to be stressed is that there is a remarkable difference between these two Nd compounds in the magnetic behavior above T_C : That is, there are evidences for the gradual onset of ferromagnetic clusters with spin-glass dynamics (as revealed by the bifurcation of ZFC-FC dc χ curves, frequency -dependent ac χ peaks and slow decay of M_{IRM}) as the temperature is lowered towards T_C for the Rh case, as though Nd 4f-Rh 4d interaction is a triggering factor for its origin. Given that this family is characterized by a triangular arrangement of rare-earth ions and that there is a crystallography-favored bond disorder, the local variations in Nd 4f covalency should be the key for above-mentioned frustrated magnetism (that is, reflected in the form of cluster spin-glass dynamics). It is intriguing that some other heavy rare-earth members of this family do not show spin-glass anomalies in polycrystalline form. Therefore, crystalline defects may not be the sole cause of spin-glass anomalies in the present cases (see below for Er case). The temperature dependence of electrical resistivity and the features (including sign reversals) in the magnetoresistance are in conformity with the conclusions made above for the Rh compound. The results overall reveal this Nd compound is an exotic magnetic material. Therefore, further studies by other experimental techniques would be rewarding,

With respect to Er_2RhSi_3 , Er is known to contain 4f electrons of localized character only, unlike Nd 4f, and hence offers an opportunity to explore anomalous magnetism of 4f in the localized limit. The results provide evidence for the onset of long-range antiferromagnetic order at 5 K, with cluster spin-glass features at the same temperature (just as the Nd case, which is however ferromagnetic). A notable finding is that this compound exhibits a characteristic feature of partially disordered antiferromagnetism, viz.,

1/3 magnetization plateau. This is fascinating as such a PDA magnetism has been proposed for some insulators with geometrically frustrated magnetism, but not so common among metals, that is, in a material with RKKY interaction, that too without any interference from other $4f$ -related hybridization phenomena. Additionally, none of the isostructural ternary rare-earth compounds has been known to show such PDA characteristics in the past, in particular, other rare-earth compounds of this Rh family (R= Gd, Dy and Ho) [64, 65] as well as the Er counterpart in the Pd-based family, Er_2PdSi_3 [13]. Clearly, this compound is also a unique magnetic material. It is not clear whether the magnetic interaction between orientated crystal-field-split ground state of $4f$ orbital of Er with Rh $4d$ -orbital in this case facilitates such an anomalous magnetism. It is also demonstrated that this compound should also serve as a prototype for transport behavior across 1/3 magnetization plateau.

In short, this work, adding the results of our investigations on Nd and Er members of R_2RhSi_3 , establishes that each member of the R_2RhSi_3 family is unique in their way in physical properties, with $4f$ orbitals in the present cases, playing a special role on certain anomalous aspects of magnetization in these compounds. Therefore, further studies of this family by various other experimental methods would be rewarding.

3.8 Bibliographical references

1. Chevalier B, Lejay P, Etourneau J, Hagenmuller P. A new family of rare earth compounds, the ternary silicides RE_2RhSi_3 (RE= Y, La, Ce, Nd, Sm, Gd, Tb, Dy, Ho, Er)-crystal structure electrical and magnetic properties. Solid state communications. 1984 Feb 1; 49(8):753-60.

2. Mallik R, Sampathkumaran EV, Strecker M, Wortmann G, Paulose PL, Ueda Y. Complex magnetism in a new alloy, Eu_2PdSi_3 , with two crystallographically inequivalent sites. *Journal of magnetism and magnetic materials*. 1998 Jun 4; 185(2):L135-43.
3. Mallik R, Sampathkumaran EV, Strecker M, Wortmann G. Observation of a minimum in the temperature-dependent electrical resistance above the magnetic-ordering temperature in Gd_2PdSi_3 . *Europhysics Letters*. 1998 Feb 1;41(3):315.
4. Mallik R, Sampathkumaran EV, Paulose PL. Large low temperature magnetoresistance and magnetic anomalies in Tb_2PdSi_3 and Dy_2PdSi_3 . *Solid state communications*. 1998 Apr 1; 106(3):169-72.
5. Saha SR, Sugawara H, Matsuda TD, Sato H, Mallik R, Sampathkumaran EV. Magnetic anisotropy, first-order-like metamagnetic transitions, and large negative magnetoresistance in single-crystal Gd_2PdSi_3 . *Physical Review B*. 1999 Nov 1; 60(17):12162.
6. Saha SR, Sugawara H, Matsuda TD, Aoki Y, Sato H, Sampathkumaran EV. Magnetic, thermal, and transport properties of single crystals of antiferromagnetic Kondo-lattice Ce_2PdSi_3 . *Physical Review B*. 2000 Jul 1; 62(1):425.
7. Majumdar S, Sampathkumaran EV, Paulose PL, Bitterlich H, Löser W, Behr G. Anisotropic giant magnetoresistance, magnetocaloric effect, and magnetic anomalies in single crystalline Tb_2PdSi_3 . *Physical Review B*. 2000 Dec 1; 62(21):14207.
8. Majumdar S. SAMPATHKUMARAN EV. *J. Magn. Magn. Mater.* 2001; 223: 247.

9. Chaika AN, Ionov AM, Busse M, Molodtsov SL, Majumdar S, Behr G, Sampathkumaran EV, Schneider W, Laubschat C. Electronic structure of R_2PdSi_3 ($R = La, Ce, Gd, \text{ and } Tb$) compounds. *Physical Review B*. 2001 Sep 11; 64(12):125121.
10. Sampathkumaran EV, Bitterlich H, Iyer KK, Löser W, Behr G. Magnetic behavior of single-crystal Ho_2PdSi_3 . *Physical Review B*. 2002 Aug 9; 66(5):052409.
11. Li DX, Nimori S, Shiokawa Y, Haga Y, Yamamoto E, Onuki Y. ac susceptibility and magnetic relaxation of R_2PdSi_3 ($R = Nd, Tb, \text{ and } Dy$). *Physical Review B*. 2003 Jul 30; 68(1):012413.
12. Paulose PL, Sampathkumaran EV, Bitterlich H, Behr G, Löser W. Anisotropic spin-glass-like and quasi-one-dimensional magnetic behavior in the intermetallic compound Tb_2PdSi_3 . *Physical Review B*. 2003 Jun 6; 67(21):212401.
13. Iyer KK, Paulose PL, Sampathkumaran EV, Frontzek M, Kreyszig A, Doerr M, Loewenhaupt M, Mazilu I, Behr G, Löser W. Novel magnetic behavior of single-crystalline Er_2PdSi_3 . *Physica B: Condensed Matter*. 2005 Jan 31; 355(1-4):158-63.
14. Nimori S, Li D. Studies of the reentrant spin-glass behavior in Dy_2PdSi_3 . *Journal of the Physical Society of Japan*. 2006; 75(Suppl):195-7.
15. Inosov DS, Evtushinsky DV, Koitzsch A, Zabolotnyy VB, Borisenko SV, Kordyuk AA, Frontzek M, Loewenhaupt M, Löser W, Mazilu I, Bitterlich H. Electronic structure and nesting-driven enhancement of the RKKY interaction at the magnetic ordering propagation vector in Gd_2PdSi_3 and Tb_2PdSi_3 . *Physical Review Letters*. 2009 Jan 26; 102(4):046401.

16. Frontzek M, Tang F, Link P, Schneidewind A, Hoffman JU, Mignot JM, Loewenhaupt M. Correlation between crystallographic superstructure and magnetic structures in finite magnetic fields: A neutron study on a single crystal of Ho_2PdSi_3 . *Physical Review B*. 2010 Nov 1; 82(17):174401.
17. Mukherjee K, Basu T, Iyer KK, Sampathkumaran EV. 4 f hybridization effect on the magnetism of Nd_2PdSi_3 . *Physical Review B*. 2011 Nov 14;84(18):184415.
18. Maiti K, Basu T, Thakur S, Sahadev N, Biswas D, Adhikary G, Xu Y, Löser W, Sampathkumaran EV. Electronic structure studies on single crystalline Nd_2PdSi_3 , an exotic Nd-based intermetallic: Evidence for Nd 4f hybridization. *Journal of Physics: Condensed Matter*. 2020 Aug 25; 32(46):46LT02.
19. Smidman M, Ritter C, Adroja DT, Rayaprol S, Basu T, Sampathkumaran EV, Hillier AD. Magnetic order in Nd_2PdSi_3 investigated using neutron scattering and muon spin relaxation. *Physical Review B*. 2019 Oct 17; 100(13):134423.
20. Paddison JA, Rai BK, May AF, Calder S, Stone MB, Frontzek MD, Christianson AD. Magnetic Interactions of the Centrosymmetric Skyrmion Material Gd_2PdSi_3 . *Physical Review Letters*. 2022 Sep 23; 129(13):137202.
21. Wang Z, Barros K, Chern GW, Maslov DL, Batista CD. Resistivity minimum in highly frustrated itinerant magnets. *Physical review letters*. 2016 Nov 8; 117(20):206601.

Wang Z, Batista CD. Resistivity minimum in diluted metallic magnets. *Physical Review B*. 2020 May 28; 101(18):184432.

22. Sampathkumaran EV. A report of (topological) Hall anomaly two decades ago in Gd_2PdSi_3 , and its relevance to the history of the field of Topological Hall Effect due to magnetic skyrmions. arXiv preprint arXiv:1910.09194. 2019 Oct 21.
23. Kurumaji T, Nakajima T, Hirschberger M, Kikkawa A, Yamasaki Y, Sagayama H, Nakao H, Taguchi Y, Arima TH, Tokura Y. Skyrmion lattice with a giant topological Hall effect in a frustrated triangular-lattice magnet. *Science*. 2019 Aug 30; 365(6456):914-8.
24. Bażela W, Wawrzyńska E, Penc B, Stüsser N, Szytuła A, Zygmunt A. Magnetic structures of R_2RhSi_3 (R= Ho, Er) compounds. *Journal of alloys and compounds*. 2003 Oct 6; 360(1-2):76-80.
25. Patil S, Medicherla VR, Singh RS, Pandey SK, Sampathkumaran EV, Maiti K. Kondo resonance in a magnetically ordered compound Ce_2RhSi_3 : Photoemission spectroscopy and ab initio band structure calculations. *Physical Review B*. 2010 Sep 24; 82(10):104428.
26. Kumar R, Iyer KK, Paulose PL, Sampathkumaran EV. Magnetic and transport anomalies in R_2RhSi_3 (R= Gd, Tb, and Dy) resembling those of the exotic magnetic material Gd_2PdSi_3 . *Physical Review B*. 2020 Apr 29; 101(14):144440.
27. Gladyshevskii RE, Cenzual K, Parthé E. Er_2RhSi_3 and R_2CoGa_3 (R= Y, Tb, Dy, Ho, Er, Tm, Yb) with Lu_2CoGa_3 type structure: new members of the A1B2 structure family. *Journal of alloys and compounds*. 1992 Dec 7; 189(2):221-8.
28. Mydosh JA. Spin glasses: an experimental introduction. CRC Press; 1993 May 13.

29. Upadhyay SK, Iyer KK, Sampathkumaran EV. Magnetic behavior of metallic kagome lattices, $Tb_3Ru_4Al_{12}$ and $Er_3Ru_4Al_{12}$. *Journal of Physics: Condensed Matter*. 2017 Jul 17; 29(32):325601.
30. Sampathkumaran EV, Iyer KK, Upadhyay SK, Andreev AV. Anisotropic re-entrant spin-glass features in a metallic kagome lattice, $Tb_3Ru_4Al_{12}$. *Solid State Communications*. 2019 Feb 1; 288:64-7.
31. Marcano N, Sal JG, Espeso JI, Barquín LF, Paulsen C. Cluster-glass percolative scenario in $CeNi_{1-x}Cu_x$ studied by very low-temperature ac susceptibility and dc magnetization. *Physical Review B*. 2007 Dec 19; 76(22):224419.
32. Yamamoto TD, Kotani A, Nakajima H, Okazaki R, Taniguchi H, Mori S, Terasaki I. Ferromagnetic Cluster Glass Phase Embedded in a Paramagnetic and Metallic Host in Non-Uniform Magnetic System $CaRu_{1-x}Sc_xO_3$. *Journal of the Physical Society of Japan*. 2016 Mar 15; 85(3):034711.
33. D. X. Li, S. Nimori, Y. Shiokawa, Y. Haga, E. Yamamoto, and Y. Onuki, *Phys. Rev. B* **68**, 172405 (2005).
34. Kumar R, Sharma J, Iyer KK, Sampathkumaran EV. Reentrant spin-glass and transport behavior of Gd_4PtAl , a compound with three sites for Gd. *Journal of Magnetism and Magnetic Materials*. 2019 Nov 15; 490:165515.
35. Joshua SJ. Power-law Form of the Temperature Dependence of the Magnon Specific Heat $C_M(T)$ in Linear, Planar and Spatial Antiferromagnets. *Australian journal of physics*. 1984; 37(3):305-8.

- Caudron R, Costa P, Lasjaunias JC, Levesque B. Power law behaviour for the specific heat of spin glasses at very low temperatures. *Journal of Physics F: Metal Physics*. 1981 Feb 1; 11(2):451.
36. Blanco JA, Sal JG, Fernandez JR, Castro M, Burriel R, Gignoux D, Schmitt D. Specific heat of $\text{GdNi}_{1-x}\text{Cu}_x$ compounds. *Solid state communications*. 1994 Jan 1; 89(4):389-92.
37. Gschneidner KA, Pecharsky VK, Tsokol AO. Recent developments in magnetocaloric materials. *Reports on progress in physics*. 2005 May 20; 68(6):1479.
38. Jaeger C, Bihler C, Vallaitis T, Gönnerwein ST, Opel M, Gross R, Brandt MS. Spin-glass-like behavior of Ge: Mn. *Physical Review B*. 2006 Jul 28;74(4):045330.
39. Goodings DA. Electrical resistivity of ferromagnetic metals at low temperatures. *Physical Review*. 1963 Oct 15; 132(2):542.
40. Mallik R, Sampathkumaran EV. Magnetic precursor effects, electrical and magnetoresistance anomalies, and heat-capacity behavior of Gd alloys. *Physical Review B*. 1998 Oct 1; 58(14):9178.
- Kumar R, Sampathkumaran EV. Magnetic frustration and paramagnetic state transport anomalies in Ho_4RhAl and Er_4RhAl : Possible test cases for newly identified roles of itinerant electrons. *Journal of Magnetism and Magnetic Materials*. 2021 Nov 15;538: 168285.
41. Das I, Sampathkumaran EV. Magnetic ordering in Ce_2RhSi_3 . *Journal of magnetism and magnetic materials*. 1994 Nov 1; 137(3):L239-42.

42. Nakano T, Sengupta K, Rayaprol S, Hedo M, Uwatoko Y, Sampathkumaran EV. Positive and negative pressure effects on the magnetic ordering and the Kondo effect in the compound Ce_2RhSi_3 . *Journal of Physics: Condensed Matter*. 2007 Jul 16; 19(32):326205.
43. Patil S, Iyer KK, Maiti K, Sampathkumaran EV. Behavior of magnetic ordering and the Kondo effect in the alloys $\text{Ce}_2\text{Rh}_{1-x}\text{Co}_x\text{Si}_3$. *Physical Review B*. 2008 Mar 31; 77(9):094443.
44. Majumdar S, Sampathkumaran EV, Brando M, Hemberger J, Loidl A. Magnetic behavior of a new series of ternary compounds of the type, R_2PtSi_3 (R= La, Ce, Pr, Nd, Gd and Y). *Journal of magnetism and magnetic materials*. 2001 Oct 1; 236(1-2):99-106.
45. Li DX, Nimori S, Shiokawa Y, Haga Y, Yamamoto E, Onuki Y. Magnetic, transport, and thermal properties of ternary intermetallic compound Nd_2PtSi_3 . *Solid state communications*. 2001 Oct 8; 120(5-6):227-32.
46. Li D, Zhao X, Nimori S. Ferromagnetic ordering and weak spin-glass-like effect in Pr_2CuSi_3 and Nd_2CuSi_3 . *Journal of Physics: Condensed Matter*. 2008 Dec 9; 21(2):026006.
47. Yubuta K, Yamamura T, Li DX, Shiokawa Y. Direct observations of ordered R_2CuSi_3 (R= Ce and Nd) cluster-glass compounds in real space by HRTEM. *Solid state communications*. 2009 Feb 1; 149(7-8):286-9.
48. Majumdar S, Mallik R, Sampathkumaran EV, Rupprecht K, Wortmann G. Magnetic behavior of Eu_2CuSi_3 : Large negative magnetoresistance above the Curie temperature. *Physical Review B*. 1999 Sep 1; 60(9):6770.

49. Nishioka T, Tabata Y, Taniguchi T, Miyako Y. Canonical spin glass behavior in Ce_2AgIn_3 . *Journal of the Physical Society of Japan*. 2000 Apr; 69(4):1012-5.
50. Li DX, Nimori S, Shiokawa Y, Tobo A, Onodera H, Haga Y, Yamamoto E, Ōnuki Y. Spin-glass behavior with short-range antiferromagnetic order in Nd_2AgIn_3 . *Applied Physics Letters*. 2001 Dec 17; 79(25):4183-5.
51. Semitelou JP, Siouris J, Yakinthos JK, Schäfer W, Schmitt D. Antiferromagnetic intermetallic Tb_2AgIn_3 . *Journal of alloys and compounds*. 1999 Feb 1; 283(1-2):12-5.
52. Siouris IM, Semitelou IP, Yakinthos JK. Susceptibility measurements of R_2CuIn_3 compounds (R= Ce, Pr, Nd, Tb, Dy, Ho, Er). *Journal of alloys and compounds*. 2000 Feb 2; 297(1-2):26-9.
53. Hoffmann RD, Pöttgen R. AlB₂-related intermetallic compounds—a comprehensive view based on group-subgroup relations. *Zeitschrift für Kristallographie-Crystalline Materials*. 2001 Mar 1; 216(3):127-45.
54. Upadhyay SK, Iyer KK, Sampathkumaran EV. Magnetic behavior of metallic kagome lattices, $\text{Tb}_3\text{Ru}_4\text{Al}_{12}$ and $\text{Er}_3\text{Ru}_4\text{Al}_{12}$. *Journal of Physics: Condensed Matter*. 2017 Jul 17; 29(32):325601.
55. Jaubert LD, Benton O, Rau JG, Oitmaa J, Singh RR, Shannon N, Gingras MJ. Are multiphase competition and order by disorder the keys to understanding $\text{Yb}_2\text{Ti}_2\text{O}_7$ *Physical review letters*. 2015 Dec 29; 115(26):267208.
56. Schmidt M, Zimmer FM, Magalhaes SG. Spin liquid and infinitesimal-disorder-driven cluster spin glass in the kagome lattice. *Journal of Physics: Condensed Matter*. 2017 Mar 16; 29(16):165801.

57. Silveira A, Erichsen Jr R, Magalhães SG. Geometrical frustration and cluster spin glass with random graphs. *Physical Review E*. 2021 May 6; 103(5):052110.
58. Butcher MW, Tanatar MA, Nevidomskyy AH. Anisotropic melting of frustrated Ising antiferromagnets. *Physical Review Letters*. 2023 Apr 19; 130(16):166701.
59. Saunders TE, Chalker JT. Spin freezing in geometrically frustrated antiferromagnets with weak disorder. *Physical review letters*. 2007 Apr 9; 98(15):157201.
60. Shinaoka H, Tomita Y, Motome Y. Spin-glass transition in bond-disordered Heisenberg antiferromagnets coupled with local lattice distortions on a pyrochlore lattice. *Physical review letters*. 2011 Jul 20; 107(4):047204.
61. See the editorial suggestion remarks for Ref. 19 online.
62. Iyer KK, Maiti K, Rayaprol S, Kumar R, Mattepanavar S, Dodamani S, Sampathkumaran EV. Emergence of partially disordered antiferromagnetism and isothermal magnetization plateau due to geometrical frustration in a metallic compound, Er_2RhSi_3 . *Physical Review Materials*. 2023 Oct 10; 7(10):L101401.
- Iyer KK, Maiti K, Rayaprol S, Kumar R, Mattepanavar S, Dodamani S, Sampathkumaran EV. Magnetic anomalies in AlB_2 -type hexagonal Ho_2RhSi_3 and Er_2RhSi_3 . In *AIP Conference Proceedings 2024 Jan 12 (Vol. 2995, No. 1)*. AIP Publishing.
63. Shirata Y, Tanaka H, Ono T, Matsuo A, Kindo K, Nakano H. Quantum magnetization plateau in spin-1 triangular-lattice antiferromagnet $\text{Ba}_3\text{NiSb}_2\text{O}_9$. *Journal of the Physical Society of Japan*. 2011 Aug 17; 80(9):093702.

Chapter 4

Magnetic and transport anomalies in Er₄PtAl, Ho₄PtAl and Dy₄RhAl compounds

4.1 Introduction

As brought out in chapters 1 and 3, discovery of new rare-earth compounds exhibiting interesting magnetic anomalies is an important aspect of research in the field of solid-state physics, even in the rare-earth compounds with localized $4f$ electrons, due to the discovery of new phenomena and their potential applications. In this chapter, we bring out that the compounds where there are multiple sites for R in the crystal structure are interesting from magnetism angle. Typical examples, for such multiple site systems, from the past literature are: Gd₅Si₂Ge₂ with five symmetrically inequivalent positions has been studied in depth, in the area of giant magnetocaloric effect [1] and R₇Rh₃ exhibiting [2–5] multiple magnetic transitions as a function of temperature and magnetic-field, with competing ferromagnetic and antiferromagnetic interactions. In this respect, the compounds of the type R_4TMX ($X = p$ block elements) [6] hitherto not paid much attention in the past literature are of interest to the aim of this chapter. These compounds are known to crystallize in Gd₄RhIn-type cubic structure [space group $F\bar{4}3m$, see, Refs. [7–9] and articles cited therein], with three sites for R . The compounds with $X = Mg, Cd$ and In , are of interest from the angles of magnetocaloric effect, cluster spin-glass and hydrogenation behavior. In the family with $X = Al$, only $TM = Ru, Rh$ and Ir based compounds have been studied [6]. Engelbert and Janka [9] reported the materials containing $TM = Pd$ and Pt , where preliminary reports with the initial magnetic measurements on some of the compounds by these authors, suggested only one magnetic transition temperature for each of these compounds. However, a detailed

study of the magnetic and transport properties in some of these compounds belonging to the family R_4PtAl ($R = Gd, Tb$ and Dy) and R_4RhAl (Gd, Tb, Ho and Er) showed that these compounds show the features of ‘frustrated magnetism’, due to competition between ferromagnetic and antiferromagnetic interaction among the multiple sites for R [10-14]. Complications in the magnetic and transport properties were seen, not only in the magnetically ordered state, but also in the paramagnetic state, as shown in some of the families in the previous chapter. For instance, Gd_4PtAl has been reported to exhibit a re-entrant spin-glass behavior around 20 K below $T_N = 64$ K [10], and Tb_4PtAl shows spin-glass features at the onset of the antiferromagnetic order itself i.e. at 50 K. Additional spin-glass anomalies at further lower temperatures were reported for this Tb compound [11]. Dy_4PtAl surprisingly undergoes a ferromagnetic order at ($T_C =$) 32.6 K, entering into spin-glass state around 20 K [12]. Some of these compounds exhibit magnetic-field induced first-order like transitions.

These results motivated us to study and understand the magnetic properties of other heavy rare earth members of these R_4PtAl and R_4RhAl families viz, Er_4PtAl , Ho_4PtAl and Dy_4RhAl . The results are reported in this chapter, to enable the scientific community in this field to arrive at a global picture of magnetism in these families.

4.2 Crystal Structure

The unit cell of the R_4TMAI is shown in figure 4.1 (a). There are 16 formula units per unit cell. The Wyckoff positions of these rare earths are $R1: 24g$, $R2: 24f$, and $R3: 16e$ respectively. Transition metal and Al occupy $16e$ sites. The building blocks and the coordination spheres of the three rare-earth sites, shown in Ref. 8, are reproduced in figure 4.1 (b). The unit cell consists of Al_4 tetrahedra, TM surrounded by R_6 trigonal prismatic

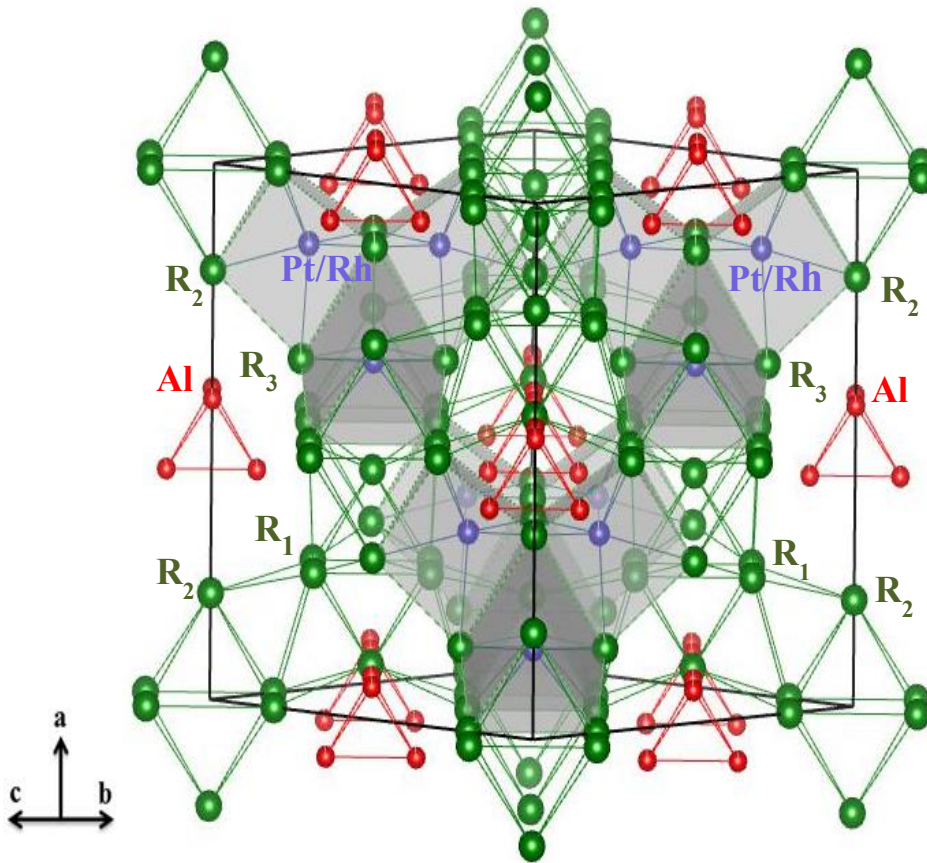


Figure 4.1a: Crystal structure of R_4TAl

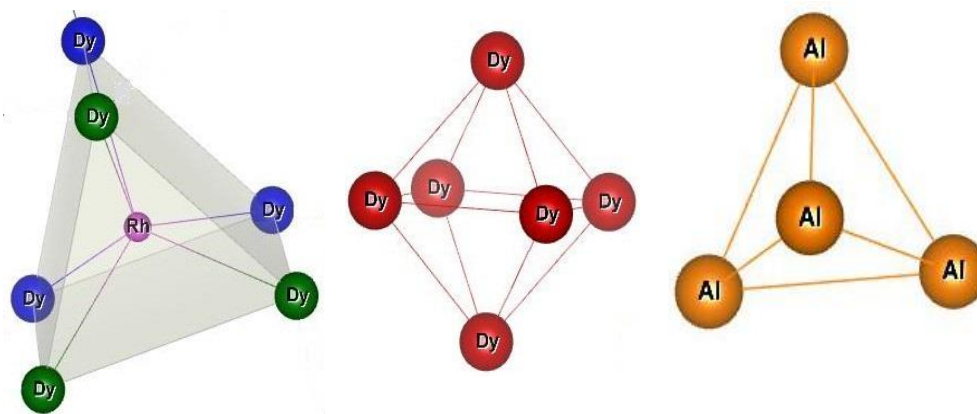


Figure 4.1b: The building blocks and coordination spheres of the $3R$ ions.

units, and R_6 octahedra, the center of which is empty. There are 4 R trigonal prisms which are arranged in a tetrahedral fashion, and these share a common triangular face with the R -

octahedra. Thus, one can clearly see that the chemical environment around each rare-earth is different. The crystallography of this family is thus complex and interesting for magnetic and transport properties investigations.

4.3 Sample preparation, characterization and experimental details.

We have studied the magnetic, transport and thermal properties for all the three samples in bulk form. Nano forms were also studied by magnetic and thermal properties. In this chapter we report the results on the bulk specimens, while the properties of nanoform specimens would be discussed in chapter 6.

The bulk specimens of the compounds were prepared using the arc melting technique. Powder x-ray diffraction patterns (Cu-K α) obtained on the as-molten ingots showed the samples to be single phase for Dy and Ho. In the case of unannealed Er sample, there was a weak extra line at $2\theta = 36^\circ$, which disappeared when the Er sample was annealed at 650°C for 8 days. The diffraction data was analyzed using Rietveld refinement and the refined diffraction patterns for all the compounds are shown in figure 4.2. All the fitted parameters are tabulated in table 4.1.

Table 4.1: Rietveld refined fitting parameters for $R_4(TM)Al$

Composition	$a = b = c (\text{\AA})$	R_p	R_{wp}	R_{exp}	χ^2
Ho ₄ PtAl	13.457 (1)	24.9	22.4	17.5	1.65
Er ₄ PtAl	13.392 (1)	21.6	19.3	14.8	1.71
Dy ₄ RhAl	13.403 (3)	39.3	30.9	25	1.53

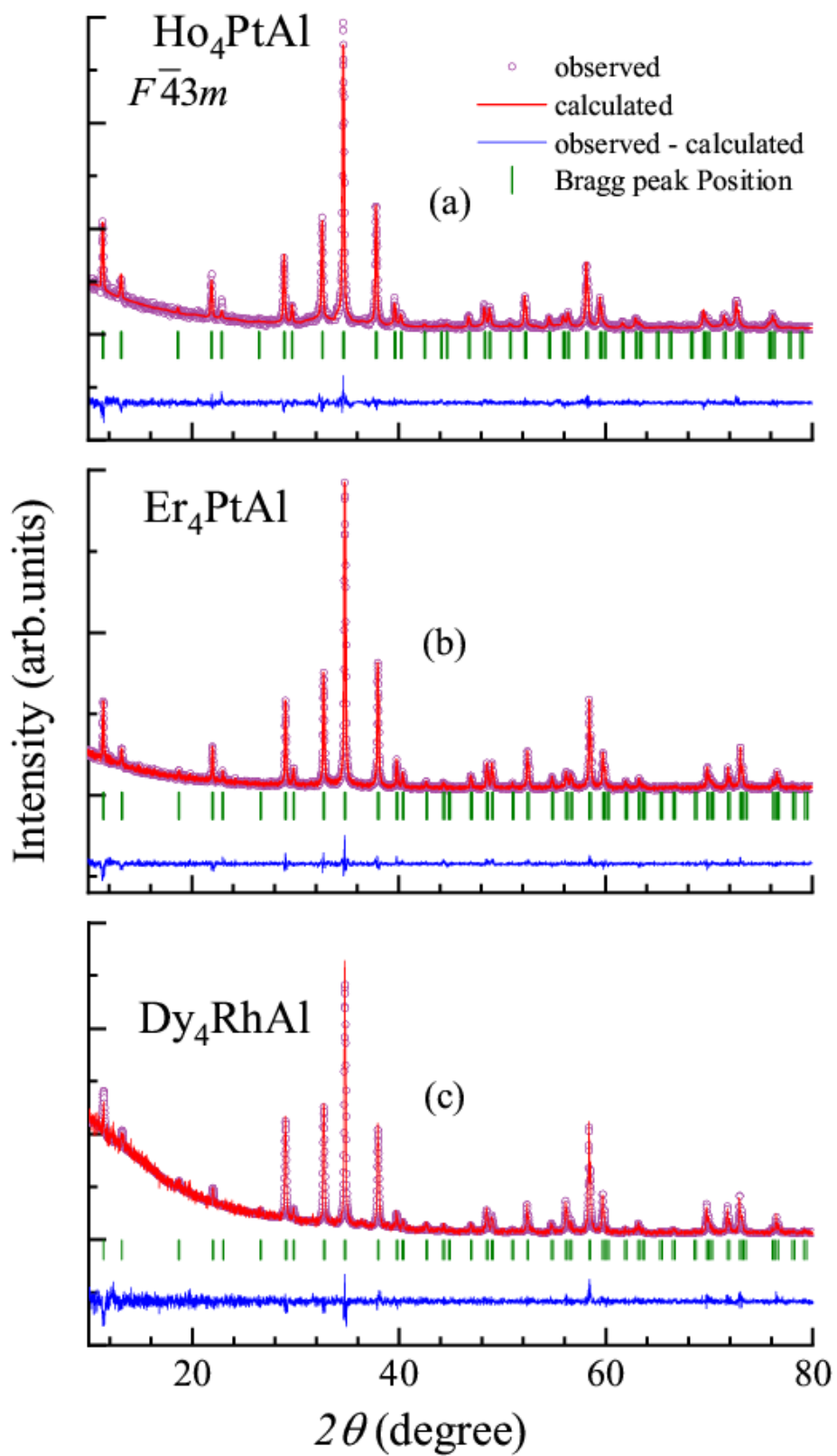


Figure 4.2: Rietveld refined powder x-ray diffraction patterns for R_4TAl obtained using $Cu K\alpha$ radiation.

4.4 Results and discussion for Ho₄PtAl.

4.4.1 Dc magnetization behavior

Figures 4.3 (a) – (b) show the magnetic susceptibility as a function of temperature measured in a field of 5 kOe as well as in 100 Oe. Inverse susceptibility data, plotted for 5 kOe, shows a linear behavior above 50 K. The values of the effective magnetic moment derived from the high temperature Curie-Weiss region is $\sim 10.7 \mu_B$ per R which is in good agreement with the theoretical values, while the paramagnetic Curie temperature is ~ 27 K with a positive sign. Positive sign of θ_p suggests dominant ferromagnetic coupling between the rare-earth ions in this compound. These features are similar to what is seen for Gd, Tb and Dy members [10-12] in the Curie-Weiss regime (even though it is seen that these compounds present a complex magnetic behavior at low temperatures). $\chi(T)$ measured in a field of 100 Oe shows a peak in the zero-field-cooled curve near 19 K (figure 4.3 (b)) which can be attributed to the onset of a long-range antiferromagnetic order. This peak is followed by an additional shoulder near 12 K and a flattening below ~ 5 K, suggesting the emergence of additional magnetic transitions. The derivative plot is shown in figure 4.3 (c) to see these features with more clarity. In the field cooled state, susceptibility shows a bifurcation below 19 K with respect to the ZFC curve, with the additional features even in this FC data; this irreversibility in the FC and ZFC curves signals a possibility of spin-glass freezing at low temperatures. The field-cooled curve shows an increase as the temperature is lowered below T_N , which is a signature of cluster spin-glass behavior [10, 15-17]. In the case of 5 kOe data, other than the 19 K magnetic ordering, additional features at 12 K and 5 K, are smeared. This indicates that the magnetism in this compound is sensitive to small

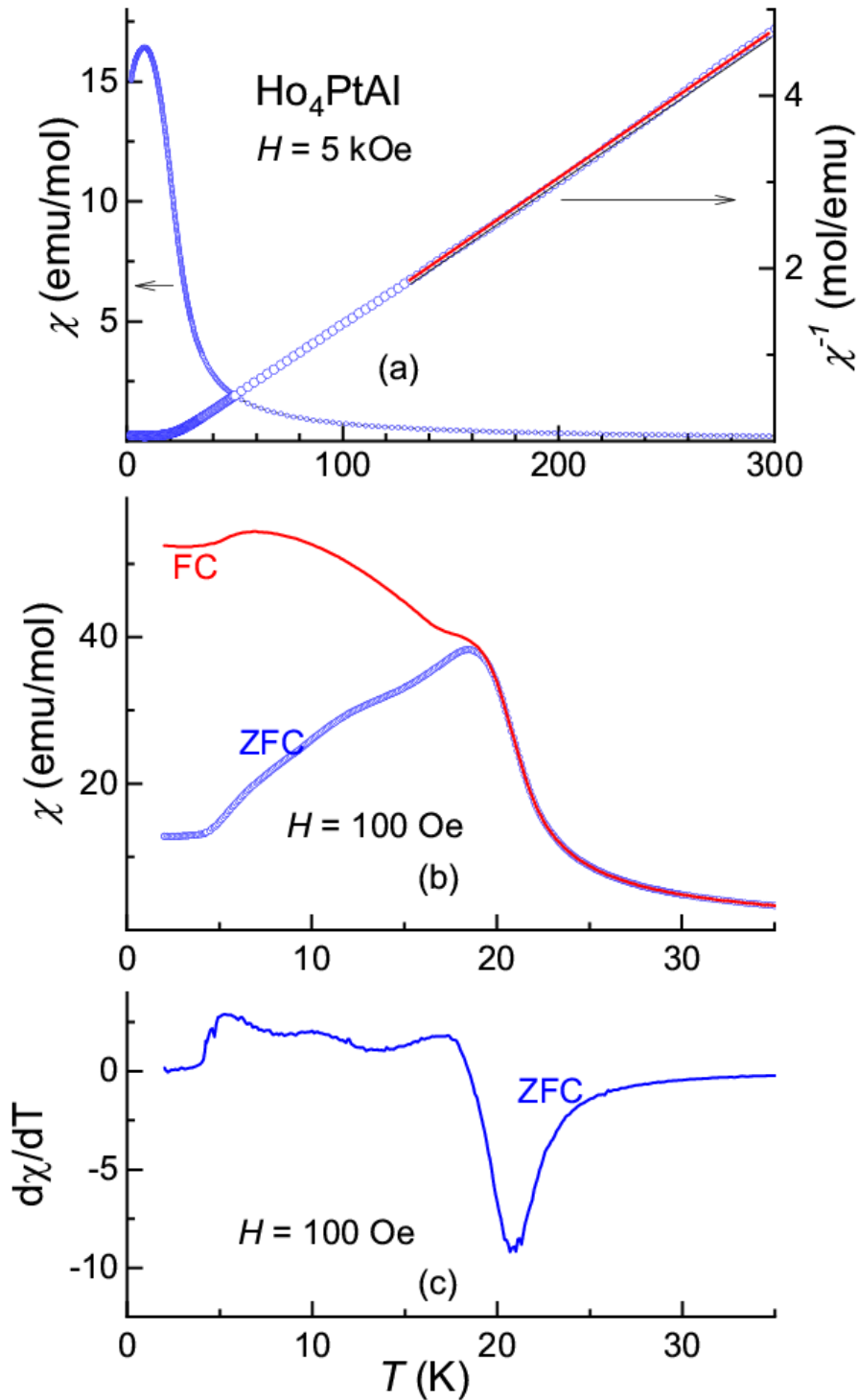


Figure 4.3: (a) Temperature dependent dc magnetic susceptibility and inverse susceptibility for Ho₄PtAl measured in 5 kOe. A line through the high temperature data points represents Curie-Weiss fitting. (b) Magnetic susceptibility measured in zero field cooled and field cooled conditions in a field of 100 Oe. (c) Derivative plot of the ZFC data in 100 Oe.

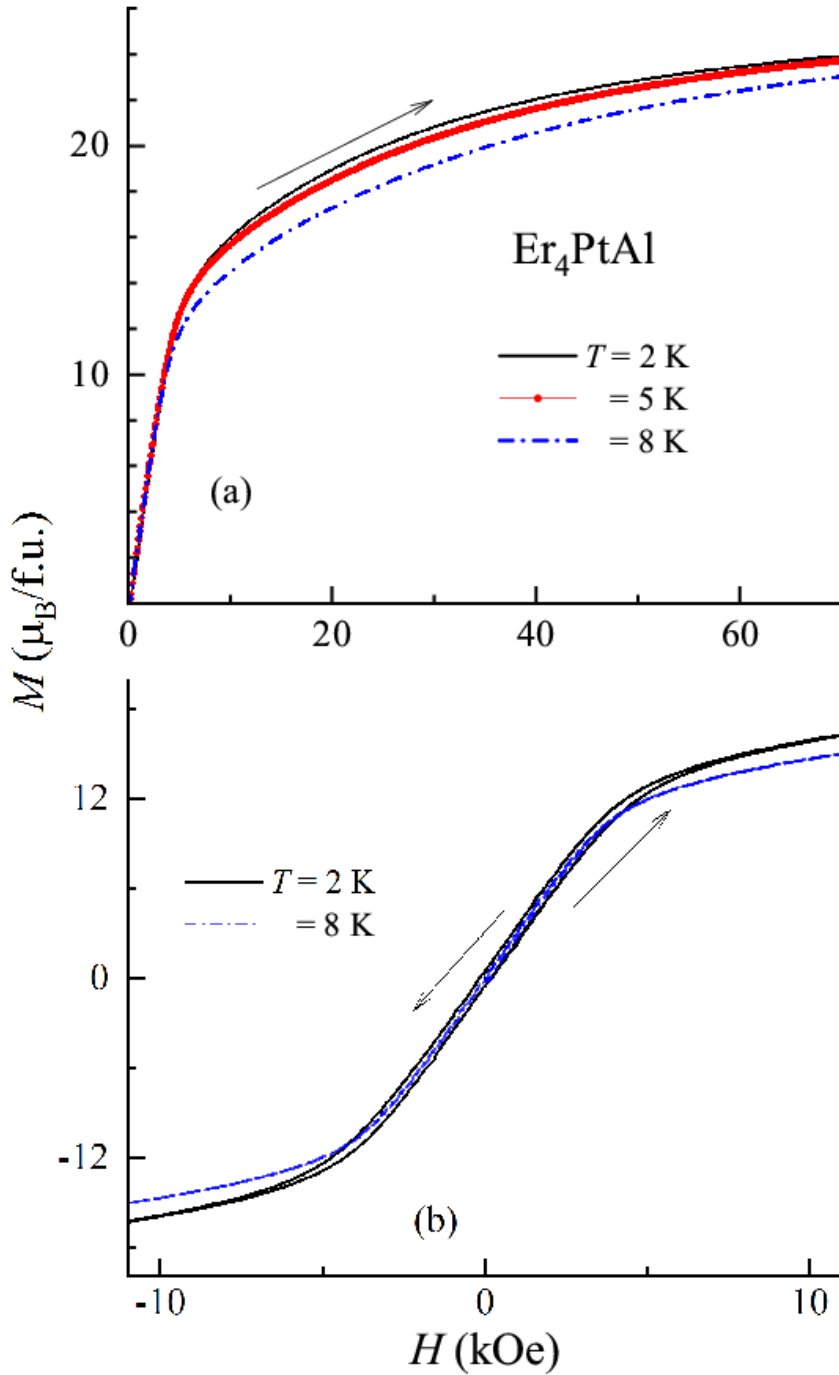


Figure 4.4: (a) Isothermal magnetization for Ho_4PtAl at 2, 8, 16 K (b) Low-field (0 to 10 to -10 to 10 kOe) hysteresis loops at 2K and 16 K. The arrows are drawn to show the direction in which field is varied.

applications of external magnetic field. The observed value of magnetic ordering temperature and θ_p are marginally higher, (19 K and 27 K) when compared to respective

de Gennes scaled values (for full degeneracy), inferred from the knowledge of ordering temperature, for Gd analogue (64 and 86 K) [10]. This is a signature of the role of anisotropy of crystal-field-split $4f$ orbital [18].

The isothermal magnetization measured up to a magnetic field of 70 kOe, in the magnetically ordered state, is plotted in figure 4.4 (a). Magnetization curves show a sharp increase in response to initial applications of magnetic field, indicating that there is a tendency towards ferromagnetic alignment by such fields. The magnetization data shows a distinct upward slope around 5 kOe, establishing that the zero-field state for this compound is not a perfect ferromagnet, but must be a canted antiferromagnet undergoing spin reorientation with H . Magnetization does not saturate even in 70 kOe, indicating the persistence of canted antiferromagnetism at higher magnetic fields as well.

We have also measured the low field hysteresis (-10 kOe to 10 kOe) at various temperatures below the magnetically ordered state and the data for two temperatures is plotted in figure 4.4 (b). Low field magnetization shows a distinct hysteretic behavior (even though weak) at a temperature well below T_N , suggesting the existence of a ferromagnetic component. Looking together magnetic susceptibility and the magnetization results, a canted antiferromagnetic nature of the virgin state at the onset of magnetic order is established.

4.4.2 Ac susceptibility and Isothermal remanent magnetization behavior

Since the compound shows a positive sign for θ_p which supports the existence of ferromagnetic correlations, while in the virgin state isothermal magnetization curve reveals the presence of antiferromagnetic component, it is important to look for spin glass features,

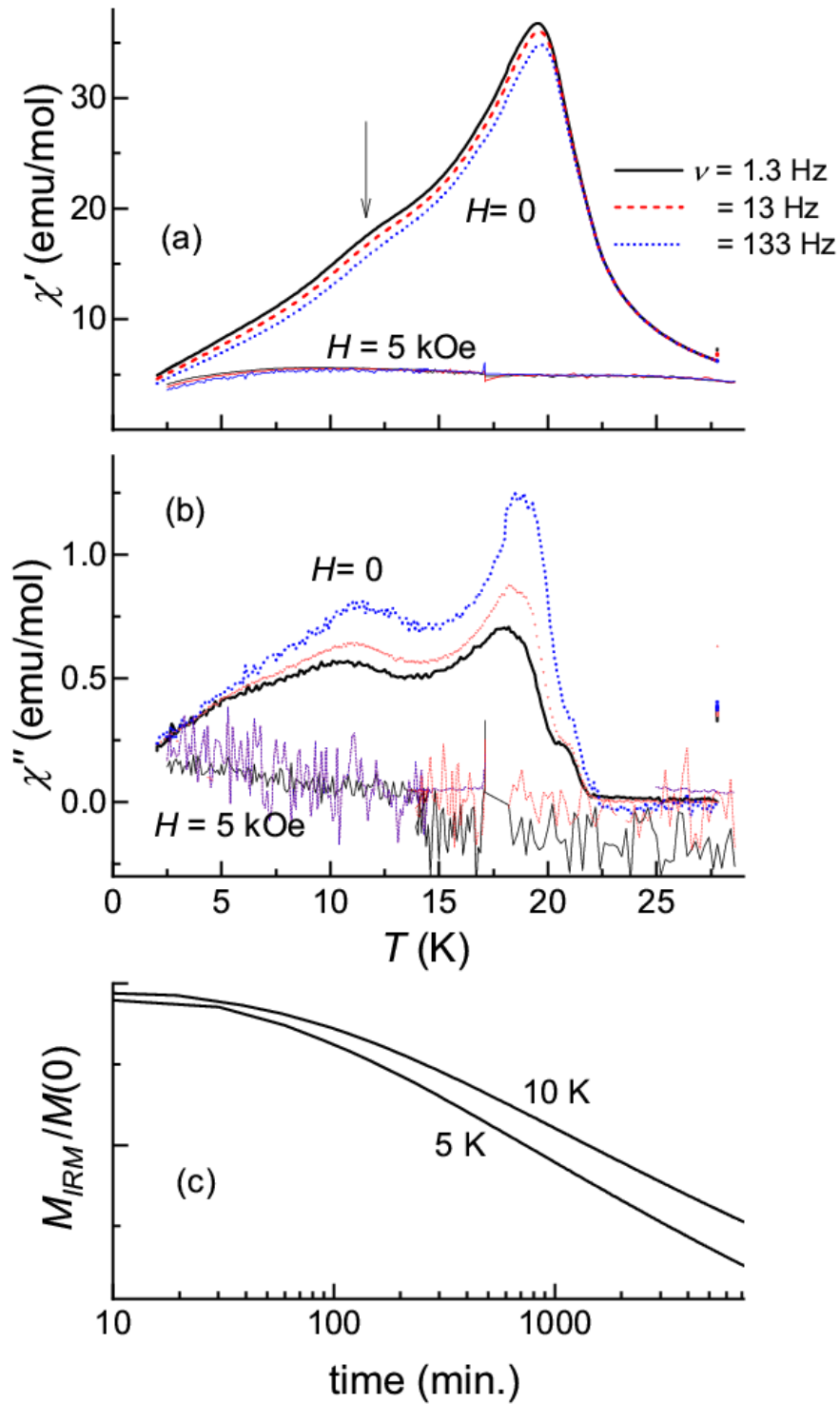


Figure 4.5: (a) Real part (b) imaginary part of ac susceptibility for Ho_4PtAl and (c) time dependence of isothermal remnant magnetization measured at 5 and 10 K, The value at $t = 0$, $M(0)$ at 5 K is ~ 14 emu/g and the respective value at 10 K is ~ 6.3 emu/g.

therefore, we measured the ac susceptibility to get further insight into the nature of the magnetically ordered state of the system. The data for the real part is plotted in figure 4.5 (a) and imaginary part is plotted in figure 4.5 (b). The χ' data measured in zero field exhibits a peak at 19 K with an additional shoulder around 12 K. These features are seen even in the χ'' curves also. There is no prominent feature around 5 K as seen in the dc susceptibility data, except a change of slope in χ'' . These features vanish when the ac susceptibility is measured in an applied field of 5 kOe. These findings support the existence of a spin-glass component at low temperatures. In addition, there is a very weak frequency dependence of the peak seen in the zero-field ac susceptibility. It is notable that such frequency dependence can be seen even at the onset of long-range magnetic order. Therefore, the possibility of spin-glass dynamics of antiferromagnetic clusters of this compound below 5 K exists.

To render further support to spin glass behavior, we have measured isothermal M_{IRM} at select temperatures below T_N ; and the curves are shown in figure 4.5 (c) for 5 K and 10 K. The starting point of measurement was labelled $M(0)$. M_{IRM} versus time shows a slow decay. This decay becomes slower as the temperature is increased towards T_N . It was difficult to ascertain the functional form of the decay because (in logarithmic form) the data shows two logarithmic regions, which could be due to the multiple sites for R . In any case, the slow decay of M_{IRM} is consistent with the glassy behavior, at least in the region close to 5 K.

4.4.3 Heat capacity and isothermal entropy change behavior

Having established the presence of spin-glass anomalies, it is important to see whether a well-defined magnetic structure coexists. We therefore measured the heat-capacity as a

function of temperature below 80 K. The data is plotted in figure 4.6 both in the form of C versus T (figure 4.6 (a)) as well as of C/T versus T (figure 4.6 (b)). In the absence of an external magnetic field, as the temperature is lowered, the compound shows a well-defined feature, i.e. an upturn followed by a peak, as the magnetic ordering temperature is approached. In addition, the heat capacity shows a shoulder around 12 K. This feature is more evident from the $C(T)$ versus (T) plot (shown in figure 4.6 (b)). One can also see a weak upturn in $C(T)$ below about 5 K, which could possibly arise due to subtle changes in the orientation of magnetic moments. With the application of magnetic field of 10 kOe, the peak at 19 K shifts marginally to a lower temperature, with the feature due to the onset of magnetic order partly overlapping with the one due to 12 K transition. This finding establishes that the magnetic structure for this compound at the onset of magnetic order is of an antiferromagnetic type, rather than being a ferromagnetic type. As the applied magnetic field is increased further (say 30 kOe and 50 kOe), the peak is not discernable, and we see a monotonic decrease of C with T down to 5 K. Below 10 K, we don't find any evidence for $T^{3/2}$ behavior expected for ferromagnets / spin-glasses or T^3 behavior which is expected for antiferromagnets. Such a functional form establishes that the magnetism at lower temperatures is in fact quite complex for this compound.

The isothermal entropy change was derived from the heat capacity data, by integrating the plots of C/T , is plotted in figure 4.6 (c). It can be seen that the plots of $-\Delta S$ exhibit a peak in the positive quadrant, even for an application of a field as small as 10 kOe; this positive sign is typical of ferromagnetic behavior [16].

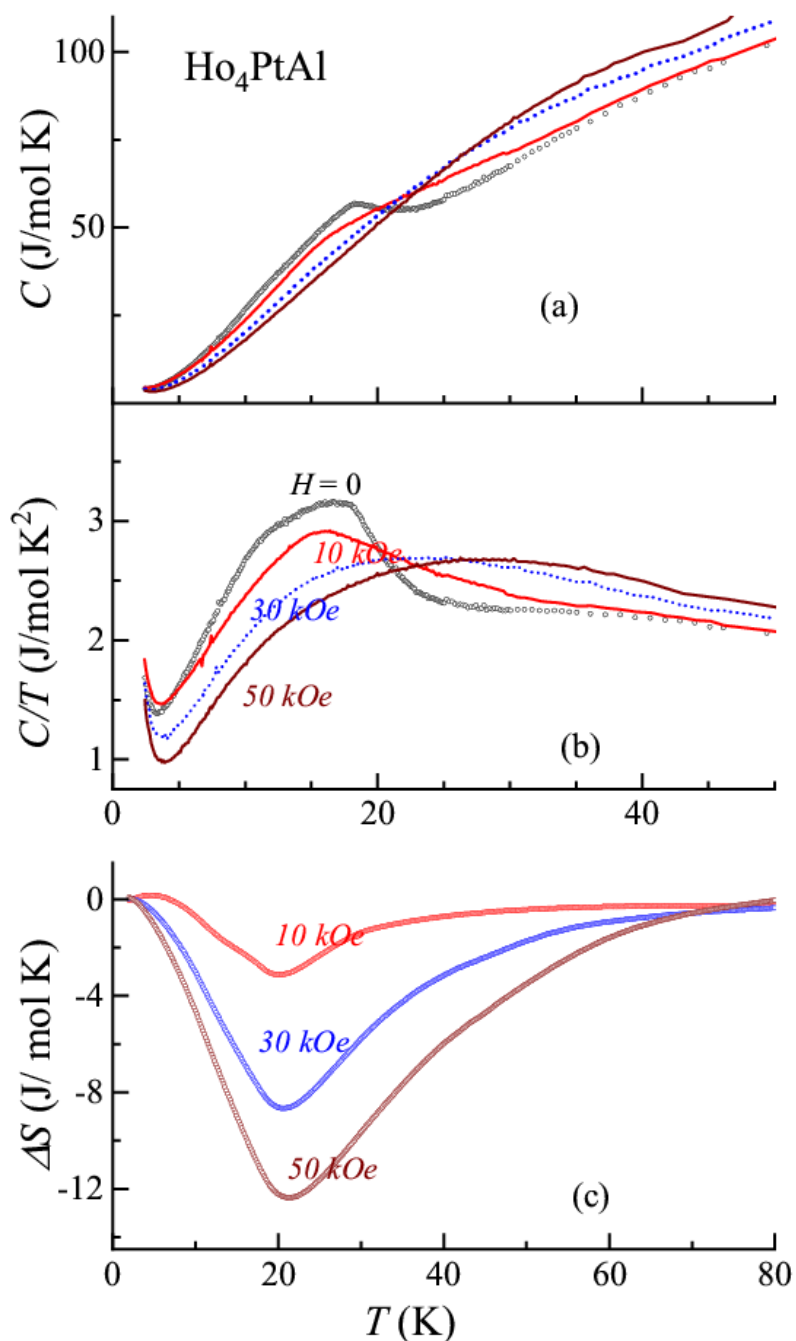


Figure 4.6: (a) Heat-capacity as a function of temperature (<50 K) for Ho_4PtAl , in zero field as well as in the presence of external magnetic fields. (b) Heat-capacity divided by temperature as a function of T . (c) Isothermal entropy change as a function of temperature (2-90 K) for different final fields starting from zero-field, derived from the heat capacity data.

This supports the inference of domination of a ferromagnetic component even for such low fields (though AF component still persists as discussed above), made from the

$M(H)$ data. It can be seen that the peak values of $(-\Delta S)$ are quite large when, compared to that of analogous Gd, and Tb members in the family [6-8]. For instance, the value of $(-\Delta S)$ for Ho for a magnetic field of 50 kOe is about ~ 12.5 J/mol K, whereas the value for the Gd case is ~ 6 J/mol K and that for Tb case is ~ 6.5 J/mol K. As shown for other family members of this compound, the plot of $(-\Delta S)$ exhibits a long tail over a wide T -range above respective T_N . This tail possibly arises from the gradual formation of ferromagnetic clusters as the temperature is lowered, thus behaving like classical spin-liquid [6, 9-11], as discussed in chapter 3.

4.4.4 Electrical resistivity and magnetoresistance behavior

We show electrical resistivity behavior as a function of temperature in zero field and in the presence of applied magnetic fields (figure 4.7). The data in the entire measured T range is plotted on the right-hand side and in the expanded form below 50 K at the left-hand side. At high temperatures resistivity exhibits a positive temperature coefficient, expected for metals. In addition, there is a minimum at 26 K in the paramagnetic state before the onset of magnetic ordering. Such a minimum in the resistivity has been reported earlier in some of the heavy R systems as a precursor to long range magnetic order [10, 20, 21] as discussed in chapter 3 (section 3.4.5) [22]. This resistivity minimum vanishes gradually with the application of external magnetic field. In the magnetically ordered state, the resistivity shows a drop below 15 K, arising due to the loss of spin-disorder contribution, supporting the onset of magnetic ordering with a well-defined magnetic structure at this temperature.

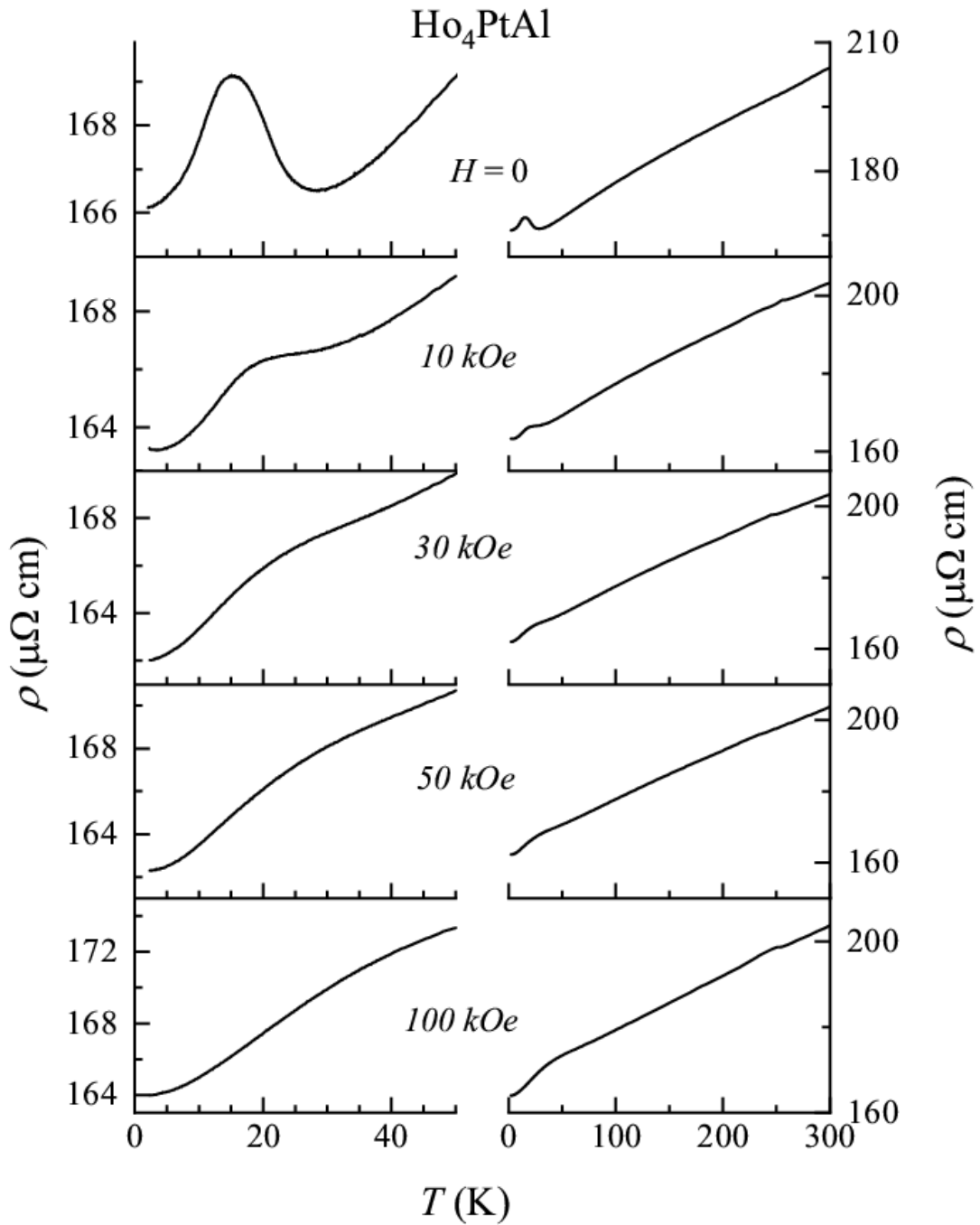


Figure 4.7: Electrical resistivity measured as a function of temperature (left side < 50 K, right side 2-300 K) for Ho₄PtAl, measured in zero field and the presence of external magnetic fields.

Note that the drop does not occur at T_N (19 K), but ρ shows an upturn below 19 K initially; such an upturn is usually attributed to the formation of magnetic Brillouin-zone formation (chapter 1 section 1.2.1).

Isothermal magnetoresistance shows interesting features. In the paramagnetic state, close to T_N , MR shows a competition between positive contribution arising from the Lorentz motion of the conduction electrons (that is, classical metallic part, which varies quadratically with H) and the negative contribution from the suppression of spin fluctuation contribution by H . For instance, just above T_N , say, at 25 K (see the right side of the MR figure), the spin contribution dominates as revealed by the negative sign till about 25 kOe and gets overcompensated at higher fields by the metallic part. At higher temperatures, the $MR(H)$ curve stays in the positive quadrant only.

Below the magnetic ordering temperature, the sign of MR remains negative which can be either due to antiferromagnetic gap formation and/or spin-glass component. Evidence for the formation of the antiferromagnetic-gap comes from the fact that as mentioned in section 4.4.4, ρ (in the zero-field curve) shows an upturn (in the zero-field curve) as soon as the magnetically ordered state is entered peaking around 15 K; with the upturn getting suppressed by a field of 10 kOe (see figure 4.7). One of the notable findings in the isothermal MR curves is that, in the low field range (<4 kOe), the virgin curve lies prominently outside the envelope loop below 12 K with a significant hysteresis, supporting that there could be a presence of disorder-broadened first-order magnetic transition in this compound at such low fields.

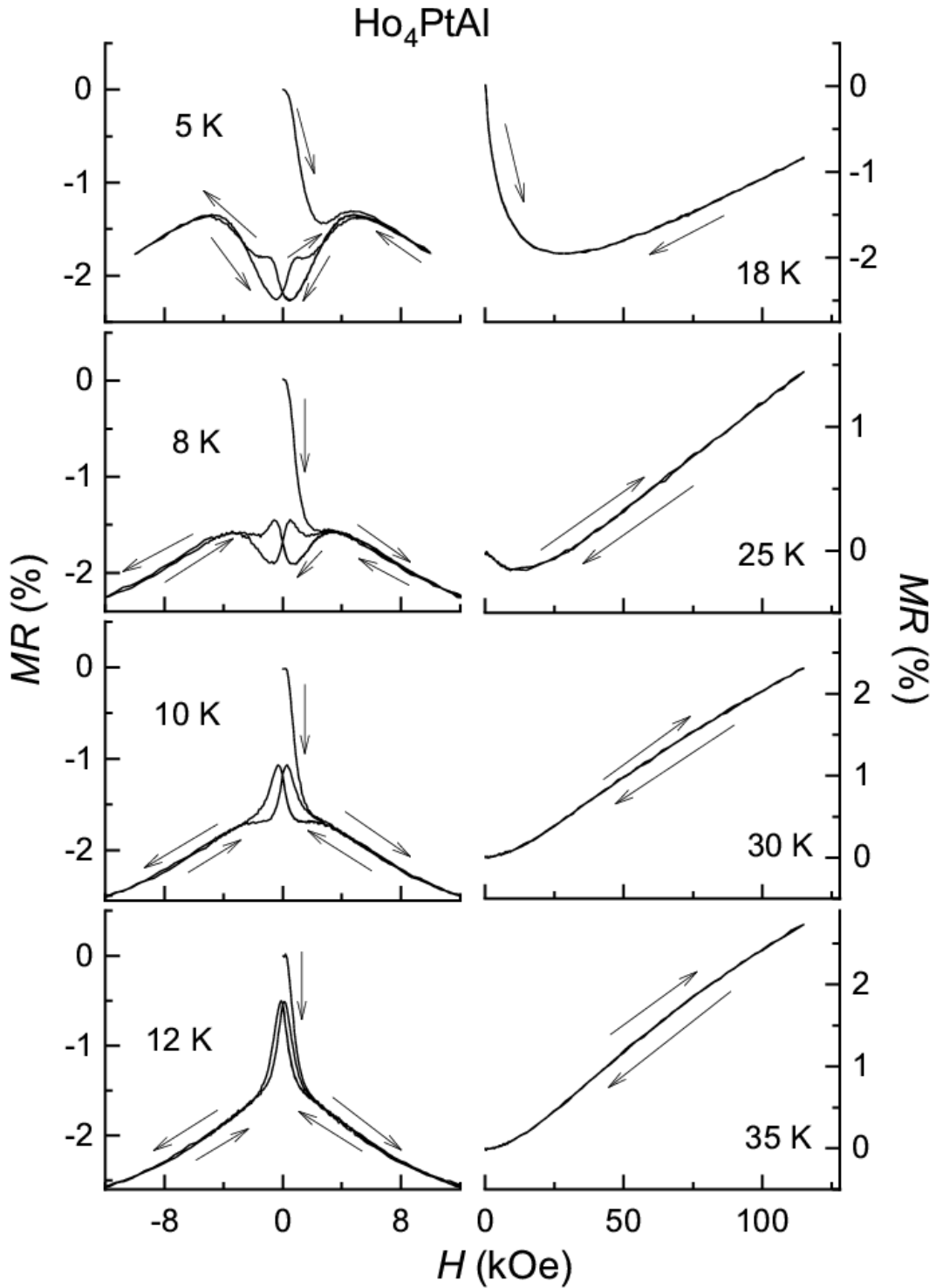


Figure 4.8: Magnetoresistance measured as a function of magnetic fields (left side for a field of -10 kOe to 10 kOe and the right side for a field of 0 to 120 kOe) for Ho_4PtAl , measured at various temperatures below and above the magnetic ordering. The arrows are drawn to show the way the magnetic field is varied.

Thus, the compound Ho₄PtAl exhibits re-entrant spin-glass behavior, with the onset of an antiferromagnetic type of magnetic order. At 19 K, the compound undergoes subtle changes in the magnetically ordered state, which are sensitive to an application of a small external field.

4.5 Results and discussion for Er₄PtAl.

4.5.1 Dc Magnetization behavior

Magnetic susceptibility measured as a function of temperature, in an applied magnetic field of 5 kOe is shown in figures 4.9 (a). Inverse susceptibility shows a linear behavior above 40 K. The value of the effective magnetic moment is found to be $\sim 9.82 \mu_B$ per Er which is in good agreement with the theoretical values for Er³⁺ ion. The paramagnetic Curie temperature is ~ 16 K. Similar to the case of Ho, positive sign of θ_p indicates dominant ferromagnetic coupling between the rare-earth moments in the Curie-Weiss regime.

The plot of $\chi(T)$ in a field of 100 Oe, are shown for both zero-field-cooled and field-cooled conditions in figure 4.9 (b). As the temperature is lowered below 50 K, susceptibility measured in the zero-field cooled condition, shows a sudden flattening near 12 K, followed by an additional slope change near 5 K. The 5 K feature is clear from the derivative plot of the ZFC curve shown in figure 4.9 (c). Similar to the case of Ho, the nature of the magnetic ordering at 12 K seems to be of an antiferromagnetic type (*vide infra*). There is a weak bifurcation seen in the ZFC-FC curves below 12 K in the magnetically ordered state and the curve in the field-cooled state shows an increase with decreasing temperature, though weak (compared to what is seen for the Ho case) below T_N , indicating cluster spin-glass behavior at low temperatures [10,15–17]. Similar to the case

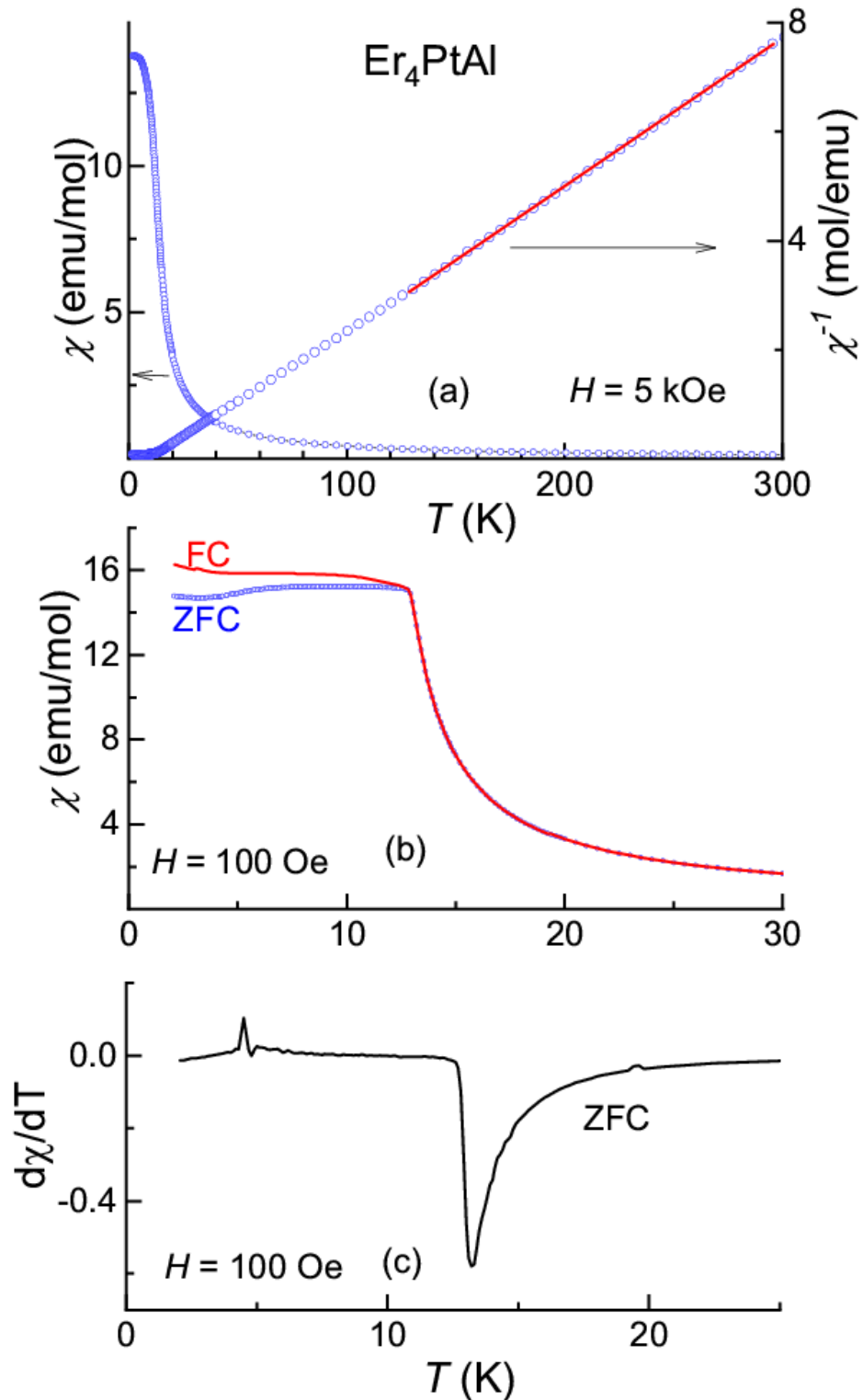


Figure 4.9: (a) Temperature dependent dc magnetic susceptibility and inverse susceptibility for Er_4PtAl measured in 5 kOe (b) magnetic susceptibility measured for zero field cooled and field cooled conditions in a field of 100 Oe. (c) derivative plot of the ZFC data in 100 Oe.

of Ho compound, the observed values of magnetic ordering temperatures and θ_p are marginally higher (12 K and 16 K) compared to the de Gennes scaled value (for full degeneracy).

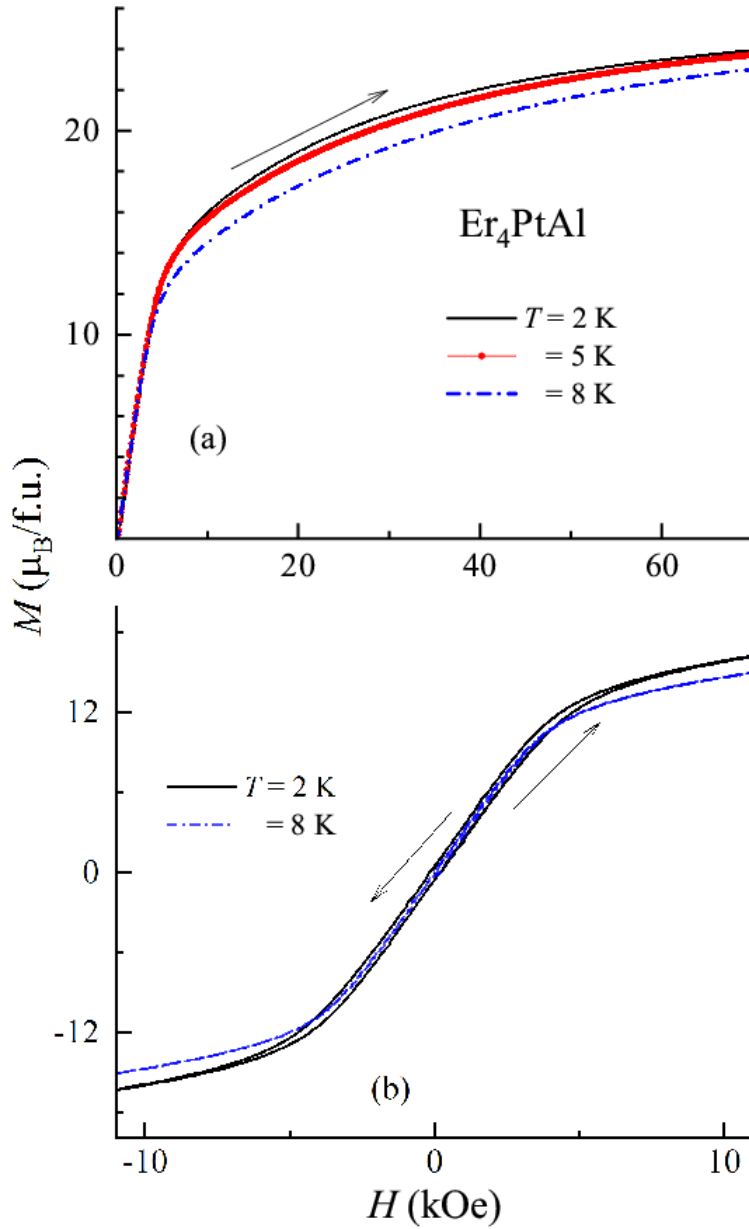


Figure 4.10: (a) Isothermal magnetization for Er_4PtAl at 2, 5, and 8 K; (b) low-field (0 to 10 to -10 to 10 kOe) hysteresis loops at 2K and 8 K.

Isothermal magnetization as a function of field was measured in the magnetically ordered state up to a magnetic field of 70 kOe, and plotted in figure 4.10a. Magnetization data shows a sharp increase in magnetization in response to the initial applications of magnetic field indicating possible tendency towards ferromagnetic alignment. $M(H)$ curves do not show a tendency to saturate even at 70 kOe. The hysteresis (figure 4.10 (b)) in the magnetically ordered state, say at 2 K, is so weak that it is difficult to attach any significance to this. The results overall suggest that the compound exhibits canted antiferromagnetism at the onset of magnetic order.

4.5.2 Ac susceptibility and Isothermal remanent magnetization behavior

Since many of the materials including Ho_4PtAl exhibit spin glass anomalies, we considered it important to investigate magnetism of Er_4PtAl in more depth by other bulk measurements. In this respect, the real and imaginary parts of the ac susceptibility data are shown in figure 4.11 (a) and (b) respectively. In zero field, χ' exhibits a peak at ~ 12 K, which is followed by a distinct change of slope around 5 K. These features are consistent with the dc susceptibility data presented above. χ' also shows a shoulder around 10 K, the origin of which was not clear. This feature could possibly arise due to the presence of additional spin-reorientation, which was subtly sensitive to small fields.

This can be easily missed in fields even as low as 100 Oe in dc χ measurements. The frequency dependence of the susceptibility peaks is not clearly discernable, even though one could find some ν -dependence in the left side of the peaks. However, the χ'' curves bring out a distinct frequency-dependent peak at about 5 K without any peak at

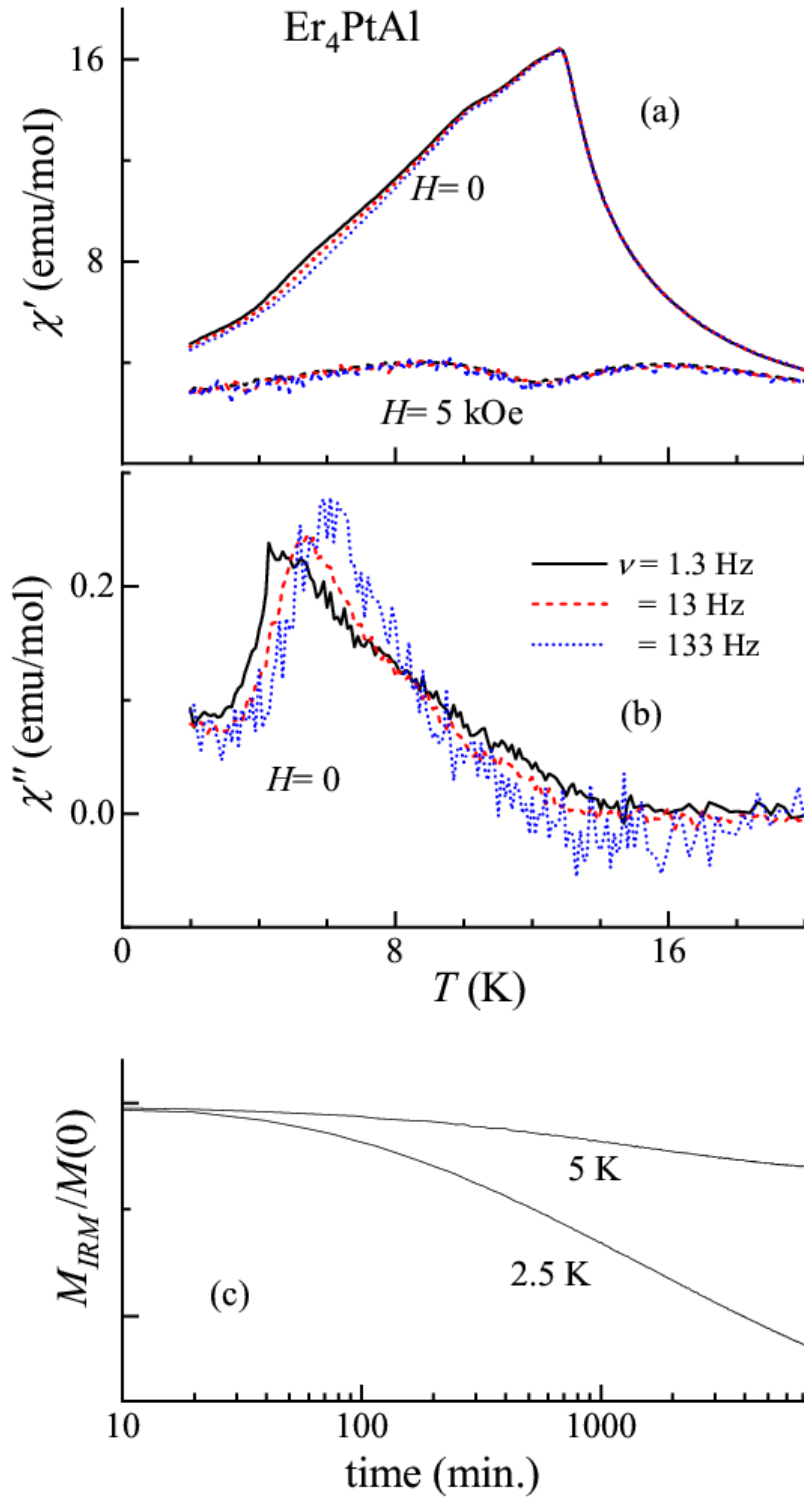


Figure 4.11:(a) Real part (b) imaginary part of ac susceptibility for Er_4PtAl (c) time dependence of isothermal remnant magnetization measured at 2.5 and 5K, measured values of $M(0)$ at 2.5 K and at 5 K are 2.7 emu/g and 1.5 emu/g respectively.

higher temperatures. This means that the 5 K-feature alone could arise from spin-glass freezing. These features in the ac susceptibility got suppressed with the application of a dc magnetic field of 5 kOe. Thus, viewing together all the features along with the behavior of low-field dc susceptibility curves and dc magnetization, it can be concluded that the compound exhibits (virgin state) antiferromagnetism below 5 K, behaving like (cluster) spin-glasses.

In order to probe further the glassiness of this compound, we measured M_{IRM} at selected temperatures below T_N . As seen in figure 4.11 (c), M_{IRM} at $t = 0$, shows a decrease with increasing temperature and also decays slowly with time. Since there were two logarithmic regions in the M_{IRM} data, it was difficult to determine the functional form of the decay with time, as in the case of Ho, attributable to complexities associated with multiple site magnetic interaction. This slow decay seen in the M_{IRM} data is consistent with the conclusion of the glassy nature of the compound, at least in the close vicinity of 5 K.

4.5.3 Heat capacity and isothermal entropy change behavior

Figure 4.12 shows the heat-capacity measured as a function of temperature in the form of C versus T (figure 4.12 (a)) as well as of C/T versus T (figure 4.12 (b)) to understand magnetically ordered state better. In zero field, the heat capacity shows a well-defined feature showing a sharp rise below 14 K, followed by a peak around 12 K. C/T v/s T plot (figure 4.12 (b)) shows an additional sharp anomaly around 5 K, which supports the presence of a magnetic feature around this temperature, as indicated by ac χ . With the application of magnetic field these features are seen to shift to lower temperatures confirming that the low temperature ground state is of an antiferromagnetic type. Similar

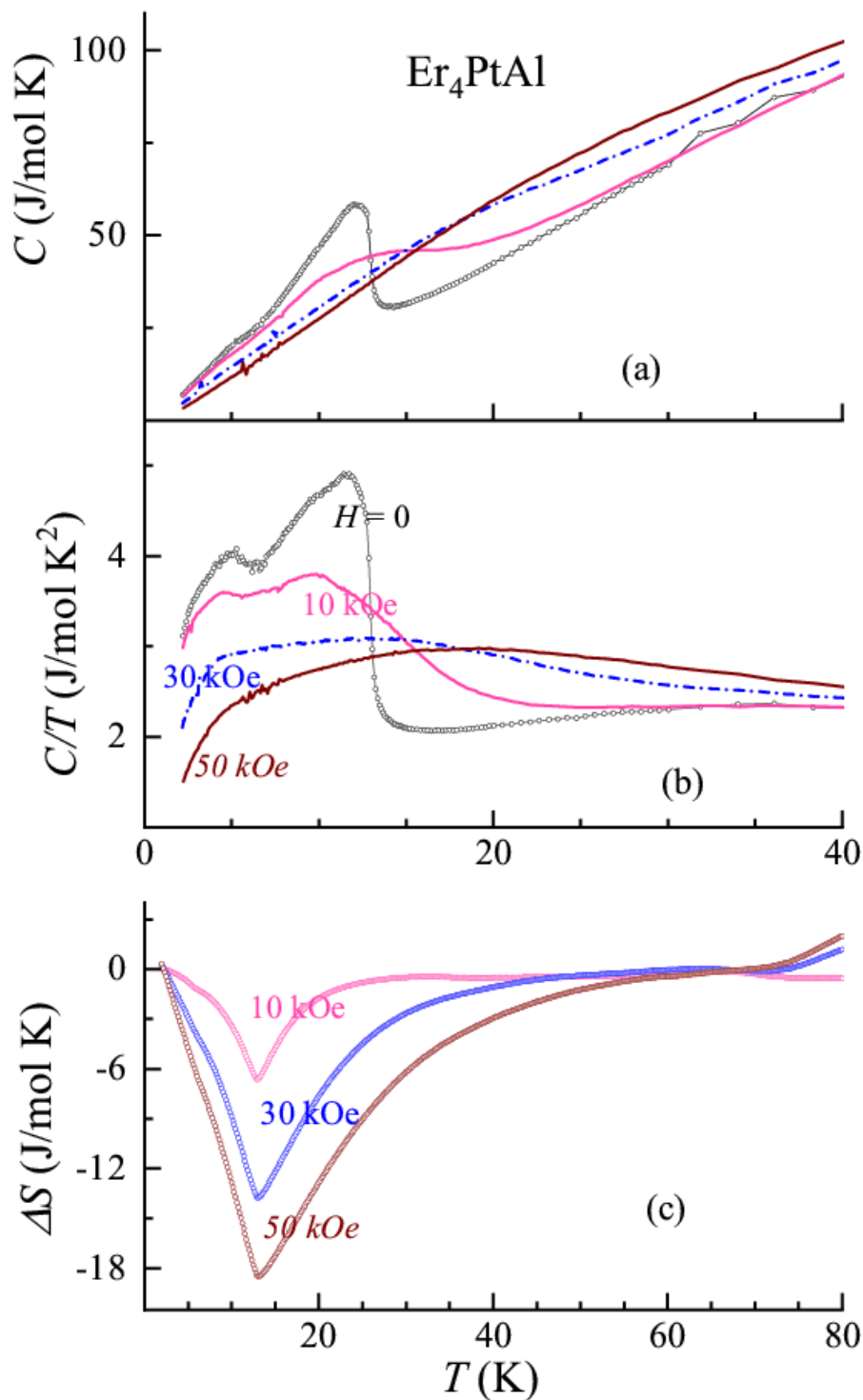


Figure 4.12: (a) Heat-capacity as a function of temperature (<40 K) for Er_4PtAl , measured in zero field and external magnetic fields, (b) heat-capacity divided by temperature, (c) isothermal entropy change as a function of temperature (2-80 K) for different final fields with initial field being zero.

to the case of Ho, it was difficult to determine the functional forms of the heat capacity data, below 10 K, as the heat capacity data does not show any evidence for $T^{3/2}$ or T^3 behavior, expected for ferromagnets/spin-glasses and antiferromagnets, respectively. This shows that the magnetism in this compound, is also quite complex. It is not clear whether a shoulder in C/T near 10 K can be correlated to the ac χ feature at this temperature.

The isothermal entropy change derived from the heat capacity data is plotted in figure 4.12 (c). The plots of ΔS exhibit a peak in the negative quadrant, even for an application of field as small as 10 kOe (similar to what is seen for the *Ho* case), typical of ferromagnetic behavior [19] supporting the inference of domination of a ferromagnetic component for an application of even low fields (though AFM component still persists as discussed above). In addition to determination of ΔS from heat capacity data, we have obtained the same from the isothermal magnetization, employing the Maxwell's equation. For obtaining this data, the isothermal magnetization measurements were carried out in close temperature intervals (every 3 K). The values and the features thus obtained are found to be in good agreement with that derived from the $C(T)$ data. A point to be emphasized is that the peak values of ΔS are relatively large, compared to that of analogous Gd and Tb members in the family [10-12]. That is, for a field of 50 kOe, the peak value of ΔS is about ~ 18.5 J/mol K, whereas the corresponding values of ΔS are lower for Gd (~ 6 J/ mol K). Similarly for Tb and Dy cases, the corresponding peak values of ΔS are ~ 6 and 13 J/ mol K respectively. Thus, the value of ΔS is clearly large for the Er compound within this family. The magnetic refrigeration capacity, defined as the product of the full-width at half maximum and the peak value, is about 420 J/kg K. This value is quite large and comparable to many other magnetocaloric materials in this temperature range of interest [20]. Also, it

can be noted that the peak values of the Er and Ho compounds in this family are much larger than those of the respective member of the isostructural Rh family [13,14,21]. If we make a comparison of the peak values of ΔS between the Pt and Rh families, we find that the values of ΔS is rather large for the Pt counterparts, for a given R . For example, for Gd_4PtAl and Gd_4RhAl , the values are ~ 6 and ~ 2.3 J/mol K, respectively [10,13]. We therefore infer [13] that the anisotropy of the (crystal-field-split) $4f$ orbital (that is, aspherical nature) plays a key role for such an enhancement. We, therefore, wonder spin-orbit coupling effect of the Pt $5d$ electrons with respect to the $4d$ band which are relatively larger plays a role in enhancing MCE.

Similar to the other rare-earth members, the plot of ΔS exhibits a long tail over a wide T -range above T_N which could possibly arise from a gradual formation of ferromagnetic clusters when the temperature is lowered as discussed for other materials. Looking at the non-hysteretic isothermal magnetization curves coupled with a large value of ΔS , it is concluded that this compound can be added to the list of materials for magnetic refrigeration below 40 K. This conclusion gains importance considering that, in the literature, there is often emphasis to find materials with large value of magnetic refrigeration capacity having such a reversible behavior [27, 28].

4.5.4 Resistivity and magnetoresistance behavior

Figure 4.18 shows the resistivity as a function of temperature for zero field and applied magnetic fields for Er_4PtAl . The curves for the range 2-300 K are shown on the right-hand side graphs. To reveal the features in the magnetically ordered state with clarity, the data below 40 K is shown in the left-hand side. There is no noticeable anomaly in the high

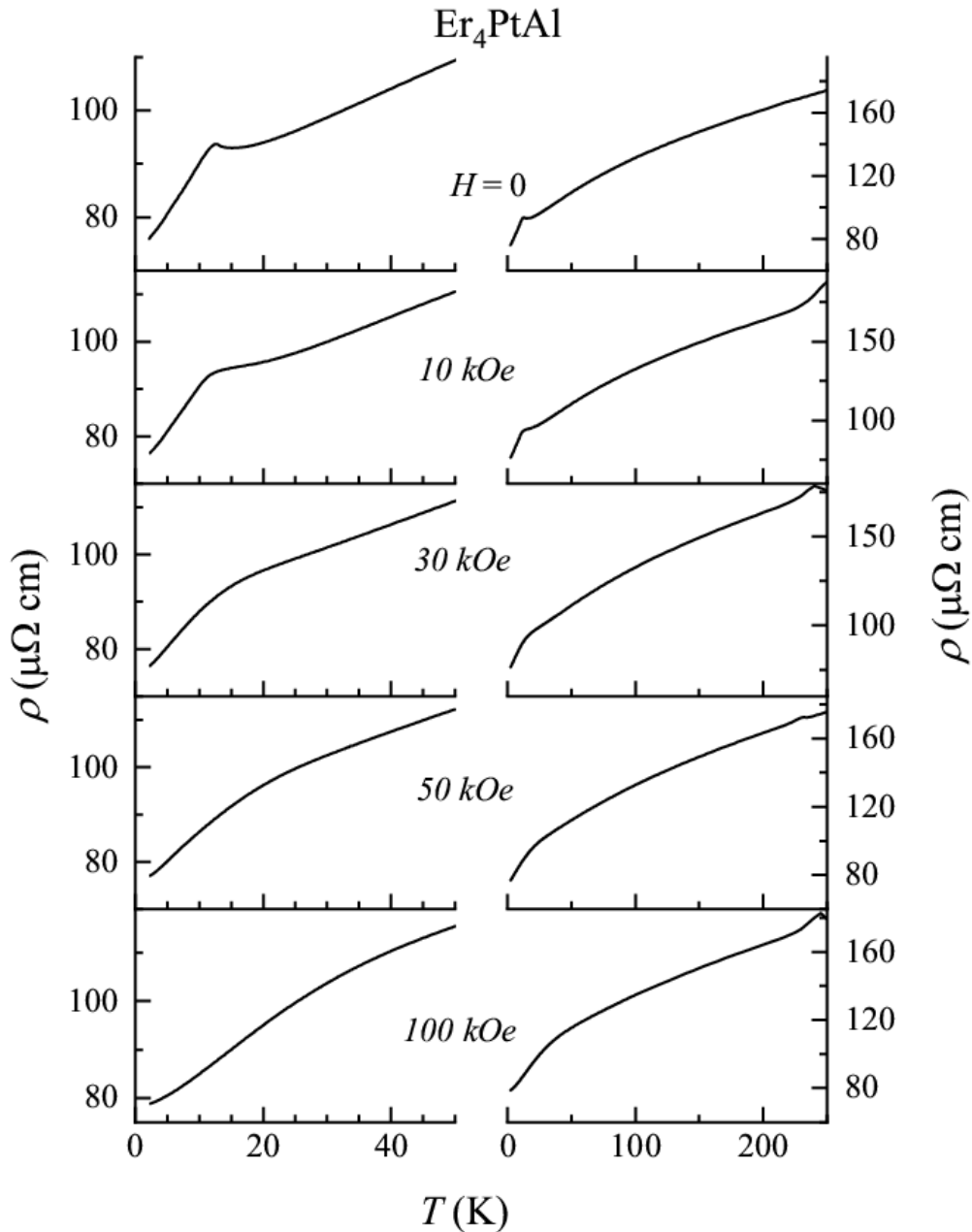


Figure 4.13: Electrical resistivity measured as a function of temperature (left side < 50 K, right side 2-300 K), measured in zero field and the presence of external magnetic fields.

temperature range (> 20 K) where metallic behavior is seen. As the temperature is lowered towards T_N , there is a minimum, in the paramagnetic state, just above the ordering temperature of 14 K, in zero field as discussed for Ho_4PtAl . This resistivity minimum

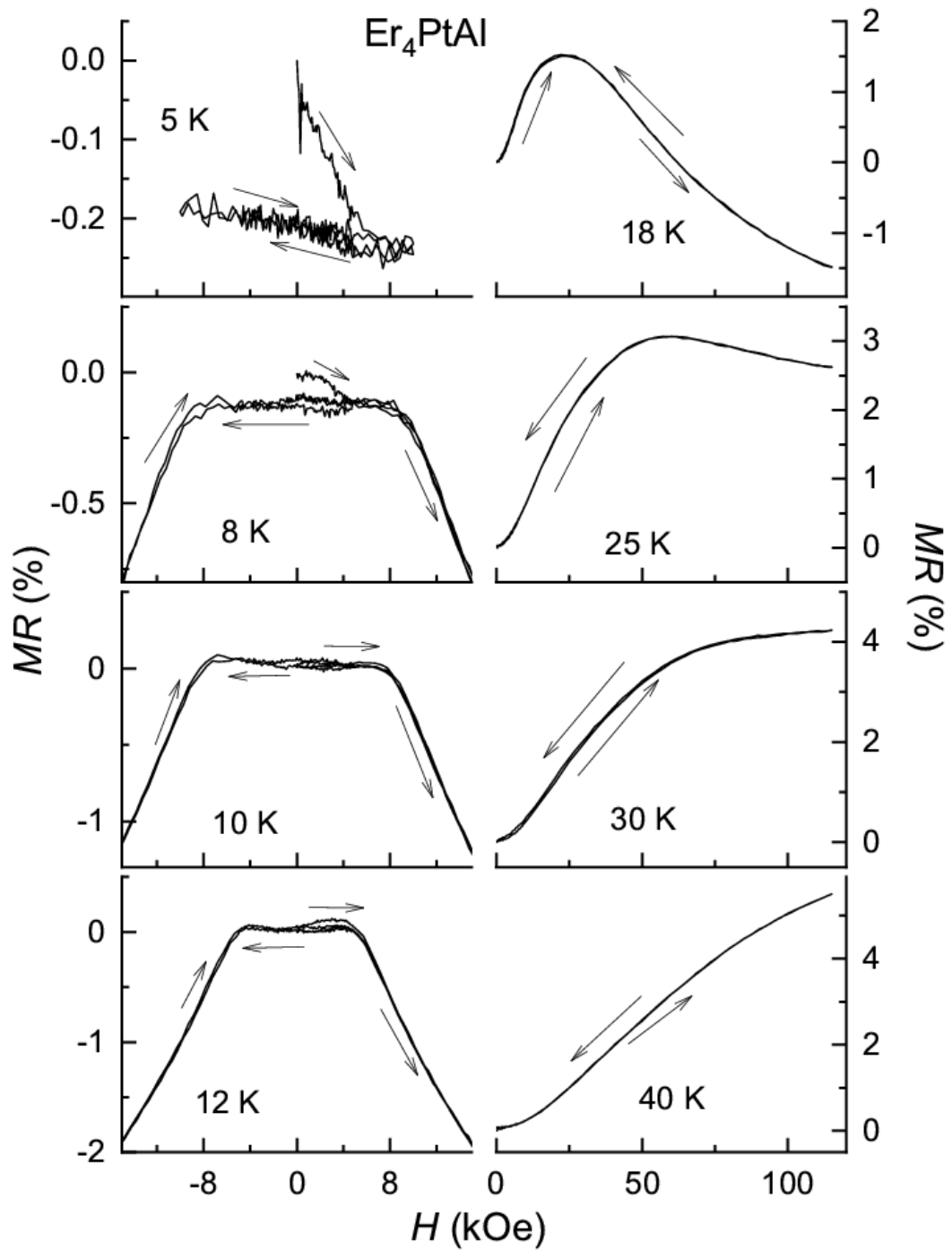


Figure 4.14: Magnetoconductance measured as a function of magnetic fields (left side -10 kOe to 10 kOe and, right for a field of 0 to 120 kOe), measured at various temperatures below and above the magnetic ordering.

vanishes gradually with the application of an external magnetic field. As the material enters a magnetically ordered state, there is a drop as expected.

Similar to the case of Ho, the magnetoresistance in the paramagnetic state shows interesting features (figure 4.13, right side graphs), due to a competition between the positive contribution and the negative contribution, both as a function of H and T . For instance, at 18 K (close to T_N), MR shows an initial increase in the positive quadrant due to metallic contribution, followed by a peak around 25 kOe and then a fall with the magnetoresistance curve entering the negative quadrant around 55 kOe due to the suppression of spin fluctuations. At higher temperatures, say at 25 K, MR curve remains in the positive quadrant because of the weakening of spin contribution with respect to the contribution from the metallic part.

In the magnetically ordered state (left side graphs of figure 4.13), the sign of MR remains negative, which could be either due to antiferromagnetic gap formation and/or spin-glass component. In the case of Er as well, we presented evidence for the formation of antiferromagnetic-gap. The magnitude of MR is so small that hysteresis in $MR(H)$ could be considered negligible. We could not observe any signature of a disorder-broadened first-order magnetic transition at low fields in contrast to that for *Ho* case.

4.6 Results and discussion for Dy₄RhAl.

As discussed in the introduction part of this chapter, Dy₄PtAl has been reported to undergo a ferromagnetic ordering, which is quite surprising, compared to that of the other rare-earth members in the family, ordering antiferromagnetically [12]. Therefore, it was of interest to study the effect of isoelectronic substitution of Rh for Pt and see how the magnetism in the

compound evolves, to compare with that of other R members of the family. With this motivation, we synthesized the polycrystalline samples of Dy_4RhAl and studied its magnetic and transport properties.

4.6.1 Dc Magnetization behavior

Magnetic susceptibility behavior as a function of temperature in two different fields is plotted in figure 4.15. ZFC and FC curves in 100 Oe are plotted in figure 4.15 (b). The susceptibility data in 100 Oe shows a distinct peak at 18 K suggesting the onset of antiferromagnetic order at this temperature. There are additional weak peaks at about 4 and 12 K, indicating the existence of magnetic anomalies at lower temperatures in the magnetically ordered state. With the application of 5 kOe field, the 12K-feature is smeared (figure 4.15 (a)), revealing sensitivity of this low-temperature magnetic state to the magnetic field in the low-field range. The inverse χ plot for 5 kOe data shows a linear behavior over a wide T range well above T_N . The value of μ_{eff} derived from the Curie-Weiss fit is found to be $11 \mu_B/\text{Dy}$, which is marginally higher than the theoretical expected value of $10.48 \mu_B$ for Dy^{3+} . The excess μ_{eff} may be attributed to the polarization of the Rh d band by the large magnetic moment on Dy^{3+} . The value of θ_P is -16 K; this magnitude and the sign are in good agreement with antiferromagnetic ordering setting in the compound around 18 K. Below T_N in the 100 Oe data ZFC and FC shows a bifurcation, with the FC curve exhibiting an upturn with decreasing temperature as in the other cases discussed in this thesis [15]. Looking at the data together, the features indicate possible antiferromagnetic cluster glass behavior at low temperatures. The χ plots for 100 Oe and 5 kOe in figure 4.15 (c) show that the two curves do not overlap at T_N , these do so but well

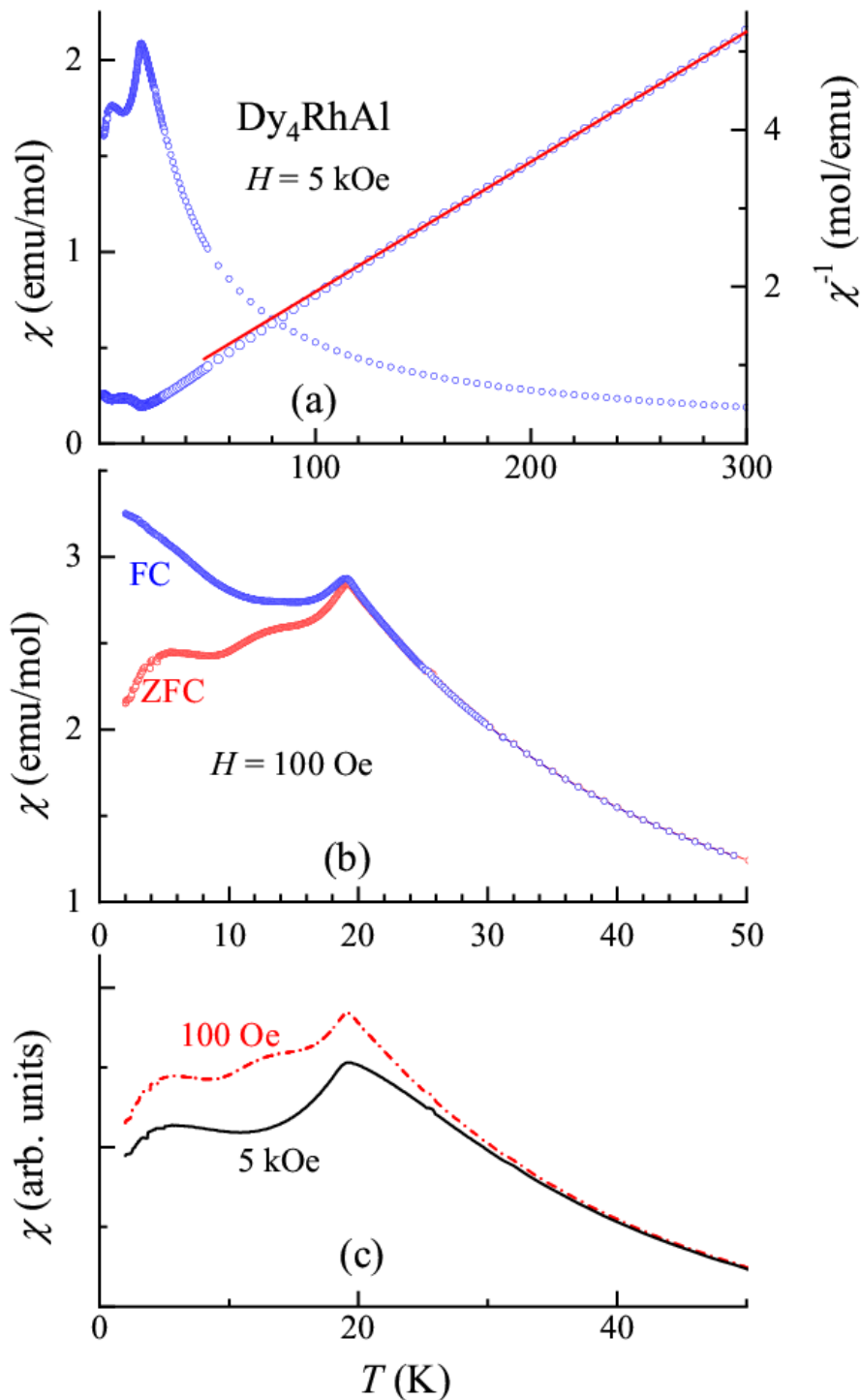


Figure 4.15: a) Temperature dependent dc magnetic susceptibility and inverse susceptibility measured in 5kOe. A red line is drawn to show the Curie-Weiss fit. (b) Temperature dependent dc magnetic susceptibility measured in 100 Oe (for zero-field-cooled and field-cooled conditions). (c) comparison of the plots of susceptibility measured in 100 Oe and 5 kOe in the vicinity of T_N to bring out the existence of short-range magnetic correlations in Dy_4RhAl .

above T_N only, indicating the existence of subtle magnetic anomalies, before long-range magnetic ordering sets in [see the articles cited in [14]].

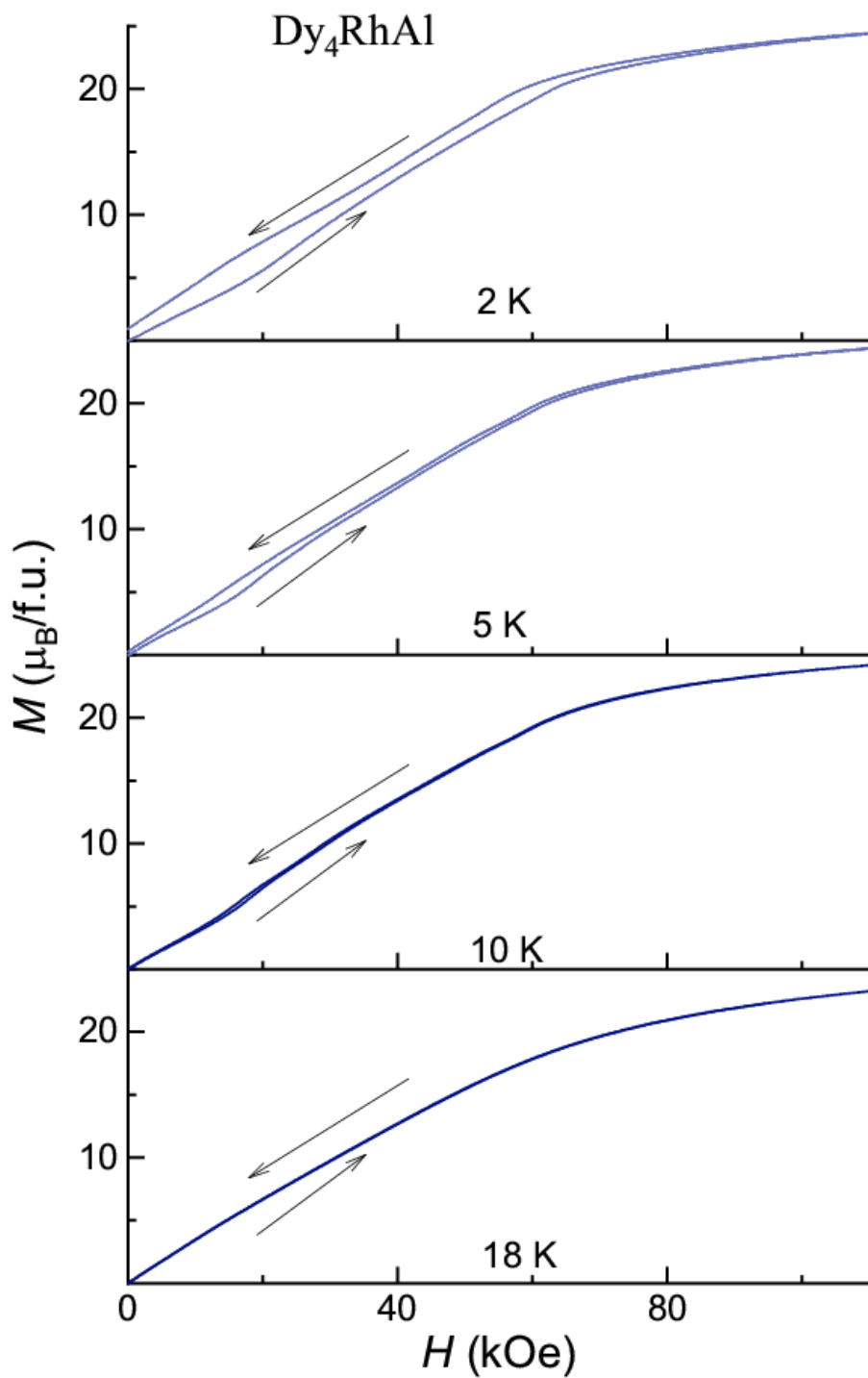


Figure 4.16: Isothermal magnetization for Dy_4RhAl at 2, 5, 10 and 18 K.

We measured the isothermal magnetization at 2, 5, 10 and 18 K and the data is plotted in figure 4.16. Magnetization shows a gradual increase with H at these temperatures, with a tendency to saturate beyond about 60 kOe. A weak hysteresis is visible at lower temperatures. There is an upward curvature in the data around 20-40 kOe below 18 K. This is a characteristic of disorder-broadened first-order field-induced magnetic transition at low temperatures. This finding supports the conclusion that the zero-field state of this compound is not ferromagnetic. The magnetic moment values at very high fields, as well as the zero-field value, obtained from the linear extrapolation of high-field linear region) are far less than that expected for the free ion. This can arise from crystal-field-effects.

4.6.2 Heat capacity and isothermal entropy change behavior

Heat capacity data is plotted in figure 4.17. In zero field the $C(T)$ data (see figure 4.17) shows an upturn below 20 K, followed by a peak at 18 K. As the temperature is lowered further, the heat capacity shows a gradual fall with decreasing temperature. There are no additional well-defined peaks in the heat capacity data well-below 18 K, indicating the absence of any additional long-range magnetic ordering at lower temperatures. The C/T versus T curve for zero field (figure 4.17 (b)) shows a change of slope around 5-10 K. This implies that there is actually a subtle faster decrease (compared to higher temperature linear region) of the heat-capacity. This can be attributed to the spin-glass component. With the application of magnetic fields, the peak seen in the data at 18 K gets suppressed and shifts

to lower temperatures, supporting the onset of antiferromagnetic order at this temperature with a well-defined magnetic structure.

The $C(T)$ data was fitted below 7 K to the functional form of, $C = \beta T^3 + \alpha T^n e^{-\Delta/T}$, where α , β and n are constants, and Δ is the spin-gap between the lower and upper band of the spin wave spectrum. The value of Δ and n are found to be ~ 2.2 K and ~ 0.8 .

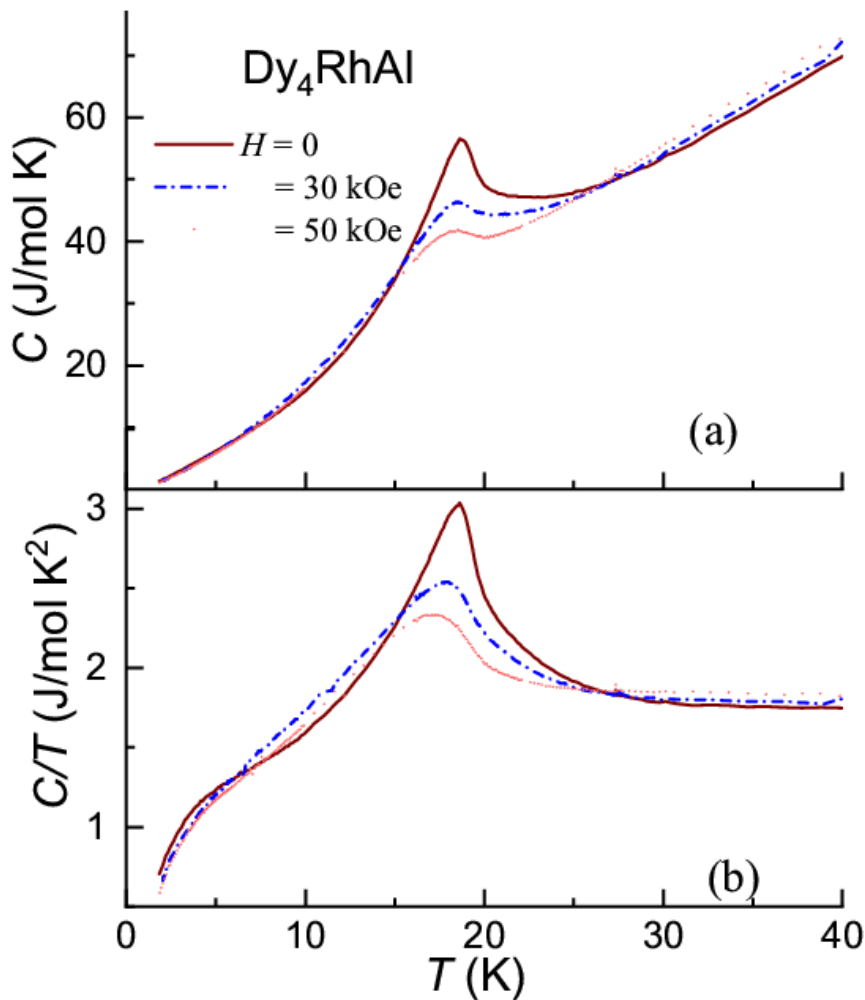


Figure 4.17: (a) Heat-capacity as a function of temperature (<40 K) for Dy_4RhAl , measured in zero field and applied magnetic fields. (b) Curves showing heat-capacity divided by temperature.

Isothermal entropy change, ΔS as a function of temperature, derived from the heat capacity data, by integrating C/T versus T curves is shown in figure 4.18. Plots of ΔS obtained for $H= 30$ and 50 kOe exhibit a peak in the negative quadrant at a temperature (about 25 K) slightly above T_N ; this feature combined with the sign indicates that [19] short-range magnetic correlations sets in (inferred from the combined plot of χ shown in figure 4.15 (c)) before long-range magnetic order and that these correlations are of a ferromagnetic-type. In addition, there is a weaker peak around 18 K in the positive quadrant, and the sign is consistent with the inference of

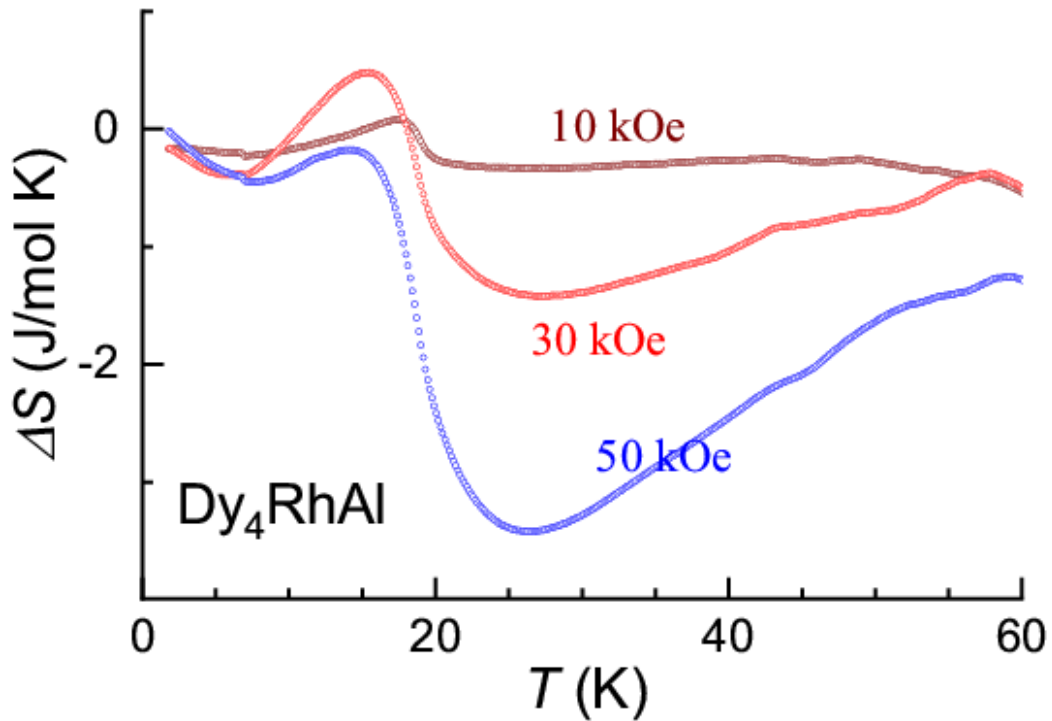


Figure 4.18: Isothermal entropy change as a function of temperature (for final fields 10, 30 and 50 kOe) below 40 K for Dy_4RhAl .

antiferromagnetic order setting in at 18 K. ΔS shows additional sign-crossovers at lower temperatures, which may be consistent with subtle magnetic effects, mentioned earlier. The peak values of ΔS are not large, when compared to those for other Rh compounds in the

family, for example the value of ΔS in isostructural Tb, Ho and Er are ~ 6.1 , 5.9 and 8.2 J/mol K respectively [13,14]. For a field of 10 kOe the values of ΔS are too small to attach any significance to the sign changes with T .

4.6.3 Ac susceptibility and isothermal remanent magnetization behavior

In view of the fact that ZFC-FC dc χ curves show a bifurcation at T_N (figure 4.15b), we measured the ac susceptibility to gather knowledge about possible spin-glass freezing. The real part and imaginary parts are shown in figure 4.19 (a) and (b) respectively. Corresponding data measured in a field of 5 kOe is noisy for 133 and 1339 Hz, hence the curves are shown for 1.3 and 13 Hz only. A ν -dependence of the peak in the $\chi'(T)$ is quite transparent in the vicinity of T_N , even though the curves for 133 and 1333 Hz are noisy (for instance, ~ 20 and ~ 24 K for 1.3 and 1333 Hz respectively). These results support the spin-glass freezing. Using the peak temperature values (T_p) for the two extreme frequencies, we derived the magnitude of the factor, $(\Delta T_p / T_p) \Delta(\log \nu)$, and the value comes out to be about 0.07. This value is rather large when compared to that expected for canonical spin-glasses (which is < 0.01) [33]. Since the T_p for the lowest frequency (1.3 Hz) matches with the value of T_N , it is concluded that the spin-glass freezing and antiferromagnetism set in simultaneously. Since, at low temperatures, low-field FC χ (figure 4.15 (b)) show an upturn, the spin-glass state revealed by ac χ also is of a cluster-type, arising from antiferromagnetic clusters. We do not find any peak in χ'' down to 2 K (being noisy at higher frequencies the data is shown for two frequencies only). The presence of a worthwhile signal in χ'' is a necessary criterion for spin-glass freezing [33].

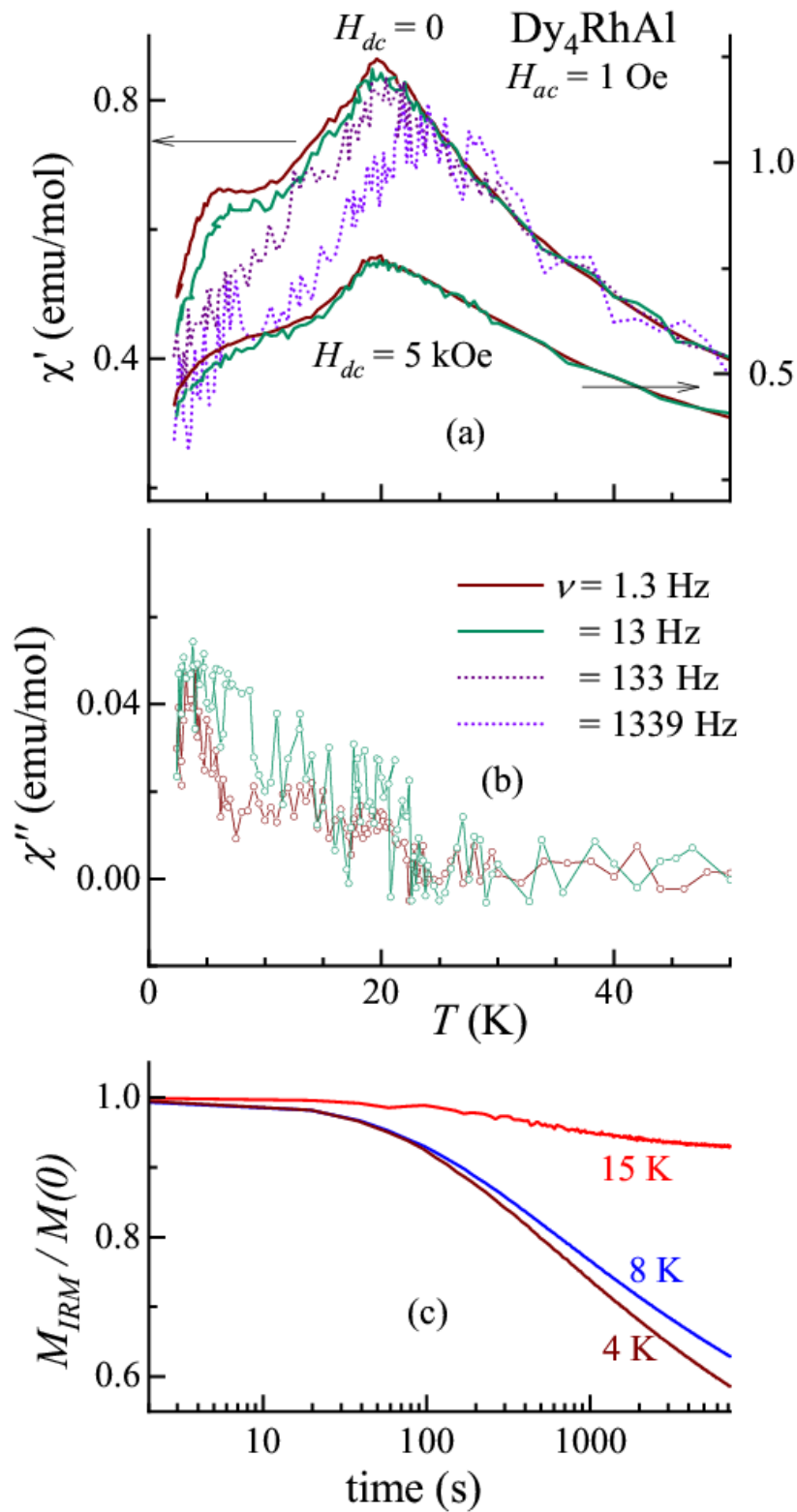


Figure 4.19: (a) Real part and, (b) imaginary part of ac susceptibility for Dy_4RhAl , (c) time dependence of isothermal remnant magnetization measured at 4, 8 and 15K.

We therefore infer that the spin-glass dynamics of the antiferromagnetic clusters is so weak that it escapes detection by χ'' measurement. The peak in χ' gets suppressed marginally with the application of a magnetic field of 5 kOe, which is in sharp contrast to the complete suppression expected in the case of conventional spin-glasses and previous cases discussion in the thesis (Nd₂RhSi₃, section 3.4.3; Er₂RhSi₃, section 3.5.2; Ho₄PtAl, Section 4.4.2 and Er₄PtAl, Section 4.5.2), endorsing our inference on the weakness of spin-glass feature. In addition to the above features, there is a drop in χ' below 5 K, as seen in dc χ data, showing a distinct frequency dependence like the one seen at 18 K. These features indicate that the spin-glass behavior coexists with antiferromagnetism, down to 2K, as soon as long-range magnetic ordering sets in.

For rendering further support to spin-glass freezing, the time dependence of M_{IRM} in the magnetically ordered state below T_N is shown in figure. 4.19c for the temperatures 4, 8 and 15 K. The M_{IRM} data, exhibits a slow decay (essentially logarithmically after waiting for about a minute) at all temperatures, as expected for spin-glass systems. However, we find the magnitude of M_{IRM} at $t=0$ decreases as the measurement temperature is increased, which reflects a corresponding change in the strength of spin-glass component. Above the magnetically ordered state, say at 25 K, M_{IRM} does not show any such decay.

4.6.4 Electrical resistivity and magnetoresistance behavior

Resistivity as a function of temperature was measured both in zero field and in the presence of various external fields (30, 50, 70 and 100 kOe), and the curves are shown in figure 4.20. To clearly show the low temperature features, the data is plotted below 100 K in figure

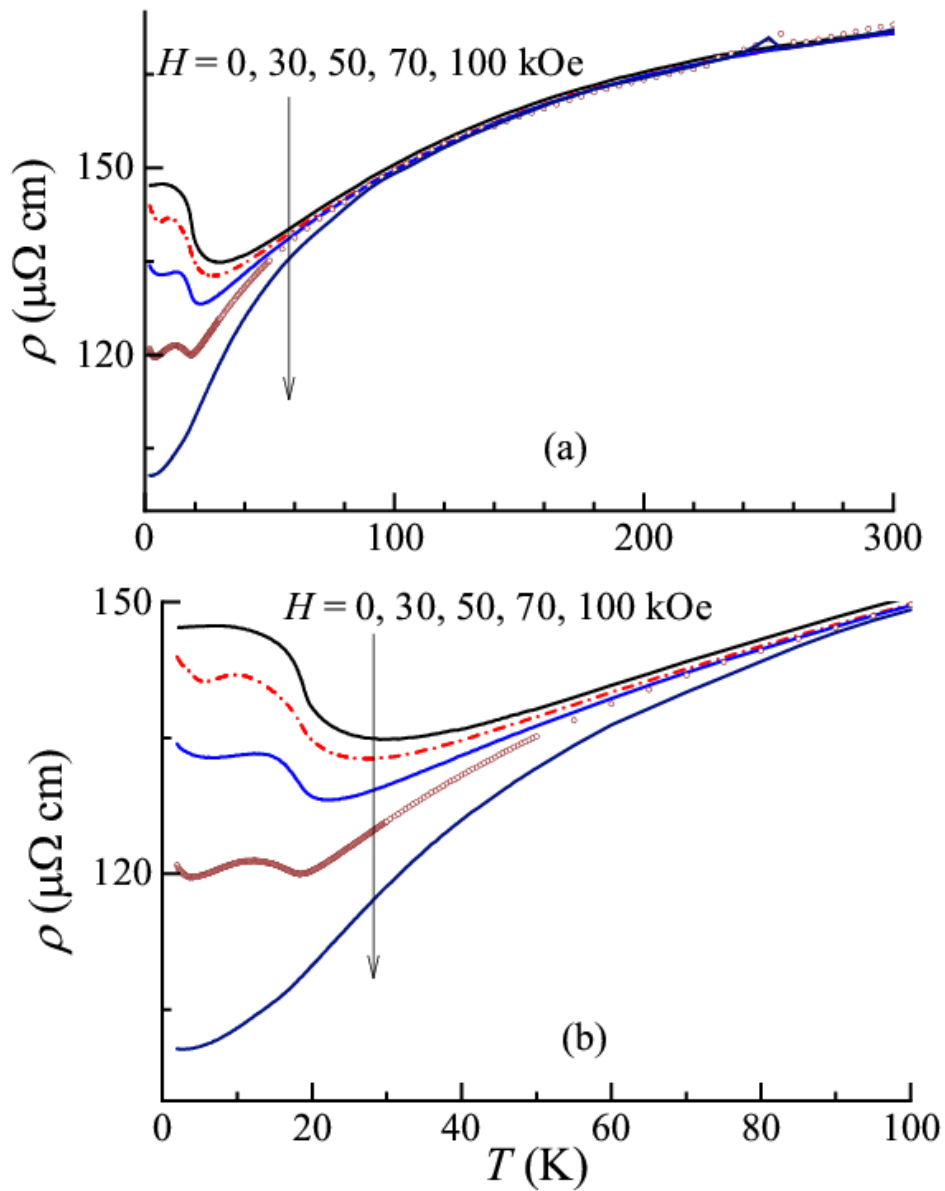


Figure 4.20: (a) Electrical resistivity measured as a function of temperature (full range) for Dy_4RhAl , measured in the presence of external magnetic fields as well. (b) Expanded portion of data below 100 K for sake of clarity of the features at low temperatures.

4.20 (b). For all fields, in the paramagnetic state, resistivity shows metallicity as the temperature is lowered below 300 K. However, the magnitude of resistivity undergoes pronounced depression with increasing magnetic fields as the temperature is lowered, revealing a gradual increase of MR with lowering temperatures across T_N like in previous

cases, reported in this thesis. As the temperature is lowered further, resistivity shows an upturn as soon as magnetic ordering sets in (in zero field). This feature, establishes the formation of magnetic Brillouin-zone gap, which is consistent with antiferromagnetic nature of the magnetic order [34]. This feature undergoes a gradual suppression with increasing magnetic fields due to suppression of antiferromagnetic energy gap. Naturally MR is large in the magnetically ordered state. For getting a better picture of the magnetoresistive behavior and its magnitude, the isothermal MR curves, were obtained at 5, 8, 12, 16 and 25 K (figure 4.21).

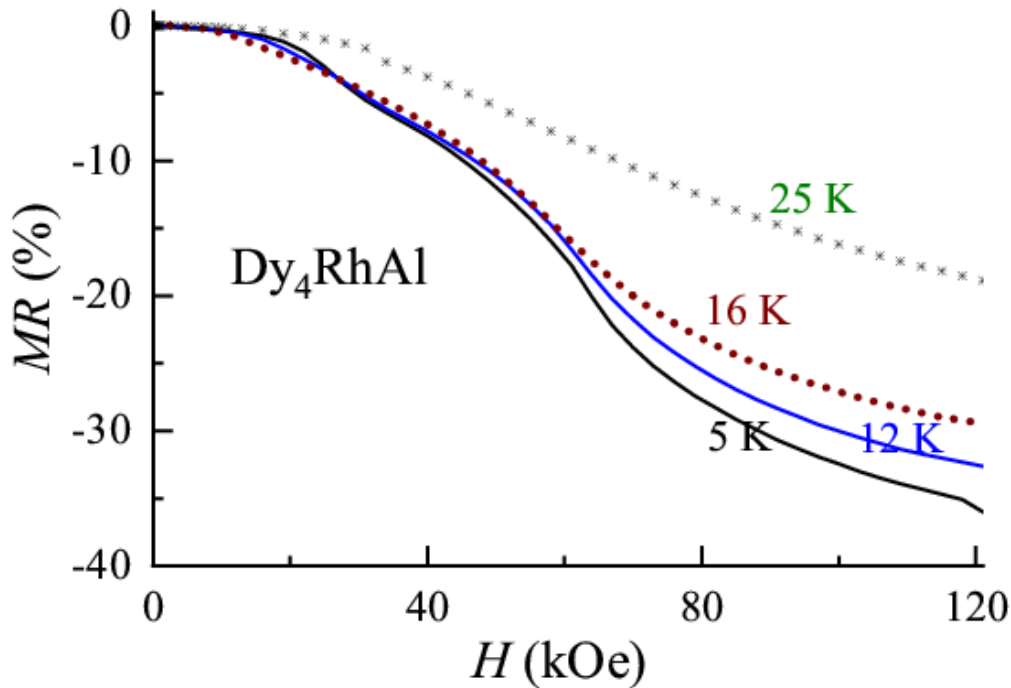


Figure 4.21: Magnetoresistance measured as a function of field at various temperatures.

A noteworthy finding from the magnetoresistance plot is that MR at 5 K, shows a very broad step around the field of 20-50 kOe and the curve is weakly hysteretic in nature which supports the conclusion from the $M(H)$ data, that there could be a disorder-broadened first-order field-induced magnetic transition in this compound at low

temperatures. At higher temperatures, this feature gets gradually smeared. At 25 K, MR shows a quadratic field-dependence which is expected for paramagnets.

4.7 Discussions and conclusions

- Looking at all the results together, it is clear that both the compounds, Ho_4PtAl and Er_4PtAl , exhibit a re-entrant cluster spin-glass behavior, with the onset of an antiferromagnetic type of magnetic order. This behavior is similar to that observed for the other rare-earth members in the family, except that of Dy_4PtAl , which is known to exhibit a ferromagnetic ordering [12]. From the degree of suppression of ac χ peaks by the application of the magnetic fields, it is concluded that the spin glass dynamics in Dy_4RhAl is relatively weaker. Within this family of compounds, both Ho_4PtAl and Er_4PtAl , exhibit the largest value of isothermal entropy change, at the onset of magnetic order, with a large tail above T_N . Since the values exceed that of an S -state ion, this finding suggests that the topology of the $4f$ orbital can enhance the magnetocaloric effect. The intriguing conclusion inferred from the comparison of the MCE behavior between the Pt-based family and the Rh-based family, is the following: It seems that the Pt $5d$ spin-orbit coupling also plays a role in the enhancement of the MCE values. Such a correlation should provide clues for the advancement of theories in the field of MCE . This will in turn be helpful in engineering of materials for magnetic refrigeration at room temperature. The reversible isothermal entropy curves establish that the Er compound meets the criterion [28] for magnetocaloric applications in the low temperature range.

- In the case of Dy₄RhAl, the results establish that the compound undergoes antiferromagnetic order which is different from the ferromagnetic ordering seen in the case of Dy₄PtAl. This result provides an indirect support to the fact that the ferromagnetism seen in the case of Dy₄PtAl is interesting and unusual. It is quite possible that the Pt *5d* orbital, extended more spatially when compared to Rh *4d* orbital, plays an important role by strong interaction with crystal-field-split anisotropic orbitals of Dy giving rise to the anomalous magnetism seen in the case of Dy₄PtAl. In addition, the *5d* electrons are relatively less correlated with stronger spin-orbit coupling than the *4d* electrons. These results suggest an important role of transition metal bands, which interact with the Dy *4f* electrons, determining the magnetism of these systems. It would be worthwhile to carry out a comparative study of both these Dy compounds, by spin-polarized band structure calculations, electron spectroscopy and neutron diffraction (for determining the magnetic structure), which would further aid to understand the role of transition band correlations on the magnetism of strictly localized *4f* orbital. In addition, inelastic neutron scattering studies would also enable to learn about crystal-field scheme in these materials.

- There are clear evidences for the presence of resistivity minimum above T_N for Ho and Er cases, in zero field, which got suppressed with the application of H . This is not expected for such rare-earths with localized *4f* electrons, and hence the comparison fall into the family of rare-earth materials with novel magnetic precursor effects [35]. Though such a minimum is not apparent for Dy₄RhAl, magnetoresistance behavior mentioned below offers support for such a phenomenon in this case as well.

- There are various other interesting features, e.g. antiferromagnetic energy gap formation, large magnetoresistive behavior, not only in the magnetically ordered state but also in the paramagnetic state, well above T_N extending to $T > 3T_N$, and spin-orientation effects as a function of T and H in the magnetically ordered state, leading to complex sign reversals with the variation of such external parameters.

Finally, this work brings out the complex nature of magnetism in these compounds, in the magnetically ordered state, arising from the different sites of rare-earth ions. It is of interest to theoretically explore, as to how the interaction among three sites of rare-earth plays a role in deciding the magnetic behaviour of the system.

4.8 Bibliographical references

1. Pecharsky VK, Gschneidner Jr KA. Giant magnetocaloric effect in $Gd_5(Si_2Ge_2)$. Physical review letters. 1997 Jun 9; 78(23):4494.
2. Tsutaoka T, Tokunaga T, Kosaka M, Uwatoko Y, Suzuki H, Kitazawa H, Kido G. Magnetic properties of R_7Rh_3 ($R = Tb, Dy$ and Ho) in high magnetic fields. Physica B: Condensed Matter. 2001 Jan 1; 294:199-202.
3. Sengupta K, Sampathkumaran EV. An anomalous magnetic phase transition at 10 K in Nd_7Rh_3 . Journal of Physics: Condensed Matter. 2006 Jul 21; 18(31):L401.
4. Sengupta K, Sampathkumaran EV. Field-induced first-order magnetic phase transition in an intermetallic compound Nd_7Rh_3 : Evidence for kinetic hindrance,

- phase coexistence, and percolative electrical conduction. *Physical Review B*. 2006 Jan 12; 73(2):020406.
5. Rayaprol S, Siruguri V, Hoser A, Ritter C, Sampathkumaran EV. Microscopic evidence for magnetic-phase coexistence in the intermetallic compound Nd₇Rh₃. *Physical Review B*. 2014 Oct 21; 90(13):134417.
 6. Tappe F, Schwickert C, Linsinger S, Pöttgen R. New rare earth-rich aluminides and indides with cubic Gd₄RhIn-type structure. *Monatshefte für Chemie-Chemical Monthly*. 2011 Nov; 142:1087-95.
 7. Doğan A, Rayaprol S, Pöttgen R. Structure and magnetic properties of RE₄CoCd and RE₄RhCd (RE= Tb, Dy, Ho). *Journal of Physics: Condensed Matter*. 2007 Feb 2; 19(7):076213.
 8. Kersting M, Matar SF, Schwickert C, Poettgen R. Segregation of calcium and magnesium into different substructures. Ca₄Ag_{0.948}Mg and other compounds with Gd₄RhIn-type structure. *Zeitschrift für Naturforschung B*. 2012 Jan 1; 67(1):61-9.
 9. Engelbert S, Janka O. RE₄TAl (RE= Y, Sm, Gd–Tm, Lu; T= Pd, Pt)–Synthesis and magnetism of new aluminum representatives with the Gd₄RhIn type structure. *Intermetallics*. 2018 May 1; 96:84-9.
 10. Kumar R, Sharma J, Iyer KK, Sampathkumaran EV. Reentrant spin-glass and transport behavior of Gd₄PtAl, a compound with three sites for Gd. *Journal of Magnetism and Magnetic Materials*. 2019 Nov 15; 490:165515.
 11. Kumar R, Iyer KK, Paulose PL, Sampathkumaran EV. Spin-glass features at multiple temperatures and transport anomalies in Tb₄PtAl. *Journal of Applied Physics*. 2019 Sep 28; 126(12).

12. Kumar R, Iyer KK, Paulose PL, Sampathkumaran EV. Ferromagnetism to spin-glass transition and magnetotransport anomalies in Dy₄PtAl. AIP Conference Proceedings 2020 Nov 5 (Vol. 2265, No. 1). AIP Publishing.
13. Kumar R, Iyer KK, Paulose PL, Sampathkumaran EV. Competing magnetic interactions and magnetoresistance anomalies in cubic intermetallic compounds, Gd₄RhAl and Tb₄RhAl, and enhanced magnetocaloric effect for the Tb case. Physical Review Materials. 2021 May 14; 5(5):054407.
14. Kumar R, Iyer KK, Paulose PL, Sampathkumaran EV. Competing magnetic interactions and magnetoresistance anomalies in cubic intermetallic compounds, Gd₄RhAl and Tb₄RhAl, and enhanced magnetocaloric effect for the Tb case. Physical Review Materials. 2021 May 14; 5(5):054407.
15. Marcano N, Sal JG, Espeso JI, Barquín LF, Paulsen C. Cluster-glass percolative scenario in CeNi_{1-x}Cu_x studied by very low-temperature ac susceptibility and dc magnetization. Physical Review B. 2007 Dec 19; 76(22):224419.
16. Yamamoto TD, Kotani A, Nakajima H, Okazaki R, Taniguchi H, Mori S, Terasaki I. Ferromagnetic Cluster Glass Phase Embedded in a Paramagnetic and Metallic Host in Non-Uniform Magnetic System CaRu_{1-x}Sc_xO₃. Journal of the Physical Society of Japan. 2016 Mar 15; 85(3):034711.
17. Upadhyay SK, Iyer KK, Sampathkumaran EV. Magnetic behavior of metallic kagome lattices, Tb₃Ru₄Al₁₂ and Er₃Ru₄Al₁₂. Journal of Physics: Condensed Matter. 2017 Jul 17; 29(32):325601.

18. Noakes DR, Shenoy GK. The effect of a crystalline electric field on the magnetic transition temperatures of rare-earth rhodium borides. *Physics Letters A*. 1982 Aug 16;91(1):35-6
- Dunlap BD, Hall LN, Behroozi F, Crabtree GW, Niarchos DG. Crystal-field effects and the magnetic properties of rare-earth rhodium borides. *Physical Review B*. 1984 Jun 1;29(11):6244
- Adroja DT, Malik SK. Magnetic-susceptibility and electrical-resistivity measurements on RPdSn (R= Ce–Yb) compounds. *Physical Review B*. 1992 Jan 1; 45(2):779.
19. Gschneidner KA, Pecharsky VK, Tsokol AO. Recent developments in magnetocaloric materials. *Reports on progress in physics*. 2005 May 20; 68(6):1479.
20. Li L, Yan M. Recent progresses in exploring the rare earth based intermetallic compounds for cryogenic magnetic refrigeration. *Journal of Alloys and Compounds*. 2020 May 15;823: 153810.
21. Iyer KK, Matteppanavar S, Dodamani S, Maiti K, Sampathkumaran EV. Magnetic behavior of cubic Dy₄RhAl with respect to isostructural Dy₄PtAl, revealing a novel 4f d-band interaction. *Journal of Magnetism and Magnetic Materials*. 2023 Feb 15; 568:170406.
22. Takayama T, Chaloupka J, Smerald A, Khaliullin G, Takagi H. Spin–orbit-entangled electronic phases in 4 d and 5 d transition-metal compounds. *Journal of the Physical Society of Japan*. 2021 Jun 15; 90(6):062001.

23. Medicherla VR, Patil S, Singh RS, Maiti K. Origin of ground state anomaly in LaB6 at low temperatures. *Applied physics letters*. 2007 Feb 5; 90(6).
24. Bindu R, Maiti K, Khalid S, Sampathkumaran EV. Structural link to precursor effects. *Physical Review B*. 2009 Mar 9; 79(9):094103.
25. Bindu R, Adhikary G, Sahadev N, Lalla NP, Maiti K. Pseudogap and charge ordering in a large-bandwidth electron-doped manganite. *Physical Review B*. 2011 Aug 29; 84(5):052407.
26. Maiti K, Singh RS, Medicherla VR, Rayaprol S, Sampathkumaran EV. Origin of charge density wave formation in insulators from a high resolution photoemission study of BaIrO₃. *Physical review letters*. 2005 Jun 30; 95(1):016404.
27. Chaudhary V, Chen X, Ramanujan RV. Iron and manganese based magnetocaloric materials for near room temperature thermal management. *Progress in Materials Science*. 2019 Feb 1; 100:64-98.
28. Law JY, Moreno-Ramírez LM, Díaz-García Á, Franco V. Current perspective in magnetocaloric materials research. *Journal of Applied Physics*. 2023 Jan 28; 133(4).
29. Mallik R, Sampathkumaran EV. Magnetic precursor effects, electrical and magnetoresistance anomalies, and heat-capacity behavior of Gd alloys. *Physical Review B*. 1998 Oct 1; 58(14):9178.
30. Kumar R, Iyer KK, Paulose PL, Sampathkumaran EV. Magnetic and transport anomalies in R₂RhSi₃ (R= Gd, Tb, and Dy) resembling those of the exotic magnetic material Gd₂PdSi₃. *Physical Review B*. 2020 Apr 29; 101(14):144440.

31. Wang Z, Barros K, Chern GW, Maslov DL, Batista CD. Resistivity minimum in highly frustrated itinerant magnets. *Physical review letters*. 2016 Nov 8; 117(20):206601.
32. Zhao B, Hu X, Dong F, Wang Y, Wang H, Tan W, Huo D. The magnetic properties and magnetocaloric effect of $\text{Pr}_{0.7}\text{Sr}_{0.3}\text{MnO}_3$ thin film grown on SrTiO_3 substrate. *Materials*. 2022 Dec 21; 16(1):75.
33. Binder K, Young AP. Spin glasses: Experimental facts, theoretical concepts, and open questions. *Reviews of Modern physics*. 1986 Oct 1; 58(4):801. Mydosh JA. Spin glasses: an experimental introduction. CRC Press; 1993 May 13.
34. S. Legvold, *Magnetic Properties of Rare-earth Metals*, Plenum, 1972.
35. S. R. Saha, H. Sugawara, T. D. Matsuda, H. Sato, R. Mallik and E.V. Sampathkumaran, *Phys. Rev. B* **60**, 12162 (1999).

Chapter 5

Pressure effects on the magnetic properties of spin-chain compounds $\text{Tb}_2\text{BaNiO}_5$ and $\text{Tb}_2\text{BaCoO}_5$

5.1 Introduction

In the previous chapters, certain exotic properties of $4f$ electrons in a metallic environment were brought out. No other element in the compounds discussed in those chapters possess magnetic moment on their own (barring a small induced moment on $4d$ metals). There are often situations where $4f$ electrons compete with magnetic moments of other types of ions in the lattice, even without *RKKY* interactions, that is in insulators, leading to complex magnetism controlling other phenomena present in these compounds. These interactions can be tuned by external as well as chemical pressures. The purpose of this chapter is to bring out such exotic nature of $4f$ electrons, by choosing suitable examples. The phenomena under discussion in this chapter is ferroelectricity coupled to magnetism, which is commonly known as ‘Multiferroicity’, known among transition metal systems due to $3d/4d$ electrons, and the exotic materials chosen are insulating spin-chain compounds, $\text{Tb}_2\text{BaNiO}_5$ and $\text{Tb}_2\text{BaCoO}_5$. Therefore, a brief introduction is given below to this phenomenon and the materials.

For the past few decades, a large number of materials have been studied to find those exhibiting multiferroicity. Multiferroics have been defined [1] as those materials, which exhibit two or all of the following properties together occur in the same phase, viz ferroelectricity, ferromagnetism, and ferroelasticity. Though either of these phenomena can have independent source, the materials which are of great current interest are those in which one property influences the other, for instance, ferroelectricity and ferromagnetism which

are antagonistic (type II). Main reason behind this antagonistic nature of these properties is the “ d^0 -ness” of the material [2], in the case of transition metals, for ferroelectricity. For any kind of magnetic ordering in a material, it is necessary to have unpaired d electrons. For any ferroelectric behavior, distortion of the center of symmetry is crucial, which in most cases (like the conventional perovskite ferroelectrics) is often achieved by an off-center displacement of the cation from the center of the oxygen octahedron. In the case of type-1 multiferroics, like BiFeO_3 , the $6s$ lone pair electrons of Bi have been known to give rise to ferroelectricity and the $3d$ -electrons of Fe lead to canted antiferromagnetic order [3]. In the case of type-II multiferroic materials, like orthorhombic RMnO_3 [4] and RMn_2O_5 [5], three microscopic mechanisms, have been shown to give rise to multiferroicity i.e. the inverse Dzyaloshinskii–Moriya (DM) interaction leading to spin canting, exchange-striction, and spin-dependent p - d hybridization [6,7]. The spin-induced ferroelectric behavior has been often observed among magnetic systems [8], but not due to $4f$ magnetism. In addition, geometrically frustrated antiferromagnetic behavior has also been known to induce multiferroicity. TbMnO_3 was the first compound of this type on which type-II multiferroicity was reported. This compound exhibits two antiferromagnetic transitions, one at 41 K and the other at 28 K, with ferroelectric transition being triggered by the 28 K magnetic transition. [9]. Spin-driven multiferroic behavior has been observed in two dimensional ($2D$) systems like $\text{Ni}_2\text{V}_2\text{O}_8$, CuFeO_2 etc., and quasi $1D$ systems like $\text{Ca}_3\text{CoMnO}_6$, LiVCuO_4 etc. [10-14].

In this regard, the Haldane spin-chain [14] family, R_2BaNiO_5 ($\text{R} = \text{Gd}, \text{Dy}, \text{Er}, \text{Sm}, \text{Nd}, \text{Ho}$ and Tb) [15-18], crystallizing in a centrosymmetric orthorhombic structure ($Immm$ space-group) have been recently reported to exhibit multiferroic behavior. In this chapter,

we focus on $\text{Tb}_2\text{BaNiO}_5$ and $\text{Tb}_2\text{BaCoO}_5$, as within the entire family, these Tb compound have been reported to exhibit an exceptionally large magnetodielectric coupling (*MDE*) (~ 18 to 54 %) following metamagnetic transition. Such a large value of *MDE* was quite rare among polycrystalline multiferroic compounds [18]. $\text{Tb}_2\text{BaNiO}_5$ was reported to exhibit two antiferromagnetic transitions one at $T_1 = 63$ K and the other at $T_2 = 25$ K, arising from magnetic ordering of Tb and Ni sublattices simultaneously, with ferroelectric behavior being induced by the 25 K magnetic transition, despite being centrosymmetric crystallographically and collinearity of magnetic moments of Ni and Tb within the respective sublattices. There is a mutual canting of the $3d(\text{Ni})$ and $4f(\text{Tb})$ moments [19]. This canting angle undergoes a sharp change at T_2 with exchange striction anomalies [20]. A critical canting angle is required to attain ferroelectricity, which is a novelty in the field of multiferroics. It was also shown that the Haldane gap was not an important criterion needed to observe the multiferroic anomalies, because the isostructural $\text{Tb}_2\text{BaCoO}_5$ is also multiferroic with still enhanced MDE coupling [21]. Another interesting aspect of $\text{Tb}_2\text{BaNiO}_5$ compound is that Tb $4f$ was shown to be crucial to observe multiferroicity [22] unlike in transition metal systems. With respect to the compound $\text{Tb}_2\text{BaCoO}_5$ [21] this has been shown to order antiferromagnetically below 18.8 K with the onset of coupled ferroelectricity. Both these compounds are characterized by metamagnetic transitions in the range 40-60 kOe. Considering that external pressure studies on some of the most celebrated multiferroics were quite informative, e.g., RMnO_3 , RMn_2O_5 , CuCrO_2 , and $\text{Ni}_3\text{V}_2\text{O}_8$, (where R = rare-earth), [23–30], we considered it worthwhile to study $\text{Tb}_2\text{BaNiO}_5$ and $\text{Tb}_2\text{BaCoO}_5$ under pressure to understand the changes in the magnetic properties. Under pressure, various interactions compete with each other, like first and second nearest-

neighbor isotropic interactions, magnetic anisotropy, antisymmetric Dzyaloshinskii-Moriya interactions, symmetric exchange interactions and $p-d$ hybridization. Chemical pressure effect on magnetism of Tb_2BaNiO_5 induced by small doping of Sr in place of Ba is also reported for comparison purpose.

5.2 Crystal structure

The compounds, Tb_2BaNiO_5 and Tb_2BaCoO_5 , are known to crystallize in an orthorhombic structure, with space group $Immm$. These compounds are known to exhibit dimorphism, $Immm$ and $Pnma$ space groups based on the sintering temperatures of the sample.

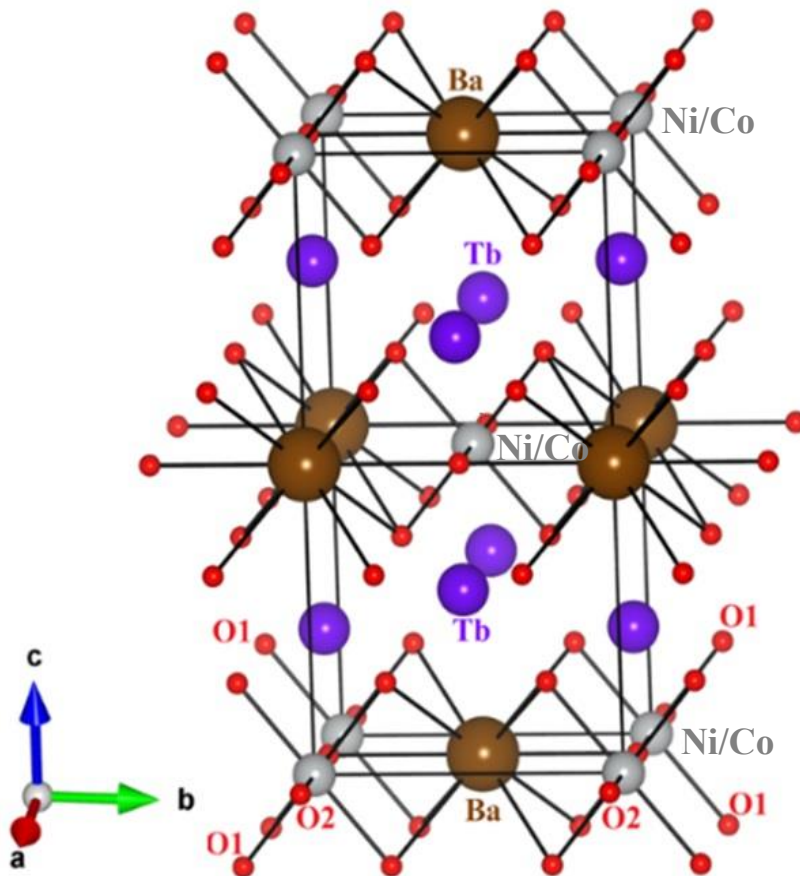


Figure 5.1: Crystal structure of Tb_2BaNiO_5

We have focused our studies on the samples crystallizing in *Immm* space group, where the crystal structure is characterized by vertex-sharing Ni/Co chains (running along the a-axis). These Ni/Co chains are isolated from each other by intervening *R* and Ba ions (see figure 5.1). The NiO₆ (CoO₆) octahedron in this space group is distorted, with the apical distance (1.88 Å) being shorter than the basal Ni-O distance (2.18 Å), for instance in Tb₂BaNiO₅.

5.3 Sample preparation, characterization and experimental details.

The parent composition as well as Sr-doped specimens, Tb₂Ba_{1-x}Sr_xNiO₅ ($x = 0, 0.025, 0.05, 0.075, \text{ and } 0.1$) and Tb₂BaCoO₅, were prepared in the polycrystalline form using the solid-state reaction method. The rare-earth carbonate was first heated to 500° C for 24 hours to remove the adsorbed moisture, if present. Following this, stoichiometric quantities of high purity carbonates and oxides, Tb₂(CO₃)₂·nH₂O, NiO, BaCO₃, SrCO₃, and CoO were ground together and heated at 1200° C for 20 hours followed by pelletizing and sintering at 1250° C, with intermediate grindings. Powder x-ray diffraction studies have been done with Cu-K_α and the Rietveld refined patterns are shown in figure 5.2 (a) for Tb₂Ba_{1-x}Sr_xNiO₅ and for Tb₂BaCoO₅ in 5.2 (b). The refined parameters and the lattice constants have been tabulated in table 5.1. The fitting of the XRD patterns confirm the samples to be in single phase. Since a small shift (at least for $x > 0.05$ at higher angle side) of XRD peaks are seen in the Sr doped specimen, it can be ascertained that Sr goes into the lattice even in such small amounts. In addition, SEM and EDAX measurements confirmed the stoichiometry and homogeneity of the samples. To determine if there is any change in the crystal symmetry or crystallographic features at low temperatures, the XRD measurements

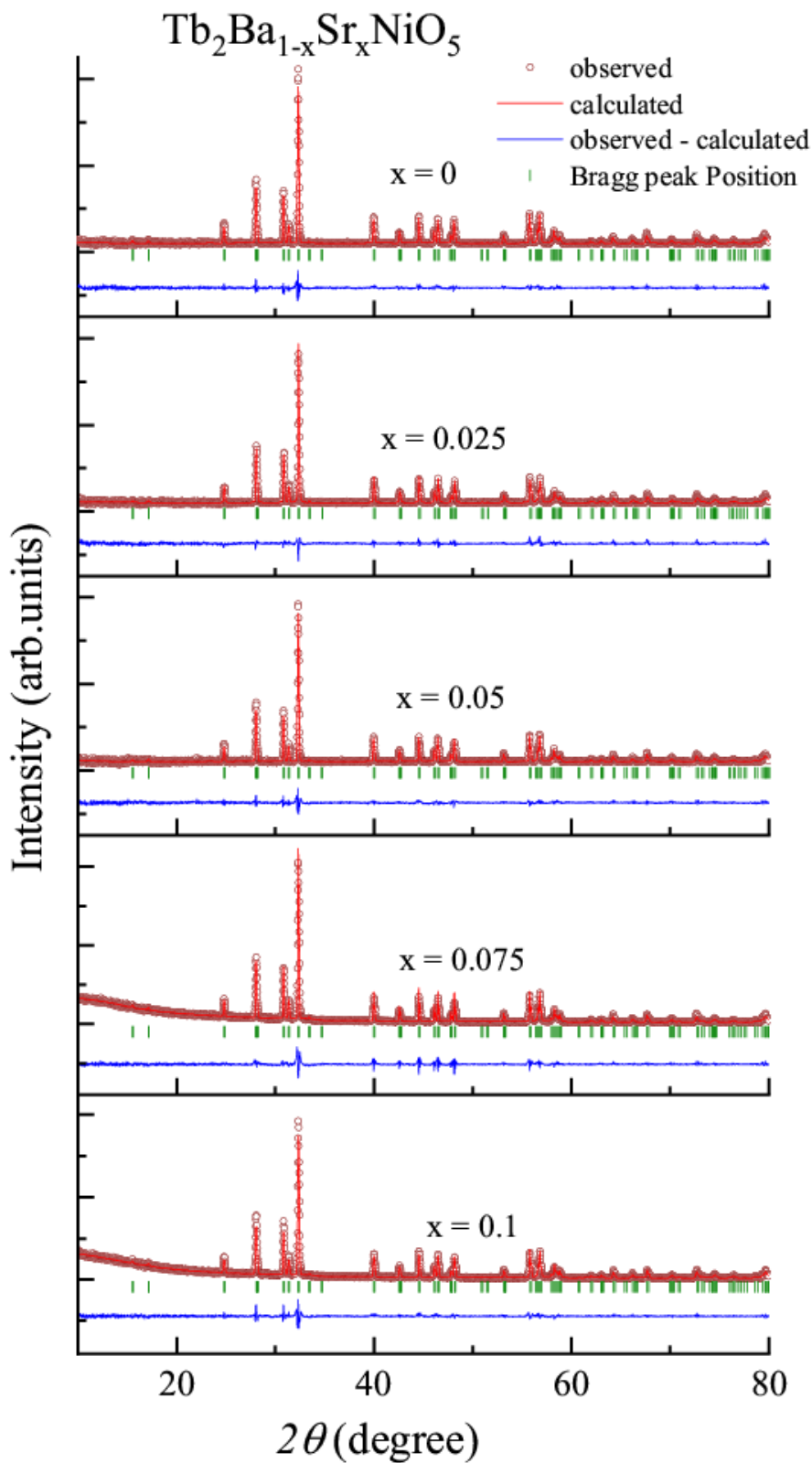


Figure 5.2a: Rietveld refined powder x-ray diffraction patterns for parent and Sr doped $\text{Tb}_2\text{BaNiO}_5$ using $\text{Cu K}\alpha$ radiation.

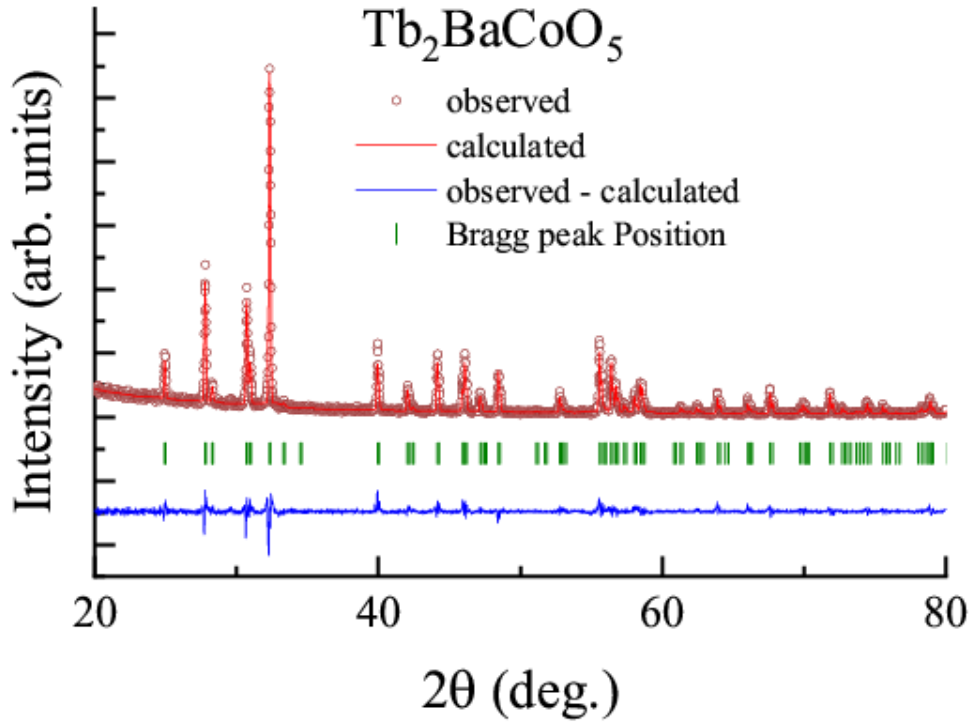


Figure 5.2b: Rietveld refined powder x-ray diffraction patterns for Tb_2BaCoO_5 using $Cu K_\alpha$ radiation.

Table 5.1: Rietveld refined fitting parameters for $Tb_2Ba_{1-x}Sr_xNiO_5$ and Tb_2BaCoO_5 .

Composition	a (Å)	b (Å)	c (Å)	R_{exp}	χ^2
Tb_2BaNiO_5	3.7799 (5)	5.7989 (8)	11.4108 (18)	18.1	1.216
$Tb_2Ba_{0.975}Sr_{0.025}NiO_5$	3.7792 (6)	5.7982 (9)	11.4099 (15)	19	1.052
$Tb_2Ba_{0.95}Sr_{0.05}NiO_5$	3.7785 (4)	5.7969 (8)	11.4083 (19)	18.8	1.224
$Tb_2Ba_{0.925}Sr_{0.075}NiO_5$	3.7772 (6)	5.7962 (10)	11.4067 (21)	15.1	2.398
$Tb_2Ba_{0.9}Sr_{0.1}NiO_5$	3.7766 (7)	5.7941 (10)	11.4058 (21)	16.3	2.383
Tb_2BaCoO_5	3.7546(4)	5.8220 (6)	11.5529 (12)	17.6	1.451

of $\text{Tb}_2\text{BaNiO}_5$, $\text{Tb}_2\text{Ba}_{0.9}\text{Sr}_{0.1}\text{NiO}_5$ and $\text{Tb}_2\text{BaCoO}_5$ was carried out down to 2 K, on Indian beamline, BL-18B at High Energy Accelerator Research Organization (KEK)-Photon Factory, Japan, using x-ray radiation with wavelength 0.883 Å. The beamline energy was $E = 14.02$ keV, and it was calibrated using LaB_6 standard.

Study of the effects of external pressures on the magnetic properties of the parent samples were done under high pressure (0.3, 0.6, and 1 GPa) in a hydrostatic pressure medium employing a commercial high-pressure cell procured from Easy-Lab Technologies Ltd, U.K. Application of pressure on the sample was done at room temperature and the calibration of pressure on the sample was done by measuring the shift in the superconducting transition temperature of Sn in the low temperature range. Temperature dependent χ behavior (1.8 K -300 K), in a field of 5 kOe and 100 Oe, was tracked for all the samples under ambient pressure conditions, while the magnetic properties of the stoichiometric compounds $\text{Tb}_2\text{BaNiO}_5$ and $\text{Tb}_2\text{BaCoO}_5$ were done in both ambient and under applied external hydrostatic pressures.

5.4 Magnetic susceptibility under external pressure.

5.4.1 $\text{Tb}_2\text{BaNiO}_5$

We first discuss the influence of pressure on the magnetism of $\text{Tb}_2\text{BaNiO}_5$. Figures 5.3 and 5.4 show the results of magnetic susceptibility as a function of temperature measured in a field of 5 kOe and 100 Oe respectively for $\text{Tb}_2\text{BaNiO}_5$. The data was collected in both low and high fields to ensure that the trends are reliable and to ensure that any change in the field induced magnetism are not missed out. For sake of clarity of the features, the curves have been shifted marginally upwards, as the overlap of curves tends

to mask the features. In addition, the data is plotted only below 100 K, since there is no feature to be emphasized at higher temperatures. Under ambient pressure, the curve follows the trend that has been reported in literature [18]. That is, there is a Curie- Weiss behavior as the temperature is lowered from 300 K, and a kink at 63 K representing the onset of antiferromagnetic transition. This transition is established by a distinct anomaly in the heat capacity data reported earlier [18]. There is a broad peak in $\chi(T)$ around 40 K, which has been attributed to the persistence of Haldane gap due to Ni one-dimensional magnetism in the magnetically ordered state [15]. Since the kink at T_{N1} is very weak, to get a clear picture of the changes in the properties under applied pressure, the derivative plot of the data is shown in figure 5.3 (b) and 5.4 (b) for respective applied magnetic fields. Careful measurements were done to track the changes seen in susceptibility under applied pressures to track this weak feature. It can be inferred from figures 5.3 (b) and 5.4 (b) that T_{N1} tends to shift to higher temperatures gradually with increasing applied pressures. e.g. for an applied pressure of 10 kBar, T_{N1} shifts by about 2 K from 63 K (ambient pressure) to 65 K. However, In the case of T_{N2} it is not very straightforward to infer the shift in the susceptibility from the plot of $\chi(T)$, because below the peak, the fall in susceptibility, arising due to the magnetic gap, is rather steep. Therefore, in this region, the derivative curves have been used to infer the trend of change in features. In these plots there is a sudden increase in the slope around 25 K under ambient pressure condition, and this characteristic temperature shifts downward marginally, however small it may be, as the pressure is increased to 10 kbar (about 0.5 K for $P = 10$ kbar). Thus, external pressure acts in the opposite way at these two magnetic features.

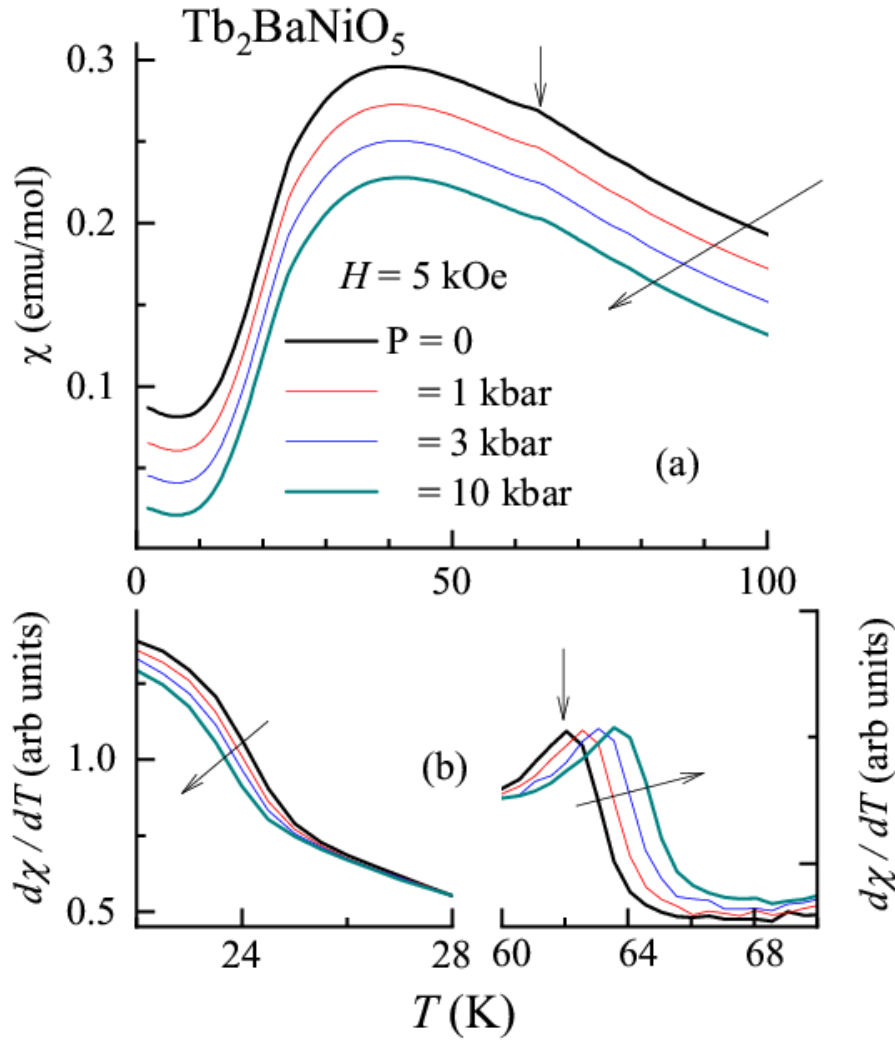


Figure 5.3: For Tb_2BaNiO_5 a) magnetic susceptibility measured as a function of temperature for ambient and external pressure conditions in a field of 5 kOe. b) The derivative plots around the two transition temperatures. Vertical arrows represent T_N . Other arrows are drawn to identify the curves with increasing external pressures.

The applied pressure did not have any effect on the effective magnetic moment within experimental error, obtained from the Curie-Weiss region above 100 K, in the 5 kOe data. The values of the effective magnetic moment for ambient pressure and applied pressures came out to be around $9.63 \mu_B/Tb$ in good agreement with the theoretically expected value of $9.72 \mu_B$ for trivalent Tb ion. The paramagnetic Curie temperature ($\theta_p = -20 \pm 1K$) was also found to be insensitive to the applied external pressure. Looking at the

susceptibility data, it is also obvious, that there are no additional changes in the features under applied pressure, thereby establishing that the external pressure up to 10 kbar does not have any effect on the Haldane gap.

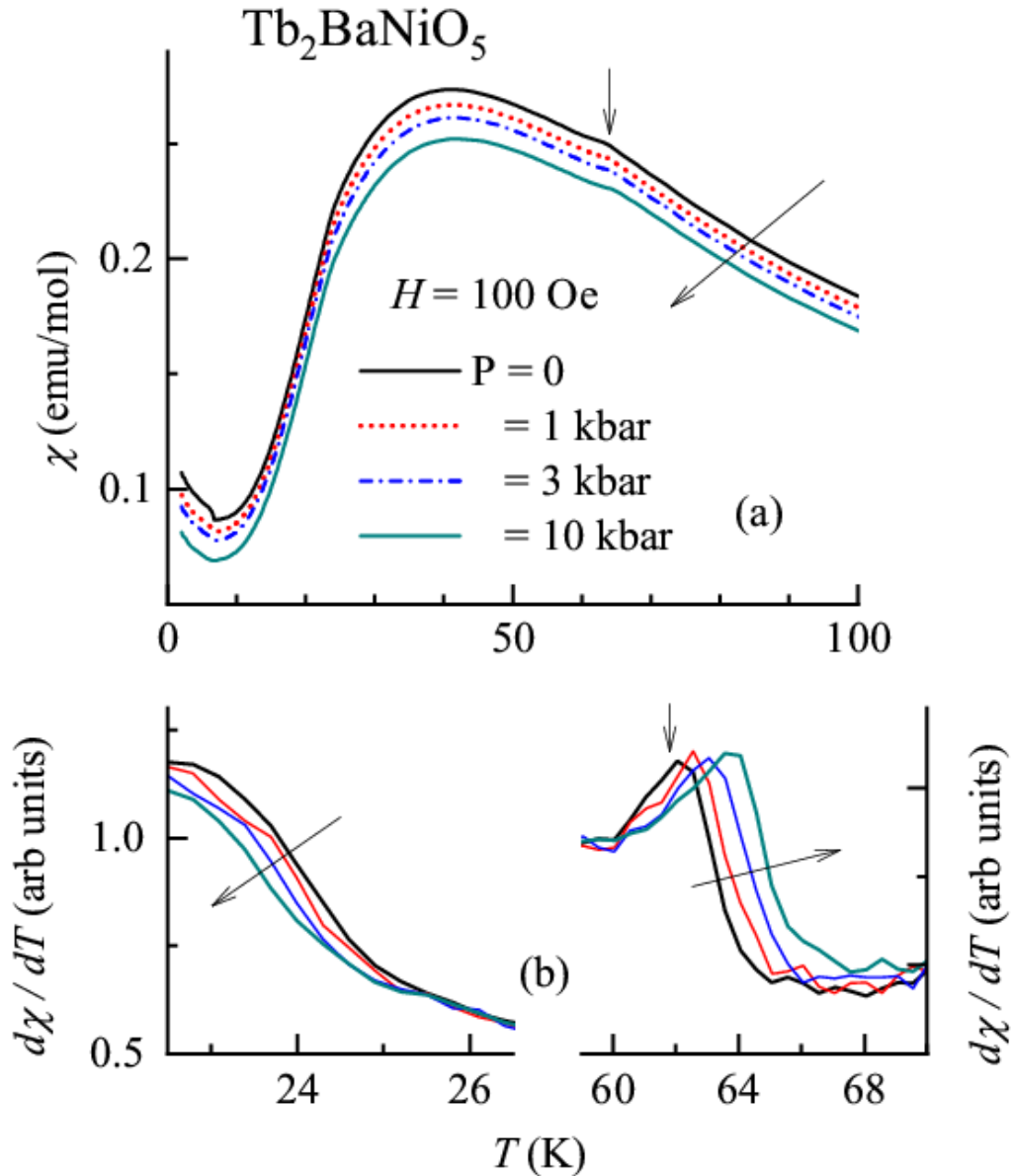


Figure 5.4: For $\text{Tb}_2\text{BaNiO}_5$ a) magnetic susceptibility measured as a function of temperature for ambient and applied external pressures in a field of 100 Oe. b) The derivative plots around the two transition temperatures. Vertical arrows represent T_N . Other arrows are drawn to identify the curves with increasing external pressures.

5.4.2 Tb_2BaCoO_5

Now turning to Tb_2BaCoO_5 , figures 5.5 and 5.6 show the results of magnetic susceptibility as a function of temperature below 100 K, in a field of 100 Oe and 5 kOe respectively, both under ambient and applied external pressures. The curves have been shifted marginally downwards, for sake of clarity of the features. Under ambient pressure, Curie-Weiss behavior in the paramagnetic state above 100 K was observed (and hence not shown here). Below 100 K, susceptibility exhibits a monotonous increase below 20 K, with a peak at 18.8 K, which is followed by a steep drop signaling the onset of an antiferromagnetic transition at $(T_{NI}) \sim 18.8$ K. These features are similar to what has been reported earlier in literature [21]. For the sake of clarity of the changes in the magnetic susceptibility features, the derivative plot of the data is shown in figures 5.5 (b) and 5.6 (b) for respective magnetic fields. Features in the plots remain unaffected by the applied external pressures. A careful look into the derivative plots at low temperatures shows the development of additional peak like features around 5 K and 2.5 K, and the origin of these features is unknown.

The values of the effective magnetic moment, obtained from the Curie-Weiss region above 100 K, for the 5 kOe data remains unaffected by increasing applied pressures. These values of the effective magnetic moments derived from the Curie-Weiss region, for ambient and applied pressures comes out to be around $9.78 \mu_B/Tb$ which is very close to the theoretical value. The paramagnetic Curie temperature ($\theta_p = -24 \pm 1K$) was also found to be insensitive to the applied external pressure.

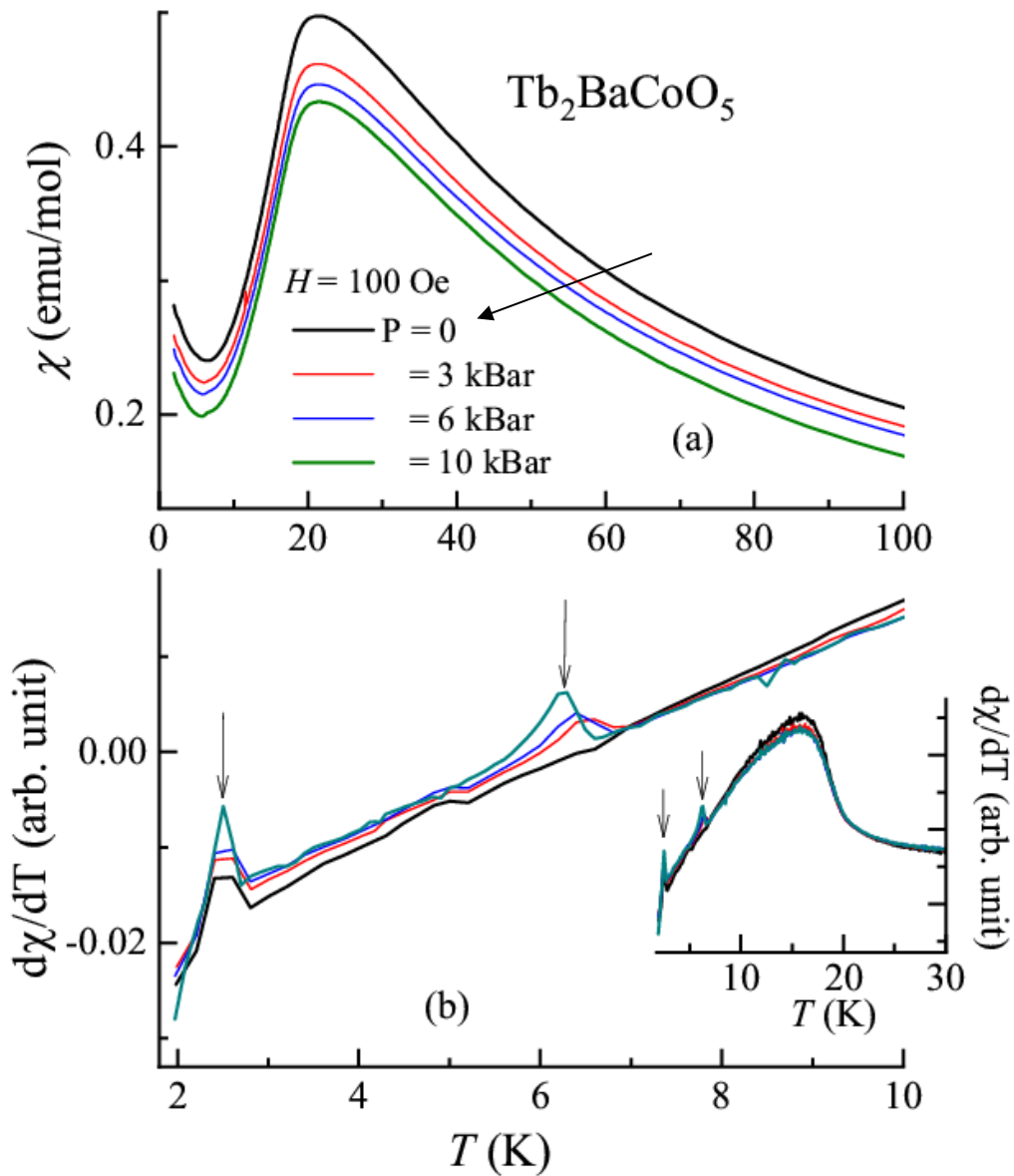


Figure 5.5: a) Magnetic susceptibility measured as a function of temperature for ambient and applied external pressures in a field of 100 Oe. b) expanded region of the derivative plots below 10 K; inset derivative plots plotted till 30 K. Vertical arrows mark additional magnetic feature, slanted arrow represents how the curves move under increasing pressures.

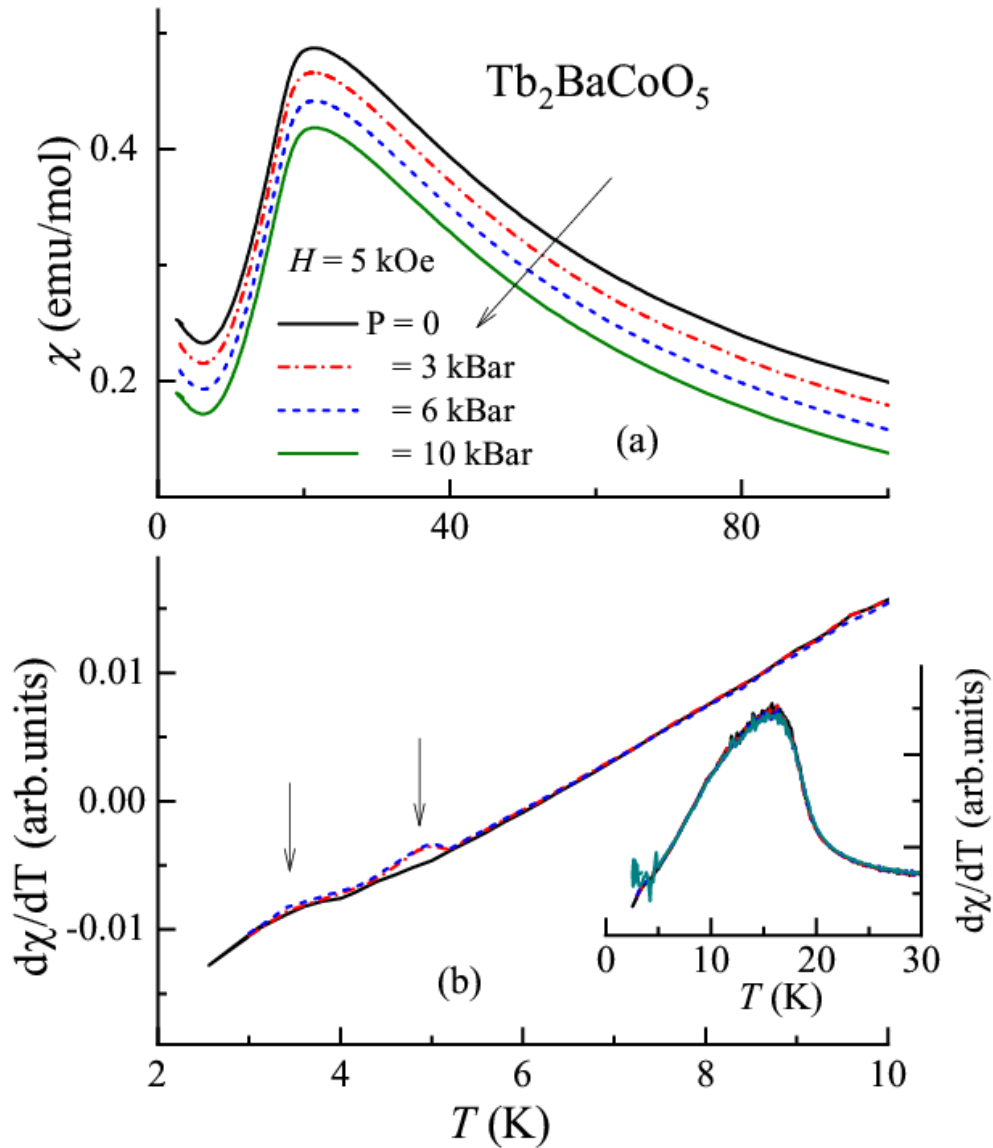


Figure 5.6: a) Magnetic susceptibility measured as a function of temperature for ambient and applied external pressures in a field of 5 kOe. b) Derivative plots below 10 K; inset derivative plots plotted till 30 K. Vertical arrows mark additional magnetic feature, slanted arrow represents how the curves move under increasing pressures.

5.4.3 Magnetic susceptibility under chemical pressure by partial doping of Sr at the Ba Site in $\text{Tb}_2\text{BaNiO}_5$: $\text{Tb}_2\text{Ba}_{1-x}\text{Sr}_x\text{NiO}_5$ ($x = 0, 0.025, 0.05, 0.075$ and 0.1)

It is needless to state that Sr^{2+} is smaller in size compared to Ba^{2+} . Therefore, to study positive chemical pressure effects, the family of $\text{Tb}_2\text{Ba}_{1-x}\text{Sr}_x\text{NiO}_5$ is ideal. We report here

our results for ($x = 0, 0.025, 0.05, 0.075$ and 0.1). The magnetic susceptibility of these compositions in an applied magnetic field of 100 Oe and 5 kOe is plotted in figure 5.7 and figure 5.8 respectively to learn the features as a function of T qualitatively. In an earlier report [32] on higher Sr substitutions in this compound, it was shown that there was an abrupt change in the features and composition, beyond $x = 0.2$. In order to avoid the changes in properties arising from these abrupt changes, the present studies are restricted to compositions till $x = 0.1$ only. We found that the ferroelectricity is destroyed for a composition of $x = 0.15$, that is till $x = 0.1$ composition, ferroelectric features still persist. There appears to be sample dependence with respect to the composition where ferroelectricity vanishes ($x = 0.1$ to 0.15), depending upon the preparative conditions. Therefore, we restrict our discussions on the trends of magnetic susceptibility for compositions till $x = 0.1$ only. Looking at the figures 5.7 and 5.8, it is quite evident that the magnetic feature at the transition temperature T_{N1} shows a gradual downward shift with increasing Sr concentration, and this shift is clear even for a small doping concentration of $x = 0.025$. The magnetic features show a shift of around 5 K from $x = 0$ to $x = 0.1$ composition. Qualitatively speaking, it is quite evident, from the observed trend in the features, that the chemical pressure has a different effect on the magnetic transition at T_{N1} when compared with the effect of external applied pressures. Now, to infer the effect of chemical pressure on the magnetic transition at T_{N2} , one has to rely on the change of slope seen in the derivative plots (see figures 5.7 (b) and 5.8 (b)), in the vicinity of 25 K. The derivative plots show that the sudden increase in the slope, seen in the case of parent compound at 25 K, exhibits a gradual shift towards low temperature range, as the Sr

concentration is increased to $x = 0.1$, which is a signature of corresponding lowering of T_{N2} .

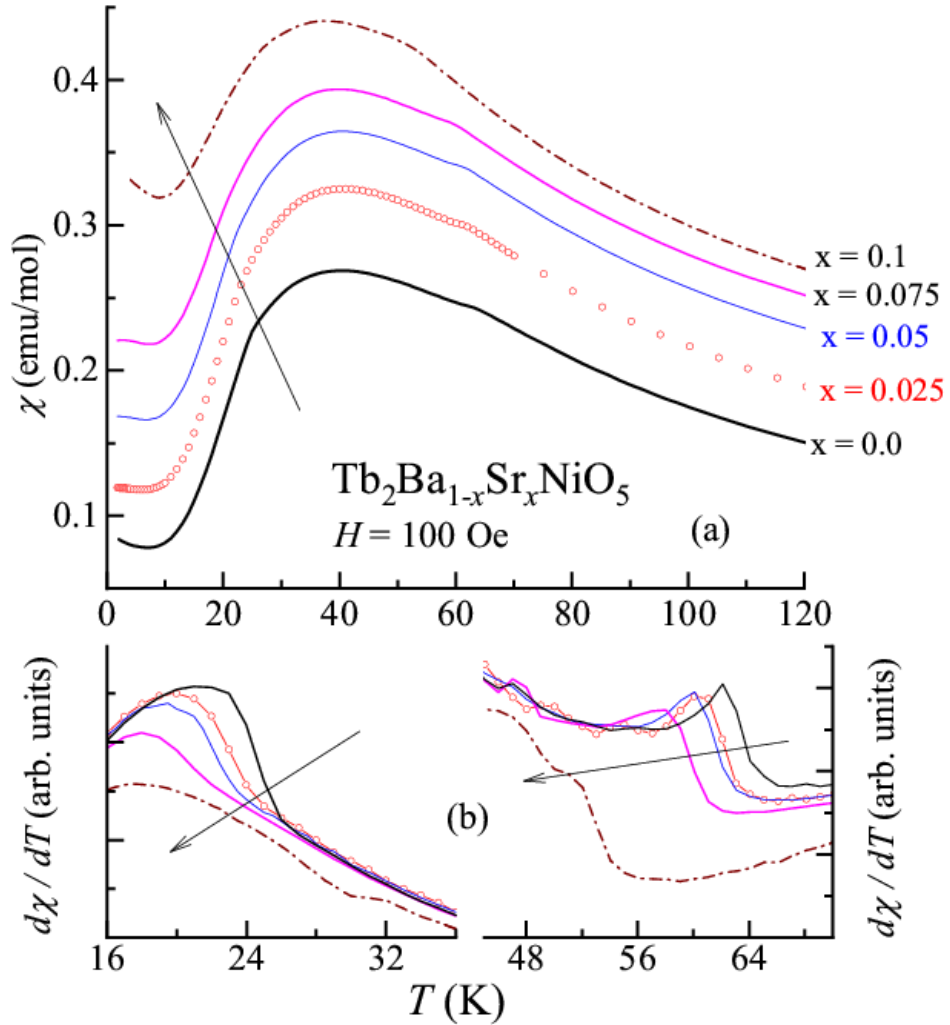


Figure 5.7: a) Magnetic susceptibility measured as a function of temperature for Sr based samples in a field of 100 Oe. b) Derivative curves are shown in an expanded form in the vicinity of the two magnetic transitions.

Thus, the chemical pressure tends to decrease both the transition temperatures T_{N1} and T_{N2} , due to the pressure exerted on the Ba layer. This observation is in contrast to the pressure effects seen under the influence of external pressures. Thus, the results indicate that T_{N1} is sensitive to changes in local hybridization due to doping.

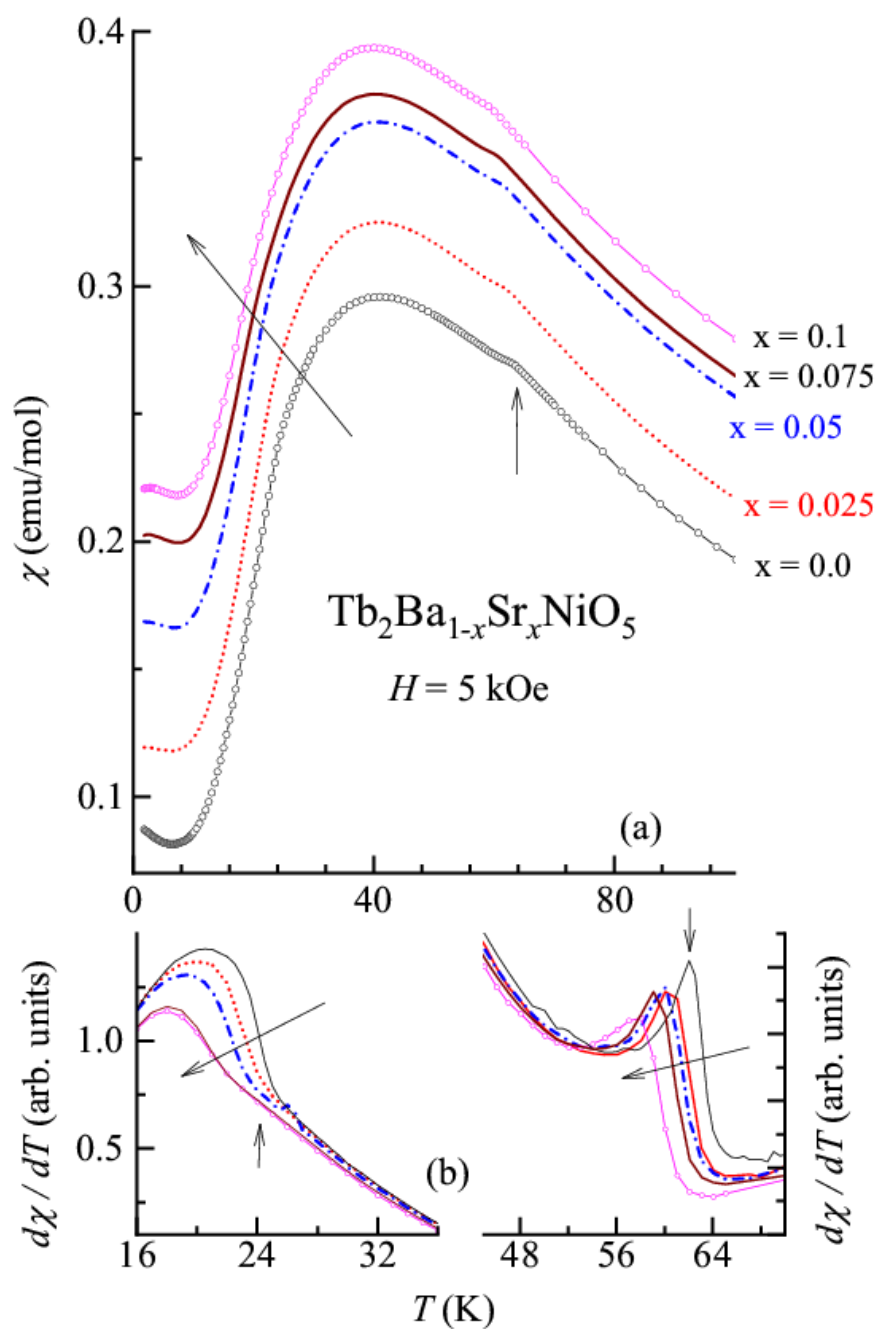


Figure 5.8: a) Magnetic susceptibility measured as a function of temperature for Sr based samples in a field of 5 kOe. b) Derivative curves shown in expanded form in the vicinity of the two magnetic transitions.

The three lattice parameters (see table 5.1) a , b , and c , undergo a weak reduction (in the third decimal place only) and there is an overall reduction in the unit-cell volume

by about 0.6 \AA^3 ($\sim 0.24\%$) as composition of Sr increases from $x = 0$ to $x = 0.1$, thereby suggesting the observed shift in magnetic features arises from chemical pressure effects. Since the bulk modulus of the parent compound is not known, it is difficult to quantify the pressure exerted by this change in the unit-cell volume.

These findings can be compared with the data reported on the effects of chemical pressures induced by the substitution of Y on the Tb sublattice i.e. on $\text{Tb}_{2-x}\text{Y}_x\text{BaNiO}_5$, reported in Ref 30. In this series, the magnitude of reduction of the unit-cell volume for $x = 0.5$ is comparable to the composition of $x = 0.2$ in the Sr-doped series. It can be seen that the magnetic features at T_{N1} and T_{N2} show a linearly diminishing trend with increasing x within Y family (as investigated up to a composition of $x = 1.5$). Since the substitution of Y involves dilution of the Tb sublattice, for comparing the changes in the features with Sr-doped series, one has to normalize to the concentration of Tb (i.e., to $2-x$). These normalized values are found to be about 73 K and 27 K respectively. This trend is similar to the upward shift of T_{N1} , seen in the case of external applied pressures. However, if we assume a linear variation of T_{N1} with pressure, one would need an external applied pressure as large as about 60 kbar to attain a value of 73 K at T_{N1} . In the crystal structure, the vertex-shared (compressed) octahedra of NiO_6 chains are separated by Tb and Ba polyhedra. Therefore, the super-super exchange mechanism of the types $\text{Ni}^{2+}\text{-O}^2\text{-R}^{3+}\text{-O}^2\text{-Ni}^{2+}$ and $\text{Ni}^{2+}\text{-O}^2\text{-Ba}^{2+}\text{-O}^2\text{-Ni}^{2+}$ control magnetic ordering. A dilution of R sublattice (by Y) has of course a natural destructive influence on the transition temperatures. But the fact that this dilution causes a large increase in the scaled- T_{N1} (instead of attaining a constant value) implies that the superexchange pathway via R^{3+} is predominant, getting further stronger with the lattice pressure. If Sr is replaced by Ba (that is, in the solid solutions, under study),

T_{NI} does not track the external pressure effect. Therefore, it is concluded that the superexchange path involving Ba opposes the one caused by pressure. The behavior of normalized T_{N2} however is different in the sense that, the increasing trend with Y-induced chemical pressure in the Tb sublattice is opposite to that observed by external pressure or Sr-doping. We attribute it to the changes in bonding strengths caused by isoelectronic substitution which bear a profound effect on the properties.

5.5 Isothermal magnetization behavior under pressure.

The compound, Tb_2BaNiO_5 , has been reported to undergo a metamagnetic transition near (H_C) 60 kOe and this field value is a bit T dependent [32]; corresponding value of Tb_2BaCoO_5 is about 50 kOe. In order to understand the effects of external applied pressure and the chemical pressure on the metamagnetic transition fields, we have measured the isothermal magnetization for these compounds in the magnetically ordered state.

5.5.1 Tb_2BaNiO_5

The results for Tb_2BaNiO_5 are shown in figure 5.9. The data was collected at various temperatures upto 20 K for all the applied pressures. Since the features are similar for all measured temperatures, the results for 5 K only are shown. A full range profile (0 to 160 kOe) for the magnetization measured at 5 K in ambient pressure conditions (figure 5.9 (b)) is similar to that reported earlier in the literature [16, 18, 19]. Magnetization shows a weak hysteresis around H_c . The magnetization plots of the virgin state in the vicinity of the field-induced transition, are shown in figure 5.9 (a). The metamagnetic transition seen around 60 kOe, under ambient pressures shows a marginal shift to higher magnetic fields as the external applied pressure is increased.

5.5.2 Tb_2BaNiO_5

The results for Tb_2BaCoO_5 are shown in figure 5.10 measured under applied external pressures. The results for 4 K data are shown, expanding the vicinity of the metamagnetic

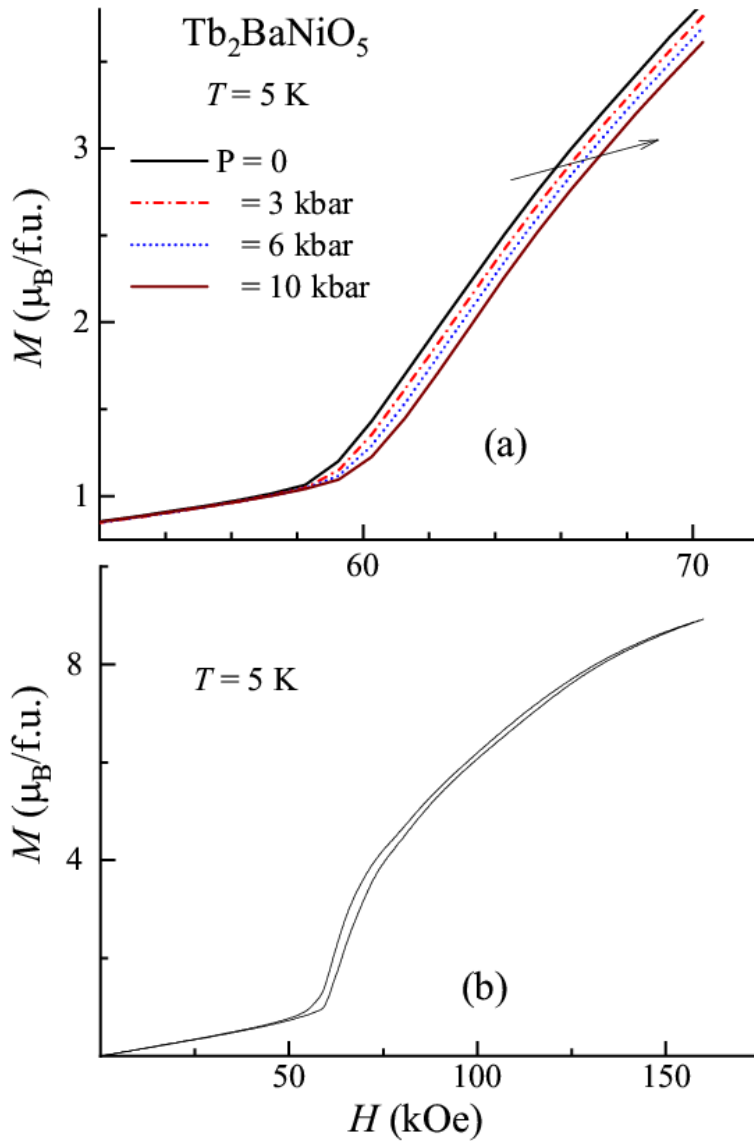


Figure 5.9: (a) Isothermal magnetization at 5 K for Tb_2BaNiO_5 under external applied pressure in the range 0-70 kOe (b) Profile of the curve in the range 0-160 kOe measured under ambient pressure up to 160 kOe.

transition for clarity of the trends. The profile at 2 K for the ambient pressure conditions as in [21] can be seen in figure 5.10 (b).

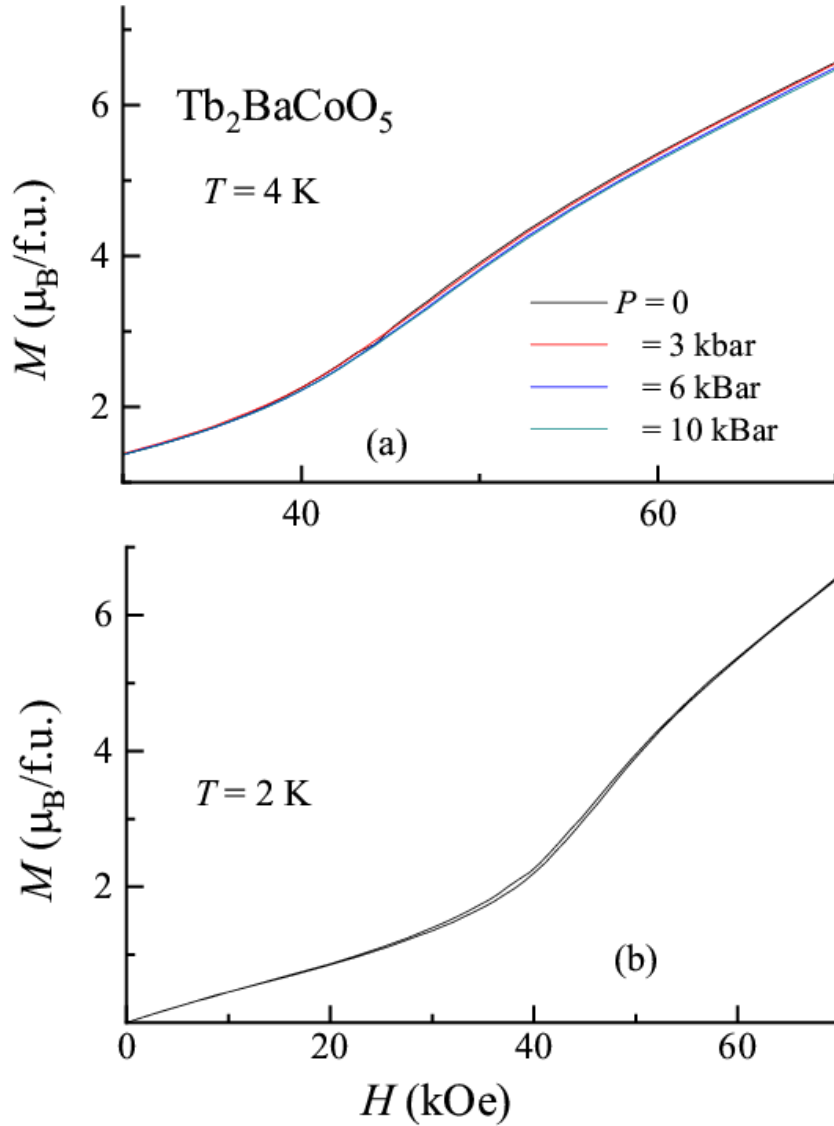


Figure 5.10: (a) Isothermal magnetization at 4 K for $\text{Tb}_2\text{BaCoO}_5$ under external applied pressure expanded around the metamagnetic transition region (b) Profile of the curve in the range 0-70 kOe measured under ambient pressure at 2 K.

There is an upturn around 40 kOe in the magnetization under ambient pressures due to the existence of a metamagnetic transition. In the case of $\text{Tb}_2\text{BaCoO}_5$ the external pressure does not have any effect on the magnetization features or the field induced

metamagnetic transition in this compound, which is interestingly different from what is seen for the Tb_2BaNiO_5 . The origin of this difference is not clear.

5.5.3 Isothermal magnetization under chemical pressure by partial doping of Sr at the Ba Site in Tb_2BaNiO_5 : $Tb_2Ba_{1-x}Sr_xNiO_5$ ($x= 0, 0.025, 0.05, 0.075$ and 0.1)

The isothermal magnetization for all the Sr-doped compositions have also been measured at various temperatures to infer chemical pressure effects on H_c . For the sake of comparison, the data measured at 5 K are plotted together for all the doped composition and shown in figure 5.11. For clarity of the changes in features, the graphs have been expanded around the metamagnetic transition and only the virgin curves in the upward field cycle have been shown in figure 5.11 (a). In addition, the data up to 120 kOe measured under ambient pressure conditions is shown for the $x= 0.1$ composition in figure 5.11b. It is clearly seen from the graph in figure 5.11 (b) that the field induced metamagnetic transition features persist for all composition suggesting that Sr-doping has not drastically changed the field induced magnetization properties. However, the magnetization curves around H_c shows slight broadening as the Sr-doping is increased, attributable to increasing chemical disorder.

It is straightforward to conclude that H_c gets depressed with increasing Sr doping, which is opposite to what is seen from the effects of external applied pressure discussed above. Y substitution has been shown [31] to depresses the H_c . Thus, looking together all these data we conclude that, as far as H_c is concerned, one cannot find any correlation with chemical and external pressure data. We attribute it to the electronic structure changes

caused by substitutions at any site has a dominating effect on the properties of this compound.

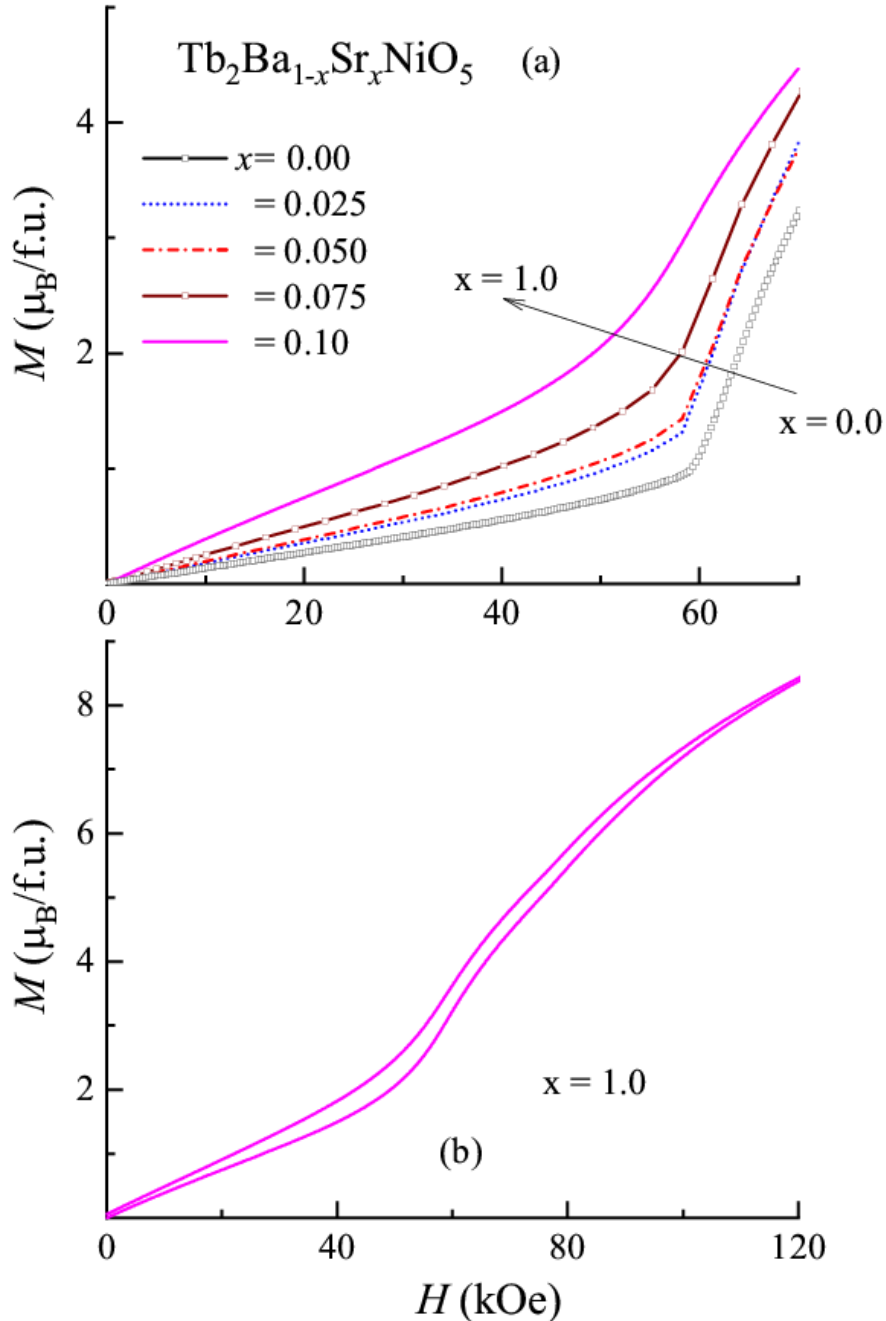


Figure 5.11: (a) Isothermal magnetization at 5 K for the Sr doped specimens. Inclined arrows are shown the direction in which the curves shift with increasing chemical pressure/composition. (b) Profile of the curve in the range 0-120 kOe for $x=0.1$ composition, at 5 K, to show the existence of field induced metamagnetic transition in MH measured under ambient pressure conditions.

5.6: Temperature dependent x-ray diffraction behavior.

In order to ascertain that the changes seen on the magnetic properties of this compound in response to the external pressures, do not arise from any crystallographic changes, the low temperature powder XRD measurements were carried out at the synchrotron facility, BL-14 at KEK-Japan down to 2 K. The results on the two stoichiometric compounds and on one Sr-doped sample ($x = 0.1$) are shown in figure 5.12, at selected temperatures in the three temperature ranges, $T < T_{N2}$, $T_{N2} < T < T_{N1}$, and $T > T_{N1}$. XRD patterns do not reveal any kind of changes in the crystallographic symmetry, down to 2 K (barring a preferred orientation effect for a few Bragg peaks).

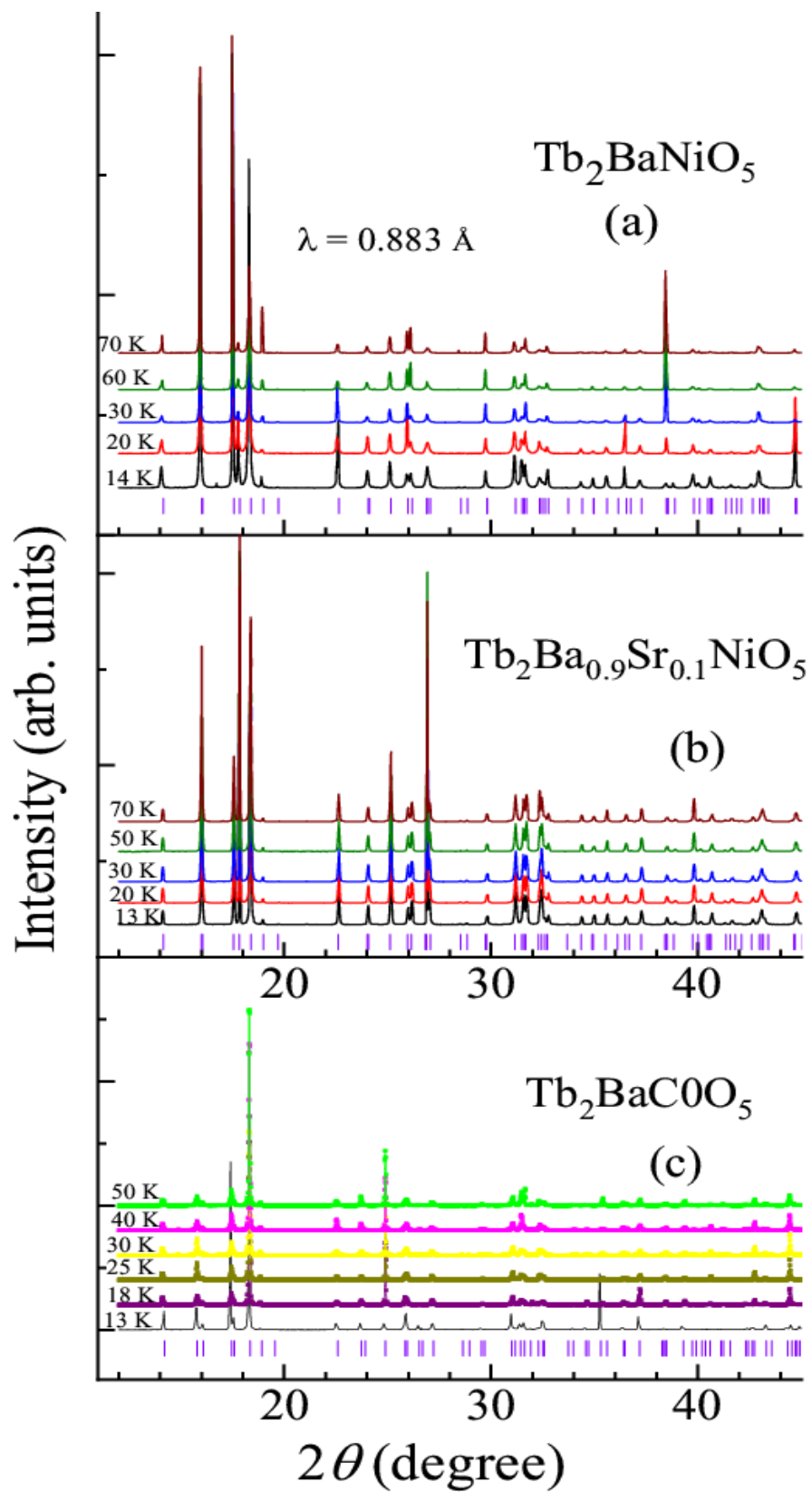


Figure 5.11: (a) Synchrotron based powder x-ray diffraction (S-PXRD) patterns of selected temperatures for $\text{Tb}_2\text{BaNiO}_5$, b) $\text{Tb}_2\text{Ba}_{0.9}\text{Sr}_{0.1}\text{NiO}_5$ and c) $\text{Tb}_2\text{BaCoO}_5$

5.7 Discussion and conclusions

High pressure magnetization studies have been performed on the exotic multiferroic compounds, $\text{Tb}_2\text{BaNiO}_5$ and $\text{Tb}_2\text{BaCoO}_5$ with the maximum external hydrostatic pressure applied being 10 kbar. In addition, the effects of chemical pressures induced by doping of Sr at the Ba site in $\text{Tb}_2\text{BaNiO}_5$ have also been probed for comparison. It is known that under ambient pressure conditions, both Tb and Ni/Co moments order at the same temperature (interestingly with the involvement of Tb 4*f* in inducing ferroelectricity, a situation which is not encountered in the case of rare-earth based manganites). Our study shows that the externally applied pressure does not have any effect on the magnetic properties of $\text{Tb}_2\text{BaCoO}_5$, indicating a robust nature of magnetism, in contrast to the opposite effect on the two magnetic transitions (63 K and 25 K) in the case of $\text{Tb}_2\text{BaNiO}_5$. T_{N1} is found to get enhanced to higher temperatures, and T_{N2} , at which multiferroicity sets in, is interestingly depressed to lower temperatures. Such an effect of applied external pressures, on the two magnetic features, at two different temperatures, in a same compound, is quite interesting, because both Tb and Ni have been known to order magnetically at the same temperature. Since there is no change in magnetic symmetry across T_{N2} , one would expect that both the transitions behave in the same way with the application of external pressure. This observation is different from that noted for the Mn sublattice in the well-known type-II multiferroic materials, TbMnO_3 [6, 7] and RMn_2O_5 [8], including the magnetic transition temperature at which ferroelectric transition sets-in in these examples. Therefore, it can be concluded that the local distortions due to ferroelectricity in this compound influences the pressure dependence of corresponding magnetic transition temperature.

In addition, the study of the magnetic properties under the influence of chemical pressures induced by doping of Sr at the Ba site shows a difference in variations of both the magnetic transition temperatures under the influence of chemical pressures. If these results are compared with the reported changes in the magnetic features seen by other isoelectronic substitution at Tb and Ba sites, we conclude that the subtle distortions cause a profound effect on magnetic characteristics of this compound.

Thus, this chapter brings out a case of rare-earth in insulating environment (that is without *RKKY* interaction), in which localized *4f* electrons (as far as magnetization is concerned) behave in a complex fashion to the application of external and chemical pressures.

5.8 Bibliographical references

1. Schmid H. Multi-ferroic magnetoelectrics. *Ferroelectrics*. 1994 Jan 1; 162(1):317-38.
2. Hill NA. Why are there so few magnetic ferroelectrics?. *The journal of physical chemistry B*. 2000 Jul 27; 104(29):6694-709.
3. Wang JB, Neaton JB, Zheng H, Nagarajan V, Ogale SB, Liu B, Viehland D, Vaithyanathan V, Schlom DG, Waghmare UV, Spaldin NA. Epitaxial BiFeO₃ multiferroic thin film heterostructures. *Science*. 2003 Mar 14; 299(5613):1719-22.
4. Kimura T, Goto T, Shintani H, Ishizaka K, Arima TH, Tokura Y. Magnetic control of ferroelectric polarization. *Nature*. 2003 Nov 6; 426(6962):55-8.

5. Hur N, Park S, Sharma PA, Ahn JS, Guha S, Cheong SW. Electric polarization reversal and memory in a multiferroic material induced by magnetic fields. *Nature*. 2004 May 27; 429(6990):392-5.
6. Dong S, Liu JM, Cheong SW, Ren Z. Multiferroic materials and magnetoelectric physics: symmetry, entanglement, excitation, and topology. *Advances in Physics*. 2015 Nov 2; 64(5-6):519-626.
7. Tokura Y, Seki S. Multiferroics with spiral spin orders. *Advanced materials*. 2010 Apr 12; 22(14):1554-65.
8. Rao CN, Sundaresan A, Saha R. Multiferroic and magnetoelectric oxides: the emerging scenario. *The journal of physical chemistry letters*. 2012 Aug 16; 3(16):2237-46.

Tokura Y, Seki S, Nagaosa N. Multiferroics of spin origin. *Reports on Progress in Physics*. 2014 Jul 3; 77(7):076501.

Dong S, Liu JM, Cheong SW, Ren Z. Multiferroic materials and magnetoelectric physics: symmetry, entanglement, excitation, and topology. *Advances in Physics*. 2015 Nov 2; 64(5-6):519-626.
9. Kimura T, Goto T, Shintani H, Ishizaka K, Arima TH, Tokura Y. Magnetic control of ferroelectric polarization. *Nature*. 2003 Nov 6; 426(6962):55-8.
10. Yamasaki Y, Miyasaka S, Kaneko Y, He JP, Arima T, Tokura Y. Magnetic reversal of the ferroelectric polarization in a multiferroic spinel oxide. *Physical review letters*. 2006 May 26; 96(20):207204.

11. Lawes G, Harris AB, Kimura T, Rogado N, Cava RJ, Aharony A, Entin-Wohlman O, Yildirim T, Kenzelmann M, Broholm C, Ramirez AP. Magnetically driven ferroelectric order in $\text{Ni}_3\text{V}_2\text{O}_8$. *Physical review letters*. 2005 Aug 19; 95(8):087205.
Kimura T, Lashley JC, Ramirez AP. Inversion-symmetry breaking in the noncollinear magnetic phase of the triangular-lattice antiferromagnet CuFeO_2 . *Physical Review B*. 2006 Jun 12; 73(22):220401.
12. Choi YJ, Yi HT, Lee S, Huang Q, Kiryukhin V, Cheong SW. Ferroelectricity in an Ising chain magnet. *Physical review letters*. 2008 Jan 29; 100(4):047601.
Naito Y, Sato K, Yasui Y, Kobayashi Y, Kobayashi Y, Sato M. Ferroelectric transition induced by the incommensurate magnetic ordering in LiCuVO_4 . *Journal of the Physical Society of Japan*. 2007 Feb 13; 76(2):023708.
13. Schollwöck U, Richter J, Farnell DJ, Bishop RF, editors. *Quantum magnetism*. Springer; 2008 May 14.
14. Haldane FD. Continuum dynamics of the 1-D Heisenberg antiferromagnet: Identification with the $O(3)$ nonlinear sigma model. *Physics letters a*. 1983 Feb 14; 93(9):464-8.
15. Singh K, Basu T, Chowki S, Mahapatra N, Iyer KK, Paulose PL, Sampathkumaran EV. Magnetoelectric coupling in the Haldane spin-chain system $\text{Dy}_2\text{BaNiO}_5$. *Physical Review B*. 2013 Sep 27;88(9):094438.
16. Basu T, Paulose PL, Iyer KK, Singh K, Mohapatra N, Chowki S, Gonde B, Sampathkumaran EV. A reentrant phenomenon in magnetic and dielectric properties of $\text{Dy}_2\text{BaNiO}_5$ and an intriguing influence of external magnetic field. *Journal of Physics: Condensed Matter*. 2014 Apr 11; 26(17):172202.

17. Basu T, Singh K, Mohapatra N, Sampathkumaran EV. Magnetic and dielectric behavior of the spin-chain compound $\text{Er}_2\text{BaNiO}_5$ well below its Néel temperature. *Journal of Applied Physics*. 2014 Sep 21; 116(11).
18. Upadhyay SK, Paulose PL, Sampathkumaran EV. Extraordinarily large intrinsic magnetodielectric coupling of the Tb member within the Haldane spin-chain family R_2BaNiO_5 . *Physical Review B*. 2017 Jul 14; 96(1):014418.
19. Garcia-Matres E, Martinez JL, Rodríguez-Carvajal J. Neutron diffraction study of the magnetic ordering in the series R_2BaNiO_5 (R= Rare Earth). *The European Physical Journal B-Condensed Matter and Complex Systems*. 2001 Nov; 24:59-70.
20. Kumar R, Rayaprol S, Rajput S, Maitra T, Adroja DT, Iyer KK, Upadhyay SK, Sampathkumaran EV. Existence of a critical canting angle of magnetic moments to induce multiferroicity in the Haldane spin-chain system $\text{Tb}_2\text{BaNiO}_5$. *Physical Review B*. 2019 Mar 29; 99(10):100406.
21. Upadhyay SK, Sampathkumaran EV. Multiferroicity in a spin-chain compound, $\text{Tb}_2\text{BaCoO}_5$, with exceptionally large magnetodielectric coupling in polycrystalline form. *Applied Physics Letters*. 2018 Jun 25; 112(26).
22. Ram Kumar, S. Rajput, T. Maitra, A. Hoser, S. Rayaprol, Sanjay K. Upadhyay, K.K. Iyer, K. Maiti, E.V. Sampathkumaran, *Journal of Alloys and Compounds*, **862**, 158514, (2021).
23. Kimura H, Nishihata K, Noda Y, Aso N, Matsubayashi K, Uwatoko Y, Fujiwara T. Pressure-induced commensurate magnetic order in multiferroic HoMn_2O_5 . *Journal of the Physical Society of Japan*. 2008 Jun 15; 77(6):063704-.

24. Aoyama T, Miyake A, Kagayama T, Shimizu K, Kimura T. Pressure effects on the magnetoelectric properties of a multiferroic triangular-lattice antiferromagnet CuCrO_2 . *Physical Review B*. 2013 Mar 4; 87(9):094401.
25. Aoyama T, Iyama A, Shimizu K, Kimura T. Multiferroicity in orthorhombic RMnO_3 (R=Dy,Tb, and Gd) under high pressure. *Physical Review B*. 2015 Feb 18; 91(8):081107.
26. Deutsch M, Hansen TC, Fernandez-Diaz MT, Forget A, Colson D, Porcher F, Mirebeau I. Pressure-induced commensurate phase with potential giant polarization in YMn_2O_5 . *Physical Review B*. 2015 Aug 21; 92(6):060410.
27. Aoyama T, Yamauchi K, Iyama A, Picozzi S, Shimizu K, Kimura T. Giant spin-driven ferroelectric polarization in TbMnO_3 under high pressure. *Nature communications*. 2014 Sep 12; 5(1):4927.
28. Noriki Terada, Dmitry D. Khalyavin, Pascal Manuel, Toyotaka Osakabe, Akiko Kikkawa, and Hideaki Kitazawa, arXiv1903.01319.
29. C. R. dela Cruz, B. Lorenz, Y. Y. Sun, Y. Wang, S. Park, S-W. Cheong, M. M. Gospodinov, and C. W. Chu, *Phys. Rev. B* **76**, 174106 (2007).
30. Chaudhury RP, Yen F, Dela Cruz CR, Lorenz B, Wang YQ, Sun YY, Chu CW. Pressure-temperature phase diagram of multiferroic $\text{Ni}_3\text{V}_2\text{O}_8$. *Physical Review B*. 2007 Jan 22; 75(1):012407.
31. Sanjay K. Upadhyay and E.V. Sampathkumaran, *J. Appl. Phys.* **125**, 174106 (2019).
32. Sanjay K Upadhyay and E.V. Sampathkumaran, *J. Phys.: Condens. Matter* **31**, 39LT01 (2019).

33. See, for instance, for such studies on MnWO_4 , J. Ruiz-Fuertes, S. Lopez-Moreno, J. Lopez-Solano, D. Errandonea, A. Segura, R. Lacomba-Perales, A. Munoz, S. Radescu, P. Rodriguez-Hernandez, M. Gospodinov, L. L. Nagornaya, and C. Y. Tu, *Phys. Rev. Lett.* **86**, 125202 (2012).
34. M. Castro, R. Burriel, A. Salinas-Sánchez, R. Sáez-Puche, *J. Magn. Magn. Mater.* **104**, 619 (1992).

Chapter 6

Magnetic behavior of nanoform of intermetallic compounds and antimicrobial properties.

6.1 Introduction

In the previous chapters, we brought out certain exotic properties exhibited by compounds containing $4f$ electrons, both in metallic and insulating environments, focusing our studies on the bulk form. It has been known in the literature that the reducing the particle size of any material can induce unusual properties, which can be useful for many technological applications. Therefore, in this chapter, we focus our study on the magnetic and thermal properties of the nanoform specimens of the metallic compounds reported in the previous chapters, namely, R_2RhSi_3 ($R = Nd$ and Er), R_4PtAl ($R = Ho$ and Er) and R_4RhAl ($R = Dy$).

When the particle size is reduced to nanoform (at least in one dimension measuring, 100 nm or less), exotic properties emerge. For example, gold nanoparticles exhibit an optical property, called surface plasmon resonance, in which the nanoparticles give vibrant colors depending on their size, shape, and surrounding medium [1], quantum confinement effects significantly alter the electronic properties of semiconducting nanoparticles [2], enhanced mechanical properties like exceptional strength and flexibility due to unique atomic structure demonstrated for carbon nanotubes and graphene [3], magnetic nanoparticles such as iron oxide nanoparticles exhibit superparamagnetic properties [4], and improved catalytic activity in the case of platinum nanoparticles [5] etc., to name a few.

These nanomaterials can be grown using various approaches, like the top-down approach or the bottom-up approach. In the case of a bottom-up approach, the nanomaterial

is constructed atom by atom or molecule by molecule in which the materials grow due to its self-assembling properties. While in the case of top-down approach the material is derived from a larger size of the material under study. Various techniques have been employed for the synthesis of such nanomaterials, viz, chemical methods like the polyol method, thermal decomposition technique, microemulsions, electrochemical synthesis and physical methods like, pulsed laser deposition, chemical vapour deposition, sono-chemical reduction and ball milling technique.

There has also been an increased focus on these nanomaterials from the application point of view. Some examples of these applications are: in electronic industry, nanomaterials like carbon nanotubes, graphene, and quantum dots are extensively used because of their excellent electrical conductivity, high surface area, and unique electronic properties. These materials have been used for synthesis of transistors, displays, sensors, batteries etc [6,7]. The nanomaterials have also been useful in energy industry where these materials find extensive application in lithium-ion batteries, fuel cells, solar cells, and supercapacitors to improve the efficiency, at the same time reducing the device weight, and enhancing the performance.[8] These materials have been useful for water purification, air filtration, and soil remediation. It has been shown that these materials have been efficient in removal of pollutants, heavy metals, and contaminants from the environment [9]. In petroleum mining and refining industry these materials find usefulness due to their catalytic properties and large surface to volume ratio making their adsorption properties useful in filtration and separation systems [10]. One of the major efforts of nanomaterials research has been on the use of their properties in the field of biotechnology and biomedicine. In the field of biomedicine, some applications are targeted drug delivery, imaging,

diagnostics, and regenerative medicine [11] and for managing multidrug resistant infections [12-19]. Combining the antibiotics with nanoparticles has been shown to increase the antibiotic efficacy as compared to the general antibiotics which are clinically being used [20]. Such a combination is useful in reducing the bacterial resistance development, and helps in reduction of the treatment duration, and antibiotic dose [21]. Platinum-based chemotherapeutics are used widely in majority of cancer treatments [22]. Gold-containing auranofin is an approved drug that is used for the treatment of rheumatoid arthritis and is currently under investigation for its anticancer as well as antimicrobial properties [23-28].

Various synthesis methods have been adopted for producing nanomaterials for biomedicine and biotechnology applications [29]. Natural products are still one of the major sources of new drug molecules, which are derived from prokaryotic bacteria, eukaryotic microorganisms, plants and various animal organisms which occupy a major part of the antimicrobial compounds. Metal complexes to be used as antibiotics have only a niche presence in biomedical field, even though some compounds like cisplatin, have been shown to have profound impact for treatment of cancer. However, metal complexes have been largely been ignored for antibiotic development even when these compounds have access to unique modes of action and exist in a wider range of three-dimensional geometries than purely organic compounds. Such properties offer a scope for the development of new drugs. In the past decade, study in this field has been focused on elements and complexes of titanium, iron, ruthenium, gallium, palladium, silver, gold, bismuth, and copper [30-44]. There is some recent work on bimetallic nanoparticles as well. But to our knowledge till date there has been no work reported on the study of efficacy

of any of the rare-earth based intermetallic compounds, containing both rare earth and transition metal elements.

Some work has been focused recently on understanding the magnetic properties of rare-earth based compounds like, RCO_2 [45-46], RMn_2Ge_2 [47,48], $\text{RCr}_2\text{Si}_2\text{C}$ [49-50], YbAl_3 [51], CeAl_2 , CePt_2 [52, 53], CeRu_2Si_2 [54], etc where the study was aimed at understanding of how the magnetic properties of these compounds get altered when driven to nanoform. One of the important results shown in the field of magnetism was in the case of exchange-enhanced Pauli paramagnets (in bulk form), like YCo_2 , LuCo_2 , and ZrCo_2 , known to undergo itinerant electron meta-magnetism at very high fields (>500 kOe) in the bulk form, were reported to show ferromagnetic behavior at room temperature with reduction in particle size [47-48]. Medical applications are yet to be explored using such magnetic anomalies.

This situation prompted us to study the effects of particle size reduction on the magnetic and thermal properties of the intermetallic compounds studied in the thesis work viz, the families of R_2RhSi_3 ($R = \text{Nd, Er}$), R_4PtAl ($R = \text{Ho, Er}$) and R_4RhAl ($R = \text{Dy}$), obtained by high-energy-ball-milling, and also to probe whether these compounds show any antibacterial or antifungal efficacy. One reason why studies on nanoform of rare-earth intermetallics, for medical applications have not been pursued, could be that there is no method of preparation available to stabilize such compounds in nanoform due to high reactivity of these compounds when driven to nanoform. The reason why we have chosen this route of synthesis (high-energy ball milling) is that it was reported [55] that toluene used as a medium in ball milling forms a protective layer on the surface of the nanoparticle, thus stabilizing the nanoparticles from oxidation or turning pyrophoric.

We discover remarkable changes in the magnetic behavior (with respect to the bulk form) are observed in Dy₄RhAl and hence this chapter focusses on this compound only to demonstrate that one has to be careful while extrapolating magnetic behavior of the bulk form to nanoform in medicinal applications. Since other compounds do not reveal any noteworthy changes, the results are presented in the tabular form in Appendix 6.1 for the sake of brevity.

6.2 Sample preparation, characterization and experimental details.

For preparing the nanoform specimens, bulk samples, 5 gms. each, were synthesized using the arc-melting technique via the procedure specified in chapters 4 and 5 for respective compounds. Before grinding, bulk specimens were checked for stoichiometry and phase formation using XRD and SEM-EDAX analysis.

Once the phase and stoichiometry of these compounds were confirmed, the ingots were powdered using high-energy ball milling technique, a mechanical method well-established by materials engineers to synthesize nano particles [55]. After grinding for 150 minutes at a speed of 500 rpm in toluene medium, the samples were removed and stored under toluene to prevent oxidation (if any). Characterization by XRD, SEM-EDAX and TEM of the ground specimens was carried out to determine the phase and stoichiometry. Comparison of the x-ray diffraction patterns for bulk and nanoform specimens are shown in figures 6.1 and 6.2. SEM and TEM images (showing the diffraction rings on one particle) for Dy₄RhAl has been shown in figure 6.3. The average particle size calculated using Scherrer formula from the XRD patterns showed an average particle size varying in the range of 50 nm to 200 nm for each specimen.

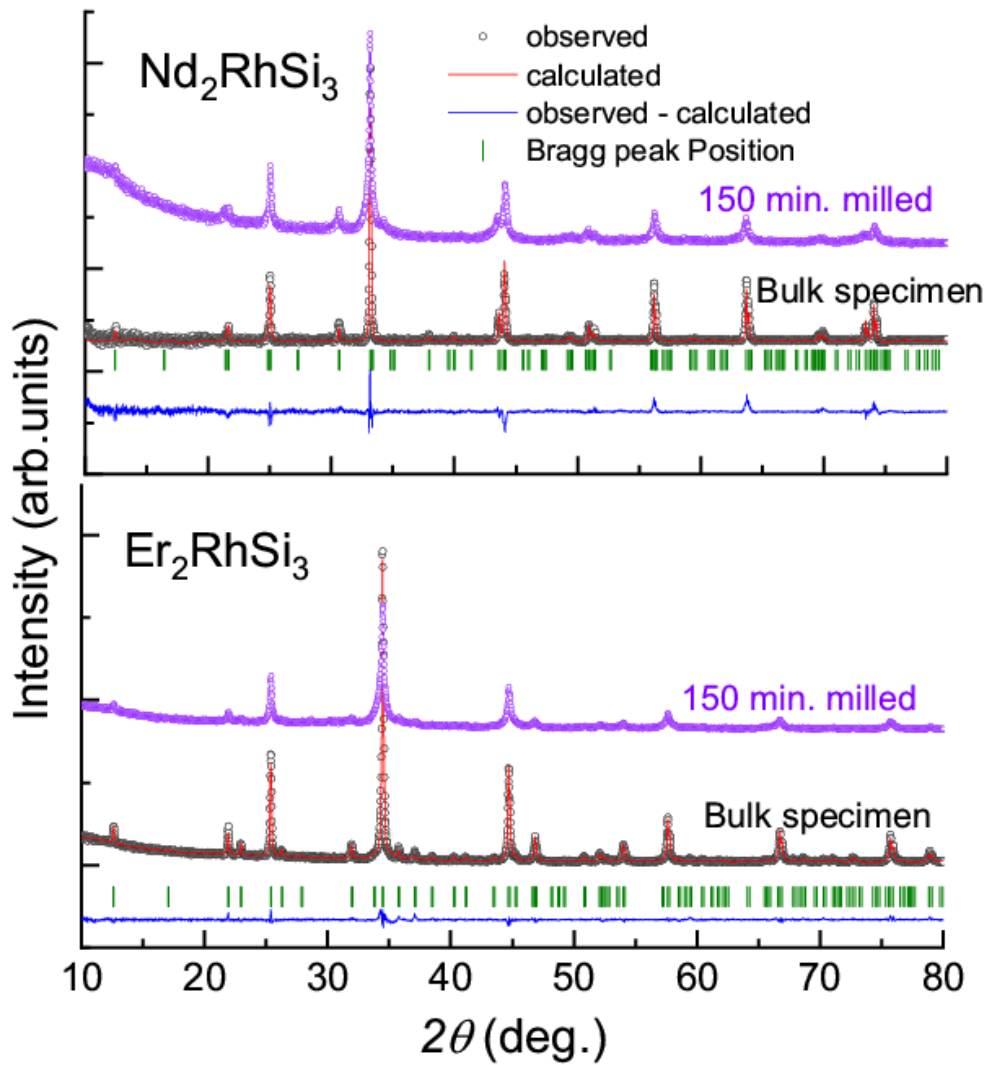


Figure 6.1: Comparison of powder x-ray diffraction patterns of bulk and nanoforms of $R_2\text{RhSi}_3$ using $\text{Cu } K_\alpha$ radiation.

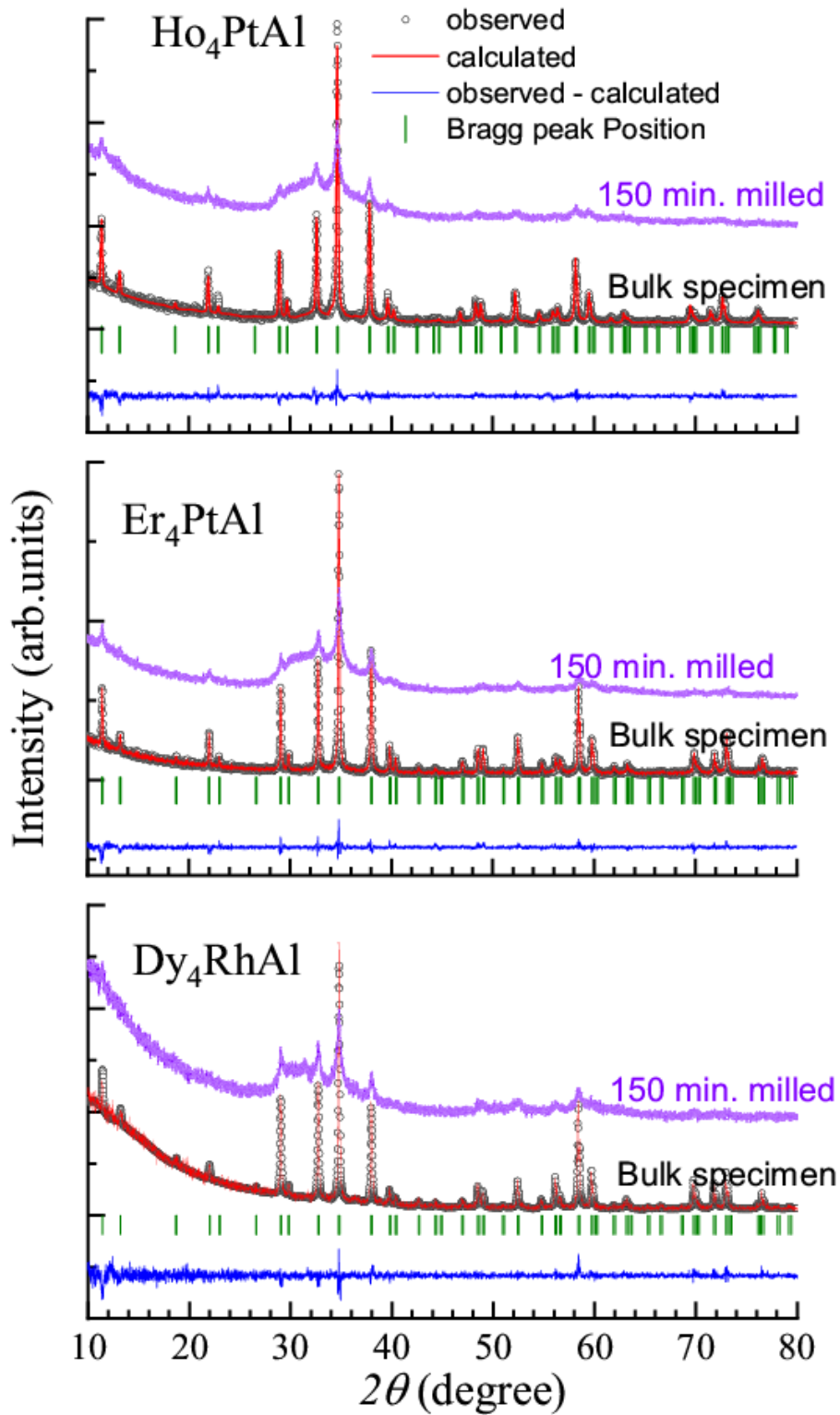


Figure 6.2: Comparison of powder x-ray diffraction patterns of $R_4(TM)Al$ bulk and nanoform specimens using $Cu K_\alpha$ radiation.

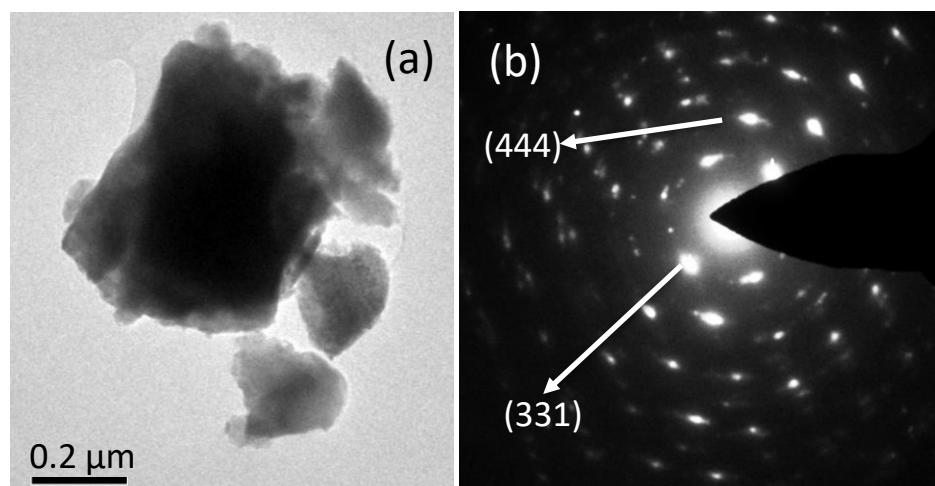


Figure 6.3: (a) SEM image showing the particle size of ground specimen of Dy_4RhAl (b) TEM image showing diffraction rings obtained on one of the particles; diffraction rings indexed with the (hkl) , which matched with the XRD pattern confirming the phase of ground specimen.

Study of the magnetic properties and the thermal properties of the nanoform specimens were carried out by making a small ball of the dried powder mixed with GE varnish. GE varnish was added to avoid the preferred orientation of the particles during the course of measurements leading to noise in the measured data. Antibacterial and antifungal efficacy of the bulk and the nanoform powders were studied using the spread plate technique, well diffusion and disk diffusion techniques. The magnetic and transport properties are reported in section 6.3 for the ball milled Dy_4RhAl and the antimicrobial efficacy studies on the bulk and nanoform specimens of all the samples have been reported in section 6.4.

6.3 Magnetic and thermal properties of Dy_4RhAl .

The readers may refer to chapter 4 for the behavior of the bulk form of Dy_4RhAl . Figures 6.4 (a)–(b) show the magnetic susceptibility as a function of temperature measured in a

field of 100 Oe as well as in 5 kOe. Inverse susceptibility data, plotted for 5 kOe, shows a linear behavior above 50 K (figure 6.4 (b)). The values of the effective magnetic moment derived from the high temperature Curie-Weiss region is $\sim 9.25 \mu_B$ per R which is slightly less than the theoretical value expected for Dy^{3+} ; a lower value of the magnetic moment could be because of the error in the estimation of the sample weight due to GE varnish, employed to glue the particles. The value of θ_P obtained from the linear region shows a value close to ~ 8 K, with the positive sign. Positive sign of θ_P indicates the presence of ferromagnetic correlations which is in contrast to the negative sign (~ -16 K) seen in the case of bulk specimens indicating dominant antiferromagnetic nature. As the temperature is lowered below 50 K, the peak seen around 18 K for the bulk specimen gets smeared, while a distinct peak is seen around 8 K. It is difficult to determine if the peak at 8 K corresponds to the 10 K feature seen in the case of bulk specimen. The plots of $\chi(T)$ in a field of 100 Oe, measured for both ZFC and FC conditions are shown in figure 6.4 (a). There is a prominent bifurcation seen in χ around 30 K, with a broad shoulder at this temperature, followed by a peak around 12 K.

This feature is different from the $\chi(T)$ seen for 100 Oe in the bulk specimen, where a weak bifurcation in the ZFC-FC features is seen around 17 K. The 12 K peak is similar to the broad shoulder seen in the case of bulk specimen, except that this shoulder becomes more prominent with a reduction in particle size. The FC curves show an increasing trend with decreasing temperature (rather than staying flat), which is a signature of cluster spin-glasses, as discussed in the earlier chapters in this thesis.

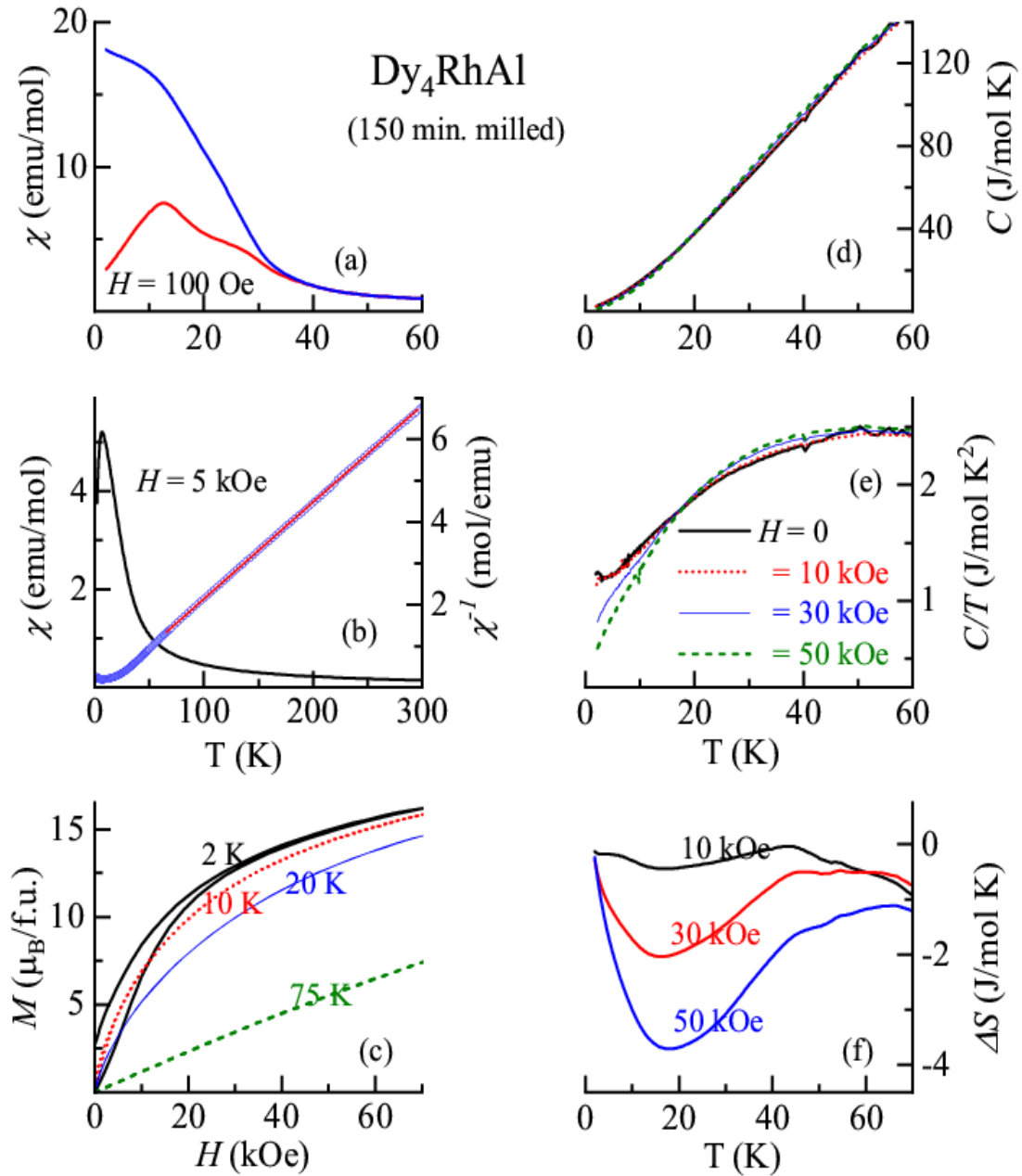


Figure 6.4: a) Magnetic susceptibility as a function of temperature obtained in a field of 100 Oe for both zero-field-cooled and field-cooled conditions for nanoform specimen of Dy₄RhAl. b) Magnetic susceptibility and inverse of magnetic susceptibility in a field of 5 kOe. Curie-Weiss fitting above 100 K is also shown. c) Isothermal magnetization measured at 2, 10, 20 and 75 K. d) Heat-capacity as a function of temperature (<60 K) measured in the presence of external magnetic fields as well. e) Heat-capacity divided by temperature. (f) Isothermal entropy change as a function of temperature (2-70 K) for different final fields starting from zero-field.

For understanding the changes in the magnetic properties of the nanoform specimens in the magnetically ordered state, we measured the heat capacity as a function of temperature and the data is shown in the form of C versus T (figure 6.4 (d)) as well as of C/T versus T (figure 6.4 (e)). $C(T)$ shows a monotonic variation down to the lowest measured temperature of 1.8 K, without any signature for a peak, as seen in the case of bulk specimen around 18 K. This feature supports our inference that the antiferromagnetic ordering seen for the bulk specimen gets smeared with the reduction in particle size, with no signature of a long-range magnetic order. The $C(T)$ data measured in a field of 30 and 50 kOe, show similar features and curves appear to overlap with each other. A careful look at the $C(T)$ versus T plots however shows that the data exhibit a change of slope around 10 K with a very weak variation for the applied fields of 30 and 50 kOe, clearly suggesting the existence of magnetic contribution. This indicates the presence of some magnetic features in the nanoform specimens.

The isothermal entropy change derived from the heat-capacity data is shown in figure 6.4 (f). It can be seen that ΔS shows a broad peak in the negative quadrant, similar to what is seen in the case of bulk specimens indicating a tendency of a field induced ferromagnetic alignment. Thus, looking together with the features in $\chi(T)$, where a bifurcation in ZFC-FC curves occurs around 30 K, and the suppression of the features in the $C(T)$ data, it is quite evident that the antiferromagnetic nature seen in the bulk specimen, get suppressed with an increase in the glassy nature, when the particle size of the compound is reduced.

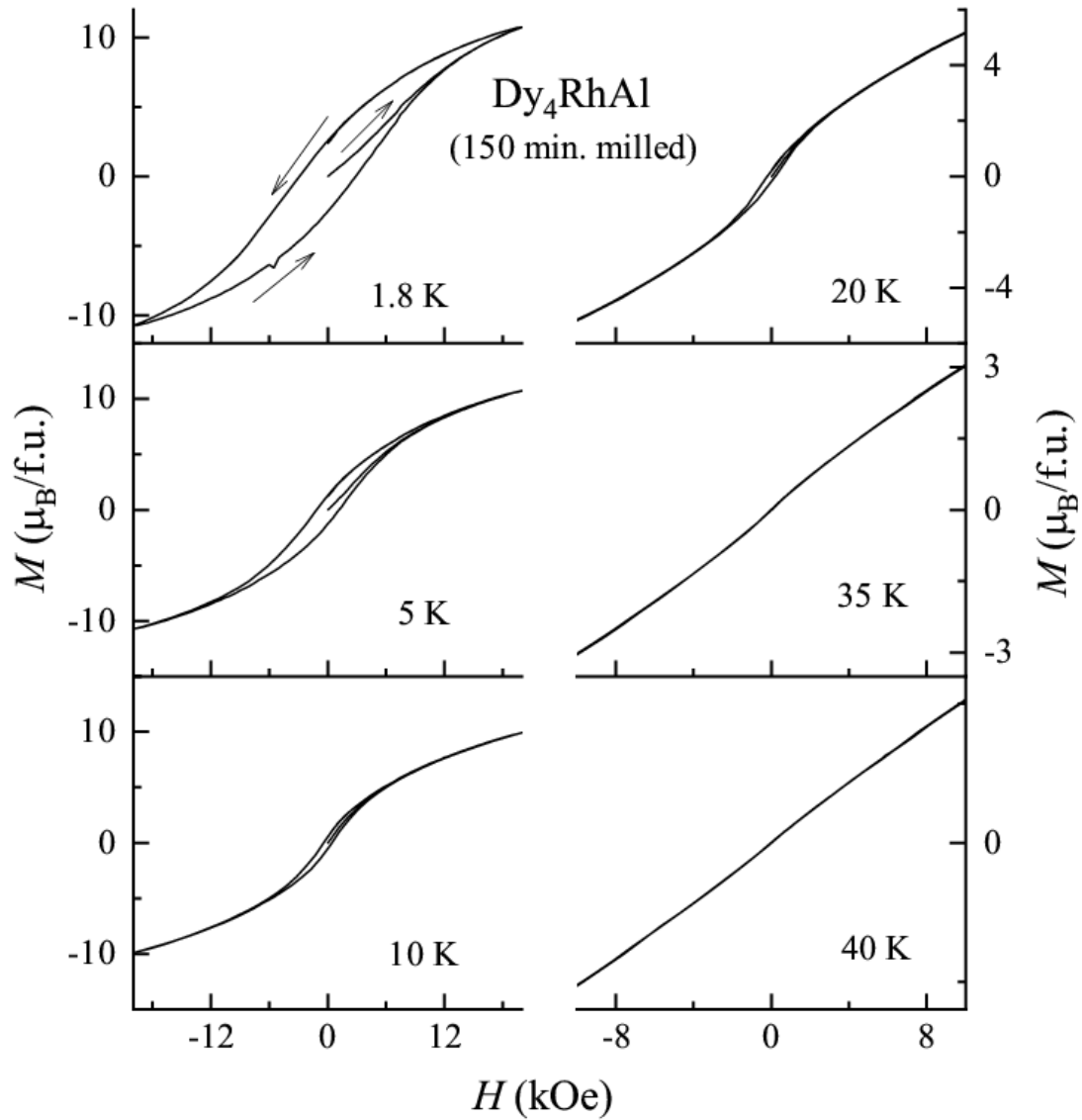


Figure 6.5: Magnetic hysteresis loops in a field range of -15 kOe to 15 kOe at various temperatures from 1.8 K to 40 K. Arrows shown in the 1.8 K data is for tracking the path of data with increasing magnetic field.

Isothermal magnetization as a function of field was measured in the magnetically ordered state, up to a magnetic field of 70 kOe, and plotted in figure 6.4 (c). $M(H)$ curve for 2 K and 5 K (distinctly) shows an increasing trend with a hysteretic nature in the magnetically ordered state, and without any tendency to saturate even for a field as high as

70 kOe. These features are typical of spin glasses and antiferromagnetism. The hysteresis gradually vanishes as the temperature is increased.

For getting a better understanding of the changes in the magnetic properties, we measured the hysteresis behavior of the ball milled specimens at various temperatures and the curves are shown in figure 6.5 in a field range of -15 to +15 kOe, which supports the conclusions made above on hysteretic behavior.

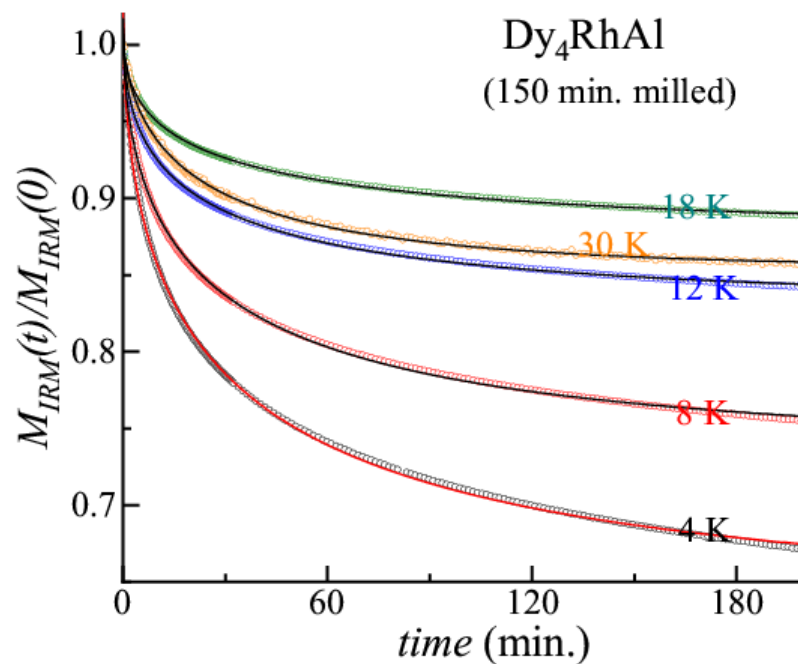


Figure 6.6: Isothermal remnant magnetization as a function of time, obtained at various temperatures. Continuous lines through the data points are obtained by a fit to a stretched exponential form as described in the text. $M(0)$ values are 5.135, 4.013, 2.607, 1.679 and 0.1003 emu/g for 4, 8, 12, 18 and 30 K respectively.

In order to ascertain the increase in glassiness, we measured M_{IRM} as a function of time at various temperatures below 35 K and the curves are shown in figure 6.6. It can be clearly seen that M_{IRM} shows a slow decay with increasing time and the magnitude of this decay e.g. $M(0)$ values decreases with increasing temperatures. This decay even though weak can be seen even for a temperature of 30 K, which confirms the increase in glassy

nature of the compound with reduction of particle size. The decay curves follow a stretched exponential form. We interpret that all these features indicate Griffiths-phase-like regime at low temperatures. Griffiths phase [56–60] was proposed for those systems which contain ferromagnetic clusters which are randomly distributed in a paramagnetic matrix, in such a way that the contribution of the ferromagnetic clusters to χ gets overshadowed by paramagnetic contribution, thus, making it difficult to detect by magnetic studies. Such systems are not known to undergo any long-range magnetic ordering.

In order to confirm the presence of a Griffiths-phase-like regime, we studied the field-dependent behavior of $\chi(T)$ at various applied magnetic fields. The curves of $\chi^{-1}(T)$ are shown in figure 6.7(a). Beyond 50 K, all the curves tend to overlap. The most notable point is that the feature seen in the $\chi(T)$ curve below 10 K, in the form of a broad upturn in the ZFC data, shows a downward shift to lower temperatures with increasing magnetic fields. This downward trend continues till this characteristic temperature reaches 3 K for a 20 kOe magnetic field. There was no worthwhile feature seen in the $\chi^{-1}(T)$ curves as the magnetic field was increased further. Thus, the main point being emphasized is that the sudden change in slope around 30 K seen in the low field curves gets smeared gradually with increasing H .

As mention earlier, Griffiths phase was proposed for systems containing ferromagnetic clusters, which are randomly distributed in a paramagnetic matrix without any signature of a long-range magnetic order. However, recent reports, on dense magnetic systems, mostly oxides, show the magnetic behavior mimicking the Griffiths phase. [see, for instance, Refs. [64–65]]. Many Ce based intermetallic systems which are characterized

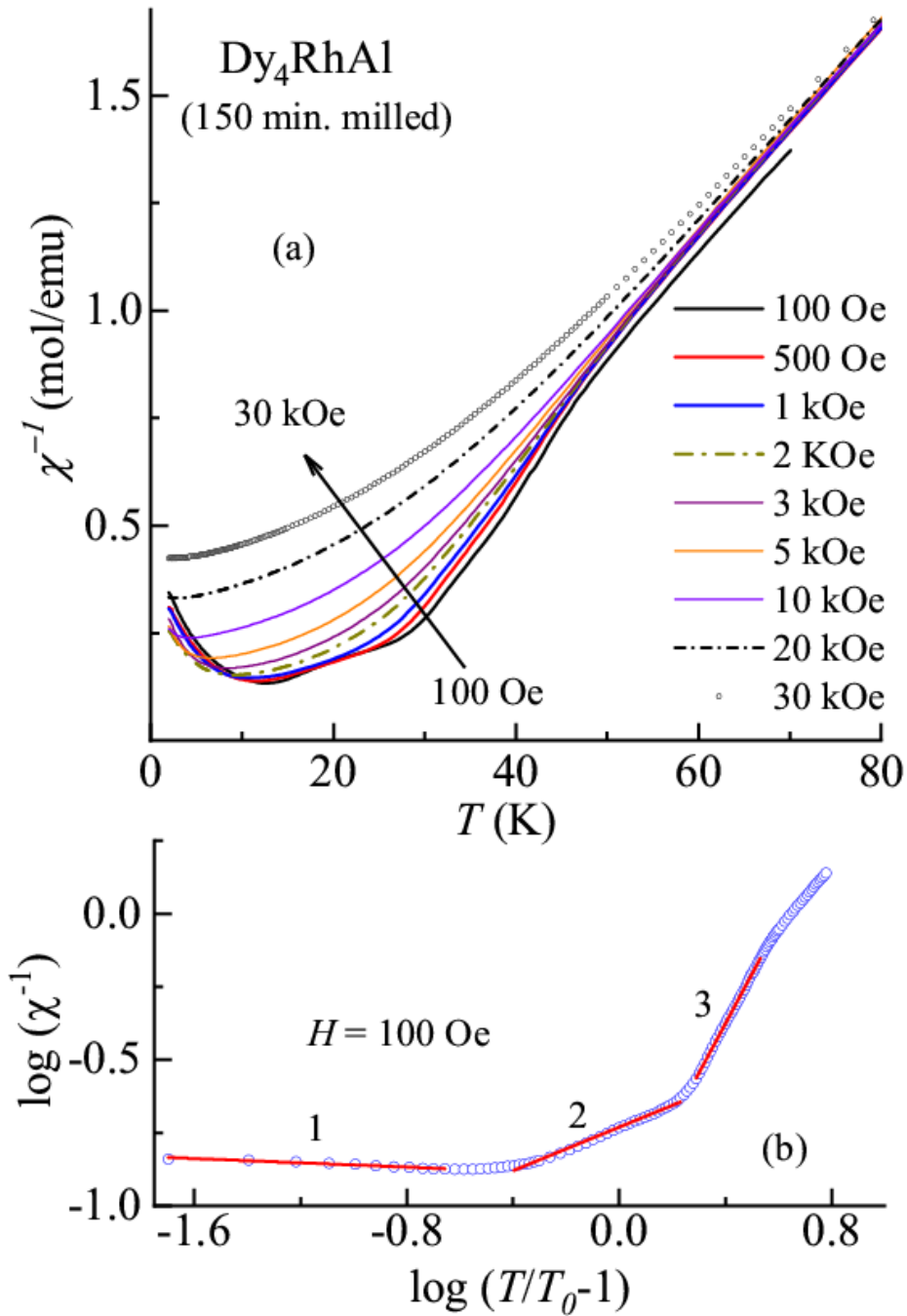


Figure 6.7: a) Inverse magnetic susceptibility as a function of temperature in the presence of dc magnetic fields. b) Data for 100 Oe, plotted as $\log \chi^{-1}$ versus $\log(T/T_0 - 1)$. The three red lines are the results of a linear fit in regions marked, as 1, 2, and 3.

by extended $4f$ orbital, near the quantum critical point and exhibiting a non-Fermi liquid behavior have also been known to exhibit similar characteristics [60,67–69]. But such a

behavior has not been reported in stable valent rare-earth intermetallics which are known to have a well-localized $4f$ orbital [70]. Thus, it is interesting to see a Griffiths-like behavior in a ball-milled nano form specimen of a heavy rare-earth compound, which has a strictly localized $4f$ orbital, exhibiting antiferromagnetic ordering in the bulk crystalline form.

In order to ascertain if the features can be related to the existence of a Griffiths phase, we have tried to determine the exponent in the expression $\chi^{-1}(T) \propto (T - T_0)^{1-\lambda}$ ($0 < \lambda < 1$) which is expected in case of a Griffiths phase behavior. The plot of χ^{-1} versus $(T/T_0 - 1)$ is shown in Fig. 6.7 (b). There are three regions marked as 1, 2 and 3 where we have tried to do a linear fit and derived the values of λ from the slopes. The values thus obtained are as follows: $\lambda \sim 1$ for $10.2 \text{ K} < 12 \text{ K}$; $\lambda \sim 0.6$ for $13 \text{ K} < 27 \text{ K}$, and $\lambda \sim -0.7$ for $30 \text{ K} < 45 \text{ K}$. Thus, it can be concluded that in a temperature regime of 10 K to 30 K, the value of λ comes out to be (+ve and < 1) suggest the presence of a Griffiths phase in this temperature range [64, 65], before a different kind of inhomogeneous magnetic state evolves below 10 K.

Summary

The results of Dy_4RhAl show that the dominant antiferromagnetic ordering seen in the case of bulk specimen disappears when the particle size is reduced to nanoform, with the evolution of a Griffiths-phase like behavior in the range 10–30 K. Demonstration of such a particle-size induced transformation to Griffith's phase-like features in an intermetallic compound due to localized $4f$ electrons is generally quite rare. In the case of other intermetallic compounds studied here, the reduction in particle size does not show drastic change in the magnetic properties, with the reduction in the particle size. Subtle differences

seen in the magnetic properties of these compounds have been tabulated in the appendix of this thesis along with a brief summary for each specimen.

6.4 Study of the antimicrobial efficacy.

We have carried out the antibacterial and antifungal efficacy studies on both bulk as well as nanoform specimens of the family R_2RhSi_3 ($R = Nd, Er$), R_4PtAl ($R = Ho, Er$) and R_4RhAl ($R = Dy$). These studies were carried out on the gram-positive bacteria *S. Aureus*, *E. Faecalis*, *P. Acnes* and the gram-negative bacteria *E. coli* and *Pseudomonas aeruginosa*. The anti-fungal studies were carried out on *Candida albicans*. To carry out the efficacy studies, we employed the disk diffusion technique, well diffusion technique and serial dilution bio-reaction technique. The data thus obtained is discussed below.

Before carrying out the efficacy studies, the solubility test of our samples was carried out in various solutions. The solubility tests were done using polar solvents like DMF, DMSO, Water, Acetone, Methanol, isopropanol, Acetonitrile as well as non-polar solvents like Benzene, Toluene, Acetic Acid, Chloroform, Diethyl ether etc. It was found that these intermetallic compounds are highly insoluble in any of these solvents, and hence we performed our efficacy studies by directly using either the hand ground samples or the nanoform specimens.



Figure 6.8: Agar Plate with Ho_4PtAl (A), Er_4PtAl (B), Ho_2RhSi_3 (C), Nd_2RhSi_3 (D), Er_2RhSi_3 (E) sample disks

For a preliminary assessment of antibacterial activity of our samples, we tried studying the efficacy using the disk diffusion technique on thin disk cut out of bulk form of each sample. In this method we made a sterile agar plate using the brain heart infusion (BHI) agar and placed our sample disks of Ho_4PtAl (A), Er_4PtAl (B), Ho_2RhSi_3 (C), Nd_2RhSi_3 (D), Er_2RhSi_3 (E) on this agar plates as shown in figure 6.8. The entire plate along with the samples was placed under UV light for 15 minutes to ensure there was no parasitic growth on these plates or samples before inoculation. Later these plates were lawned with *E. coli* and incubated at 37°C for two days. After two days of inoculation the growth of *E. coli* on these samples were checked to determine the zone of inhibition around the sample disks.

As seen in figure 6.9, no zone of inhibition was found around the study samples, indicating that the samples might be inefficacious towards inhibiting the growth of *E. coli*.

Similar studies were carried out on *Pseudomonas* and *S. Aureus* (figures not shown), but the results were negative for these microbes as well indicating an inefficacious nature of our samples. We felt the inefficacy might also be because of the insolubility of the samples, which leads to zero diffusivity of the samples into the agar medium which is needed to show activity.

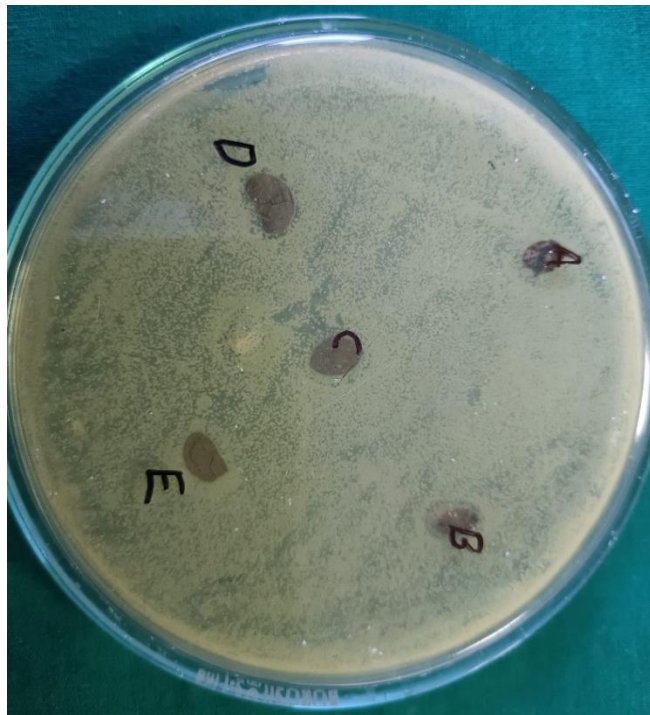


Figure 6.9: Agar Plate with Ho_4PtAl , Er_4PtAl , Ho_2RhSi_3 , Nd_2RhSi_3 , Er_2RhSi_3 disks, lawned with *E. coli* and incubated for 2 days

In order to verify if the hand ground powders show some activity, we tried hand grinding of these samples and dispersing these powders in freshly prepared BHI broth. The mixture was prepared using 5 mg (by weight) of our sample powders which was mixed with 1 ml of broth. The tubes containing the mixture of sample and broth were kept for thorough mixing, for 24 hours at 25° C, in media shakers, along with control tubes containing only broth media. After 24 hours, additional vortex mixing was carried out for a better dispersion of these powders in the broth. Since the sample powders were of a

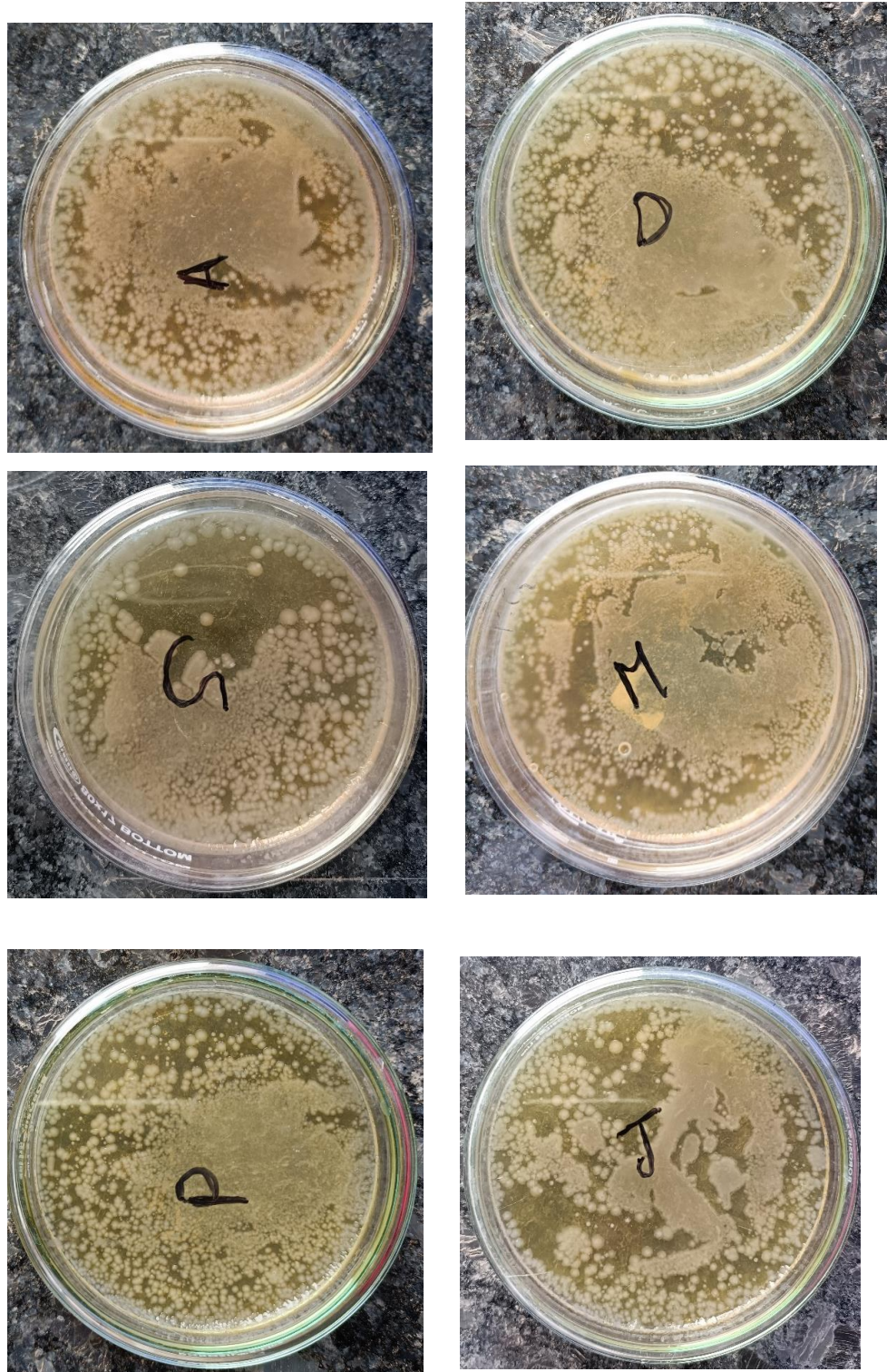


Figure 6.10: Agar Plate lawned with sixth dilution of mixture of *E. coli*, BHI broth and powders of Dy_4RhAl (A), Er_4PtAl (D), Ho_4PtAl (G), Er_2RhSi_3 (M), Ho_2RhSi_3 (P), Nd_2RhSi_3 (J) and incubated for 2 days.

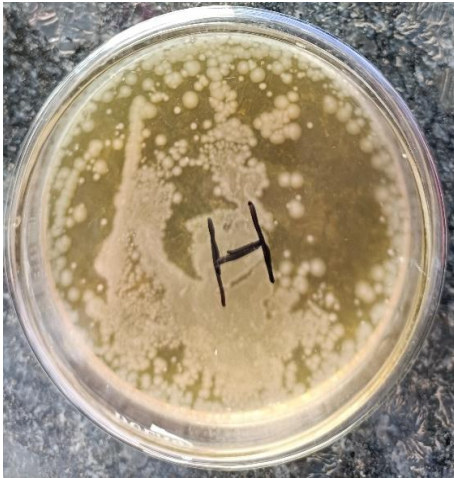


Figure 6.11: Agar Plate lawned with sixth dilution of mixture of *Pseudomonas*, BHI broth and powders of Dy_4RhAl (B), Er_4PtAl (E), Ho_4PtAl (H), Er_2RhSi_3 (N), Ho_2RhSi_3 (Q), Nd_2RhSi_3 (K) and incubated for 2 days



Figure 6.12: Agar Plate lawned with sixth dilution of mixture of *S. Aureus*, BHI broth and powders of Dy₄RhAl (C), Er₄PtAl (F), Ho₄PtAl (I), Er₂RhSi₃ (O), Ho₂RhSi₃ (R), Nd₂RhSi₃ (L), and incubated for 2 days.

higher density, these powders showed a tendency to settle down at the bottom of the vials without mixing congruently in the broth. These vials were inoculated with *E. coli*, *Pseudomonas* and *S. Aureus*, by adding 5 μ l each of bacterium to the respective vials. The inoculated tubes were again set for shaking and incubation for two days at 37° C in media shakers. These incubated tubes were later diluted using a serial dilution technique described in chapter 2. Serial dilution enables the reduction of bacteria in the vials to be lawned on agar plates, which in turn helps in counting of colonies for a comparative study with the control plates after growth.

The sixth diluted vial was taken up for lawning using the spread plate technique. Sterile BHI agar plates (prepared earlier) were used for lawning of the diluted mixture for with 1 μ l each of the mixture was placed on the agar plated and lawned using sterile cotton swabs. These spread plates were then incubated for two days at 35° C. After two days of incubation, the plates were removed and taken up for counting of microbial colonies. It was found that the entire plate had a quite large amount of growth, of the bacterial colonies, (based on a superficial examination of the spread plates). Thus, it was evident that none of the hand ground samples showed antibacterial efficacy. The images of the incubated spread plates have been shown in figures 6.10, 6.11 and 6.12 for *E. coli*, *Pseudomonas* and *S. Aureus*.

It was clear from the images that the hand ground samples were also ineffective in inhibiting the growth of bacterial colonies. We repeated the same procedure for *Candida albicans* as well and the results were found to be negative for these specimens as well.

The well diffusion technique was used to determine the efficacy of hand ground Dy_4RhAl , Ho_4PtAl , Er_4PtAl and Ho_2RhSi_3 on the microbe *P. Acnes*. In this technique the powders were filled in wells created on sterile BHI agar plates and lawned with *P. Acnes*. This plate was then incubated at $37^\circ C$ for 48 hours. The images of as lawned and the incubated plates are shown in figure 6.13. It is evident from the images that none of these hand ground samples were effective in inhibiting the growth of *P. Acnes*.



Figure 6.13: Left image shows agar plate with wells filled with Dy_4RhAl (A), Ho_4PtAl (B), Er_4PtAl (C) and Ho_2RhSi_3 (D) on day 0 and right image shows the growth after 28 hours of Incubation at $37^\circ C$ for *P. Acne*.

As mentioned earlier, the main reason behind the negative results could be the insolubility of the bulk and hand ground samples, which prevents the diffusion of the compounds into the media rendering it inefficacious against the microbes. Thus, we felt that it was necessary to carry out these studies on the nanoform specimens of our samples, before arriving at a final conclusion.

The efficacy studies were carried out on the nanoform specimens on which we reported the magnetic properties in the earlier subsection. These studies were carried out on *E. coli*, *Pseudomonas aeruginosa*, *S. Aureus*, *E. Faecalis* and *Candida albicans* using the

disk diffusion technique, and the bioreactor serial dilution technique. In this study, the nanoform specimens were weighed (~5 mg) and mixed with 1 ml of BHI broth and left for mixing in media shaker for 24 hours. After 24 hours, this mixture was again dispersed with vortex shaker mixer for dispersing the nano-powders in the broth media. These tubes were placed under UV light for sterilization before inoculation to remove any stray growth. Microbes (5 µl) were added to the designated vials containing the broth and sample mixture. These vials were incubated for 24 hours at 37° C with continuous shaking in media shaker. After 24 hours of incubation, serial dilution was carried out and the 10th dilution was used for spread plating by using 1 µl of the mixture. These lawned spread plates were incubated again for 24 hours. For each bacterium a control plate was also incubated for sake of comparison of the efficacy. After incubation the agar plates were checked for growth of colonies and photographed. The images are shown in figures 6.14 to 6.37 below where the just lawned plates are shown on the left side and the incubated plates are shown in the right side. In both the images, half image on the right-hand side contains image of the control plates for each microbe, which has been placed for sake of comparison.

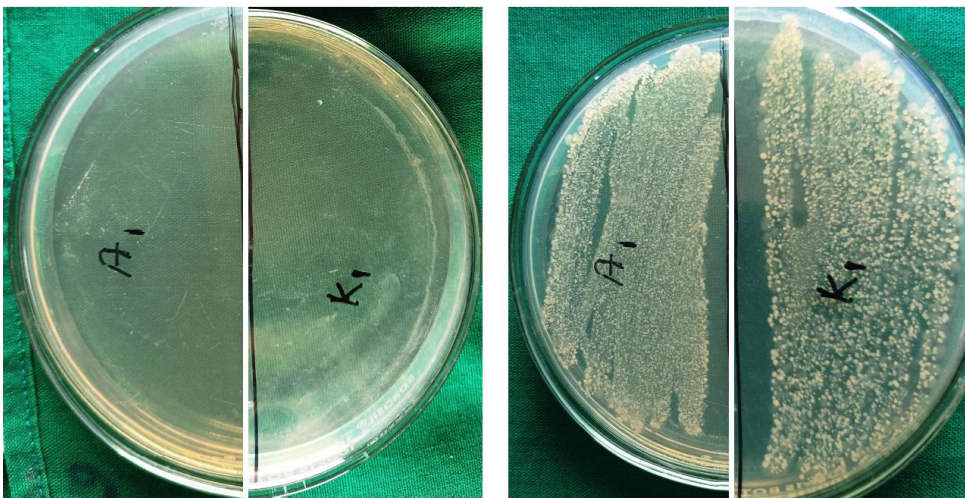


Figure 6.14: *S. Aureus* with Er₄PtAl nano powder and K region acts as control

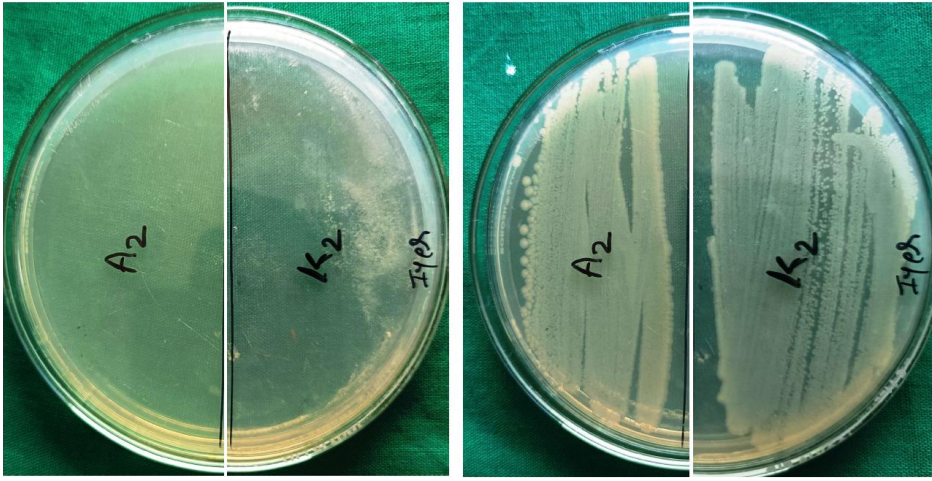


Figure 6.15: *E. coli* with Er_4PtAl nano powder and K region acts as control

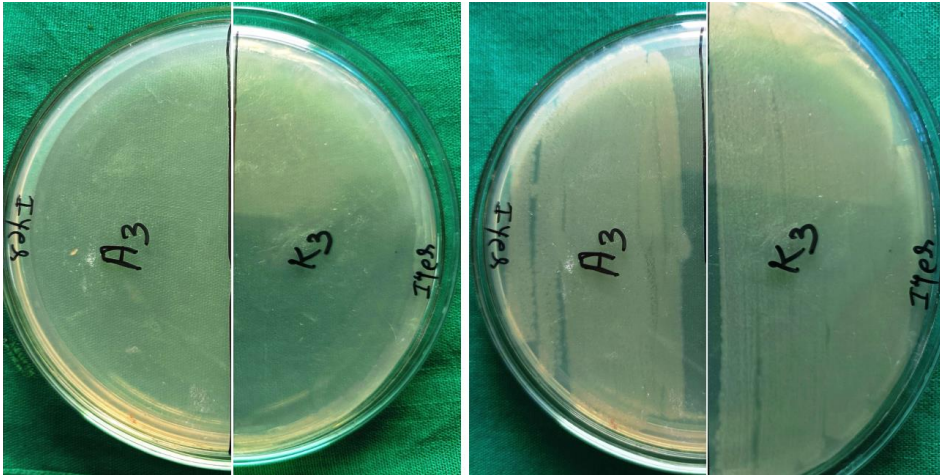


Figure 6.16: *Pseudomonas* with Er_4PtAl nano powder and K region acts as control

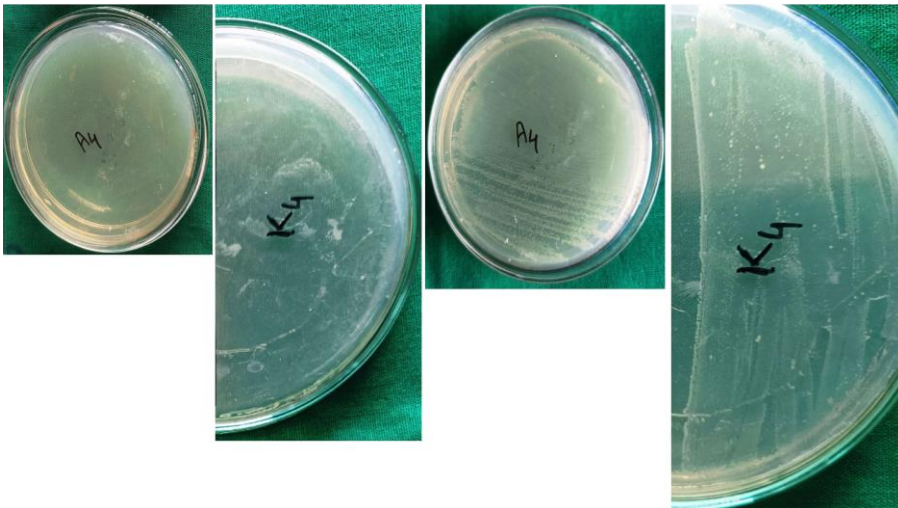


Figure 6.17: *E. Faecalis* with Er_4PtAl nano powder and K region acts as control

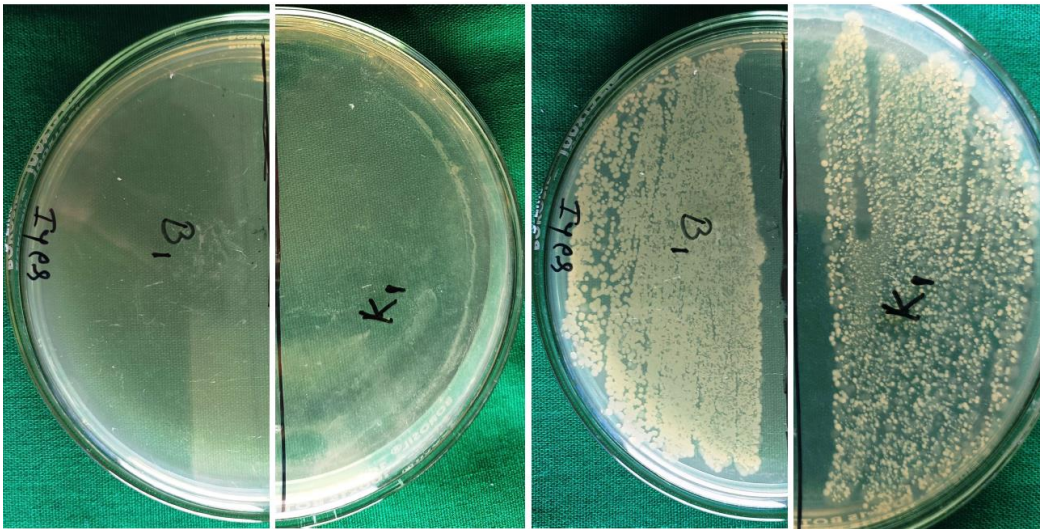


Figure 6.18: *S. Aureus* with Ho₄PtAl nano powder and K region acts as control

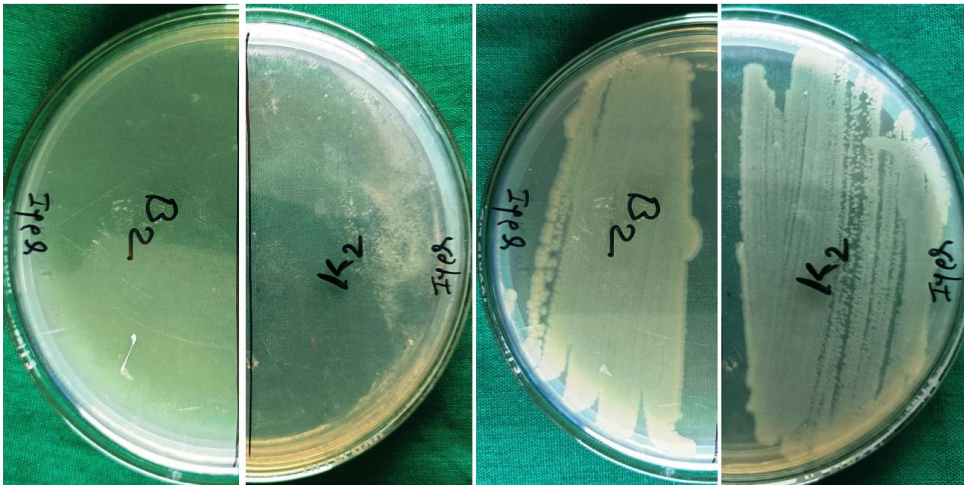


Figure 6.19: *E. coli* with Ho₄PtAl nano powder and K region acts as control

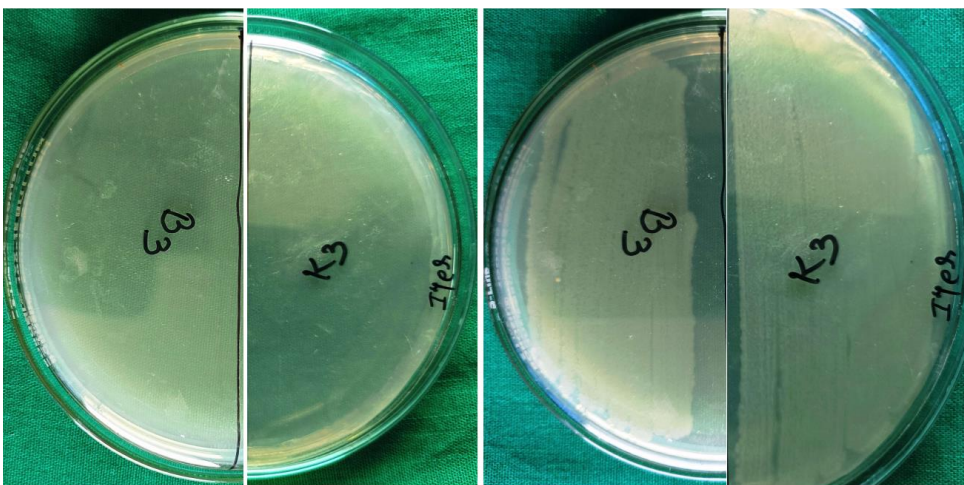


Figure 6.20: *Pseudomonas* with Ho₄PtAl nano powder and K region acts as control

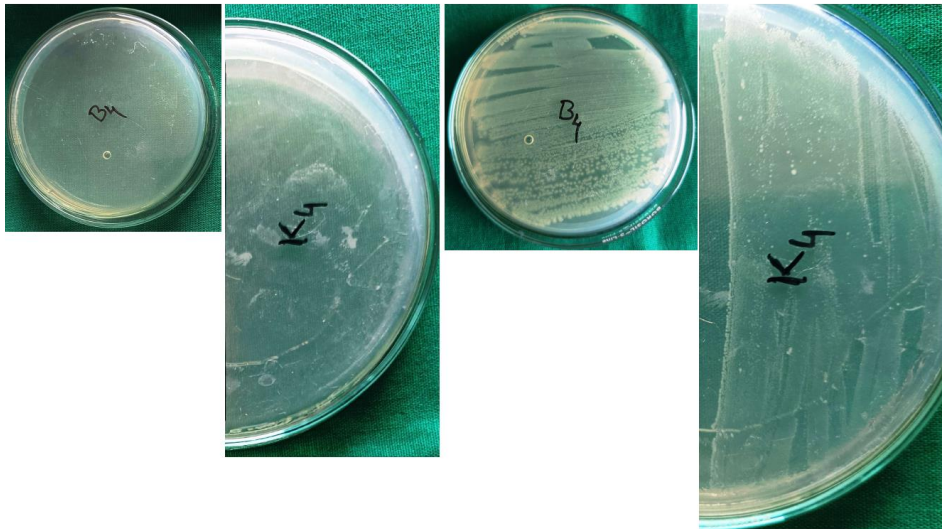


Figure 6.21: *E. Faecalis* with Ho_4PtAl nano powder and *K* region acts as control

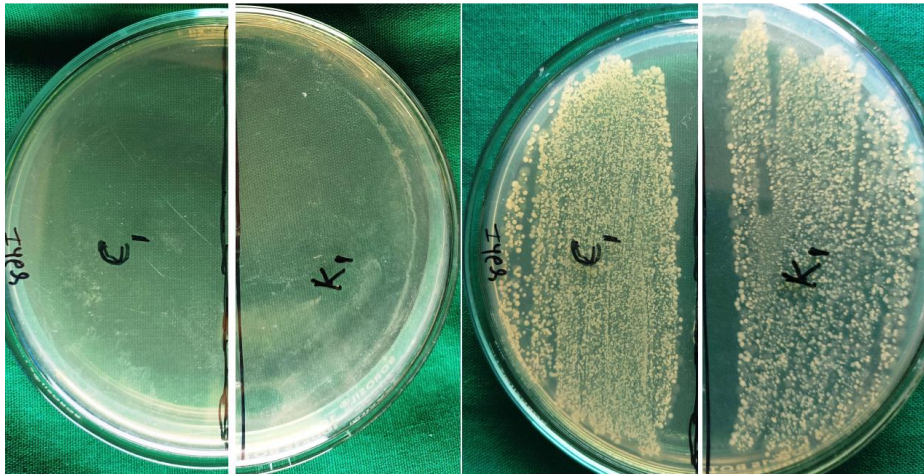


Figure 6.22: *S. Aureus* with Dy_4RhAl nano powder and *K* region acts as control

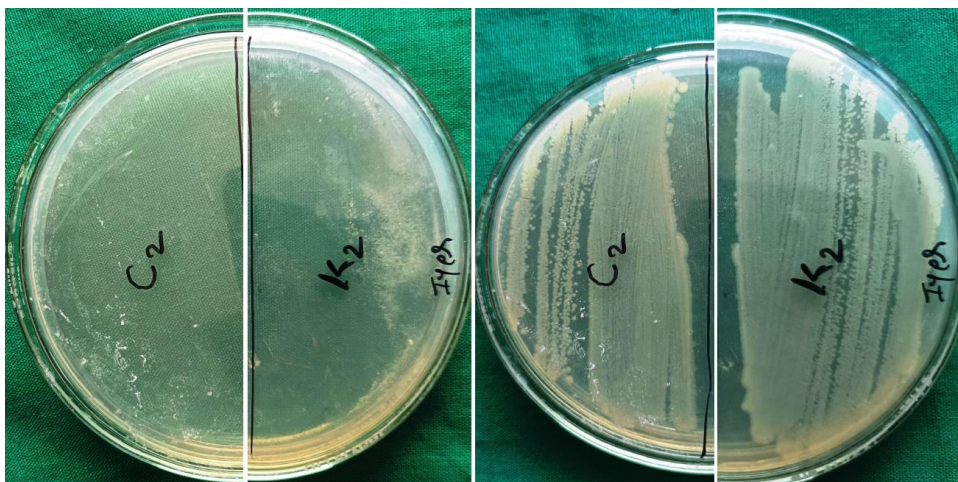


Figure 6.23: *E. coli* with Dy_4RhAl nano powder and *K* region acts as control

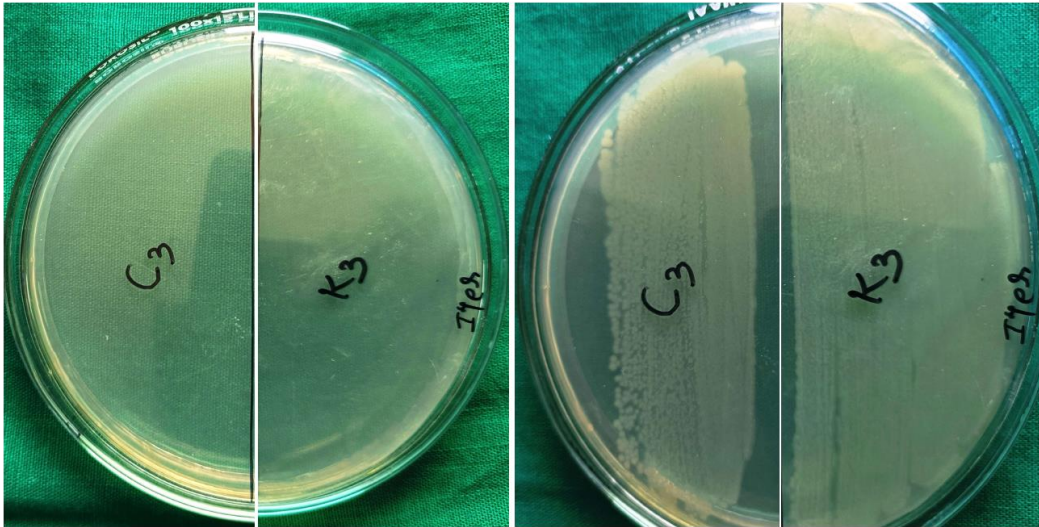


Figure 6.24: *Pseudomonas* with Dy_4RhAl nano powder and K region acts as control



Figure 6.25: *E. Faecalis* with Dy_4RhAl nano powder and K region acts as control

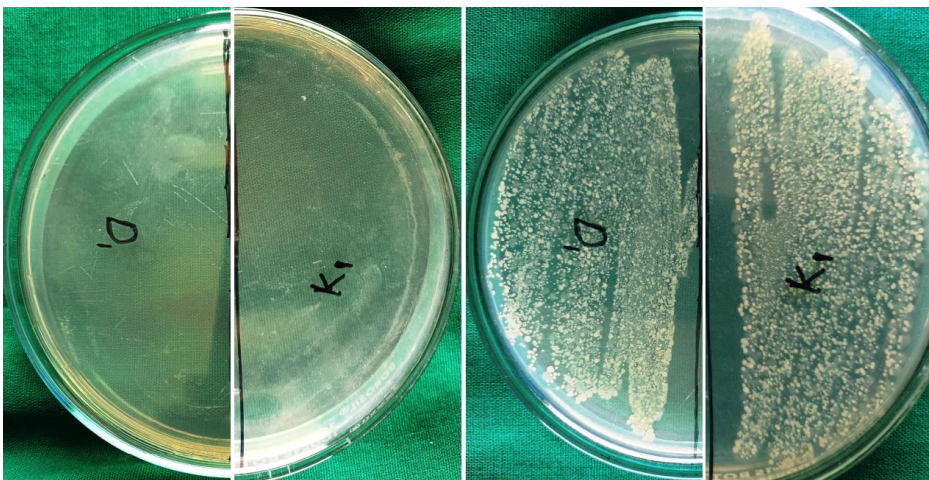


Figure 6.26: *S. Aureus* with Er_2RhSi_3 nano powder and K region acts as control

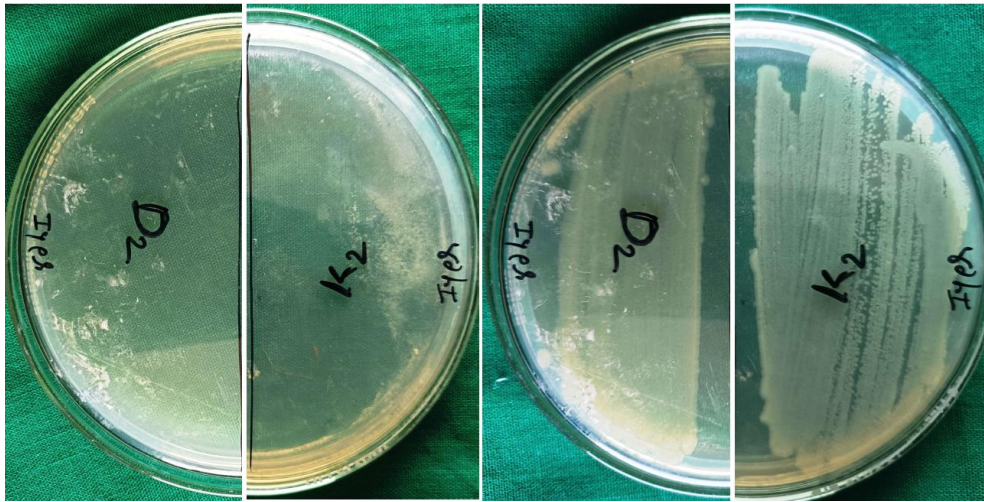


Figure 6.27: *E. coli* with Er_2RhSi_3 nano powder and K region acts as control

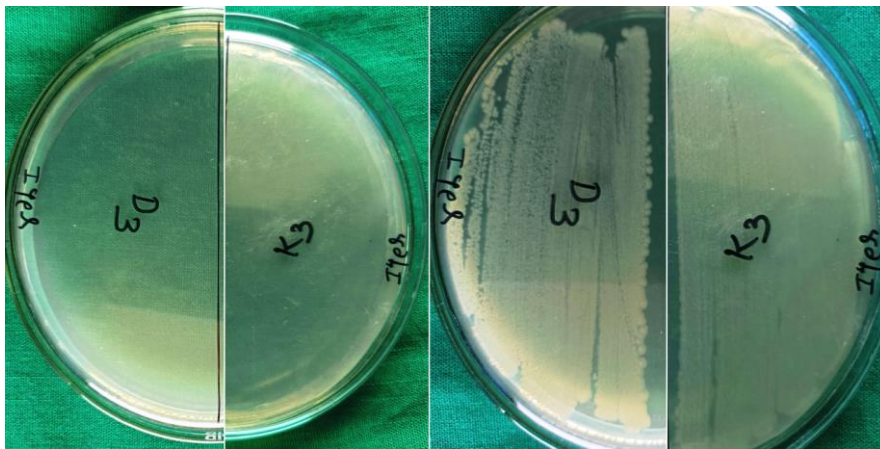


Figure 6.28: *Pseudomonas* with Er_2RhSi_3 nano powder and K region acts as control

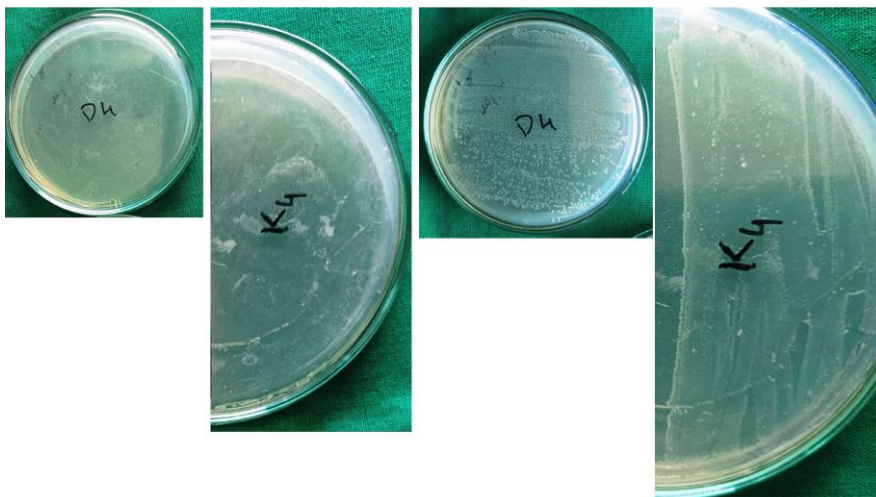


Figure 6.29: *E. Faecalis* with Er_2RhSi_3 nano powder and K region acts as control

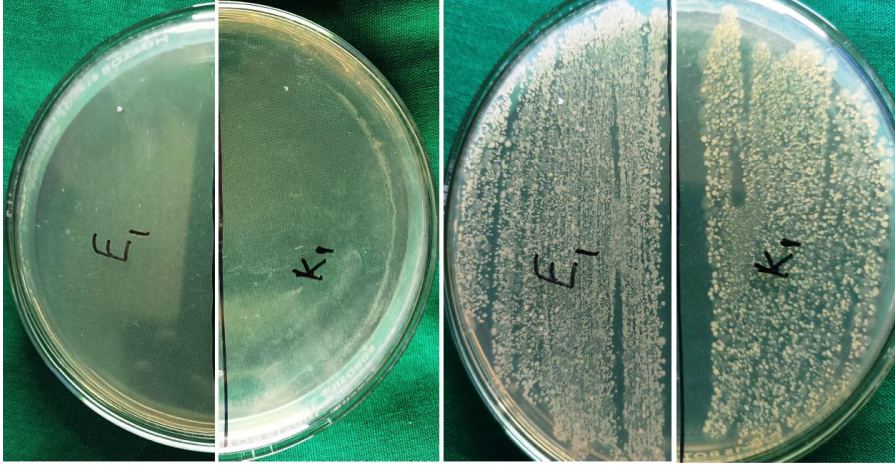


Figure 6.30: *S. Aureus* with Ho_2RhSi_3 nano powder and K region acts as control

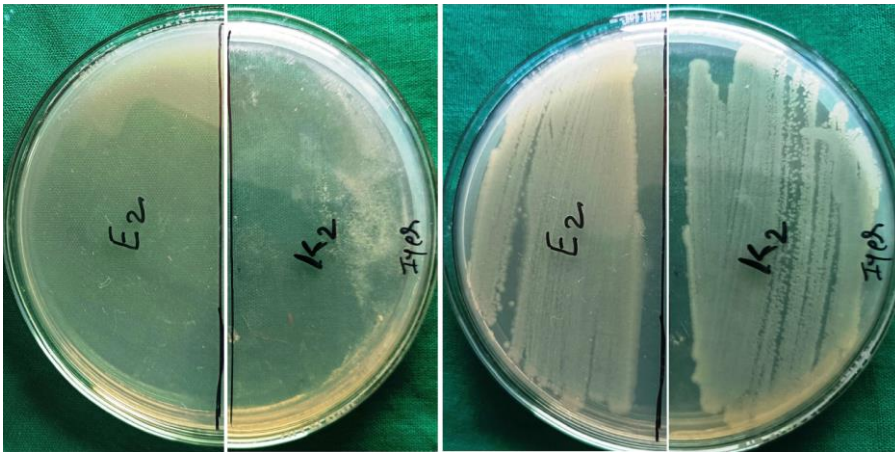


Figure 6.31: *E. coli* with Ho_2RhSi_3 nano powder and K region acts as control

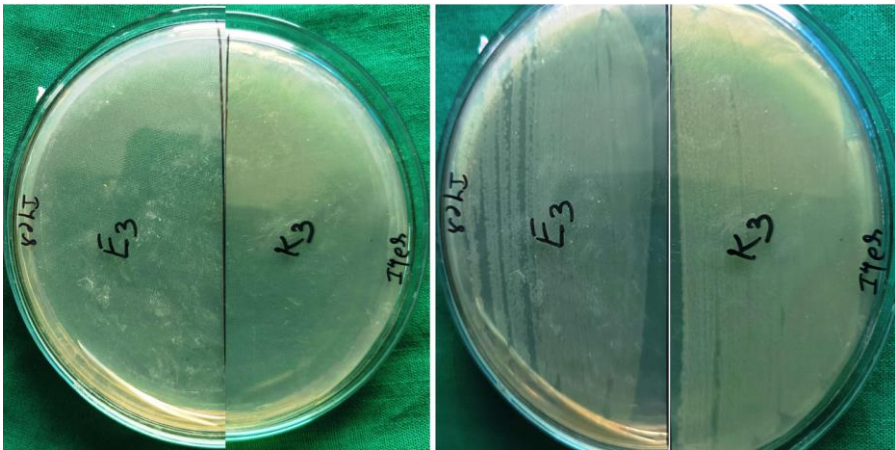


Figure 6.32: *Pseudomonas* with Ho_2RhSi_3 nano powder and K region acts as control

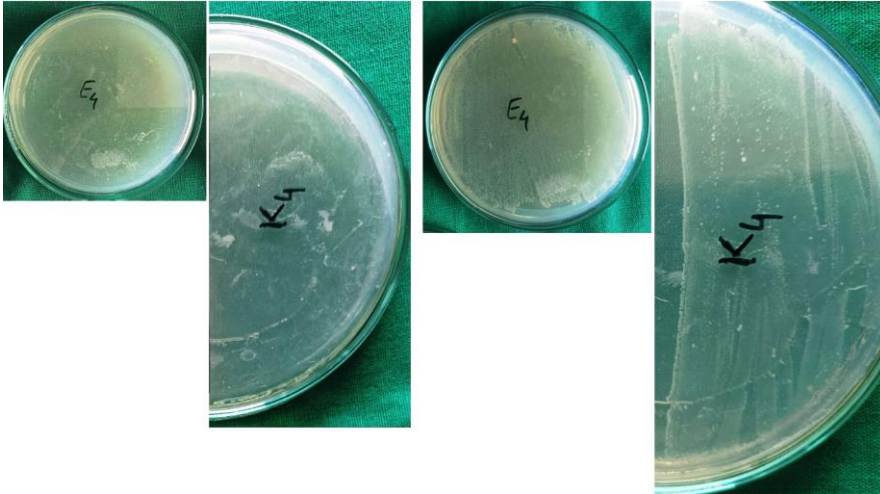


Figure 6.33: *E. Faecalis* with Ho_2RhSi_3 nano powder and K region acts as control

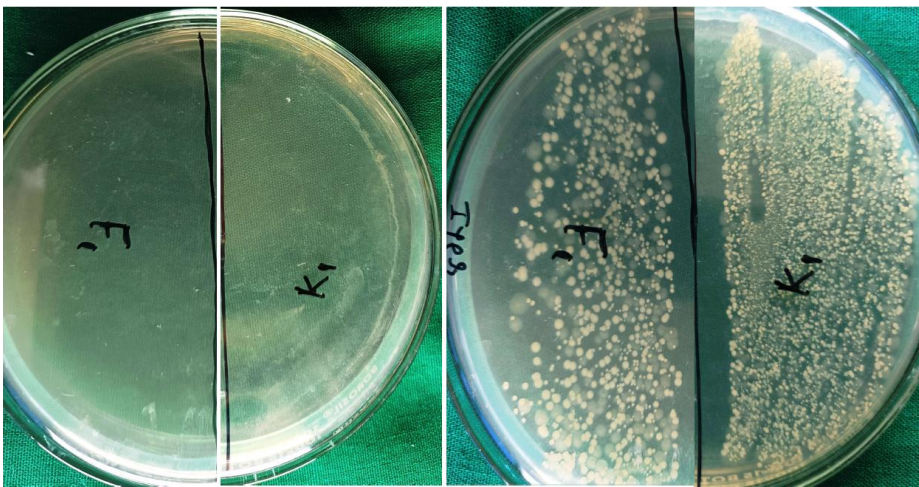


Figure 6.34: *S. Aureus* with Nd_2RhSi_3 nano powder and K region acts as control

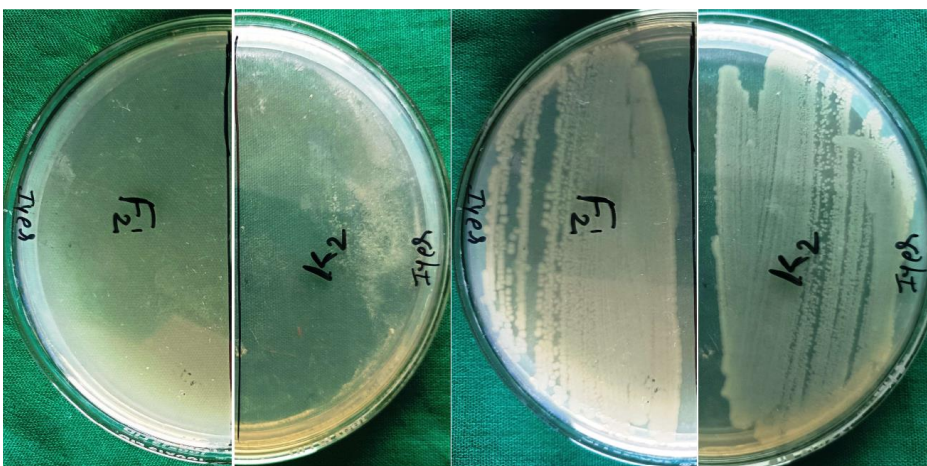


Figure 6.35: *E. coli* with Nd_2RhSi_3 nano powder and K region acts as control

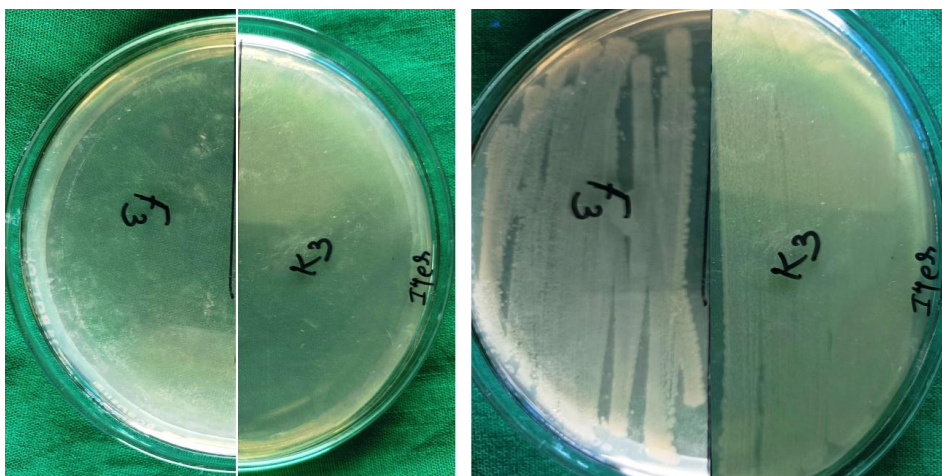


Figure 6.36: *Pseudomonas* with Nd_2RhSi_3 nano powder and *K* region acts as control

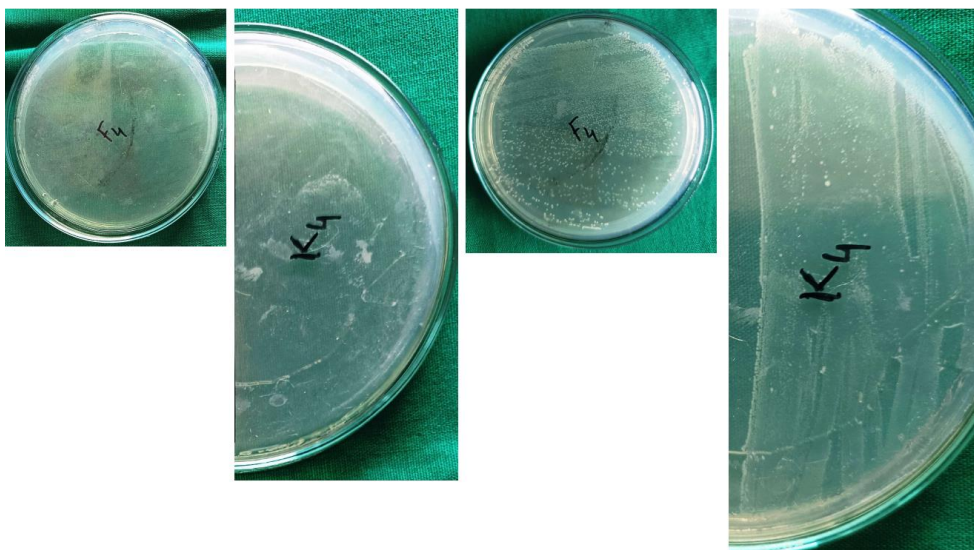


Figure 6.37: *E. Faecalis* with Nd_2RhSi_3 nano powder and *K* region acts as control

Some of the plates where there was doubt about the growth after inoculation, we repeated the entire process starting from the fresh broth and sample mixture before arriving at a conclusion.

Looking at the growth of colonies and comparing with the control plates, it is evident that these samples are not efficacious in inhibiting the growth of microbes (both bacteria or fungus). A careful look into some of these plates, indicated more growth of microbes when compared with the growth on the control plates (based on superficial

examination), probably indicating that some of these compounds are actually aiding the bacterial growth and acting as probiotic instead of antibiotic material.

6.5 Conclusions

We have compared and contrasted the magnetic behaviors of the bulk and nanoforms of the intermetallic compounds studied in this thesis. The nanoform of Dy₄RhAl present a novel magnetic property. In the case of Ho₄PtAl and Er₄PtAl, the reduction in the particle size increases the glassy nature of the compounds, while suppressing the antiferromagnetic properties, surprisingly, the isostructural Dy₄RhAl compound shows the signature of magnetic susceptibility behavior mimicking Griffith's phase around 30 K, a feature not seen in the case of Ho₄PtAl and Er₄PtAl with the same particle size reduction. Demonstration of such a particle-size induced transformation of magnetic property to Griffith's phase-like features, in an intermetallic compound, containing localized 4*f* electrons is generally quite rare. The results also reveal that one has to be careful while extrapolating magnetic behavior of the bulk form to nanoform in medicinal applications.

The results of the antimicrobial efficacy on these compounds (both bulk and nanoform specimens) shows that these samples are ineffective in inhibition of bacterial and fungal growth.

6.6 Bibliographical References

1. El-Sayed IH, Huang X, El-Sayed MA. Surface plasmon resonance scattering and absorption of anti-EGFR antibody conjugated gold nanoparticles in cancer diagnostics: applications in oral cancer. *Nano letters*. 2005 May 11; 5(5):829-34.

2. Neikov OD, Yefimov NA, Naboychenko S. Handbook of non-ferrous metal powders: technologies and applications. Elsevier; 2009 Feb 24.
3. Urade AR, Lahiri I, Suresh KS. Graphene properties, synthesis and applications: a review. *Jom*. 2023 Mar; 75(3):614-30.
4. Cannas C, Gatteschi D, Musinu A, Piccaluga G, Sangregorio C. Structural and magnetic properties of Fe₂O₃ nanoparticles dispersed over a silica matrix. *The Journal of Physical Chemistry B*. 1998 Oct 1; 102(40):7721-6.
5. Mayer AB, Mark JE. Polymer-protected, colloidal platinum nanocatalysts. *Polymer Bulletin*. 1996 Nov; 37:683-90.
6. Mhetre H, Kanse D, Patil D. Nanomaterials: Applications in Electronics. *Int J Adv Eng Nano Technol*. 2021 Sep; 4:7-19.
7. Matsui I. Nanoparticles for electronic device applications: a brief review. *Journal of chemical engineering of Japan*. 2005; 38(8):535-46.
8. Mahmud MZ. A Concise Review of Nanoparticles Utilized Energy Storage and Conservation. *Journal of Nanomaterials*. 2023 Nov 14; 2023.
9. Baby R, Hussein MZ, Abdullah AH, Zainal Z. Nanomaterials for the treatment of heavy metal contaminated water. *Polymers*. 2022 Jan 31; 14(3):583.
10. Alsaba MT, Al Dushaishi MF, Abbas AK. A comprehensive review of nanoparticles applications in the oil and gas industry. *Journal of Petroleum Exploration and Production Technology*. 2020 Apr; 10(4):1389-99.
11. Mansour A, Romani M, Acharya AB, Rahman B, Verron E, Badran Z. Drug delivery systems in regenerative medicine: an updated review. *Pharmaceutics*. 2023 Feb 18; 15(2):695.

12. Salata OV. Applications of nanoparticles in biology and medicine. *Journal of nanobiotechnology*. 2004 Dec; 2:1-6.
13. Khan I, Saeed K, Khan I. Nanoparticles: Properties, applications and toxicities. *Arabian journal of chemistry*. 2019 Nov 1; 12(7):908-31.
14. Sekar RP *Journal of Biomedical and Pharmaceutical Sciences* 3: 28 (2018).
15. Weindling P. *Epidemics and genocide in Eastern Europe, 1890-1945*. OUP Oxford; 2000 Feb 3.
16. Apostolou P, Toloudi M, Chatziioannou M, Ioannou E, Knocke DR, Nester J, Komiotis D, Papatotiriou I. Anvirzel™ in combination with cisplatin in breast, colon, lung, prostate, melanoma and pancreatic cancer cell lines. *BMC Pharmacology and Toxicology*. 2013 Dec; 14:1-6.
17. Akbar Vaseghi, Babak Bakhshinejd, Majide Sadeghizade et.al. (2014) *Science and Researcher Branch, Islamic Azad University, Ardabil, Iran*
18. Idris DS, Roy A. Synthesis of bimetallic nanoparticles and applications—an updated review. *Crystals*. 2023 Apr 7; 13(4):637.
19. Muzammil S, Hayat S, Fakhar-E-Alam M, Aslam B, Siddique MH, Nisar MA, Saqalein M, Atif M, Sarwar A, Khurshid A, Amin N. Nanoantibiotics: Future nanotechnologies to combat antibiotic resistance. *Front. Biosci*. 2018 Mar 1; 10(2):352-74.
20. Adeniji OO, Ojemaye MO, Okoh AI. Antibacterial activity of metallic nanoparticles against multidrug-resistant pathogens isolated from environmental samples: nanoparticles/antibiotic combination therapy and cytotoxicity study. *ACS Applied Bio Materials*. 2022 Sep 26; 5(10):4814-26.

21. Jones F, Hu Y, Coates A. The efficacy of using combination therapy against multi-drug and extensively drug-resistant *Pseudomonas aeruginosa* in clinical settings. *Antibiotics*. 2022 Feb 28; 11(3):323.
22. Johnstone TC, Suntharalingam K, Lippard SJ. The next generation of platinum drugs: targeted Pt (II) agents, nanoparticle delivery, and Pt (IV) prodrugs. *Chemical reviews*. 2016 Mar 9; 116(5):3436-86.
23. Champion GD, Graham GG, Ziegler JB. Chrysotherapy, treatment with gold-based drugs. *Ballieres Clin. Rheumatol*. 1990; 4:491-534.
24. Kean WF, Kean IR. Clinical pharmacology of gold. *Inflammopharmacology*. 2008 Jun; 16(3):112-25.
25. Barnard PJ, Berners-Price SJ. Targeting the mitochondrial cell death pathway with gold compounds. *Coordination Chemistry Reviews*. 2007 Jul 1; 251(13-14):1889-902.
26. Mirzadeh N, Reddy TS, Bhargava SK. Advances in diphosphine ligand-containing gold complexes as anticancer agents. *Coordination Chemistry Reviews*. 2019 Jun 1; 388:343-59.
27. Harbut MB, Vilchèze C, Luo X, Hensler ME, Guo H, Yang B, Chatterjee AK, Nizet V, Jacobs Jr WR, Schultz PG, Wang F. Auranofin exerts broad-spectrum bactericidal activities by targeting thiol-redox homeostasis. *Proceedings of the National Academy of Sciences*. 2015 Apr 7; 112(14):4453-8.
28. Wu B, Yang X, Yan M. Synthesis and structure–activity relationship study of antimicrobial auranofin against ESKAPE pathogens. *Journal of medicinal chemistry*. 2019 Aug 6; 62(17):7751-68.

29. Rezić I. Nanoparticles for biomedical application and their synthesis. *Polymers*. 2022 Nov 16; 14(22):4961.
30. ClinicalTrials.gov a Database of Privately and Publicly Funded Clinical Studies Conducted around the World. Available online: www.clinicaltrials.gov (accessed on 5 December 2019).
31. Biot C, Nosten F, Fraisse L, Ter-Minassian D, Khalife J, Dive D. The antimalarial ferroquine: from bench to clinic. *Parasite: journal de la Société Française de Parasitologie*. 2011 Aug; 18(3):207.
32. Monro S, Colon KL, Yin H, Roque III J, Konda P, Gujar S, Thummel RP, Lilge L, Cameron CG, McFarland SA. Transition metal complexes and photodynamic therapy from a tumor-centered approach: challenges, opportunities, and highlights from the development of TLD1433. *Chemical reviews*. 2018 Oct 8; 119(2):797-828.
33. Zeng L, Gupta P, Chen Y, Wang E, Ji L, Chao H, Chen ZS. The development of anticancer ruthenium (II) complexes: from single molecule compounds to nanomaterials. *Chemical Society Reviews*. 2017; 46(19):5771-804.
34. Kenny RG, Marmion CJ. Toward multi-targeted platinum and ruthenium drugs—a new paradigm in cancer drug treatment regimens? *Chemical reviews*. 2019 Jan 14; 119(2):1058-137.
35. Korfel A, Scheulen ME, Schmoll HJ, Gründel O, Harstrick A, Knoche M, Fels LM, Skorzec M, Bach F, Baumgart J, Sass G. Phase I clinical and pharmacokinetic study of titanocene dichloride in adults with advanced solid tumors. *Clinical cancer*

- research: an official journal of the American Association for Cancer Research. 1998 Nov 1; 4(11):2701-8.
36. Marková Z, Šišková KM, Filip J, Cuda J, Kolar M, Safarova K, Medrik I, Zboril R. Air stable magnetic bimetallic Fe–Ag nanoparticles for advanced antimicrobial treatment and phosphorus removal. *Environmental science & technology*. 2013 May 21; 47(10):5285-93.
37. Perdikaki A, Galeou A, Pilatos G, Karatasios I, Kanellopoulos NK, Prombona A, Karanikolos GN. Ag and Cu monometallic and Ag/Cu bimetallic nanoparticle–graphene composites with enhanced antibacterial performance. *ACS Applied Materials & Interfaces*. 2016 Oct 19; 8(41):27498-510.
38. Perdikaki A, Galeou A, Pilatos G, Prombona A, Karanikolos GN. Ion-based metal/graphene antibacterial agents comprising mono-ionic and bi-ionic silver and copper species. *Langmuir*. 2018 Aug 26; 34(37):11156-66.
39. Perdikaki AV, Tsitoura P, Vermisoglou EC, Kanellopoulos NK, Karanikolos GN. Poly (ethylene oxide)-b-poly (propylene oxide) amphiphilic block copolymer-mediated growth of silver nanoparticles and their antibacterial behavior. *Langmuir*. 2013 Sep 10;29(36):11479-88.
40. Pilatos G, Perdikaki AV, Sapalidis A, Pappas GS, Giannakopoulou T, Tsoutsou D, Xenogiannopoulou E, Boukos N, Dimoulas A, Trapalis C, Kanellopoulos NK. Graphene by one-step chemical vapor deposition from ferrocene vapors: Properties and electrochemical evaluation. *Journal of Applied Physics*. 2016 Feb 14;119(6).
41. Pilatos G, Vermisoglou EC, Perdikaki A, Devlin E, Pappas GS, Romanos GE, Boukos N, Giannakopoulou T, Trapalis C, Kanellopoulos NK, Karanikolos GN.

- One-step, in situ growth of unmodified graphene–magnetic nanostructured composites. *Carbon*. 2014 Jan 1;66: 467-75.
42. Abd-Elsalam KA. Bimetallic Nanoparticles as Antimicrobials.(2016) *J Nanotech Mater Sci* 3 (1): 1-2. *J Nanotech Mater Sci.*; 3(1).
43. Arora N, Thangavelu K, Karanikolos GN. Bimetallic nanoparticles for antimicrobial applications. *Frontiers in Chemistry*. 2020 May 28;8:412.
44. Frei A. Metal complexes, an untapped source of antibiotic potential? *Antibiotics*. 2020 Feb 18; 9(2):90.
45. Jammalamadaka SN, Sampathkumaran EV, Narayana Murthy VS, Markandeyulu G. Room temperature soft ferromagnetism in the nanocrystalline form of YCo_2 , A well-known bulk Pauli paramagnet. *Applied Physics Letters*. 2008 May 12; 92(19).
46. Das SD, Mohapatra N, Iyer KK, Bapat RD, Sampathkumaran EV. Magnetic behavior of nanocrystalline $ErCo_2$. *Journal of Physics: Condensed Matter*. 2009 Jul 3;21(29):296004.
47. Das SD, Jammalamadaka SN, Iyer KK, Sampathkumaran EV. Magnetic ordering in the fine particles of some bulk Pauli paramagnets. *Physical Review B*. 2009 Jul 1; 80(2):024401.
48. Jammalamadaka SN, Das SD, Chalke BA, Sampathkumaran EV. Magnetic behavior of nanocrystalline $LaMn_2Ge_2$. *Journal of magnetism and magnetic materials*. 2008 Nov 1; 320(21):L129-31.
49. Mukherjee K, Iyer KK, Sampathkumaran EV. Ferromagnetic feature from Mn near room temperature in the fine particles of $GdMn_2Ge_2$ and $TbMn_2Ge_2$. *Europhysics Letters*. 2010 May 5; 90(1):17007.

50. Mukherjee K, Iyer K K and Sampathkumaran E V J. *Phys.: Condens. Matter* 22 29560.
51. Rojas D P, Barquin L F, Espeso, Fernandez J R and Chaboy J 2008 *Phys. Rev. B* 78 094412.
52. Chen Y Y, Yao Y D, Wang C R, Li W H, Chang C L, Lee T K, Hong T M, Ho J C and Pan S F 2000 *Phys. Rev. Lett.* 84 4990
53. Han S W, Booth C H, Bauer E D, Huang P H, Chen Y Y and Lawrence J W 2006 *Phys. Rev. Lett.* 97 0972
54. E V Sampathkumaran *et al* 2011 *J. Phys.: Condens. Matter* **23** 094209
55. Suryanarayana C 2001 *Prog. Mat. Sci.* 46 1
56. de Paula VG, Silva MG, da Silva LM, dos Santos AO, Lang R, Otubo L, Coelho AA, Cardoso LP. Structural disorder effects on the magnetic entropy change of DyCo₂ intermetallic: Mechanical milling and the weakening of the itinerant electron metamagnetism mechanism. *Intermetallics*. 2018 Mar 1; 94:1-9.
57. Griffiths RB. Nonanalytic behavior above the critical point in a random Ising ferromagnet. *Physical Review Letters*. 1969 Jul 7; 23(1):17.
58. Bray AJ. Dynamics of dilute magnets above T_C. *Physical review letters*. 1988 Feb 22; 60(8):720.
59. Salamon MB, Lin P, Chun SH. Colossal magnetoresistance is a Griffiths singularity. *Physical review letters*. 2002 Apr 25; 88(19):197203.
60. Neto AC, Castilla G, Jones BA. Non-Fermi liquid behavior and Griffiths phase in f-electron compounds. *Physical review letters*. 1998 Oct 19; 81(16):3531.

61. Gschneidner KA, Pecharsky VK, Tsokol AO. Recent developments in magnetocaloric materials. Reports on progress in physics. 2005 May 20; 68(6):1479.
62. Duc NH, Anh DK, Brommer PE. Metamagnetism, giant magnetoresistance and magnetocaloric effects in RCo₂-based compounds in the vicinity of the Curie temperature. Physica B: Condensed Matter. 2002 Jul 1;319(1-4):1-8.
J. H. K Buschow (Ed.), Handbook on Magnetic Materials, vol. 12, North-Holland, Amsterdam, 1999, p. 395. (Chapter 4).
63. Banerjee BK. On a generalised approach to first and second order magnetic transitions. Physics letters. 1964 Sep; 12(1):16-7.
64. Sampathkumaran EV, Mohapatra N, Rayaprol S, Iyer KK. Magnetic anomalies in the spin-chain compound Sr₃CuRhO₆: Griffiths-phase-like behavior of magnetic susceptibility. Physical Review B. 2007 Feb 28; 75(5):052412.
65. Fita I, Troyanchuk IO, Zajarniuk T, Iwanowski P, Wisniewski A, Puzniak R. Exchange bias effect and Griffiths phase coexistence in the disordered cobaltite Gd_{0.5}Sr_{0.5}CoO_{3-δ}. Physical Review B. 2018 Dec 28; 98(21):214445.
66. Kumar J, Panja SN, Dengre S, Nair S. Identification of a Griffiths singularity in a geometrically frustrated antiferromagnet. Physical Review B. 2017 Feb 1; 95(5):054401.
67. Tripathi R, Adroja DT, Muro Y, Sharma S, Biswas PK, Namiki T, Kuwai T, Hiroto T, Strydom AM, Sundaresan A, Langridge S. Quantum Griffiths singularity in the stoichiometric heavy-fermion system CeRh₄Al₁₅. Physical Review B. 2023 Oct 23; 108(14):144427.

68. Ślebarski A, Spalek J, Fijałkowski M. Thermodynamic and electrical transport properties of $\text{CeRhSb}_{1-x}\text{Te}_x$ systems: Transition from Kondo insulating to the Griffiths and non-Fermi liquid states. *Journal of Magnetism and Magnetic Materials*. 2023 Dec 1; 587:171239.
69. Tripathi R, Das D, Biswas PK, Adroja DT, Hillier AD, Hossain Z. Quantum Griffiths phase near an antiferromagnetic quantum critical point: Muon spin relaxation study of $\text{Ce}(\text{Cu}_{1-x}\text{Co}_x)_2\text{Ge}_2$. *Physical Review B*. 2019 Jun 17; 99(22):224424.
70. Magen C, Algarabel PA, Morellon L, Araújo JP, Ritter C, Ibarra MR, Pereira AM, Sousa JB. Observation of a Griffiths-like phase in the magnetocaloric compound $\text{Tb}_5\text{Si}_2\text{Ge}_2$. *Physical review letters*. 2006 Apr 26;96(16):167201.

Appendix

The curves of the dc χ (measured in a field of 100 Oe for both ZFC-FC conditions and a field of 5 kOe in ZFC condition), $M(H)$ (measured at various temperatures), heat capacity (measured both in zero field and applied magnetic fields) and the isothermal entropy change (derived from the heat capacity data) are shown in the figures for ball-milled nano-specimens of R_2RhSi_3 ($R = Nd, Er$) and R_4PtAl ($R = Ho, Er$). A comparison of the changes seen in the properties between the bulk and nanoform specimens is also tabulated.

1. Nd_2RhSi_3

Table A.1: Comparison of the magnetic features of the bulk and ball milled Nd_2RhSi_3 .

	Bulk Specimen (for details see chapter 3)	Nanoform Specimen
μ_{eff}	$\sim 5.2 \mu_B$ /f.u. or $\sim 3.7 \mu_B$ per $Nd^{3+} \Rightarrow$ consistent with the theoretical value of Nd^{3+}	$\sim 4.46 \mu_B$ /f.u. or $\sim 3.15 \mu_B$ per $Nd^{3+} \Rightarrow$ lower value may be related to the error in the estimation of mass in the presence of GE varnish
θ_p	~ 0.7 K \Rightarrow Similar in magnitude for ferromagnetic and antiferromagnetic correlations.	~ 1.8 K
Features in 100 Oe ZFC-FC χ -curves	Bifurcation seen in ZFC -FC curves below 40 K, an upturn seen below 16.5 K with a peak at 14.5 K and an additional weak feature in ZFC at 10 K. \Rightarrow Cluster magnetism just above T_C of 16.5 K.	Bifurcation seen in ZFC -FC curves below 18 K, followed by a peak at 11.5 K with an additional weak peak at ~ 3 K in ZFC curve. \Rightarrow Signature of cluster magnetism above T_C of about 16 K is absent.

Features in 5 kOe χ -curves	Sharp jump in χ around 16.5 K with a peak at ~ 6.5 K at low temperatures \Rightarrow An additional transition well below 16.5 K.	Monotonic variation seen in χ , with no signature of long range magnetic ordering down to 2 K. \rightarrow Inhomogeneous magnetism?
$M(H)$	<p>Magnetization curves do not show a tendency to saturate till the highest measured field of 70 kOe, suggesting presence of an antiferromagnetic component and crystal-field effects.</p> <p>Hysteretic behavior (seen in a field range of -20 to +20 kOe) in the magnetically ordered state, with a large coercive field, indicating ferromagnetic component.</p>	<p>No tendency of saturation seen in the $M(H)$, till the highest measured field of 70 kOe, as for bulk form.</p> <p>Hysteretic behavior (as seen from $M(H)$ curves) gets marginally suppressed with the loops seen only in a field range of (-10 to +10 kOe) with reduction in particle size.</p> <p>\Rightarrow Not much change in the magnetic properties below T_C of 16 K.</p>
C versus T	<p>Upturn at 18 K followed by a peak at 15 K, with midpoint at 16.5 K supporting long range magnetic ordering setting in at this temperature.</p> <p>\Rightarrow Field dependence of $C(T)$ curves shifting to low temperatures confirm the antiferromagnetic component as well.</p>	<p>Monotonic variation in the $C(T)$ curves down to 2K, with no feature attributable to long range magnetic ordering in $C(T)$ curves \Rightarrow Inhomogeneous magnetism due to probable size inhomogeneity.</p>

C/T versus T	Additional shoulder around 10 K, shifting to low temperature with increasing magnetic fields. \Rightarrow Supports additional low-temperature feature.	Change of slope seen below 18 K, with a very weak peak like feature around ~ 12 K, which gets suppressed with increasing magnetic fields. This feature may correspond to the shoulder seen around 10 K seen in the bulk specimen.
ΔS	Sign of ΔS stays in negative quadrant with a peak value of -4.5 J/mol K around ~ 16.5 K. \Rightarrow presence of ferromagnetic correlations.	Sign of ΔS stays in negative quadrant for a field of 10 kOe with a broad hump around 30 K followed by a weak peak like feature at low temperature. Peak values gets suppressed to ~ -3 J/mol K. \Rightarrow Indicating the presence of inhomogeneous magnetism.

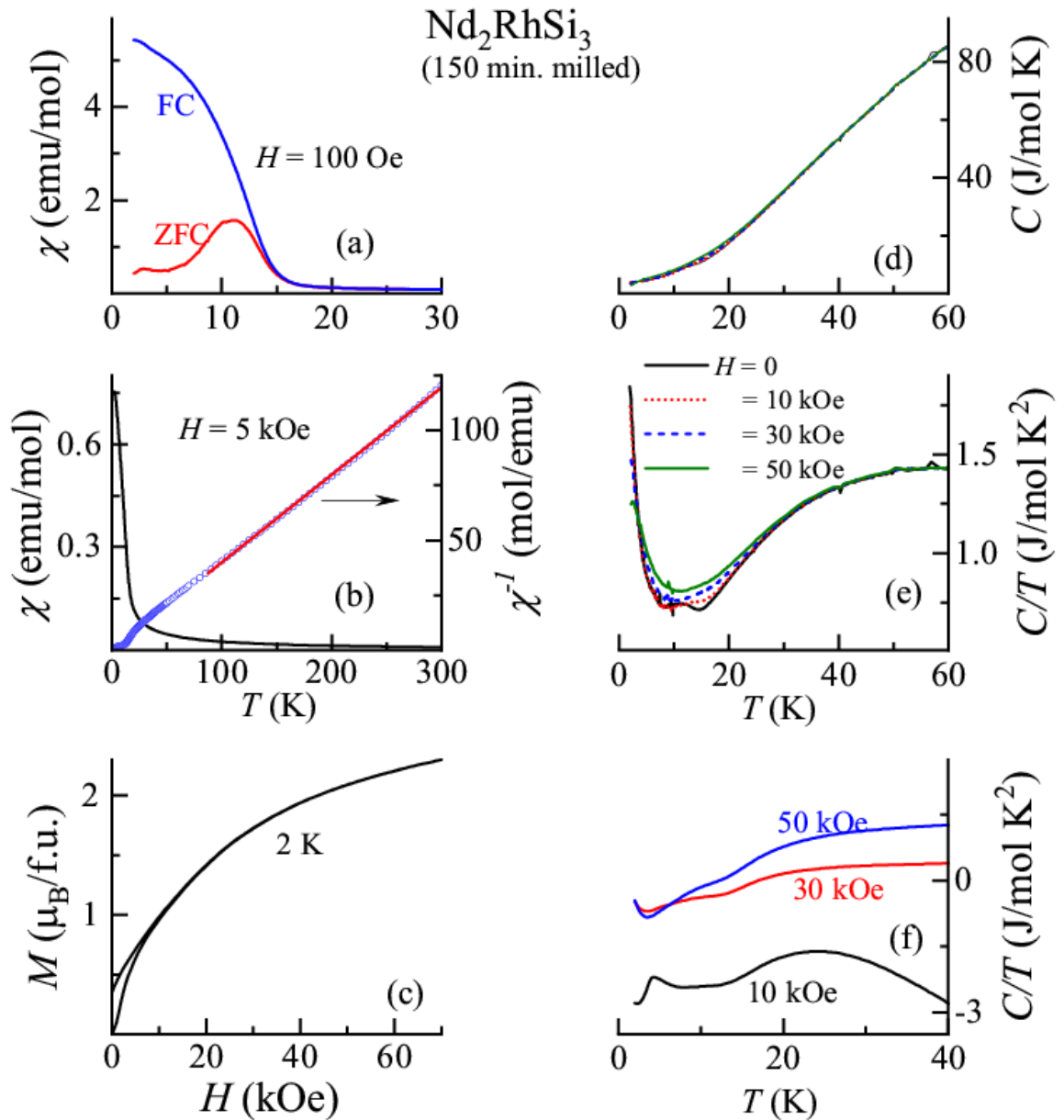


Figure A.1: a) Magnetic susceptibility as a function of temperature obtained in a field of 100 Oe in both zero-field-cooled and field-cooled conditions for nanoform specimen of Nd₂RhSi₃. b) Magnetic susceptibility and inverse of magnetic susceptibility in a field of 5 kOe. Curie-Weiss fitting above 100 K is also shown. c) Isothermal magnetization measured at 2 K. d) Heat-capacity as a function of temperature (<60 K) measured in the presence of external magnetic fields as well. e) Heat-capacity divided by temperature f) Isothermal entropy change as a function of temperature (2-100 K) for different final fields starting from zero-field.

2. Er_2RhSi_3

Table A.2: Comparison of the features of the bulk and ball milled Er_2RhSi_3 .

	Bulk Specimen (for details see chapter 3)	Nanoform Specimen
μ_{eff}	$\sim 13.70 \mu_B$ /f.u. or $\sim 9.69 \mu_B$ per $Er^{3+} \Rightarrow$ consistent with the theoretical value of Er^{3+}	$\sim 12.03 \mu_B$ /f.u. or $\sim 8.50 \mu_B$ per $Er^{3+} \Rightarrow$ lower value may be related to the error in the estimation of mass in the presence of GE varnish
θ_P	~ 1.3 K	~ 0.21 K
Features in 100 Oe ZFC-FC χ -curves	Bifurcation seen in ZFC - FC curves below 5.2 K, with a change of slope at T_N followed by a peak at low temperatures, around 3.5 K \Rightarrow Coexistence of antiferromagnetism and spin glass nature at T_N of 5.2 K.	Weak bifurcation seen in ZFC -FC curves below 5.2 K, with a change of slope and flattening below 4.3 K in ZFC χ -curve. \Rightarrow Essentially no worthwhile change in T_N and the features.
Features in 5 kOe χ curves	Change of slope in χ around 5.2 K followed by an upturn at low temperatures	Sharp change of slope in χ at low temperature with no peak seen till 2 K. \Rightarrow no worthwhile change
$M(H)$	Non hysteretic curves, with 1/3 rd magnetization step at 2 K \Rightarrow Characteristic of partially disordered antiferromagnetism arising	Non hysteretic curves, with 1/3 rd magnetization step getting smeared out with a weak change of slope seen in the same H range.

	due to geometrical frustration.	⇒Smearing possibly due to inhomogeneity in the particle size.
C versus T	Well defined peak at 5.2 K in zero field, with the curves getting suppressed as H is increased ⇒ Supporting antiferromagnetic ordering component.	Well defined peak at 5.2 K in zero field, followed by an upturn and a change in slope at low temperatures, curves get suppressed with increasing H . ⇒ No qualitative change in antiferromagnetism.
ΔS	ΔS sharply changes sign at the onset of magnetic ordering in 10 kOe field, with a positive sign. ⇒ Implying possibility of antiferromagnetic cluster existing before the onset of magnetic ordering. All other curves lie in negative quadrant ⇒ Implying dominant ferromagnetic component at high fields.	ΔS shows a shoulder like feature around $T_N \sim 5$ K. A shoulder at ~ 2.5 K (as in bulk, evident from the 10 kOe data) supporting the presence of an additional feature at a low temperature. This low temperature feature seen as a change of slope even for a field of 30 kOe. All curves lie in negative quadrant implying dominant ferromagnetic component at high fields. ⇒ The results overall support inferences on magnetic ordering observed from the studies on bulk specimen.

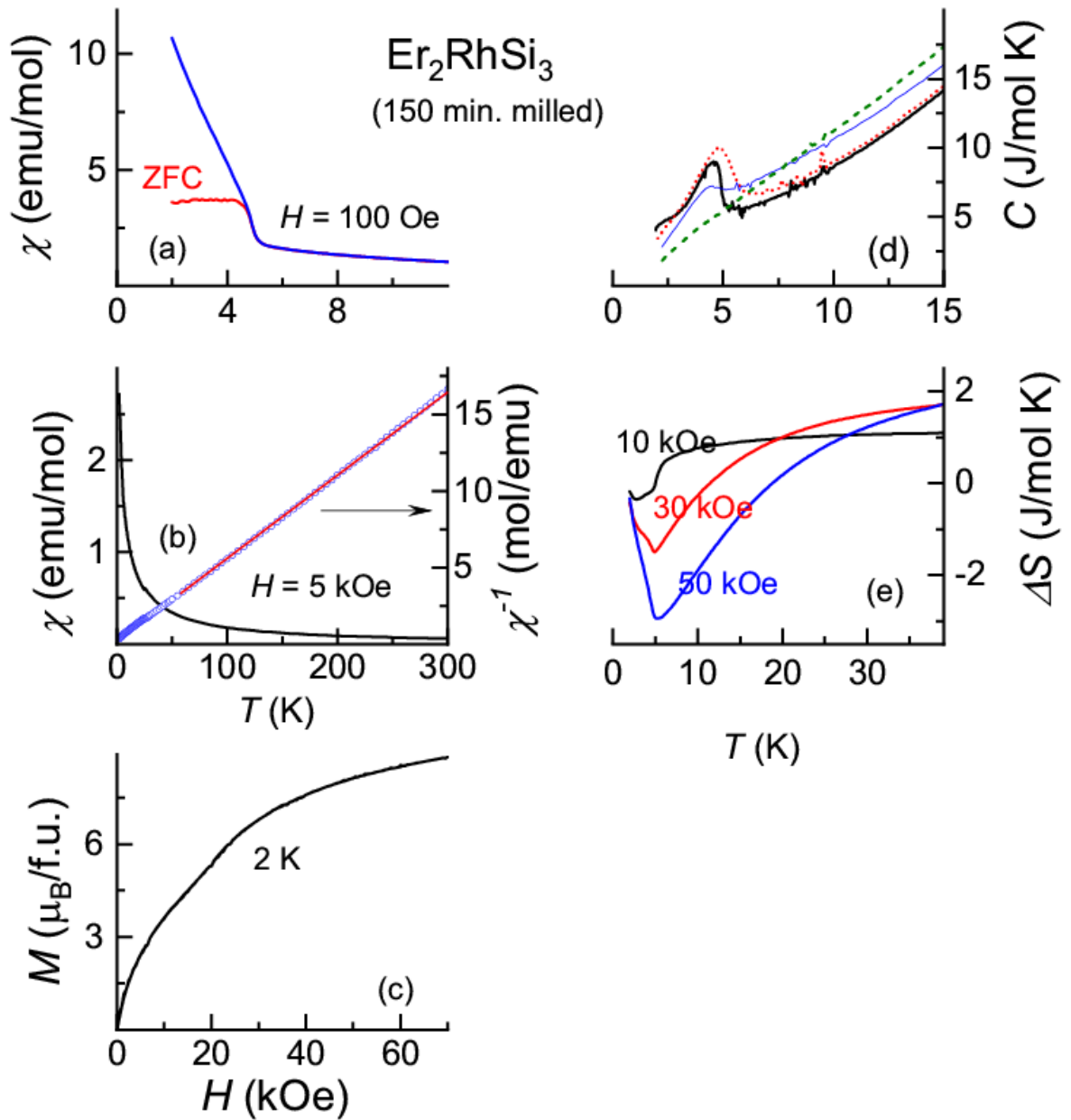


Figure A.2: a) Magnetic susceptibility as a function of temperature obtained in a field of 100 Oe in both zero-field-cooled and field-cooled conditions b) Magnetic susceptibility and inverse of magnetic susceptibility in a field of 5 kOe. Curie-Weiss fitting above 100 K is also shown, see red line through the data points. c) Isothermal magnetization measured at 2 K. d) Heat-capacity as a function of temperature (<15 K) measured in the presence of external magnetic fields as well. e) Isothermal entropy change as a function of temperature (2-40 K) for different final fields starting from zero-field.

3. Ho_4PtAl

Table A.3: Comparison of the features of the bulk and ball milled Ho_4PtAl .

	Bulk Specimen (for details see chapter 4)	Nanoform Specimen
μ_{eff}	$\sim 21.5 \mu_{\text{B}}$ /f.u. or $\sim 10.7 \mu_{\text{B}}$ per $\text{Ho}^{3+} \Rightarrow$ consistent with the theoretical value of Ho^{3+}	$\sim 18.8 \mu_{\text{B}}$ /f.u. or $\sim 9.4 \mu_{\text{B}}$ per $\text{Ho}^{3+} \Rightarrow$ lower value may be related to the error in the estimation of mass in the presence of GE varnish
θ_P	$\sim 19 \text{ K} \Rightarrow$ Positive sign of θ_P indicates the presence of ferromagnetic correlations.	$\sim 15 \text{ K} \Rightarrow$ slightly smaller value in nano-form
Features in 100 Oe ZFC-FC χ -curves	<p>Peak in ZFC curve at $\sim 19 \text{ K}$, followed by a shoulder at 12 K and flattening below 5 K.</p> <p>\Rightarrow Onset of a long-range antiferromagnetic order at 19 K with additional magnetic features at low temperatures.</p> <p>Bifurcation in the ZFC-FC curves below 19 K</p> <p>\Rightarrow Attributed to spin-glass freezing at low temperatures</p>	<p>Bifurcation in the ZFC-FC curves sets in at a higher temperature of $\sim 35 \text{ K}$, in contrast to what is seen for the bulk form.</p> <p>A broad shoulder around $\sim 19 \text{ K}$, with a change of slope and a peak around $\sim 7.5 \text{ K}$.</p> <p>\Rightarrow Inhomogeneous magnetism with spin glass features seen at a higher temperature. (Absence of Griffiths-like feature was verified by H-dependent studies).</p>

Features in 5 kOe χ -curves	Other than the 19 K magnetic ordering, additional features at 12 K and 5 K, are smeared. \Rightarrow Magnetism is sensitive to small applications of magnetic field.	Monotonic variation seen in χ , with no signature of magnetic ordering down to 2 K. \Rightarrow An application of a higher field smears the features seen in low field data similar to the case of bulk specimen.
$M(H)$	Sharp increase in M with initial application of H , at 2 K, indicating tendency towards ferromagnetic alignments. No evidence of saturation of M even for an applied H of 70 kOe, supporting the existence of antiferromagnetic part as well; crystal-field effects also can play a role. Distinct weak hysteretic features seen in $M(H)$ at low temperatures.	No evidence of saturation of M even for an applied H of 70 kOe, as in bulk. Hysteretic nature in $M(H)$ seen at 2 K seems to get suppressed with a reduction in particle size. Coercive field in $M(H)$ is zero as in the case of soft ferromagnets.
C versus T	Well defined peak at 19 K in zero field; peak getting suppressed with increasing H , \Rightarrow Confirming antiferromagnetic component	No feature attributable to magnetic ordering seen till the lowest measured temperature of 2 K. \Rightarrow Inhomogeneous magnetic ordering due to possible size distribution.
ΔS	Peak values of $-\Delta S \sim 12.5$ J/mol K for magnetic field of	Peak value of $-\Delta S \sim 6.5$ J/mol K, gets suppressed

	50 kOe is quite large when compared with other members in the family, with a long tail over a wide T - range.	with a decrease in particle size.
--	---	-----------------------------------

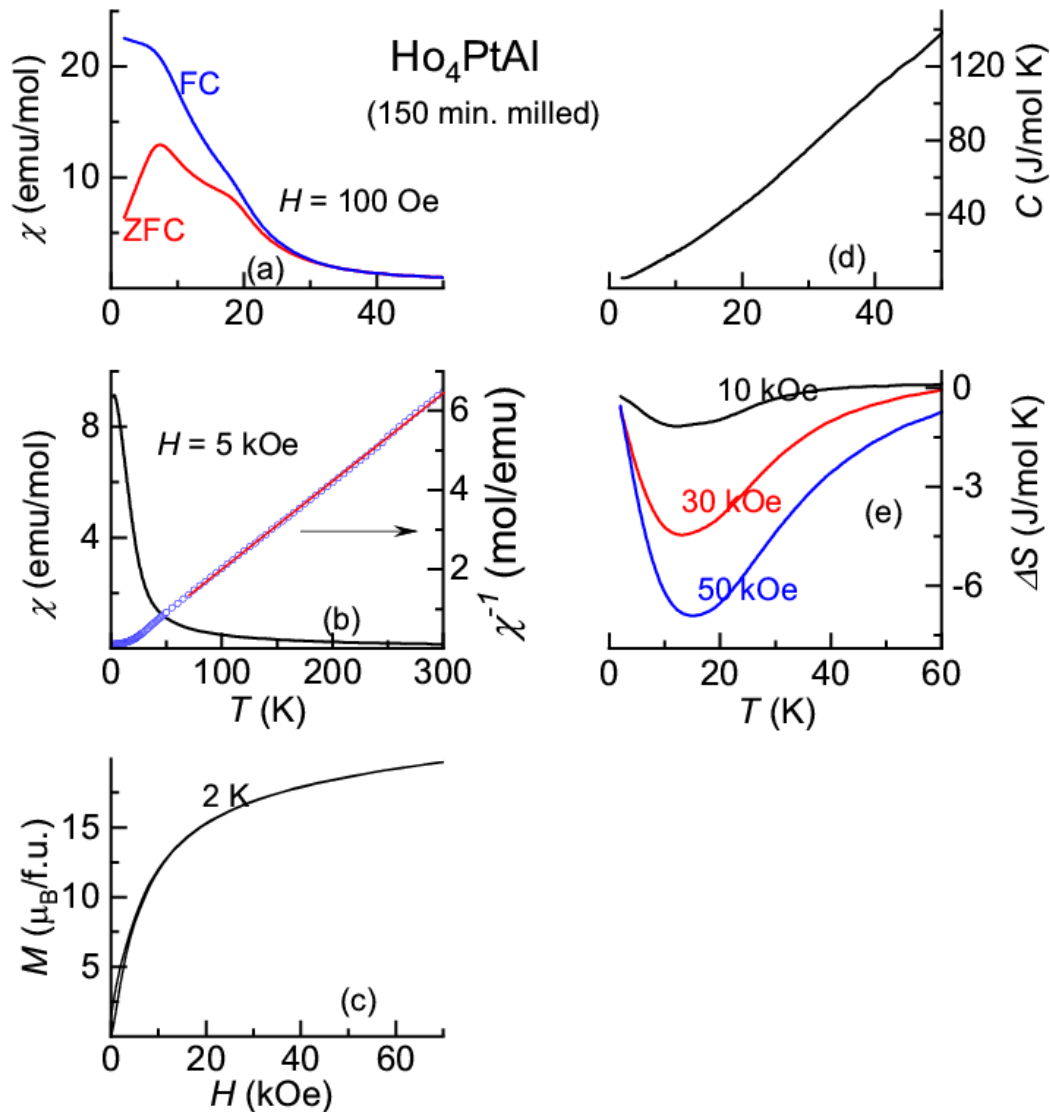


Figure A.3: a) Magnetic susceptibility as a function of temperature obtained in a field of 100 Oe in both zero-field-cooled and field-cooled conditions for nanoform specimen of Ho_4PtAl . b) Magnetic susceptibility and inverse of magnetic susceptibility in a field of 5 kOe. Curie-Weiss fitting above 100 K is also shown. c) Isothermal magnetization measured at 2 K. d) Heat-capacity as a function of temperature (<50 K) measured in the presence of external magnetic fields as well. e) Isothermal entropy change as a function of temperature (2-60 K) for different final fields starting from zero-field.

4. *Er₄PtAl*

Table A.4: Comparison of the features of the bulk and ball milled Er₄PtAl.

	Bulk Specimen (for details see chapter 4)	Nanoform Specimen
μ_{eff}	$\sim 19.7 \mu_B/f.u.$ or $\sim 9.8 \mu_B$ per $Er^{3+} \Rightarrow$ consistent with the theoretical value of Er^{3+}	$\sim 16.6 \mu_B/f.u.$ or $\sim 8.3 \mu_B$ per $Er^{3+} \Rightarrow$ lower value may be related to the error in the estimation of mass in the presence of GE varnish
θ_P	$\sim 12.6 K \Rightarrow$ Positive sign of θ_P indicates the presence of ferromagnetic correlations.	$\sim 4.6 K \Rightarrow$ marginal change seen in the values of θ_P . Positive sign reveal the existence of ferromagnetic correlations.
Features in 100 Oe ZFC-FC χ -curves	Peak in ZFC curve at $\sim 12 K$, with additional feature around $5 K$. \Rightarrow Onset of a long-range antiferromagnetic order at $5 K$ with additional magnetic features at low temperatures. Bifurcation in the ZFC-FC χ -curves below $12 K$. \Rightarrow Attributed to spin-glass freezing.	Bifurcation in the ZFC-FC curves seen at a higher temperature of $\sim 20 K$ with a broad shoulder at $14 K$, as in the case of Ho_4PtAl , with a change of slope and a prominent peak around $\sim 3.6 K$. \Rightarrow Spin glass feature possibly develops at a higher temperature, with some evidence of magnetic ordering.
Features in 5 kOe χ -curves.	Only the $12 K$ magnetic ordering feature is seen while	Change of slope in χ around $20 K$ followed by a sharp upturn at low temperatures.

	<p>the other feature at 5 K is smeared.</p> <p>⇒ Magnetism is sensitive to external magnetic field.</p>	<p>Features attributable to magnetic ordering as seen in 100 Oe are smeared in 5 kOe.</p> <p>⇒ Magnetism is sensitive to external magnetic field.</p>
$M(H)$	<p>Increase in M in response to initial application of magnetic fields. No evidence of saturation of M even for an applied H of 70 kOe, as in previous cases. $M(H)$ is non-hysteretic at all temperatures.</p>	<p>$M(H)$ shows a sharp increase in response to initial magnetic fields with no tendency to saturate even for an applied H of 70 kOe.</p> <p>$M(H)$ shows a non-hysteretic nature at all temperatures.</p> <p>⇒ Essentially no change with respect to the bulk form.</p>
C versus T	<p>Well defined peak at 12 K in zero field, with curves shifting to low temperatures as H is increased</p> <p>⇒ Consistent with antiferromagnetic component.</p>	<p>No feature attributable to magnetic ordering seen till the lowest measured temperature of 2 K. Only a weak hump seen in the zero-field data below 5 K.</p> <p>⇒ There must be a distribution in the magnetic ordering temperature, due to particle size inhomogeneity.</p>
C/T versus T	<p>In addition to the 12 K feature, there is a sharp anomaly (shoulder like feature) around 5 K.</p>	<p>Sharp change of slope followed by an upturn below 5 K and the upturn gets suppressed with increasing magnetic fields.</p>

		⇒Sensitivity to H suggests the presence of magnetic correlations, though the λ -anomaly is smeared due to inhomogeneity.
ΔS	A large value of $\Delta S \sim 18.5$ J/mol K for a magnetic field of 50 kOe, compared with other members in the family, with a long tail over a wide T - range.	Value of $\Delta S \sim 4.5$ J/mol K for a magnetic field of 50 kOe, gets suppressed with a reduction in particle size.

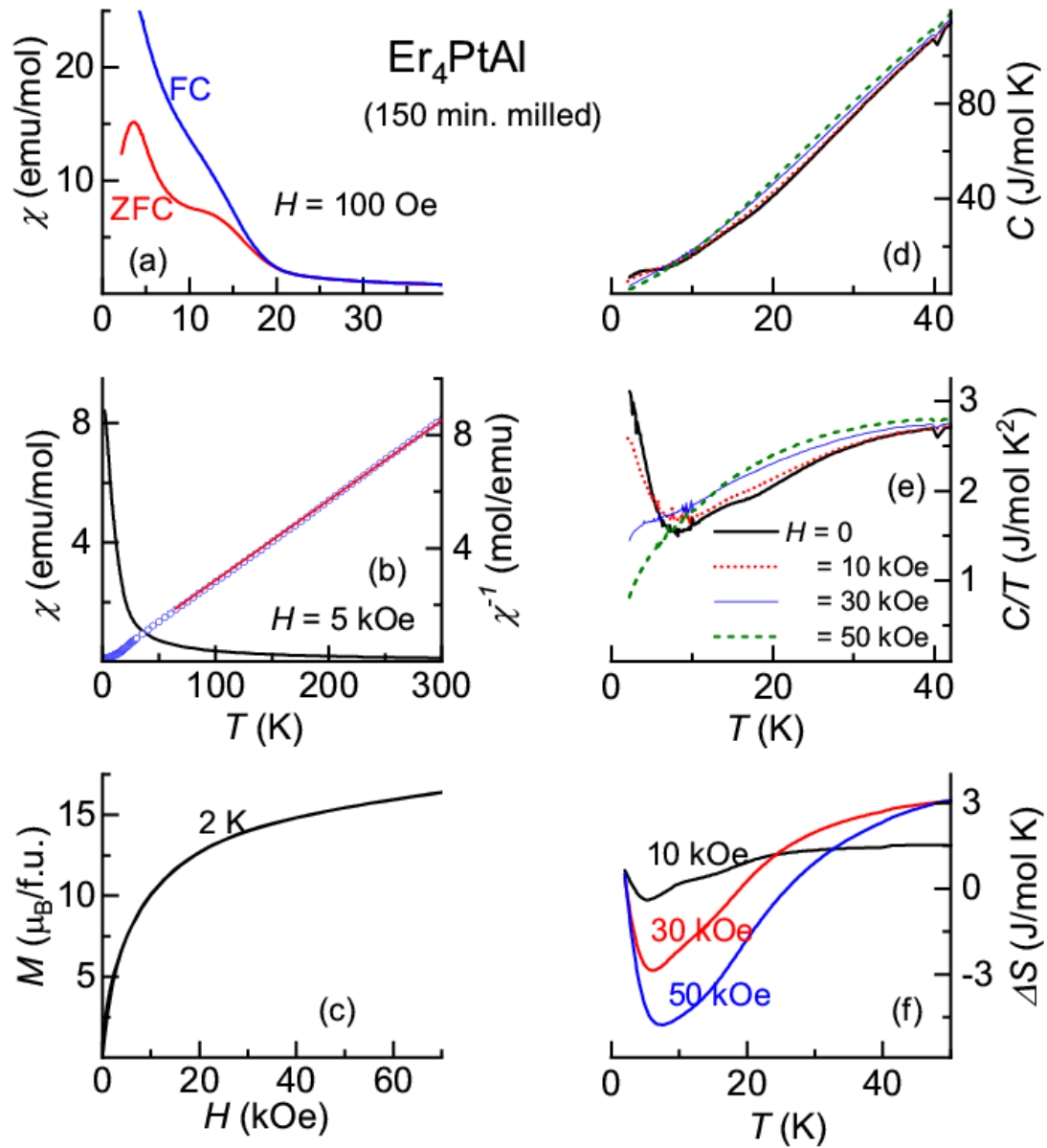


Figure A.4: a) Magnetic susceptibility as a function of temperature obtained in a field of 100 Oe in both zero-field-cooled and field-cooled conditions for nanoform specimen of Er_4PtAl . b) Magnetic susceptibility and inverse of magnetic susceptibility in a field of 5 kOe. Curie-Weiss fitting above 100 K is also shown by a red line. c) Isothermal magnetization measured at 2K d) Heat-capacity as a function of temperature (<40 K) measured in the presence of external magnetic fields as well. e) Heat-capacity divided by temperature. f) Isothermal entropy change as a function of temperature (2-50 K) for different final fields starting from zero-field.

Conclusion

In the summary, magnetic properties of the rare-earth intermetallics studied in chapters 3 and 4 are studied in the ball-milled nanoforms. A finding common to all these compounds in the nanoform is that magnetism becomes inhomogeneous (as indicated by the smearing of λ -anomalies due to magnetic ordering in heat-capacity), attributable to a distribution in particle sizes. However, for the compounds reported in this Appendix, there is no result leading to a conceptual change in magnetism, unlike, in Dy_4RhAl , in which case the reduction in particle size induces a Griffiths phase like behavior (as indicated by magnetic-field dependent inverse susceptibility plots). However, subtle changes as noted in the tables occur. For instance, a reduction in the particle size of Nd_2RhSi_3 suppresses cluster glass features observed above the magnetic ordering temperature, while in the case of Er_2RhSi_3 , there was no significant effect of particle size reduction on the nature of magnetism, except smearing of the step-like feature (attributable to an inhomogeneity in particle size) in isothermal magnetization due to the PDA magnetism arising from geometrical frustration; in the case of Ho_4PtAl and Er_4PtAl , a reduction in the particle size shifts possible onset of (spin)glassy nature to a higher temperature (with respect to respective magnetic ordering temperatures), as indicated by the bifurcation temperature of the ZFC-FC susceptibility curves. In general, the peak values of the isothermal entropy change noted for the bulk form get suppressed with the reduction in particle size.

Thus, the results overall suggest that a reduction in particle size may in some cases lead to a conceptual change in magnetic behavior, whereas in some other cases, the changes could be minor, reinforcing the fact that one needs to be cautious while employing nanoparticles for medicinal applications based on the properties of the bulk forms.

List of Publications (relevant to Thesis)

- 1) Exotic Nd 4f electron magnetism in Nd₂RhSi₃
E. V. Sampathkumaran, **Kartik K Iyer**, Sudhindra Rayaprol, and Kalobaran Maiti.
Journal of Magnetism and Magnetic Materials, (Communicated).
- 2) Emergent Griffiths-phase-like behavior in the ball-milled nanocrystalline Dy₄RhAl and its implication
KK Iyer, K Maiti, S Rayaprol, BA Chalke, EV Sampathkumaran
Journal of Magnetism and Magnetic Materials 597, 172018, 2024.
- 3) Emergence of partially disordered antiferromagnetism and isothermal magnetization plateau due to geometrical frustration in a metallic compound, Er₂RhSi₃
Kartik K Iyer, Kalobaran Maiti, Sudhindra Rayaprol, Ram Kumar, S. Mattepanavar, S. Dodamani, and E.V. Sampathkumaran
Physical Review Materials 7 (10), L101401, 2023.
- 4) Magnetic and Transport Anomalies and Large Magnetocaloric Effect in Cubic R₄PtAl (R = Ho and Er)
KK Iyer, S Rayaprol, R Kumar, S Mattepanavar, S Dodamani, K Maiti, & E.V. Sampathkumaran
Magnetochemistry 9 (3), 85 2023.
- 5) Magnetic behavior of cubic Dy₄RhAl with respect to isostructural Dy₄PtAl, revealing a novel 4f d-band interaction
KK Iyer, S Mattepanavar, S Dodamani, K Maiti, EV Sampathkumaran
Journal of Magnetism and Magnetic Materials, 170406, 2023.
- 6) Magnetic Anomalies in AlB₂-type Hexagonal Ho₂RhSi₃ and Er₂RhSi₃
Kartik K Iyer, K. Maiti, Sudhindra Rayaprol, Ram Kumar, S. Mattepanavar, S. Dodamani, and E.V. Sampathkumaran
AIP Conference proceedings 2995 (1) 2023.
- 7) Pressure-induced anomalies in the magnetic transitions of the exotic multiferroic material Tb₂BaNiO₅
KK Iyer, R Kumar, S Rayaprol, K Maiti, EV Sampathkumaran
Physical Review Materials 5 (8), 084401 2021.

List of Publications

- 1) Exotic Nd 4f electron magnetism in Nd₂RhSi₃
E. V. Sampathkumaran, **Kartik K Iyer**, Sudhindra Rayaprol, and Kalobaran Maiti.
Journal of Magnetism and Magnetic Materials, (Communicated).
- 2) Emergent Griffiths-phase-like behaviour in the ball-milled nanocrystalline Dy₄RhAl and its implication
KK Iyer, K Maiti, S Rayaprol, BA Chalke, EV Sampathkumaran
Journal of Magnetism and Magnetic Materials 597, 172018, 2024.
- 3) Exceptional magnetic anomalies in TbIrIn₅
AA Biswal, **KK Iyer**, K Maiti
(communicated)
- 4) Emergence of partially disordered antiferromagnetism and isothermal magnetization plateau due to geometrical frustration in a metallic compound, Er₂RhSi₃
Kartik K Iyer, Kalobaran Maiti, Sudhindra Rayaprol, Ram Kumar, S. Mattepanavar, S. Dodamani, and E.V. Sampathkumaran
Physical Review Materials 7 (10), L101401, 2023.
- 5) Magnetic and Transport Anomalies and Large Magnetocaloric Effect in Cubic R₄PtAl (R = Ho and Er)
KK Iyer, S Rayaprol, R Kumar, S Mattepanavar, S Dodamani, K Maiti, & E.V. Sampathkumaran
Magnetochemistry 9 (3), 85 2023.
- 6) Magnetic behavior of cubic Dy₄RhAl with respect to isostructural Dy₄PtAl, revealing a novel 4f d-band interaction
KK Iyer, S Mattepanavar, S Dodamani, K Maiti, EV Sampathkumaran
Journal of Magnetism and Magnetic Materials, 170406, 2023.
- 7) Magnetic Anomalies in AlB₂-type Hexagonal Ho₂RhSi₃ and Er₂RhSi₃
Kartik K Iyer, K. Maiti, Sudhindra Rayaprol, Ram Kumar, S. Mattepanavar, S. Dodamani, and E.V. Sampathkumaran
AIP Conference proceedings 2995 (1) 2023.
- 8) Evolution of extremely large magnetoresistance in a Weyl semimetal, with Ni-doping
A Singh, S Sasmal, **KK Iyer**, A Thamizhavel, K Maiti
Physical Review Materials 6 (12), 124202 2022

- 9) Magnetic-field induced melting of long-range magnetic order in Tb_5Si_3 : A possible case for Kitaev physics
*S Rayaprol, **KK Iyer**, A Hoser, M Reehuis, AV Morozkin, V Siruguri, K Maiti, ...*
J. Phys.: Condens. Matter (35) 305801
- 10) Extremely High magnetoresistance and quantum Oscillation study of WTe_2 , Weyl Semimetal
*A Singh, S Sasmal, **KK Iyer**, A Thamizhavel, K Maiti*
Journal of Physics: Conference Series 2164 (1), 012061 2022
- 11) Anomalies in the temperature evolution of Dirac states in the topological crystalline insulator SnTe
*A Maiti, RP Pandeya, B Singh, **KK Iyer**, A Thamizhavel, K Maiti*
Physical Review B 104 (19), 195403, 2021
- 12) Pressure-induced anomalies in the magnetic transitions of the exotic multiferroic material Tb_2BaNiO_5
***KK Iyer**, R Kumar, S Rayaprol, K Maiti, EV Sampathkumaran*
Physical Review Materials 5 (8), 084401 2021
- 13) Competing magnetic interactions and magnetoresistance anomalies in cubic intermetallic compounds, and enhanced magnetocaloric effect for the Tb case
*R Kumar, **KK Iyer**, PL Paulose, EV Sampathkumaran*
Physical Review Materials 5 (5), 054407 2021
- 14) Origin of destruction of multiferroicity in Tb_2BaNiO_5 by Sr doping and its implications
*R Kumar, S Rajput, T Maitra, A Hoser, S Rayaprol, SK Upadhyay, **KK Iyer**, E.V. Sampathkumaran*
Journal of Alloys and Compounds 862, 158514 2021
- 15) Insight into exotic multiferroicity of Tb_2BaNiO_5 through neutron diffraction studies
*R Kumar, **KK Iyer**, S Rayaprol, EV Sampathkumaran, DT Adroja, A Hoser*
Proceedings of the seventh conference on neutron scattering-programme 2021

- 16) Magnetic behavior of $\text{HfMnMo}_3\text{O}_{12}$, a material exhibiting negative thermal expansion
KK Iyer, R Kumar, EV Sampathkumaran
AIP Conference Proceedings 2265 (1), 030562 2020
- 17) Ferromagnetism to spin-glass transition and magneto transport anomalies in Dy_4PtAl
R Kumar, KK Iyer, PL Paulose, EV Sampathkumaran
AIP Conference Proceedings 2265 (1), 030509, 2020
- 18) Magnetic and transport anomalies in R_2RhSi_3 ($\text{R} = \text{Tb}$, and Dy) resembling those of the exotic magnetic material
R Kumar, KK Iyer, PL Paulose, EV Sampathkumaran
Physical Review B 101 (14), 144440 2020
- 19) Reentrant spin-glass and transport behavior of Gd_4PtAl , a compound with three sites for Gd
R Kumar, J Sharma, KK Iyer, EV Sampathkumaran
Journal of Magnetism and Magnetic Materials 490, 165515, 2019
- 20) Spin-glass features at multiple temperatures and transport anomalies in Tb_4PtAl
R Kumar, KK Iyer, PL Paulose, EV Sampathkumaran
Journal of Applied Physics 126 (12), 123906 2019
- 21) Neutron diffraction study of a metallic kagome lattice, $\text{Tb}_3\text{Ru}_4\text{Al}_{12}$
S Rayaprol, A Hoser, KK Iyer, SK Upadhyay, EV Sampathkumaran
Journal of Magnetism and Magnetic Materials 477, 83-87, 2019
- 22) Existence of a critical canting angle of magnetic moments to induce multiferroicity in the Haldane spin-chain system $\text{Tb}_2\text{BaNiO}_5$
R Kumar, S Rayaprol, S Rajput, T Maitra, DT Adroja, KK Iyer, and E.V. Sampathkumaran
Physical Review B 99 (10), 100406, 2019
- 23) Anisotropic re-entrant spin-glass features in a metallic kagome lattice, $\text{Tb}_3\text{Ru}_4\text{Al}_{12}$
EV Sampathkumaran, KK Iyer, SK Upadhyay, AV Andreev
Solid State Communications 288, 64-67, 2019
- 24) Eu valence transition behavior in the nano form of EuPd_2Si_2
KK Iyer, T Basu, PL Paulose, EV Sampathkumaran
Journal of Magnetism and Magnetic Materials 465, 515-518, 2018

- 25) Dielectric and multiferroic behavior in $\text{Sm}_2\text{BaNiO}_5$, a Haldane spin-chain compound
SK Upadhyay, KK Iyer, EV Sampathkumaran
 Physica B: Condensed Matter 524, 123-126, 2017
- 26) Magnetic behavior of new compounds, Gd_3RuSn_6 and Tb_3RuSn_6
SK Upadhyay, KK Iyer, EV Sampathkumaran
 Journal of Magnetism and Magnetic Materials 441, 180-187, 2017
- 27) Magnetic behavior of metallic kagome lattices, $\text{Tb}_3\text{Ru}_4\text{Al}_{12}$ and $\text{Er}_3\text{Ru}_4\text{Al}_{12}$
SK Upadhyay, KK Iyer, EV Sampathkumaran
 Journal of Physics: Condensed Matter 29 (32), 325601, 2017
- 28) Pyrocurrent anomalies and intrinsic magnetodielectric behavior near room temperature in $\text{Li}_2\text{Ni}_2\text{Mo}_3\text{O}_{12}$, a compound with distorted honeycomb and spin-chains
SK Upadhyay, KK Iyer, S Gohil, S Ghosh, PL Paulose and E.V. Sampathkumaran
 Scientific reports 7 (1), 1-9, 2017
- 29) Magnetic behavior of $\text{Li}_3\text{Co}_2\text{RuO}_6$
SK Upadhyay, KK Iyer, EV Sampathkumaran
 AIP Conference Proceedings 1832 (1), 130001, 2017
- 30) Re-entrant spin-glass freezing and magneto-dielectric behaviour of $\text{Li}_3\text{NiRuO}_5$, a layered rock-salt related oxide
SK Upadhyay, KK Iyer, S Rayaprol, V Siruguri, EV Sampathkumaran
 Journal of Materials Chemistry C 5 (21), 5163-5169, 2017
- 31) Insight into the magnetism of a distorted Kagome lattice, $\text{Dy}_3\text{Ru}_4\text{Al}_{12}$, based on polycrystalline studies
V Chandragiri, KK Iyer, EV Sampathkumaran
 Intermetallics 76, 26-32, 2016
- 32) A rock-salt-type Li-based oxide, $\text{Li}_3\text{Ni}_2\text{RuO}_6$, exhibiting a chaotic ferrimagnetism with cluster spin-glass dynamics and thermally frozen charge carriers
SK Upadhyay, KK Iyer, S Rayaprol, PL Paulose, EV Sampathkumaran
 Scientific reports 6 (1), 1-10, 2016

- 33) Dielectric anomalies and magnetodielectric coupling behavior of single crystalline $\text{Ca}_3\text{Co}_2\text{O}_6$, a geometrically frustrated magnetic spin-chain system
*T Basu, **KK Iyer**, PL Paulose, EV Sampathkumaran*
 Journal of Alloys and Compounds 675, 364-369, 2016
- 34) Magnetism of a rhombohedral-type pyrochlore-derived Kagome series, $\text{Mn}_2\text{R}_3\text{Sb}_3\text{O}_{14}$ (R= Rare-earths)
*V Chandragiri, **KK Iyer**, K Maiti, EV Sampathkumaran*
 Materials Research Express 3 (6), 066102, 2016
- 35) Magnetic behavior of $\text{Gd}_3\text{Ru}_4\text{Al}_{12}$, a layered compound with distorted kagomé net
*V Chandragiri, **KK Iyer**, EV Sampathkumaran*
 Journal of Physics: Condensed Matter 28 (28), 286002, 2016
- 36) Spin-glass behavior and pyroelectric anomalies in a new lithium-based oxide, $\text{Li}_3\text{FeRuO}_5$
*SK Upadhyay, PL Paulose, **KK Iyer**, EV Sampathkumaran*
 Physical Chemistry Chemical Physics 18 (33), 23348-23353, 2016
- 37) Enhanced magnetic ordering temperature and dielectric behavior in off-stoichiometric $\text{Ca}_3\text{Cu}_{1-x}\text{Mn}_{1+x}\text{O}_6$ ($x= 0.07$)
*S Rayaprol, SD Kaushik, **KK Iyer**, EV Sampathkumaran*
 Solid State Communications 223, 67-73, 2015
- 38) Magnetic and magneto transport behavior of RFe_5Al_7 (R= Gd and Dy): Observation of reentrant inverse-magnetocaloric phenomenon and asymmetric magnetoresistance behavior
*V Chandragiri, **KK Iyer**, EV Sampathkumaran*
 Physical Review B 92 (1), 014407, 2015
- 39) Dielectric and magnetodielectric behavior of polycrystalline $\text{Ca}_3\text{CoRhO}_6$, a geometrically frustrated magnetic system
***KK Iyer**, T Basu, K Singh, EV Sampathkumaran*
 AIP Conference Proceedings 1665 (1), 140045, 2015
- 40) Anisotropic magnetodielectric coupling behavior of $\text{Ca}_3\text{Co}_{1.4}\text{Rh}_{0.6}\text{O}_6$ due to geometrically frustrated magnetism
*T Basu, **KK Iyer**, K Singh, K Mukherjee, PL Paulose, EV Sampathkumaran*
 Applied Physics Letters 105 (10), 2014

- 41) Anisotropic magnetodielectric coupling behavior of $\text{Ca}_3\text{Co}_{1.4}\text{Rh}_{0.6}\text{O}_6$ due to geometrically frustrated magnetism
*T Basu, **KK Iyer**, K Singh, K Mukherjee, PL Paulose, EV Sampathkumaran*
 Applied Physics Letters 105 (10), 102912, 2014
- 42) A reentrant phenomenon in magnetic and dielectric properties of $\text{Dy}_2\text{BaNiO}_5$ and an intriguing influence of external magnetic field
*T Basu, PL Paulose, **KK Iyer**, K Singh, N Mohapatra, S Chowki, B Gonde, ...*
 Journal of Physics: Condensed Matter 26 (17), 172202, 2014
- 43) Novel dielectric anomalies due to spin-chains above and below Néel temperature in $\text{Ca}_3\text{Co}_2\text{O}_6$
*T Basu, **KK Iyer**, K Singh, EV Sampathkumaran*
 Scientific reports 3 (1), 1-6, 2013
- 44) Magnetoelectric coupling in the Haldane spin-chain system $\text{Dy}_2\text{BaNiO}_5$
*K Singh, T Basu, S Chowki, N Mahapatra, **KK Iyer**, PL Paulose, ...*
 Physical Review B 88 (9), 094438, 2013
- 45) Magnetic study under external high pressure and magnetic field in low dimensional honeycomb lattice $\text{In}_3\text{Cu}_2\text{VO}_9$
***KK Iyer**, T Basu, AK Singh, K Mukherjee, PL Paulose, ...*
 AIP Conference Proceedings 1536 (1), 1049-1050, 2013
- 46) Robust nature of frustrated antiferromagnetism in ACrO_2 (A= Pd,Li) compounds
*AK Singh, T Basu, **KK Iyer**, K Mukherjee, PL Paulose & E.V. Sampathkumaran*
 AIP Conference Proceedings 1536 (1), 1039-1040, 2013
- 47) Electronic transport minimum in SmCuAs_2 at low temperatures and structural anomalies
*K Sengupta, **KK Iyer**, R Ranganathan, EV Sampathkumaran, T Doert.*
 Solid state communications 159, 29-31, 2013
- 48) Microscopic evidence for f localization with reduced particle size in correlated electron system CePd_3
*SK Mohanta, SN Mishra, **KK Iyer**, EV Sampathkumaran*
 Physical Review B 87 (12), 125125, 2013
- 49) Superparamagnetism in nanocrystalline: Bulk magnetization and TDPAC studies
*SN Mishra, SK Mohanta, SM Davane, **K Iyer**, EV Sampathkumaran*
 AIP Conference Proceedings 1512 (1), 196-197, 2013

- 50) Magnetodielectric properties of frustrated antiferromagnet LiCrO_2
*AK Singh, K Singh, T Basu, **KK Iyer**, PL Paulose, EV Sampathkumaran*
 AIP Conference Proceedings 1512 (1), 1274-1275, 2013
- 51) Destruction of magnetic frustration by a partial replacement of Ca by Gd in a spin chain compound $\text{Ca}_3\text{Co}_2\text{O}_6$
*T Basu, **KK Iyer**, PL Paulose, EV Sampathkumaran*
 AIP Conference Proceedings 1512 (1), 1150-1151, 2013
- 52) Unusual pressure response of electronic transport properties of a Kondo insulator CeRu_4Sn_6
*K Sengupta, **KK Iyer**, R Ranganathan, EV Sampathkumaran*
 Journal of Physics: Conference Series 377 (1), 012029, 2012
- 53) The nature of 4f electron magnetism in the diluted ferromagnetic Kondo lattice, CeIr_2B_2
*K Mukherjee, **KK Iyer**, EV Sampathkumaran*
 Journal of Physics: Condensed Matter 24 (26), 266006, 2012
- 54) Observation of spin glass-like behavior in fine particles of Nd_2PdSi_3
*K Mukherjee, T Basu, **KK Iyer**, EV Sampathkumaran*
 AIP Conference Proceedings 1447 (1), 1097-1098, 2012
- 55) Magnetic behavior of nano-crystalline ruthenium perovskites, CaRuO_3 and SrRuO_3
***KK Iyer**, N Mohapatra, EV Sampathkumaran*
 AIP Conference Proceedings 1447 (1), 1157-1158, 2012
- 56) Magnetoresistance and magnetocaloric effect in Er_5Si_3
*N Mohapatra, K Mukherjee, **KK Iyer**, EV Sampathkumaran*
 AIP Conference Proceedings 1447 (1), 1165-1166, 2012
- 57) Contrasting magnetic behavior of fine particles of some Kondo lattices
*K Mukherjee, **KK Iyer**, EV Sampathkumaran*
 Solid state communications 152 (7), 606-611, 2012
- 58) Magnetic anomalies in single crystalline Tb_5Si_3
***KK Iyer**, K Mukherjee, PL Paulose, EV Sampathkumaran, Y Xu, W Löser*
 Solid state communications 152 (6), 522-524, 2012

- 59) Magnetic anomalies in CeIn₂
*K Mukherjee, **KK Iyer**, EV Sampathkumaran*
 Journal of Physics: Condensed Matter 24 (9), 096006, 2012
- 60) A first-order magnetic phase transition near 15 K with novel magnetic-field-induced effects in Er₅Si₃
*N Mohapatra, K Mukherjee, **KK Iyer**, EV Sampathkumaran*
 Journal of Physics: Condensed Matter 23 (49), 496001, 2011
- 61) 4 *f* hybridization effect on the magnetism of Nd₂PdSi₃
*K Mukherjee, T Basu, **KK Iyer**, EV Sampathkumaran*
 Physical Review B 84 (18), 184415, 2011
- 62) Evolution of a metastable phase with a magnetic phase coexistence phenomenon and its unusual sensitivity to magnetic field cycling in the alloys Tb_{5-x}Lu_xSi₃ (x ≤ 0.7)
*K Mukherjee, **KK Iyer**, EV Sampathkumaran*
 Journal of Physics: Condensed Matter 23 (20), 206002, 2011
- 63) Magnetism of fine particles of Kondo lattices, obtained by high-energy ball-milling
*EV Sampathkumaran, K Mukherjee, **KK Iyer**, N Mohapatra, SD Das*
 Journal of Physics: Condensed Matter 23 (9), 094209, 2011
- 64) Enhanced electrical resistance at the field-induced magnetic transitions in some non-stoichiometric and stoichiometric Tb-based ternary germanides
*K Mukherjee, **KK Iyer**, EV Sampathkumaran*
 Journal of Physics: Condensed Matter 23 (6), 066003, 2011
- 65) Transport and magnetic behavior under pressure and high-resolution photoemission studies of Ce₂Rh_{0.7}Co_{0.3}Si₃, an alloy on the verge of quantum
*K Mukherjee, **KK Iyer**, S Patil, K Maiti, EV Sampathkumaran*
 Journal of Physics. Conference Series (Online) 273, 012010, 2011
- 66) Physical Properties of Eu₃Ba₂Mn₂Cu₂O₁₂
*N Kumar, K Singh, NK Gaur, S Rayaprol, SD Kaushik, A Dogra, G Anjum, **KK Iyer** & E.V. Sampathkumaran.*
 AIP Conference Proceedings 1313 (1), 2010

- 67) Magnetic behavior of bulk and fine particles of $\text{RCr}_2\text{Si}_2\text{C}$ (R= La, Ce) compounds: possible magnetic ordering from Cr
*K Mukherjee, **KK Iyer**, EV Sampathkumaran*
Journal of Physics: Condensed Matter 22 (29), 295603, 2010
- 68) Anomalous butterfly-shaped magnetoresistance loops in the alloy Tb_4LuSi_3
*K Mukherjee, SD Das, N Mohapatra, **KK Iyer**, EV Sampathkumaran*
Physical Review B 81 (18), 184434, 2010
- 69) Ferromagnetic feature from Mn near room temperature in the fine particles of GdMn_2Ge_2 and TbMn_2Ge_2
*K Mukherjee, **KK Iyer**, EV Sampathkumaran*
EPL (Europhysics Letters) 90 (1), 17007, 2010
- 70) Raman study of $\text{Ca}_3\text{Co}_2\text{O}_6$ single crystals
*G Smita, **KK Iyer**, P Aswathi, S Ghosh, EV Sampathkumaran*
Journal of Applied Physics 108 (10), 103517_1-103517_5, 2010
- 71) Influence of pressure on the magnetic behavior and the anomalous magnetoresistance in Tb_5Si_3
*N Mohapatra, SD Das, K Mukherjee, **KK Iyer**, EV Sampathkumaran*
Physical Review B 80 (21), 214425, 2009
- 72) Sharp fall of electrical resistance for a small application of magnetic field on a metastable form of a compound, Tb_5Si_3 , under pressure
***KK Iyer**, EV Sampathkumaran*
Applied Physics Letters 95 (14), 142504, 2009
- 73) Magnetic anomalies in nanocrystalline $\text{Ca}_3\text{CoRhO}_6$, a geometrically frustrated spin-chain compound
*N Mohapatra, **KK Iyer**, BA Chalke, EV Sampathkumaran*
Solid state communications 149 (39-40), 1641-1645, 2009
- 74) Magnetic behavior of nanocrystalline ErCo_2
*SD Das, N Mohapatra, **KK Iyer**, RD Bapat, EV Sampathkumaran*
Journal of Physics: Condensed Matter 21 (29), 296004, 2009
- 75) Magnetic ordering in the fine particles of some bulk Pauli paramagnets
*SD Das, SN Jammalamadaka, **KK Iyer**, EV Sampathkumaran*
Physical Review B 80 (2), 024401, 2009

- 76) Magnetic behavior of nanocrystals of the spin-chain system $\text{Ca}_3\text{Co}_2\text{O}_6$: Absence of multiple steps in the low-temperature isothermal magnetization
*N Mohapatra, **KK Iyer**, SD Das, BA Chalke, SC Purandare, & E.V. Sampathkumaran*
 Physical Review B 79 (14), 140409, 2009
- 77) Magnetic anomalies in $\text{Gd}_6\text{Co}_{1.67}\text{Si}_3$ and $\text{Tb}_6\text{Co}_{1.67}\text{Si}_3$
*SN Jammalamadaka, N Mohapatra, SD Das, **KK Iyer**, and E.V. Sampathkumaran*
 Journal of Physics: Condensed Matter 20 (42), 425204, 2008
- 78) Large magnetocaloric effect and magnetoresistance behavior in Gd_4Co_3
*N Mohapatra, **KK Iyer**, EV Sampathkumaran*
 The European Physical Journal B 63 (4), 451-454, 2008
- 79) Stability of the geometrically frustrated magnetic state of $\text{Ca}_3\text{CoRhO}_6$ to applications of positive and negative pressure
*N Mohapatra, **KK Iyer**, S Rayaprol, SN Jammalamadaka, and E.V. Sampathkumaran*
 Journal of Physics: Condensed Matter 20 (25), 255247, 2008
- 80) Profound changes on the geometrically frustrated magnetism of $\text{Ca}_3\text{CoRhO}_6$ by the disturbance of the non-magnetic site
*N Mohapatra, **KK Iyer**, EV Sampathkumaran*
 Physica B: Condensed Matter 403 (5-9), 1443-1444, 2008
- 81) Magnetic anomalies in single crystalline ErPd_2Si_2
*EV Sampathkumaran, N Mohapatra, **KK Iyer**, CD Cao, W Löser, G Behr*
 Journal of magnetism and magnetic materials 320 (8), 1549-1552, 2008
- 82) Behavior of magnetic ordering and the Kondo effect in the alloys $\text{Ce}_2\text{Rh}_{1-x}\text{Co}_x\text{Si}_3$
*S Patil, **KK Iyer**, K Maiti, EV Sampathkumaran*
 Physical Review B 77 (9), 094443, 2008
- 83) Superconducting behavior of the solid solution, $\text{Y}_2\text{Pd}_{1-x}\text{Pt}_x\text{Ge}_3$
***KK Iyer**, EV Sampathkumaran*
 Physica. C, Superconductivity 466, 2007
- 84) Heavy fermion behaviour in $\text{Ce}_2\text{Ni}_{1.88}\text{Cd}$
*EV Sampathkumaran, **KK Iyer**, N Mohapatra, S Rayaprol, R Poettgen*
 Zeitschrift für Naturforschung B 62 (7), 891-895, 2007

- 85) Geometrically frustrated magnetic behavior of $\text{Sr}_3\text{NiRhO}_6$ and $\text{Sr}_3\text{NiPtO}_6$
*N Mohapatra, **KK Iyer**, S Rayaprol, EV Sampathkumaran*
 Physical Review B 75 (21), 214422, 2007
- 86) Magnetic anomalies in the spin-chain compound $\text{Sr}_3\text{CuRhO}_6$: Griffiths-phase-like behavior of magnetic susceptibility
*EV Sampathkumaran, N Mohapatra, S Rayaprol, **KK Iyer***
 Physical Review B 75 (5), 052412, 2007
- 87) Influence of High Pressure and Magnetic Fields on the Magnetic and Transport Anomalies in Nd_7Rh_3
*E V. Sampathkumaran, **K K. Iyer**, P L. Paulose, K Sengupta*
 Journal of the Physical Society of Japan 76 (Suppl. A), 39-42, 2007
- 88) Magnetic and magnetoresistance behavior of Tb_7Rh_3 , an intermetallic compound with a negative temperature coefficient of electrical resistivity in the paramagnetic state
*K Sengupta, **KK Iyer**, EV Sampathkumaran*
 Solid state communications 139 (7), 351-354, 2006
- 89) Large magnetoresistance and magnetocaloric effect above 70 K in $\text{Gd}_2\text{Co}_2\text{Al}$, $\text{Gd}_2\text{Co}_2\text{Ga}$, and Gd_7Rh_3
*K Sengupta, **KK Iyer**, EV Sampathkumaran*
 Physical Review B 72 (5), 054422, 2005
- 90) Novel magnetic behavior of single-crystalline Er_2PdSi_3
***KK Iyer**, PL Paulose, EV Sampathkumaran, M Frontzek, A Kreyssig, ...*
 Physica B: Condensed Matter 355 (1-4), 158-163, 2005
- 91) A transition from antiferromagnetism to spin-glass freezing in single crystalline, Dy_2PdSi_3
***KK Iyer**, PL Paulose, EV Sampathkumaran, H Bitterlich, G Behr*
 AIP Conference Proceedings 0412387, 2004
- 92) 30aYB-4 Magnetic and transport anomalies in RCuAs (R= rare-earths)
*EV Sampathkumaran, K Sengupta, S Rayaprol, **KK Iyer**, D Thomas,*
 Collection of Lectures of the Physical Society of Japan
 59, 344, 2004

- 93) Long-range magnetic ordering in the spin-chain compound $\text{Ca}_3\text{CuMnO}_6$ with multiple bond distances
*K Sengupta, S Rayaprol, **KK Iyer**, EV Sampathkumaran*
Physical Review B 68 (1), 012411, 2003
- 94) Enhanced Electrical Resistivity before Néel Order in the Metals RCuAs_2 (R= S m, Gd, Tb, and Dy)
*EV Sampathkumaran, K Sengupta, S Rayaprol, **KK Iyer**, T Doert,*
Physical review letters 91 (3), 036603, 2003
- 95) Magnetic behavior of single-crystal Ho_2PdSi_3
*EV Sampathkumaran, H Bitterlich, **KK Iyer**, W Löser, G Behr*
Physical Review B 66 (5), 052409, 2002

Pressure-induced anomalies in the magnetic transitions of the exotic multiferroic material $\text{Tb}_2\text{BaNiO}_5$

K. K. Iyer,¹ Ram Kumar,¹ S. Rayaprol,² K. Maiti,¹ and E. V. Sampathkumaran^{2,3}

¹*Department of Condensed Matter Physics and Materials Science, Tata Institute of Fundamental Research, Homi Bhabha Road, Colaba, Mumbai 400005, India*

²*UGC-DAE-Consortium for Scientific Research, Mumbai Centre, BARC Campus, Trombay, Mumbai 400085, India*

³*Homi Bhabha Centre for Science Education, Tata Institute of Fundamental Research, V. N. Purav Marg, Mankhurd, Mumbai 400088, India*



(Received 7 June 2021; accepted 26 July 2021; published 5 August 2021)

We have studied the influence of external pressure up to 1 GPa on the magnetic transitions of the orthorhombic Haldane-spin chain compound $\text{Tb}_2\text{BaNiO}_5$, an exotic multiferroic material. This parent compound is known to undergo Néel ordering at $T_{N1} = 63$ K and another magnetic transition at $T_{N2} = 25$ K at which ferroelectricity sets in, however, without any change in the magnetic symmetry, but with only a sharp change in the canting angle of Tb $4f$ and Ni $3d$ magnetic moments. There is a subtle difference in the antiferromagnetic state above and below T_{N2} , which is supported by the fact that there is a metamagnetic transition below T_{N2} only (for 5 K, at ~ 60 kOe). We report here that, with the application of external pressure, there is an upward shift of T_{N1} , while T_{N2} shifts towards lower temperatures. It is interesting that the two magnetic transitions in the same compound behave differently under pressure and the opposite behavior at T_{N2} is attributed to local distortion leading to ferroelectricity. The results are augmented by temperature dependent x-ray diffraction and positive chemical pressure studies. The chemical pressure caused by the isoelectronic doping at Ba site by Sr reduces both the transition temperatures. Clearly, the external pressure favors antiferromagnetic coupling (that is, leading to T_{N1} enhancement), whereas the chemical pressure reduces T_{N1} , suggesting an important role of the changes in local hybridization induced by doping on magnetism in this material.

DOI: [10.1103/PhysRevMaterials.5.084401](https://doi.org/10.1103/PhysRevMaterials.5.084401)

I. INTRODUCTION

The investigation of the mutual influence of two historically known antagonistic phenomena, namely, magnetism and ferroelectricity in the same compound, has been one of the active topics of research in condensed matter physics. The spin-induced ferroelectric behavior, called type-II multiferroicity, is now commonly known in many compounds with magnetism from the transition metal ions playing a key role on the so-called multiferroic phenomenon [1]. This becomes interesting because ferroelectricity historically is associated with d^0 -ness, whereas magnetism requires unpaired electrons in the d orbitals. The magnetic frustration arising out of certain (e.g., triangular, kagome) geometrical arrangement of antiferromagnetically coupled transition metal ions has been known to be an essential factor to induce multiferroicity in many materials. There are sufficient experimental evidences on some of the most celebrated multiferroics, e.g., RMnO_3 , RMn_2O_5 , CuCrO_2 , and $\text{Ni}_3\text{V}_2\text{O}_8$, (where R = rare-earth), for the influence on ferroelectricity by a change in magnetic structure induced by external parameters, for example, high pressure, P [2–9]. This is due to the fact that the external pressure in general can lead to a change of the magnetic exchange coupling constants by compressing the lattice, decreasing the interatomic distances and possibly changing the bond angles between different ions, which in turn can affect the magnetically ordered phases as well as the

ferroelectric displacements. Additionally, the presence of magnetic rare earths, ordering magnetically at much lower temperatures can complicate magnetoelectric coupling and pressure dependence of ferroelectric properties further in rare-earth containing multiferroics. As a result, many of these materials, in particular rare-earth containing manganites, are characterized by a cascade of magnetic phase transitions with decreasing temperature. It was found that various interactions compete with each other under pressure, e.g., first and second nearest-neighbor isotropic Heisenberg interactions as well as magnetic anisotropy, antisymmetric Dzyaloshinskii-Moriya interactions, symmetric exchange interactions and p - d hybridization, depending on the material on hand. If one disregards rare-earth induced low-temperature magnetic transitions and focuses on the magnetic ordering of the Mn sublattice responsible for ferroelectricity, it was found that the initial antiferromagnetic ordering temperature and the lower one responsible for ferroelectricity are found to increase with pressure in the case of RMnO_3 [6,7] and RMn_2O_5 [8]. In the case of the delafossite, CuCrO_2 , the spin spiral state onset temperature (at 24 K), at which ferroelectric order occurs, increases with pressure [3]. In the kagome lattice, $\text{Ni}_3\text{V}_2\text{O}_8$, the temperature (around 6.5 K) at which helical spin density wave structure breaks the spatial inversion symmetry decreases marginally with pressure [9]. Clearly, no systematics have evolved until now with respect to pressure dependence of multiferroic temperature. Barring such reports, high pressure

studies on multiferroics are less abundant and it is therefore of interest to gather knowledge about the influence of pressure on different spin-induced multiferroics.

With this background, we performed high pressure studies on the Haldane spin-chain compound, $\text{Tb}_2\text{BaNiO}_5$ [10,11], crystallizing in the orthorhombic structure (space group $Immm$) [12–15]. In this structure, the corner-sharing NiO_6 octahedra run along a axis forming chains (isolated by Tb and Ba ions) and these octahedra are distorted in the sense that Ni-O apical distance is less than that in the basal plane and O-Ni-O bond angle is also reduced compared to that for regular octahedron. This compound provides a different and unique opportunity for high pressure studies with respect to the situation in the compounds mentioned above, as elaborated here. This compound has been recently reported to be exotic in its magnetic, multiferroic and magnetodielectric (MDE) coupling properties [16–20]. This insulating compound exhibits two antiferromagnetic transitions [16], one at about $T_{N1} = 63$ K and the other at about $T_{N2} = 25$ K, and, unlike in manganites mentioned above, the onset of magnetic order for both Tb-4f and Ni-3d magnetic moments occurs at the same temperature [12]. The magnetic structure is made up of mutually canted collinear $3d(\text{Ni})$ and collinear $4f(\text{Tb})$ sublattices even across T_{N2} with temperature (T) dependent canting angles with respect to c axis (θ_{Tb} , and θ_{Ni}) as well as relative canting angle ($\Delta\theta = |\theta_{\text{Tb}} - \theta_{\text{Ni}}|$). Otherwise, there is no change in the magnetic symmetry down to 2 K. However, multiferroicity is observed below T_{N2} only. The fact that there is a subtle difference in the magnetic states above and below T_{N2} is revealed by the observation of a metamagnetic transition below this temperature only. It was established [17] that there is a sudden increase in the canting angle of Ni and Tb magnetic sublattices at 25 K at which spontaneous electric polarization sets in with a lowering of temperature. Crystallographic features do not provide any evidence for geometrically frustrated magnetism unlike in the compounds discussed above and it appears that a new theory based on exchange striction coupled with critical canting angle may be required to explain multiferroicity in this compound [17]. In support of this, a small doping (10 at. %) of Sr for Ba destroys ferroelectricity and the mutual canting angle of the two magnetic sublattices are below the critical value [20]. Thus, multiferroicity in this compound is conceptually different from other compounds, providing a new landscape in the field of multiferroicity.

It may also be added that the magnetism of this compound is special within this rare-earth family, $R_2\text{BaNiO}_5$ [21], as the onset of antiferromagnetic ordering temperature, T_{N1} , is the largest within this family, attributable to the dominant role of single-ion $4f$ anisotropy as stated in Ref. [16]. A strong MDE coupling is reported below T_{N2} (as large as about 18%) which is unusual for a polycrystalline material [16]. Subsequent studies showed that this can be further enhanced by a small Y doping [18] and also superseded by the Co analog [22]. This compound also presents a rare situation in which the rare-earth plays a crucial role to induce ferroelectricity [18], unlike many other oxides in which the magnetism of transition metal ions is responsible for this phenomenon. Naturally, this compound offers an opportunity to understand the role of spin-orbit coupling [23] on ferroelectricity.

We therefore consider it important to understand magnetism of this exotic compound under pressure. With this motivation, we have carried out dc magnetic susceptibility (χ) studies up to 1 GPa down to 2 K on $\text{Tb}_2\text{BaNiO}_5$. To augment the line of arguments, we present the results of our investigation on the influence of chemical pressure, induced by small Sr doping, that is, in the series $\text{Tb}_2\text{Ba}_{2-x}\text{Sr}_x\text{NiO}_5$, and of T -dependent x-ray diffraction (XRD) patterns.

II. EXPERIMENTAL DETAILS

The parent compound as well as Sr-doped specimens, $\text{Tb}_2\text{Ba}_{1-x}\text{Sr}_x\text{NiO}_5$ ($x = 0, 0.025, 0.05, 0.075, \text{ and } 0.1$), were prepared in the polycrystalline form using the solid-state reaction route starting from stoichiometric amounts of high purity oxides, $\text{Tb}_2(\text{CO}_3)_2 \cdot n\text{H}_2\text{O}$, NiO, BaCO_3 , and SrCO_3 . The samples thus prepared were found to be single phase forming in the orthorhombic $Immm$ space group by Rietveld fitting of the XRD ($\text{Cu } K_\alpha$) patterns at room temperature, similar to the ones shown in Ref. [19]. The fact that Sr goes into the lattice was further ascertained from the shift of the XRD peaks, which is found to be distinctly visible at least for $x > 0.05$ at higher angle side, however small it may be. In addition, the homogeneity of the samples was confirmed by scanning electron microscope. Further characterization of $\text{Tb}_2\text{BaNiO}_5$ and $\text{Tb}_2\text{Ba}_{0.9}\text{Sr}_{0.1}\text{NiO}_5$ was carried out by T -dependent XRD studies down to 2 K using x-ray radiation with wavelength 0.883 Å on Indian beamline, BL-18B at High Energy Accelerator Research Organization (KEK)-Photon Factory, Japan. The beamline energy was $E = 14.02$ keV, and it was calibrated using LaB_6 standard sample data. The dc magnetization (M) measurements were performed as a function of both magnetic-field (H) and temperature with the help of a commercial (M/s . Quantum Design) superconducting quantum interference device. The magnetism under high pressure (0.3, 0.6, and 1 GPa) was studied for the parent compound (2–300 K) in a hydrostatic pressure medium (daphne oil) employing a commercial pressure cell (EasyLab Technologies Ltd, U.K.). The pressure applied on the sample was calibrated by measuring the superconducting transition temperature of Sn in the low temperature range.

III. RESULTS AND DISCUSSIONS

The results of magnetization ($H = 5$ kOe and 100 Oe) measurements under external pressure are shown in Fig. 1(a) below 100 K and the curves under external pressure are shifted for the sake of clarity, as the overlap of the curves mask the features we want to highlight. We measured with two fields to convince the readers that the trends discussed here are reliable. The features in the $\chi(T)$ were discussed in several places in the previous literature. Following Curie-Weiss behavior in the paramagnetic state as known earlier [16], there is a kink due to the onset of antiferromagnetic order at T_{N1} [marked by a vertical arrow in Fig. 1(a)] at which heat-capacity was shown to exhibit a distinct anomaly [16]; a broad peak at a lower temperature (at ~ 40 K) appears which has been attributed to the persistence of Haldane gap due to Ni one-dimensional magnetism in the magnetically ordered state. The kink is very weak and therefore one has to carefully do the measurements

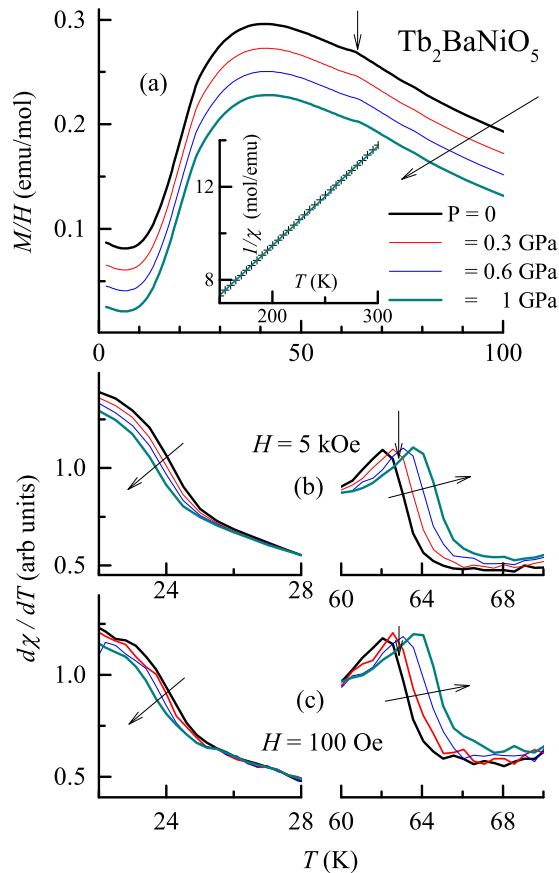


FIG. 1. Magnetic susceptibility (χ) curves obtained as a function of temperature for $\text{Tb}_2\text{BaNiO}_5$ under various external pressures in the range 2–100 K measured in 5 kOe are shown in (a). The high pressure $\chi(T)$ curves are shifted for the sake of clarity, as otherwise the curves are essentially indistinguishable. Derivative curves, also for the data measured in 100 Oe, are shown in (b) and (c) in an expanded form in the vicinity of magnetic transitions (T_{N1} and T_{N2}) described in the text. Vertical arrows mark the T_{N1} and T_{N2} under ambient pressure conditions. Inclined arrows are shown as guide to the eye for the reader to show the direction in which the curves move with pressure around the transition. The plot of inverse susceptibility above 150 K is shown in the inset of (a) in the absence of external pressure (points) and for 1 GPa (continuous line), to highlight that the paramagnetic Curie temperatures and the effective magnetic moment do not change with pressure.

under pressure to track its behavior. It can be inferred from the $\chi(T)$ plots as well as from the derivative plots [Figs. 1(b) and 1(c)] that T_{N1} tends to increase gradually with P , e.g., by about 2 K for an increase of P to 1 GPa. However, it is not straightforward to infer T_{N2} from the $\chi(T)$ plot, as the fall in χ below the peak due to the magnetic gap is rather steep and, therefore, the derivative curves are used to infer the trend. The derivative curves, $d\chi/dT$, shown in Figs. 1(b) and 1(c) reveal a sudden increase in slope near 25 K under ambient pressure conditions, but the fact remains that there is a marginal downward shift of the curve around this temperature, however small it may be, with increasing pressure (by about 0.5 K for $P = 1$ GPa). Clearly, the external pressure acts in the opposite way at these two magnetic features. Finally, the effective magnetic

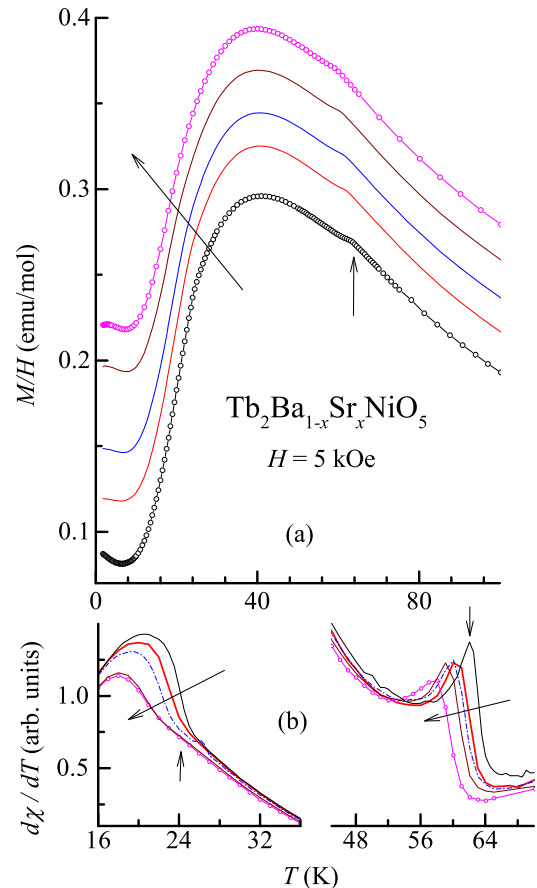


FIG. 2. (a) Magnetic susceptibility (χ) as a function of temperature for Sr-doped specimens, $\text{Tb}_2\text{Ba}_{1-x}\text{Sr}_x\text{NiO}_5$ in the range 2–100 K, measured with 5 kOe. In (b), the derivative curves are shown in an expanded form in the vicinity of T_{N1} and T_{N2} . Vertical arrows mark T_{N1} and T_{N2} . Inclined arrows are guides to the eyes to show how the transitions shift with x ($x = 0.0, 0.025, 0.05, 0.075, \text{ and } 0.1$).

moment ($\mu_{\text{eff}} = 9.63 \mu_B/\text{Tb}$) obtained from the Curie-Weiss region (say, above 100 K) is found to be insensitive to pressure within experimental error ($<0.05 \mu_B$) and the value is in good agreement with that for trivalent Tb ion ($9.72 \mu_B$); the paramagnetic Curie temperature ($\vartheta_p = -20 \pm 1$ K) is also found to be independent of pressure [see inset of Fig. 1(a), comparing inverse χ plots in the high- T region for 0 and 1 GPa]. It is also obvious from Fig. 1 that there is no other change in the features, thereby establishing that the Haldane gap is not affected by external pressure up to 1 GPa.

We now compare results of high-pressure measurements of $\text{Tb}_2\text{BaNiO}_5$ with the observations made in the experiments with $\text{Tb}_2\text{Ba}_{1-x}\text{Sr}_x\text{NiO}_5$ in which a chemical pressure was induced by the partial substitution of Ba atoms by Sr atoms (Fig. 2). The curves for doped compositions are shifted along y axis for the sake of clarity. Though we had earlier reported magnetic, and magnetodielectric coupling properties of this Sr-doped series, $\text{Tb}_2\text{Ba}_{1-x}\text{Sr}_x\text{NiO}_5$, [19] for $x = 0, 0.1, \text{ and } 0.2$, we felt the need to study the magnetic properties at closer intervals of x below $x = 0.1$ synthesized under identical conditions (that is, same batch), considering abrupt changes

in the multiferroic properties for initial doping beyond $x = 0.1$. [Beyond $x = 0.2$, we see sample inhomogeneities, unlike Y doping which can replace Tb completely]. We find that ferroelectricity is destroyed for $x = 0.15$ in this batch of specimens, and not for $x = 0.10$, thereby revealing that there is a small spread in the composition at which multiferroicity vanishes depending on the batch of specimens. We restrict the discussions here for the trends in magnetic behavior only for selected compositions, $x = 0, 0.025, 0.05, 0.075$, and 0.1 . The $\chi(T)$ and the derivative curves below 100 K, measured with 5 kOe are shown in Fig. 2. It is clear that the feature due to the transition at T_{N1} shifts downwards gradually with increasing x , visible even for a doping as small as $x = 0.025$. There is an overall decrease by about 5 K for $x = 0.1$ in this investigation. T_{N1} reported for $x = 0.2$ [15] also follows this trend. As shown earlier [19], all the three lattice parameters, a , b , and c , undergo a weak reduction (in the third decimal place only) and the overall reduction in the unit-cell volume as x is varied from 0 to 0.1 is 0.6 \AA^3 ($\sim 0.24\%$). Since the bulk modulus of the parent compound is not known, it is difficult to quantify the pressure exerted by this change in the unit-cell volume. Nevertheless, it is straightforward to conclude that, qualitatively speaking, chemical pressure acts differently with respect to that caused by external pressure as far as T_{N1} is concerned. Now, with respect to the behavior of T_{N2} , though it is not straightforward to infer this characteristic temperature precisely, one gets an idea by looking at the slope change of the derivative curves [Fig. 2(b)] in the vicinity of 25 K. It is clear that the sudden increase in the slope at 25 K noted for the parent compound gradually shifts towards low temperature range, which is a signature of corresponding lowering of T_{N2} . We, therefore, conclude that both T_{N1} and T_{N2} decrease with the increasing chemical pressure, exerted on the Ba layer, in contrast to the ones seen under external pressure. This means that T_{N1} is sensitive to changes in local hybridization due to doping.

It is of interest to see the trend under chemical pressure by isoelectronic substitution at the Tb site. For this purpose, the readers may see Ref. [18] for the results on $\text{Tb}_{2-x}\text{Y}_x\text{BaNiO}_5$, in which the magnitude of unit-cell volume reduction for $x = 0.5$ is comparable to that for $x = 0.2$ of the Sr-doped series. Therefore, one can assume that the magnitudes of internal pressure are similar for these compositions. Both T_{N1} and T_{N2} were found to diminish linearly with x , investigated up to $x = 1.5$, interestingly with the persistence of magnetically coupled ferroelectric order even in this dilute limit of Tb; for example, for $x = 0.5$, $T_{N1} = \sim 55 \text{ K}$ and $T_{N2} = \sim 20 \text{ K}$. Since Y substitution involves dilution of the Tb sublattice, for a comparison with Sr-doped series, it is necessary to normalize to Tb concentration (that is, to $2-x$). The normalized values are about 73 and 27 K respectively. Clearly, while the trend in $T_{N1}(x)$ in Y series is the same as that in high pressure, the increase of the normalized value by about 10 K compared to that for the parent compound under external pressure is quite profound. Assuming a linear variation of T_{N1} with P , a pressure as large as about 6 GPa would be required to attain a value of 73 K. Y dilution studies clearly suggested Tb 4f plays a major role on the onset of ferroelectric ordering [18], as the transition temperatures decrease gradually with Y doping. In the crystal structure, the vertex-shared (compressed)

octahedra of NiO_6 chains are isolated by Tb and Ba polyhedra and therefore the super-superexchange mechanism of the types $\text{Ni}^{2+}-\text{O}^{2-}-\text{R}^{3+}-\text{O}^{2-}-\text{Ni}^{2+}$ and $\text{Ni}^{2+}-\text{O}^{2-}-\text{Ba}^{2+}-\text{O}^{2-}-\text{Ni}^{2+}$ are known to be operative to induce magnetic ordering. As stated in the introduction, both the magnetic sublattices order at the same temperature. A dilution of R sublattice (by Y) has of course a natural destructive influence on the transition temperatures. But the fact that this dilution tends to enhance the scaled- T_{N1} significantly (rather than remaining constant as expected for scaling with the concentration of magnetic ions) implies that the superexchange pathway involving R^{3+} is the dominating one, getting stronger with the lattice pressure. While Ba is replaced by Sr, T_{N1} does not follow the external pressure effect, and therefore we are tempted to argue that the superexchange path involving Ba counteracts the one caused by pressure. It is interesting that the behavior of normalized T_{N2} is different; that is, the increasing trend with Y-induced chemical pressure in the Tb sublattice is opposite to that observed by external pressure or Sr-doping. We therefore believe that the changes in bonding strengths caused by isoelectronic substitution bear a profound effect on the properties.

We have also measured isothermal M to see the influence of pressure on the metamagnetic transition field (H_c), occurring at 60 kOe at 2 K, for the parent compound. The results obtained under pressure are shown in Fig. 3(a), and for Sr-doped compositions in Fig. 3(b). Though we measured at various temperatures below 20 K, we show the curves for 5 K only. There is a weak hysteresis around H_c as reproduced in the inset of Fig. 3(a) from our past work [16,18,19], but we restrict the plots here to the virgin curves only in the mainframe of Fig. 3(a), that too in the vicinity of the field-induced transition for the sake of clarity. The curves around H_c are broadened with increasing Sr-doping [Fig. 3(b), clearly due to increasing chemical disorder. The point to be noted is that there is a marginal increase in H_c with external P . However, H_c gets depressed by Sr doping. It may be recalled [18] that the chemical pressure induced by Y substitution also depresses H_c . It is thus obvious that, as far as H_c is concerned, there is no correlation of these results obtained by external pressure, on the one hand, and the chemical pressure (induced at the R site as well as at Ba site) on the other. This endorses the conclusion made in the previous paragraph that the electronic structure changes caused isoelectronic substitutions at any site has a dominating effect on the properties.

We now offer evidence for the fact that the observed pressure effects are free from any ambiguities due to a possible change in the crystallographic symmetry. To show the absence of temperature induced changes in crystal structure down to 2 K, we measured XRD patterns with the synchrotron facility at several temperatures for $x = 0$ and 0.1 . In Fig. 4, we show such synchrotron-based powder XRD (S-PXRD) patterns at selected temperatures in the three temperature ranges, $T < T_{N2}$, $T_{N2} < T < T_{N1}$, and $T > T_{N1}$. The patterns, apart from establishing that the specimens are single phase ($Immm$ space group) with the diffracting peaks appearing at expected angles only, reveal that there is no change in the patterns down to 2 K for both the compositions. Though there is a preferred orientation effect for a few Bragg peaks, we could index all the patterns using LeBail fit. The main point to emphasize here is that there is no change in the crystal symmetry down to

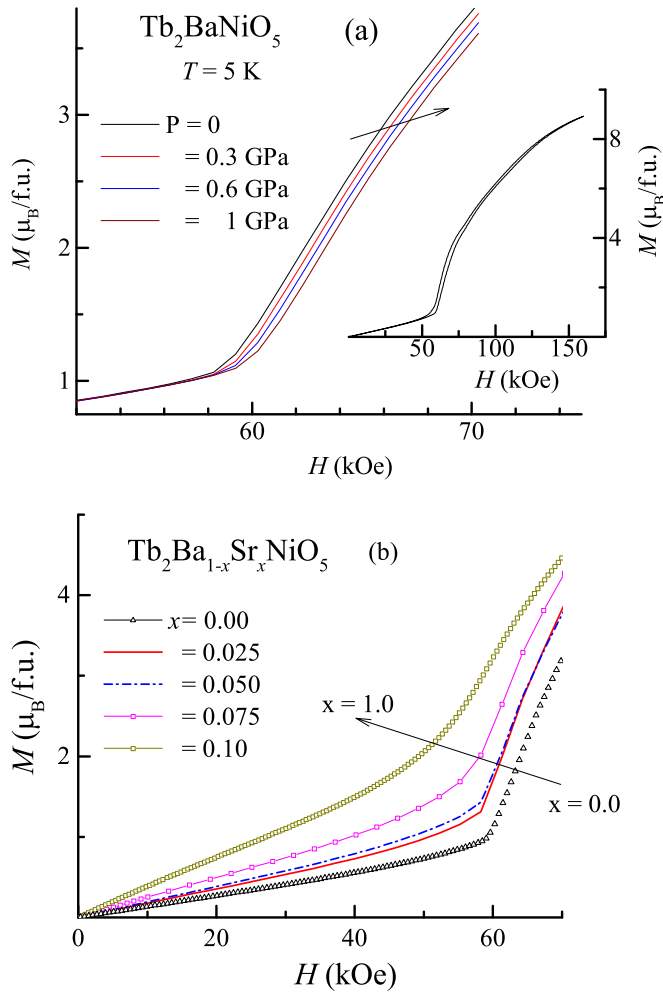


FIG. 3. (a) Isothermal magnetization (virgin) at 5 K for Tb_2BaNiO_5 under pressure in the metamagnetic transition region. The profile of the curve in the range 0–160 kOe under ambient pressure is shown in the inset. (b) Isothermal magnetization at 5 K for the Sr-doped specimens. Inclined arrows are showing the direction in which the curves shift with increasing pressure/composition.

2 K. This conclusion was inferred by low temperature neutron diffraction studies as well on both the compositions [17,20]. Since Sr substitutions exert chemical pressure without any change in the crystal symmetry, it is reasonable to assume that the external pressure of about 1 GPa also would not have caused any crystallographic change.

As mentioned earlier, there is no change in the magnetic symmetry as well down to 2 K for the parent compound, although canting angles change with varying temperature [17]. Since Sr content (measured for $x = 0.1$) also does not change magnetic symmetry [20], additional magnetic structural complexities are not expected to occur under pressure for the parent. We take this opportunity to clarify how the loss of inversion symmetry occurs in this compound, an issue remained unresolved till now. In order to understand this, we used the program FINDSYM [24] to find the magnetic space group and point group. Using the atomic positions of Tb and Ni (both magnetic ions), and assuming that moments are placed along the z direction, the program suggests the magnetic point

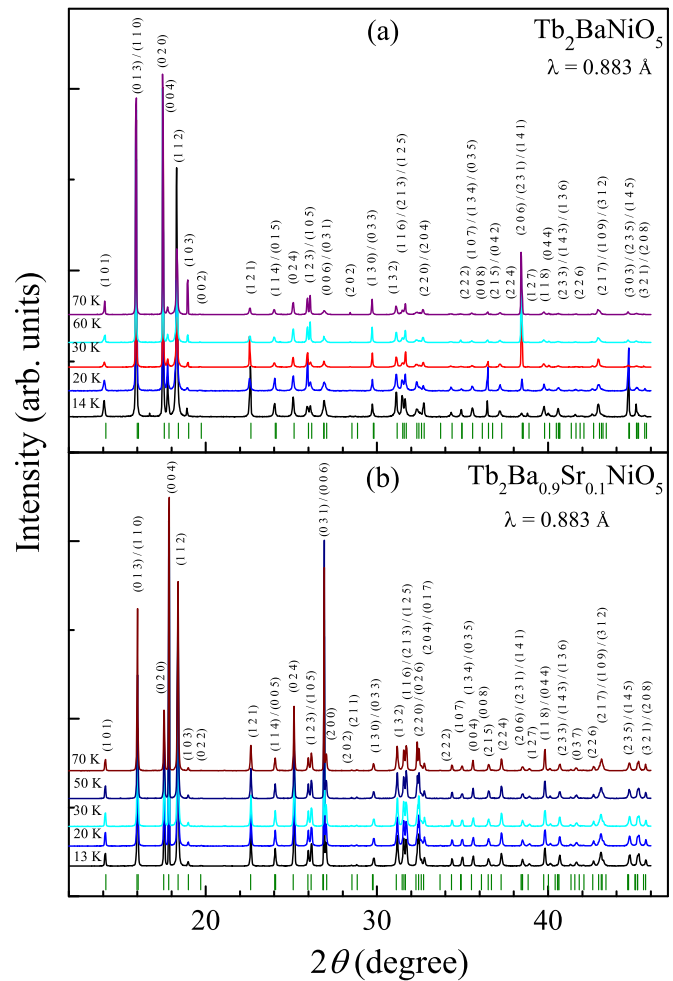


FIG. 4. Synchrotron based powder x-ray diffraction (S-PXRD) patterns of selected temperatures for Tb_2BaNiO_5 and $Tb_2Ba_{0.9}Sr_{0.1}NiO_5$ are shown to highlight that there is no change in structural symmetry across the magnetic transitions. Vertical bars are shown to mark the expected positions of Bragg peaks.

group to be $m'm'2$, which is a noncentrosymmetric, polar space group ($Im'm'2$), which allows polarization along the z direction. However, the magnetic structure refinement of the neutron diffraction experimental data, shown in the Supplemental Material of Ref. [17], revealed that there is a magnetic moment component along the x direction also in addition to the z component (though $M_z > M_x$), which implies canting of the moments in the ac plane. Therefore, considering this (that is, assigning moments along x and z directions), the magnetic point group obtained is m' (magnetic space group Cm'). This is also a noncentrosymmetric, polar space group allowing polarization in the x and z directions. In a nutshell, for both the samples, i.e., Tb_2BaNiO_5 and $Tb_2Ba_{0.9}Sr_{0.1}NiO_5$, by carrying out the magnetic structural refinement across both long-range antiferromagnetic ordering temperatures considering the canting, the magnetic symmetry remains the same (Cm') until the lowest temperature. In short, though canting of the Tb and Ni moments with respect to c axis changes, resulting in the change of magnetic moment (M_x , M_z and net moment M) as temperature is reduced, there is no change in

the magnetic symmetry. This finding emphasizes the importance of an additional criterion for the multiferroic properties in $\text{Tb}_2\text{BaNiO}_5$, which we attribute to the existence of a critical canting angle.

IV. SUMMARY

We have performed high pressure magnetization studies on an exotic multiferroic compound, $\text{Tb}_2\text{BaNiO}_5$, in which both Tb and Ni moments order at the same temperature with the involvement of Tb $4f$ in inducing ferroelectricity; a situation not encountered in the manganites. While the antiferromagnetic ordering onset temperature is enhanced by external pressure, the lower characteristic temperature, T_{N2} , at which multiferroicity has been known to set in, gets depressed by the external pressure. It is interesting that the external pressure has the opposite effect on the magnetic features at the two temperatures in the same compound. This situation is different from that noted for the Mn sublattice in the most celebrated multiferroic materials, TbMnO_3 [6,7] and RMn_2O_5 [8], including the magnetic transition temperature that is tied to the onset of ferroelectric transition. Given that both Tb and Ni order magnetically at the same temperature without any change in magnetic symmetry across T_{N2} , one would naively expect that both the transitions respond in the same way to the application of external pressure, in contrast to the observation. We, therefore, conclude that the local distortions leading to ferroelectricity influences the pressure dependence of concurrent magnetic transition temperature. We have also compared and contrasted the changes in the magnetic features with those seen by chemical pressure by isoelectronic substitution at Tb and Ba sites. Readers may recall [17] that there are prominent local lattice distortions (as reflected in O-Tb-O bond angles and Ni-O bond distances) at T_{N2} , where ferroelectricity also sets in, for the parent compound, which naturally gets modified by chemical and external pressure as inferred from the analysis of neutron diffraction data presented in Ref. [20] for

a Sr-doped specimen. There are less prominent and gradual changes in the lattice constants across T_{N1} as well when T is lowered [see Fig. S2 in Ref. [17]] for the parent due to magnetostriction as one enters the state magnetically and this also must get influenced by pressure, thereby changing hybridization. We conclude that the subtle distortions cause a profound effect on magnetic characteristics of this compound. We hope this work serves as a motivating force to extend the magnetic, optical, and magnetoelectric studies by various experimental methods including neutron diffraction to much higher pressures, also in the presence of high magnetic fields, on this exotic material, as this material provides another avenue to understand various factors (including band gap changes [25]) in the evolution of the cross-coupling phenomena.

ACKNOWLEDGMENTS

K.K.I. and K.M. acknowledge financial support from the Department of Atomic Energy, Govt. of India (Project Identification No. RTI4003, DAE OM No. 1303/2/2019/R&D-II/DAE/2079 dated 11.02.2020). E.V.S. thanks Department of Atomic Energy, Government of India, for awarding Raja Ramanna Fellowship (Order No. 1003/4/2021/RRF/R&D-II/8335, dated 22.07.2021). K.M. acknowledges financial assistance under Award No. DAE-SRC-OI, DAE, Government of India. S.R. and K.K.I thank the Department of Science and Technology, India for the financial support, and Saha Institute of Nuclear Physics and Jawaharlal Nehru Center for Advanced Scientific Research for facilitating the experiments at the Indian Beamline, Photon Factory, KEK, Japan, under the proposal number JNC/KEK-JAP/IN-56 for synchrotron XRD measurements on Indian beamline (BL-18B) at PF, KEK, Japan. The authors also thank G. Manna and S. Karmakar for their help during the synchrotron x-ray powder diffraction experiments. We thank H. J. Zhao, University of Arkansas, Fayetteville, AR, USA for his guidance on carrying out symmetry analysis.

-
- [1] C. N. R. Rao, A. Sundaresan, and R. Saha, *J. Phys. Chem. Lett.* **3**, 2237 (2012); Y. Tokura, S. Seki, and N. Nagaosa, *Rep. Prog. Phys.* **77**, 076501 (2014); S. Dong, J.-M. Liu, S.-W. Cheong, and Z. Ren, *Adv. Phys.* **64**, 519 (2015).
- [2] H. Kimura, K. Nishihata, Y. Noda, N. Aso, K. Matsubayashi, Y. Uwatoko, and T. Fujiwara, *J. Phys. Soc. Jpn.* **77**, 063704 (2008).
- [3] T. Aoyama, A. Miyake, T. Kagayama, K. Shimizu, and T. Kimura, *Phys. Rev. B* **87**, 094401 (2013).
- [4] T. Aoyama, A. Iyama, K. Shimizu, and T. Kimura, *Phys. Rev. B* **91**, 081107(R) (2015).
- [5] M. Deutsch, T. C. Hansen, M. T. Fernandez-Diaz, A. Forget, D. Colson, F. Porcher, and I. Mirebeau, *Phys. Rev. B* **92**, 060410(R) (2015).
- [6] T. Aoyama, K. Yamauchi, A. Iyama, S. Picozzi, K. Shimizu, and T. Kimura, *Nat. Comm.* **5**, 4927 (2014).
- [7] N. Terada, D. Dmitry, P. Khalyavin, T. Manuel, Osakabe, A. Kikkawa, and H. Kitazawa, *Phys. Rev. B* **93**, 081104(R) (2016).
- [8] C. R. delaCruz, B. Lorenz, Y. Y. Sun, Y. Wang, S. Park, S.-W. Cheong, M. M. Gospodinov, and C. W. Chu, *Phys. Rev. B* **76**, 174106 (2007).
- [9] R. P. Chaudhury, F. Yen, C. R. delaCruz, B. Lorenz, Y. Q. Wang, Y. Y. Sun, and C. W. Chu, *Phys. Rev. B* **75**, 012407 (2007).
- [10] J. Hernandez-Velasco and R. Saez-Puche, *J. Alloys Compd.* **225**, 147 (1995).
- [11] E. Garcia-Matres, J. L. Garcia-Munoz, J. L. Martinez, and J. Rodriguez-Carvajal, *J. Magn. Magn. Mater.* **149**, 363 (1995).
- [12] E. Garcia-Matres, J. L. Martinez, and J. Rodriguez-Carvajal, *Eur. Phys. J. B.* **24**, 59 (2001).
- [13] J. Amador, E. Gutierrez-Puebla, M. A. Monge, I. Rasines, C. Ruiz-Valero, F. Fernandez, R. Saez-Puche, and J. A. Campa, *Phys. Rev. B* **42**, 7918 (1990).
- [14] J. A. Alonso, J. Amador, J. L. Martinez, I. Rasines, J. Rodriguez-Carvajal, and R. Saez-Puche, *Solid State Commun.* **76**, 467 (1990).

- [15] M. Castro, R. Burriel, A. Salinas-Sánchez, and R. Sáez-Puche, *J. Magn. Magn. Mater.* **104**, 619 (1992).
- [16] S. K. Upadhyay, P. L. Paulose, and E. V. Sampathkumaran, *Phys. Rev. B* **96**, 014418 (2017).
- [17] R. Kumar, S. Rayaprol, S. Rajput, T. Maitra, D. T. Adroja, K. K. Iyer, S. K. Upadhyay, and E. V. Sampathkumaran, *Phys. Rev. B* **99**, 100406(R) (2019).
- [18] S. K. Upadhyay and E. V. Sampathkumaran, *J. Appl. Phys.* **125**, 174106 (2019).
- [19] S. K. Upadhyay and E. V. Sampathkumaran, *J. Phys.: Condens. Matter* **31**, 39LT01 (2019).
- [20] R. Kumar, S. Rajput, T. Maitra, A. Hoser, S. Rayaprol, S. K. Upadhyay, K. K. Iyer, K. Maiti, and E. V. Sampathkumaran, *J. Alloys Compd.* **862**, 158514 (2021).
- [21] J. Darriet, and L. P. Regnault, *Solid State Commun.* **86**, 409 (1993); T. Yokoo, T. Sakaguchi, K. Kakurai, and J. Akimitsu, *J. Phys. Soc. Jpn.* **64**, 3651 (1995); A. Zheludev, E. Ressouche, S. Maslov, T. Yokoo, S. Raymond, and J. Akimitsu, *Phys. Rev. Lett.* **80**, 3630 (1998); A. Zheludev, S. Maslov, T. Yokoo, S. Raymond, S. E. Nagler, and J. Akimitsu, *J. Phys.: Condens. Matter* **13** R525 (2001); S. Raymond, T. Yokoo, A. Zheludev, S. E. Nagler, A. Wildes, and J. Akimitsu, *Phys. Rev. Lett.* **82**, 2382 (1999).
- [22] S. K. Upadhyay and E. V. Sampathkumaran, *Appl. Phys. Lett.* **112**, 262902 (2018).
- [23] S. Dong, H. Xiang, and E. Dagotto, *Natl. Sci. Rev.* **6**, 629 (2019).
- [24] H. T. Stokes, D. M. Hatch, and B. J. Campbell, FINDSYM, ISOTROPY Software Suite, iso.byu.edu; H. T. Stokes, and D. M. Hatch, Program for Identifying the Space Group Symmetry of a Crystal, *J. Appl. Crystallogr.* **38**, 237 (2005).
- [25] See, for instance, for such studies on MnWO_4 , J. Ruiz-Fuertes, S. Lopez-Moreno, J. Lopez-Solano, D. Errandonea, A. Segura, R. Lacomba-Perales, A. Munoz, S. Radescu, P. Rodriguez-Hernandez, M. Gospodinov, L. L. Nagornaya, and C. Y. Tu, *Phys. Rev. B* **86**, 125202 (2012).



Magnetic behavior of cubic Dy₄RhAl with respect to isostructural Dy₄PtAl, revealing a novel 4f d-band interaction

ARTICLE INFO

Keywords

Dy₄RhAl
Dy₄PtAl
4f-5d band correlation
Magnetic susceptibility
Electrical resistance
Magnetoresistance
Heat capacity

ABSTRACT

We have investigated for the first time the magnetic behaviour of an intermetallic compound, Dy₄RhAl, crystallizing in Gd₄RhIn-type cubic structure containing 3 sites for rare-earth (R), by several bulk measurements down to 1.8 K. This work is motivated by the fact that the isostructural Dy compound in the R₄PtAl family surprisingly orders ferromagnetically unlike other members of this series, which order antiferromagnetically. The results reveal that the title compound undergoes antiferromagnetic order at about 18 K, similar to other heavy R members of R₄RhAl family, unlike its Pt counterpart, indicating a subtle difference in the role of conduction electrons to decide magnetism of these compounds. Besides, spin-glass features coexisting with antiferromagnetic order could be observed, which could mean cluster antiferromagnetism. The electrical resistivity and magnetoresistance behaviours in the magnetically ordered state are typical of magnetic materials exhibiting antiferromagnetic gap. Features attributable to spin-reorientation as a function of temperature and magnetic field can be seen in the magnetization data.

1. Introduction

The ternary compounds of the type R₄TX (where R = rare-earths, T = transition metals and X = p-block metals) forming in the cubic Gd₄RhIn-type structure [1–4] are of special interest, as these compounds provide an opportunity to understand magnetism due to the interactions between 3 independent crystallographic sites of the rare-earth. We have carried out extensive bulk measurements on many heavy rare-earth members of the families, R₄PtAl (R = Gd, Tb, Dy, Ho and Er) and R₄RhAl (R = Gd, Tb, Ho and Er) and we have observed re-entrant spin-glass behaviour in all the compounds, apart from many other interesting magnetic, thermal, transport and magnetocaloric features [5–10]. A novel observation pertinent to the aim of this article is that the onset of magnetic order is of an antiferromagnetic (AF) type for R = Gd [5], Tb [6], Ho and Er [10], within the R₄PtAl family, whereas Dy member [7] enters into a ferromagnetic (F) state from the paramagnetic state. It is puzzling why Dy₄PtAl behaves differently in this respect. It is therefore of great interest to understand the magnetism of Dy counterpart in another family, viz., R₄PtAl, as Gd, Tb, Ho and Er members of this family also order antiferromagnetically with pronounced spin-glass features. With this primary motivation, we have carried out ac and dc magnetization (*M*), heat-capacity (*C*), electrical resistivity (*ρ*), and magnetoresistance (MR) measurements on Dy₄RhAl, the results of which are presented in this article. It may be remarked that, subsequent to initial synthesis report of this compound [2] about a decade ago, to our knowledge, there is no further literature on the magnetism of this compound. The point of main emphasis, apart from other findings, is that this compound also orders antiferromagnetically similar to other members in this family - unlike Dy₄PtAl - forming clusters behaving like spin-glass.

2. Experimental details

The sample in the polycrystalline form was prepared by melting together stoichiometric amounts of high purity Dy (>99.9%), Rh (99.99%) and Al (>99.99%) in an atmosphere of high purity argon in an arc furnace. Powder x-ray diffraction pattern (XRD) (Cu K_α) confirmed single phase of the specimen within the detection limit of this technique (<2%). The results of Rietveld refinement to the cubic phase with the space group *F* $\bar{4}3m$ are shown in Fig. 1. The lattice constant is obtained to be 13.403(3) Å, which is in good agreement with the reported value of 13.468 Å [2]. We have also characterized the sample by scanning electron microscope (SEM) and we could not detect any additional phase. Energy Dispersive X-ray (EDX) analysis confirmed that the chemical composition is uniform (4:1:1) in the sample. Therefore, within the detection limit of these techniques (<1%), the specimen is a single phase. Dc magnetic susceptibility (χ) (1.8–300 K), and isothermal *M* were performed using a commercial PPMS (Physical Properties Measurement system, Quantum Design) -VSM and ac χ (with an ac field of 1 Oe) measurements were carried out with the help of a commercial (Quantum Design) superconducting quantum interference device. Heat-capacity and electrical resistivity as well as MR measurements as a function of temperature (*T*) and magnetic field (*H*) were carried out using a commercial PPMS. The measurements in general were carried out for the zero-field-cooled (ZFC) condition of the specimens.

3. Results and discussions

In Fig. 2a, we show $\chi(T)$ measured in 100 Oe for the ZFC condition as well as for the field-cooled (FC) condition of the specimen in the low temperature range of interest. There is a distinct peak at $T_N = 18$ K suggesting the onset of AF order. In addition to this peak, there are

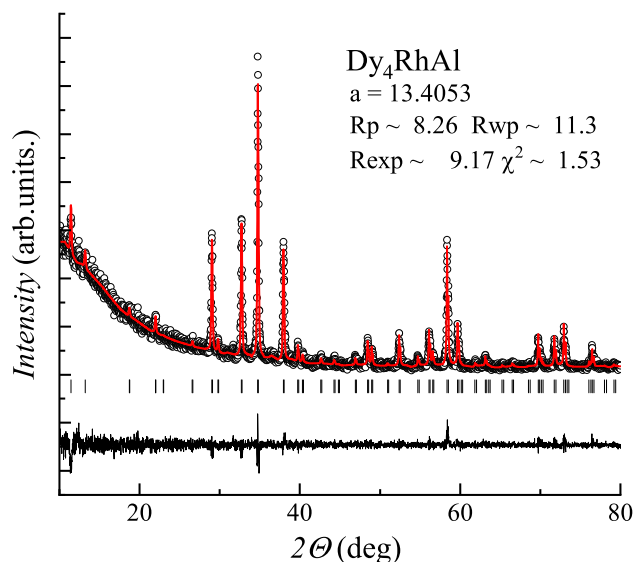


Fig. 1. X-ray diffraction pattern of Dy₄RhAl at room temperature, along with Rietveld fitting results.

additional weak peaks at about 4 and 12 K, indicating further magnetic anomalies with a lowering of temperature. The 12 K-feature is smeared when measured in a field of 5 kOe (Fig. 2b), implying subtle nature of such low-temperature magnetic state, but we do not know whether possible traces of other magnetic impurities below the detection limit of XRD, SEM and EDX cause this feature. Inverse χ plot for 5 kOe data in Fig. 2c is linear over a wide T range (that is, above 25 K) and a Curie-Weiss fit yielded a value of the effective moment of $11 \mu_B/\text{Dy}$, which is marginally higher than the theoretical value of $10.48 \mu_B$ for Dy^{3+} , usually attributed to a contribution from conduction electron polarization. The paramagnetic Curie temperature is obtained to be -16 K; this magnitude and the sign are in good agreement with AF ordering setting in around 18 K. Finally, the low-field curves for ZFC and FC conditions separate at T_N , and the FC curve exhibits an upturn with decreasing temperature typical of cluster spin-glasses [11–13]. All these results already indicate possible antiferromagnetic cluster glass behaviour. We would also like to mention that the χ curves of 100 Oe and 5 kOe do not overlap at T_N , but well above T_N only, as shown in the inset of Fig. 2c, and this signals the existence of short-range magnetic correlations before long-range magnetic ordering sets in, as demonstrated for many heavy rare-earth systems [see the articles cited in [9]].

Fig. 3a shows isothermal magnetization at 2, 5 and 10 K. M increases gradually with H at these temperatures, tending to saturate beyond about 60 kOe. A careful look at the curve suggests that there is an upward curvature around 20–40 kOe and a weak hysteresis is clearly visible as the temperature is lowered to 2 K. This implies that there could be a disorder-broadened first-order field-induced magnetic transition. All these features are consistent with the conclusion that the zero-field state is not ferromagnetic. The values of the magnetic moment at very high fields (as well as the zero-field value following linear extrapolation of high-field linear region) are far less than that of the free ion and this can arise from crystal-field-effects.

In Fig. 4a and b, we show $C(T)$ and $C(T)/T$ behaviour in zero field as well as in the presence of 10, 30 and 50 kOe. In the plot of $C(T)$ versus T , in zero-field, there is an upturn below 20 K, followed by a peak at 18 K and a gradual fall thereafter with decreasing temperature. There is no well-defined peak well-below 18 K suggesting the absence of any additional long-range magnetic ordering, but not inconsistent with possible presence of spin-glass freezing. A careful look at the C/T curves reveals a change of slope around 5–10 K in the zero-field curve, thereby implying that there is actually a subtle faster decrease (compared to higher temperature linear region) in heat-capacity attributable to the spin-glass

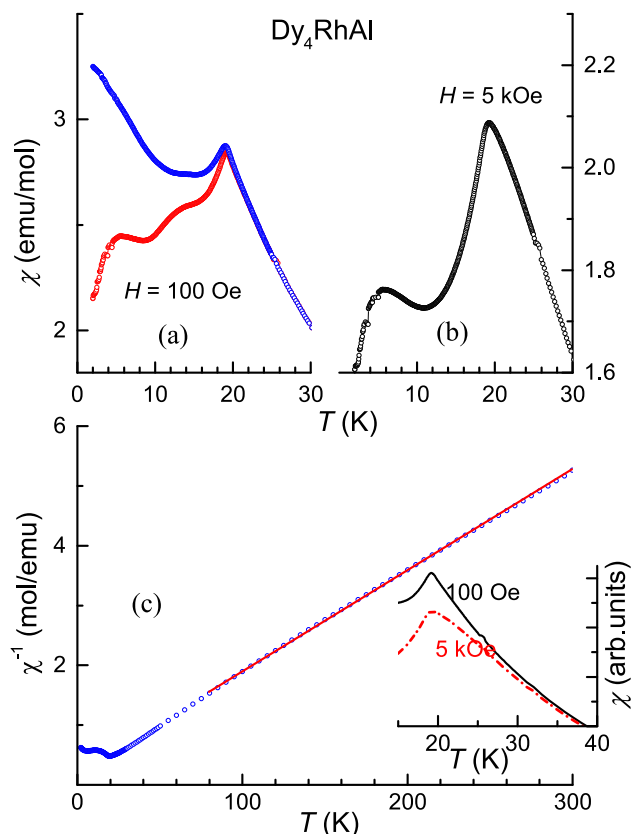


Fig. 2. The temperature dependent (a, b) dc magnetic susceptibility measured in 100 Oe (for zero-field-cooled and field-cooled condition) and in 5 kOe (zero-field-cooled) in the low temperature range and (c) inverse susceptibility with the continuous line representing Curie-Weiss fit, for Dy₄RhAl. Inset compares the plots of susceptibility measured in 100 Oe and 5 kOe in the vicinity of T_N to bring out the existence of short-range magnetic correlations.

component. The support for the onset of antiferromagnetic order can be seen from the gradual suppression of the peak with increasing H . We have also obtained isothermal entropy change, $\Delta S = S(H) - S(0)$, as a function of temperature by integrating the C/T versus T curves. The plots of $-\Delta S$ (Fig. 4c) thus obtained for $H = 30$ and 50 kOe exhibit a positive peak at a temperature (about 25 K) slightly above T_N ; this finding, along with the positive sign, implies [14] that short-range magnetic correlations (inferred from the inset of Fig. 2c) setting in before long-range magnetic order is of a ferromagnetic-type. There is also a weaker peak in the negative quadrant around 18 K, and the sign is consistent with AF order. There are additional sign-crossovers at lower temperatures, which may be consistent with subtle magnetic effects, mentioned above. The peak values are not large, as in other Rh compounds [8,9]. The values for $H = 10$ kOe are too small to attach any significance to the sign changes with T . Finally, we are able to fit the $C(T)$ data below 7 K to the functional form, $C = \beta T^3 + \alpha T^n e^{-\Delta/T}$, where α , β and n are constants, and Δ is the spin-gap between the lower and upper band of the spin wave spectrum. The value of Δ and n are found to be ~ 2.2 K and ~ 0.8 .

In order to explore possible presence of spin-glass features, we have measured ac susceptibility with four frequencies (ν). We show the real (χ') and imaginary (χ'') parts in Fig. 5. Since the curves are noisy for 133 and 1333 Hz, we show the curves for 1.3 and 13 Hz only for 5 kOe. Though the data for higher frequencies are noisy, a ν -dependence of the peak is transparent in the real part in the vicinity of T_N (for instance, ~ 20 and ~ 24 K for 1.3 and 1333 Hz respectively), attributable to spin-glass freezing. From the values of the peak temperature (T_p) for the two extreme frequencies, the magnitude of the factor, $\Delta T_p / T_p \Delta(\log \nu)$, is

derived to be about 0.07, which is rather large compared to that for canonical spin-glasses (which is < 0.01) [15]. The fact that the T_p at the lowest frequency (1.3 Hz) matches with the value of T_N , suggests that spin-glass freezing sets in simultaneously with antiferromagnetic ordering. Combined with the observation that there is an upturn in the low-field FC χ in the magnetically ordered state (mentioned above) with decreasing temperature, we infer that the spin-glass is of a cluster-type, arising from antiferromagnetic clusters. However, there is no such feature in χ'' down to 2 K (shown for two frequencies only). The presence of a worthwhile signal in χ'' is a necessary criterion for spin-glass freezing [15]. We therefore infer that the spin-glass dynamics of the AF clusters is so weak that it escapes detection by χ'' measurement. An application of a dc field (say, 5 kOe) suppresses the peak in χ' marginally (in sharp contrast to the complete suppression in conventional spin-glasses) and this endorses weakness of spin-glass feature. Finally, there is a drop in χ' below 5 K, as in dc χ data, which is also distinctly frequency dependent behaving like the one at 18 K. Thus, down to 2 K, spin-glass behaviour coexists with AF as soon as long-range magnetic ordering sets in.

In order to render further support to spin-glass freezing, time (t) dependence of isothermal remnant magnetization (M_{IRM}) was measured below T_N . For this purpose, the sample was cooled to desired temperature in zero field, and then a field of 5 kOe was switched on for 5 mins. Immediately after switching off the field, M_{IRM} was tracked as a function of t , and the results are shown in Fig. 3b for 4, 8 and 15 K. It is clear that there is a slow decay of M_{IRM} (essentially logarithmically after waiting for about a minute) at all temperatures, characteristic of many spin-glass

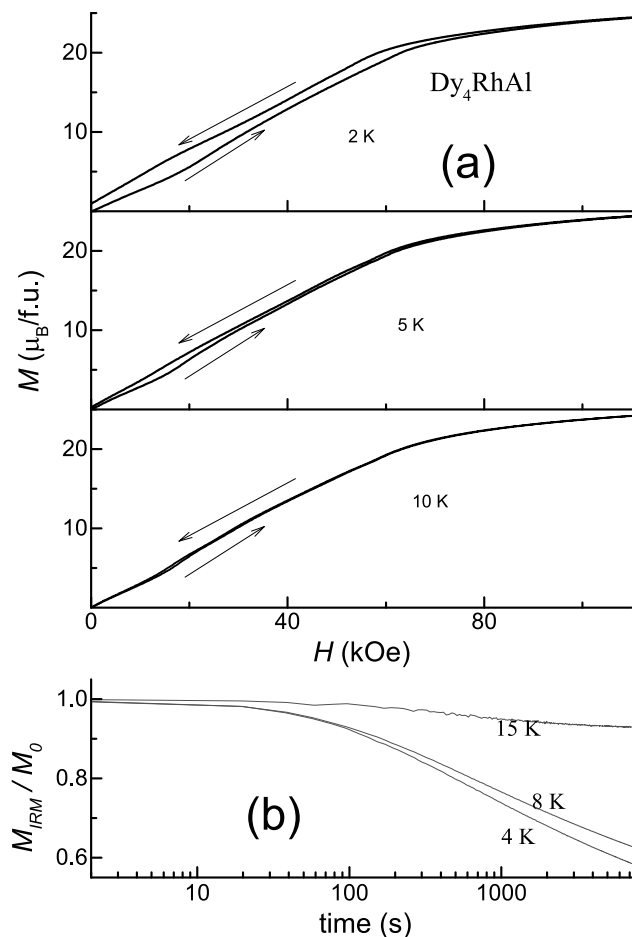


Fig. 3. (a) Isothermal magnetization at 2, 5 and 10 K, and (b) isothermal remnant magnetization as a function of time, normalized to respective values ($\sim 0.5, 0.25, 0.05$ emu/g) immediately after the field was switched off, at 4, 8, and 15 K for Dy_4RhAl .

systems; however, the magnitude of M_{IRM} at $t = 0$ decreases with increasing T , reflecting a change in the strength of spin-glass component with respect to antiferromagnetic part. Above T_N , say at 25 K, no such decay was observed.

The behaviour of $\rho(T)$ in the presence of various external fields (0, 30, 50, 70 and 100 kOe) and isothermal MR, defined as $[\rho(H) - \rho(0)]/\rho(0)$, at 5, 8, 12, 16 and 25 K are shown in Fig. 6a and 6b respectively. The derivative, $d\rho/dT$, in the paramagnetic state is metallic for all fields. The magnitude of ρ however undergoes pronounced depression with increasing H as the T is lowered, revealing a gradual increase of MR as the magnetic ordering is approached. In the past, several rare-earth intermetallics have been demonstrated to show this behaviour due to a peculiar magnetic precursor effect [16], which is recently understood in terms of an interplay between indirect exchange interaction and magnetic frustration [17]. With a further lowering of temperature, an upturn is observed as soon as magnetic ordering sets in (in zero field). This establishes the formation of magnetic Brillouin-zone formation, consistent with antiferromagnetic nature of the magnetic order [18]. This feature undergoes a gradual suppression with increasing H . Naturally, MR is large in the magnetically ordered state. In order to get a better picture of the magnitude of MR, the readers may see the isothermal MR

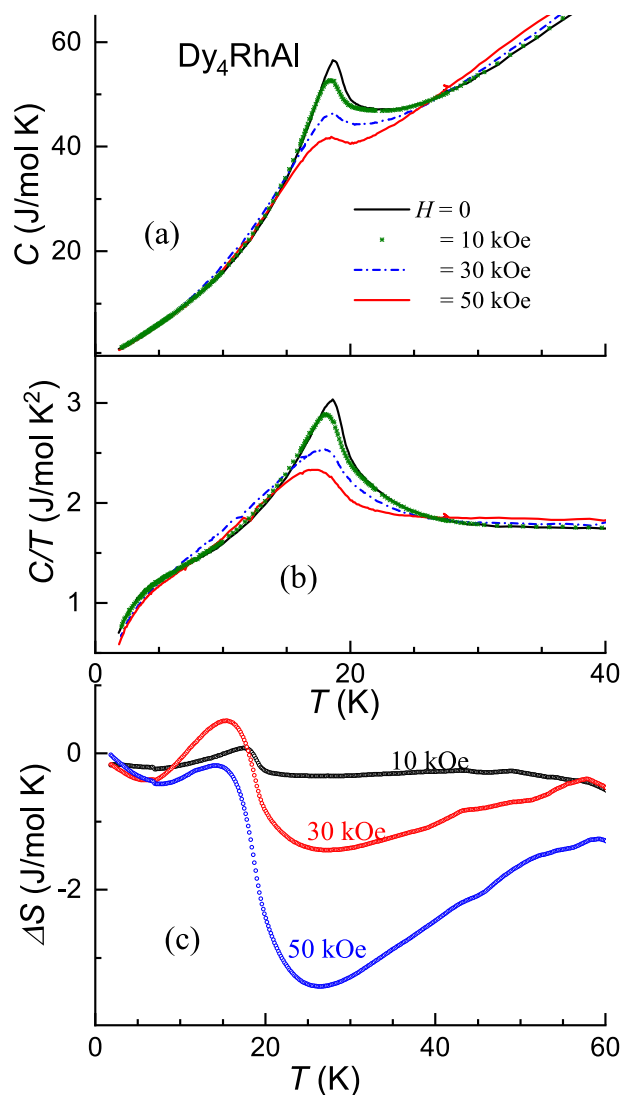


Fig. 4. The plots of (a) heat-capacity (C), (b) heat-capacity divided by temperature and (c) isothermal entropy change (ΔS) as a function of temperature (for final fields 10, 30 and 50 kOe) in the vicinity of magnetic ordering temperature for Dy_4RhAl .

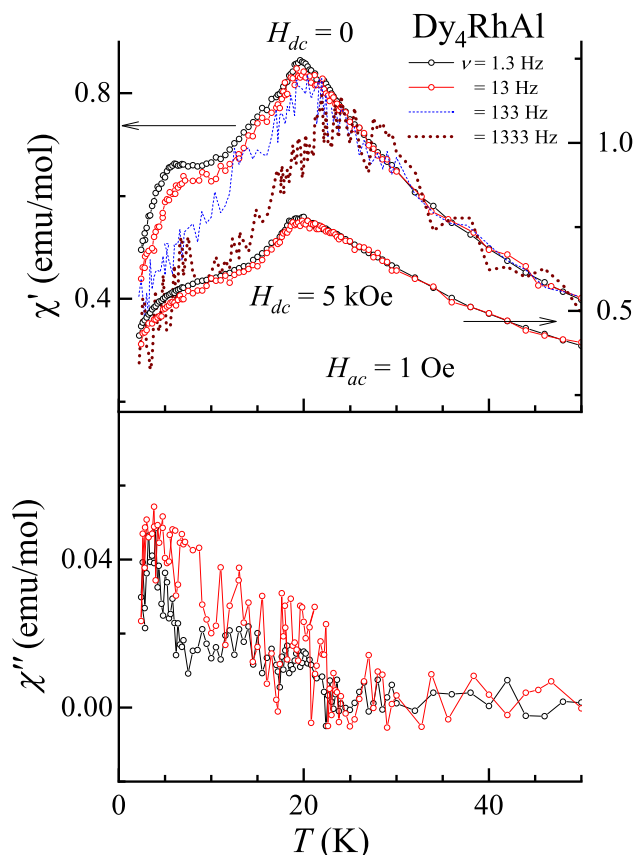


Fig. 5. Real (χ') and imaginary (χ'') parts of ac susceptibility for Dy_4RhAl . The lines through the data points are guides to the eyes.

curves, shown in Fig. 6b. A noteworthy finding in this figure is that there is a very broad step around 20–50 kOe at 5 K and the curve is weakly hysteretic supporting the conclusion from $M(H)$ data. This feature gradually gets smeared with increasing T . At 25 K, a quadratic field-dependence expected for paramagnets could be seen.

4. Conclusions

Several bulk measurements establish that the compound Dy_4RhAl undergoes antiferromagnetic order unlike its counterpart in Pt series. The present results therefore offer an indirect support for the fact that the ferromagnetic behaviour of Dy_4PtAl is interesting and unusual. It is possible that the Pt 5d orbital, which is more spatially extended compared to Rh 4d orbital plays a role by strong interaction with crystal-field-split anisotropic orbitals of Dy for the anomalous magnetism of Dy_4PtAl . Moreover, 5d electrons are relatively less correlated with stronger spin-orbit coupling than the 4d electrons. This suggests an important role of conduction electrons interacting with the Dy 4f electrons in determining the magnetism of these systems.

We hope that a comparative study of both these Dy compounds by spin-polarized band structure calculations, electron spectroscopy and neutron diffraction (to determine magnetic structure), would offer an ideal opportunity to throw light on the role of 5d band correlations on the magnetism of strictly localized 4f orbital. Inelastic neutron scattering studies are also warranted to learn about crystal-field scheme in these materials.

There are various other interesting observations with respect to the properties of the title compound, viz., evidence for antiferromagnetic energy gap formation, weak spin-glass behaviour of antiferromagnetic clusters, large magnetoresistance not only in the magnetically ordered state but also well above T_N extending to $T > 3T_N$, spin-orientation

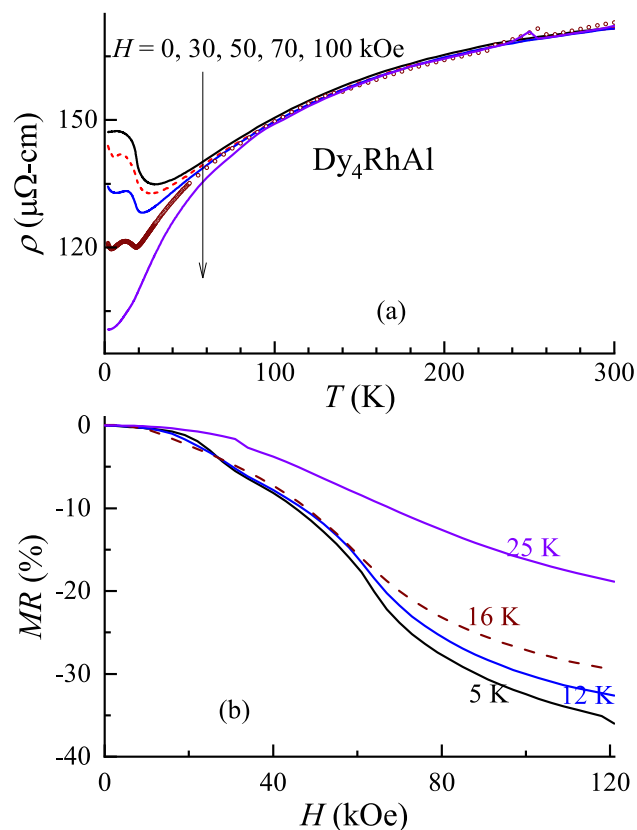


Fig. 6. (a) Electrical resistivity as a function of temperature in several fields, and (b) isothermal magnetoresistance at some temperatures for Dy_4RhAl .

effects as a function of T and H . It is of interest to explore theoretically how the interaction among 3 sites of rare-earth plays a role in deciding the magnetic behaviour.

Declaration of Competing Interest

The authors declare that they have no known competing financial interests or personal relationships that could have appeared to influence the work reported in this paper.

Data availability

Data will be made available on request.

Acknowledgements

E.V.S. acknowledges the support of Atomic Energy Department, Government of India, by way of awarding Raja Ramanna Fellowship. K. M. thanks financial support from BRNS, DAE under the DAE-SRC-OI program. SM thanks support from Vision Group on Science and Technology-GRD No 852.

References

- [1] A. Doan, S. Rayaprol, R. Pöttgen, *J. Phys. Condens. Matter.* **19** (2007), 076213.
- [2] F. Tappe, C. Schwickert, S. Linsinger, R. Pöttgen, *Monatsh. Chem.* **142** (2011) 1087.
- [3] M. Kersting, S.F. Matar, C. Schwickert, R. Pöttgen, *Z. Naturforsch.* **67b** (2012) 61.
- [4] S. Engelbert, O. Janka, *Intermetallics* **96** (2018) 84.
- [5] Ram Kumar, Jyoti Sharma, Kartik K Iyer, E.V. Sampathkumaran, *J. Magn. Magn. Mater* **490** (2019) 165515.
- [6] R. Kumar, K.K. Iyer, P.L. Paulose, E.V. Sampathkumaran, *J. Appl. Phys.* **126** (2019), 123906.
- [7] Ram Kumar, Kartik K Iyer, P.L. Paulose, E.V. Sampathkumaran, *AIP Conf. Proc.* **2265** (2020) 030509.

- [8] R. Kumar, K.K. Iyer, P.L. Paulose, E.V. Sampathkumar, *Phys. Rev. Mat.* 5 (2021), 054407.
- [9] Ram Kumar, E.V. Sampathkumar, *J. Magn. Mag. Mater* 538 (2021) 168285.
- [10] K. K. Iyer, Ram Kumar, S. Rayaprol, S. Matteppanavar, S. Dodamani, K. Maiti, E.V. Sampathkumar (to be published).
- [11] N. Marcano, J.C. Gómez Sal, J.I. Espeso, L. Fernández Barquín, C. Paulsen, *Phys. Rev.* 76 (2007), 224419.
- [12] T.D. Yamamoto, A. Kotani, H. Nakajima, R. Okazaki, H. Taniguchi, S. Mori, I. Terasaki, *J. Phys. Soc. Jpn.* 85 (2016), 034711.
- [13] Sanjay Kumar Upadhyay, Kartik K Iyer, E.V. Sampathkumar, *J. Phys. Condens. Matter* 29 (2017), 325601.
- [14] K.A. Gschneidner Jr, V.K. Pecharsky, A.O. Tsokol, *Rep. Prog. Phys.* 68 (2005) 1479.
- [15] K. Binder, A.P. Young, *Rev. Mod. Phys.* 58 (1986) 80; J.A. Mydosh, *Spin glasses: An Experimental Introduction*, Taylor and Francis, London, 1993.
- [16] R. Mallik, E.V. Sampathkumar, *Phys. Rev. B* 58 (1998) 9178.
- [17] Z. Wang, K. Barros, G.-W. Chern, D.L. Maslov, C.D. Batista, *Phys. Rev. Lett.* 117 (2016), 206601.
- [18] S. Legvold, *Magnetic Properties of Rare-earth Metals*, Plenum, 1972.

K.K. Iyer^{a,b,c}, S. Matteppanavar^{b,c}, S. Dodamani^b, K. Maiti^a, E. V. Sampathkumar^{d,*}

^a *Tata Institute of Fundamental Research, Homi Bhabha Road, Colaba, Mumbai 400005, India*

^b *Dr. Prabhakar Kore Basic Science Research Centre, KLE Academy of Higher Education and Research, Belagavi 590010, India*

^c *KLE Society's, Basavaprabhu Kore College of Arts, Science & Commerce, Chikodi 591110, India*




^d *Homi Bhabha Centre for Science Education, Tata Institute of Fundamental Research, V.N. Purav Marg, Mankhurd, Mumbai 400088, India*

* Corresponding author.

E-mail addresses: iyerkk@gmail.com (K.K. Iyer), sampathev@gmail.com (E.V. Sampathkumar).

Article

Magnetic and Transport Anomalies and Large Magnetocaloric Effect in Cubic R_4PtAl ($R = Ho$ and Er)

Kartik K. Iyer^{1,2,*}, Sudhindra Rayaprol³, Ram Kumar^{1,4}, Shidaling Matteppanavar⁵, Suneel Dodamani², Kalobaran Maiti¹ and Echur V. Sampathkumaran^{6,*}¹ Tata Institute of Fundamental Research, Homi Bhabha Road, Colaba, Mumbai 400005, India² KLE Society's Dr. Prabhakar Kore Basic Science Research Centre, KLE Academy of Higher Education and Research, Belagavi 590010, India³ UGC-DAE-Consortium for Scientific Research—Mumbai Centre, BARC Campus, Trombay, Mumbai 400085, India⁴ Maryland Quantum Materials Center and Department of Physics, University of Maryland, College Park, MD 20742, USA⁵ KLE Society's Basavaprabhu Kore Arts, Science & Commerce College, Chikodi 591201, India⁶ Homi Bhabha Centre for Science Education, TIFR, V. N. Purav Marg, Mumbai 400088, India

* Correspondence: iyer@tifr.res.in (K.K.I.); sampathev@gmail.com (E.V.S.); Tel.: +91-22-22782439 (K.K.I.)

Abstract: We report the electronic properties of R_4PtAl ($R = Ho$, and Er), which contains three sites for R , by the measurements of magnetization (ac and dc), heat-capacity, transport, and magnetoresistance (MR). Dc magnetization data reveal antiferromagnetic order below 19 K and 12 K in Ho and Er compounds, respectively. Additional features observed at lower temperatures (12 K for Ho_4PtAl and 5 K for Er_4PtAl) are akin to the cluster spin-glass phase. Resistivity data exhibit a weak minimum at a temperature marginally higher than their respective Néel temperature (T_N), which is unusual for such rare-earths with well-localized $4f$ states. Isothermal magnetization and magnetoresistance data well below T_N exhibit signatures of a subtle field-induced magnetic transition for a small magnetic field (<10 kOe). Notably, the isothermal entropy change at T_N has the largest peak value within this rare-earth family; for a field change from zero to 50 kOe, the entropy change is ~ 14.5 J/kg K (Ho_4PtAl) and ~ 21.5 J/kg K (Er_4PtAl) suggesting a role of anisotropy of $4f$ orbital in determining this large value. The results provide some clues for the advancement of the field of magnetocaloric effect. The magnetocaloric property of Er_4PtAl is nonhysteretic, meeting a challenge to find materials with reversible magnetocaloric effect.

Keywords: rare earth intermetallics; magnetocaloric effect; antiferromagnetism

Citation: Iyer, K.K.; Rayaprol, S.; Kumar, R.; Matteppanavar, S.; Dodamani, S.; Maiti, K.; Sampathkumaran, E.V. Magnetic and Transport Anomalies and Large Magnetocaloric Effect in Cubic R_4PtAl ($R = Ho$ and Er). *Magnetochemistry* **2023**, *9*, 85. <https://doi.org/10.3390/magnetochemistry9030085>

Academic Editors:

Devashibhai Adroja and Dmitry Alexandrovich Filippov

Received: 4 March 2023

Revised: 16 March 2023

Accepted: 18 March 2023

Published: 20 March 2023



Copyright: © 2023 by the authors. Licensee MDPI, Basel, Switzerland. This article is an open access article distributed under the terms and conditions of the Creative Commons Attribution (CC BY) license (<https://creativecommons.org/licenses/by/4.0/>).

1. Introduction

There is a general consensus that the technology of “magnetic refrigeration” can increase the efficiency of cooling when compared to the conventional gas-compression route. Therefore, there are constant efforts in the current literature to find clues to improve the magnetocaloric effect (MCE) as well as to discover new solid materials which are cost-efficient, as well as those that minimize the problems due to irreversibility in magnetic-field (H) cycling. Gd metal, being a large magnetic-moment element, seems to remain the benchmark for applications, even after several decades of intense research. It is needless to emphasize that the exceptional MCE behavior of $Gd_5Si_2Ge_2$ reported by Pecharsky and Gschneidner [1] in 1997 has been at the centerstage of the field of MCE, but its application has been limited due to the hysteretic nature of the first-order magnetic-field induced magnetic transition. Naturally, the search for new rare-earth (R) compounds with magnetic anomalies continues to be an important direction of research to find favorable MCE materials in different temperature (T) ranges. Keeping this scenario in mind, we have investigated the magnetic and MCE behavior of two rare-earth compounds, R_4PtAl ($R = Ho$ and Er).

The compounds of the type R_4TX (T = transition metals and X = p-block metal) with the cubic Gd_4RhIn -type structure [2–5] provide a new platform in the field of “frustrated magnetism”, as multiple sites for R seem to favor a spin-glass state, competing with antiferromagnetism (AF) and ferromagnetism (F) [6–11]. The crystal structure is shown in Figure 1 to bring out the surrounding of the three R ions. Complexities of crystallography for this family have been discussed by Engelbert and Janka in the literature [5] and also presented in our earlier publication [7].

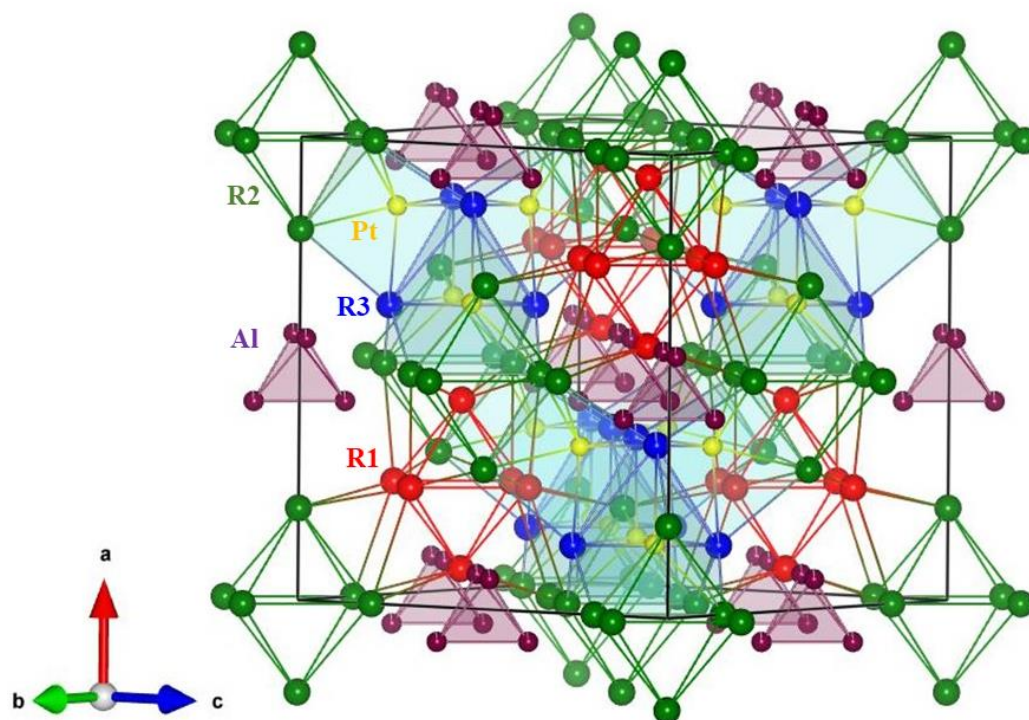


Figure 1. Crystal structure of R_4PtAl (R = Rare-earth). The rare-earths with different chemical environments can be seen. The rare-earths R1 (red) and R2 (green) form separate octahedra and R2 and R3 form an octahedra with Pt (yellow) at the center. The rare-earth R3 (blue) forms a tetrahedra. Al forms a tetrahedra.

Recent investigations on some members of this class of compounds have established that there are novel transport anomalies, not only in the magnetically ordered state, but also in the paramagnetic state [6–11]. Here, we focus on the heavy R members of the Pt-based family, R_4PtAl , where the $4f$ states are far away from the Fermi level (thereby avoiding the complex, well-known phenomena due to $4f$ -hybridization in light rare-earths); Pt $5d$ electrons are expected to be weakly correlated, although possessing strong spin-orbit coupling. Extensive studies in recent years revealed that Gd_4PtAl shows re-entrant spin-glass behavior around 20 K below its Néel temperature ($T_N = 64$ K) [6], whereas Tb_4PtAl exhibits spin-glass features at the onset of the AF order at 50 K and an additional spin-glass anomaly at a further lower temperature [7]. Curiously, the Dy analogue undergoes a ferromagnetic transition at (T_C) 32.6 K, indicating an unusual role of Pt $5d$ states on the magnetism of a rare-earth with well-localized $4f$ orbital [11], which transforms to a spin-glass phase around 20 K [8]. There are magnetic-field-induced features as well, attributable to first-order transitions in most of these compounds. The experimental results presented in this article on Ho and Er compounds reveal fascinating magnetic and transport anomalies with an exceptional MCE, as inferred from the values of the isothermal entropy change (ΔS), in comparison with the values reported earlier for this family; this finding at low-temperatures provides some clues for further theoretical advancement in the field of MCE to enable the discovery of new materials for room temperature applications.

2. Materials and Methods

Samples were prepared in polycrystalline form by arc-melting stoichiometric amounts of constituent elements in an argon atmosphere. The Er compound needed to be annealed at 650 °C for 8 days. Powder x-ray diffraction patterns (XRD), shown in Figure 2, were obtained using Cu-K α radiation, and these were found to be in good agreement with those reported in Ref. [5]. Rietveld refinement further helped in understanding the diffraction patterns. Such an analysis enabled us to ascertain the formation of the cubic phase with the space group $F\bar{4}3m$. It may be mentioned that the XRD pattern showed a weak extra line around 36° for the unannealed Er sample, which disappeared after annealing. Scanning electron microscopic images revealed the homogeneity of the samples without showing any extra phase. Dc magnetic susceptibility (χ) (1.8 to 300 K) and isothermal magnetization (M) measurements were performed with the help of a commercial (Quantum Design) superconducting quantum interference device; ac χ data were also collected in a T -region of interest with an ac field of 1 Oe with different frequencies ($\nu = 1.3, 13$ and 133 Hz) with the same magnetometer. Heat-capacity (C) and electrical resistivity (ρ) and magnetoresistance (MR) measurements down to 1.8 K and also as a function of H were carried out using a commercial (Quantum Design Physical Property Measurement System). Unless otherwise stated, all the measurements were performed for the zero-field-cooled (ZFC) condition of the specimens.

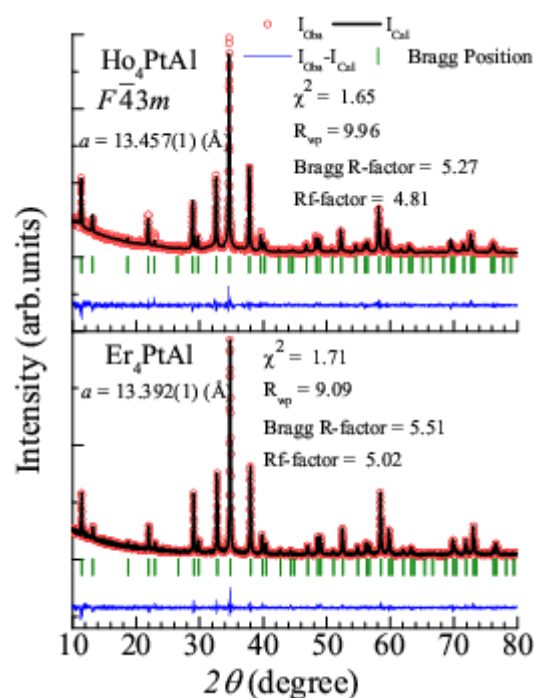


Figure 2. X-ray diffraction patterns of Ho₄PtAl and Er₄PtAl at room temperature, along with Rietveld fitting results.

3. Results and Discussions

Figures 3a,b and 4a,b show $\chi(T)$ measured in 5 kOe magnetic field as well as in 100 Oe field for both the samples. Inverse χ , plotted for 5 kOe data in the mainframe, is linear above 50 K.

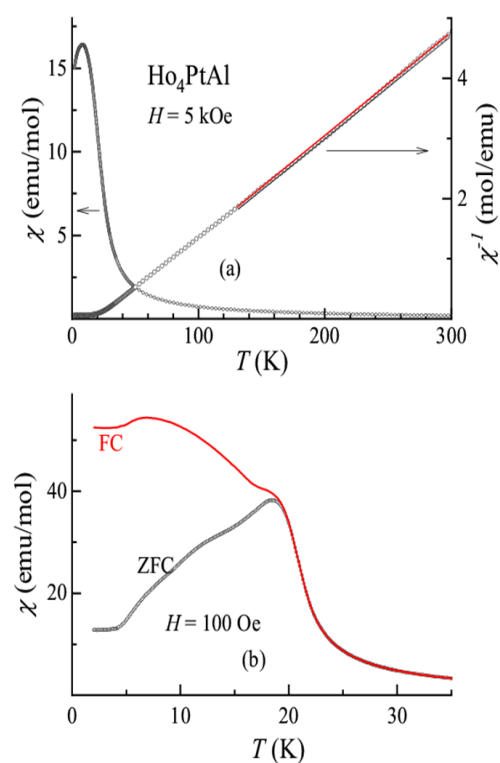


Figure 3. The temperature-dependent dc magnetic susceptibility and inverse susceptibility for Ho_4PtAl , measured in (a) 5 kOe and (b) 100 Oe. In (b), the curve obtained for field-cooled warming conditions is also included. In (a), a straight line in the inverse χ plot above 120 K represents Curie–Weiss fitting.

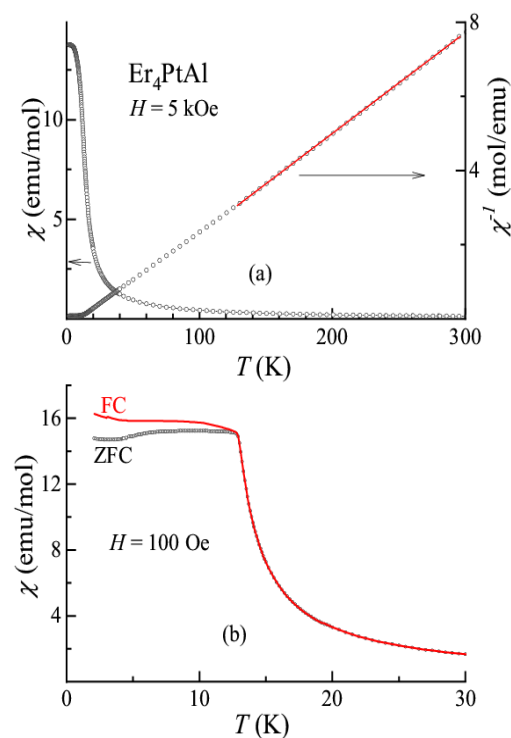


Figure 4. The temperature-dependent dc magnetic susceptibility and inverse susceptibility for Er_4PtAl , respectively, measured in (a) 5 kOe and (b) 100 Oe. In (b), the curve obtained for field-cooled warming conditions is also included. In (a), a straight line in the inverse χ plot above 120 K represents Curie–Weiss fitting.

The values of the effective magnetic moments ($\sim 10.7 \mu_B$ and $9.82 \mu_B$ per Ho and Er, respectively) derived from the high-temperature paramagnetic region are in good agreement with the theoretical values (10.6 and $9.59 \mu_B$, respectively) (see, for instance, Ref. [12]). The corresponding values of paramagnetic Curie temperature (θ_p) are ~ 27 K and 16 K. The positive sign of θ_p indicates that ferromagnetic coupling between the rare-earth moments is dominant in these compounds in the Curie–Weiss regime, as also observed in the cases of Gd, Tb, and Dy members [6–8]; the situation is more complex at lower temperatures as described below. For the Ho compound, as the T is lowered, there is a peak in $\chi(T)$ in the ZFC curve for $H = 100$ Oe near 19 K (Figure 3b) attributable to the long range antiferromagnetic order, followed by a shoulder near 12 K and a flattening below about 5 K, as though there are additional magnetic transitions. The ZFC curve obtained in 5 kOe field smeared out these additional magnetic features. This suggests that the magnetism is sensitive to external magnetic fields. Irreversibility appeared in the 100 Oe field-cooled (FC) and ZFC curves (Figure 3b) at around 19 K, signaling a possibility of the spin-glass phase, though other factors (like domain wall boundary effects) have also been known to result in such a feature in ferromagnetic and antiferromagnetic materials. In the case of the Er sample, the features appear similar with magnetic ordering (presumably of an AF type, *vide infra*) setting in at 12 K along with an additional feature (a change of slope) around 5 K for the curves measured in 100 Oe (Figure 4b); the bifurcation of the low-field ZFC-FC curves in the magnetically ordered state can be seen even for this compound at around 12 K. It is important to note that the FC curves in both the cases tended to show an increase with decreasing temperature (though it is weak for the Er case) below T_N , which is a signature of cluster spin-glass behavior [6,13–15]. The observed values of magnetic ordering temperatures and θ_p are marginally higher compared to the respective de Gennes scaled values (for full degeneracy), as inferred from the knowledge of the corresponding values (64 K and 86 K) for the Gd analogue [6]. This means that anisotropy of the crystal-field-split $4f$ orbital probably plays a role in such a breakdown [16–18].

In Figure 5a,b, we show the $M(H)$ curves up to 70 kOe at selected temperatures in the magnetically ordered state for both compounds. The points to be noted are: (i) in these curves, there was a sharp increase of M for initial applications of H , indicating a possible tendency towards ferromagnetic alignment at a small H ; there is a distinct step around 5 kOe for the Ho compound at 2 K in support of the fact that the zero-field state cannot be classified as a ferromagnet, but as a canted antiferromagnet undergoing spin reorientation; (ii) even at fields as high as 70 kOe, there is no evidence for saturation, supporting further the canted nature of magnetic structure persisting at high fields; (iii) distinct hysteresis, though weak, is observed for the Ho compound at 2 K, which was found to diminish gradually with increasing temperature well below T_N , as shown in Figure 4c for 16 K, in the low-field hysteresis measurements; this hysteresis suggests the existence of a ferromagnetic component; (iv) hysteresis is absent in the $M(H)$ curves for the Er compound down to 2 K (Figure 5d). The results overall suggest the canted antiferromagnetic nature of the virgin state at the onset of magnetic order.

We have measured ac χ to get more insight into the nature of the magnetically ordered state, given that the sign of θ_p positively supports the existence of ferromagnetic correlations, whereas the virgin specimens reveal the onset of antiferromagnetic order (as discussed above). The real (χ') and imaginary (χ'') parts are shown in Figure 6. In the case of Ho compound, χ' (in zero field) exhibits a peak at 19 K, followed by a shoulder around 12 K; there are upturns at similar temperatures in the χ'' . No feature could be clearly resolved around 5 K, though χ'' exhibits a change of slope. All these features vanish in an applied field of 5 kOe, clearly revealing the existence of a spin-glass component. The ν -dependence of the peak, though weak, is discernable; the fact that it is seen even at the onset of long-range magnetic order does not rule out the possibility of antiferromagnetic cluster spin-glass behavior. In the case of Er compound, χ' (in zero field) exhibits a peak at ~ 12 K, followed by a distinct change of slope around 5 K, consistent with the dc χ data presented above. There is also a shoulder around 10 K, the origin of which is not clear; pos-

sibly, there is an additional spin-reorientation at this temperature, which is subtly sensitive to small fields, escaping detection in the dc χ measurements even in fields as low as 100 Oe. It appears that such subtle additional magnetic features could be observed under favorable circumstances due to complex interaction between the three non-equivalent magnetic sites, as also observed for the Tb analogue [7]. The frequency dependence of the peak is not well resolved, though the left side of the peak shows some dependence. However, the χ'' curves reveal a distinct frequency-dependent peak at about 5 K without any notable peak at higher temperatures. These findings imply that the 5 K-feature alone could arise from spin-glass freezing. An application of a dc magnetic field of 5 kOe completely suppresses the peaks. Viewing together with the behavior of low-field dc χ curves and dc M , we conclude that (virgin state) antiferromagnetism below 5 K behaves like (cluster) spin-glasses for the Er case.

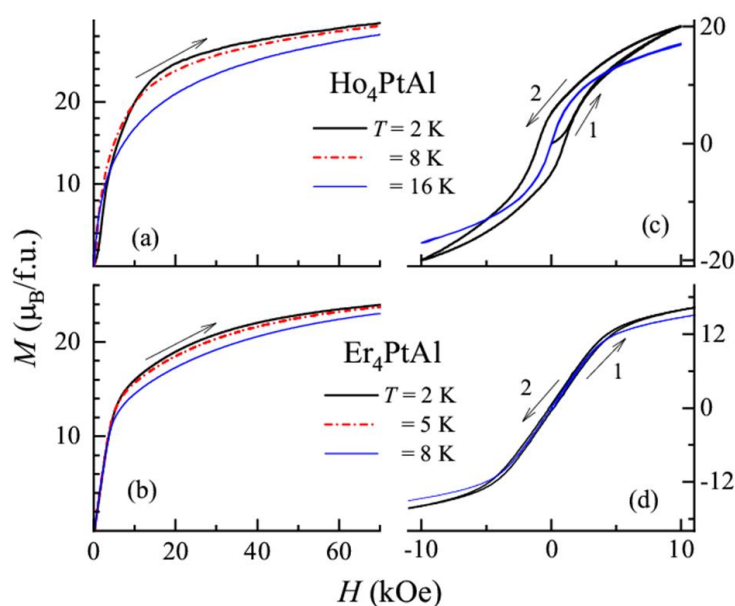


Figure 5. Isothermal magnetization (per formula unit) at selected temperatures for (a) Ho_4PtAl and (b) Er_4PtAl . In (c,d), respective low-field (0 to 10 to -10 to 10 kOe) hysteresis loops are shown for two temperatures.

In order to render support to the above conclusions for both the materials, we have measured isothermal remanent magnetization (M_{IRM}) at selected temperatures below T_N ; for this purpose, we cooled the samples in 5 kOe to desired temperatures, switched off the field and measured M_{IRM} as a function of time. It is noted (Figure 6e,f) that the value M_{IRM} , measured immediately after the field was switched off (labeled $M(0)$), decreases with the increase of T and also decreases slowly with time. Though the functional form of the decay with time appears to be complicated (e.g., two logarithmic regions are seen in Figure 6e,f), possibly due to the presence of multiple sites for R, the slow decay is consistent with the glassy behavior, at least in the close vicinity of 5 K for both the cases.

Figure 7 shows heat-capacity as a function of temperature for both the compounds in the form of C versus T as well as of C/T versus T below 40 K. It is clear that there is a well-defined feature (upturn followed by a peak) as the magnetic ordering temperature is approached from the paramagnetic state for both the compounds in the absence of a magnetic field. Additionally, for the Ho compound, there is a shoulder around 12 K in the plot of $C(T)$ (Figure 7a), which is more transparent in the plot of $C(T)/T$ (Figure 7b). There is also a weak upturn in $C(T)$ below about 5 K, and it is possible that it is due to subtle changes in the orientation of magnetic moments. As the magnetic field is applied, for $H = 10$ kOe, the peak temperature is marginally decreased with the feature due to the onset of magnetic order partly overlapping with the one due to 12 K transition. This established that the magnetic structure at the onset of magnetic order is of an AF type and not of an

F-type as proposed earlier [5]. For further higher fields (30 and 50 kOe), the peak is smeared and there was a monotonic decrease of C with T down to 5 K (Figure 7c). With respect to the Er case, it is clear that, following a sharp rise below 14 K, the peak appears around 12 K (in zero field). The C/T plot (Figure 7d) shows an additional sharp anomaly around 5 K in support of a magnetic feature around this temperature, as indicated by ac χ . Below 10 K, there is no evidence for $T^{3/2}$ or T^3 behavior, expected for ferromagnets/spin-glasses and antiferromagnets, respectively, thereby revealing that the magnetism is, in fact, quite complex. It is not clear whether a shoulder in C/T near 10 K can be correlated to the ac χ feature at this temperature (see above). The H -dependence of the magnetic feature is somewhat similar to that of the Ho case, and the downward shift of the peak with H is consistent with the AF ordering at the onset of the magnetic transition.

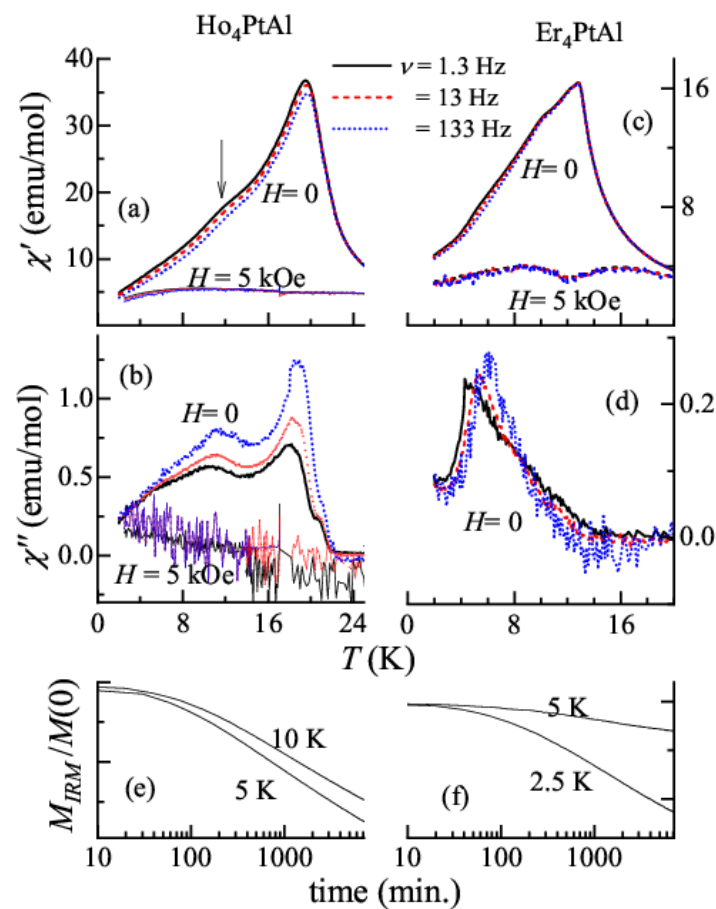


Figure 6. Real (χ') and imaginary (χ'') parts of ac susceptibility for Ho_4PtAl are shown in (a,b) and corresponding parts for Er_4PtAl are plotted in (c,d). A vertical arrow in (a) is drawn to show the temperature where the shoulder occurs. Time dependence of isothermal remnant magnetization at selected temperatures are plotted in (e) for the former and in (f) for the latter. In (d), the 5kOe-data is not plotted, as it is very noisy and featureless. The values of M_{IRM} , labeled $M(0)$, immediately after the field is switched off, are: For Ho, -14 and 6.3 emu/g for 5 and 10 K, and, for Er, 2.7 and 1.5 emu/g for 2.5 and 5 K, respectively.

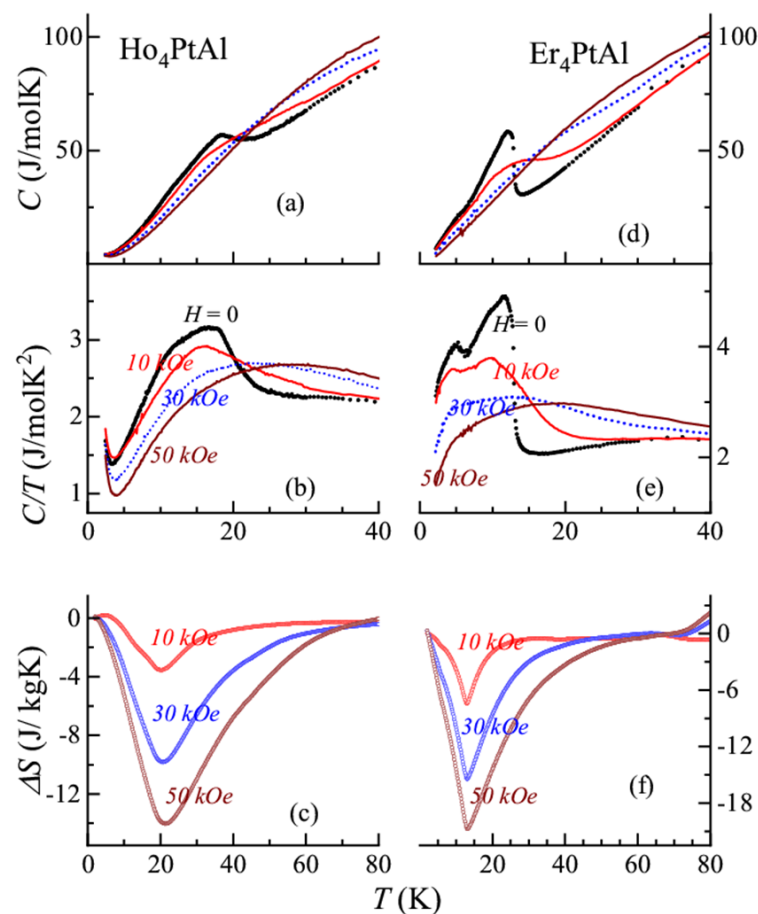


Figure 7. The plots of heat-capacity (C), heat-capacity divided by temperature, and isothermal entropy change (ΔS) as a function of temperature for Ho_4PtAl are shown in (a–c), respectively. Corresponding plots for Er_4PtAl are shown in (d–f).

We have derived isothermal entropy change, $\Delta S = S(H) - S(0)$, by integrating the plots of C/T , and the results obtained are shown in Figure 6c,f, for selected final fields. The plots of ΔS exhibit a peak in the negative quadrant for both cases, even for an application of a field as small as 10 kOe; this sign is typical of ferromagnetism [19] and, therefore, this supports the inference made from $M(H)$ for the appearance of a ferromagnetic component even for such low fields (though AF component still persists as discussed above). We had also obtained ΔS from isothermal M data employing Maxwell's equation for the Er case by measuring isothermal M in close intervals of temperature (every 3 K, not shown here); the values and the features are in good agreement with that derived from the $C(T)$ data. We would like to emphasize the following outcome: (i) the peak values of ΔS are relatively large for both the compounds, compared to that of analogous Gd, and Tb members [6–8]. For instance, for a field of 50 kOe, the values for Ho and Er members are about ~ 14.5 and ~ 21.5 J/kg K, whereas the corresponding values are lower for Gd (~ 6 J/kg K). For Tb and Dy cases, the corresponding peak values are ~ 6 and 13 J/kg K, respectively. Clearly, the value for the Er sample is the largest within this family. The magnetic refrigeration capacity, defined as the product of the full-width at half maximum and the peak value, is quite large—about 420 J/kg K—and comparable to many best magnetocaloric materials in this temperature range of interest [20]. This finding, therefore, reinforces [9] that the anisotropy of the (crystal-field-split) 4f orbital (that is, aspherical nature) plays a key role for such an enhancement. (ii) The peak values of these two Pt compounds are far higher than those of the respective member of the isomorphous Rh family as well [9–11]. In fact, a comparison of the peak values of ΔS between Pt and Rh families suggests that this is in general true for a given R, e.g., for Gd_4PtAl and Gd_4RhAl , the values are ~ 6 and ~ 2.3 J/kg K,

respectively [6,9]. It is known that the electronic correlation within the 4d bands is usually stronger than that within 5d bands in transition metal systems; on the other hand, the spin-orbit coupling is stronger for the latter. We, therefore, wonder spin-orbit coupling effect of the Pt 5d electrons plays a role in enhancing MCE. It is needless to elaborate that the correlated electrons in the event of stronger spin-orbit coupling (compared to crystal-field splitting and electron hopping amplitude) resulted in a rich variety of spin-orbit entangled phenomena, as demonstrated in recent years for oxide systems (see, for a review, Ref. [21]); (iii) as discussed for other compounds of this family [6,9–11], the plot of ΔS exhibits a long tail over a wide T -range above T_N , possibly arising from a gradual formation of ferromagnetic clusters with a lowering of temperature (behaving like a classical spin-liquid). The readers may note that interesting magnetic precursor effects have been brought out in different contexts, as well in the past, in insulating materials [22–25]. (iv) The isothermal magnetization curves were non-hysteretic for the Er case, and, in view of this, this compound can be added to the list of materials for magnetic refrigeration below 40 K, considering that it is often emphasized in the literature to find materials with such a reversible behavior [26,27].

The $\rho(T)$, as expected for metals, exhibits a positive temperature coefficient as the temperature is lowered below 300 K (Figure 8a,b) but exhibits a minimum in the paramagnetic state just above the ordering temperature in both the cases in zero field (at 26 K and 14 K, respectively) (Figure 8c,d, insets). Such a minimum, though not expected for rare-earths with localized 4f electrons like Ho and Er, was encountered in some heavy rare-earth systems as a precursor to long-range magnetic order [10,28,29]. Recent new theoretical ideas attribute it to classical spin-liquid behavior due to geometrically frustrated magnetism [30]. Such a minimum vanished gradually with the application of an external magnetic field, as shown in Figure 8c,d, for an application of 10 kOe. As the material enters a magnetically ordered state, the drop due to the loss of spin-disorder contribution (see zero field curves) could be seen. Following interesting observations were made on the magnetoresistance ($MR = [\rho(H) - \rho(0)]/\rho(0)$) data, even in the paramagnetic state (Figure 9). There was a competition between positive contribution due to the Lorentz motion of the conduction electrons (that is, classical metallic part, varying quadratically with H) and negative contribution due to the suppression of spin fluctuation contribution by H as a function of H and T . Thus, at 18 K (close to T_N), for the Er case, there was initially an increase in the positive quadrant due to metallic contribution, followed by a peak around 25 kOe and then a fall with the curve entering the negative quadrant around 55 kOe due to spins. At higher temperatures, say at 25 K, MR curve remains in the positive quadrant due to the weakening of spin contribution with respect to the metallic part. On the other hand, for the Ho compound, just above its T_N , say, at 25 K, the spin contribution dominated, as revealed by the negative sign, until about 25 kOe, and it was overcompensated at higher fields by the metallic part at higher fields. At higher temperatures, the $MR(H)$ curve stays in the positive quadrant only. Concerning the behavior below T_N (Figure 10), the sign of MR remains negative, either due to antiferromagnetic gap formation and/or spin-glass component. The fact that the antiferromagnetic-gap formation occurs is evidenced, at least for the Ho case, by the observation that there was initially a (weak) upturn in ρ (in the zero-field curve) as soon as the magnetically ordered state was entered; this upturn was suppressed by a field of 10 kOe (see Figure 8). A notable finding in the isothermal MR curves is that the virgin curve lay prominently outside the envelope loop below 12 K in the low-field range (<4 kOe) with a significant hysteresis for the Ho case, supporting that there could be a disorder-broadened first-order magnetic transition at such low fields; however, in the Er case, the magnitude of MR was so small that hysteresis $MR(H)$ could be considered negligible.

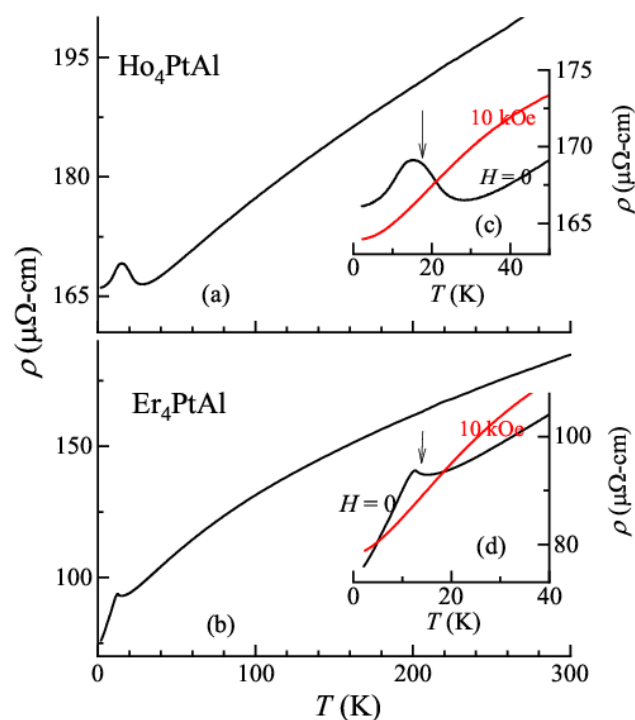


Figure 8. Zero-field electrical resistivity in the range 2–300 K are shown for Ho_4PtAl and Er_4PtAl in (a,b), respectively. The data below 50 K for the Ho case and below 40 K for the Er case in zero-field and in 10 kOe are shown in the insets c–f in an expanded form to show the existence of a resistivity minimum. Vertical arrows mark Néel temperature, inferred from other measurements presented in the text.

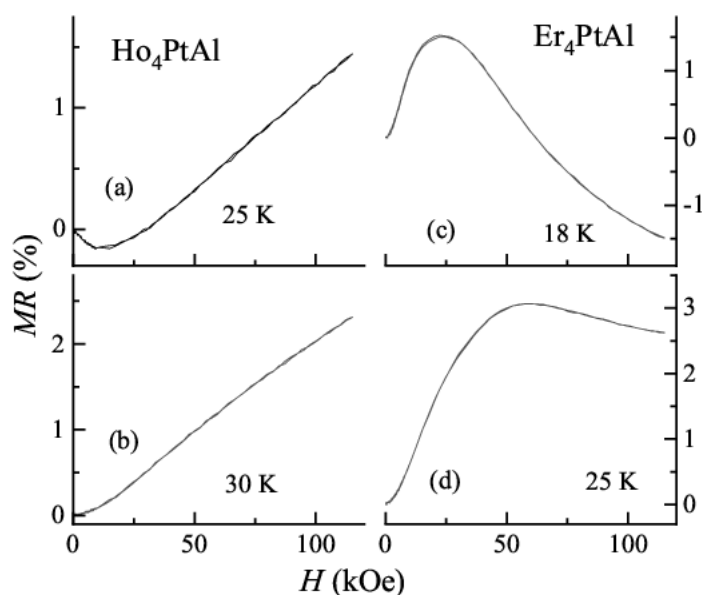


Figure 9. Isothermal magnetoresistance $[\rho(H) - \rho(0)]/\rho(0)$ as a function of the magnetic field at selected temperatures above T_N ; (a) 25 K and (b) 30 K for Ho_4PtAl ; and (c) 18 K and (d) 25 K for Er_4PtAl .

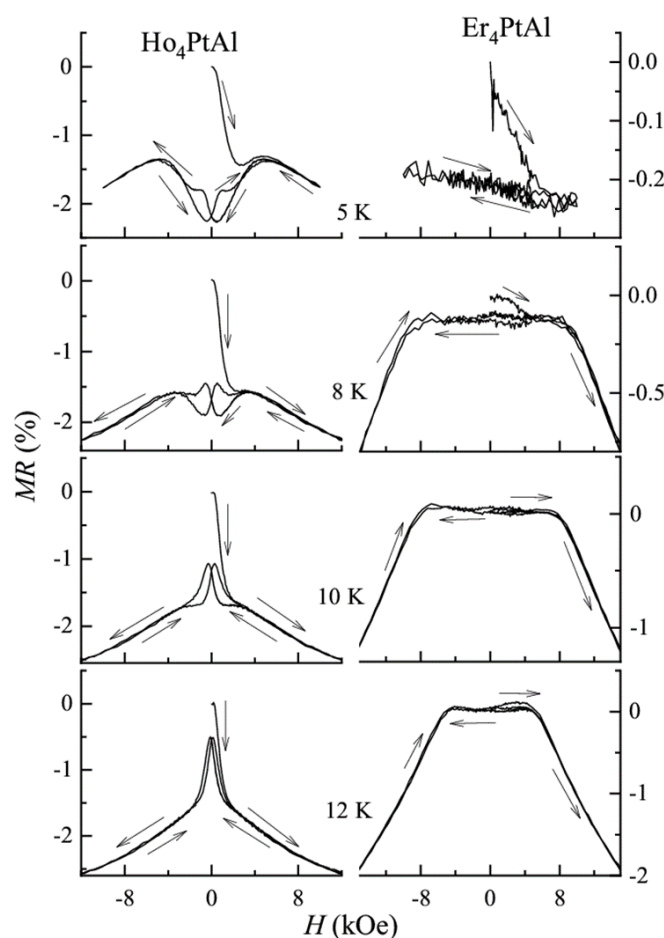


Figure 10. Magnetoconductance hysteresis loops at 5, 8, 10, and 12 K for Ho_4PtAl and Er_4PtAl .

4. Conclusions

The present results establish that Ho_4PtAl and Er_4PtAl , are interesting magnetic materials with re-entrant spin-glass behavior with the onset of magnetic order of an antiferromagnetic type, but undergoing subtle changes in this magnetic state by an application of a small external field. A notable finding is that these compounds show the largest value of isothermal entropy change (a measure of magnetocaloric effect) at the onset of magnetic order within this family, in particular with respect to the isomorphous Gd compound. Since the values surpass that of an S-state ion, this finding suggests that the topology of the $4f$ orbital can enhance the magnetocaloric effect. Another intriguing outcome, based on the comparison of the MCE behavior of Pt-based family with that of Rh family, is that Pt $5d$ spin-orbit coupling also may play a role in this regard. We hope these inferences provide clues for the advancement of theories in the field of MCE to enable the engineering of materials for magnetic refrigeration at room temperature (see, for instance, Ref. [31] for a report on thin film route of a manganite to enhance MCE with respect to Gd metal at room temperature). This entropy behavior of the Er compound meets the much-needed [27] characteristic of “reversibility” for magnetocaloric applications in the low temperature range. Finally, neutron diffraction studies would be rewarding to understand the magnetic structure changes with temperature and magnetic field in these materials.

Author Contributions: Conceptualization, E.V.S.; methodology, K.K.I. and R.K.; validation, K.K.I., R.K., K.M., and E.V.S.; formal analysis, K.K.I. and S.R.; data curation, K.K.I. and R.K.; writing—original draft preparation, K.K.I.; writing—review and editing, E.V.S., S.R. and K.M.; visualization, E.V.S.; supervision, E.V.S. and K.M.; project administration, K.M.; funding acquisition, K.M., E.V.S., S.D. and S.M. All authors have read and agreed to the published version of the manuscript.

Funding: Financial support from the DAE, Govt. of India (Project Identification No. RTI4003, DAE OM No. 1303/2/2019/R&DII/DAE/2079 dated 11-02-2020) is thankfully acknowledged. K.M. thanks financial support from BRNS, DAE under the DAE-SRC-OI program. S.M. thanks support from Vision Group on Science and Technology-GRD No 852.

Institutional Review Board Statement: Not applicable.

Informed Consent Statement: Not applicable.

Data Availability Statement: The data presented in this study are available on request from the corresponding author.

Acknowledgments: E.V.S. thanks the Atomic Energy Department, Government of India, for awarding the Raja Ramanna Fellowship.

Conflicts of Interest: The authors declare no conflict of interest.

References

1. Pecharsky, V.K.; Gschneidner, K.A. Giant Magnetocaloric effect in $Gd_5(Si_2Ge_2)$. *Phys. Rev. Lett.* **1997**, *78*, 4494–4497. [[CrossRef](#)]
2. Tappe, F.; Schwickert, C.; Linsinger, S.; Pöttgen, R. New rare earth-rich aluminides and indides with cubic Gd_4RhIn -type structure. *Monatsch. Chem.* **2011**, *142*, 1087. [[CrossRef](#)]
3. Doğan, A.; Rayaprol, S.; Pöttgen, R. Structure and magnetic properties of RE_4CoCd and RE_4RhCd ($RE = Tb, Dy, Ho$). *J. Phys. Condens. Matter.* **2007**, *19*, 0762131–07621313. [[CrossRef](#)]
4. Kersting, M.; Matar, S.F.; Schwickert, C.; Pöttgen, R. Segregation of Calcium and Magnesium into Different Substructures. $Ca_4Ag_{0.948}Mg$ and Other Compounds with Gd_4RhIn -type Structure. *Z. Naturforsch.* **2012**, *67*, 61–69. [[CrossRef](#)]
5. Engelbert, S.; Janka, O. RE_4TAl ($RE = Y, Sm, Gd-Tm, Lu; T = Pd, Pt$)—Synthesis and magnetism of new aluminum representatives with the Gd_4RhIn type structure. *Intermetallics* **2018**, *96*, 84–89. [[CrossRef](#)]
6. Kumar, R.; Sharma, J.; Iyer, K.K.; Sampathkumaran, E.V. Reentrant spin-glass and transport behavior of Gd_4PtAl , a compound with three sites for Gd. *J. Magn. Mag. Mater.* **2019**, *490*, 165515. [[CrossRef](#)]
7. Kumar, R.; Iyer, K.K.; Paulose, P.L.; Sampathkumaran, E.V. Spin-glass features at multiple temperatures and transport anomalies in Tb_4PtAl . *J. Appl. Phys.* **2019**, *126*, 123906. [[CrossRef](#)]
8. Kumar, R.; Iyer, K.K.; Paulose, P.L.; Sampathkumaran, E.V. Ferromagnetism to spin-glass transition and magnetotransport anomalies in Dy_4PtAl . *AIP Conf. Proc.* **2020**, *2265*, 030509.
9. Kumar, R.; Iyer, K.K.; Paulose, P.L.; Sampathkumaran, E.V. Competing magnetic interactions and magnetoresistance anomalies in cubic intermetallic compounds, Gd_4RhAl and Tb_4RhAl , and enhanced magnetocaloric effect for the Tb case. *Phys. Rev. Mater.* **2021**, *5*, 054407. [[CrossRef](#)]
10. Kumar, R.; Sampathkumaran, E.V. Magnetic frustration and paramagnetic state transport anomalies in Ho_4RhAl and Er_4RhAl : Possible test cases for newly identified roles of itinerant electrons. *J. Magn. Mag. Mater.* **2021**, *538*, 168285. [[CrossRef](#)]
11. Iyer, K.K.; Mattepanavar, S.; Dodamani, S.; Maiti, K.; Sampathkumaran, E.V. Magnetic behavior of cubic Dy_4RhAl with respect to isostructural Dy_4PtAl , revealing a novel $4f d$ -band interaction. *J. Magn. Mag. Mater.* **2023**, *568*, 170406. [[CrossRef](#)]
12. Buschow, K.H.J. Intermetallic compounds of rare-earths and non-magnetic metals. *Rep. Prog. Phys.* **1979**, *42*, 1373. [[CrossRef](#)]
13. Marcano, N.; Gómez Sal, J.C.; Espeso, J.I.; Fernández Barquín, L.; Paulsen, C. Cluster-glass percolative scenario in $CeNi_{1-x}Cu_x$ studied by very low-temperature ac susceptibility and dc magnetization. *Phys. Rev.* **2007**, *76*, 224419. [[CrossRef](#)]
14. Yamamoto, T.D.; Kotani, A.; Nakajima, H.; Okazaki, R.; Taniguchi, H.; Mori, S.; Terasaki, I. Ferromagnetic Cluster Glass Phase Embedded in a Paramagnetic and Metallic Host in Non-Uniform Magnetic System $CaRu_{1-x}Sc_xO_3$. *J. Phys. Soc. Jpn.* **2016**, *85*, 034711. [[CrossRef](#)]
15. Upadhyay, S.K.; Iyer, K.K.; Sampathkumaran, E.V. Magnetic behavior of metallic kagome lattices, $Tb_3Ru_4Al_{12}$ and $Er_3Ru_4Al_{12}$. *J. Phys. Condens. Mater.* **2017**, *29*, 325601. [[CrossRef](#)] [[PubMed](#)]
16. Noakes, D.R.; Shenoy, G.K. The effect of a crystalline electric field on the magnetic transition temperatures of rare-earth rhodium borides. *Phys. Lett. A* **1982**, *91*, 35–36. [[CrossRef](#)]
17. Dunlap, B.D.; Hall, L.N.; Behroozi, F.; Crabtree, G.W.; Niarchos, D.G. Crystal-field effects and the magnetic properties of rare-earth rhodium borides. *Phys. Rev. B* **1984**, *29*, 6244. [[CrossRef](#)]
18. Adroja, D.T.; Malik, S.K. Magnetic-susceptibility and electrical-resistivity measurements on $RPdSn$ ($R = Ce-Yb$) compounds. *Phys. Rev. B* **1992**, *45*, 779. [[CrossRef](#)]
19. Gschneidner, K.A., Jr.; Pecharsky, V.K.; Tsokol, A.O. Recent developments in magnetocaloric materials. *Rep. Prog. Phys.* **2005**, *68*, 1479. [[CrossRef](#)]
20. Li, L.; Yan, M. Recent progresses in exploring the rare earth based intermetallic compounds for cryogenic magnetic refrigeration. *J. Alloys Compd.* **2020**, *823*, 153810. [[CrossRef](#)]
21. Takayama, T.; Chaloupka, J.; Smerald, A.; Khaliullin, G.; Takagi, H. Spin-orbit entangled electronic phases in 4d and 5d transition metal compounds. *J. Phys. Soc. Jpn.* **2021**, *90*, 062001. [[CrossRef](#)]

22. Medicherla, V.R.R.; Patil, S.; Singh, R.S.; Maiti, K. Origin of ground state anomaly in LaB₆ at low temperatures. *Appl. Phys. Lett.* **2007**, *90*, 062507. [[CrossRef](#)]
23. Bindu, R.; Maiti, K.; Khalid, S.; Sampathkumaran, E.V. Structural link to precursor effects. *Phys. Rev. B* **2009**, *79*, 094103. [[CrossRef](#)]
24. Bindu, R.; Adhikary, G.; Sahadev, N.; Lalla, N.P.; Maiti, K. Pseudogap and charge ordering in a large-bandwidth electron-doped manganite. *Phys. Rev. B* **2011**, *84*, 052407. [[CrossRef](#)]
25. Maiti, K.; Singh, R.S.; Medicherla, V.R.R.; Rayaprol, S.; Sampathkumaran, E.V. Origin of charge density wave formation in insulators from a high resolution photoemission study of BaIrO₃. *Phys. Rev. Lett.* **2005**, *95*, 016404. [[CrossRef](#)]
26. Chaudhary, V.; Chen, X.; Ramanujan, R.V. Iron and manganese based magnetocaloric materials for near room temperature thermal management. *Prog. Mater. Sci.* **2019**, *100*, 64–98. [[CrossRef](#)]
27. Law, J.Y.; Moreno-Ramirez, L.M.; Diaz-Garcia, A.; Franco, V. Current perspective in magnetocaloric materials research. *J. App. Phys.* **2023**, *133*, 040903. [[CrossRef](#)]
28. Mallik, R.; Sampathkumaran, E.V. Magnetic precursor effects, electrical and magnetoresistance anomalies, and heat-capacity behavior of Gd alloys. *Phys. Rev. B* **1998**, *58*, 9178. [[CrossRef](#)]
29. Kumar, R.; Iyer, K.K.; Paulose, P.L.; Sampathkumaran, E.V. Magnetic and transport anomalies in R₂RhSi₃ (R = Gd, Tb, and Dy) resembling those of the exotic magnetic material Gd₂PdSi₃. *Phys. Rev. B* **2020**, *101*, 144440. [[CrossRef](#)]
30. Wang, Z.; Barros, K.; Chern, G.-W.; Maslov, D.L.; Batista, C.D. Resistivity Minimum in Highly Frustrated Itinerant Magnets. *Phys. Rev. Lett.* **2016**, *117*, 206601. [[CrossRef](#)]
31. Zhao, B.; Hu, X.; Dong, F.; Wang, Y.; Wang, H.; Tan, W.; Huo, D. The magnetic properties and magnetocaloric effect of Pr_{0.7}Sr_{0.3}MnO₃ thin film grown on SrTiO₃ substrate. *Materials* **2023**, *16*, 75. [[CrossRef](#)] [[PubMed](#)]

Disclaimer/Publisher's Note: The statements, opinions and data contained in all publications are solely those of the individual author(s) and contributor(s) and not of MDPI and/or the editor(s). MDPI and/or the editor(s) disclaim responsibility for any injury to people or property resulting from any ideas, methods, instructions or products referred to in the content.

Emergence of partially disordered antiferromagnetism and isothermal magnetization plateau due to geometrical frustration in a metallic compound, Er_2RhSi_3

Kartik K. Iyer^{1,2,*}, Kalobaran Maiti¹, Sudhindra Rayaprol³, Ram Kumar⁴, S. Mattepanavar⁵, S. Dodamani² and E. V. Sampathkumaran^{6,†}

¹Tata Institute of Fundamental Research, Homi Bhabha Road, Colaba, Mumbai 400005, India

²KLE Society's Dr. Prabhakar Kore Basic Science Research Centre, KLE Academy of Higher Education and Research, Belagavi 590010, India

³UGC-DAE Consortium for Scientific Research, Mumbai Centre, BARC Campus, Trombay, Mumbai 400085, India

⁴Maryland Quantum Materials Center, University of Maryland, College Park, Maryland 20742, USA

⁵KLE Society's Basavaprabhu Kore Arts, Science and Commerce College, Chikodi 591201, India

⁶Homi Bhabha Centre for Science Education, TIFR, V. N. Purav Marg, Mankhurd, Mumbai 400088, India



(Received 16 June 2023; accepted 14 September 2023; published 10 October 2023)

Partially disordered antiferromagnetism (PDA) (in which one of the three magnetic ions in a triangular network remains magnetically disordered) has been known commonly among geometrically frustrated insulating materials. The $1/3$ plateau in isothermal magnetization M of such materials has been of great theoretical interest. Here we report these properties in an AlB_2 -structure-derived metallic material, Er_2RhSi_3 , in which the Er sublattice has triangular networks. The presence of a well-defined λ anomaly in the temperature T dependence of heat capacity and its magnetic-field H dependence and the loss of spin-disorder contribution to electrical resistivity ρ confirm antiferromagnetic order below $T_N = 5$ K. On the other hand, the separation of zero-field-cooled and field-cooled dc magnetic susceptibility χ curves, the decay of isothermal remnant magnetization, and the frequency dependence of real and imaginary components of ac χ suggest the onset of spin-glass freezing concomitant with the antiferromagnetic order. In addition, interestingly, we observe the $1/3$ plateau in $M(H)$ below 20 kOe for $T < T_N$. The change in ρ as a function of H at a given temperature well below T_N is also revealing, with this compound exhibiting a plateau below 20 kOe, with complexities at higher fields. Therefore, this compound serves as a prototype for theoretical understanding of transport behavior across the $1/3$ plateau due to PDA magnetism in a metal without any interference from the $4f$ delocalization phenomenon.

DOI: [10.1103/PhysRevMaterials.7.L101401](https://doi.org/10.1103/PhysRevMaterials.7.L101401)

The phenomenon of highly frustrated magnetism due to the geometrical arrangement of the magnetic ions, referred to as geometrically frustrated (GF) magnetism, is one of the modern topics of research in condensed matter physics, as such a frustration has been known to lead to a variety of interesting magnetic states [1–9]. This article essentially focuses on two of these aspects, viz., partially disordered antiferromagnetism (PDA) and magnetization plateaus. The concept of PDA magnetism was originally invoked to describe a situation for materials containing a triangular magnetic framework, in which the magnetic ions at two vertices are antiferromagnetically coupled, while the third one is left random due to geometrical frustration [1,2]. This kind of magnetism has been of interest due to the fact that all the magnetic ions are crystallographically equivalent yet exhibiting different magnetic behavior. Very early examples for PDA magnetism are CsCoCl_3 and CsCoBr_3 [1,2], and during the past two decades $\text{Ca}_3\text{CoRhO}_6$ [3–5] and $\text{Ca}_3\text{Co}_2\text{O}_6$ [6–8] have been attracting attention. With respect to the magnetization plateaus, this is in general a subject of considerable theoretical and experimental investigation in terms of Shastry-Sutherland, square, kagome,

and triangular insulating systems, as multiple plateaus can arise not only due to GF magnetism, but also due to various other magnetic interaction frustrations (see, for instance, Refs. [9–12]). Quantum effects have been shown to play a major role. The PDA magnetism arising from GF magnetism in triangular magnetic lattices is often characterized, in particular, by a plateau at $1/3$ of the saturation magnetization M . There has been a flurry of activity in recent years studying this $1/3$ plateau in, e.g., $\text{Ba}_3\text{NiSb}_2\text{O}_9$, $\text{Ba}_3\text{NiNb}_2\text{O}_9$ [13,14], volborthite [15], Cs_2CoBr_4 [16], CoGeO_3 [17], and $\text{Cu}_3\text{Bi}(\text{TeO}_3)_2\text{O}_2\text{Cl}$ [18]. Readers may also refer to the seminal theoretical work by Chubukov and Golosov [19]. Such plateaus occur irrespective of the spin value of the magnetic ion (see, for instance, [11,12,17–33] and references therein). Besides many such insulators, a semiconducting triangular system Eu_3InAs_3 has been reported very recently [34].

Clearly, the identification of materials exhibiting such quantized steps, in particular the $1/3$ plateau, is an important direction of research in the field of GF magnetism. Obviously, any kind of PDA magnetic structure, even in other GF families, is of great interest in condensed matter physics, e.g., $\text{Gd}_2\text{Ti}_2\text{O}_7$ [35]. However, such reports in a metallic environment are scarce and sporadic, e.g., UNi_4B [36], CePdAl [37], $\text{Tb}_3\text{Ru}_4\text{Al}_{12}$ [38], and very recently EuRh_2Al_8 [39]. The compound TbRh_6Ge_6 [40] has been recently

*Iyerkk@gmail.com

†sampathev@gmail.com

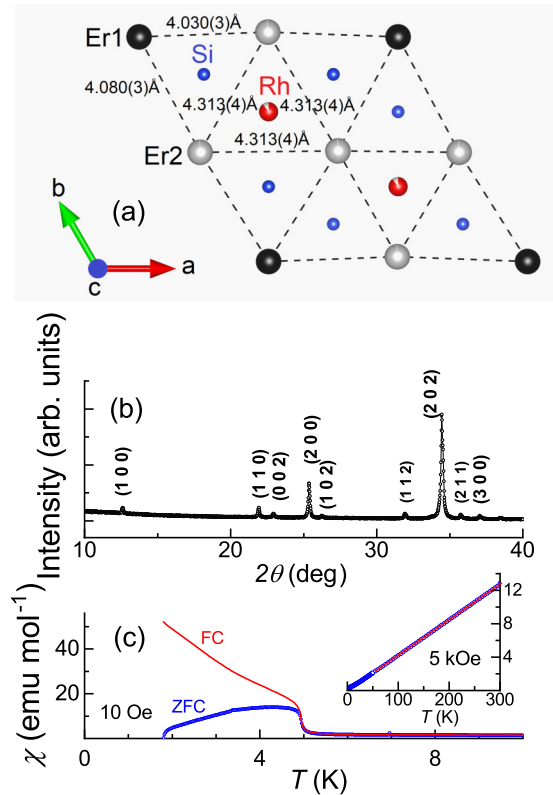


FIG. 1. (a) Unit cell of Er_2RhSi_3 viewed along the c axis, showing triangular arrangement of Er ions in the Er layer; intralayer distances between Er atoms are given. An adjacent Rh-Si layer is also shown. (b) X-ray-diffraction pattern ($\text{Cu } K_\alpha$) below $2\theta = 40^\circ$ to show weak superstructure lines (100) and (110). (c) Magnetic susceptibility as a function of temperature below 10 K for the zero-field-cooled and field-cooled conditions of the specimens, measured with 10 Oe. The inset shows the inverse χ in a field of 5 kOe, with a straight line through the Curie-Weiss regime.

reported to show a $1/9$ plateau, in addition to a $1/3$ plateau. The question therefore arises whether the Rudermann-Kittel-Kasuya-Yosida (RKKY) indirect exchange interaction usually mediating magnetic ordering in metals, in particular among rare-earth metals R , is not generally favorable to cause these features of geometric frustration. It is therefore of great interest to search for materials, without interference from other exotic phenomena due to f -electron delocalization (as in CePdAl [37]), exhibiting features characteristic of PDA magnetism and the $1/3$ plateau to provide relatively simple examples to enable the theorists to work further in this direction. In this article we present evidence of such magnetic characteristics in Er_2RhSi_3 , derived from an AlB_2 -derived hexagonal structure [41].

A good number of ternary rare-earth compounds of the type $R_2(T)X_3$ (where T is a transition metal ion in this paragraph and $X = \text{Si}$ or Ge) have been derived from an AlB_2 hexagonal crystal structure. The sites for T and X are $4f$ and $12i$, respectively forming T - X layers. The layers of T - X form a honeycomb network and the layers of the triangular network of R ions [Fig. 1(a)] alternate with T - X in the c direction. In the event of the ordered replacement of the boron site by T and X , two types of rare-earth compounds, viz., $2b$ and $6h$, can be

visualized depending on whether the nearest hexagons in the adjacent layers contain ordered T - X or X atoms. As a result of this difference in the chemical surrounding, the interatomic distances undergo subtle differences, as discussed in Ref. [42] for Er_2RhSi_3 [and shown in Fig. 1(a) for Er-Er distances]. This is presumably responsible for doubling of the unit-cell parameters with respect to those expected for the disordered distribution of T and X [in which case the chemical formula can be written as $R(T)_{0.5}X_{1.5}$]. For crystallographic details, the readers are referred to Ref. [41] and the Supplemental Material [42]. Among these, many novel magnetic and transport anomalies have been reported (see references in [43–56]) for the past three decades for several members of the $R_2\text{PdSi}_3$ family. The most notable one is Gd_2PdSi_3 , the transport anomalies of which include Kondo-like electrical resistivity ρ [46]; it is intriguing that Hall anomaly typical of the topological Hall effect was reported two decades ago, long before this concept was recognized in metals, as noted in Ref. [49]. Gd_2PdSi_3 is the first centrosymmetric case to exhibit magnetic skyrmion behavior [48,50–52], strongly modulated by the Pd/Si superlattice [51]. Therefore, it is important to investigate Rh analogs. Other than some initial studies long ago [41,57,58], in particular on the Ce case in depth [59–67], Gd, Tb, and Dy members [68] are special as these exhibit magnetic and transport properties comparable to those of Gd_2PdSi_3 . The properties of the isomorphous Er compound [69] presented in this paper reveal uniqueness in the context of PDA magnetism and one-third magnetization plateau.

A polycrystalline sample was prepared by melting together stoichiometric amounts of constituent elements in an arc furnace in an atmosphere of argon under partial pressure, followed by annealing at 1073 K for about a week in an evacuated sealed quartz tube. The x-ray-diffraction pattern (recorded with $\text{Cu } K_\alpha$ radiation) was analyzed by the Rietveld refinement method, which confirmed the single-phase nature of molten ingot (see the Supplemental Material [42]). The pattern was found to be in excellent agreement with that of Ref. [41], including the appearance of superstructure lines [Fig. 1(b)] establishing doubling of the unit-cell parameters ($a = \sim 8.1043$ and $c = \sim 7.7518 \text{ \AA}$). Details of the temperature T and magnetic-field H dependences of ac and dc M , heat-capacity C , and electrical resistivity ρ measurements can be found in Ref. [42].

In the inset of Fig. 1(c) we show the T dependence of the inverse susceptibility χ obtained in a field of 5 kOe. The plot is found to be linear over a wide T range well above 10 K. The effective moment μ_{eff} obtained from the slope of the plot (approximately $9.7\mu_B$) is the same as the theoretical value of $9.7\mu_B$ for trivalent Er ions. The paramagnetic Curie temperature is found to be approximately 1.4 K; the positive sign is indicative of ferromagnetic correlations between Er ions, which is different from other rare-earth cases in the same family [68]. We note that, as the temperature is lowered, there is an upturn of χ around 5 K beyond the value expected from the high-temperature Curie-Weiss behavior followed by a peak, as though antiferromagnetic ordering sets in, as shown in Fig. 1(c) for the 10 Oe measuring field. The zero-field-cooled (ZFC) and field-cooled (FC) curves for this low field tend to deviate from each other at the onset of magnetic

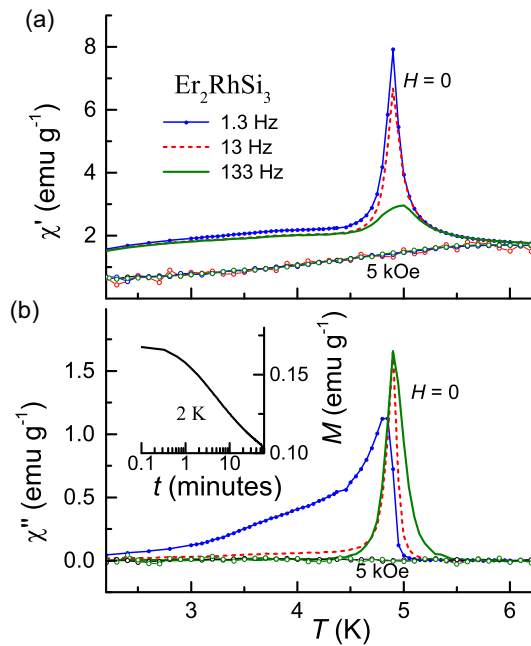


FIG. 2. (a) Real and (b) imaginary parts of ac susceptibility of Er_2RhSi_3 below 6 K, obtained with different frequencies in zero field as well as in 5 kOe. The curves for 5 kOe for all frequencies overlap and are featureless. The inset shows isothermal remnant magnetization at 2 K.

order itself, with the FC curve continuing to rise down to 2 K, typical of spin glasses in many concentrated magnetic materials [38,70,71]. For another interesting χ behavior in the vicinity of the T region of 2–20 K at low fields (20, 50, and 100 Oe), readers are referred to the Supplemental Material [42].

In order to explore further the origin of the above features, we have measured ac χ in the low-temperature region with frequencies 1.3, 13, 133, and 1333 Hz; the results obtained as a function of T in the vicinity of the magnetic transition are shown in Fig. 2. The curves are featureless at higher temperatures. It is apparent from this figure that not only the real part χ' but also the imaginary part χ'' exhibits prominent peaks in magnitude, with the sharp upturn occurring at 5 K, as expected for spin glasses [72]. There is a weak frequency ν dependence of the peak temperature, say, in χ' , that is, 0.2 K for a variation of ν from 1.3 to 133 Hz. (The peak values also undergo a decrease with increasing ν , with significant suppression for 1333 Hz, which is curious). The peaks vanish for a small application of a dc magnetic field (say, 5 kOe), as revealed by the flatness of the plot in the figure. The results establish that this compound undergoes spin-glass freezing. The most notable observation, as inferred from the peak temperature in χ' , is that the spin freezing occurs exactly at the onset of magnetic ordering. In order to render further support to the existence spin-glass freezing, we have measured isothermal remnant magnetization M_{IRM} as a function of time t at 2 K. This curve, shown in the inset of Fig. 2, was obtained as follows: After zero-field cooling of the specimen at 2 K, the specimen was left in a magnetic field of 5 kOe for 5 min; immediately after switching off the field, M_{IRM} was measured

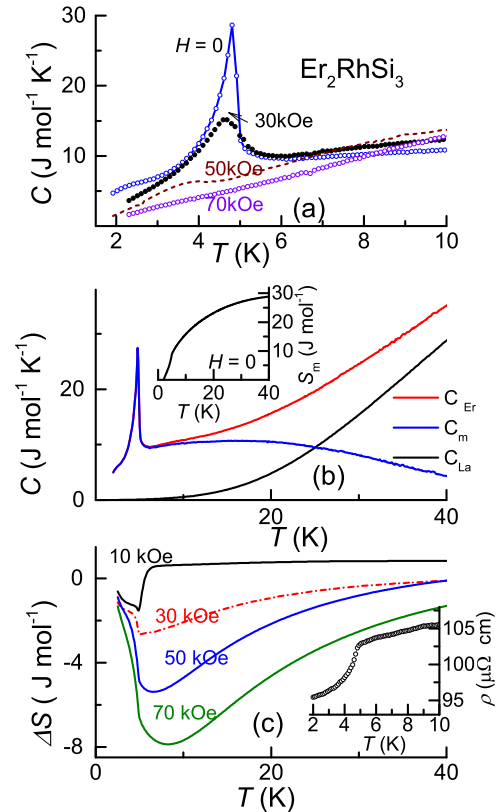


FIG. 3. (a) Zero-field and in-field heat capacity below 10 K and (b) zero-field heat capacity in a wider temperature range of 2–40 K for Er_2RhSi_3 . (b) Magnetic contribution to heat capacity C_m for Er_2RhSi_3 , employing the heat capacity of La_2RhSi_3 (also shown) for the nonmagnetic part, along with the magnetic entropy S_m curve, derived from C_m versus T for the Er sample in the inset. (c) Isothermal entropy change curves as a function of temperature (see the text for details) for different final fields starting from zero field; the inset shows the electrical resistivity data at low temperatures.

as a function of t for about an hour. From the inset of Fig. 2 it is clear that there is a slow decay of M_{IRM} , varying essentially logarithmically with t (barring slower decay for a few initial seconds), consistent with what is expected for spin glasses.

Having established the onset of spin-glass freezing at 5 K, support for long-range magnetic order pointing to a well-defined magnetic structure comes from the $C(T)$ data, apart from the appearance of magnetic Bragg peaks in the neutron diffraction data [57]. We show the $C(T)$ data in the T region of interest only (much less than 10 K) in Fig. 3(a), as there is no worthwhile feature measured up to 150 K. It is evident from Fig. 3(a) that the zero-field data exhibit a strong λ anomaly with a sharp upturn at 5 K. This is a characteristic feature of long-range magnetic ordering arising from a well-defined magnetic structure. Spin-glass freezing alone would have resulted in smearing of the feature at the onset of freezing. Therefore, viewed together with the features in the ac and dc magnetization presented above, this establishes that spin-glass freezing and a well-defined magnetic structure set in essentially at the same temperature, namely, at 5 K. With respect to the behavior in the presence of external fields, there is a gradual smearing and broadening of the peak and the

peak moves towards a lower temperature, for example, for 30 and 50 kOe to 4.5 and 3.8 K, respectively. This establishes that the strong λ anomaly arises from antiferromagnetism. In short, these results establish that PDA magnetism occurs at the magnetic ordering temperature of $T_N = 5$ K. Finally, we have also derived the magnetic contribution C_m to $C(T)$ by measuring $C(T)$ of the La analog as in Ref. [68], which is shown in Fig. 3(b). The magnetic entropy S_m [Fig. 3(b), inset] obtained by integrating C_m/T versus T is approximately 8 J/mol K at T_N . If one assumes that the magnetic ordering arises from the crystal-field-split doublet ground state (as Er^{3+} is a Kramers ion), the minimum expected value for the magnetic entropy at T_N should be $2R\ln 2 = 11.52$ J/mol K. Therefore, the observed lower value supports that a significant fraction of Er ions are magnetically disordered. It may be remarked that the theoretical value of magnetic entropy for full degeneracy of the $4f$ orbital of Er^{3+} (for which the total orbital angular momentum is $J = 15/2$) is equal to $(2R\ln 16 =) 46.1$ J/mol K, which is far above the observed value at T_N . Clearly, crystal-field splitting of the $4f$ orbital is present, which is also supported by a similar lower value of magnetic moment determined by neutron diffraction [57].

We have derived the isothermal entropy change, defined as $\Delta S = S(H) - S(0)$, from the area under the curves of C/T versus T , measured at different fields, and the results obtained are shown in Fig. 3(c). The curves fall in the negative quadrant with a negative peak, typical of a dominant ferromagnetic component in such fields [73]. This demonstrates field-induced changes in the magnetic structure in the magnetically ordered state. The peak values are reasonably large, say, for 0–50 kOe field variation, with the curve spreading over a wide T range above T_N . Surprisingly, ΔS changes sign sharply at the loss of magnetic order above 5 K for 10 kOe, and the positive sign above T_N implies possible field-induced magnetic fluctuations in such low fields. The sign becomes negative in the paramagnetic state for $H > 10$ kOe as expected, but the large magnitude over a wide T range may be due to the antiferromagnetic clusters giving rise to an effective ferromagnetic alignment. The results overall imply that this compound may be an example of interesting magnetic precursor effects [46,47,73–75] in the paramagnetic state, which has also been addressed theoretically in recent times [47,76,77].

We present isothermal magnetization behavior for 1.8, 4, and 6 K in Figs. 4(a)–4(c) to reveal the $1/3$ plateau. There is a sharp rise at 1.8 K for the application of an initial small H and there is a plateau immediately thereafter until 20 kOe. The sharpness of these features is a bit smeared in the 4 K plot. There is an upturn near about 20 kOe after the plateau and the variation is weak beyond about 30 kOe. The plot of $M(H)$ tends to flatten, varying weakly beyond 60 kOe until the measured field of 120 kOe [Fig. 4(a), inset], as though there is a tendency to saturate. All these $M(H)$ curves are found to be nonhysteretic. A linear extrapolation of the high-field curve to zero field yields a value of about $6.5\mu_B$ per Er ion. This value is far below the saturation value expected for fully degenerate trivalent Er ions ($9\mu_B$ per Er ion) and so the reduced value can be attributed to a decrease in the magnetic moment and possible strong anisotropy resulting from crystal-field effects. The most intriguing observation relevant to the aim of this article is that the value of the similarly extrapolated magnetic

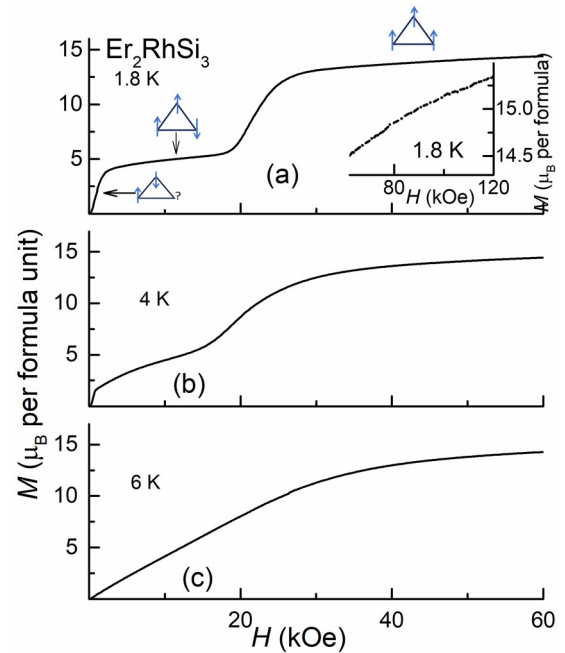


FIG. 4. Isothermal magnetization of Er_2RhSi_3 below 60 kOe at (a) 1.8, (b) 4, and (c) 6 K for the forward variation of the magnetic field. The inset shows the behavior in the range 60–120 kOe at 1.8 K. Also shown in (a) is a schematic representation of a scenario [5] for the orientation of magnetic moments in a triangular network; the question mark represents magnetically disordered ions.

moment in the plateau region is approximately $2.15\mu_B$ per Er ion, which is essentially one-third of the extrapolated value from the high-field data (obtained above). A simple picture for the origin of $1/3$ magnetization plateau, advanced for a triangular lattice $\text{Ca}_3\text{Co}_2\text{O}_6$ [5] is as follows: The magnetic ion at one of the three vortices of the triangle is magnetically disordered as evidenced by spin-glass features discussed above, while the other two are coupled antiparallel in zero field in the virgin state; in the plateau region, the magnetic moment of the disordered magnetic ion gets oriented along the field, leaving the other two aligned antiparallel to each other, leading to a ferrimagnetic state. It is not straightforward to understand why such an intermediate state is stable against perturbation by a magnetic field, in our case, up to 20 kOe; presumably, the antiparallel interaction is too strong to flip the moments of Er with this external field. Beyond 30 kOe, all three sites tend to align ferromagnetically, resulting in three times the magnetic moment of the plateau region. For the sake of the reader, a schematic representation of this scenario is shown for a triangle in Fig. 4. Thus, the $1/3$ isothermal magnetization plateau could be consistently interpreted with the idea of partially disordered antiferromagnetism. Note that the plateau vanishes as soon as the long-range magnetic order regime is crossed, as seen for the $M(H)$ curve for 6 K.

Previous neutron diffraction studies [57] suggest that there is no crystal structure change in the magnetically ordered state. In that work, both Er ions are assumed to carry an equal magnetic moment of $5.9\mu_B$ per Er ion, which is below the value of $9\mu_B$ for the fully $4f$ -degenerate trivalent Er ion, suggesting the presence of crystal-field splitting. We would

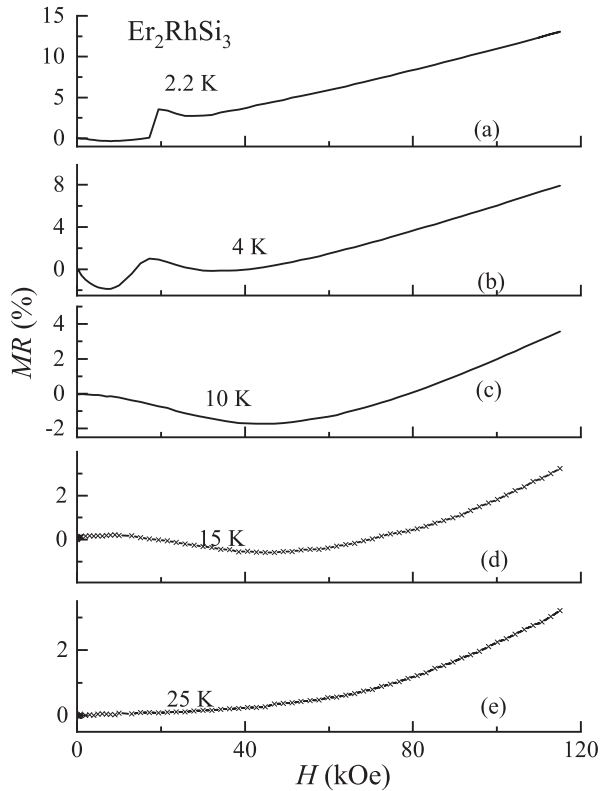


FIG. 5. Isothermal magnetoresistance, defined as $[\rho(H) - \rho(0)]/\rho(0)$, for Er_2RhSi_3 , at (a) 2.2, (b) 4, (c) 10, (d) 15, and (e) 25 K.

like to state that it is difficult to reconcile the PDA magnetic structure proposed here with the conclusions obtained from these neutron diffraction studies. It is not uncommon, particularly within this ternary family, that reinvestigations by modern facilities and/or better quality samples have yielded results contradicting previous magnetic structure proposals, for example, for Tb_2PdSi_3 [78,79] and for Nd_2PdSi_3 [44,78]. Besides, a PDA system would be characterized by a broad background below the sharp magnetic peaks, suggestive of quasielastic peaks arising from spin-glass component, as in $\text{Ca}_3\text{CoRhO}_6$ [80,81]. A careful look at the background below the intense peaks in the reported neutron diffraction pattern [57] indeed provides an indication of the same. In view of these findings, we call for detailed neutron diffraction studies to search for some kind of PDA magnetic structure, before attaching any significance to the apparent discrepancy with the present conclusion.

We now demonstrate the behavior of magnetoresistance (in the transverse geometry) across the $1/3$ plateau regime in this metallic system, serving as a subject warranting further theoretical work to understand transport anomalies in the $1/3$ plateau regime, as such an opportunity is not provided by insulating PDA systems. The $\rho(T)$ plot [see Fig. 3(c), inset] shows distinct evidence for the loss of the spin-disorder contribution to ρ at T_N . Figures 5(a)–5(e) show the behavior of isothermal magnetoresistance (MR) at various temperatures across T_N . Here MR is defined as $[\rho(H) - \rho(0)]/\rho(0)$. The

curves are essentially nonhysteretic. Looking at the MR curve at 2.2 K [see Fig. 5(a)], the magnitude is negligibly small below 20 kOe, but a negative sign emerges after a small change in applied H (possibly due to grain boundaries or spin-glass component); it is notable that MR otherwise is almost flat in the $1/3$ magnetization plateau region, as though magnetism is topologically protected, apparently avoiding even conventional magnetic and nonmagnetic contributions for the scattering process. After this plateau region is crossed, there is a distinct upturn to the positive quadrant, followed by a weak drop around 30 kOe, possibly due to the ferromagnetic alignment contribution. With a further increase of H , that is, in the region where there is a tendency for magnetization to saturate, MR surprisingly keeps increasing, remaining in the positive quadrant. Such a linear MR variation in the essentially ferromagnetically aligned state is puzzling (as ferromagnets are usually characterized by negative MR with a nonlinear dependence on H). It is not clear whether the classical contribution due to conduction electrons dominates the ferromagnetic contribution at higher fields, leading to positive MR. At 4 K, the features are similar, except that the initial drop is more prominent. Just above T_N , say, at 10 K, there is a competition between the well-known paramagnetic contribution (negative sign with an H^2 dependence) and the positive classical contribution, leading to a minimum at the intermediate-field range. With increasing T , since the paramagnetic contribution should gradually weaken, the minimum gradually vanishes, as shown for 10, 15, and 25 K [Figs. 5(c)–5(e)].

In conclusion, we have reported the results of our bulk measurements on Er_2RhSi_3 containing essentially localized $4f$ electrons in a triangular network, hitherto not paid much attention in the literature. A fascinating finding is that this compound exhibits characteristic features of PDA magnetism, also characterized by the $1/3$ magnetization plateau in this case, in a material with RKKY interaction, that too without any interference from other $4f$ -related phenomena (like the Kondo effect typical of Ce or U systems). It may be remarked that none of the isostructural ternary rare-earth compounds has been known to show such PDA characteristics in the past, in particular, other rare-earth compounds of this Rh family ($R = \text{Gd}, \text{Tb}, \text{Dy}, \text{and Ho}$) [68,69] as well as the Er counterpart in the Pd-based family, Er_2PdSi_3 [56]. This is puzzling and renders support to the conclusion that this compound is a unique magnetic material, possibly suggesting an interesting magnetic interaction between the orientated crystal-field-split ground state of the $4f$ orbital of Er with the Rh $4d$ orbital and therefore it is worth probing this aspect further. Finally, this compound may also serve as a prototype for transport behavior across the $1/3$ magnetization plateau.


The authors acknowledge financial support from the Department of Atomic Energy (DAE), Government of India (Project No. RTI4003, DAE OM No. 1303/2/2019/R&D-II/DAE/2079). E.V.S. is grateful to the Department of Atomic Energy, Government of India, for financial support through a Raja Ramanna Fellowship. K.M. is grateful for financial support from BRNS, DAE under the DAE-SRC-OI program. S.M. is grateful for support from Vision Group on Science and Technology–GRD through Grant No. 852.

- [1] M. Mekata, *J. Phys. Soc. Jpn.* **42**, 76 (1977).
- [2] W. B. Yelon, D. E. Cox, and M. Eibschutz, *Phys. Rev. B* **12**, 5007 (1975).
- [3] S. Niitaka, H. Kageyama, M. Kato, K. Yoshimura, and K. Kosuge, *J. Solid State Chem.* **146**, 137 (1999); S. Niitaka, H. Kageyama, K. Yoshimura, K. Kosuge, S. Kawano, N. Aso, A. Mitsuda, H. Mitamura, and T. Goto, *J. Phys. Soc. Jpn.* **70**, 1222 (2001).
- [4] E. V. Sampathkumaran and A. Niazi, *Phys. Rev. B* **65**, 180401(R) (2002).
- [5] H. Kageyama, K. Yoshimura, K. Kosuge, H. Mitamura, and T. Goto, *J. Phys. Soc. Jpn.* **66**, 1607 (1997).
- [6] A. Maignon, C. Michel, A. C. Masset, C. Martin, and B. Raveau, *Eur. Phys. J. B* **15**, 657 (2000).
- [7] S. Rayaprol, K. Sengupta, and E. V. Sampathkumaran, *Solid State Commun.* **128**, 79 (2003).
- [8] F. Levy, I. Sheikin, C. Berthier, M. Horvatic, M. Takigawa, H. Kageyama, T. Waki, and Y. Ueda, *Europhys. Lett.* **81**, 67004 (2008).
- [9] For a recent review on quantum spin liquids see V. R. Shaginyan, V. A. Stephanovich, A. Z. Msezane, G. S. Japaridze, J. W. Clark, M. Y. Amusia, and E. V. Kirichenko, *J. Mater. Sci.* **55**, 2257 (2020).
- [10] H. O. Jeschke, H. Nakano, and T. Sakai, *Phys. Rev. B* **99**, 140410(R) (2019).
- [11] D. Flavián, J. Nagl, S. Hayashida, M. Yan, O. Zaharko, T. Fennell, D. Khalyavin, Z. Yan, S. Gvasaliya, and A. Zheludev, *Phys. Rev. B* **107**, 174406 (2023).
- [12] Z. W. Ouyang, Y. C. Sun, J. F. Wang, X. Y. Yue, R. Chen, Z. X. Wang, Z. Z. He, Z. C. Xia, Y. Liu, and G. H. Rao, *Phys. Rev. B* **97**, 144406 (2018).
- [13] Y. Shirata, H. Tanaka, T. O. A. Matsuo, K. Kindo, and H. Nakano, *J. Phys. Soc. Jpn.* **80**, 093702 (2011).
- [14] J. Hwang, E. S. Choi, F. Ye, C. R. Dela Cruz, Y. Xin, H. D. Zhou, and P. Schlottmann, *Phys. Rev. Lett.* **109**, 257205 (2012).
- [15] H. Ishikawa, M. Yoshida, K. Nawa, M. Jeong, S. Krämer, M. Horvatić, C. Berthier, M. Takigawa, M. Akaki, A. Miyake *et al.*, *Phys. Rev. Lett.* **114**, 227202 (2015).
- [16] L. Facheris, K. Y. Povarov, S. D. Nabi, D. G. Mazzone, J. Lass, B. Roessli, E. Ressouche, Z. Yan, S. Gvasaliya, and A. Zheludev, *Phys. Rev. Lett.* **129**, 087201 (2022).
- [17] H. Guo, L. Zhao, M. Baenitz, X. Fabrèges, A. Gukasov, A. Melendez Sans, D. I. Khomskii, L. H. Tjeng, and A. C. Komarek, *Phys. Rev. Res.* **3**, L032037 (2021).
- [18] X. Liu, Z. Ouyang, D. Jiang, J. Cao, T. Xiao, Z. Wang, Z. Xiao, and W. Tong, *J. Magn. Magn. Mater.* **565**, 170228 (2023).
- [19] A. V. Chubukov and D. I. Golosov, *J. Phys.: Condens. Matter* **3**, 69 (1991).
- [20] A. Farchakh, A. Boubekri, and M. El Hafidi, *J. Low Temp. Phys.* **206**, 131 (2022).
- [21] T. Sakai, K. Okamoto, and T. Tonegawa, *Phys. Rev. B* **100**, 054407 (2019).
- [22] Y. Kamiya, L. Ge, Tao Hong, Y. Qiu, D. L. Quintero-Castro, Z. Lu, H. B. Cao, M. Matsuda, E. S. Choi, C. D. Batista, M. Mourigal, H. D. Zhou, and J. Ma, *Nat. Commun.* **9**, 2666 (2018).
- [23] M. E. Zhitomirsky, A. Honecker, and O. A. Petrenko, *Phys. Rev. Lett.* **85**, 3269 (2000).
- [24] K. Hida and I. Affleck, *J. Phys. Soc. Jpn.* **74**, 1849 (2005).
- [25] *Magnetization Plateaus*, edited by C. Lacroix, P. Mendels, and F. Mila (Springer, Heidelberg, 2011), Chap. 10.
- [26] L. Seabra, P. Sindzingre, T. Momoi, and N. Shannon, *Phys. Rev. B* **93**, 085132 (2016).
- [27] M. Goto, H. Ueda, C. Michioka, A. Matsuo, K. Kindo, K. Sugawara, S. Kobayashi, N. Katayama, H. Sawa, and K. Yoshimura, *Phys. Rev. B* **97**, 224421 (2018).
- [28] E. Parker and L. Balents, *Phys. Rev. B* **95**, 104411 (2017).
- [29] V. S. Abgaryan, N. S. Ananikian, L. N. Ananikyan, and V. V. Hovhannissyan, *Solid State Commun.* **224**, 15 (2015).
- [30] H. Nakano and T. Sakai, *J. Phys. Soc. Jpn.* **84**, 063705 (2015).
- [31] O. Götze, J. Richter, R. Zinke, and D. J. J. Farnell, *J. Magn. Magn. Mater.* **397**, 333 (2016).
- [32] T. Liu, W. Li, and G. Su, *Phys. Rev. E* **94**, 032114 (2016).
- [33] K. Morita, T. Sugimoto, S. Sota, and T. Tohyama, *Phys. Rev. B* **97**, 014412 (2018).
- [34] K. Jia, C.-X. Wang, X. Dong, N. Chen, J. Cong, G. Li, H. L. Feng, H. Zhao, and Y. Shi, *Phys. Rev. Res.* **3**, 043178 (2021).
- [35] J. A. M. Paddison, G. Ehlers, A. B. Cairns, J. S. Gardner, O. A. Petrenko, N. P. Butch, D. D. Khalyavin, P. Manuel, H. E. Fischer, H. Zhou *et al.*, *npj Quantum Mater.* **6**, 99 (2021).
- [36] S. A. M. Mentink, A. Drost, G. J. Nieuwenhuys, E. Frikkee, A. A. Menovsky, and J. A. Mydosh, *Phys. Rev. Lett.* **73**, 1031 (1994).
- [37] A. Dönni, G. Ehlers, H. Maletta, P. Fischer, H. Kitazawa, and M. Zolliker, *J. Phys.: Condens. Matter.* **8**, 11213 (1996); V. Fritsch, S. Lucas, Z. Huesges, A. Sakai, W. Kittler, C. Taubenheim, S. Woitschach, B. Pedersen, K. Grube, B. Schmidt *et al.*, *J. Phys.: Conf. Ser.* **807**, 032003 (2017); A. Oyamada, S. Maegawa, M. Nishiyama, H. Kitazawa, and Y. Isikawa, *Phys. Rev. B* **77**, 064432 (2008); S. Lucas, *Phys. Rev. Lett.* **118**, 107204 (2017).
- [38] S. K. Upadhyay, K. K. Iyer, and E. V. Sampathkumaran, *J. Phys.: Condens. Matter.* **29**, 325601 (2017); E. V. Sampathkumaran, K. K. Iyer, S. K. Upadhyay, and A. V. Andreev, *Solid State Commun.* **288**, 64 (2019).
- [39] M. He, X. Xu, Z. Wu, C. Dong, Y. Liu, Q. Hou, S. Zhou, Y. Han, J. Wang, and Z. Qu, *Phys. Rev. Mater.* **7**, 033401 (2023).
- [40] Y. Chen, Y. Zhang, R. Li, H. Su, Z. Shan, M. Smidman, and H. Yuan, *Phys. Rev. B* **107**, 094414 (2023).
- [41] B. Chevalier, P. Lejay, J. Etourneau, and P. Hagenmuller, *Solid State Commun.* **49**, 753 (1984).
- [42] See Supplemental Material at <http://link.aps.org/supplemental/10.1103/PhysRevMaterials.7.L101401> for experimental methods, crystallographic information, Rietveld fitting of the x-ray-diffraction pattern, and the magnetic susceptibility behavior at some low fields around the magnetic transition for Er₂RhSi₃.
- [43] K. Mukherjee, T. Basu, K. K. Iyer, and E. V. Sampathkumaran, *Phys. Rev. B* **84**, 184415 (2011).
- [44] M. Smidman, C. Ritter, D. T. Adroja, S. Rayaprol, T. Basu, E. V. Sampathkumaran, and A. D. Hillier, *Phys. Rev. B* **100**, 134423 (2019).
- [45] K. Maiti, T. Basu, S. Thakur, N. Sahadev, D. Biswas, G. Adhikary, Y. Xu, W. Löser, and E. V. Sampathkumaran, *J. Phys.: Condens. Matter* **32**, 46LT02 (2020).
- [46] R. Mallik, E. V. Sampathkumaran, M. Strecker, and G. Wortmann, *Europhys. Lett.* **41**, 315 (1998).
- [47] Z. Wang, K. Barros, G.-W. Chern, D. L. Maslov, and C. D. Batista, *Phys. Rev. Lett.* **117**, 206601 (2016).

- [48] S. R. Saha, H. Sugawara, T. D. Matsuda, H. Sato, R. Mallik, and E. V. Sampathkumaran, *Phys. Rev. B* **60**, 12162 (1999).
- [49] E. V. Sampathkumaran, [arXiv:1910.09194](https://arxiv.org/abs/1910.09194).
- [50] T. Kurumaji, T. Nakajima, M. Hirschberger, A. Kikkawa, Y. Yamasaki, H. Sagayama, H. Nakao, Y. Taguchi, T. Arima, and Y. Tokura, *Science* **365**, 914 (2019).
- [51] J. A. M. Paddison, B. K. Rai, A. F. May, S. Calder, M. B. Stone, M. D. Frontzek, and A. D. Christianson, *Phys. Rev. Lett.* **129**, 137202 (2022).
- [52] T. Nomoto and R. Arita, *J. Appl. Phys.* **133**, 150901 (2023).
- [53] R. Mallik, E. V. Sampathkumaran, and P. L. Paulose, *Solid State Commun.* **106**, 169 (1998).
- [54] S. Majumdar, E. V. Sampathkumaran, P. L. Paulose, H. Bitterlich, W. Loser, and G. Behr, *Phys. Rev. B* **62**, 14207 (2000).
- [55] P. L. Paulose, E. V. Sampathkumaran, H. Bitterlich, G. Behr, and W. Löser, *Phys. Rev. B* **67**, 212401 (2003).
- [56] K. K. Iyer, P. L. Paulose, E. V. Sampathkumaran, M. Frontzek, A. Kreyssig, M. Doerr, M. Loewenhaupt, I. Mazilu, G. Behr, and W. Löser, *Physica B* **355**, 158 (2004).
- [57] W. Bazela, E. Wawrzynska, B. Penc, N. Stusser, A. Szytula, and A. Szymunt, *J. Alloys Compd.* **360**, 76 (2003).
- [58] R. E. Gladyshevskii, K. Cenzual, and E. Parthe, *J. Alloys Compd.* **189**, 221 (1992).
- [59] I. Das and E. V. Sampathkumaran, *J. Magn. Magn. Mater.* **137**, L239 (1994).
- [60] J. Lecejewicz, N. Stüsser, A. Szytula, and A. Szymunt, *J. Magn. Magn. Mater.* **147**, 45 (1995).
- [61] M. Szlawska, D. Kaczorowski, A. Slebarski, L. Gulay, and J. Stepien-Damm, *Phys. Rev. B* **79**, 134435 (2009).
- [62] N. Kase, T. Muranaka, and J. Akimitsu, *J. Magn. Magn. Mater.* **321**, 3380 (2009).
- [63] T. Nakano, K. Sengupta, S. Rayaprol, M. Hedo, Y. Uwatoko, and E. V. Sampathkumaran, *J. Phys.: Condens. Matter* **19**, 326205 (2007).
- [64] S. Patil, K. K. Iyer, K. Maiti, and E. V. Sampathkumaran, *Phys. Rev. B* **77**, 094443 (2008).
- [65] S. Patil, V. R. R. Medicherla, R. S. Singh, S. K. Pandey, E. V. Sampathkumaran, and K. Maiti, *Phys. Rev. B* **82**, 104428 (2010).
- [66] S. Patil, V. R. R. Medicherla, R. S. Singh, E. V. Sampathkumaran, and K. Maiti, *Europhys. Lett.* **97**, 17004 (2012).
- [67] K. Mukherjee, K. K. Iyer, S. Patil, K. Maiti, and E. V. Sampathkumaran, *J. Phys.: Conf. Ser.* **273**, 012010 (2011).
- [68] R. Kumar, K. K. Iyer, P. L. Paulose, and E. V. Sampathkumaran, *Phys. Rev. B* **101**, 144440 (2020).
- [69] Initial magnetization results were presented in *Proceedings of the DAE Solid State Physics Symposium*, (Ranchi, 2022), edited by A. K. Mishra, M. Tyagi, and D. V. Udupa (AIP, Melville, 2022), Vol. 56.
- [70] N. Marcano, J. C. Gómez Sal, J. L. Espeso, L. Fernández Barquín, and C. Paulsen, *Phys. Rev. B* **76**, 224419 (2007); T. D. Yamamoto, A. Kotani, H. Nakajima, R. Okazaki, H. Taniguchi, S. Mori, and I. Terasaki, *J. Phys. Soc. Jpn.* **85**, 034711 (2016); D. X. Li, S. Nimori, Y. Shiokawa, Y. Haga, E. Yamamoto, and Y. Onuki, *Phys. Rev. B* **68**, 172405 (2003).
- [71] R. Kumar, J. Sharma, K. K. Iyer, and E. V. Sampathkumaran, *J. Magn. Magn. Mater.* **490**, 165515 (2019).
- [72] J. A. Mydosh, *Spin Glasses: An Experimental Introduction* (Taylor & Francis, London, 1993).
- [73] K. A. Gschneidner, V. K. Pecharsky, Jr., and A. O. Tsokol, *Rep. Prog. Phys.* **68**, 1479 (2005).
- [74] R. Mallik and E. V. Sampathkumaran, *Phys. Rev. B* **58**, 9178 (1998).
- [75] R. Kumar and E. V. Sampathkumaran, *J. Magn. Magn. Mater.* **538**, 168285 (2021), and references therein.
- [76] M. W. Butcher, M. A. Tanatar, and A. H. Nevidomskyy, *Phys. Rev. Lett.* **130**, 166701 (2023).
- [77] A. Silveira, R. Erichsen, Jr., and S. G. Magalhaes, *Phys. Rev. E* **103**, 052110 (2021).
- [78] A. Szytula, M. Hofmann, B. Penc, M. Slaski, S. Majumdar, E. V. Sampathkumaran, and A. Zygmunt, *J. Magn. Magn. Mater.* **202**, 365 (1999).
- [79] M. Frontzek, A. Kreyssig, M. Doerr, A. Schneidewind, J.-U. Hoffmann, and M. Loewenhaupt, *J. Phys.: Condens. Matter* **19**, 145276 (2007).
- [80] S. Niitaka, K. Yoshimura, K. Kosuge, M. Nishi, and K. Kakurai, *Phys. Rev. Lett.* **87**, 177202 (2001).
- [81] M. Loewenhaupt, W. Schafer, A. Niazi, and E. V. Sampathkumaran, *Europhys. Lett.* **63**, 374 (2003).

RESEARCH ARTICLE | JANUARY 12 2024

Magnetic anomalies in AIB_2 -type hexagonal Ho_2RhSi_3 and Er_2RhSi_3

Kartik K. Iyer ; K. Maiti; Sudhindra Rayaprol; Ram Kumar; S. Mattepanavar; S. Dodamani; E. V. Sampathkumaran



AIP Conf. Proc. 2995, 020153 (2024)

<https://doi.org/10.1063/5.0177980>



View
Online



Export
Citation



APL Energy

Latest Articles Online!

Read Now



Magnetic Anomalies in AIB_2 -type Hexagonal Ho_2RhSi_3 and Er_2RhSi_3

Kartik K Iyer,^{1,2,3 a)} K. Maiti,¹ Sudhindra Rayaprol,⁴ Ram Kumar⁵,
S. Mattepanavar,^{2,3} S. Dodamani,² and E. V. Sampathkumaran⁶

¹*DCMPMS, Tata Institute of Fundamental Research, Homi Bhabha Road, Colaba, Mumbai, India – 400005.*

²*KLE Society's Dr. Prabhakar Kore Basic Science Research Centre, KAHER Belagavi, India- 59001.0*

³*KLE Society's, Basavaprabhu Kore Arts, Science & Commerce College Chikodi, India -591201.*

⁴*UGC-DAE-Consortium for Scientific Research, BARC Campus, Trombay, Mumbai, India – 400085.*

⁵*Maryland Quantum Materials Center, University of Maryland, College Park, MD20742, USA.*

⁶*Homi Bhabha Centre for Science Education, TIFR, V. N. Purav Marg, Mankhurd, Mumbai, India – 400088.*

^{a)}Corresponding author: iyer@tifr.res.in

Abstract. We report the results of initial magnetic measurements on the rare-earth (R) ternary compounds, R_2RhSi_3 (R= Ho and Er), crystallizing in a AIB_2 -derived hexagonal structure, hitherto not paid much attention in the past literature. While the results establish the existence of a magnetic transition around 5 K for both the compounds, dc magnetization (M) and heat-capacity behavior as a function of temperature and magnetic field based on these studies are already quite revealing. In the case of the Er compound, interestingly enough, the magnetic transition appears to be first-order-like and there is a 1/3 plateau in the isothermal magnetization curves in the magnetically ordered state, expected for 'partially disordered antiferromagnetism (PDA)' sometimes known for geometrically frustrated triangular magnetic insulators; there is also a bifurcation of zero-field-cooled (ZFC) and field-cooled (FC) low-field dc magnetic susceptibility (χ) curves in the magnetically ordered state – a characteristic feature of spin-glasses. The results overall reveal that there is a subtle competition between antiferromagnetism and ferromagnetism in this compound. In the case of the Ho compound, there is no indication for spin-glass anomalies and the isothermal M data reveal the existence of magnetization jumps, which are hysteretic.

INTRODUCTION

It is well-known that the Ce, Eu and Yb compounds exhibit exotic properties due to some degree of $4f$ electron delocalization. On the other hand, the compounds of heavy rare-earth (R) members have not drawn much attention due to essentially localized nature of the $4f$ electrons. However, some of heavy R intermetallic compounds were shown to exhibit Kondo-like anomalies (typical of Ce intermetallics) a few decades ago [1,2], which also led to new theoretical approaches in recent years [3]. In this respect, the rare-earth compounds of the type R_2PdSi_3 , crystallizing in a AIB_2 -derived hexagonal crystal structure [4], turned out to be novel in many aspects. The most notable one is Gd_2PdSi_3 , which was shown to exhibit unusual paramagnetic transport [1] as well as Hall anomalies across two metamagnetic transitions in the magnetically ordered state more than two decades ago [5], which is now called 'Topological Hall effect' in the current literature. In other words, this concept of great current interest in solid state physics branch is actually much older than what is believed to be [6]. Considering such recent upsurge in exploring interesting properties of such ternary heavy rare-earth compounds, it is important to investigate isostructural Rh based compounds. This family was not explored in depth for a long time after initial reports a few decades ago [4, 7], though Ce compound was studied in depth [8]. Recently, it was reported [9] that R=Gd, Tb and Dy members of R_2RhSi_3 family are characterized by magnetic and transport properties comparable to those of Gd_2PdSi_3 . In this study, we report the magnetic properties of Ho_2RhSi_3 and Er_2RhSi_3 where the $4f$ states are further away from the Fermi level having relatively less contributions in the conduction band. The results bring out hitherto unknown magnetic anomalies for these compounds.

Before we present the results of our investigations, it is important to recall crystallographic features relevant to this article and the readers may find the details in earlier reports [4, 9]. Si and Rh atoms are ordered in planes perpendicular to c -axis, forming a honeycomb network. The rare-earth layer made up of triangular network alternate along c -axis with respect to Rh-Si layer. Due to the ordering of Pd and Si, the lattice parameters, a and c , are doubled with respect to that for AIB_2 structure, as evidenced by weak superstructure lines at the low angle side in the x-ray diffraction pattern.

EXPERIMENTAL DETAILS

Polycrystalline samples have been prepared by melting together stoichiometric amounts of constituent elements in an arc furnace in an atmosphere of argon under partial pressure, followed by annealing at 1073 K for about a week in evacuated sealed quartz tubes. Experimental details are curtailed due to space limitations, but are available in the past literature [4,7,8,9]. An analysis of the x-ray diffraction patterns by Rietveld refinement methods confirms single phase nature of these compounds (not shown due to space limitations). Dc susceptibility (χ), isothermal magnetization (M) and heat-capacity (C) measurements were performed as a function of temperature (T) and magnetic field (H), as described in Ref. 9.

RESULTS AND DISCUSSIONS

We first focus on the Er compound. In fig.1, we show the behavior of $\chi(T)$ measured with 100 Oe and 5 kOe in various ways. Inverse $\chi(T)$ measured in 5 kOe is found to be linear over a wide T -range (10 – 300 K) and the effective moment (μ_{eff}) obtained from the slope of the plot ($\sim 9.69 \mu_B$) is in excellent agreement with the theoretical value of $9.7\mu_B$ for trivalent Er ions. The paramagnetic Curie temperature (θ_p) is ~ 1.4 K with the positive sign suggesting the existence of ferromagnetic interactions. As the temperature is lowered (for the zero-field-cooled (ZFC) condition), there is a rather broad upturn around 5 K (when measured with 5 kOe) (see, left inset of fig.1a). In order to have a closer look of this upturn, we have obtained the $\chi(T)$ data below 20 K for the ZFC, field-cooled (FC) and field-cooled-warming (FCW) conditions with 100 Oe; the curves obtained are shown in fig. 1b in the T -region of interest, 2-7K. It is distinctly clear that there is a sharp jump in the ZFC curve, as though the virgin state exhibits a first-order-like transition; in support of this, the FCC and FCW curves, though broadened and shifted strangely to lower temperature marginally (by about 0.4 K, the reason for which is unclear), are found to be hysteretic. Additionally, unlike the curve in fig. 1a inset obtained in 5 kOe, there is a peak in ZFC curve at about 3.2 K and FCW curve deviates from ZFC curve at this temperature, increasing down to 2 K. This finding is a characteristic feature of cluster spin-glasses

We now focus on the isothermal $M(H)$ behavior (measured with ZFC condition) in the magnetically ordered state, shown in fig. 1c for 1.8 and 4 K. The curves are essentially nonhysteretic. It is transparent that, following an initial sharp increase possibly due to the response from the magnetic domains to the application of H , there is a plateau till 20 kOe and then a sharp increase in the $M(H)$ plot of the data at 1.8 K; this step is a bit smoothed in the 4 K plot. The variation of M with H is very weak beyond 50 kOe (not shown), as though there is a tendency to saturate. The linear extrapolation of the high-field curve to zero field yields a value of about $6.5 \mu_B/\text{Er}$, which is lower than the saturation value expected for fully degenerate trivalent Er ions ($9 \mu_B$); such a reduction could be due to crystal-field effects. The most intriguing observation is that the value of the magnetic moment by a similar extrapolation in the plateau region is $\sim 2.15\mu_B/\text{Er}$, which is essentially one-third of the extrapolated high-field saturation moment. Such a $1/3$ magnetization plateau in triangular lattices is expected for a situation when the magnetic ions at one of the three vortices of the triangle is magnetically disordered, while the other two are antiferromagnetically coupled in zero field in the virgin state; when the compound is in a field in the plateau region, the magnetic moment of the ‘disordered’ Er ion gets oriented and becomes antiparallel to one of the two Er ions, leaving behind a net spontaneous moment from the third Er ion; at higher fields beyond 25 kOe, the magnetic moment from all the three Er ions get ferromagnetically aligned resulting in thrice of magnetic moment at the plateau. This kind of magnetism in zero-field for the virgin state is called ‘Partially Disordered Antiferromagnetism (PDA)’ due to geometrical frustration of the magnetic moments. Typical examples for such a PDA magnetism known in the past literature [10, 11] are CsCoCl_3 and $\text{Ca}_3\text{CoRhO}_6$, containing triangular magnetic lattices and such compounds are insulators. Such a PDA magnetism was not considered in the analysis of neutron diffraction pattern in the previous report (reported for 1.5 K only) [7].

We now bring out an interesting feature in the $C(T)$ data, measured also in the presence of external fields while warming after ZFC to 2 K. There is no worthwhile feature in the data above 8 K (measured till 150 K) and therefore we show the data in fig. 1d below 10 K only. As expected, in the zero-field data, there is a λ -anomaly well below 6 K, with the upturn and the sharp peak occurring very close to 5 K due to the onset of magnetic ordering; no additional prominent peak could be detectable down to 2 K, even in the C/T curve.

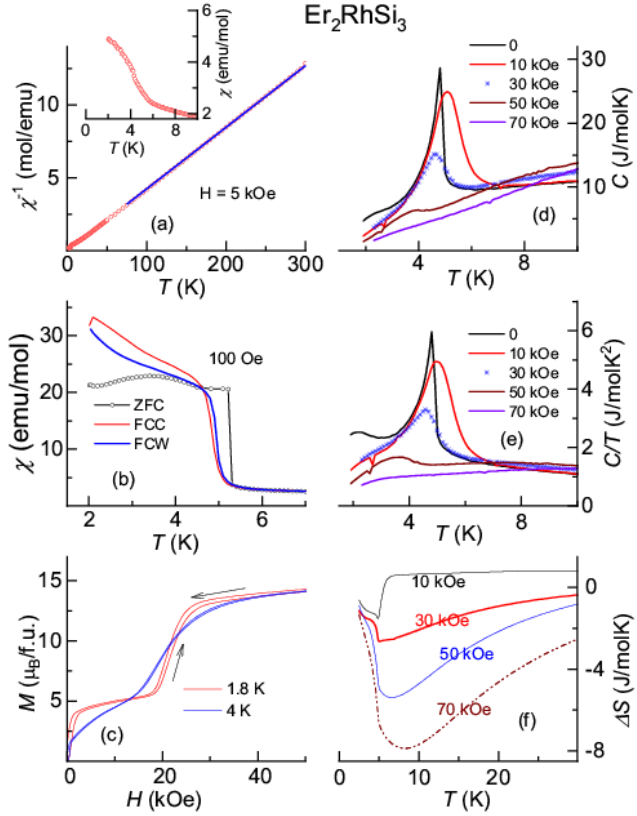


FIGURE 1: (a) Inverse susceptibility ($1/\chi$) as a function of temperature (T) below 300 K with the Curie-Weiss fit line (mainframe) and the χ below 10 K (inset), (b) χ for zero-field-cooled, field-cooled-cooling and field-cooled-warming conditions below 10 K, (c) isothermal magnetization behavior at 1.8 and 4 K up to 50 kOe, (d) heat-capacity as a function of T below 10 K in various fields, (e) C/T curves, and (f) isothermal entropy changes below 30 K, for Er_2RhSi_3 .

The interesting finding is that, for $H=10$ kOe, the λ -peak is shifted to a marginally higher temperature, which is usually a characteristic feature of ferromagnetism; further applications of H suppresses the peak temperature, typical of antiferromagnets. Clearly, there is a subtle competition between ferromagnetism and antiferromagnetism with the application of H . The isothermal entropy change, defined as $\Delta S = S(H) - S(0)$, obtained by integrating C/T curves, exhibits a negative peak typical of field-induced ferromagnetic alignment (fig. 1f). Surprisingly, it changes sign sharply at the onset of magnetic transition for 10 kOe, as though there are antiferromagnetic clusters before the onset of long range magnetic order; the peak values are reasonably large, say, for $0 \rightarrow 50$ kOe field-variation, spread over a wide T -range to enable possible applications at low temperatures, given that isothermal M curves are nonhysteretic.

We now focus on the Ho compound. We show the results of χ , isothermal M , and C measurements in fig. 2. $\chi(T)$ exhibits Curie-Weiss behavior (fig. 2b, inset) above its magnetic transition temperature of 5.2 K, with the value of μ_{eff} ($\sim 10.63 \mu_B$) in agreement with the theoretical value of Ho^{3+} ion. The value of θ_p is ~ -5.4 K with the negative sign suggesting antiferromagnetic correlations; since the magnitude is in good agreement with the observed ordering temperature, we infer that there is negligible competition from ferromagnetic correlations, at least in low fields. There is a peak at 5.2 K, without any worthwhile bifurcation of ZFC-FC curves measured in 100 Oe (fig. 2a), thereby implying absence of glassiness of magnetism down to 2 K. An interesting finding in the ZFC curve measured with 100 Oe is that there is a drop of χ at 5.1 K – that is, as soon as the compound enters magnetically ordered state – followed by a relatively broader peak; such a drop is not observed in FCC and FCW curves. Clearly, there is a subtle magnetic anomaly around 5 K sensitive to the way the measurements are done for this compound. Isothermal M behavior is shown for 1.8 and 4 K in fig. 2b. The curve at 1.8 K is found to be hysteretic and a careful look of the

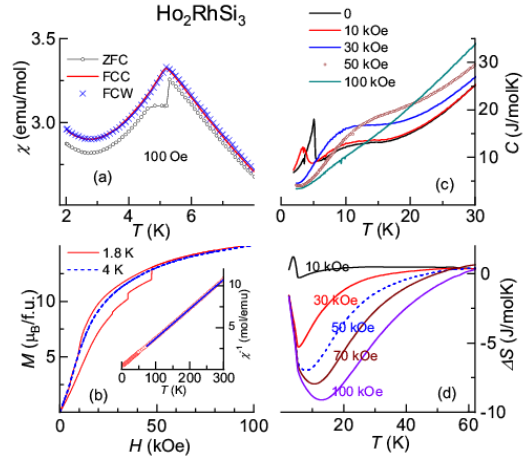


FIGURE 2: (a) Magnetic susceptibility (χ) as a function of temperature (T) below 8 K for zero-field-cooled, field-cooled-cooling and field-cooled-warming conditions, measured with 100 Oe (b) isothermal magnetization behavior at 1.8 and 4 K up to 100 kOe, & the inverse χ below 300 K with the Curie-Weiss fit (inset) (c) heat-capacity as a function of T below 30 K in various fields, and (d) isothermal entropy change below 60 K, for Ho_2RhSi_3 .

virgin curve reveals that there is an upward curvature around 5 kOe, attributable to spin-reorientation. There are additional sharp jumps at higher fields (35 and 47 kOe); while reversing the field, these jumps vanish, but the change of slope due to spin-reorientation persists. At 4 K, these steps are absent, though a careful look at the curve provides evidence for spin-reorientation in the low-field range.

In fig. 2c, we show the $C(T)$ data below 30 K (though measured till 60 K). There is a well-defined λ -anomaly with a sharp peak at 5 K in zero field due to magnetic ordering, which is suppressed to about 3 K for an application of 10 kOe; for higher fields, this feature is suppressed to a temperature below 2 K (as indicated by a weak upturn in C/T below 4 K, not shown here). There is also a broad peak in zero-field in the range 5-20 K, possibly due to Schottky anomaly associated with crystal-field effects; this peak persists for 10 kOe, but it is smeared for higher fields. The ΔS , shown in fig. 2d, below 60 K, exhibits a peak, shifting to higher temperatures with increasing (final) H due to the depression of magnetic transition temperature. The fact that the sign is negative suggests field-induced ferromagnetic alignment. The values at the minimum of the curve are reasonably large, as in the case of Er compound, say, for a change of field 50 kOe.

CONCLUSIONS

We bring out interesting magnetic anomalies in Ho_2RhSi_3 and Er_2RhSi_3 , based on initial magnetic investigations. In the case of Ho compound, there is an interesting magnetic transition around 5.2 K and the magnetic features are sensitive to the way measurements are done and isothermal M is hysteretic showing spin reorientation effects. Jumps in the virgin isothermal magnetization data below 5 K are observed. With respect to Er compound, which is found to order at 5 K, it is notable that the Er compound exhibits an interesting magnetic transition around 5 K, in addition characterized by ‘partially disordered antiferromagnetic’ features due to geometrically frustrated magnetism – an observation unusual among intermetallics. In order to get better insight into this, ac χ and remnant magnetization studies will be carried out. Details will be published elsewhere. It would be rewarding to carry out neutron diffraction studies as a function of temperature and magnetic field.

ACKNOWLEDGMENTS

E.V.S. thanks Department of Atomic Energy, Government of India, for awarding Raja Ramanna Fellowship. K.M. thanks financial support from BRNS, DAE under the DAE-SRC-OI program. SM thanks support from Vision Group on Science and Technology-GRD No 852.

REFERENCES

1. R. Mallik E.V. Sampathkumaran, M. Strecker, and G. Wortmann, *Europhys Lett.* **41**, 315-320 (1998).
2. E.V. Sampathkumaran and R. Mallik, in “Concepts in Electron Correlations”, edited by A.C. Hewson and V. Zlatic (Kluwer Academic Publishers, Netherlands, 2003), p353-361;
3. Z. Wang, K. Barros, G.-W. Chern, et.al, *Phys. Rev. Lett.* **117**, 206601(1-5) (2016).
4. B. Chevalier, P. Lejay, J. Etourneau, and P. Hagenmuller, *Solid State Commun.* **49**, 753-760 (1984).
5. S.R. Saha et al., *Phys. Rev.* **B60**, 12162-12165 (1999).
6. E.V. Sampathkumaran, [arXiv:1910.09194](https://arxiv.org/abs/1910.09194).
7. W. Bazela, E. Wawrzynska, B. Penc, et.al, *J. Alloys and Compd.* **360**, 76-80 (2003).
8. S. Patil, V.R.R. Medicherla, et.al *Phys. Rev. B* **82**, 104428 (pg1-4) (2010) and references cited therein.
9. Ram Kumar, Kartik K Iyer, P.L. Paulose, et.al, *Phys. Rev. B* **101**, 144440 (Pg1-7) (2020).
10. M. Mekata, *J. Phys. Soc. Jpn.* **42**, 76-82 (1977).
11. E.V. Sampathkumaran, and A. Niazi, *Phys. Rev. B* **65**, 180410(R) (pg1-3) (2002).



Emergent Griffiths-phase-like behavior in the ball-milled nanocrystalline Dy₄RhAl and its implication

ARTICLE INFO

Keywords

Nanocrystals
Magnetism
Griffiths phase

ABSTRACT

We report the results of dc susceptibility and heat capacity measurements on the (ball-milled) nanocrystalline rare-earth (R) ternary compound, crystallizing in Gd₄RhIn-type, cubic Dy₄RhAl compound (space group $F\bar{4}3m$, No. 216, cF96). The bulk form of this compound has been known to undergo antiferromagnetic ordering at ($T_N =$) 18 K with concomitant cluster spin-glass anomalies. The present studies on the nano-form obtained by ball-milling reveal that this antiferromagnetic ordering is suppressed with the reduction of particle size with no feature attributable to a well-defined long-range magnetic ordering down to 1.8 K, but showing an inhomogeneous magnetism below 10 K. The point being stressed is that the results show the dominance of a feature around 30 K in the magnetic susceptibility data - well above T_N of the bulk form - mimicking Griffiths phase. We infer that surface magnetism dominates before long-range magnetic ordering occurs in this material.

One of the current trends in the field of magnetism is to look for various manifestations of magnetic frustration due to the competition between antiferromagnetic and ferromagnetic interactions in a material, attributable to geometrical arrangement of the magnetic ions in the lattice. It is now realized that a consequence of such a competition is the ‘Topological Hall Effect,’ the signatures of which were reported on Gd₂PdSi₃ [1], a decade before this terminology was applied to magnetic systems [2], and magnetic skyrmions [3,4]. Considering the application potential of such systems, there are constant efforts to identify such exotic magnetic materials and to find ways and means of tuning the same. A very recent theoretical effort by Hayami [5] emphasized the need to focus on multi (magnetic) substructure systems to understand such a magnetic frustration. However, it should be noted that such multi-substructure systems among rare-earth (R) intermetallics are rather scarce, some examples being Gd₅Si₂Ge₂ [6] and R₇Rh₃ [7,8]. In this respect, the compounds of the type R₄TX ($T =$ Transition metal and $X =$ p block elements), which are characterized by three different crystallographic sites for the rare-earths [9–13] are of great interest, as the bulk specimens of the heavy rare-earth members R₄RhAl ($R =$ Gd, Tb, Ho and Er) showed [14–18] exotic magnetic and transport properties. In the case of R₄PtAl family, ($R =$ Gd, Tb, Dy, Ho, Er), all the members are known to order antiferromagnetically, with the Er and Ho members exhibiting a larger value of isothermal entropy change (ΔS), at the onset of magnetic ordering within this family [19]. It may be mentioned that microscopic studies are not available at present to understand whether the observed anomalies in the bulk measurements are the result of the formation of magnetic skyrmions or any other modern magnetic concept like altermagnetism [20] (given that many of these compounds including the title compound are characterized by antiferromagnetic as well as ferromagnetic features and that the local symmetries for the three magnetic sites of R are different).

In this Letter, we focus on the compound Dy₄RhAl [21], which has been reported to exhibit antiferromagnetic ordering at ($T_N =$) 18 K

setting it concomitantly with spin glass features, apart from other subtle magnetic anomalies as a function of temperature (T) and magnetic field (H). The study on fine particles was motivated by the fact that some of the rare-earth intermetallics showed interesting changes in properties when going from bulk to nanoform including conversion of Pauli paramagnetism to magnetic ordering, e.g., YCo₂ [22], and a well-known heavy-fermion CeRu₂Si₂ [23]. This work is further motivated by the importance of understanding magnetism of multi-substructures systems in different forms. The results reveal suppression of antiferromagnetism in the nano form, leading to a Griffiths-phase-like state – a magnetic state proposed for a situation in which ferromagnetic clusters are distributed in a paramagnetic state [24–28] – in the H dependent $\chi(T)$ data. We argue that there is a qualitative change in the magnetic properties when traversing from the bulk to the surface of complex magnetic materials, particularly the ones with multiple magnetic sites.

A polycrystalline sample of Dy₄RhAl was prepared by melting together stoichiometric amounts of constituent elements in an arc furnace in an argon atmosphere. The phase and stoichiometry of the ingots were ascertained using x-ray diffraction (XRD) and Energy Dispersive Analysis of X-rays (EDAX). The ingot was ground using a high energy ball mill (Pulverisette 7, M/s. Fritsch GMBH, Germany) for 150 min at a speed of 500 RPM in a zirconia bowl with zirconia balls of 5 mm diameter. A small amount of milled sample was mixed with a drop of diluted GE-Varnish and allowed to dry to get a single pellet. This pellet was used for measurements. A transmission electron microscope (TEM, Technai-200 kV) was used to characterize the phase and the particle size. Dc χ , isothermal magnetization (M) and heat-capacity (C) measurements were performed as a function of T and H , as described in Ref. [21].

Fig. 1a shows the XRD data for the powders of molten ingot and the ball-milled materials. The main panel of the figure shows the profile fitted using Rietveld refinement method along with the observed powder XRD data for the bulk sample. The fit clearly shows the formation of

<https://doi.org/10.1016/j.jmmm.2024.172018>

Received 7 March 2024; Received in revised form 23 March 2024; Accepted 29 March 2024

Available online 30 March 2024

0304-8853/© 2024 Elsevier B.V. All rights reserved.

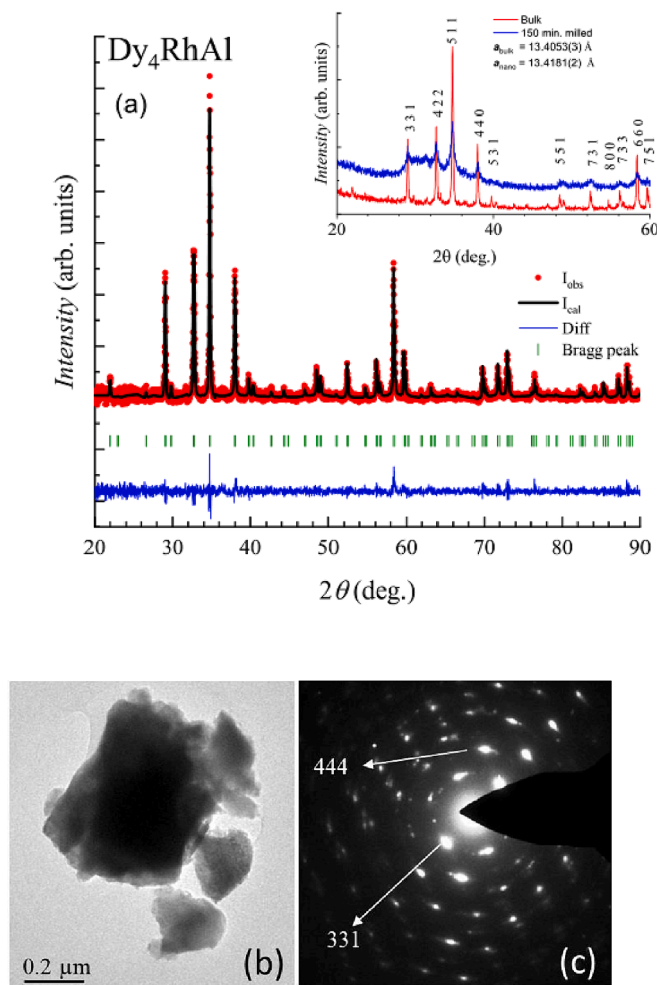


Fig. 1. (a) Powder x-ray diffraction pattern for the bulk sample fitted to a Rietveld refined structural model is shown in the main panel. The plot shows the observed data (I_{obs}), calculated profile (I_{cal}) along with the Bragg peak positions shown as vertical tick marks. (The inset shows powder X-ray diffraction patterns for bulk and nanoform specimen (obtained by ball milling for 150 min) of Dy_4RhAl at room temperature. (b) TEM images to reveal particle sizes and (c) electron diffraction pattern obtained on a single nano particle to establish phase formation.

the sample in Gd_4RhIn -type Dy_4RhAl cubic structure (space group $F\bar{4}3m$, No. 216, $cF96$), with no additional peaks. The peaks in the XRD pattern for the milled sample show broadening. We calculated the particle size for this specimen from the XRD measurements by Debye-Scherrer formula and the average particle size was found to be in the range of 20-50 nm. Table 1 summarizes the values of refined cell parameters. The transmission electron microscopic pictures, shown in Fig. 1(b), show the presence of nanoparticles of higher sizes as well (a few up to 500 nm), suggesting an inhomogeneity in particle sizes, which

Table 1

Values of unit cell parameters obtained from the refinement of powder diffraction data is summarized here. The table also lists the values of paramagnetic Curie temperature and effective magnetic moment obtained from the magnetic susceptibility data for bulk and nanosized samples of Dy_4RhAl .

Sample	Cell parameter (a , Å)	Paramagnetic Curie temperature (θ_p)	Effective magnetic moment (μ_B) per formula unit
Bulk	13.4053(3)	-16 K	21.9
Nano	13.4181(2)	7.6 K	18.5

is inevitable in the ball-milling procedure. The electron diffraction pattern shown in Fig. 1(c) was obtained on a particle of about 200 nm and confirms that there is no change in the structure after milling (as inferred from the indexing of some of the diffraction lines).

We now focus on the effects of the reduction in particle size on the magnetism in this compound. In Fig. 2(a), we show the χ and inverse χ data measured in a magnetic field of 5 kOe down to 1.8 K for the nanoform specimens; inverse χ remains linear down to 50 K and obeys Curie-Weiss behaviour. The paramagnetic Curie temperature (θ_p) obtained for the linear region is close to 7.6 K, with the positive sign indicating effective ferromagnetic correlations in contrast to the negative sign of θ_p ($=-16$ K) for the bulk form typical of antiferromagnetic interactions [21]. Table 1 gives a comparison of the values of θ_p and μ_{eff} for bulk and nano samples. As the temperature is lowered, there is no feature around 18 K attributable to the magnetic ordering seen in bulk specimen, but we find a distinct peak appearing at 8 K in this 5kOe-curve. It is not clear whether it is the same additional feature seen in the bulk specimen around 10 K, when measured with 5 kOe. As seen in Fig. 2(b), for a magnetic field of 100 Oe, χ shows a prominent bifurcation in the ZFC-FC curves in the vicinity of 30 K for the milled specimen, which is absent in similar measurements on the bulk form, as shown in the same figure. However, note that even in the bulk form [21], there is a weak bifurcation of the two curves, obtained by measuring with 100 Oe and 5 kOe, well before magnetic ordering sets in, as though there is a weak magnetic anomaly above T_N . In addition to a shoulder around 30 K in this ZFC curve, we see a broad peak appearing around 12 K which is similar to the shoulder around 12 K for the bulk specimen in the data measured with 100 Oe, except that this shoulder has become relatively more prominent and broadened in the nanoform specimen. Finally, the FC curve, rather than remaining flat at the temperature of bifurcation from the ZFC curve, keeps increasing with decreasing temperature, typical of cluster spin-glasses.

In order to throw more light on the changes observed in the magnetic ordering behaviour, the heat capacity results are shown in Fig. 3(a) and

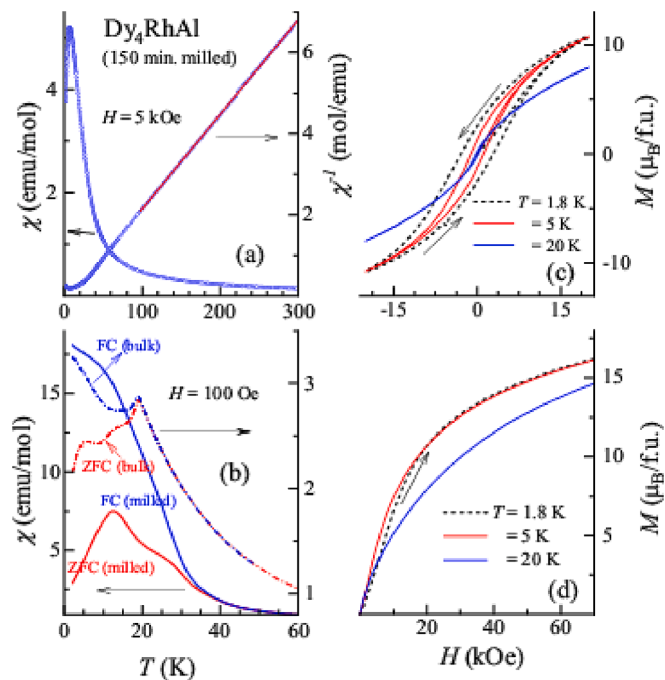


Fig. 2. Temperature dependent dc susceptibility measured in (a) 5 kOe (zero-field cooled condition) and (b) 100 Oe (for zero field cooled and field cooled conditions) for milled specimens. The curves for the bulk form are reproduced from Ref. 20. (c) Magnetic hysteresis loops at 1.8, 5 and 20 K. (d) Isothermal magnetization in units of Bohr magneton per formula unit (f. u.) at selected temperatures measured up to 70 kOe.

3(b), along with the zero-field data [reproduced from Ref. [21]] for the bulk specimen. We find that C varies monotonically down to 1.8 K, without any evidence for a λ -anomaly, seen prominently for the bulk specimen around 18 K, supporting the absence of long-range antiferromagnetic ordering in nanoform specimens. We find that the $C(T)$ data for 30 kOe and 50 kOe almost overlap with the $H = 0$ data down to 1.8 K (and hence not shown in Fig. 3(a) for the sake of clarity). However, a careful look at the $C(T)/T$ plots (Fig. 3(b)) shows that, there is a subtle variation of the heat capacity values for a field of 30 kOe and 50 kOe, which points to the persistence of some sort of magnetism. Incidentally, we have also derived isothermal entropy change $[\Delta S = S(H) - S(0)]$ from the heat-capacity data by integrating C/T over temperature and the sign of the ΔS remains negative with a broad peak, similar to that noted for the bulk form [21] (and hence not shown here); this negative sign is a signature [29] for a tendency for the field-induced ferromagnetic alignment. Combined with the fact that the bifurcation in the $\chi(T)$ curves begins in the range 30 to 35 K for $H = 100$ Oe, the $C(T)$ data, provides evidence for the inference that the glassy nature gets enhanced and the long-range antiferromagnetic order gets suppressed when the sample is driven to the nanoform in this compound.

We present the $M(H)$ data for the nanoform specimen in Fig. 2(c) and 2(d). We find that the $M(H)$ curves are distinctly hysteretic at 1.8 and 5 K (in the range -20 to $+20$ kOe) supporting the existence of a spin-glass-like or ferromagnetic component. However, the hysteresis is negligible at 20 K. The (virgin) curves extended to higher fields are shown in Fig. 2(d). There is no evidence for saturation even for a field as high as 70 kOe, which is typical of spin-glass and antiferromagnetism. Arrott plots (Fig. 4) offer an additional insight into the low temperature magnetism. These plots - H/M versus M^2 - are shown at different temperatures for

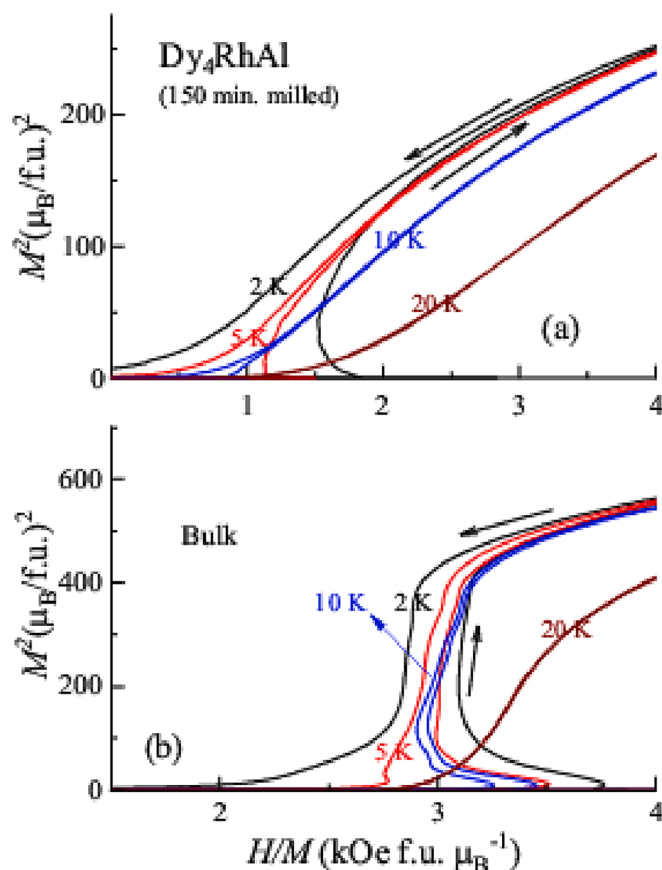


Fig. 4. Arrott plots for the bulk and milled forms of Dy_4RhAl at the temperatures specified. Arrows are drawn to show the direction in which the H/M increases.

both the bulk form as well as milled form. The slope of the virgin curve (that is, for the upward cycle of field variation) remains positive for temperatures well above 10 K, whereas a negative slope appears in the virgin curves for $T = 2, 5$ and 10 K. This is true for the bulk form also. This signals [30,31] that the zero-field magnetic state at such low temperatures, presumably containing some antiferromagnetic component (as inferred in Ref. [21]), undergoes a disorder-broadened first-order field-induced transition to a ferromagnetic-like component. The fact that, in the return cycle, the slope remains positive for the milled form after a high magnetic field cycling is in support of a first-order field-induced transition for the virgin state only. This behavior is different from that of the bulk, as the negative curvature is retained in the reverse cycle of field variation as well. Thus, there are also subtle changes when reducing the particle size. Finally, a careful look at the $M(H)$ curves at 2 K, for both bulk and milled forms, shows a feeble upward curvature at low-fields (< 4 kOe) typical of an antiferromagnetic component in zero-field, which is smeared in the 5 and 10 K curves (Fig. 2(c)). Thus, there are features attributable to spin-glass-like, ferromagnetic-like as well as antiferromagnetic behavior at very low temperatures ($< \sim 10$ K). It is not clear at present whether this apparent inhomogeneous magnetic state is due to a distribution in particle size, a surface phenomenon or it implies a more complex magnetism for small particles.

To get an insight into field-dependent behavior of magnetism of the specimen above 10 K - which is the central point of this Letter - we have performed the $\chi(T)$ measurements for different applied magnetic fields, the results of which are shown as $\chi^{-1}(T)$ plots in Fig. 5(a). The curves above 50 K tend to overlap. We find that the feature below about 10 K (a broad upturn) shifts towards a low temperature marginally with the increase in the magnetic field initially, except for a magnetic field of 5

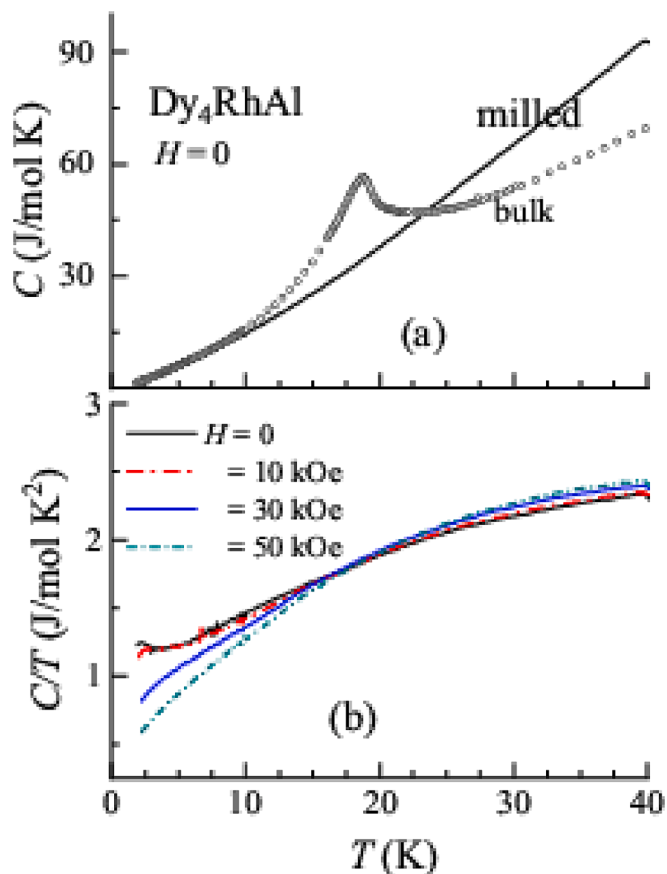


Fig. 3. Plots of (a) heat capacity (C), and (b) heat capacity divided by temperature as a function of temperature (in the presence of 10, 30 and 50 kOe) in the vicinity of magnetic ordering. The heat-capacity data for the bulk (Ref. 20) is also shown in (a).

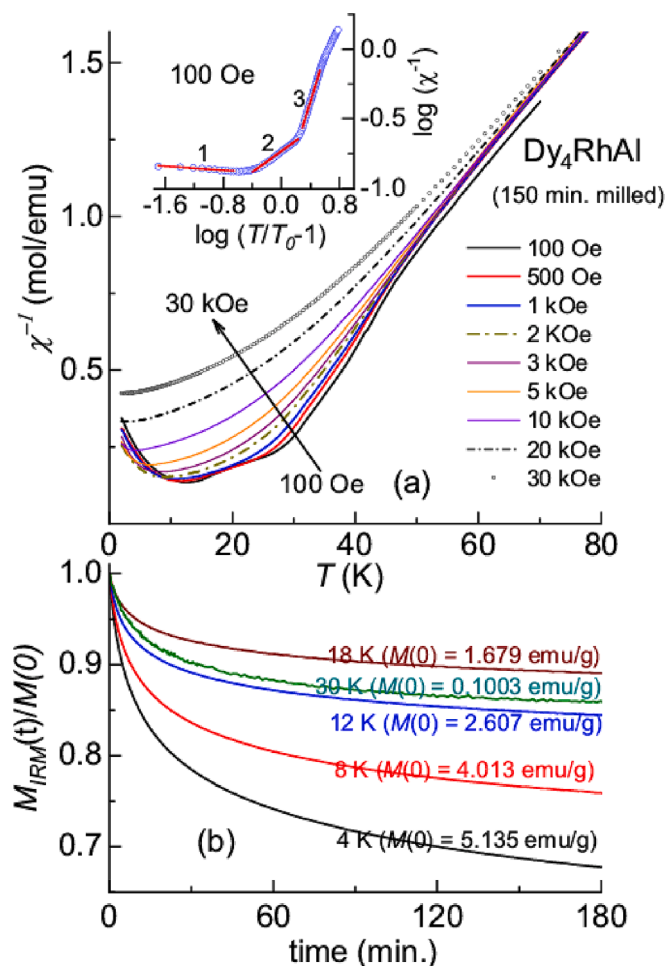


Fig. 5. (a) Inverse magnetic susceptibility as a function of temperature in the presence of dc magnetic fields. Inset shows data for 100 Oe, plotted as $\log(\chi^{-1})$ versus $\log(T/T_0-1)$. The three red lines are the results of a linear fit in regions marked, as 1, 2, and 3, (b) Isothermal remnant magnetization curves obtained at several temperatures, and the lines through the data points obtained by a fit as described in the text; the values are normalized to the respective initial values (M_0) immediately after switching of the field.

kOe, where we find a sharp drop of temperature from 8.5 K for $H = 3$ kOe to 5 K for $H = 5$ kOe. This trend continues till this characteristic temperature reaches 3 K for a magnetic field of 20 kOe, beyond which we do not find any such worthwhile feature in the $\chi^{-1}(T)$ as the magnetic field is increased. This may be correlated to the anomalies seen at such low temperatures in the $\chi(T)$ data discussed above (Fig. 2(b)). *The main point we emphasize is that there is a sudden change of slope around 30 K in the low-field curves, which is gradually smeared with increasing H .* Qualitatively speaking, such a dependence of the $\chi^{-1}(T)$ with applied magnetic fields is the fingerprint of Griffiths Phase. Such a magnetic phase was conceptualized long ago [24–28] to explain a situation where traces of ferromagnetic clusters are distributed randomly in a paramagnetic matrix in such a manner that its contribution to χ is overshadowed by paramagnetic contribution. Thus, it is generally not easy to detect by magnetic studies. However, this magnetic behaviour, mimicking Griffiths phase has been recently claimed to occur in dense magnetic systems also, more frequently among oxides [see, for instance, Refs. [32–34]]. Many Ce based intermetallics, characterized by extended 4f orbital, near the quantum critical point exhibiting non-Fermi liquid behaviour have also been shown to exhibit the characteristics of this phenomenon [28,35–37]. But it is less commonly demonstrated in stable valent rare-earth intermetallics with well-localized 4f orbital [38]. It is in this context that, for a heavy rare-earth compound with strictly localized 4f

orbital showing antiferromagnetism in the crystalline form, the observation of Griffiths-like behavior in the ball-milled nano form is interesting. To further ascertain that the features observed in Fig. 5(a) signal Griffiths phase, we have looked for the T -region where the theoretical prediction [26–28] is obeyed. That is, $\chi^{-1}(T)$ should be proportional to $(T-T_0)^{1-\lambda}$ where λ should be in the range 0 to 1. The plot of χ^{-1} versus (T/T_0-1) is shown in Fig. 5(a) (inset) for the data measured in 100 Oe. We can identify three linear regions in this plot, as shown in this figure. The values of λ derived from the slopes are: ~ 1 (~ 10.2 to ~ 12 K), ~ 0.6 (~ 13 to ~ 27 K), ~ -0.7 (~ 30 K to ~ 45 K) On the basis of this, one can conclude that approximately in the range $10 \text{ K} < T < 30 \text{ K}$ only, the value of λ turns out to be positive and less than 1. The value of T_0 is 10 K. In the linear region above 30 K, the sign of this exponent is unrealistically negative. Thus, the results show the signature of Griffiths phase in this compound below 30 K when the particle size is reduced to nanoform, before a different kind of inhomogeneous magnetic state evolves below 10 K. We believe that non-overlapping curves for different H in Fig. 5 at higher temperatures is due to conventional short-range magnetic correlations (given that λ value does not obey Griffiths formula), which are often encountered in many bulk magnetic materials before long-range magnetic order sets in.

We have also measured isothermal remnant magnetization (M_{IRM}) as a function of time (t) at selected temperatures below 30 K. This measurement was performed first by cooling the sample in the magnetometer from 100 K to a desired temperature, thereafter, leaving in a field of 5 kOe for about 5 mins; the field was then switched off and subsequently M_{IRM} behavior was tracked as a function of t . The curves thus obtained are shown in Fig. 5(b) and it is clear that there is a slow decay of M_{IRM} , suggesting that the Griffiths-phase-like regime (see the curves for 12, 18 and 30 K) exhibits spin-glass dynamics [39,40]. This slow decay persists down to 1.8 K, attributable to glassiness. The decay curves are also found to obey a stretched exponential form, $M_{IRM}(t) = M_{IRM}(0) + A \exp(-t/\tau)^{1-n}$, where A is a constant, and the time constant τ and the exponent n are related to the relaxation rate of the clusters.

To summarize, the present fine particles (< 500 nm) studies of Dy_4RhAl reveal that the antiferromagnetic ordering dominating in the bulk specimen, disappears in the nanocrystalline form, while a new magnetic state emerges in the range 10–30 K. Considering that this feature is feebly present for the bulk form as well below ~ 35 K, visible in some form when measured with different low fields, we attribute this magnetic state to the surface layers (naturally characterized by disorder due to incomplete coordination or strain) since the total area of the surface gets enhanced when the particle size is reduced. The magnetism of such a state is characterized by a magnetic susceptibility behavior mimicking Griffith's phase around 30 K. Demonstration of such a particle-size induced transformation to Griffith's phase-like features in an intermetallic compound due to localized 4f electrons is generally quite rare. It is of interest to explore how common this is in other exotic magnetic systems.

Funding

Authors acknowledge financial support from the Department of Atomic Energy (DAE), Govt. of India (Project Identification no. RTI4003, DAE OM no. 1303/2/2019/R&D-II/DAE/2079 dated 11.02.2020). E.V.S. thanks Department of Atomic Energy, Government of India, for awarding Raja Ramanna Fellowship. We thank Jayesh Parmar for his help during characterization by TEM.

CRediT authorship contribution statement

Kartik K. Iyer: Conceptualization, Formal analysis, Investigation. **Kalobaran Maiti:** Writing – review & editing, Resources, Project administration, Investigation, Formal analysis, Funding acquisition. **S. Rayaprol:** Investigation, Formal analysis. **B.A. Chalke:** Investigation. **E. V. Sampathkumaran:** Writing – review & editing, Writing – original

draft, Project administration, Investigation, Funding acquisition, Conceptualization, Formal analysis.

Declaration of competing interest

The authors declare that they have no known competing financial interests or personal relationships that could have appeared to influence the work reported in this paper.

Data availability

The data that support the findings of this study are available from the corresponding authors upon reasonable request.

References

- [1] S.R. Saha, H. Sugawara, T.D. Matsuda, H. Sato, R. Mallik, E.V. Sampathkumaran, *Phys. Rev. B* 60 (1999) 12162.
- [2] E.V. Sampathkumaran, arXiv:1910.09192; also see, A brief e-letter can be found at the Science journal site: <https://science.sciencemag.org/content/365/6456/914/tab-e-letters>.
- [3] S. Mühlbauer et al., *Science* 323, 915 (2009); X.Z. Yu et al., *Nature* 465, 901 (2010).
- [4] See, for instance, Bom Soo Kim, *J. Phys.: Condens. Matter* 31, 383001 (2019).
- [5] S. Hayami, *Phys. Rev. B* 109 (2024) 014415.
- [6] V.K. Pecharsky, K.A. Gschneidner Jr., *Phys. Rev. Lett.* 78 (1997) 4494.
- [7] T. Tsutaoka, T. Tokunaga, M. Kosaka, Y. Uwatoko, H. Suzuki, H. Kitazawa, G. Kido, *Phys. B* 294–295 (2001) 199.
- [8] S. Rayaprol, V. Siruguri, A. Hoser, C. Ritter, E.V. Sampathkumaran, *Phys. Rev. B* 90 (2014) 134417.
- [9] A. Doğan, S. Rayaprol, R. Pöttgen, *J. Phys. Condens. Matter* 19 (2007) 076213.
- [10] F. Tappe, C. Schwickert, S. Linsinger, R. Pöttgen, *Monatsch. Chem.* 142 (2011) 1087.
- [11] M. Kersting, S.F. Matar, C. Schwickert, and R. Pöttgen, *Z. Naturforsch.* 67b, 61 (2012).
- [12] S. Engelbert, O. Janka, *Intermetallics* 96 (2018) 84.
- [13] R. Pöttgen, *Handb. Phys. Chem. Rare Earths* 58 (2020) 1–38.
- [14] R. Kumar, J. Sharma, K.K. Iyer, E.V. Sampathkumaran, *J. Magn. Mag. Mater* 490, 165515 (2019).
- [15] R. Kumar, K.K. Iyer, P.L. Paulose, E.V. Sampathkumaran, *J. Appl. Phys.* 126 (2019) 123906.
- [16] R. Kumar, K.K. Iyer, P.L. Paulose, E.V. Sampathkumaran, *AIP Conf. Proc.* 2265 (2020) 030509.
- [17] R. Kumar, K.K. Iyer, P.L. Paulose, E.V. Sampathkumaran, *Phys. Rev. Mat.* 5 (2021) 054407.
- [18] R. Kumar, E.V. Sampathkumaran, *J. Magn. Mag. Mater.* 538, 168285 (2021).
- [19] K.K. Iyer, S. Rayaprol, R. Kumar, S. Matheppanavar, S. Dodamani, K. Maiti, E.V. Sampathkumaran, *Magnetochemistry*, 9, 85 (2023).
- [20] See, for instance, S.-W. Cheong, F.-T. Huang, *Npj Quantum Mater.* 9, 13 (2024).
- [21] K.K. Iyer, S. Matheppanavar, S. Dodamani, K. Maiti, E.V. Sampathkumaran, *J. Magn. Mag. Mater.* 568 (2023) 170406.
- [22] S. Narayana Jammalamadaka, E.V. Sampathkumaran, V. Satya Narayanamurthy, G. Markandeyulu, *Appl. Phys. Lett.* 92 (2008) 192506.
- [23] S.D. Das, S.N. Jammalamadaka, K.K. Iyer, E.V. Sampathkumaran, *Phys. Rev. B* 80, 024401 (2009); E.V. Sampathkumaran, K. Mukherjee, K.K. Iyer, N. Mohapatra, S.D. Das, *J. Phys.: Condens. Matter* 23, 094209 (2011). and references cited therein.
- [24] V.G. de Paula, M. Gomes Silva, L.M. da Silva, A.O. dos Santos, R. Lang, L. Otubo, A. A. Coelho, L.P. Cardoso, *Intermetallics* 94 (2018) 1.
- [25] R.B. Griffiths, *Phys. Rev. Lett.* 23 (1969) 17.
- [26] A.J. Bray, M.A. Moore, *J. Phys. C* 15, L765 (1982); A. J. Bray, *Phys. Rev. Lett.* 59, 586, (1987).
- [27] M.B. Salamon, P. Lin, S.H. Chun, *Phys. Rev. Lett.* 88 (2002) 197203.
- [28] A.H. Castro Neto, G. Castilla, B.A. Jones, *Phys. Rev. Lett.* 81 (1998) 3531.
- [29] K.A. Gschneidner, V.K. Pecharsky, A.O. Tsokol, *Rep. Prog. Phys.* 68 (2005) 1479.
- [30] N.H. Duc, D.T. Kim Anh, P.E. Brommer, *Physica B* 319, 1 (2002); N.H. Duc, P.E. Brommer, in: J. H. K Buschow (Ed.), *Handbook on Magnetic Materials*, vol. 12, North-Holland, Amsterdam, 1999, p. 395. (Chapter 4).
- [31] S.K. Banerjee, *Phys. Lett.* 12 (1964) 16.
- [32] E.V. Sampathkumaran, N. Mohapatra, S. Rayaprol, K. Kiyer, *Phys. Rev. B* 75 (2007) 052412.
- [33] I. Fita, I.O. Troyanchuk, T. Zajarniuk, P. Iwanowski, A. Wisniewski, R. Puzniak, *Phys. Rev. B* 98 (2018) 214445.
- [34] J. Kumar, S.N. Panja, S. Dengre, S. Nair, *Phys. Rev. B* 95 (2017) 054401.
- [35] D.T. Rajesh Tripathi, Y.M. Adroja, P.K. Shivani Sharma, T. Biswas, T. Namiki, T. Kuwai, A.M. Hiroto, A.S. Strydom, S. Langridge, *Phys. Rev. B* 108 (2023) 144427.
- [36] A. Ślebarkski, J. Spalek, M. Fijałkowski, *J. Magn. Mag. Mater.* 587 (2023) 171239.
- [37] R. Tripathi, P.K. Debarchan Das, D.T. Biswas, A.D. Adroja, *Phys. Rev. B* 99 (2019) 224424.
- [38] C. Magen, P.A. Algarabel, L. Morellón, J.P. Araújo, C. Ritter, M.R. Ibarra, A. M. Pereira, J.B. Sousa, *Phys. Rev. Lett.* 96 (2006) 167201.
- [39] J.A. Mydosh, *Spin glasses: an Experimental introduction*, Taylor and Francis, London, 1993.
- [40] K. Binder, A.P. Young, *Rev. Mod. Phys.* 58 (1986) 801.

Kartik K. Iyer^a, Kalobaran Maiti^{a,*}, S. Rayaprol^b, B.A. Chalke^a, E. V. Sampathkumaran^{c,*}

^a Tata Institute of Fundamental Research, Homi Bhabha Road, Colaba, Mumbai 400005, India

^b UGC-DAE-Consortium for Scientific Research -Mumbai Centre, BARC Campus, Trombay, Mumbai 400085, India

^c Homi Bhabha Centre for Science Education, TIFR, V. N. Purav Marg, Mankhurd, Mumbai 400088, India

* Corresponding authors.

E-mail addresses: kbmaiti@tifr.res.in (K. Maiti), sampathev@gmail.com (E.V. Sampathkumaran).

Presentation Certificates

65th DAE Solid State Physics Symposium
Organised by: Bhabha Atomic research centre, Mumbai
Sponsored by: Board of research in nuclear sciences (BRNS)
Department of Atomic Energy, Government of India

CERTIFICATE

of Participation

Karthik K Iyer

has presented a paper and participated in this symposium
held at Bhabha Atomic Research Centre, Mumbai,
during 15 - 19 December 2021

Arup Biswas
Arup Biswas
Scientific secretary
DAE SSPS 2021

Ajaya
Ajay K Mishra
Scientific secretary
DAE SSPS 2021

Dif
Dinesh Udupa
Convener
DAE SSPS 2021

Dated: 19 Dec 2021

REG-322



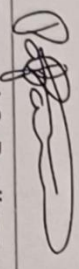


Certificate

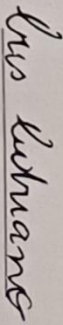
We hereby certify that

Kartik Iyer

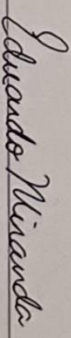
attended the SCES 2020 - International Conference on Strongly Correlated Electron Systems,
held in online format, from September 27th to October 02nd, 2021.



Pascoal G. Pagliuso
Conference Chair



Cris Adriano
Co-Chair



Eduardo Miranda
Co-Chair

66th DAE Solid State Physics Symposium

Organised by: Bhabha Atomic research centre, Mumbai
Sponsored by: Board of research in nuclear sciences (BRNS)
Department of Atomic Energy, Government of India

CERTIFICATE of Participation

Karthik Iyer

has presented a paper and participated in this symposium
held at Birla Institute of Technology Mesra, Ranchi,
during 18 - 22 December 2022

Ajay Mishra

Ajay Mishra

Scientific secretary
DAE SSPS 2022

Mohit Tyagi

Mohit Tyagi

Scientific secretary
DAE SSPS 2022

Dinesh Udupa

Dinesh Udupa

Convener
DAE SSPS 2022

Dated: 22 Dec 2022





CERTIFICATE

This is to certify that

Garbhik R Siper

Tata Institute of Fundamental Research, Mumbai

has attended the
XIX-School on

Neutrons as Probes of Condensed Matter (NPCM-2022)

organized by

UGC-DAE Consortium for Scientific Research, Mumbai Centre

&
Solid State Physics Division, BARC, Mumbai

during November 14 - 19, 2022

at

Multipurpose Hall, TSH, Anushaktinagar, Mumbai



NPCM22-MM-37

[Signature]
(Dr. Sudhindra Rayaprol)
UGC-DAE CSR Mumbai

Coordinators

[Signature]
(Dr. Mayanak K. Gupta)
SSPD, BARC



CERTIFICATE OF ATTENDANCE

This is to certify that

Karthik Iyer

Tata Institute of Fundamental Research, India

has attended in the International Conference on
Strongly Correlated Electron Systems 2023 [SCES 2023]
held from July 2 to 7, 2023 in Incheon, Korea.

Je-Geun Park *Je-Geun Park*
Conference Chair, SCES 2023

KPS
The Korean Physical Society



KLE ACADEMY OF HIGHER EDUCATION & RESEARCH (Formerly known as KLE University, Belagavi)

[Declared as Deemed-to-be-University vis 3 of the UGC Act, 1956, vide Government of India Notification No. F.9-19/2000-USA]
Placed in Category 'A' by MHRD, Govt. of India Accredited 'A+' Grade by NAAC 3rd Cycle
Nehru Nagar, Belagavi - 590 010, Karnataka State, India

Ph. : 0831-2444444 FAX : 0831-2493777 Web: <http://www.kledeemeduniversity.edu.in> E-mail: info@kledeemeduniversity.edu.in

UNIVERSITY DEPARTMENT OF EDUCATION FOR HEALTH PROFESSIONALS

This is to certify that

Dr./Mr./Mrs. Karthik Iyer

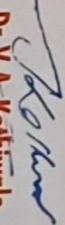
has participated in the workshop entitled

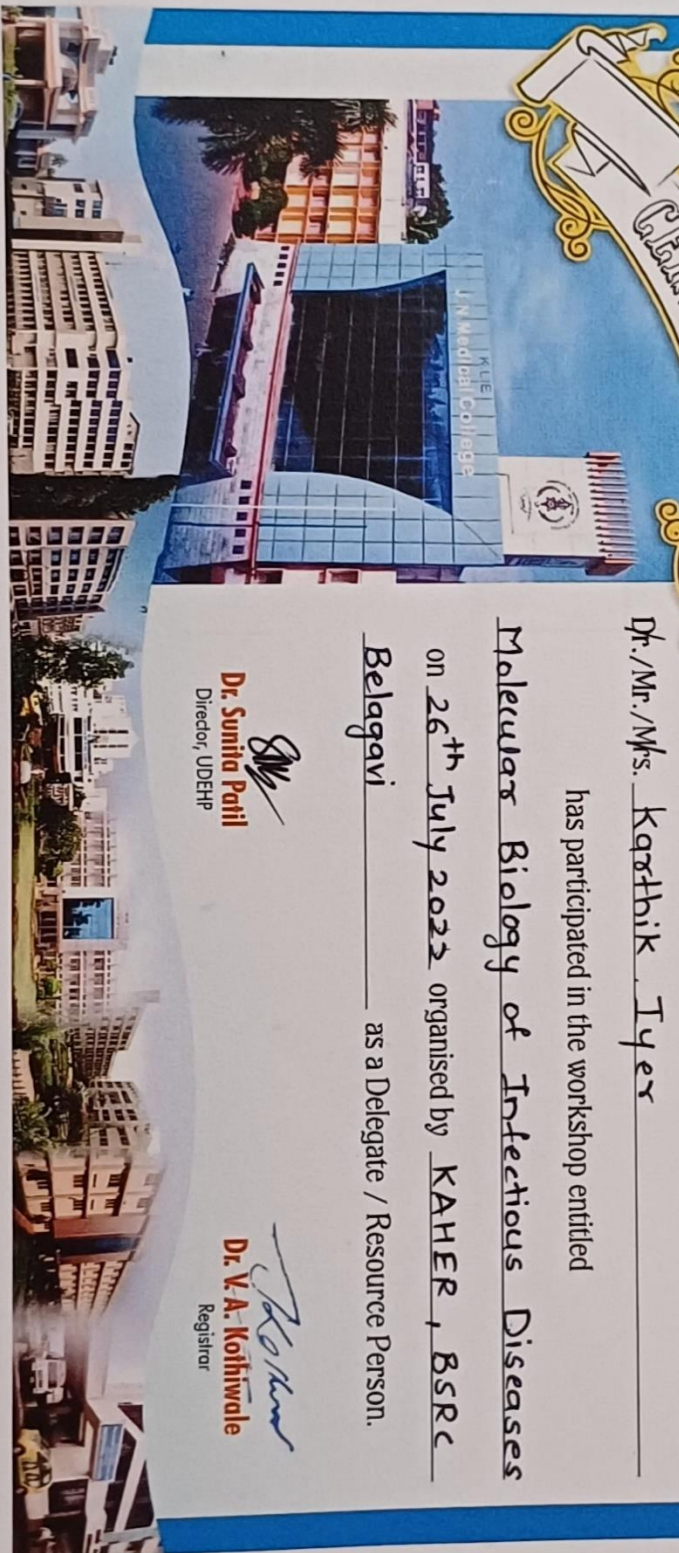
Molecular Biology of Infectious Diseases

on 26th July 2022 organised by KAHER, BSRc

Belagavi as a Delegate / Resource Person.


Dr. Sunita Patil
Director, UDEHP


Dr. V. A. Kothiwale
Registrar



This certificate is computer generated and can be verified by scanning the QR code given below.

To: **KARTHIK IYER**
REGISTRATION NO: 27
MICHIGY KANVAL, STATION ROAD
MUMBAI (EAST)
MAHARASHTRA - 401005
PH. NO: 9970821931

Roll No: NPTEL22H503533940327



Score	Type of Certificate
>= 60	Distinction
75-89	Elite-Silver
>= 70	Elite
60-69	Merit
< 60	No Certificate

No. of credits recommended by NPTEL
An additional 1 credit may be awarded if the University/Institution is fully based on the actual student effort displayed.



NPTEL Online Certification



Elite

(Funded by the MoE, Govt. of India)

This certificate is awarded to
KARTHIK IYER
for successfully completing the course

Health Research Fundamentals
NIE: ICM e-Certificate course: HRCR 101

with a score of **75** %

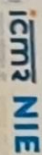
Online Assignments	23.21/25	Proctored Exam	51.75/75
--------------------	----------	----------------	----------

Total number of candidates certified in this course: 674

Sohi

Dr. Ranajit Bhattacharya

Senior & Associate Professor, PCCOEE



Baran Bhargava

Prof. Baran Bhargava

Senior Lecturer, School of Public Health & Community Science, PCCOEE

Jan-Mar 2022
(8 week course)

Andrew Hanganai

Prof. Andrew Hanganai

Senior Lecturer, School of Public Health & Community Science, PCCOEE



Roll No: NPTEL22H503533940327

To verify and check score: <https://npel.ac.in>



NIDA Clinical Trials Network

Certificate of Completion

is hereby granted to

Karthik Iyer

to certify your completion of the six-hour required course on:

GOOD CLINICAL PRACTICE

MODULE:	STATUS:
Introduction	N/A
Institutional Review Boards	Passed
Informed Consent	Passed
Confidentiality & Privacy	Passed
Participant Safety & Adverse Events	Passed
Quality Assurance	Passed
The Research Protocol	Passed
Documentation & Record-Keeping	Passed
Research Misconduct	Passed
Roles & Responsibilities	Passed
Recruitment & Retention	Passed
Investigational New Drugs	Passed

Course Completion Date: 23 November 2021

CTN Expiration Date: 23 November 2024

Tracee Williams, Training Coordinator
NIDA Clinical Coordinating Center

Good Clinical Practice, Version 5, effective 03-Mar-2017

This training has been funded in whole or in part with Federal funds from the National Institute on Drug Abuse, National Institutes of Health, Department of Health and Human Services, under Contract No. HHSN27201201000024C.

KLE ACADEMY OF HIGHER EDUCATION AND RESEARCH

[Deemed-to-be-University u/s 3 of the UGC Act, 1956 vide Government of India Notification No. F-9-19/2000-U-3(A)]
Accredited 'A' Grade by NAAC (2nd Cycle)

Placed in 'A' Category by MHRD (GoI)

Department of Epidemiology and Biostatistics

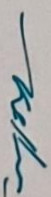
KAHER/EBD/NI221/D-011



This is to certify that **Mr. Karthik Krishnan Iyer**
has attended the 'Intensive Course in Research Methodology and Biostatistics'
held from 1st December to 31st December, 2021 at KAHER, Belagavi
and passed with **78 Percent (Grade A)**



Dr. J. B. Prasad
Asst. Professor
Department of Epidemiology & Biostatistics,
KAHER, Belagavi



Dr. V. A. Kothiwale
Registrar,
KAHER, Belagavi



Rd/No. KAHER/EBD/21-22/W017

KLE ACADEMY OF HIGHER EDUCATION AND RESEARCH

(Declared as Deemed-to-be-University u/s 3 of the UGC Act, 1956)
Accredited 'A' Grade by NAAC (2nd cycle) Placed in Category 'A' by MHRD (GoI)

Department of Epidemiology and Biostatistics


CERTIFICATE

Workshop on

Sample Size Estimation, Systematic Review and Meta-Analysis using EXCELS/SPSS
held from 5th to 7 July 2021

This is to certify that Mr. Iyer Karthik Krishnan
has participated as an online Delegate in the workshop


Dr. N. K. Tyagi
Professor & Head,
Department of Epidemiology & Biostatistics, KAHER, Belagavi


Dr. V. A. Kohliwale
Registrar,
KAHER, Belagavi

KLE ACADEMY OF HIGHER EDUCATION AND RESEARCH

(Declared as Deemed-to-be-University u/s 3 of the UGC Act, 1956)

Accredited 'A' Grade by NAAC (2nd Cycle) Placed in Category 'A' by MHRD (GoI)

Ref No. KAHER/EBD/21-22/W/1221-015

Department of Epidemiology and Biostatistics





CERTIFICATE

Workshop on

*Multivariate Statistical Method and Diagnostic Evaluation using Excel & SPSS
held from 13th to 17th December 2021*

This is to certify that **Mr. Karthik Krishnan Iyer**
has participated as a Delegate in the workshop


Dr. J. B. Prasad
Asst. Professor,
Department of Epidemiology & Biostatistics, KAHER, Belagavi


Dr. V. A. Kothiwale
Registrar,
KAHER, Belagavi

REG-275

67th DAE Solid State Physics Symposium

Organised by: Bhabha Atomic Research Centre, Mumbai

Sponsored by: Board of Research in Nuclear Sciences
(BRNS) Department of Atomic Energy, Government of
India

CERTIFICATE of Participation Karthik K Iyer

TIFR, Mumbai & KAHER, Belagavi

has presented a paper in the form of ORAL and POSTER and
participated in this symposium held at GITAM Deemed to be
University, Visakhapatnam, during 20- 24 December 2023

L. M. Pant
Convener
DAE SSPS 2023



Mohit Tyagi
Scientific secretary
DAE SSPS 2023



Jitendra Bahadur
Scientific secretary
DAE SSPS 2023



Dated: 24 Dec 2023